

MCLOEB 21(1-4) 1-552 (1999)

ISSN: 1058-7268

Volume 21, Numbers 1-4 (1999)

ISBN: 90-5699-262-7

MCLC S & T

SECTION B

Nonlinear Optics

Principles, Materials, Phenomena, and Devices

Editor: Takayoshi Kobayashi, University of Tokyo, Japan

Consultant Editors: M M Labes, A F Garito

East European and CIS Editor: Vladilen S Letokhov

North American Editor: Jerome D Swalen

West European Editor: François Kajzar

Proceedings of

**First International Workshop on
Optical Power Limiting**

CANNES (France)

28 June – 1 July, 1998

Guest Editor

François Kajzar

(CEN) de Saclay, France

Public Release
on Unlimited

19990903 176



GORDON AND BREACH SCIENCE PUBLISHERS

MCLC S & T—Section B:

NONLINEAR OPTICS

PRINCIPLES, MATERIALS, PHENOMENA, AND DEVICES

Editor

Takayoshi Kobayashi, Department of Physics, University of Tokyo, Hongo, Tokyo 113, Japan

Consultant Editors

M M Labes, Department of Chemistry, Temple University, Philadelphia, Pennsylvania 19122, USA

A F Garito, Department of Physics, University of Pennsylvania, Philadelphia, Pennsylvania 19104, USA

East European and CIS Editor: *Fladilen S Letokhov*, Institute of Spectroscopy, Troitzk, Russia

North American Editor: *Jerome D Swalen*, Department of Physics, University of California, Santa Cruz, CA, 94720, USA

West European Editor: *François Kajzar*, DEIN LPEM, CEN Saclay, Gif-sur-Yvette, 91191, France

Editorial Advisory Board

East Europe and CIS: *N I Koroteev*, Moscow State University, Moscow, Russia • *V V Ragul'skii*, Institute of Problems of Mechanics, Moscow, Russia • *V F Svirnov*, General Physics Institute, Moscow, Russia

North America: *Daniel S Chenla*, University of California, Berkeley, California, USA • *Stephen T Kowel*, University of Alabama, Huntsville, Alabama, USA • *RS Lytel*, AMP Corporation, Palo Alto, California, USA

• *Gerald R Meredith*, E I Dupont de Nemours and Co, Wilmington, Delaware, USA • *Nasser Peyghambarian*, University of Arizona, Tucson, Arizona, USA • *YR Shen*, University of California, Berkeley, California, USA

• *Kenneth Singer*, Case Western Reserve University, Cleveland, Ohio, USA • *Eric W Van Stryland*, CREOL, University of Florida, Orlando, Florida, USA • *David J Williams*, Eastman Kodak Company, Rochester, New York, USA

West Europe: *David Bloor*, Durham University, Durham, UK • *Jean-Luc Brédas*, Université den Mons, Mons, Belgium • *David Cotter*, British Telecom Research Laboratories, Ipswich, UK • *Christos Flytzanis*, Laboratoire d'Optique Quantique du CNRS, Palaiseau, France • *Peter Günter*, Institute of Quantum Electronics, Zürich, Switzerland • *Yves Lévy*, Institut d'Optique, Orsay, France • *Gerd Marowsky*, Laser Laboratorium Göttingen e. V., Göttingen, Germany • *Arnold Migus*, École Polytechnique ENSTA, Palaiseau, France • *Jean-Paul Pocholle*, Thomson CSF, Orsay, France • *Joseph Zyss*, CNET, Bagneux, France

Japan: *Tadashi Itoh*, Osaka University, Osaka • *Yuzo Ito*, Hitachi Ltd, Hitachi-shi • *Toshikuni Kaino*, NTT Optoelectronics Laboratory, Tokai • *Ken'ichi Kubodera*, NTT Science and Core Technology Laboratory Group, Atsugi • *Arai Nakamura*, Nagoya University, Nagoya • *Hachiro Nakanishi*, Tohoku University, Sendai • *Hiroyuki Nakatsuka*, University of Tsukuba, Tsukuba • *Hiroyuki Sasabe*, RIKEN, Wako • *Shinsuke Umegaki*, Keio University, Yokohama • *Masamichi Yamanishi*, Hiroshima University, Hiroshima

Aims and Scope

Nonlinear Optics publishes primary papers reporting original research, review articles, and rapid communications. The journal is divided into four main sections. 1. Principles—covering studies into the fundamental theoretical understanding of the origins and mechanisms of nonlinear optical processes, such as squeezing, phase conjugation, and optical bistability, and theoretical calculations of susceptibilities either by band theory or by quantum mechanical theory. 2. Materials—including work on the solid state physics of semiconductors and dielectrics, and organic and polymer compounds exhibiting nonlinear and electrooptical behaviour. 3. Phenomena—devoted to papers on: the discovery of new nonlinear optical phenomena; measurement of nonlinear optical processes; determination of nonlinear optical constants and figures of merit; observation of ultrafast and fast nonlinear optical processes; and the characterization of nonlinear optical materials by new measurement methods. 4. Device—featuring fundamental research articles on applications to devices, optical switches, optical bistable devices, phase conjugation, and optical logics. The journal recognizes the multidisciplinary nature of this field, and will include materials science and device implementation material, as well as the physicochemical aspects. The editors place great emphasis on the importance of the development of applications of nonlinear optical materials to practical devices.

Notes for contributors can be found at the back of the journal.

© 1999 OPA (Overseas Publishers Association) N.V. Published by license under the Gordon and Breach Science Publishers imprint. All rights reserved.

Except as permitted under national laws or under the Photocopy License described below, no part of this publication may be reproduced or transmitted in any form or by any means, electronic, mechanical, photocopying or otherwise, or stored in a retrieval system of any nature, without the advance written permission of the Publisher.

A CD-ROM ARCHIVE version (which may include visual data such as 3-D animations and video clips) is available for this journal at a nominal extra charge to subscribers.

World Wide Web Addresses

Additional information is also available through the Publisher's web home page site at <http://www.gbhap.com>. Full text on-line access and electronic author submissions may also be available.

Editorial enquiries by e-mail: <editlink@gbhap.com>.

Order Information

Four issues per volume. Subscriptions are renewed on an annual basis. 1999 Volume (s): 22–24

Orders may be placed with your usual supplier or at one of the addresses shown below. Journal subscriptions are sold on a per volume basis only; single issues of the current volume are not available separately. Claims for

(Continued on inside back cover)

REPORT DOCUMENTATION PAGE

Form Approved OMB No. 0704-0188

Public reporting burden for this collection of information is estimated to average 1 hour per response, including the time for reviewing instructions, searching existing data sources, gathering and maintaining the data needed, and completing and reviewing the collection of information. Send comments regarding this burden estimate or any other aspect of this collection of information, including suggestions for reducing this burden to Washington Headquarters Services, Directorate for Information Operations and Reports, 1215 Jefferson Davis Highway, Suite 1204, Arlington, VA 22202-4302, and to the Office of Management and Budget, Paperwork Reduction Project (0704-0188), Washington, DC 20503.

1. AGENCY USE ONLY (Leave blank)		2. REPORT DATE 1999		3. REPORT TYPE AND DATES COVERED Conference Proceedings	
4. TITLE AND SUBTITLE First International Workshop on Optical Power Limiting				5. FUNDING NUMBERS F617089	
6. AUTHOR(S) Conference Committee					
7. PERFORMING ORGANIZATION NAME(S) AND ADDRESS(ES) Dept. of Electronics & Nuclear Instrumentation Research Center in Saclay Gif-sur-Yvette Cedex 91191 France				8. PERFORMING ORGANIZATION REPORT NUMBER N/A	
9. SPONSORING/MONITORING AGENCY NAME(S) AND ADDRESS(ES) EOARD PSC 802 BOX 14 FPO 09499-0200				10. SPONSORING/MONITORING AGENCY REPORT NUMBER CSP 98-1047	
11. SUPPLEMENTARY NOTES					
12a. DISTRIBUTION/AVAILABILITY STATEMENT Approved for public release; distribution is unlimited.				12b. DISTRIBUTION CODE A	
13. ABSTRACT (Maximum 200 words) The Final Proceedings for First Int'l Workshop on Optical Power Limiting, 28 June 1998 - 1 July 1998 This is an interdisciplinary conference. Topics include modeling of beam propagation, liquid crystalline, organic, semiconductor, photochromic and nanostructured materials, nonlinear absorption, thermal lensing, characterization techniques, and systems.					
14. SUBJECT TERMS EOARD, Optical systems, Optical power limiting				15. NUMBER OF PAGES 551	
				16. PRICE CODE N/A	
17. SECURITY CLASSIFICATION OF REPORT UNCLASSIFIED	18. SECURITY CLASSIFICATION OF THIS PAGE UNCLASSIFIED	19. SECURITY CLASSIFICATION OF ABSTRACT UNCLASSIFIED	20. LIMITATION OF ABSTRACT UL		

NSN 7540-01-280-5500

Standard Form 298 (Rev. 2-89)
Prescribed by ANSI Std. Z39-18
298-102

F61775-98-WE090

PROCEEDINGS OF

CSP98-1047

**First International Workshop on
Optical Power Limiting**

CANNES (France)

28 June-1 July, 1998

Organizing Committee

Chairman

François Kajzar
LETI-Commissariat à l'Energie Atomique
(Technologies Avancées), CE Saclay, France

Co-Chairmen

Christophe Jurczak
Délégation Générale pour l' Armement, Paris

Donald McGillen
US European Office for Aerospace Research
and Development (London)

Paras N. Prasad
State University of New York at Buffalo (USA)

Secretary

Fabrice Charra
Commissariat à l'Energie Atomique (DSM),
CE Saclay, France

Treasurer

Pierre Alain Chollet
LETI-Commissariat à l'Energie Atomique
(Technologies Avancées), CE Saclay, France

DTIC QUALITY INSPECTED 4

AQF99-12-2194

Scientific Program Committee

Jean-Claude Dubois, Thomson CSF, LCR, France
Richard C. Hollins, Defence Research Agency, England
Charles Y.-C. Lee, Air Force Office for Scientific Research, USA
Keith Lewis, Defence Research Agency, England
François Micheron, Thomson CSF Optronique, France
Jean- Michel Nunzi, LETI – CEA (Technologies Avancées),
CE Saclay, France
Joseph W. Perry, Jet Propulsion Laboratory, USA
Bruce A. Reinhardt, Wright Patterson Labs, USA
James S. Shirk, Office of Naval Research Labs, USA
Eric W. Van Stryland, CREOL, University of Orlando, USA

Organized by

Commissariat à l'Energie Atomique- LETI (France)
Délégation Générale pour l' Armement (France)
State University of New York at Buffalo (USA)
US European Office for Aerospace Research and Development
(London)

CONTENTS

Volume 21(1-4)

Foreword	vii
D. H. SLINEY: Retinal Injury from Laser Radiation	1
J. A. ZUClich, D. J. LUND, P. R. EDSALL, R. C. HOLLINS, P. A. SMITH, B. E. STUCK and L. N. McLIN: Experimental Study of the Variation of Laser-induced Retinal Damage Threshold with Retinal Image Size	19
E. W. VAN STRYLAND, M. J. SOILEAU, S. ROSS and D. J. HAGAN: Passive Optical Limiting: Where are we?	29
P. N. PRASAD, G. S. HE, M. P. JOSHI, J. SWIATKIEWICZ, G. MANCHALA, M. LAL, A. BISWAS and K.-S. KIM: Nanostructured Materials and Composites for Optical Power Limiting	39
R. C. HOLLINS: Optical Limiters: Spatial, Temporal and Spectral Effects	49
J. BONESS, R. HILDEBRANDT and G. MAROWSKY: High-intensity Laser-matter Interactions	63
V. GROlier-MAZZA: The Specification of Laser Protection	73
I. C. KHOO, M. V. WOOD, P. H. CHEN and M. Y. SHIH: Nonlinear Optical Liquid Cored Fiber Array and Liquid Crystalline Film for Optical Limiting of Frequency Agile Picosecond Pulsed-CW Laser	85
S. BARTKIEWICZ, A. MINIEWICZ, F. KAJZAR and M. ZAGÓRSKA: All-optical Switching of Light in Hybrid Liquid Crystal Structures	99
R. A. LESSARD, C. LAFOND, I. PETKOV and V. BARACHEVSKY: Use of Photochromic Molecules as Optical Power Limiters	115
J. LIVAGE and C. SANCHEZ: Optical Properties of Sol-gel Films	125
R. SIGNORINI, S. SARTORI, M. MENEGHETTI, R. BOZIO, M. MAGGINI, G. SCORRANO, M. PRATO, G. BRUSATIN and M. GUGLIELMI: Hybrid Sol-gel Glasses Containing Fullerene Derivatives for Bottleneck Optical Limiting with Multilayer Structures	143

B. DUPUIS, I. JOUANIN, C. BIED-CHARRETON, J. DELAIRE, P. ROBIN, P. FENEYROU and V. DENTAN: Reverse Saturable Absorption using Photoinduced Intramolecular Electron Transfer in Porphyrin-Viologen Dyads and Porphyrin-Tetraviologen Array.	163
J. P. SEGAUD, B. DILLEMANN and O. GIRAUDO: Modeling of Pulsed Laser Irradiation of VO ₂ Thin Films	175
B. HÖNERLAGE, J. SCHELL and R. LEVY: Optical Limiting in C ₆₀ Doped Solid Sol-gel Glasses	189
B. CAMPAGNE, A. COURJAUD, A. BRUN, F. CHAPUT and J.-P. BOILLOT: Thermally Induced Lens in Nigrosin Doped Xerogels	201
J. P. SEGAUD, O. GIRAUDO, C. INDRIGO, E. CAVANNA and J. LIVAGE: VO ₂ and Au-VO ₂ Thin Films Prepared by Sputtering and Sol-gel for Infrared Optical Power Limiting	211
J. W. PERRY, S. BARLOW, J. E. EHRLICH, A. A. HEIKAL, Z.-Y. HU, I.-Y. S. LEE, K. MANSOUR, S. R. MARDER, H. RÖCKEL, M. RUMI, S. THAYUMANAVAN and X. L. WU: Two-photon and Higher-order Absorptions and Optical Limiting Properties of Bis-Donor Substituted Conjugated Organic Chromophores	225
L. R. DALTON, R. J. LARSEN and F. STROHKENDL: Measurement of Two-photon Absorption Coefficients Employing Femtosecond, Phase-mismatched DFWM and nDFWM Spectroscopy	245
M. K. CASSTEVENS, D. KUMAR, S. GHOSAL, R. BURZYNSKI, C. SPANGLER and EL HADJ ELANDALOUSSI: The Optical Behavior of New TPA Dyes in Nanoporous Glasses	263
P. FENEYROU, D. BLOCK, M. PIERRE, A. IBANEZ and P. L. BALDECK: Nonlinear Transmission of Optically Thick Two-photon Absorptive Materials	279
S. DELYSSE, F. KAJZAR, J.-M. NUNZI, M. TRZANDEL and M. ZAGORSKA: Two Photon Absorption in Regio-regular Poly(3-alkylthiophenes)	287
P.-A. CHOLLET, V. DUMARCHER, J.-M. NUNZI, P. FENEYROU and P. BALDECK: Dispersion of Optical Power Limiting in Stilbene 3 Solutions	299

CONTENTS

v

C. NGUEFACK, T. ZABULON, R. ANÉMIAN, C. ANDRAUD, A. COLLET, S. TOPÇU and P. L. BALDECK: Engineering of Transparent Diphenylpolyene Derivatives for Optical Power Limiting at Visible Wavelengths	309
A. ADINOLFI, M. C. NETTI, M. LEPORE, R. TOMMASI and I. M. CATALANO: Measurements of Multiphoton Absorption Coefficients in $\text{ZnSe/ZnS}_x\text{Se}_{1-x}$ Strained-layer Superlattices	317
A. ADINOLFI, T. CASSANO, R. TOMMASI and M. FERRARA: Z-scan Measurements of Optical Nonlinearities in Bulk LiNbO_3	327
A. AGARWAL, K. KAMADA, Y. SHIMIZU and K. OHTA: Coherent Dip in Optical Kerr Measurement Arising from Grating Formation in Weakly Absorptive Media	335
S. A. ASHER, G. PAN and R. KESAVAMOORTHY: Crystalline Colloidal Array Optical Switches and Limiters	343
K. M. NASHOLD, D. P. WALTER, J. M. VOSS, G. S. FRYSSINGER and R. L. SHARPLESS: Comparing the Scattering Process in Particle Suspensions in Liquids and Gases for Use as Optical Limiters	353
D. B. JAMES AND K. J. McEWAN: Bubble and Refractive Processes in Carbon Suspensions	377
D. RIEHL and F. FOUGEANET: Thermodynamic Modeling of Optical Limiting Mechanisms in Carbon-black Suspensions (CBS)	391
M. J. POTASEK: Spatiotemporal Effects in Nonlinear Dispersive and Diffractive Media using Ultrashort Optical Pulses	399
D. VINCENT: High-performance Optical Limiter Based on Fine Carbon Particles Suspended in an Organic Solvent	413
V. JOUDRIER, P. BOURDON, F. HACHE and C. FLYTZANIS: Nonlinear Light Scattering in a Two-component Medium: Optical Limiting Application	423
F. FOUGEANET and D. RIEHL: Investigation of Optical Limiting Mechanisms in Carbon-black Suspensions	435

J.-P. FAURE and O. GIRAUDO: Modelling of Parametric Beam Conversion: Application to Image Amplification with Optical Self-limiting	447
D. BELJONNE, T. KOGEJ, S. R. MARDER, J. W. PERRY and J. L. BRÉDAS: Theoretical Design of Organic Chromophores with Large Two-photon Absorption Cross-sections	461
S. P. KARNA: Microscopic Theory and Modeling of Organic Optical Power Limiting Materials	481
S. P. McGEOCH, I. THOMSON, A. CHRISTIE, R. C. HOLLINS and J. MILWARD: Design Considerations for using Optical Limiters in Sighting Systems	491
P. ASCHIERI, P. BALDI, L. CHANVILLARD, M. P. DE MICHELI, D. B. OSTROWSKY, G. BELLANCA and P. BASSI: Optical Power Limiting using Nonlinear Periodic Segmented Waveguides	503
A. J. IKUSHIMA and T. FUJIWARA: Large-second-order Optical Nonlinearity in Ge-doped Silica Glass	515
D. WOLFERSBERGER, N. FRESSENGEAS, J. MAUFOY and G. KUGEL: Experimental Evidence of Laser Beam Self-focussing in Photorefractive Media from the Nanosecond Time-scale to Steady-state	525
J. SANETRA, J. NIZIOŁ, P. ARMATYS, R. CHRZASZCZ, S. NIZIOŁ, I. KITYK and A. MEFLEH: Electrooptical Properties of Polyvinylhalogencarbazole's	535
B. SAHRAOUI, X. NGUYEN PHU, I. V. KITYK, P. HUDHOMME and A. GORGUES: Photoinduced Transparency and Two-photon Absorption in Some Modified Fullerenes	543

FOREWORD

The First International Workshop on Optical Power Limiting was held 28 June – 1st July, 1998, in Cannes, the famous French Mediterranean resort. The meeting was attended by about 80 participants from France, USA, Germany, Canada, Japan and Poland. It consisted of invited plenary lectures, given by leading specialists in this field and contributed papers addressing more specific topics. A poster session was also organized. A large amount of time was devoted to discussions.

The problem of optical power limiting has been a subject of increasing interest for more than a decade now. The interest is motivated by the increasing presence of the laser sources in our life and hazards connected with their utilisation. Light-absorbing protections have been less and less safe for three main reasons:

- (i) limited operation wavelength
- (ii) saturation absorption effects (bleaching)
- (iii) colored vision

The first point comes to be more and more important because of increasing use of tunable laser sources (OPO's, dye lasers, Raman lasers, etc.) not only in the laboratory, but also in large areas of industry, medicine and for military applications.

The dyes used in absorbing protections bleach at high fluences and become transparent, offering no more protection. Moreover, their use increases the probability of injury as the holders of such a kind of protection believe they are protected, while they are not at high input intensities. Also the use of dyes implies a coloration of vision which is not always acceptable. Therefore, large band and efficient protection against laser light aggression is not only interesting for military applications, but is also important in industry, medicine and in research laboratories.

Several types of protection are actually under study at present. Their common point is the dependence of light transmission on incident fluence. The proposed solutions are:

- Nonlinear absorption
- Reverse saturable absorption
- Nonlinear scattering
- Thermal lensing

These different approaches to the problem of optical power limiting are discussed in the papers of these proceedings, together with laser injury, system application and theoretical calculations of either optical beam propagation in nonlinear media or of quantum mechanical calculations of nonlinear absorption.

The next meeting on optical power limiting is planned to be organized in the US in 2000.

For the organizing committee

François Kajzar
(chair)

Saclay, August 1998

ACKNOWLEDGEMENTS

The organizers of this meeting wish to thank the following sponsors:

Commissariat à l'Energie Atomique - LETI,
Technologies Avancées (France)
Délégation Générale pour l'Armement (France)
The United States Air Force European Office of
Aerospace Research and Development (UK)
The United States Army Research,
Development and Standardization Group (UK)
The United States Office for Naval Research Europe,
for their contribution to the success of the conference.

RETINAL INJURY FROM LASER RADIATION

DAVID H. SLINEY

US Army Center for Health Promotion and Preventive Medicine, Laser/Optical
Radiation Program, Aberdeen Proving Ground, MD 21010-5422 USA

Abstract During the past 35 years, a wide body of biomedical research has been conducted to understand the biophysical factors which influence laser induced retinal injury. Although, the optical effects which influence the retinal imaging and the initial physical events which lead to the absorption and dissipation of the laser energy are well understood, the stages of biological damage which take place after the deposition of energy and for hours or even days later are not so well understood. Occupational health and safety standards which provide maximum permissible exposure (MPE) limits are based both upon the theoretical understanding and a large body of experimental data and human accident experience. Current laser safety research has recently focussed almost exclusively on deriving retinal injury thresholds for sub-nanosecond exposures. Setting limits in this temporal region has been difficult, since there have been conflicting data sets and there are limited data to extrapolate to other spectral regions.

INTRODUCTION

The very high radiance ("brightness") of a laser (MW and $\text{TW} \times \text{cm}^{-2} \times \text{sr}^{-1}$) is responsible for the laser's great value in material processing and laser surgery, but it also accounts for its significant hazard to the eye (Figure 1). When compared to a xenon arc or the sun, even a small He-Ne alignment laser is typically ten times brighter (Figure 2). A collimated beam entering the relaxed human eye will experience an increased irradiance of about 10^5 , i.e., $1 \text{ W} \times \text{cm}^{-2}$ at the cornea become $100 \text{ kW} \times \text{cm}^{-2}$ at the retina.¹⁻³ Of course the retinal image size is only about 10-20 mm, considerably smaller than the diameter of a human hair. So you may wonder: so what if I have a such a small lesion in my retina? You do have millions of cone cells in your retina. The retinal injury is always larger because of heat flow and acoustic transients following the initial absorption of energy, and even a small disturbance of the retina can be significant. This is particularly important in the region of central vision referred to by eye specialists as the *macula lutea* (yellow spot), or simply the "macula." The central region of the macula, the *fovea centralis*, is responsible for

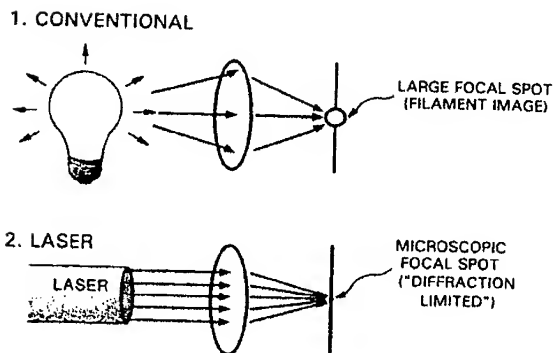


FIGURE 1. Unlike a conventional light source, the high radiance of a laser permits a laser beam to be focused to a much smaller spot leading to material processing applications but also to an increased retinal hazard.

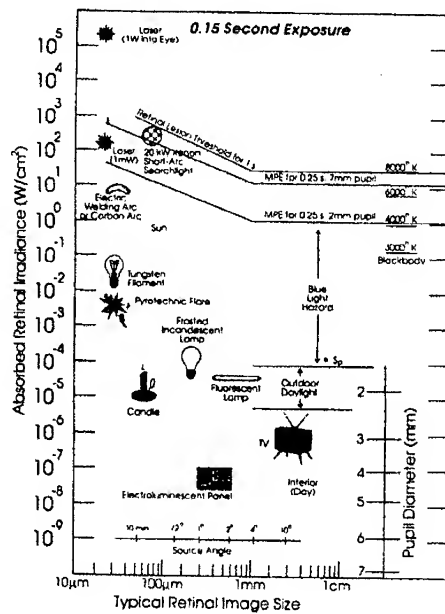


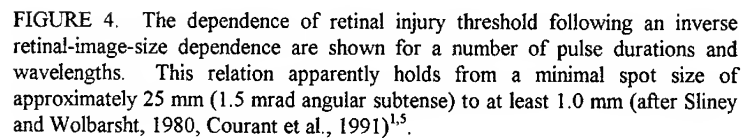
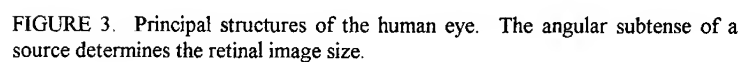
FIGURE 2. Examples of retinal irradiances from conventional light sources are compared to the irradiance produced by intrabeam viewing of a laser.¹ Note the spot-size dependence of retinal thermal injury.

detailed "20/20" or "6/6" vision (Fig 3). Damage to this extremely small (about 150 μ m diameter) central region can result in severe vision loss even though 99% of the total retinal area remains unscathed. The peripheral retina surrounding the macula is useful for movement detection and other tasks but possesses little acuity [After all, this is why your eye moves across a line of print, because your detailed vision is very small angular subtense]. Outside the 400-1400 nm retinal hazard region the cornea--and even the lens--can be damaged by laser beam exposure.¹

Under certain conditions, such as viewing by diffuse reflection, larger areas of the retina may be exposed to laser radiation.¹⁻³ In this regard, the threshold energy for thermal injury increases with increasing image size. However, if the retinal image size doubles, with a resulting four-fold increase in retinal area the increased energy necessary to reach a damage threshold does not increase by four, but only by a factor of approximately two. This result is due to reduced efficiency of the retina to dissipate energy by radial heat flow for larger images.^{1,2,3,4} This inverse relationship of thermal injury threshold with increasing spot size is valid from approximately 25 mm to nearly 1.3 - 1.7 mm (Fig 4). In any attempt to employ nonlinear optical (NLO) phenomena to limit retinal exposure from a pulsed laser, it is important to consider the way that laser energy may be distributed over the retina and how this and temporal distributions of that energy affect the risk of retinal injury. These factors and the current laser safety MPEs and their basis will be therefore be presented.

RETINAL INJURY MECHANISMS

There are a number of biophysical and physiological factors which influence the size, nature and degree of retinal photocoagulation. Since the primary interaction mechanism for laser pulses of durations ranging from microseconds to many seconds is thermal, and from nanoseconds to microseconds appears to be thermal and thermo-acoustic, it is worthwhile to consider how the nature of retinal injury scales with wavelength, energy distribution and spot-size on the retina. Our understanding of the nature of thermal damage of subcellular structures and thermal denaturation of proteins is partially lacking for pulse durations less than about 100 ms. It is well accepted that heat conduction plays



a key role in the redistribution of energy not only during the laser exposure, but also *following the exposure*, and the duration that each cell is located in either the irradiated area or adjacent area of elevated temperature is critical (Barnes, 1974; Priebe and Welch, 1978; Ham, 1987; Sliney and Wolbarsht, 1980; Sliney, 1982).^{1,3-10} This is referred to as the "time-temperature history," and the thermochemical denaturation of proteins depends not only upon the peak temperature, but the entire duration (of many milliseconds or seconds) that the temperature remains elevated.^{7,10-25} Therefore, the geometry of the tissue exposure will influence the resulting lesion. It was most unexpected some years ago to discover that the spot-size dependence existed for sub-microsecond exposures, since it had been thought that since both thermal and thermal-acoustic energy deposition and temperature buildup in tissue occurs during the pulse and there would be no time for heat dissipation and damage during the pulse.^{1,5,22-26} The spot-size dependence did not appear in flat (*in vitro*) preparations of retinal pigment epithelium exposed to laser radiation under a laboratory microscope.²⁶ Of course, the actual spot-size dependence clearly shows that most of the cellular damage occurs after the exposure and not during the impulse.

Probably the most extensive series of fundamental studies relate to retinal photocoagulation, where lesion size and the scaling of photocoagulation threshold has been shown to vary in much the same way regardless of the pulsed exposure duration (Fig 4).^{1,5,22-28} Whether laser energy was delivered in nanoseconds or seconds, the spot size dependence of retinal (apparently thermochemical) damage scaled as $1/(\text{spot size})$ for spot sizes up to 1-2 mm. For spot sizes greater than about 1.7 mm (corresponding to a light-source angular subtense of 0.1 radian), only retinal radiant exposure (J/cm^2) or irradiance (W/cm^2) is necessary to describe the threshold. This can only be explained by the impact of heat flow. Figure 4 shows the spot-size dependence of experimental retinal injury thresholds.^{1,5,22} The accumulated data suggest that *at threshold*, simple coagulation of proteins is the dominant effect resulting in cell death and visible damage, although photodisruption of tissue by acoustic mechanisms dominates the injury effect at suprathreshold levels an order of magnitude higher in irradiance.

BASIC STUDIES OF THERMAL INJURY

The only retinal lesions which have been shown to be sharply defined and dependent only upon the light distribution on the retina result from either ultrashort, sub-nanosecond non-linear damage mechanism, or photochemical damage mechanisms which dominate for minutes of blue-light exposure.²³ These non-thermal mechanisms will not be discussed here. It is also known from theoretical models that factors such as: blood-flow, a competition between photochemical and thermal effects, and even eye movements affect the zone of retinal damage when exposures last for seconds, and these effects also will not be considered here (ICNIRP, 1999).²⁹ Our greatest understanding relates to clinical laser retinal photocoagulation to treat retinal disease, but this medical procedure is normally performed with ion or diode CW lasers with exposure durations of the order of 0.1 - 0.5 s. Ophthalmologists have traditionally avoided exposures shorter than about 10 ms (except for high repetition rate, quasi-CW conditions) to prevent retinal hemorrhages (Sliney and Marshall, 1992).⁹

Thermal injury of biological tissue has been studied for many decades with important studies dating at least from those of Henriques (1947), who studied skin injury by observational, histological and theoretical methods.⁷ His group clearly showed that thermal injury is strongly dependent upon heat conduction from the irradiated tissue. In more recent decades many of the careful scientific studies of localized thermal injury and thermochemical rate processes for proteins have resulted from studies of laser photocoagulation, where the thermal energy can be carefully applied by a well defined radiant exposure. Hu and Barnes (1970) studied the critical temperatures as a function of time (i.e., the thermochemical rate process) for protein denaturation and enzyme inactivation by irradiating different proteins and enzymes with a CO-2 laser, adding to the earlier, basic studies on proteins and enzymes by Wood (1956).^{6,10}

During the past decade, there have been many further basic studies of «heat-shock» proteins and the inactivation or denaturation of different types of biological macromolecules by elevated temperatures (Lepock, 1997).¹¹ However, most of this research was conducted with moderate temperature elevations to 39-46° C and heating durations of minutes and hours. Nevertheless, these studies refine and clarify our understanding of the complex thermal mechanisms of damage to large biomolecules, and

most are based upon the studying of cell killing (Craig 1985; Dewey, 1989; Hahn and W, 1990; Jung, 1986; Kushner, 1977; Zale, 1986).¹⁰⁻²⁰ The multitude of thermal damage mechanisms at elevated temperature leads us to hypothesize that different mechanisms dominate for sub-millisecond heating durations. Whereas the damage for exposure durations of seconds or more might result from protein conformational changes, other mechanisms such as «order-disorder transitions» in complex proteins like RNA, membrane damage or damage of organelles probably dominate in the sub-millisecond domain. To explain the spot-size dependence of sub-millisecond pulses, it would be reasonable to hypothesize a two-state damage process, where the pulsed thermal insult predisposes the tissue to the slower process of protein deformation.

MATHEMATICAL MODELS

The mathematical models of retinal thermal injury have been quite successful in predicting thresholds for ophthalmoscopically visible retinal lesions for single-exposure conditions for a large variety of retinal image sizes for exposure durations varying between less than a millisecond to many seconds. The Arrhenius function for thermal denaturation of proteins shows the importance of time-temperature history (Allen and Polhamus, 1977; Mainster et al., 1970).^{4-7,24-25} Much of the injury occurring from pulsed exposures actually occurs during the cool-off time when local tissue remains elevated; hence, the retinal image-sized dependence of injury.^{1,9,28} However, to date, these mathematical models with currently used rate-process coefficients have not been successful in predicting the N-0.25 thermal additivity rule for small image sizes (Sloney and Marshall, 1992),⁹ nor the lowering of thresholds below about 0.1 ms.^{21,25}

From a phenomenological standpoint it is clear that most thermal denaturation of proteins must take place after about 10-100 ms, and the exact time of delivery for shorter pulses does not play an important role *at threshold*, judging from the retinal threshold data shown in Figure 5. From about 1 ns to 20 ms the thresholds follow a nearly constant radiant exposure. The retinal spot-size dependence shown in Figure 4 of short pulse durations, can therefore be explained in this way. For a minimal spot size (e.g., 25 mm or less), a spherical heat wave is produced since unexposed tissue exists in all directions

around the absorbing site to dissipate the thermal energy. For intermediate size images of 25 - 1,000 μm , radial heat flow plays less and less a role, and for very large images, radial heat flow plays only a small role, and blood-flow plays a role in dissipating the more substantial total energy which now moves in two directions along the z-axis. At the larger spot sizes of 1.7 mm or greater, laser safety standards assume a constant retinal irradiance (i.e., source radiance in $\text{W}\times\text{cm}^{-2}\times\text{sr}^{-1}$) specifies the threshold.²⁹ Thermal models have been used to determine the approach in dealing with different types of retinal images as now recommended in safety standards.²⁹⁻³⁰

Much has been written about thermoacoustic damage from short-pulse lasers. In this regard, interest centers upon the very high temperatures reached in the melanin granules in the RPE. Hayes and Wolbarsht (1968) first introduced the idea that damage to subcellular organelles as well as individual protein and enzyme systems surrounding the 1-2 μm melanin pigment granules might be responsible for the unexpectedly low thermal damage thresholds found experimentally in the nanosecond time regime with Q-switched lasers.²⁷ This is still the best explanation of all known phenomena, although one could also postulate two thermal denaturation time constants—one for conventional injury dominating for seconds of exposure and one dominating at sub-microsecond exposures. However, this latter hypothesis of retinal would not appear to predict a spot-size dependence. Likewise, a spot-size dependence would not be predicted by a more recently published model of retinal injuries proposed by Gerstman et al. (1996), who argue that the lower injury thresholds resulted from microbubble formation around the melanin granules.³¹ This latter hypothesis appeared to be bolstered by experimental studies reported by Lin and Kelly (1998) in which *in vitro* cell cultures of cells interlaced with carbon microparticles or RPE cells themselves were irradiated by focal Q-switched laser pulses.³² The experimentally determined thresholds for bubble formation and substantial acoustic transients they measured using a pump-probe technique corresponded to retinal injury thresholds for small 20-40 μm diameter images in the RPE cells; however, this mechanism did not explain the far lower thresholds found for much larger retinal images.^{5,21-22} While these mechanisms do explain photodisruption at higher levels which produce the formation of a retinal hole by microexplosion, they fail to explain the dependence at threshold. It is interesting that earlier *in vitro* studies of RPE cell cultures

reported by King and Geeraets (1968) also showed no spot-size dependence in their preparation. Perhaps, the heat-flow conditions were different than in live eyes (*in vivo*).

Retinal injury thresholds for repetitively pulsed exposures give further support for a thermal damage mechanism at threshold for pulsed laser injury. For all pulse durations longer than the cool-off time, the injury threshold for a train of pulses is lowered by a factor that corresponds to the "total on-time" of the train of pulses. In other words, for a train of 50 100-ms pulses, the thermal injury threshold for the group of pulses is equivalent to a total-on-time-pulse (TOTP) of $(50)(0.1 \text{ ms}) = 5 \text{ ms}$. Since the allowed energy threshold increases as a $t^{0.75}$ function of exposure duration, this results in lowering the effective threshold for a single pulse in the train expressed as a correction factor known as $N^{0.25}$. Therefore, the single-pulse threshold would be lowered by one order of magnitude for 10,000 pulses, and this has been experimentally verified.^{23,33-36} This rule applies to any pulse, and the $N^{0.25}$ rule is more general than the TOTP rule, since it applies to pulse durations less than 50 microseconds as well as longer pulse durations. Corneal damage thresholds from 10.6 mm thermal injury also follows the TOTP rule.³⁶ This lends further support to the thermal injury mechanism and tells us that some subcellular injury occurs with each pulse, and that buildup of the number of damaged molecules eventually leads to cell death and the macroscopic, visible lesion in the retina.^{9,23,28} All of this data points to the need for revised rate-constants for thermal injury, or to a more likely two-step damage mechanism. It would appear that the acoustic transient predisposes the cell to thermal injury. For example, the acoustic transient is known to damage membranes, and this could lead to a lowering of the thermal damage threshold, such that the thermal energy remaining after the short pulse damages the cell--or interferes with rapid repair. This would explain the same spot-size dependence of thermal injuries from the sub-nanosecond regime³⁷⁻³⁹ to exposures of 1 second or more.

We are left with a phenomenological model that suggests that thermal coagulation of proteins and subcellular organelles dominates from nanosecond exposure durations to many seconds and minutes--at least for laser wavelengths between 500 and 1300 nm. The mathematical models could be corrected with a short-pulse term that represents the lowering of damage threshold due to melanin granule super-heating, and this would be a simple matter of fitting the large number of experimental threshold data. It may even be

possible that the form of the Arrhenius integral needs to be re-evaluated in light of all of the experimental results of pulsed thermal injury. It has even been postulated that the apparent "hump" in the sub-microsecond data (Figure 5) may have resulted from the thermoacoustic mechanism serving to more effectively dissipate energy in the 100 ns time domain, thus raising the thermal injury threshold.²⁵ Another interesting effect that is not at all surprising is the near elimination of the inflection in the threshold curve of Figure 5 when threshold data for the 800-nm spectral region is plotted as a function of pulse duration (Lund, 1998).⁴⁰ This result appears to be explained by the fact that a far greater absorbing volume begins to occur in the near-infrared spectral region and more energy is absorbed beneath the RPE in the melanin granules in the choroidal layers.

Still more baffling are the data from Lund and associates, which show strong fluctuations of the retinal injury threshold with wavelength—an effect much more pronounced for q-switched pulse duration than exposures of the order of 0.1-1 second.⁴⁰ This effect remains the most puzzling of all experimentally observed phenomena, but it might be explained by very thermally labile enzymes which may have special wavelength absorption bands in this spectral region (Biscar, 1976).⁴¹

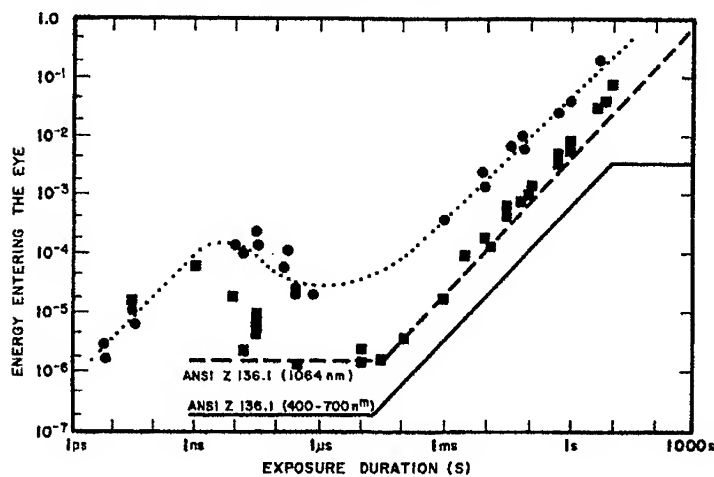


FIGURE 5. Dependence of retinal injury threshold for an ophthalmoscopically visible minimal retinal lesion ("point-source" viewing condition) with exposure duration. The current exposure limits for visible and Nd:YAG laser wavelengths are also shown.

LASER ACCIDENTS

Much of our understanding of laser retinal injuries in humans comes from careful studies of laser accidental injuries. Those accidental injuries which are reported are almost always at energies far above injury threshold, and generally result from q-switched laser exposures which result in a thermoacoustic microexplosion in the retina leading to a temporary retinal hole--frequently allowing blood to pass from the choroid into the space between the nerve layers of the retina and the jelly-like central substance of the eye--the vitreous. Although only a "drop" of blood may be involved, if pressed in this space between the vitreous and retina, it can cover the fovea and much of the retina, thus obscuring the victim's central vision. Depending upon the exact focal position in the retinal zone, the detailed nature of the retinal injury will vary and the potential for recovery will differ. For example, if the micro-explosion created at the focal zone of the laser energy occurs just behind the nerve layers at the retinal pigment epithelium (RPE), then a tiny separation of the retina--a retinal detachment--may result. Since the RPE has the highest concentration of optical absorption (the melanin granules), threshold injury always is localized in and adjacent to the RPE. However, if optical breakdown occurs in the vitreous or neural retina, prior to this absorption site, then the microexplosion would be expected to puncture a hole in the retina (Sloney, 1996).⁴²⁻⁴³

Most typically the accident scenario is in a governmental or university research laboratory.⁴³⁻⁴⁴ For example, a postdoctoral fellow in a physical chemistry laboratory is aligning a Nd:YAG pumped OPO laser beam to direct it into a gas cell to study photodissociation parameters for a particular molecule. Leaning over a beam director, he glances down over an upward, secondary beam and approximately 80 mJ enters his left eye. The impact produces a microscopic hole in his retina and a small hemorrhage is produced over his central vision. The victim sees only red in his or her left eye. Within an hour he is rushed to an eye clinic where an ophthalmologist tells him he has only 20/400 (6/120) vision.⁴³ The good news was that in this incident, the blood resolved within days and the small retinal hole closed up, with vision returning within weeks to 10/20 (6/6). Not so lucky have been those accident victims where retinal scars developed. It appears that the healing process determines the visual outcome.

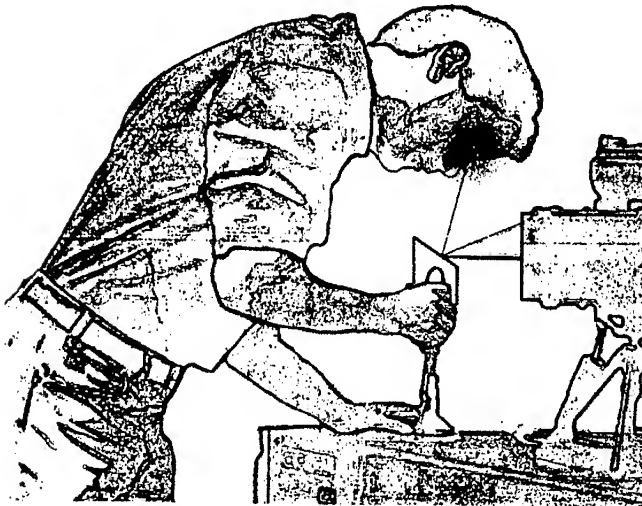


FIGURE 6. Typical scenario for an accidental laser induced retinal injury.

EXPOSURE LIMITS FOR THE HUMAN EYE

Exposure limits for laser radiation are used by a number of different groups.^{1, 29, 33, 46-47} The primary user is the occupational health specialist, such as the health physicist or industrial hygienist who must determine in a given situation whether human exposure is safe for incidental or continuous exposure. The exposure limits (ELs), whether they are called Threshold Limit Values (TLVs) or Maximum Permissible Exposures (MPEs), are developed by health-based groups such as the American Conference of Government Industrial Hygienists (ACGIH),⁴⁶ the American National Standards Institute,⁴⁷ and the International Commission on Non-ionizing Radiation (ICNIRP),²⁹ working with the World Health Organization (WHO) and similar groups. For pulsed durations between 1 ns and 10 s, these limits for small retinal images have remained the same for a quarter century.

The development of exposure limits in the sub-nanosecond time domain has been very difficult because of the presence of different interaction mechanisms of laser radiation

with biological tissues. The non-linear damage mechanisms do not scale in the same way with wavelength, with pulse duration, and with retinal image size as do thermal and thermal acoustic damage mechanisms. For this reason, it has been necessary to perform a number of studies of damage mechanisms (Cain, et al, 1996).³⁸⁻³⁹ Likewise the range of effects that occur at sub-visible threshold levels had to be studied by histological techniques and the consequences of exceeding the threshold, i.e., supra-threshold effects, had to be understood prior to setting exposure limits. Fortunately, a consensus has evolved on the understanding of sub-nanosecond damage factors. Figure 7 shows the evolution of damage levels in the sub-nano-second regime and some currently proposed initial MPE values upon which to base discussions. The ICNIRP and the research biophysicists from the ANSI Z136.1 Bioeffects Committee, have only tentatively reached agreement on these proposed MPEs.

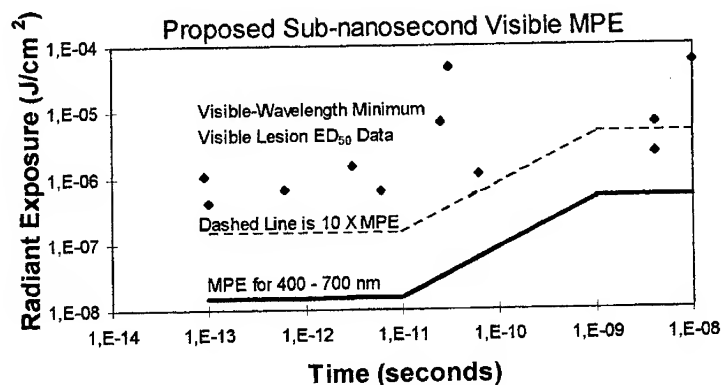


FIGURE 7. Proposed MPEs for sub-nanosecond laser exposures.

CONCLUSIONS

It is well to remember, that unlike laser damage of materials such as metals, glasses and polymers (which frequently have only one, or at most only a few types of molecules), laser damage is far more complex when the target is biological tissue.²¹ A wide variety of biological molecules perform varying functions in cells. The presence of living

Table 1. Retinal Hazard Laser Ocular Exposure Limits

Wavelength l (nm)	Expos. Duration t t (s)	Exposure Limit (EL) (J/cm ² or W/cm ²)	Restric- tions
400 to 700	1 ns to 18 ms	0.5 mJ/cm ²	
400 to 700	18 ms to 10 s	$1.8t^{3/4}$ mJ/cm ²	7-mm
700 to 1050	1 ns to 18 ms	0.5 C _A mJ/cm ²	aperture
700 to 1050	18 ms to 1 ks	$1.8 C_A t^{3/4}$ mJ/cm ²	
1051 to 1400	1 ns to 50 ms	5 C _C mJ/cm ²	
1051 to 1400	50 ms to 10 s	$9.0 C_C t^{3/4}$ mJ/cm ²	

NOTES:

Time: All values of t in s.

Spectral Correction Factors

$C_A = 1$ for $l = 400$ to 700 nm; $C_A = 10^{[0.02(l-700)]}$ if $l = 700 - 1050$ nm

$C_C = 1$ for $l \leq 1150$; $C_C = 10^{0.0181(l-1150)}$ for $1150 < l < 1200$;

$C_C = 8$ for $1200 \leq l < 1400$

Extended Source TLVs For extended-source laser radiation (e.g., diffuse reflection) viewing at wavelengths between 400 nm and 1400 nm, the intrabeam viewing TLVs can be increased by the following correction factor C_E provided that the angular subtense of the source (measured at the viewer's eye) is greater than a_{min} , where a_{min} is:

$$a_{min} = 1.5 \text{ mrad for } t < 0.7 \text{ s,}$$

$$a_{min} = 2 t^{3/4} \text{ mrad for } 0.7 \text{ s} \leq t < 10 \text{ s}^*$$

*a is likely to change to 1.5 mrad for all $t < 10$ s in 1999.

$$C_E = a/a_{min} \text{ for } a_{min} < a < 100 \text{ mrad.}$$

The angle of 100 mrad may also be referred to as a_{max} at which point the extended source limits can be expressed as a constant radiance using the value at a_{max} . Alternatively, one need not measure or determine any energy spread out over more than 0.1 radian, since it does not contribute to the hazard if it is not of a higher radiance than the central cone of 0.1 radian half-angle.

Terminology The term Exposure Limit (EL) is used by ICNIRP. The same values are termed MPEs (Maximum Permissible Exposure Limits) by ANSI and termed TLVs (Threshold Limit Values) by ACGIH. Essentially all groups have the same limit values.

microstructures such as cells with membranes and subcellular organelles clearly complicate the picture. While the delivery and transfer of thermal and acoustic energy can be modelled with some degree of accuracy, it is absurd to think that we can readily compute biological damage thresholds. Indeed the biological threshold data determined at 5 minutes post-exposure is almost always a factor higher than the threshold determined at 24 hours post-exposure—a result of "biological amplification" of the thermal insult described by Hayes and Wolbarsht in 1968.²⁷ Hopefully, with the advent of frequency agile eye protection, the risk of retinal injury from short-pulsed lasers will be reduced, and the fixed-wavelength eye protection of today⁴⁸⁻⁵⁰ will be replaced by broad-wavelength protection.

REFERENCES

1. Sliney D. H. and M. L. Wolbarsht (1980) *Safety with Lasers and Other Optical Sources*. New York: Plenum Publishing Corp.
2. Solon L.R., R. Aronson and G. Gould (1961), Physiological implications of laser beams, *Science*, 134:1506-1508.
3. Sliney, D.H., (1996). Laser Effects on Vision and Ocular Exposure Limits, *Appl Occup Environ Hyg* 11(4):313-319.
4. Allen, R.G., and Polhamus, G.D., Ocular thermal injury from intense light, in (M. L. Wolbarsht, Ed.), *Laser Applications in Medicine and Biology*, Vol. 4, pp 247-278, Plenum Press, New York, 1989.
5. Courant, D., Ph.D., Court, L., and Sliney, D., "Research Relative to Safety Formulations for Retinal Damage from Extended Source and Large Retinal Image," *Proceedings of the International Laser Safety Conference*, Laser Institute of America, Orlando, FL., pp. 4-25, (1991).
6. Barnes, F.S., Biological damage resulting from thermal pulses, in (M.L. Wolbarsht, Ed.) *Laser Applications in Medicine and Biology*, Vol. 2., Plenum Press, New York, pp 205-221, 1974.
7. Henriques, F. C., Jr., Studies of thermal injury V. The predictability and the significance of thermally induced rate processes leading to irreversible epidermal injury. *Amer J Pathol*, 23: 489-502, 1947.
8. Hillenkamp, F. Interaction between laser radiation and biological systems, in Hillenkamp, F., Pratesi, R., Sacchi, C.A. (Eds.), *Lasers in Biology and Medicine*, NATO Advanced Study Institutes Series A #4. New York, Plenum Press, 1980.
9. Sliney, D.H., and Marshall, J., "Tissue specific damage to the retinal pigment epithelium: mechanisms and therapeutic implications," *Lasers and Light in Ophthalmology*, 5(1):17-28, (1992).
10. Wood, T. H., Lethal effects of high and low temperatures on unicellular organisms in *Advances in Biological Medical Physics*, Vol 4, Academic Press, New York, 1956.
11. Lepock, J.R., «Protein Denaturation During Heat Shock,» in *Advances in Molecular and Cell Biology*, JAI Press (1997).

12. Biltonen, R.L., Freire, E., «Thermodynamic characterization of conformational states of biological macromolecules using differential scanning calorimetry, *CRC Crit Revs, Biochem*, 5: 85-124 (1978).
13. Craig, E.A., «The heat shock response,» *CRC Crit Revs, Biochem*, 18:239-280 (1985).
14. Dewey, W.C., «The search for critical cellular targets damaged by heat,» *Radiat. Res*, 120: 191-204 (1989).
15. Hahn, G.M., *Hyperthermia and Cancer*, Plenum Press, New York, pp. 90-94, (1982).
16. Jung, H., «A generalized concept of cell killing by heat,» *Radiat. Res.*, 106: 56-72 (1986).
17. Kushner, V.P., *Conformational Flexibility and Denaturation of Biopolymers*, Nauka Press, Leningrad, (1977).
18. Lazlo, A., «The effects of hyperthermia on mammalian cell structure and function,» *Cell. Prolif.*, 25: 59-87 (1992).
19. Lepock, J.R., «Involvement of membranes in cellular responses to hyperthermia,» *Radiat. Res.*, 92: 433-438.
20. Zale, S.E. and Klibanov, A.M., «Why does ribonuclease irreversibly inactivate at high temperatures? *Biochemistry*, 25: 5432-5444.
21. Sliney, D.H., "Interaction Mechanisms of Laser Radiation with Ocular Tissues: Implications for Human Exposure Limits," *Kvantovaya Elektronika*, 8(12):2640-2649, (1981) [in Russian; English Translation in *Soviet Journal of Quantum Electronics*, 11(12):1606-1611, (1981)].
22. E. S. Beatrice and G. D. Frisch, Retinal laser damage thresholds as a function of image diameter, *Arch. Environ. Health*, 27:322-326, 1973.
23. Ham, W. T., Jr. (1983) The photopathology and nature of the blue-light and near-UV retinal lesion produced by lasers and other optical sources (M. L. Wolbarsht, ed.) *Laser Applications in Medicine and Biology*, New York, Plenum Publishing Corp. (1989).
24. M. A. Mainster, T.J. White, J.H. Tins and P.W. Wilson, Retinal temperature increases produced by intense light sources, *J. Opt. Soc. Am.*, 60:264-270, 1970.
25. Sliney, D.H., "Interaction Mechanisms of Laser Radiation with Ocular Tissues," in [Court, L. A., Duchene, A., and Courant, D., eds.], *First International Symposium on Laser Biological Effects and Exposure Limits: Lasers et Normes de Protection*, pp. 64-83, Commissariat a l'Energie Atomique, Departement de Protection Sanitaire, Fontenay-aux-Roses, (1988).
26. R. G. King and W. J. Geeraets, The effect of q-switched laser radiation upon the retinal pigment epithelium *in vitro*, *Acta Ophthalmologica*, 46:617-632, 1968.
27. J.R. Hayes and M.L. Wolbarsht, Thermal model for retinal damage induced by pulsed lasers, *J. Aerospace Med.*, 39:474-480, 1968.
28. D. H. Sliney, D.H. and W. J. Marshall, Bioeffects of repetitively pulsed lasers, in (S. S. Charscan, Ed.), *Proceedings of the International Laser Safety Conference*, Cincinnati, OH, November 1990, pp. 4:15-4:24, Orlando, Laser Institute of America, 1991.
29. International Commission on Non-Ionizing Radiation Protection (ICNIRP), Guidelines on Limits for Laser Radiation of Wavelengths between 180 nm and 1,000 nm, *Health Phys*, 71(5): 804-819, 1996.
30. Freund, d.e., McCally, R.L., Farrell, R.A., and Sliney, D.H., A Theoretical Comparison of Retinal Temperature Changes Resulting from Exposure to Rectangular

- and Gaussian Beams, *Lasers in the Life Sciences*, 7(2): 71-89 (1996).
31. B. S. Gerstman, C.R. Thompson, S.L. Jacques and M.E. Rogers, Laser induced bubble formation in the retina, *Lasers Surg. Med.*, 18(1):10-21, 1996.
 32. Lin C.P. and Kelly M.W., Cavitation and acoustic emission around laser heated microparticle, *Appl Phys Lett* 72:2800, 1998.
 33. Wolbarsht, M.L. and Sliney, D.H., 1991, 1992, Historical Development of the ANSI Laser Safety Standard, *Journal of Laser Applications*, 3(1):5-10 (1991) and 4(3):18-21, (1992).
 34. Stuck, B.E. Lund, D.J., and Beatrice, E.S., *Repetitive Pulse Laser Data and Changes in the Maximum Permissible Exposure Limits*. Institute Report No. 58, Letterman Army Institute of Research, Division of Non-Ionizing Radiation, Presidio of San Francisco, San Francisco (1978).
 35. Ham, W.T., Jr., Mueller, H.A., Wolbarsht, M.L., and Sliney, D.H.: Evaluation of Retinal Exposures from Repetitively Pulsed and Scanning Lasers. *Health Physics*. 54(3):337-344 (1988).
 36. Bargerion, C.B., Deters, O.J., Farrell, R.A., and McCally, R.L., "Epithelial Damage in Rabbit Corneas Exposed to CO₂ Laser Radiation," *Health Phys.* 56:85-95 (1989).
 37. Sliney D. H., "Yag Laser Safety," in (S.L. Trokel, Ed.) *YAG Ophthalmic Microsurgery*, Appleton-Century-Crofts, Norwalk, pp. 67-84, 1983.
 38. Cain, C.P., Rockwell, B. et al., Retinal damage and laser-induced breakdown produced by ultrashort-pulse lasers, *Graefe's Arch Clin Exp Ophthalmol*, 234(suppl 1):S28-S37 (1996).
 39. Cain, C.P., et al, Visible retinal lesions from ultrashort laser pulses in the primate eye, *Invest Ophthalmol Vis Sci*, 36:879-888 (1995).
 40. Lund D. J., P.R. Edsall, D. R. Fuller, and S.W. Hoxie, (1996) Ocular Hazards of Tunable Continuous-Wave Near-Infrared Laser Sources, *SPIE Proc.* 2674: 53-61.
 41. Biscar J.P., Photon enzyme activation, *Bull. Math. Biophys.*, 38:29-38, 1976.
 42. Sliney, D.H., Ocular injuries from laser accidents, in *Laser-Inflicted Eye Injuries: Epidemiology, Prevention, and Treatment*, *Proc SPIE*, 2674: 25-33 (1996).
 43. Gibbons, W. and Allen, R., "Retinal Damage from Suprathreshold Q-Switch Laser Exposure," *Health Physics*, 35:461-469, (September 1978).
 44. Hirsch, D.R., Booth, D.G., Schockett, S., and Sliney, D. H., Recovery from Pulsed-dye Laser Retinal Injury, *Arch. Ophthalmol.*, 110:1688-1689, (1992).
 45. Decker, C. D., "Accident Victim's View," *Laser Focus*, p. 6, (August 1977).
 46. American Conference of Governmental Industrial Hygienists (ACGIH), *Threshold Limit Values for Chemical Substances and Physical Agents for 1998*, Cincinnati, ACGIH, 1998.
 47. American National Standards Institute, *Safe Use of Lasers*, American National Standard Z-136.1-1993, Laser Institute of America, Orlando, FL (1993)
 48. Sliney D. H., and H. LeBodo (1990) Laser Eye Protectors, *J Laser Applications*, 2(3):9-14.
 49. Robinson, A., Marshall, Wesley J., and Dudevoir, S., Study of saturation in commercial laser goggles, *SPIE Proc.*, 1207:202-213, (1990).
 50. Sliney, D.H., "A Safety Manager's Guide to the New Welding Eye Filters, *Welding Journal*, 71(9):45-47, (1992).
 51. Roach W.P., Johnson T.E. and Rockwell B.A., "Proposed Maximum Permissible Exposure Limits for Ultrashort Laser Pulses", accepted to *Health Physics*, August 1998.

EXPERIMENTAL STUDY OF THE VARIATION OF LASER-INDUCED RETINAL DAMAGE THRESHOLD WITH RETINAL IMAGE SIZE

J.A. ZUCCLICH,¹ D.J. LUND,² P.R. EDSALL,¹ R.C. HOLLINS,³ P.A.
SMITH,⁴ B.E. STUCK,² and L.N. McLIN⁵

¹TASC, Inc., 4241 Woodcock Dr., Suite B-100, San Antonio, TX 78228,
USA; ²US Army Medical Research Detachment, Brooks AFB, TX 78235-
5138, USA; ³UK Defence Evaluation Research Agency, Malvern, WR143PS,
UK; ⁴UK Defence Evaluation Research Agency, Farnborough, GU146TD,
UK; ⁵Optical Radiation Branch, USAF/HEDO, Brooks AFB, TX 78235-
5215, USA.

Abstract The dependence of retinal damage threshold on laser spot size was examined for microsecond-duration laser pulses from a flashlamp-pumped dye laser. Threshold determinations were conducted for nominal retinal image sizes ranging from 1.5 mrad to 100 mrad of visual field, corresponding to image diameters of ~22 μm to 1.4 mm on the primate retina. In addition, a baseline collimated-beam damage threshold was determined for comparison. Together, this set of retinal damage thresholds reveals the functional dependence of threshold on spot size. The threshold dose was found to vary with the spot size diameter for small to moderate image sizes (up to ~400 μm) but with the area of the image for larger image sizes.

Keywords: *laser, eye protection, optical limiter, retina, image size*

INTRODUCTION

Non-linear optical limiter cells or optical switches have been widely explored as a broadband laser countermeasure technology.¹⁻³ To the extent that non-linear refraction and/or scattering processes diverge a laser beam passing through an optical limiter, such devices may provide eye protection beyond that which would be attributed to the absorption properties (linear and non-linear). In order to quantitate the enhanced ocular protection, one must first specify the variation of the eye's damage threshold as a function of the image size of the laser beam transmitted to the retina (i.e., as a function of the divergence of the beam reaching the eye). Such data are generally not available in the published literature. This report presents the results

of a systematic study of variation of retinal damage threshold with laser image diameter in the primate retina. These results could be used by optical limiter designers and modelers to assess the laser eye protection provided by an optical switch as the incident pulse energy is varied and, consequently, as the divergence varies of the transmitted laser pulse propagated into the eye.

EXPERIMENTAL APPROACH

The experimental subjects were rhesus monkeys (*Macaca mulatta*). All animals involved in this study were procured, maintained, and used in accordance with the Animal Welfare Act and the "Guide for the Care and Use of Laboratory Animals" prepared by the Institute of Laboratory Animal Resources, National Research Council; and the ARVO Resolution on the Use of Animals in Research. All experiments involving animals used appropriate levels of anesthesia so the subjects did not experience pain or distress.

Pre-exposure screening of subjects to insure clear ocular media and normal retinas consisted of slit-lamp and fundus camera examinations, fluorescein angiography, and refraction to the nearest 0.25 diopter. No eyes having refractive error differences of more than 0.5 diopter in any meridian were used.

The flashlamp-pumped dye laser was a laser source taken from a clinical instrument used for photocoagulation procedures (Candela Model LFDL-8). We utilized rhodamine chloride (rhodamine 6G) to yield 590-nm emission and measured a maximum pulse energy of ~1 J and a pulsewidth of 3 μ sec. The laser operated as a repetitively pulsed system with pulse repetition frequency variable from 0.1 to 10.0 Hz or it could be triggered externally as required. For this study, an external trigger switch was used to trigger single pulses for delivery to each retinal exposure site.

The beam diameter at the laser output was ~6 mm and exhibited a rather "dirty" spatial profile. However, as illustrated in the schematic diagram for the apparatus (Figure 1), a beam expander was used to yield a clean collimated beam which then passed through a final focusing lens of such a power as to achieve the desired retinal image size.

A total of four retinal image diameters were studied. In addition, the collimated beam baseline threshold, in effect, provides a fifth data point for the

study. Table I lists the retinal image sizes in terms of both angle of visual field subtended and retinal image diameter, as well as the size of the final aperture and the power of the focusing lens used to achieve each image size.

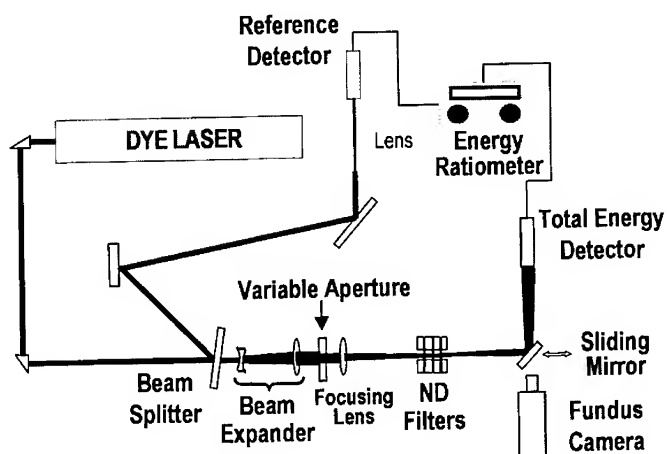


FIGURE 1 Schematic diagram of experimental apparatus.

TABLE I Retinal spot sizes.

Visual field subtended (mrad)	Retinal image diameter (μm)	Variable aperture size (mm)	Power of focusing lens (diopter)
0 ^a	-- ^b	-- ^c	-- ^c
1.5	22	1.5	1.0
5.0	72	3.5	2.0
20	280	2.9	7.0
100	1400	18	5.4

^aPoint source – nominal collimated beam incident at corneal plane

^bDiffraction limited spot size

^cNot applicable

The retinal image diameters listed in Table I were calculated assuming that a one-degree field of view corresponds to a 250- μm -diameter spot on the rhesus retina.

The diameters in the table can be scaled accordingly if a different assumption is made regarding the linear extent corresponding to one degree of visual field.

The sliding mirror seen in Figure 1 is a front surface mirror mounted on a slide with a single translational degree of freedom. With the slide at the right-hand stop, the mirror is moved away from the fundus camera so as not to interfere with the positioning of the subject in front of the camera and the viewing of the subject's retina. With the slide at the left-hand stop (shown in Figure 1) the mirror sits directly in front of the fundus camera objective and is positioned to deflect the incident laser beam along the optical axis of the fundus camera and to the selected target site on the retina. When the subject is absent, the deflected dye laser beam is directed to a detector which measures the total pulse energy which would have entered the subject's eye. With the subject absent, the pulse energy reaching the total energy detector can be cross-calibrated against that reaching a reference detector. Thus the reference detector yields an indirect measure of pulse energy to the eye when the subject is mounted in front of the fundus camera.

The fundus camera is a standard ophthalmologist's instrument manufactured by Zeiss. The eyepiece of the fundus camera has a crosshair so that a given spot on the subject's retina can be aligned to the optical axis of the fundus camera. The fundus camera and sliding mirror are positioned so that a laser beam deflected off the mirror travels along the optical axis of the fundus camera and, thus, will strike the retinal target site designated by the fundus camera crosshair. The anesthetized subject, when in place, sits on a motorized adjustable stage such that the corneal plane is ~2 inches from the fundus camera objective (required to bring the retina into focus) and ~1 inch from the deflecting mirror.

Pulse energy is measured by two Laser Precision RJP 735 detectors coupled to a Laser Precision RJ 7620 energy ratiometer. The "total energy" detector measures the laser pulse energy which would pass through the dilated pupil (~8 mm) of the subject. Alternatively, an aperture can be placed in front of this detector to collect only the "encircled" pulse energy which would be directed to the central 1.5 mrad of visual field.⁴ Laser safety standards^{5,6} define sources of laser radiation subtending an angle of ≤ 1.5 mrad at the eye as collimated beams or point sources, while pulsed lasers subtending a greater visual angle are extended sources.

Experimental exposure sessions began with the placement of "marker" lesions in the subject's eye. Marker lesions are moderately sized (~100-200 μm) retinal lesions produced by a laser; in this case by the same dye laser used for the experimental exposures (but without using a focusing lens, so that a collimated beam enters the eye). The marker lesions, generally placed just outside of the pigmented macular area of the retina, serve as retinal landmarks for the positioning of subsequent experimental exposures. The experimental exposures are directed to grid sites (macular and/or paramacular) defined by the marker lesions. When the angular subtense of the experimental laser exposures was small (≤ 5 mrad) a total of nine macular exposures were delivered in a 3 x 3 grid pattern. For the 20-mrad case (retinal spot size ~280 μm), only four macular exposures were allowed in a 2 x 2 grid pattern. For each of the above cases, numerous paramacular exposures were delivered to sites along the grid lines defined by the marker lesions. For the 100-mrad case, only one macular exposure was delivered per eye, since a single central exposure covers the entire area of the pigmented macula. Approximately 12 paramacular exposures were spaced across the 30° field of view surrounding the macula.

Lesion/no lesion readings were conducted for each exposed eye via ophthalmoscopic observation at ~1-hr and 24-hr postexposure. The 24-hr readings were used for the threshold values reported here since lesion development continued to progress beyond one hour. These binary data were used to calculate the minimum visible lesion (MVL) threshold and fiducial limits by probit analysis. A running series of probit calculations on the cumulative lesion/no lesion data was used to assess the statistical goodness of the ED_{50} threshold so that data collection could be terminated when sufficient confidence was achieved in the calculated threshold value.

RESULTS

Figures 2-5 depict retinas exposed to arrays of dye laser pulses using retinal spot sizes of 1.5, 5.0, 20, and 100 mrad, respectively.

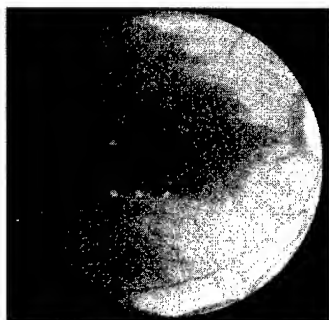


FIGURE 2 Fundus photograph of eye exposed to dye laser pulses with 1.5-mrad retinal image size.

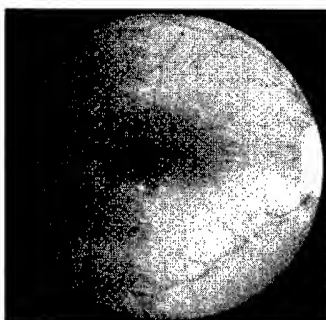


FIGURE 3 Fundus photograph of eye exposed to dye laser pulses with 5.0-mrad retinal image size.

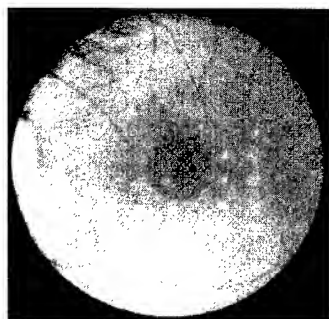


FIGURE 4 Fundus photograph of eye exposed to dye laser pulses with 20-mrad retinal image size.

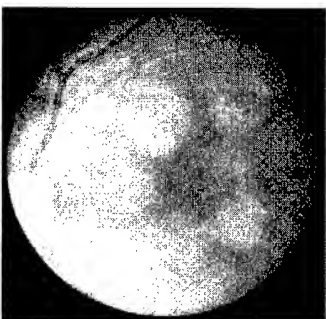


FIGURE 5 Fundus photograph of eye exposed to dye laser pulses with 100-mrad retinal image size.

Representative retinal image profiles for each case are seen in Figure 6. The spatial profiles were captured by a Spiricon laser beam analyzer using a CCD camera (Model LBA-100). As seen from Figure 6, the image profile becomes less Gaussian with increasing spot size, approaching a top-hat configuration.

Retinal Image Profiles for Spot Size Study 590 nm Dye Laser - 3 μ s pulse

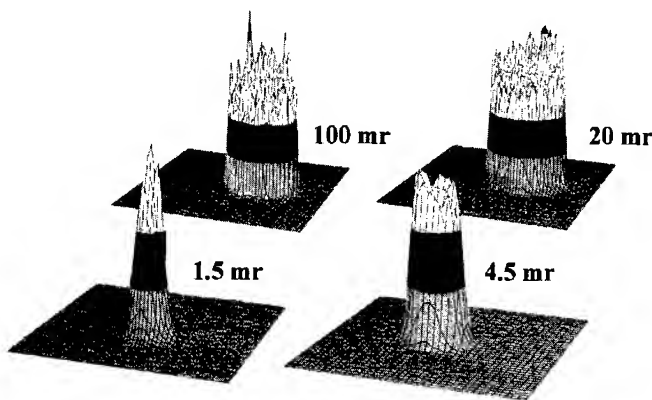


FIGURE 6 Retinal image profiles for spot size study.

Each of the eyes seen in Figures 2-5 received numerous dye laser exposures with pulse energies bracketing the estimated ED_{50} threshold for the respective retinal spot size. For the 1.5-mrad image size (Figure 2), threshold lesions are punctate, having an ophthalmoscopic appearance similar to that found following collimated beam exposures (e.g., the baseline threshold determination reported in this study).

For the 5.0-mrad spot size, the lowest pulse energies to yield ophthalmoscopically visible lesions resulted in retinal blemishes of measurable extent (perhaps 50-75 μ m in diameter) but still smaller than the marker lesions. Several examples are readily seen in Figure 3.

The 20-mrad case yields threshold lesions which are more diffuse and distinctly larger than the marker lesions. In Figure 4, it is seen that although the pulse energy delivered to each experimental exposure site varied from below threshold to ~3-4 times threshold, the observed lesion size is about the same for every case and approximates the chosen retinal spot size of 20 mrad or ~280 μ m.

Finally, an array of retinal lesions induced by the 100-mrad laser pulses is shown in Figure 5. Again the lesion size varies little, while the exposure doses across sites varied significantly. An appreciation for the lesion size is gained by comparison to the oval-shaped optic disc appearing at the left edge of the photo. In

the rhesus, the disc has a nominal size of 5° by 7° of visual angle compared to the chosen image diameter of 100 mrad or 5.7° . Again, the observed lesion size approximates the image diameter for all exposure doses.

The ED_{50} threshold data for the four retinal spot sizes as well as for the collimated beam baseline are summarized in Table II. Damage thresholds are reported for both macular and paramacular areas of the retina, but the macular results are only estimates in some cases as the total number of macular exposures is relatively small.

TABLE II Spot size dependence.

Retinal spot size	Threshold dose*
Baseline (collimated beam)	ED_{50} (macula) = 3.4 μ J (2.6-4.0) ED_{50} (paramacula) = 8.7 μ J (7.0-9.9)
1.5 mrad ($\approx 22 \mu$ m)	ED_{50} (macula) = $<6 \mu$ J ED_{50} (paramacula) = 9.7 μ J (8.6-11.2)
5.0 mrad ($\approx 70 \mu$ m)	ED_{50} (macula) = 11.8 μ J (10.0-13.9) ED_{50} (paramacula) = 16.9 μ J (15.6-18.7)
20 mrad ($\approx 280 \mu$ m)	ED_{50} (macula) = 60.7 μ J (-) ED_{50} (paramacula) = 87.8 μ J (78.1-100)
100 mrad ($\approx 1400 \mu$ m)	ED_{50} (macula) = 1.39 mJ (-) ED_{50} (paramacula) = 2.18 mJ (1.87-2.47)

* ED_{50} thresholds in terms of TIE pulse energy; fiducial limits in parentheses

DISCUSSION

Figure 7 shows the data of Table II plotted as ED_{50} threshold vs retinal image diameter (in micrometers).

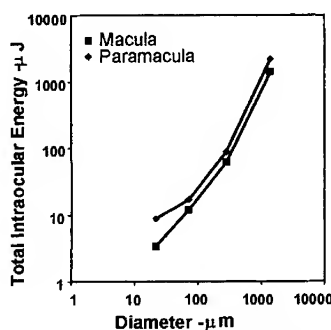


FIGURE 7 ED_{50} vs retinal image diameter.

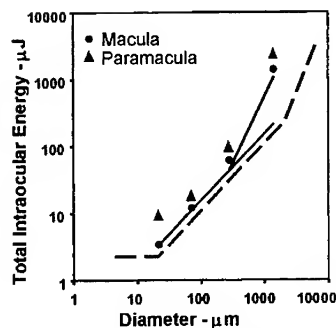


FIGURE 8 Comparison of ED_{50} to 10x MPE from laser safety standards.

The baseline threshold data are not included since the image diameter for the collimated beam is problematical (estimated at anywhere from 10 to 30 μm). However, the collimated beam thresholds closely approximate the 1.5-mrad case which we have plotted at the nominal 22- μm spot size even though ocular aberrations probably result in a somewhat larger retinal beam profile. The solid lines drawn through the data suggest that the dependence of threshold dose on image size is not strictly linear but approaches a higher order slope for large spot sizes. However, when the data for the largest spot size (100 mrad) are omitted, the remaining data show a reasonably close fit to a linear dependence.

The spot size dependence as represented by the laser safety standards^{5,6} is summarized as follows: a visual field subtense, α , of <1.5 mrad implies a point source and a maximum permissible exposure (MPE) invariant with α . For values of α between 1.5 mrad and 100 mrad, the MPE and, hence, the ED_{50} threshold is predicted to vary with α . For $\alpha > 100$ mrad, the ANSI standard states that the MPE varies as α^2 (or irradiated area). We note, however, a lack of published threshold data for extended sources subtending a visual field >100 mrad, so this aspect of the safety standards is certainly open to further discussion.

Figure 8 illustrates the current threshold data replotted and compared to the predicted linear dependence on image diameter for intermediate spot sizes and to the

predicted dependence on area for larger spot sizes. Although the ANSI standard indicates a transition from the α^1 dependence to the α^2 dependence at $\alpha = 100$ mrad or ~ 1400 μm , our data suggest that the transition might occur at somewhat smaller spot sizes – perhaps in the vicinity of 20-40 mrad or ~ 300 -550 μm . In any event, the transition would not be sharp, but would occur gradually over a range of spot sizes. It seems reasonable that in the large spot-size limit, the threshold would vary with the irradiated area since the temperature elevation profile will more closely resemble (if not initially, then after allowing some time for thermal diffusion) a top-hat distribution with a relatively slow relaxation back to ambient.

ACKNOWLEDGEMENTS

This work was supported by Contract CHS 60196 from the United Kingdom Defence Evaluation Research Agency. The work was conducted at Brooks Air Force Base, TX, under a Cooperative Research and Development Agreement between the US Army Medical Research Detachment, Brooks AFB, TX, and TASC, Inc.

REFERENCES

1. J.L. Guagliardo and R.C. Honey, Eye Protection of Military Personnel from Laser Radiation, Final Report, Stanford Research Institute Project 6057 (July 1984).
2. Ibid, Stanford Research Institute Project 7608 (May 1985).
3. K.M. Nashold et al., Optical Limiter Development, Final Report, Stanford Research Institute Project 4424 (May 1990).
4. J.A. Zuclich, Study of Ocular Protection Provided by Non-linear Optical Switches, Final Report, TASC Contract ELM/0874 (UK Defence Research Agency, March 1996).
5. ANSI Standard Z136.1, American National Standard for the Safe Use of Lasers, (American National Standards Institute, Inc., New York, 1993).
6. IEC Publication 825, Standard on Radiation Safety of Laser Products, Equipment Classification, Requirements and User's Guide (International Electrotechnical Commission, Geneva, 1993).

PASSIVE OPTICAL LIMITING: WHERE ARE WE?

Eric W. Van Stryland, M.J. Soileau, Sean Ross and David J. Hagan
CREOL, School of Optics, University of Central Florida, Orlando, Florida

Abstract We give a brief history of optical limiting with a few key references. A conclusion from these works is that we are still materials limited. Better nonlinear materials are needed to satisfy optical limiting and switching requirements. Many researchers are concentrating efforts on organic materials hoping that synthesis successes in other fields will also work for nonlinear optics. What is needed is a rapid characterization method for determining the nonlinear spectra of organic materials (both nonlinear absorption and refraction). Pump-probe experiments where the probe is a white-light continuum are ideally suited for this characterization. In principle the nonlinear spectra can be determined in a single laser firing. Since continua usually require short pulses to produce them, an added advantage is that the time resolution allows separation of ultrafast processes (two-photon absorption and the associated n_2) from cumulative nonlinearities such as excited state absorption.

HISTORY

The first passive optical limiter was built and tested by Leite et. al. in 1967.[1] It was based on thermal lensing in a liquid and used with a cw laser. Two years later two-photon absorption (2PA) was proposed and demonstrated for limiting the irradiance of pulsed lasers by Ralston and Chang [2]. In 1980 self focusing in Kerr liquids was utilized for passive optical limiting by Soileau [3], who also proposed liquid crystals in their isotropic phase for picosecond limiting in 1985 [4]. Self lensing in liquid crystals had been studied for cw lasers earlier.[5] Suspensions of carbon particles as an optical material for limiting was suggested in the late 1980's [6], with an explanation of the nonlinearity published in 1992 [7]. This material continues to be one of the best for sensor protection applications. In particular it shows the broadest bandwidth with the highest linear transmittance and no coloration. Reverse saturable absorption (RSA), which occurs for large excited-state absorption, was first investigated by Giuliano and Hess in 1967 [8], and in 1984 was used to smooth amplitude modulated pulses [9], and utilized for optical limiting in the late 1980's [10,11]. This nonlinearity is cumulative, that is, it builds up with time, and is thus good for limiting pulses of duration up to the

excited state lifetime. This nonlinearity is currently receiving the most research attention. Photorefraction has also been investigated for optical limiting in various configurations using single beam fanning [12] or 2-beam methods [13].

Advances in the field have relied heavily on our ability to properly characterize the nonlinear optical interactions in these materials, e.g. the development of Z-scan.[14] For example, the nonlinear response of semiconductors depends greatly on the input pulsewidth and often is a complicated mix of nonlinearities, e.g. 2PA plus free-carrier nonlinearities including diffusion and recombination dynamics with heating and subsequent thermal nonlinearities.[15] Understanding the scaling of 2PA with bandgap energy E_g allowed prediction of good limiting properties of narrow gap semiconductors in the IR (scales as E_g^{-3}). [16] Semiconductors, such as InSb near the 10 μm wavelength, are now being tested for their effectiveness.

Understanding the nonlinear processes allows for optimization of the utilization of the effects. For example, in semiconductors monolithic devices could be used to extend the dynamic range of devices.[17] Different geometrical arrangements are needed for other nonlinearities. For RSA, since linear absorption is needed to initiate the response, judicious placement of the nonlinear material must be used to increase the dynamic range while maintaining high linear transmittance. This led to tandem limiting devices [18], which in the limit of many elements resulted in graded density limiters [19]. Reviews of this field can be found in the following references [20-22]. Compilations of papers on the subject can be found in Refs. [23-28.]

The above is an incomplete history of optical limiting research giving a few of the key results. Much work still needs to be done and the main conclusion from examination of the history of the field is that it is still materials limited. New highly nonlinear materials are needed. Much of the current materials efforts are concentrating on organics with the thought that the successes of organic synthesis in other fields will be profitable here as well. Research is also continuing into modeling optical propagation in nonlinear materials including all forms of interaction from 2PA, ESA, and nonlinear refraction including thermally driven acoustic waves and bubble formation. Depending on the material and device design the interaction of nonlinear refraction with nonlinear absorption can be a help or hindrance. Also work on host materials such as sol-gel glasses is ongoing including looking for methods to create graded densities of dopants. In what

follows we concentrate on a new method for rapid characterization of the spectral dependence of material nonlinearities.

NONLINEAR SPECTROPHOTOMETRY

The number and variety of possible organic compounds with potentially large nonlinear response is extremely large. It is almost impossible to study all of them. What is needed is a basic understanding of how the molecular substituents and structure affect the nonlinear response. Most experiments to date have studied trends with changes in molecular structure by studying the nonlinear response with a single wavelength. It is often difficult to determine the mechanism responsible for the changes in nonlinearity. Multiwavelength measurements are clearly preferable. We have assembled what we believe to be the ideal nonlinear spectrophotometer. In addition to measuring the spectral response of the nonlinear losses, it simultaneously gives the dispersion of the nonlinear refraction.[29]

Description of Nonlinear Spectrophotometer

Figure 1 shows the basic concept of the nonlinear spectrophotometer. The sample is excited by an intense beam which changes the optical properties of the material and then this "changed sample" is probed at varying time delays with the "white-light" continuum to give its transmittance. At the same time a replica of the femtosecond continuum is sent through an unexcited portion of the sample to serve as a reference to determine the change in transmittance induced by the excitation. While the basic idea of this device is quite straightforward, the source for these measurements is quite complicated.

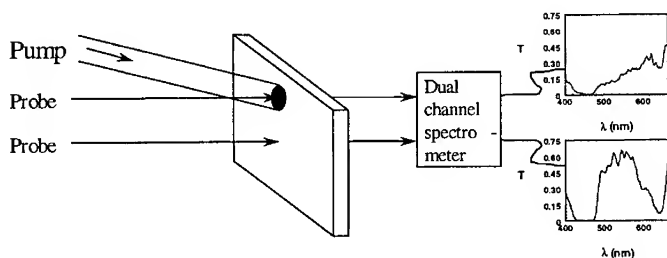


Figure 1. Schematic for the workings of the nonlinear spectrophotometer.

A modelocked fiber ring oscillator produces femtosecond pulses frequency doubled to 780 nm, stretched in time with gratings and injected into a Ti:sapphire regenerative amplifier. The amplified pulses are then compressed with another set of gratings. This system produces 1 mJ, 120 fs pulses at a 1 kHz repetition rate. The output is split in two with one of the outputs pumping an optical parametric generator/amplifier (OPG/A). A femtosecond continuum is produced by one of these outputs and used as the probe in Fig. 1 (after being split in two). The pump can either be at 780 nm, its harmonic at 390 nm, or the output of the OPG/A. This combination allows measurement of the nondegenerate nonlinear absorption (NLA) spectrum over a very large spectral range, i.e. $\Delta\alpha(\omega;\omega_c)$. We are limited with our dual diode array detection systems to wavelengths from 1.7 μm to 250 nm. This covers most of the interesting nonlinear spectral regions for organic materials. In addition this spectral range is large enough to apply causality and use Kramers-Kronig relations to calculate the dispersion of the nondegenerate nonlinear refraction, i.e. $\Delta n(\omega;\omega_c)$. Nonlinear refraction (NLR) is important for optical limiting even if the limiter is based on nonlinear absorption, since phase distortion on the beam induced by NLR can greatly change the fluence distribution at the detector. We briefly describe nonlinear Kramers-Kronig calculations in the next section.

Kramers-Kronig Relations For Nonlinear Optics

The complex response function of any linear, causal system obeys a dispersion relation relating the real and imaginary parts of the response function via a Hilbert transform pair. In optics, Kramers-Kronig (KK) relations are dispersion relations relating the frequency dependent refraction, $n(\omega)$ to an integral over all frequencies of the absorption $\alpha(\omega)$ and vice-versa. Toll [30] gave an interesting way of viewing the necessity for these dispersion relations. The electric field of an optical pulse in time, consisting of a superposition of many frequencies, arrives at an absorbing medium. If a single frequency component is completely absorbed we could naively expect that the output should be given by the difference between the input waveform and a sine wave at the absorbing frequency. However, this would obviously violate causality since there is an output signal (the negative of the sine wave) occurring at times before the incident wave train arrives. In order for causality to be satisfied, the absorption of one frequency component must be

accompanied by phase shifts of all of the remaining components in just such a manner that the field prior to the pulse vanishes. Such phase shifts result from the index of refraction and its dispersion. The KK relations are a frequency-domain representation of the causality statement. The usual KK relation that links the real χ' and imaginary χ'' parts of the susceptibility is

$$\chi'(\omega) = \frac{1}{\pi} \mathcal{P} \int_{-\infty}^{\infty} \frac{\chi''(\Omega)}{\omega - \Omega} d\Omega .$$

where \mathcal{P} indicates principle value. This allows us to directly relate the quantities of refractive index, $n(\omega)$, and absorption coefficient, $\alpha(\omega)$. These relations are:

$$n(\omega) - 1 = \frac{c}{2\pi} \mathcal{P} \int_{-\infty}^{\infty} \frac{\alpha(\Omega)}{\omega - \Omega} \frac{d\Omega}{\Omega} , \text{ or } n(\omega) - 1 = \frac{c}{\pi} \mathcal{P} \int_0^{\infty} \frac{\alpha(\Omega)}{\Omega^2 - \omega^2} d\Omega .$$

Clearly causality holds for nonlinear systems as well as for linear systems. The real and imaginary parts of $\chi^{(3)}$, are related through causality by KK relations in much the same way as n and α are related for linear optics. This may appear somewhat surprising at first glance since KK relations are derived from linear response theory, and this has caused confusion about the application of causality in NLO. The simplest way to view this process is to first linearize the problem by viewing the material plus strong perturbing light beam as a new linear system upon which we apply causality, i.e. the light interaction results in a new absorption spectrum for the material as illustrated in Fig. 2. Thus, we obtain relations between the changes in absorption, $\Delta\alpha$, and changes in refraction, Δn . An important difference here with what might first be written for this relation is that the connection is between nondegenerate nonlinearities. That is, the material plus light beam is held constant so that in the integral relation for the NLA, it is the change in absorption at frequency ω due to the presence of a strong beam at ω_k that is needed; $\Delta\alpha(\omega; \omega_k)$. [31] Thus, both the NLA and the NLR are equivalent to pump-probe spectra with a fixed pump frequency and variable probe frequency. This integral is over only one frequency argument, ω , and all other frequencies are held constant. Thus, we do not obtain a relationship between the degenerate nonlinearities but their nondegenerate counterparts $\Delta n(\omega; \omega_k)$. We can relate these changes, Δn and $\Delta\alpha$ as shown in Fig. 2. The nonlinear relation shows how the pump-probe experiment is ideally suited for determining both $\Delta\alpha$ and Δn .

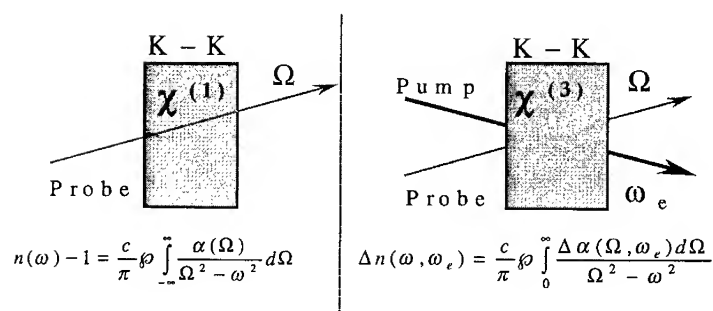


Figure 2. Illustration of Kramers-Kronig relations for linear and nonlinear systems. On the left a tunable source probes the absorption spectrum of the system (material only). On the right a tunable source probes the absorption spectrum of the system (material plus strong laser pump), and the difference between right and left gives $\Delta\alpha$ and $\Delta\beta$.

Although the calculation as illustrated above gives the nondegenerate NLR for a specific pair of frequencies, in most cases we set $\omega = \omega_k$ (after the integral is performed) and consider self-refraction.

As an example of preliminary data taken with this spectroscopy system, we show in Fig. 3 the temporally resolved nonlinear spectrum of a zinc-tetra (p-methoxyphenyl) tetrabenzporphyrine dye (TBP).[30] This figure shows the change in transmittance (signal spectrum minus reference) as a function of wavelength and time. Clearly this is a cumulative nonlinearity as it grows with time becoming nearly constant on the time scale of 10's of picoseconds. The interpretation for this material (after having performed several other experiments as well as studying the linear spectroscopy) is that the dominant nonlinearity is the creation of an excited state via linear absorption. What is being observed is the excited-state absorption dynamics after having been excited with a femtosecond pulse at 420 nm.

Experimental comparison of Spectrometer data to multiple wavelength Z-scans

We also performed single wavelength Z-scan experiments with a picosecond optical parametric oscillator as a function of wavelength.[32] Figure 4 shows a comparison of

these results that give the refractive cross section to the KK calculated nonlinear refraction measured over an extended λ range.

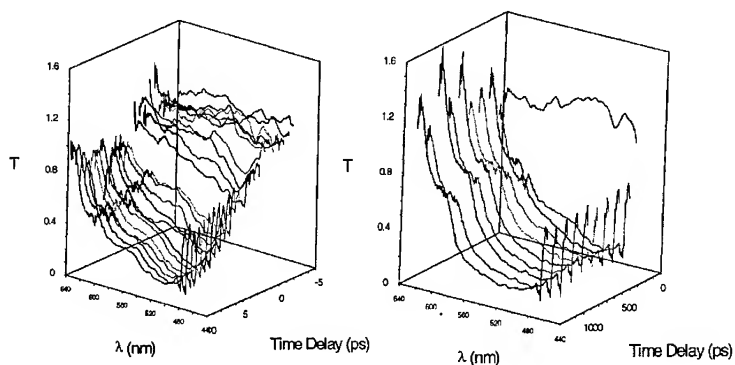


Figure 3. Excited-state absorption dynamics in a dilute sample of TBP. Left -5 to 5 ps, and Right 0 ps to 1 ns.

The agreement between these curves shows that for excited-state nonlinearities the degenerate nonlinear response is the same as the nondegenerate response. This is expected since the excitation very rapidly thermalizes to populate the lowest molecular energy levels. Thus, the probe measures the same excited spectra independent of excitation wavelength.

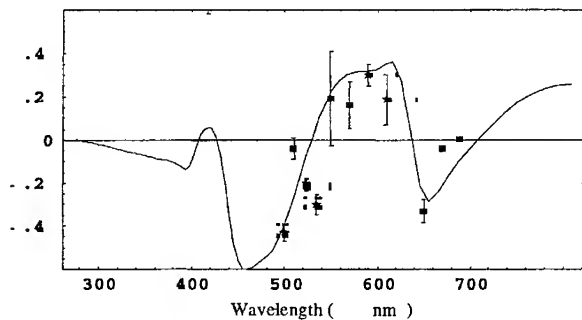


Figure 4. Refractive cross section determined from Δn versus λ both with Z-scan (dots) and continuum (line).

CONCLUSION

The nonlinear spectrophotometer described here offers the potential to rapidly determine both the nonlinear absorption spectrum and the dispersion of the nonlinear refraction. Both of these quantities are important for applications of nonlinear optical materials. Data obtained will provide a rapid increase in the information database available for developing an understanding of the fundamental bases for NLO interactions in organics. With this expanded database, observed trends will lead to scaling relations which lead to validation and/or modification of theory. A clear understanding of the NLO properties of these materials will answer questions regarding their suitability for optical devices, e.g. optical switching and routing devices and optical limiting devices. Additionally, the development of a predictive capability will enable the materials synthesis of new materials with enhanced (or diminished) NLO properties for specific applications. At the current level of understanding it is simply not possible to answer the question of whether or not particular devices will be suitable for a specific application.

ACKNOWLEDGEMENT

We gratefully acknowledge the contributions of M. Sheik-Bahae, a number of former students and post-doctoral researchers. We also thank Masato Nakashima of Natick for supplying the TBP sample. The financial support of the National Science Foundation, ECS-9510046 is greatly appreciated over the past several years as is support from the Joint Services Agile program and the Office of Naval Research contract N0000149710936.

REFERENCES

1. R.C.C. Leite, S.P.S. Porto, and P.C. Damen, "The thermal lens effect as a power limiting device", *Appl. Phys. Lett.* 10, 100 (1967).
2. J.M. Ralston and K.R. Chang, "Optical Limiting in Semiconductors", *Appl. Phys. Lett.* 15, 164 (1969).
3. M.J. Soileau, "Passive intensity limiter based on nonlinear optics", *JOSA*, 70, 1051 (1980).
4. M.J. Soileau, Shekhar Guha, William E. Williams, Eric W. Van Stryland, Juergen L.W. Pohlmann, E.J. Sharp, and Gary Wood, "Studies of the Nonlinear Switching Properties of Liquid Crystals with Picosecond Pulses," *Mol. Cryst. Liq. Cryst.* 127, 321 (1985).

5. I. C. Khoo, S. L. Zhuang and S. Shepard, "Self-focusing of low power cw laser beam via optically induced birefringence in nematic liquid crystal film., Appl. Phys. Letts., 39, 937 (1981).
6. see for example; K. M. Nashold, R. A. Brown, D. P. Walter, R. C. Honey, SPIE. 1105, 78 (1989).
7. Kamjou Mansour, M.J. Soileau and E. W. Van Stryland, "Nonlinear Optical Properties of Carbon Black Suspensions", JOSA B, 9, 1100-1109 (1992).
8. C.R. Guliano and L.D. Hess, "Nonlinear absorption of light: Optical saturation of electronic transitions in organic molecules with high intensity laser radiation", IEEE J. Quant. Electron., QE-3, 358-367 (1967).
9. D.J. Harter, M.L. Shand and Y.B. Band, J. Appl. Phys. 56, 865 (1984).
10. D.R. Coulter, V.M. Miskowsky, J.W. Perry, T.H. Wei, E.W. Van Stryland, and D.J. Hagan, "Optical Limiting in Solutions of Metallo-phthalocyanines and Naphthalocyanines", Proceedings of SPIE volume 1105, Materials for Optical Switches, Isolators, and Limiters, 42-51, 1989.
11. J.S. Shirk, R.G.S. Pong, F.J. Bartoli, and A.W. Snow, "Optical Limiter using a Lead Phthalocyanine", Appl. Phys. Lett., 63, 1880 (1993).
12. M. Cronin-Golumb and A. Yariv, "Optical Limiters using Photorefractive Nonlinearities, J. Appl. Phys., 57, 4906 (1985).
13. S.W. McCahon and M.B. Klein, "Coherent beam excisors using the photorefractive effect in BaTiO₃, Proc. SPIE, vol. 1105, Materials for Optical Switches, Isolators and Limiters, 119-124, 1989.
14. M. Sheik-bahae, A.A. Said, and E.W. Van Stryland, "High Sensitivity, Single Beam n₂ Measurements", Opt. Lett. 14, 955-957 (1989).
15. E.W. Van Stryland, Y.Y. Wu, D.J. Hagan, M.J. Soileau and Kamjou Mansour, "Optical limiting with semiconductors", JOSA B 5, 1980 (1988).
16. E. W. Van Stryland, H. Vanherzeele, M.A. Woodall, M.J. Soileau, Arthur L. Smirl, Shekhar Guha, Thomas F. Boggess, "Two-Photon Absorption, Nonlinear Refraction and Optical Limiting in Semiconductors", Opt. Eng. 24, 613 (1985).
17. D. J. Hagan, E. W. Van Stryland, M. J. Soileau and Y. Y. Wu, "Self Protecting Semiconductor Optical Limiters", Opt. Lett. 13, 315 (1988).
18. A.A. Said, T.H. Wei, J.R. DeSalvo, M. Sheik-Bahae, D.J. Hagan and E.W. Van Stryland, "Self-Protecting Optical Limiters Using Cascading Geometries", Proceedings of the SPIE, conference 1692, Orlando, FL, 1992.
19. P. A. Miles, "Bottleneck Optical Limiters: the Optimal Use of Excited-State Absorbers", Appl. Opt. 33, 6965 (1994).
20. G.L. Wood, W.W. Clark, M.J. Miller, G.J. Salamo and E.J. Sharp, "Evaluation of passive optical limiters and switches", Proc. SPIE, vol. 1105, 154 (1989).
21. E.W. Van Stryland, D. Hagan, T. Xia, and A. Said, "Application of Nonlinear Optics to Passive Optical Limiting", pp 841-860, in *Nonlinear Optics of Organic Molecular and Polymeric Materials*, ed. H.S. Nalwa and S. Miyata, CRC Press Boca Raton (1997).
22. L. W. Tutt and T. F. Boggess, "A Review of Optical Limiting Mechanisms and Devices Using Organics, Fullerenes, Semiconductors and Other Materials", Prog. Quantum Electron., 17, 299-338 (1993).
23. Proceedings of the SPIE, vol. 1307, "Electro-Optical Materials of Switches, Coatings, Sensor Optics, and Dielectrics", eds. R. Hartmann, M.J. Soileau, and V. K. Varadan, 1990.

24. Proceedings of the SPIE, vol. 2143, "Organic, Metallo-Organic, and Polymeric Materials for Nonlinear Optical Applications", eds. S. Marder and J. Perry, 1994.
25. Proceedings of the SPIE, vol. 1852, "Nonlinear Optical Properties of Advanced Materials", ed. S. Etemad, 1993.
26. Proceedings of the SPIE, vol. 1692, "Nonlinear and Electro-Optic Materials for Optical Switching", ed. M.J. Soileau, 1993.
27. *Materials for Optical Limiting*, Proceedings of the 1994 meeting of the Materials Research Society, Vol. 374, 1994.
28. *Materials for Optical Limiting II*, Proceedings of the 1994 meeting of the Materials Research Society, Vol. 479, 1997.
29. P. Buck, A. Dogariu, D.J. Hagan and E.W. Van Stryland, "Femtosecond Continuum Probe Measurements of Nonlinearities of Organic Dyes", Proceedings of the Conf. On Nonlinear Optical Liquids, SPIE, SPIE vol. 479 (1996).
30. J.S. Toll, "Causality and the dispersion relation: Logical Foundations", Phys. Rev. 104, 1760 (1956).
31. M. Sheik-Bahae, D.C. Hutchings, D.J. Hagan, and E.W. Van Stryland, "Dispersion of Bound Electronic Nonlinear Refraction in Solids", JQE, QE-27, 1296-1309 (1991).
32. T. Sean Ross, David J. Hagan, Arthur Dogariu, Paul M. Buck and Eric W. Van Stryland, "Excited-State Absorption Spectroscopy of Metallo-Porphyrin Dyes with Both Q and B-Band Excitation", CLEO 98, San Fransisco, 1998.

NANOSTRUCTURED MATERIALS AND COMPOSITES FOR OPTICAL POWER LIMITING

PARAS N. PRASAD, GUANG S. HE, MUKESH P. JOSHI, JACEK SWIATKIEWICZ, GEETHA MANCHALA, MANJARI LAL, ABANI BISWAS, and K- S. KIM
Photonics Research Laboratory, Departments of Chemistry and Physics,
State University of New York, Buffalo, New York 14260-3000, USA

Abstract This paper discusses methods used in our laboratory to design and prepare nanostructured materials and nanocomposites for optical power limiting. At the molecular level, we are studying structure-property relationship in a group of sequentially made and systematically derivatized structures with an objective to enhance the two-photon absorption cross-section. At the bulk level, nanoscale synthesis and processing in confined geometries such as those provided by the cavities in reverse micelles and pores in sol-gel glasses are utilized to prepare nanoparticles and nanocomposites. By these approaches we are able to combine a number of processes such as multiphoton absorption, reverse saturable absorption, photochromism, and nonlinear scattering, each of which can produce power limiting action under different conditions. Femtosecond time-resolved, pump-probe transient absorption experiment has been used to understand the excited state dynamics, particularly excited state absorption and its importance in power limiting action.

INTRODUCTION

Optical power limiting is an active area of research worldwide and has relevance to many applications. The optical limiting function requires the optical output power to be clamped below a certain critical value as the incident optical power increases. Therefore, it is a nonlinear optical response of the medium chosen to perform the optical limiting function. An ideal power limiting action should fulfill the following conditions:

- Complete transmission below a critical threshold intensity
- Fast response
- Broad spectral coverage

- Operation under different conditions of optical input
 - cw vs pulsed, different pulse widths
- Reversible operation with rapid recovery time
- To achieve limiting behavior well below materials damage threshold

In reality, the task of producing such a general-purpose ideal power limiter is very difficult if not impossible.

One can use a multitude of mechanisms to produce power limiting action. Some of these mechanisms are: two-photon absorption, reverse saturable absorption, nonlinear scattering, nonlinear beam fanning, beam steering, photochromism, sacrificial materials. Each has its own merits and limitations. The effort at our Photonics Research Laboratory has been mainly directed towards using two-photon absorption for optical power limiting. We have focused on direct two-photon absorption as opposed to a sequential two-photon absorption process. In this direct process a molecule simultaneously absorbs two-photons (of the same frequency in the present context) to produce an excited state. Therefore, the intermediate state for interaction is only a virtual state. Some of the merits and limitations of a two-photon based optical power limiter are as follows:

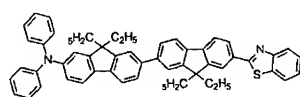
Merits: complete transmission at low intensity, instantaneous response with direct two-photon absorption, reversible operation, relatively broad two-photon absorption spectra;

Limitations: works under pulse conditions such as with nanosecond to femtosecond pulses.

EFFICIENT TWO-PHOTON ABSORBERS

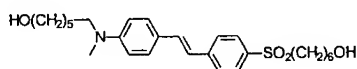
Two-photon processes have been known for a long time and suggested for optical power limiting¹. However, there has been a considerable increase of interest recently in using this mechanism for effective optical power limiting because of the availability of materials with considerably enhanced two-photon absorption-cross sections²⁻⁷. In collaboration with Bruce Reinhardt's group at the Polymer Branch of the Air Force Research Laboratory at Dayton, we have taken the approach of a systematic study of structure-property relationship to design

highly efficient two-photon absorbers.⁸⁻¹⁰ Some of the structures with large effective two-photon cross-sections (σ_2' in $\text{cm}^4 \text{ sec}$ as measured using nanosecond pulses) are listed below.



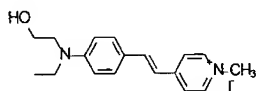
AF-250

$$\sigma_2' = 128 \times 10^{-48} \text{ cm}^4 \text{ sec}$$



APSS

$$\sigma_2' = 37 \times 10^{-48} \text{ cm}^4 \text{ sec}$$



ASPI

$$\sigma_2' = 7.3 \times 10^{-48} \text{ cm}^4 \text{ sec}$$

Recently, Reinhardt's group has synthesized another absorber AF-350 (structure proprietary) with $\sigma_2' = 238.1 \times 10^{-48} \text{ cm}^4 \text{ sec}$. The two-photon cross sections are effective cross sections measured with $\sim 8 \text{ nsec}$ pulses. Therefore they also possibly include excited state absorption contribution. All these materials are highly efficient up-converted emitters as they exhibit the following processes.

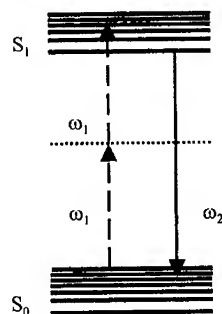


FIGURE 1 Energy level diagram showing two-photon pumped up-converted emission.

In some of these compounds (APSS and ASPI), the two-photon pumped upconverted emission process is so strong that population inversion and cavity lasing can be achieved by this mechanisms.^{2,8,9} A typical power limiting curve obtained with the AF-350 solution in THF is shown below. Even at the dilute concentration of 0.02 mol/L, we have achieved our initial goal of clamping the output fluence below 1 J/cm².

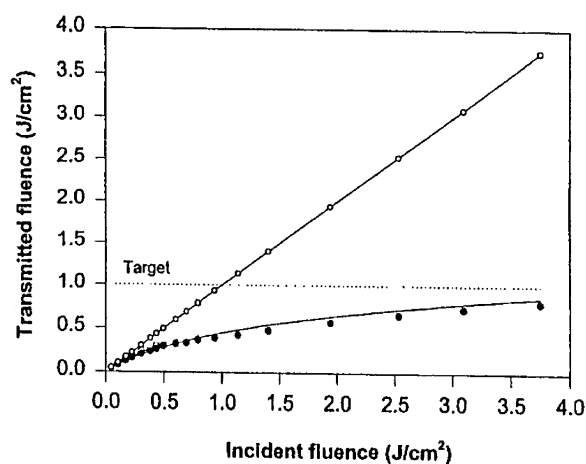


FIGURE 2. Optical limiting curve for AF-350 in THF solution using 8 ns pulses from a dye laser at the wavelength of 800 nm pumped by a Q-switched pulsed Nd-YAG laser.

NANOSTRUCTURED MATERIALS AND COMPOSITES

Nanostructured materials and composites offer opportunity to tailor the nonlinear optical response for controlling and broadening the range of optical power limiting function. At the molecular level, one can utilize nanoscale synthesis to prepare structures with control of optical band gap or conjugation length as well as make inorganic:organic hybrid structures.

We have utilized nanoscale synthesis in reverse micelle nanoreactors of controlled sizes for this purpose. A reverse micelle nanopocket can be formed by dispersing a surfactant together with water in a nonpolar liquid such as isooctane. The size of the nanopockets is determined by the ratio W_o of the amount of water and the amount of surfactant. These nanopockets are polar cavities which can be used as nanoreactors for reactions involving polar or ionic reactants. In our approach, we prepare these nanoreactors of a certain size by selecting W_o ; then introduce the polar reactants which diffuse into these nanoreactors and undergo reaction. By using this approach we have prepared a variety of structures for enhanced optical power limiting functions. Some examples are:

- Inorganic nanoparticles (CdS, Ag, Au) with controlled bandgaps
- Finite segment conjugated polymers such as poly-p-phenylene vinylene (PPV) with controlled conjugation length¹¹
- Inorganic:organic nanocomposites such as CdS:PPV
- Metal cluster: two-photon encapsulator

The last structure was made with the hypothesis that a resonance interaction between the surface plasmon resonance of the metal cluster and the two-photon state of the dye

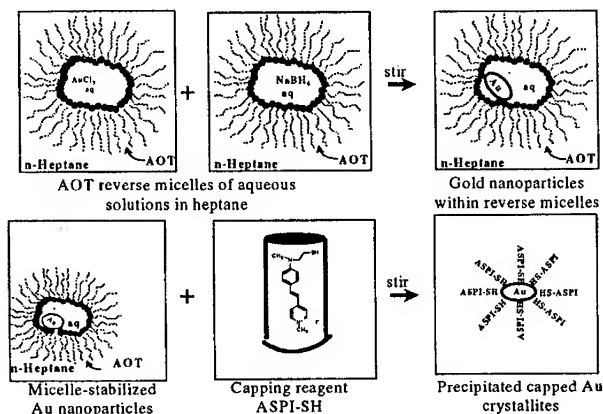


FIGURE 3 Reverse micelle synthesis of ASPI-SH capped Au nanoparticles.

encapsulator will lead to an enhancement of nonlinear absorption. A specific example of this type of structure preparation is shown in Figure 3. By judicious choice of the size of Au nanoparticle, its surface plasmon resonance was matched in energy with the two-photon absorption of ASPI-SH. Our preliminary result shows that this nanostructured material exhibits a very efficient power limiting action.

We have used processing of multiphasic domains using nanoporous glasses or polymeric structures whereby each domain is a nonlinear absorber to provide a broad spectral coverage of optical power limiting function. This method has the distinct advantage that two dissimilar materials can be introduced as separate nanodomains in the same bulk form. Yet the material is optically transparent because of nanoscale separation of domains. An example of this type of system is a sol-gel processed multiphasic nanocomposite in which C_{60} was deposited on the walls of the pores of the glass and a two-photon dye was introduced in the polymer phase filling the pores.⁴

SYNERGISM BETWEEN TWO EFFECTS

As was discussed in the introduction section, the optical power limiting requirement is very demanding and requires coverage over a broad spectral and temporal condition of optical input. It is not possible to derive such a function by using one effect such as two-photon absorption. One way to broaden the coverage is to utilize a multitude of effects (mechanisms) by using a multiphasic approach discussed above in which each domain (phase) provides power limiting by a different physical mechanism. However, there also is the possibility to use a synergistic effect between two mechanisms, or couple two mechanisms to introduce additional or broadened channel for optical power limiting. Two such examples being pursued in our laboratory are:

- Two-photon absorption coupled with photochromism
- Two-photon absorption in one molecule coupled with reverse saturable absorption in another molecule through energy transfer

We have achieved success in demonstrating both these concepts. In the first case a two-photon absorber, AF-183 (an Air Force Laboratory compound from Reinhardt's group)

was co-dispersed with a photochromic material, 6-nitro spiropyran, in PMMA. This two-photon absorber absorbs two-photons at 800 nm and exhibits up-converted blue fluorescence which is absorbed by spiropyran to produce the colored merocyanine dye which further absorbs the 800 nm photons to provide an enhanced optical power limiting function. Figure 4 shows the transmitted energy as a function of laser pulses. It clearly shows that as with the number of pulses the merocyanine number density increases, an increased optical power limiting is observed.

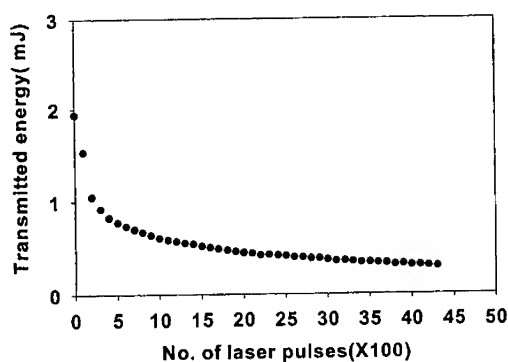


FIGURE 4 Decrease in transmission of 800 nm pulses as a function of number of pulses. Transmission was measured at the same location on the sample. Laser pulse energy and the rep rate were 2mj and 10 Hz.

CHARACTERIZATION

In order to completely formulate the conditions of effective power limiting it is essential to fully understand the nature and dynamics of two-photon absorption. For example, it is essential to determine if the nonlinear absorption giving rise to power limiting is purely a direct two-photon (or multiphoton absorption) process or a two-photon absorption followed

by a linear absorption of the same photon from the excited state generated. This possibility was pointed out by Marder and Perry⁷.

We have used a variety of techniques to characterize the two-photon properties of molecules. These are:

- Nonlinear transmission
- Z-scan
- phase sensitive nonlinear techniques
- ultrashort pulse time-resolved transient absorption
- Two-photon spectra
- Upconverted emission

To determine if the excited state absorption is playing any important role in the nonlinear transmission we have used femtosecond time-resolved transient absorption experiments in which the transmission of a weak probe beam at various time delays with respect to a strong pump beam is monitored. In the case of a direct two-photon absorption, a change in transmission of the probe beam will occur only when the pump pulse and the probe pulse coincide (zero time delay). However, if this two-photon excited state or a subsequently relaxed state also absorbs even at the wavelength of two-photon absorption, then the probe pulse will continue to be absorbed at a finite time delay until the excited state population has decayed. Figure 5(a) and (b) shows the Schematics of excited state absorption

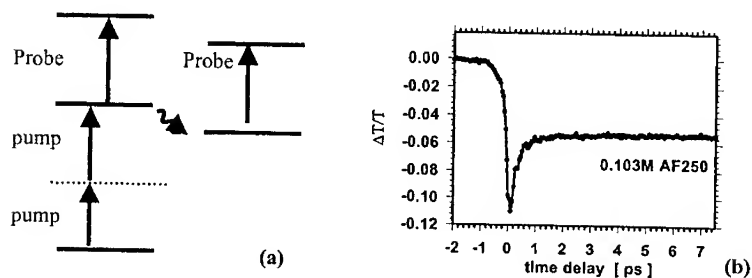


FIGURE 5 (a) Schematics of pump-probe excited state absorption and (b) Normalized differential transmittance vs time delay in a pump probe experiment with excitation pulses of 160 fs at 796 nm.

and result of our study on AF250 respectively. A continued change in the transmission of the probe beams at finite time delays clearly points out the role of excited state absorption, in addition to the direct two-photon absorption (a sharp change in transmission at zero time delays).

ACKNOWLEDGMENTS

This work was supported by the Polymer Branch of the Air Force Research Laboratory, Wright-Patterson Air Force Base and the Air Force Office of Scientific Research. We thank Bruce Reinhardt for valuable discussions and his permission to reference results on the Air Force compounds.

REFERENCES

1. E W. Van Stryland, H. Vanherzeele, M.A. Woodall, M. J. Soileau, A. L. Smirl, S. Guha, and T. F. Boggress, Opt. Eng., **24**, 613(1985).
2. J. D. Bhawalkar, G. S. He, and P. N. Prasad, Rep. Prog. Phys., **59**, 1041(1996).
3. G. S. He, R. Gvishi, P. N. Prasad, and B. A. Reinhardt, Opt. Commun. **117**, 133(1995).
4. R. Gvishi, J. D. Bhwalakar, N. D. Kumar, G. Ruland, U. Narang, and P. N. Prasad, Chem. Mater., **7**, 2199(1995).
5. G. S. He, G. C. Xu, P. N. Prasad, B. A. Reinhardt, J. C. Bhatt, and A. G. Dillard, Opt. Lett., **20**, 435(1995).
6. G. S. He, J. D. Bhawalkar, C. F. Zhao, and P. N. Prasad, Appl. Phys. Lett., **67**, 2433(1995).
7. J. E. Ehrlich, X. L. Wu, L. S. Lee, A. A. Heikal, Z. Y. Hu, H. Roeckel, S. R. Marder, and J. W. Perry, MRS Symposium Proc., **479**, 9(1998).
8. B. A. Reinhardt, L. L. Brott, S. J. Clarson, R. Kannan, and A. G. Dillard, MRS symposium Proc., **479**, 3(1998).
9. C. F. Zhao, R. Gvishi, U. Narang, G. Ruland, and P.N. Prasad, J. Phys. Chem., **100**, 4526(1996).
10. G. S. He, Y. Lixiang, N. Cheng, J. D. Bhwalkar, P.N. Prasad, L. L. Brott, S. J. Clarson, and B. A. Reinhardt, J. Opt. Soc. Am., **B14**, 1079(1997).
11. M. Lal, N. D. Kumar, M. P. Joshi, and P. N. Prasad, Chem. Mater. **10**, 1065(1998).

OPTICAL LIMITERS: SPATIAL, TEMPORAL, AND SPECTRAL EFFECTS

RICHARD C HOLLINS

Defence Evaluation & Research Agency, Malvern, Worcester WR14 3PS,
United Kingdom

Abstract This paper studies the performance of limiters and investigates limitations imposed by the weakness or absence of nonlinear effect at the edges of the spatial and temporal distribution of the beam. In many cases, spatial issues severely restrict any control over the total energy transmitted by the device, and analysis provides clear insights into how limiters should be studied for protection applications. Moreover, nonlinear devices generally affect the temporal form of a laser pulse. In some cases, the limiter dramatically shortens the pulse and the implications for protection are discussed. These effects are illustrated by results obtained using a variety of materials under study at DERA. A new diagnostic technique which permits direct measurement of the triplet yield of nonlinear dyes is also described.

INTRODUCTION

Sensor protection poses a difficult challenge to optical limiters. Any limiter which is required to operate over a wide range of input levels must exhibit very high optical densities at the highest input levels, and this can only be achieved if the nonlinear effect extends across the whole of the laser pulse. The edges of the spatial and temporal distributions present obvious problems because the optical power is inevitably low. Since the damage thresholds of imaging sensors are very low¹ (often $\sim 1 \mu\text{J}$), the nonlinear material must be very sensitive to operate throughout the whole of the pulse. This paper examines the ability of nonlinear materials to meet this challenge.

Unfortunately, the constraints and imperfections of a real optical system² intensify the problem. Practical issues such as thermal and chromatic aberrations and field curvature render the position of the focussed beam within the limiter somewhat unpredictable, and require that the thickness of the nonlinear material be increased far beyond the Rayleigh range of the focussed beam. Careful design is required to restrict

the insertion loss of the device to tolerable levels. For many nonlinear materials, the linear loss coefficient is directly linked to the concentration of some active ingredient, and the insertion loss can only be suppressed at the expense of reduced nonlinear sensitivity. Moreover, a real optical system fails to focus the laser energy into a diffraction-limited spot within the limiter, so edge effects become very important. Simple calculations and measurements are presented to illustrate the effects. Evaluation techniques designed to determine the protective characteristics of limiters are discussed.

The characteristics of some familiar classes of nonlinear materials are reviewed in the light of the above issues, and the potential for a low-loss device which operates across a broad transmission band is examined. Recent results from new porphyrin materials are also presented, and recent advances in materials and diagnostic techniques are reported.

THE EDGES OF THE FOCUSED BEAM

The problem

This section examines the focussing of light into a limiter by an $f/5$ optical system, and determines the amount of energy contained around the edges of the spot at locations where the optical power is too low for nonlinear effects. Calculations are presented for a diffraction-limited system, and supporting measurements are presented for a real optical system.

In many systems, practical requirements² dictate that the limiter cell must be at least 1-2 mm thick. If high insertion loss is to be avoided, the linear loss coefficient must therefore be below $5\text{-}10\text{ cm}^{-1}$ and most nonlinear materials of appropriate concentration exhibit nonlinear thresholds above 0.1 J/cm^2 (for Q-switched pulses). The

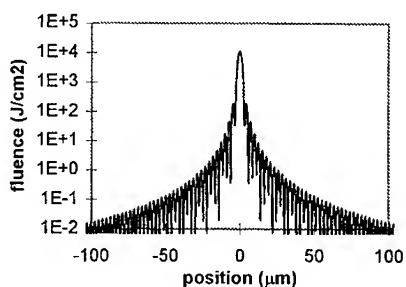


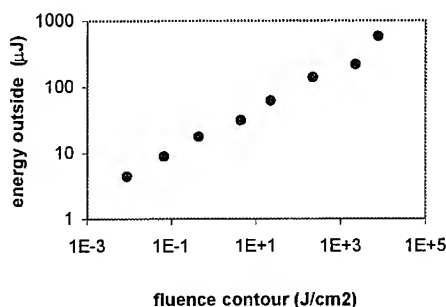
Figure 1: Airy spot pattern, $f/5$ system, $E_{in} = 1\text{ mJ}$

damage thresholds of many imaging sensors (including the retina) lie around 1 μJ , and input levels three orders of magnitude higher than this (*i.e.* $E_{in} = 1 \text{ mJ}$) are considered.

Diffraction-limited focal spot

In the absence of nonlinear effects, the focussed beam would form an Airy pattern, and the diameter of the central disc would be 6 μm . A log-linear plot of the pattern is shown in figure 1. The on-axis fluence corresponding to $E_{in} = 1 \text{ mJ}$ would be around $1.2 \times 10^4 \text{ J/cm}^2$. However, in the limiter, the focussed fluence is limited to much lower values; nevertheless, the Airy pattern provides a useful guide as to fluence levels *around the edges of the pattern* where no significant nonlinear effects occur. The Airy pattern is used to estimate the amount of energy which lies beyond the control of the nonlinear limiter. The calculations involve fluence levels as low as six orders of magnitude lower than the (assumed) on-axis value.

Figure 2 illustrates the amount of energy which lies outside any given fluence contour. The energy contained in the outer portions is enhanced by the two-dimensional nature of the calculation - the outer regions have much larger areas than the central spot. The energy E_{outer}



outside the contour I falls surprisingly slowly: $E_{outer} \propto I^{0.5}$ fluence

throughout the outer region. Most

importantly, some 10 μJ falls outside the 0.1 J/cm^2 contour below which the limiter is not expected to operate. This fluence contour lies at a diameter of $\sim 70 \mu\text{m}$, much wider than the Airy disc. Even in this diffraction-limited system, the amount of energy which lies outside the control provided by the limiter exceeds the published damage threshold of the eye.

Real optical system

The focussing performance of a real optical system (chosen to be typical of many viewing systems) is illustrated in figure 3. The measurements were performed on an $f/5$ magnifying system whose input optic was a high-quality doublet lens of focal length 250 mm, and the system was illuminated by a Q-switched 532 nm beam of

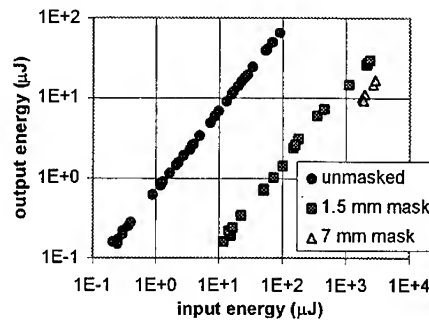


Figure 3: input-output characteristics of $f/5$ system with mask in focal plane

very low divergence. A small circular mask was fitted at the focal plane of the system to suppress remove the bright central spot of the focussed beam, thereby enabling measurement of the energy contained in the outermost portions of the focal plane. The figure exhibits input-output characteristics recorded with masks of diameter 1.5 mm and 7 mm, and with no mask. Even though the masks are much wider than the 70 μm contour indicated in the diffraction-limited calculations, significant energy passes around them. The proportion of the input energy which escapes the mask is approximately 2% (1.5 mm mask) or 0.7% (7 mm mask). The measurements vividly illustrate that, for $E_m = 1$ mJ, more than 10 μJ fails to pass through the focussed spot, and can therefore reach the sensor immune to control by any realistic limiter.

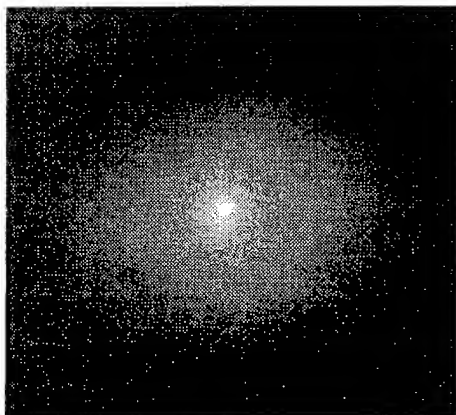
The focussing characteristics of all optical systems are degraded by a variety of well-known imperfections, including:

- aberrations inherent in the optical design
- distortion of the optical components from the desired form
- scattering from the optical surfaces.

The prospects of reducing the uncontrollable energy below the 1% level seem remote.

Implications for nonlinear protection

The energy which escapes around the edges of the focussed beam cannot be focussed tightly onto the sensor surface, and its hazard to the sensor is thereby reduced. A sensor mounted behind a limiter sees a laser image of the form indicated in figure 4: a bright, focusable spot is surrounded by an unfocussed pattern of much wider extent. In this paper, this image is



referred to as the *sensor image*. *Figure 4: image seen by sensor behind optical limiter*

The central spot has been suppressed by the limiter; the unfocussed portion has not. The above analysis shows that unfocussed region may contain large amounts of energy because of its large area, and any hazard analysis must take due account of this fact. The importance of this unfocussed region is intensified by two issues:

- the energy received by the sensor is more than sufficient to produce damage if it were tightly focussed;
- although the wide spatial extent must reduce the hazard to some extent, careful analysis is necessary. In the eye, the risk of damage is not determined entirely by the fluence; bio-optical studies^{1,3} indicate that the critical fluence is much lower for large images.

This analysis provides valuable guidance concerning the manner in which nonlinear devices should be evaluated for protection applications. The total energy transmitted by a limiter does not, in itself indicate the protective value. Comparison of this total transmitted energy against the damage threshold for a tightly-focussed beam does not indicate the true hazard; moreover, the damage thresholds for tightly-focussed

beams are too low to be matched by any limiter which can realistically be used. Study of the spatial distribution of energy across the sensor surface therefore forms an essential part of any protection study. Data relating the sensor damage threshold to the size and shape of the retinal image are also required, and bio-optical studies such as reference 3 make an invaluable input to the protection problem.

NONLINEAR SCATTERING AND REFRACTION PROCESSES

Nonlinear scattering and refraction are present in a wide variety of nonlinear limiters, and contribute to the form of the image formed on the sensor surface. In fact, the transformation of the sensor image from a tightly-focusable spot to the extended form illustrated in figure 4 might easily be attributed to these processes alone. This section examines the origins of the different portions of the sensor image. Measurements are presented of the nonlinear characteristics of the energy contained in different annular portions of the image.

The spatial form of the sensor image may conveniently be analysed in diagnostic experiments using apertures to isolate different portions of the re-imaged beam. Although high-performance silicon arrays are now available for image analysis, the use of diagnostic apertures to isolate a chosen portion offers several advantages:

- the image contains a very wide dynamic range of fluence levels ($\sim 10^4$) and imposes severe challenges on imaging sensors;
- the brightest portions of the image have very small areas, so the energies contained in different portions of the image fall within a much narrower range which lies well within the capabilities of a pyroelectric detector;
- a pyroelectric detector is immune to continuous background light.

Measurements on a carbon suspension limiter ($f/5$) are presented in figure 5. The output energy was measured using circular diagnostic apertures in the sensor plane, and the energy in annular portions of the image was determined by difference. The input-output characteristics of the energy contained in different annular portions are plotted, the different portions being identified by the field-of-view defined by each annulus. In each annulus, the energy exhibits a *sub-linear* dependence on the input energy; the high-

energy pattern is formed by the *removal* of components which were present at low energy, rather than the scattering of energy into regions which were hitherto empty. The sub-linear behaviour appears at

higher thresholds in successive annuli, and the energy delivered in angles larger than 7 mrad depends linearly on E_{in} across the full range of input levels. The influence of nonlinear scattering is clearly apparent since the output in each annulus fails to "clamp" at the highest levels.

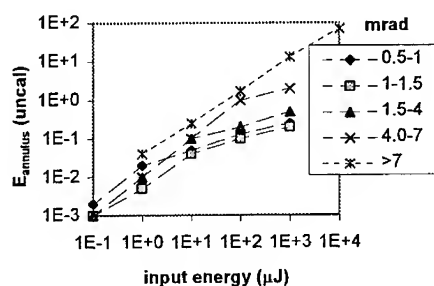


Figure 5: energy contained in annular portions of corresponding set of data pattern; carbon suspension

describing a nonlinear absorber

(C_{60}) indicates complete clamping in individual annuli. The thresholds associated with nonlinear effects at different positions are compatible with the analysis presented above.

TEMPORAL EFFECTS

The temporal distribution of the laser pulse also deserves study since the optical power is inevitably low at its edges. The initial (leading) edge of the pulse is normally the most important since the incident power rises very rapidly (particularly in gain-switched laser pulses) and the nonlinear effect is as yet unestablished. The leading edge makes an important contribution to the output since the initial transmission of the material is very high. The trailing edge is usually less important because the nonlinear effect has some inherent memory due to the finite lifetime of excited species, bubbles, *etc.*

Nonlinear effects shorten the transmitted pulse. The magnitude of the effect is closely related to the effectiveness of the limiter. Since the material is initially strongly-transmitting, high optical densities can only be achieved if the nonlinear effects are both *early* and *dramatic*. The pulse-shortening is confined largely to the bright centre of the sensor image

where the nonlinear effects are strongest - in this region, the output becomes confined to a brief flash at the start of the pulse, whereas the pulse duration is largely unaffected in the surrounding unfocusable region. Pulse-shortening of a 3 μs dye laser pulse ($E_{in} = 1$ mJ) by a carbon suspension limiter is illustrated in figure 6. The 3 μs laser pulse is shortened to around 70 ns.

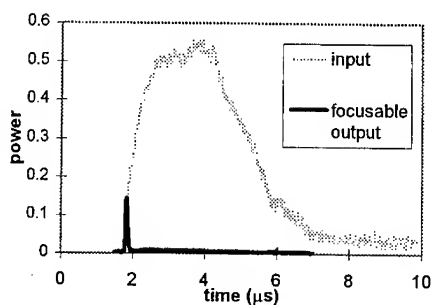


Figure 6: pulse-shortening in a carbon suspension

Pulse-shortening effects can be important to protection applications because sensor damage thresholds depend explicitly on the pulse duration. Figure 7 illustrates the dependence for the retina. Caution is required when applying sensor damage thresholds measured using a non-shortened laser pulse to predict the protective value of a limiter against that same laser. In the case of the 3 μs dye laser illustrated in figure 6, the difference may not be important for

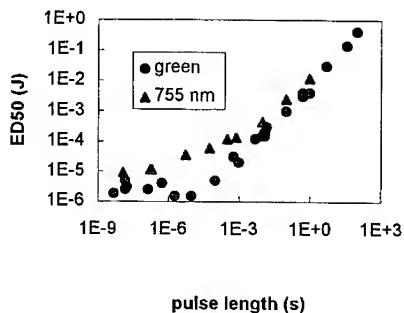


Figure 7: dependence of retinal damage threshold on pulse duration (after Lund)

eye protection because ocular damage thresholds at 3 μ s and 70 ns are quite similar. The difference may be more important for Q-switched lasers if the limiter shortens the pulse into the sub-nanosecond regime in which non-thermal injury mechanisms become quite important.

COMPARISON OF NONLINEAR MATERIALS

The suitability of different materials for an effective limiter depends on a variety of properties, among which the following are important:

- low linear optical loss across the response band of the sensor;
- sensitive nonlinear response across the same band;
- stability and resistance to optical damage;
- temperature range.

Linear transmission spectra

The linear transmission spectrum is an important selection criterion since it determines the extent to which the limiter degrades the normal operation of the sensor.

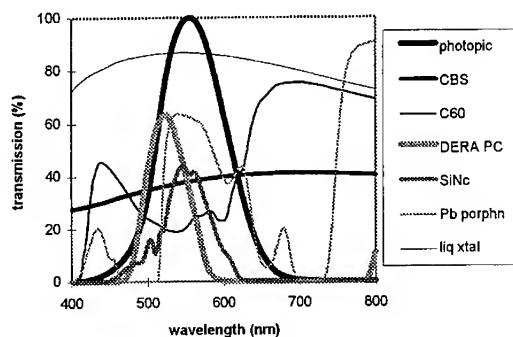


Figure 8: transmission spectra of limiter materials

In the visible band, optical loss in any portion of the band imposes coloration on the scene and removes information through reduced resolution and colour contrast.

The transmission spectra of devices containing a variety of materials are illustrated in figure 8. All curves refer to devices 2 mm thick; all are solutions or suspensions with the exception of the liquid crystal which is a mixture of several pure cyano-biphenyl materials. The photopic response curve of the eye is also displayed. The photopic transmission T_{photopic} provides a useful figure of merit of the spectrum for visual purposes.

- The most favourable transmission spectrum is that of the liquid crystal which exhibits very little absorption - its nonlinear response is initiated by optical Kerr (refractive) and two-photon absorption processes, neither of which require absorption, and most of the optical loss illustrated is associated with reflection at the cell interfaces. This is typical of many two-photon absorbing materials.
- The carbon suspension (CBS) also transmits across the whole of the visible band. For the device shown, T_{photopic} has been adjusted to approximately 37% which sets the nonlinear threshold for Q-switched pulses (532 nm) around 0.5 J/cm^2 . The device transmits an almost neutral scene. The chloroform host fluid⁴ remains fluid down to low temperatures.
- The fullerene C_{60} also has a wide transmission band, in spite of some absorption centred around the middle of the band.
- Two phthalocyanine dyes are shown: silicon naphthalocyanine (SiNc) and a substituted hydrogen phthalocyanine (DERA PC). Both dyes exhibit narrow transmission bands which are typical of the phthalocyanines. Even though they are quite well-matched to the photopic band, the dyes have a strong green colour and remove most of the colour contrast from a scene.
- A substituted lead porphyrin exhibits much broader transmission than the phthalocyanines and provides superior colour contrast. The spectrum matches the photopic curve very well. Two narrow absorption bands fall within the visible band.

Sensitivity in low-loss devices

For many nonlinear materials, the nonlinear sensitivity can be adjusted over a wide range (together with the visual loss) by varying the concentration of the solution or suspension.

The trade-off between clamping level and photopic transmission is illustrated in figure 9; measurements refer to 2 mm cells irradiated by a Q-switched 532 nm laser; the input energy is ~ 1 mJ. A different cell corresponds to each data point.

The carbon suspension performs better in low-loss devices than either C_{60} or SiNC. This difference is partially attributable to the narrower transmission bands of the latter two - their concentration would need to be reduced to very low levels to restore high transmission in all parts of the photopic band.

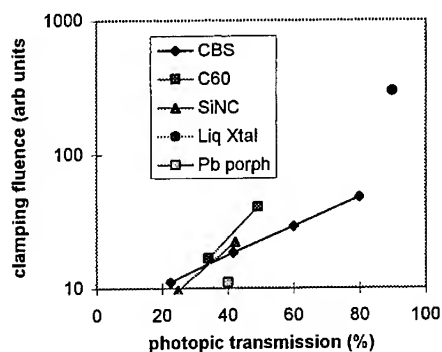


Figure 9: trade-off between nonlinear sensitivity and visual loss

The lead porphyrin exhibits very high sensitivity at the 532 nm wavelength of the measurements. Data are not yet available for a wide variety of transmission levels.

The concentration of the cyano-biphenyl liquid crystal mixture is not adjustable. The figure shows that, although this material has low visual loss, its performance is inferior to that of a suspension diluted to high transmission. The liquid crystal performance is typical of several other low-loss organics whose nonlinear response is due to two-photon absorption and optical Kerr effects.

Nonlinear response at different wavelengths

The nonlinear sensitivity of many molecular species varies strongly with wavelength, as illustrated in figure 10. The laser source was a tunable OPO, and all data refer to cells 2 mm thick adjusted to 40% photopic transmission.

For the carbon suspension, the clamping level increases quite gently with wavelength. Scattering centres are required to grow to larger size to scatter the longer wavelengths. C_{60} also exhibits a fairly gentle spectral dependence, although the clamping level rises sharply in the red due to the lack of ground-state absorption to initiate the nonlinear response.

The dyes exhibit quite sharp spectral dependence. In particular, the lead porphyrin exhibits very strong nonlinear response around 530-550 nm, but the clamping level rises very sharply at longer wavelengths. These spectral characteristics can be understood from the excited state cross-section data (for a similar compound, Zn TMSAP porphyrin) illustrated in figure 11. At wavelengths around 500-530 nm, the excited states

absorb much more strongly than the ground state. The cross-sections become much more similar at yellow wavelengths. The data in figure 11 were recorded using a broadband picosecond pump-probe technique⁵ forms a powerful tool for analysis of nonlinear absorber materials.

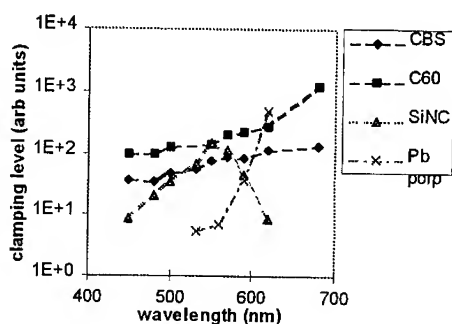


Figure 10: wavelength dependence of clamping level for several materials

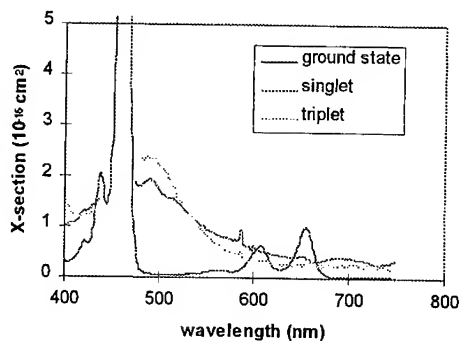


Figure 11: absorption spectra of ground and excited states of zinc TMSAP porphyrin

CONCLUSIONS

The thick limiters required for use in many optical systems cannot limit laser output to levels as low as 1 μ J. However, the total energy transmitted by the limiter provides quite a poor indication of its protective ability, and evaluation of materials and devices must consider the spatial distribution of energy across the sensor surface.

Nonlinear limiters dramatically affect the duration of a laser pulse, and this effect may affect the protective value of the device.

Materials studies must consider the nonlinear performance of a limiter against its impact on the visual performance of the corresponding sensor. Broadband materials may offer the best nonlinear performance under low-loss conditions; carbon suspensions remain a strong candidate. New lead porphyrin materials exhibit strong nonlinear response in the green, although the long-wavelength response is weaker.

ACKNOWLEDGEMENTS

The author is grateful to colleagues in DERA, UK industry, and abroad for useful discussions and collaborations over several years. Particular thanks are due to Dr K J Harrison, Dr K J McEwan, Mr D B James, Mr J M Cruickshank, Dr J Zuclich, and Mr D J Lund.

REFERENCES

1. D. Sliney and M Wolbarst, Safety with lasers and other sources, Plenum Press.
2. S McGeoch et al, Design considerations for using optical limiters in sighting systems, these proceedings (1998).
3. J A Zuclich et al, Study of the variation of laser-induced retinal damage threshold with retinal image size, these proceedings, (1998).
4. D. B. James and K. J. McEwan, Bubble and refractive processes in carbob suspensions, these proceedings, (1998).
5. K. J. Mcewan and R. C. Hollins, in MRS Symposium Proceedings Series, Vol 374, Nov 1994.

HIGH-INTENSITY LASER-MATTER INTERACTIONS

JAN BONESS, RALF HILDEBRANDT, GERD MAROWSKY
Laser-Laboratorium Göttingen e.V., Hans-Adolf-Krebs-Weg 1,
D-37077 Göttingen, Germany

Abstract Recent experimental results obtained with high-intensity laser pulses are presented. Nonlinear studies on interfaces within organic light-emitting diodes, and studies on silicon surfaces are presented as well as higher-harmonic generation in high-Z materials with laser intensities exceeding 10^{19} W/cm². Two alternative approaches to the generation of such intensities are discussed.

Keywords: Organic LED, silicon, harmonic generation, ultrashort UV pulses

INTRODUCTION

The recent advances in high-power laser physics have given rise to a multitude of new phenomena and technical applications. High-power laser pulses with both low and high pulse energy are required for different experimental aims: The nonlinear analysis of systems with a low damage threshold requires high power pulses which possess low pulse energy. As shall be discussed below, this combination of high power and low energy per pulse provides for an intense nonlinear signal and at the same time prevents damage to the sample. On the other hand, recent discoveries would not have been possible without the use of laser intensities exceeding 10^{18} W/cm². Such high intensities can only be achieved with state-of-the-art laser systems in which theoretical limits to the peak power become important. In the following, both kinds of experiments shall be presented, and the inherent power limiting parameters shall be discussed.

NONLINEAR OPTICS: THE NEED FOR HIGH INTENSITIES

Optical second-harmonic generation (SHG) is a powerful tool for the investigation of surfaces and interfaces. The interface sensitivity results from the fact that SHG is, in the dipole approximation, forbidden in the bulk of centrosymmetric media. However,

even a centrosymmetric medium can be investigated by SHG if an external electric field is applied influencing its structure¹. This EFISHG-technique (electric-field-induced SHG) is outstandingly advantageous to the investigation of electrical devices since a time-resolution up to GHz is possible with ultrashort laser pulses².

As an example we demonstrate the EFISHG-technique with organic light-emitting diodes (LEDs) which have attracted close attention in scientific and industrial research due to possible applications in display-technology. Organic materials can be produced inexpensively, structured in almost any shape and size, and tailored to emit in any region of the visible spectral range. A major drawback, however, is the limited life of the device. The inset of Fig. 1 shows an organic LED³ based on the conjugated polymer poly-phenylene-vinylene (PPV).

The PPV-layer is about 300 nm thick and located between a transparent indium tin oxide (ITO) layer and an aluminium top-electrode. The LED thus possesses various interfaces. To probe these interfaces via SHG we use 8 ns laser pulses at 1064 nm emitted by a Nd:YAG-laser at 10 Hz repetition rate. The generated second-harmonic at 532 nm is detected by a photomultiplier after passing a monochromator. We have not detected any SHG from PPV on glass whereas, with a reverse bias voltage applied to the diode, EFISHG could be observed.

As shown in Fig. 1, the second-harmonic (SH) intensity depends quadratically on the applied bias voltage. The SH minimum should be located at the diffusion voltage $U_D = 1.8$ V where the effective bias at the PPV/aluminium Schottky contact is zero. The shift of the minimum towards a negative bias can be explained by the total SH signal being a coherent superposition of two signals originating from the Schottky contact, and from the ITO/PPV interface. The observed bias dependence can be used to monitor ageing of the diodes or switching processes.

The sensitivity of such investigations is limited by the threshold at which the aluminium layer or the polymer is destroyed by the laser. In order to increase the sensitivity and still avoid damage to the device, shorter pulses have to be used which also provide better time-resolution.

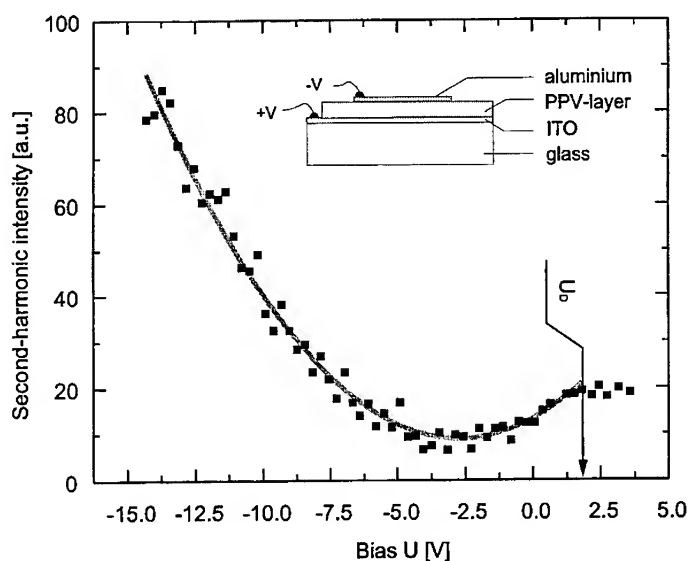


Figure 1: Dependence of the second-harmonic intensity on the applied bias voltage. Negative values imply reverse bias.

This can be seen as follows. The SH intensity is given by

$$I_{2\omega} \propto |\chi^{(2)}|^2 I_{\omega}^2 \tau \propto \frac{W_{\omega}^2}{\tau} \quad (1)$$

where $\chi^{(2)}$ is the second-order nonlinear optical susceptibility, τ denotes the pulse duration of the fundamental radiation, and I_{ω} and W_{ω} are the incident intensity and pulse energy. It is clear from Eq. (1) that by going from nanosecond to femtosecond pulses, thus shortening τ by six orders of magnitude, one can reduce the pulse energy by three orders of magnitude and still have the same SH intensity. Since destructive processes (ablation, desorption, etc.) are mainly governed by the pulse *energy*, using ultrashort pulses can be the only way to investigate delicate samples like adsorbate systems.

This is illustrated in Fig. 2. We have observed the symmetry of the Si(111)7x7 surface as prepared, and with different coverages of Na (not shown). The nonlinear

susceptibility of this surface is much smaller than that of the PPV samples described above. Therefore higher intensities are required in the experiments with Si, preferably at low pulse energies, lest the surface be damaged or the adsorbate desorbed.

The reconstructed surface was prepared by resistively heating the Si wafer material in a UHV chamber to about 1300 K. The native oxide was thus desorbed, and a clear 7x7 reconstruction was observed with LEED⁴. The laser beam was incident normal to the (111) surface.

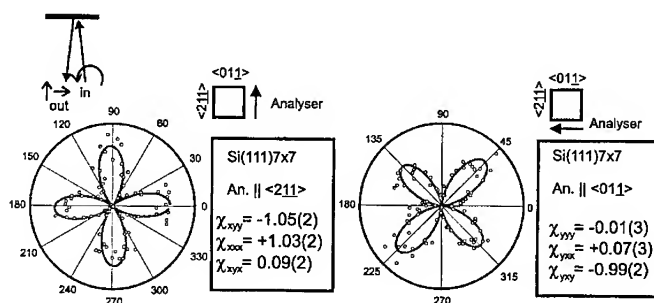


Figure 2: SH intensity plotted versus the azimuth of the input beam's electric field. Circles denote the experimental data and the solid line indicates the fit.

Figure 2 shows the SH intensity measured in two geometries, with the analyser parallel to the $[2\bar{1}\bar{1}]$, and parallel to the $[0\bar{1}\bar{1}]$ directions of the Si sample. In each graph the intensity is plotted versus the angle of the input beam's electric field, with respect to the $[0\bar{1}\bar{1}]$ direction. The values of the $\chi^{(2)}$ elements resemble the C_{3v} symmetry of the reconstructed Si(111)7x7 surface⁵. The SH generated in this geometry originates exclusively from the silicon surface, even if the surface becomes covered by a sodium film: The $\chi^{(2)}$ elements of the Na film are not excited at normal incidence. We have not observed any change in this rotational pattern for a coverage of up to two monolayers of Na. This means that the symmetry of the Si surface remains the same below the Na layer, viz., that the 7x7 reconstruction remains intact on the whole.

LIMITATIONS TO THE OPTICAL POWER

It was advantageous to use high power laser pulses with low *energy* per pulse in the experiments presented above. Before describing the experiments for higher-harmonic generation where pulses with both extremely high power *and* high energy are necessary, we shall briefly consider two crucial parameters in such experiments: the maximum power extractable from a certain laser or amplifier medium, and the highest focused intensity which can be obtained.

We define the *saturation fluence* F_{sat} (J/cm^2)

$$F_{\text{sat}} = h\nu / \sigma \quad (2)$$

Here $h\nu$ denotes the photon energy and σ the cross section for stimulated emission. Up to the saturation fluence⁶ the amplifier is considered to operate properly. Specifically, the inversion is depleted to one half of its small-signal value by the amplified pulse. This depletion becomes even more pronounced at fluences higher than F_{sat} and leads to an increasingly poor performance of the amplifier.

The minimum pulse duration τ attainable with any frequency bandwidth $\Delta\nu$ is given by $\tau \approx 1/\Delta\nu$ (apart from a constant on the order of 1, which depends on the pulse shape). Multiplying by the beam cross section A , we get the maximum extractable power per pulse:

$$P_{\text{sat}} = F_{\text{sat}} A / \tau = h\nu(\Delta\nu)A / \sigma \quad (3)$$

Since the focal cross section is about $\lambda^2 = (c/\nu)^2$, where λ is the laser wavelength, the focused peak intensity is approximately given by

$$I_{\text{max}} = h\nu^3(\Delta\nu)A/(c^2\sigma) \quad (4)$$

Equation (4) has several implications concerning the generation of high power laser pulses. First, it is desirable to use a laser medium with a large bandwidth and large cross section A . The large amplified bandwidth is crucial, since this limits the minimum pulse duration after compression and thereby the maximum power. Obviously, a laser medium with a large cross section A will emit more photons than a small one. Finally, the maximum intensity depends on the laser frequency *to the third power* due to the better focusability of short wavelength light! This means that, by going to a shorter wavelength, the accessible intensity can be tremendously increased.

Let us discuss some advantages and disadvantages of two approaches to generate high-power laser pulses: the chirped-pulse amplification (CPA) using an all-solid state laser system, and generation and amplification of UV pulses on the basis of KrF excimer systems.

Materials possessing an excellent saturation fluence (on the order of J/cm^2), like Ti:sapphire or Yb:glass, are used in all-solid state laser systems. With these materials high pulse energies can be achieved in a very compact system, i.e., *table top* in its true sense. However, when the intensity approaches about a GW/cm^2 , which can easily be the case for picosecond pulses, the refractive index of the laser medium becomes intensity dependent, and unwanted effects like self-focusing of the beam arise, resulting in damage to the system. To overcome this limitation, the CPA technique is employed: In this scheme, pico- or femtosecond pulses, being, for example, produced by a Ti:sapphire system, are first stretched into the nanosecond regime, then amplified, and afterwards recompressed. Thus the full energy storage capacity of the medium is utilised without exceeding the limit for self-focusing⁷⁻⁹. The inherent disadvantage is that before compression the beam diameter has to be increased to prevent damage to the final compression gratings, which have to be large and are therefore expensive. This cancels in part one advantage of the Ti:sapphire system, namely the small size of all stages up to the compressor. Antonetti *et al.* could produce $5 \times 10^{19} \text{ W}/\text{cm}^2$ with a system having a beam diameter of 50 mm inside the compressor¹⁰.

While solid-state laser systems employing the CPA technique can produce peak powers of several tens of terawatts¹¹, excimer-based short-pulse laser systems operate at a somewhat lower power level. However, in many experiments, not the power per pulse, but the *focused intensity* is the important parameter. Owing to their shorter wavelength, UV pulses from an excimer-based system can be focused onto a much smaller spot than the typical IR pulses from solid-state systems. Thereby, focused intensities comparable to those of a solid-state system can be achieved with a suitable KrF amplifier as Szatmári *et al.* have demonstrated recently¹². The input pulses for the KrF amplifier were generated by a hybrid excimer-pumped dye-laser system^{13,14}. It produced 150 μJ , 500 fs pulses at 497 nm. The second harmonic (248 nm) was generated by a BBO crystal and amplified via a special three-pass off-axis amplification scheme in a commercially available KrF amplifier^{12,15}. In this way diffraction limited

pulses with an energy of 15 mJ and a duration of 500 fs were produced. Owing to the special properties of the amplification scheme the input pulses were both homogenized and amplified optimally in the KrF amplifier. In addition, optical distortions by the laser medium are considerably smaller for a gaseous medium (KrF) than for a solid-state medium. Thus Szatmári *et al.* were able to focus the output pulses down to 480 nm FWHM. Consequently, the focus cross section was almost ten times smaller than the theoretical limit for, e.g., infra-red pulses from an Ti:sapphire system, and a focused intensity of 10^{19} W/cm² was obtained. The whole system including dye laser and KrF amplifier is also strictly of table-top size (2.5 m x 1 m).

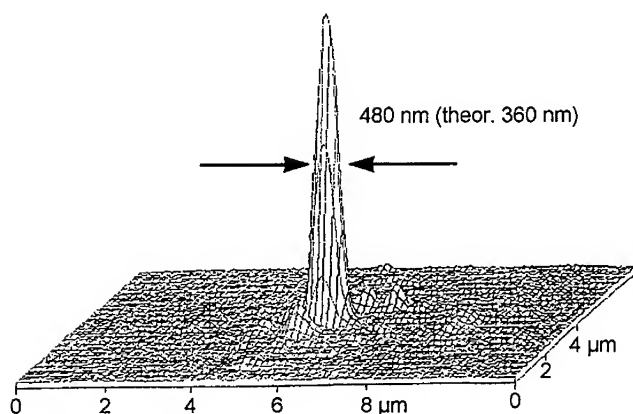


Figure 3: Intensity distribution of laser pulses at 248 nm focused with an $f/1.4$ parabolic mirror. The actual and the theoretical half-widths are shown.

COLLECTIVE ELECTRON EXCITATION BY ULTRASHORT LASER PULSES

Besides the laser power or the focused intensity, the laser wavelength itself can be a crucial parameter not only with respect to the focused intensity, but also concerning the possible excitations, even in ultrahigh intensity laser experiments. It is well known that UV laser pulses are often preferable to other wavelengths when structuring materials. In comparison to IR pulses, the ablation tends to occur with less melting of the

sample, thus producing structures with sharper contours. Furthermore, the minimum size of the structures, being determined by diffraction, is smaller for shorter laser wavelengths. But also for high harmonic generation, UV pulses seem to be preferable to IR pulses. Kondo *et al.*¹⁶ have generated high harmonics in a Xe cluster beam and demonstrated that the excitation mechanism is strongly wavelength dependent. They found that keV x-ray radiation could be generated much more efficiently with an excitation wavelength of 248 nm than with 800 nm.

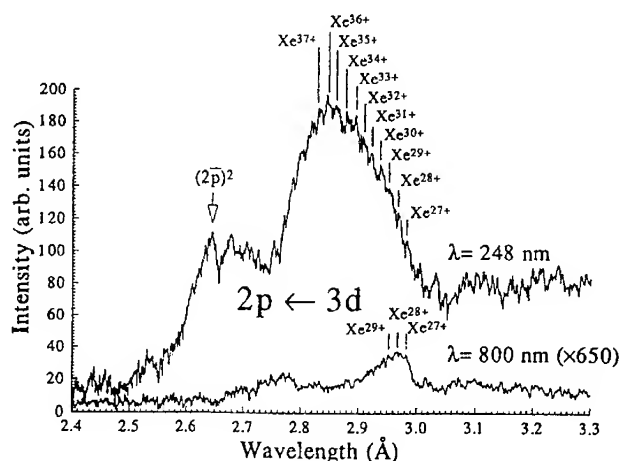


Figure 4: Xe(L) spectra produced by irradiation of Xe clusters with fs laser pulses at 248 nm and 800 nm. Note the stretched ordinate for 800 nm.

The pulse durations were 90 fs for the 800 nm pulses and 270 fs for the 248 nm radiation. The respective intensities inside the cluster beam were 1.4×10^{18} W/cm² (800 nm) and 1×10^{19} W/cm² (248 nm). The pulses at 800 nm were produced with a Ti:sapphire system, while for the generation of the terawatt pulses at 248 nm a hybrid system consisting of a first Ti:sapphire oscillator, a frequency-tripling stage, and two subsequent KrF amplifiers were used^{17,18}.

Figure 4 shows the x-ray intensity produced by irradiation of a Xe cluster beam¹⁶ by intense laser pulses at 800 nm and 248 nm. The x-ray spectra possess a rich struc-

ture due to transitions in Xe atoms in different degrees of ionisation. It is important to note that the ordinate has been stretched by a factor of 650 for the 800 nm data. The x-ray intensity is about 3000 times weaker for irradiation with IR pulses than for UV pulses, and the double vacancy $(2\bar{p})^2$ is not observed with the longer wavelength. These differences could not be explained simply by the UV intensity being ten times as high as the IR intensity. Kondo *et al.* argue that the 248 nm pulses can excite electrons collectively, while the IR pulses can only produce single-electron excitations. This is due to the electrons' dephasing time (1-2 fs) being longer than one oscillation of the electric field in 248 nm light, and consequently several electrons being driven in phase by the laser. This is not the case for 800 nm radiation. Kondo *et al.* conclude that, by using UV pulses, the matter under investigation can be excited by far more efficiently via a collective electron mechanism than by independent single-electron excitations. In this way the maximum energy transfer from the laser beam to matter can be considerably increased. In addition to this, Borisov *et al.*¹⁹ have observed that in similar experiments a channel is formed in the Xe cluster beam which compresses the incident light and guides it over a distance of some hundred micrometers. This was confirmed in a computer simulation by Pukhov and Meyer-ter-Vehn²⁰. The channel is caused by the light pressure displacing the electrons from the region of highest intensity, i.e., the centre of the laser beam. Due to the resulting change in plasma frequency, the refractive index increases in regions of higher intensity, and a waveguiding channel with a diameter of 1-2 wavelengths, determined largely by diffraction, is formed.

The experiments discussed above show that in future developments it may not be sufficient to maximize the power extractable from a laser system, but that it is worth considering how to transfer this power to the target material in the most efficient way. A proper choice of the laser wavelength can help to overcome the limits which seem insurmountable at less suited wavelengths.

ACKNOWLEDGEMENT

The authors wish to thank J. Jethwa for carefully reading the manuscript and P. Simon for helpful discussions.

REFERENCES

1. T. Dürre, R. Hildebrandt, G. Marowsky, R. Stolle. *Phys. Rev. A*, **56**, 4139 (1997)
2. O.A. Aktsipetrov, A.A. Fedyanin, E.D. Mishina, A.N. Rubtsov, C.W. van Haselt, M.A. Devillers, Th. Rasing. *Phys. Rev. B*, **54**, 1825 (1996)
3. M. Herold, J. Gmeiner, C. Drummer, M. Schwoerer. *J. Mat. Sci.*, **32**, 5709 (1997)
4. J. Boness, G. Marowsky, J. Braun, G. Witte, H.-G. Rubahn. *Surf. Sci.*, **402-404**, 513, (1998)
5. A. Yariv. *Quantum electronics* (J. Wiley, New York, 1975) 2nd Ed., Chap. 16
6. A.E. Siegman. *Lasers* (Univ. Sci. Books, Mill Valley, 1986), Chap. 7
7. M.D. Perry and G. Mourou. *Science*, **264**, 917 (1994)
8. G. Mourou. *Appl. Phys. B*, **65**, 205 (1997)
9. G. Mourou, C.P.J. Barty, and M.D. Perry. *Physics Today*, Jan. 1998, 22
10. A. Antonetti, F. Blasco, J.P. Chambaret, G. Cheriaux, G. Darpentigny, C. Le Blanc, P. Rousseau, S. Ranc, G. Rey, F. Salin. *Appl. Phys. B*, **65**, 197 (1997)
11. S. Seznec, C. Sauteret, S. Gary, E. Béchir, J.L. Bocher, A. Migus. *Opt. Commun.*, **87**, 331 (1992)
12. S. Szatmári, G. Almási, M. Feuerhake, P. Simon. *Appl. Phys. B*, **63**, 463 (1996)
13. S. Szatmári, F.P. Schäfer. *Optics Commun.*, **68**, 196 (1988)
14. S. Szatmári, F.P. Schäfer. *Appl. Phys. B*, **46**, 305 (1988)
15. M. Feuerhake, P. Simon, G. Almási, T. Nagy, S. Szatmári. *Appl. Opt.*, **36**, 4094 (1997)
16. K. Kondo, A.B. Borisov, C. Jordan, A. McPherson, W.A. Schroeder, K. Boyer, C.K. Rhodes. *J. Phys. B*, **30**, 2707 (1997)
17. B. Bouma, T.S. Luk, K. Boyer, C.K. Rhodes. *J. Opt. Soc. Am. B*, **10**, 1180 (1993)
18. F.G. Omenetto, K. Boyer, J.W. Longworth, A. McPherson, T. Nelson, P. Noel, W.A. Schroeder, C.K. Rhodes, S. Szatmári, G. Marowsky. *Appl. Phys. B*, **64**, 643 (1997)
19. A.B. Borisov, X. Shi, V.B. Karpov, V.V. Korobkin, O.B. Shiryaev, J.C. Solem, A. McPherson, K. Boyer, C.K. Rhodes. *J. Opt. Soc. Am. B*, **11**, 1941 (1994)
20. A. Pukhov and J. Meyer-ter-Vehn. *Phys. Rev. Lett.*, **76**, 3975 (1996)

THE SPECIFICATION OF LASER PROTECTION

VALERIE GROLIER-MAZZA
Thomson-CSF Optronique, rue Guynemer, BP 55, 78283 GUYANCOURT
CEDEX, FRANCE
valerie.grolier-mazza@tco.thomson.fr

Abstract: In this paper we describe the different stages necessary to specify the protection of optronic equipments against lasers.

Keywords : laser protection, optical limiting, systems

INTRODUCTION

Protection against lasers is an additional function that is to be integrated in the already elaborate architecture of optronic equipments. A critical trade-off has to be made between protection and functional impairment. Therefore, in order to avoid overprotection, the specification of protective devices against lasers must precisely take into account different parameters:

- the optronic equipment to be protected and whether the application is a ground, navy or airborne one,
- the laser threat,
- the scenario of engagement,
- the effects of the laser on the detector,
- the acceptable performance losses,
- the integration constraints.

Optronic equipments are used by infantrymen and can be found on different platforms on the battlefield (infantrymen, helicopters, tanks, aircrafts, missiles, ships) for many purposes :

- observation
- reconnaissance
- navigation

- fire control.

In order to detect objects at long distances and to bring complementary information to direct observation, optronic equipments use all the transparency windows of the atmosphere: visible-near infra-red (IR) region between 0.4 μm and 1.4 μm ; IRI window between 1.5 μm and 2.7 μm , IRII window between 3 μm and 5.8 μm and IRIII window between 7.5 μm and 14 μm .

The laser propagation through the atmosphere is a major issue to assess the range of laser systems; its modeling implies a precise knowledge of the chemical components of the atmosphere and of the mechanisms of interaction with light: absorption, scattering, scintillation.¹ In the following, we assume for simplicity that the propagation can be characterized by an exponential decay with an atmospheric attenuation coefficient depending upon the weather, the geographical location, the climate.

The equipments

In the visible-near IR window, we can distinguish two classes of equipments.

In direct vision equipments the human eye is the detector and looks through a magnifying optics (goggles) or simply an image transport optics (episcopes, periscopes).

Indirect vision systems make use of solid detectors, image intensifiers or Si matrices, and provide either night vision capacities or near IR vision for reconnaissance. In the IR II and IR III ranges, the thermal emissivity of objects is used to build an image that will be exploited by an IR seeker or by a fire control system. The detection is ensured by cooled Mercury Cadmium Telluride (MCT), InSb, Multiple Quantum Wells or by uncooled IR detectors.

The laser threat.

Compared to classical weapons, the laser presents many advantages: energy travels at the speed of the light and its range can be as high as a few kilometers at the ground level. Moreover, the fast deflexion of the beam makes of the laser a multitarget weapon.

If the laser output wavelength lies within the transparency window of the optronic equipment (in-band), this latter, due to the concentration power of the optics, is focused onto the detector, leading to very high fluences. In this case medium output energies (<1J) are sufficient to disturb significantly the system.

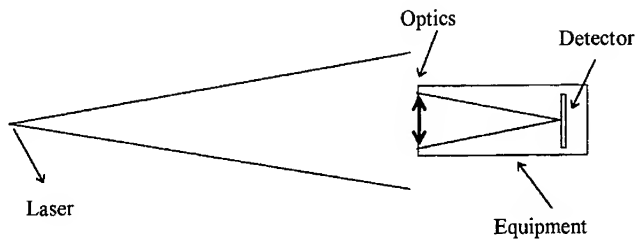


FIGURE1 : Representation of a low energy counter measure system.

Low energy laser threats can be either sophisticated countermeasure systems performing detection, tracking (eventually via cat's eye effect), accurate pointing and firing. In the short term, range finders, illuminators or lab lasers could cause accidents due to hazardous uses.

Another strategy can be chosen, in which the laser is used to destroy not the detector but the front optics or the structure of the equipment: adaptive optics and high output energies ($>1\text{kJ}$) are then necessary to compensate the turbulence effects and to obtain the proper beam shape able to reach the target with sufficient energy density (figure 2).

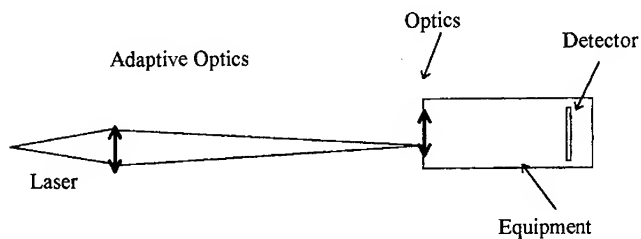


FIGURE 2 : representation of a high energy counter-measure system

In the following only low energy lasers will be considered.

Laser sources were developed for different applications in each transparency window of the atmosphere; moreover, nonlinear optical operations enable now to tune continuously

the output wavelength in very large ranges. Tables 1, 2, 3 summarize the main laser sources that can be seen as potential threats for optical equipments.

TABLE1 : Laser threats in the visible near IR region.

Laser type	Wavelength (μm)
Nd: YAG	1.064
Nd: Glass	1.06
Nd: YAG * 2	0.532
Ruby	0.694
Excimer +Raman	0.48
Ar	0.488-0.514 (lines)
Kr	0.407-0.8 (lines)
Diodes	0.7-0.9
Alexandrite	0.7-0.8 (continuously)
Dyes	0.4-0.7 (continuously)
Ti: Sapphire	0.65-1.1 (continuously)
OPO	0.4-2 (continuously)

TABLE 2 : Laser threats in the mid IR

Laser type	Wavelength (μm)
CO ₂ *2	4.5-5.6 (lines)
CO	4.6-5.2 (lines)
HF/DF	2.7/3.8
He-Ne	3.39
OPO	3-5 (continuously)

DAMAGE THRESHOLDS

The eye

Ocular media are transparent at wavelengths between 0.35 μm to 1.3 μm whereas the spectral responsivity is maximum around 0.55 μm in daylight conditions and vanishes

below 0.4 μm and above 0.7 μm . This means that the eye can be hurt by an invisible beam.

TABLE 3 : Laser threats in the far IR

Laser type	Wavelength (μm)
CO2	9-11.2 (lines)
OPO	8-12 (continuously)

The retinal damage threshold arises from photo-chemical processes in the retinal cells and depends on several parameters: the image size, the incidence of the incoming laser beam, the pulse duration and repetition rate, the photopigment concentration. Experimental studies are underway ² to understand these interactions thanks to a very precise knowledge of the optics and of the physiology of the eye.

Today protection standards exist ^{3,4} that define the maximum permitted exposure (MPE) at the entrance of the pupil; for example, the $\text{MPE} = 0.5 \mu\text{J}/\text{cm}^2$ for ns pulses at a wavelength of 0.5 μm .

Solid state sensors

For solid state sensors, there is a large dynamics between the saturation level of one pixel and the destruction level (typically 7 orders of magnitude for Si detectors). Between these two limits, the response of the detector is correlated to the read-out electronics. The mechanism responsible for damage depends on the pulse duration (figure 3). Below 1 ns, high power densities can be reached, leading to electrical breakdown. Above 1 ns, the damage originates from thermal effects that are fluence dependent as long as the pulse duration is smaller than the thermal time constant to become power density dependent above ⁵.

Few experimental data are available about image intensifiers and uncooled IR detectors. Image intensifiers are very sensitive to overilluminations and some $10 \text{ mJ}/\text{cm}^2$ is a reasonable assumed value.

Uncooled IR detectors are designed to have very good thermal insulation and we can expect lower damage thresholds than quantum detectors. This threshold is very specific of the architecture of the detector: structure, materials, thermal insulation.

Table 4 represents the damage thresholds of classical detectors^{6,7}

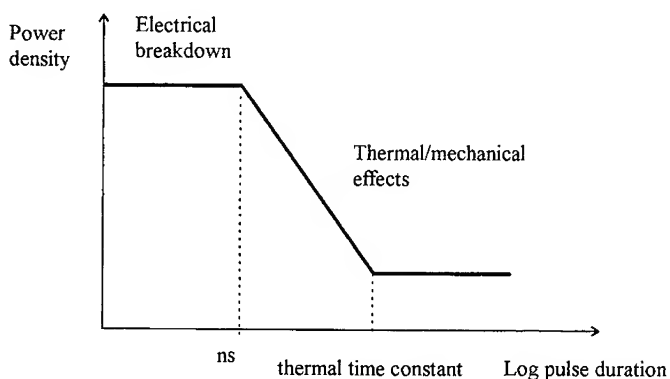


FIGURE 3: Detector damage threshold versus pulse duration

TABLE 4: Damage thresholds of detectors used in optronic equipments

Detector	Damage threshold
Si	J/cm ²
Light Intensifiers (LI)	some 10 mJ/cm ² assumed
InSb, MCT	some J/cm ²
Multiple Quantum Wells	some 10 J/cm ²
Uncooled IR detectors	< InSb, MCT

Range assessment

At this stage it is possible to perform range assessments, knowing the equipment to protect, the laser threat, the atmospheric propagation and the characteristics of the optical system and of the detector. Figure 4 and 5 show range assessments in the visible/near IR region and in band III.

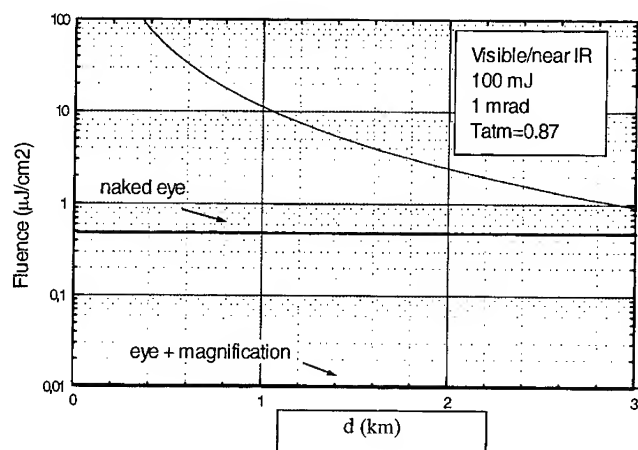


FIGURE 4: Range assessment in the visible-near IR region; the total divergence of the laser is 1 mrad, the atmospheric transmission is written (T_{atm}), d is the distance (km).

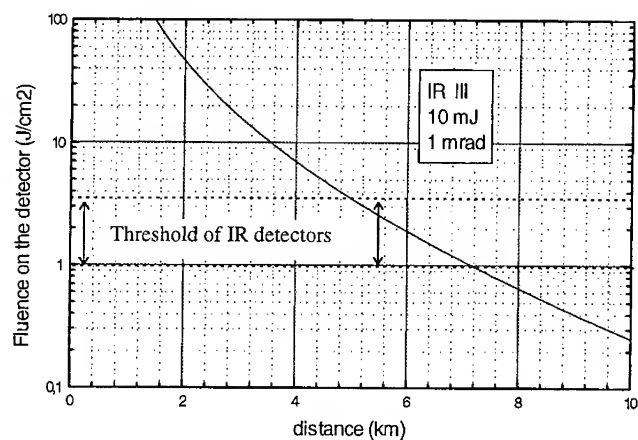


FIGURE 5: Range assessment in the band III; the total divergence of the laser is 1 mrad; $T_{atm} = 0.78$.

Therefore, these kinds of lasers are dangerous at distances corresponding to the ranges of classical weapons.

Protection level

The protective device must ensure that the energy reaching the detector or the eye is smaller than the threshold; the transmission of this filter must be smaller than a limit law T_{lim} whose shape is given on figure 6

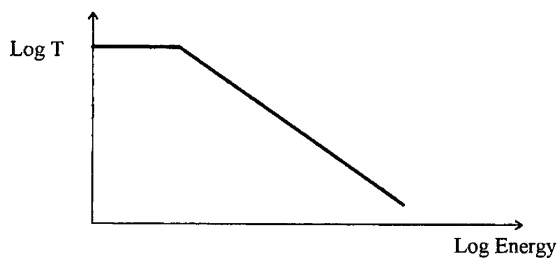


FIGURE 6 :Representation of the transmission law T_{lim} .

For small energies there is no risk of destruction: the transmission is equal to unity. Above the energy necessary to destroy the detector, T_{lim} can be written as:

$$T_{lim} = \frac{K}{E}$$

where K depends on the characteristics of the optical system: transmission, lens parameters, damage or dazzle threshold.

Therefore, the protection issue can be addressed in terms of either material optimization and/or optical design.

The condition $T < T_{lim}$ cannot be fulfilled for all energies and the validity range of this relationship is given by the range assessment. As an illustration, figure 7 shows the required optical density to protect a magnifying system (x 8) for the same condition as in fig.4. The maximum protection level depends on the safety distance and on the output energy of the laser: OD=2.2 at 2 km and OD=3.5 at 500 m.

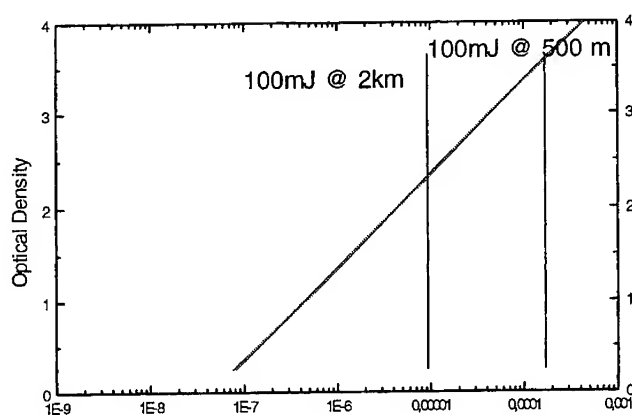


FIGURE 7: Required optical density to protect a magnifying system (x8) in the visible-near IR region.

Protection specifications

The response time of the protection device must be compatible with the pulse duration of the laser threat; in the short/mid term, this latter will operate in the ns - μ s range. In the long term, ultra-short pulses (ps or fs) could appear on the battlefield. The protection must be efficient in the whole field of view of the equipment, typically more than 50 degrees for naked eyes and 10 degrees for goggles and thermal imagers. In the short term, the main need is protection against fixed line lasers, whereas in the mid term, tunable filters will be necessary. Beside these specifications of the protection level, its angular acceptance, its spectral bandwidth, other specifications should be kept in mind as soon as the design of the filter has begun.

The integration of an extra optical component may impair the functional performances of the equipment. It is therefore necessary to know the acceptable transmission losses; in the IR range, absorption of the filter will cause an increase of the thermal background and of the noise. For the eye, two parameters must be considered, the integrated visual photopic transmission (IVPT) and the color of the filter: to what extent the changes of the pupil size can compensate the transmission losses without

significantly impairing visual acuity, to what extent the color disturbs infantrymen or pilots. Moreover, the optical quality of the filter must be as good as possible in terms of flatness, homogeneity, so as not to reduce the modulation transfer function of the equipment. Alike any component of an optronic equipment, the protection must meet some requirements (defined by military standards) regarding lifetime, sensitivity to vibrations, to radiations, temperature range for use and/or for storage, typically -40°C $+70^{\circ}\text{C}$ for ground applications.

If all these specifications are a prerequisite for integration in an optronic equipment, other optional requirements must be considered : stealthiness, protection against other threats than lasers (for example microwave weapons), possible retrofit of existing equipments and cost.

CONCLUSIONS

In the short/mid term, the laser threats than can be found on the battlefield are numerous and their possible output wavelengths cover the whole atmospheric transparency windows. Moreover their output energies are sufficient to cause permanent blindness of the eye or of the detectors at a few kilometers, not to mention dazzling.

There is therefore a strong need for protection that must be efficient against dazzle and destruction, which requires the implementation of different types of solutions: optical filters, image processing, detector optimization. If the achievement of high protection levels is the main concern when designing protective devices, other requirements should be kept in mind that ensure the best performances of the equipment and its conformity with military standards.

ACKNOWLEDGMENTS

The author thanks the French Ministry of Defense for supporting the work in laser protection; the author is also grateful to J. Jeanrot, J. Tabourel and O. Durand from the Scientific Department of Thomson-CSF Optronique for helpful discussions.

REFERENCES

1. M. E. Thomas, D.D. Duncan, Infrared and Electro-optical Systems handbook, Vol 2 Atmospheric Propagation of Radiation, F. Smith editor, SPIE Press (1993).
2. J.A. Zuclich, D. Lund, P.R. Edsall, R.C. Hollins, B.E. Stuck, L.N. McLin , in this proceedings, 1998.
3. D. H. Sliney and W.L. Wolbarsht, Safety with lasers and other optical sources (Plenum Publishing Corp. New York, 1980).
4. Laser safety standards US: ANSI Z1136.1-1993 (1993), ANSI Z136.2-1997 (1997) Europe: IEC 60825-1 (1994).
5. F. Bartoli, L. Esterowitz, M. Kruer, R. Allen, J. of Appl. Phys. **46**, 4519 (1975)
6. C. Zhang, S. E. Watkins, R. M. Walser, M. F. Becker, Optical Engineering **30** 651, (1991).
7. SPIE vol. 1105, Materials for Optical switches, Isolators and limiters (1989).

NONLINEAR OPTICAL LIQUID CORED FIBER ARRAY AND LIQUID CRYSTALLINE FILM FOR OPTICAL LIMITING OF FREQUENCY AGILE PICOSECOND PULSED - CW LASER

I. C. KHOO, M. V. WOOD, P. H. CHEN and M. Y. SHIH
Department of Electrical Engineering
Pennsylvania State University
University Park, PA 16802
USA

Abstract We have developed compact millimeter thick optical fiber arrays with nonlinear optical liquid guiding core. The fiber arrays are capable of high quality image transmission of scenery, while providing protection of the eyes and sensors against frequency agile lasers short pulses [nanosecond -picosecond] in the visible spectrum. In this paper, we present the theoretical model for the various linear and nonlinear absorption processes and nonlinear propagation of short laser pulses in the constituent fiber cores. We also discuss how a recently discovered extremely nonlinear response of nematic liquid crystal film may be employed for limiting action on longer pulse or cw lasers with nanowatt threshold power.

INTRODUCTION

Various optical, electro-optical and nonlinear- optical materials [1] and devices have been investigated for the purpose of protecting the eye and optical sensor from lasers. In order to achieve the desired limiting performance characteristics, the nonlinear material or device has to be placed at the focal plane of the optical system where the laser energy fluence is intensified. In such optical systems involving focused optics, the gain defined by the ratio [intensity at the focal plane]/[input intensity to the optical system] is typically in the range of 10^5 - 10^6 . However, as a result of diffraction, the interaction length in such tight focusing configuration is rather short. Consider for example a Gaussian beam with a focused diameter of 5 μm , the interaction length as measured by the Rayleigh range is only 0.0625 mm, c.f. Table 1.1. Such short interaction length severely limits the performance of the

material or device.

Table 1. Fiber Array Optical Characteristics and Working Parameters

Fiber Core Diameter (Index $n_{\text{core}} = 1.54$)	30 μm	10 μm	5 μm	
	[better image resolution for smaller core diameter]			
Numerical Aperture ($n_{\text{cladding}} = 1.53$)	0.1752	0.1752	0.1752	
($n_{\text{cladding}} = 1.45$)	0.519	0.519	0.519	
Acceptance angle (degrees)	20.18	20.18	20.1	$n_{\text{cladding}} = 1.53$
	62.5	62.5	62.5	$n_{\text{cladding}} = 1.45$
# of Modes	393	43	10	$n_{\text{cladding}} = 1.53$
	3448	383	95	$n_{\text{cladding}} = 1.45$
Interaction Length				
Fiber	(3 mm - 7 mm or longer; independent of core diameter)			
Bulk	2.25 mm	0.25 mm	0.0625 mm	
	(Rayleigh range for focused Gaussian Beams)			

We have developed a patented fiber array optical limiting device [2,3] where the guided wave geometry allows a long interaction length limited only by practical weight/size consideration. As illustrated in Fig.1, the fiber array is positioned within an optical

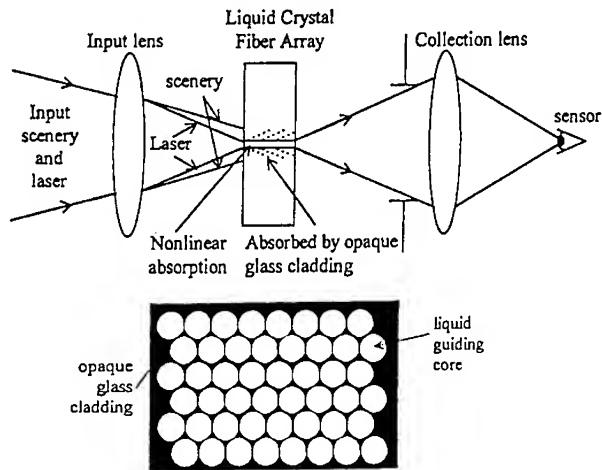


Fig. 1 Nonlinear Fiber Array in Imaging Optical Set Up for Sensor Protection.
Lower figure depicts the front cross-sectional view of the array.

system such that its entrance plane coincides with the image plane of the input optical system. The scenery from a large field of view is imaged onto an input plane area covering many (several thousands) constituent fibers; on the other hand, a threat laser originating from a distant point source is brought to a focused spot size on the order of the diameter of a single constituent fibers. By optical waveguiding, the image is transmitted to the exit end and viewed by the detection optics.

One seldom mentioned advantage of fiber array over bulk films is that in bulk films, the optical limiting thresholds are highly dependent on the location of the laser focal plane. A small shift in the focal plane will cause a tremendous increase in the transmission from the intended minimum setting. On the other hand, the construction of the fiber array is such that if the focal plane is shifted, the input threat laser will not be imaged onto the input plane of the array, and so practically no light will be coupled into the fiber core and the threat laser's transmission will be greatly attenuated by the opaque cladding.

Another advantage of the fiber arrays is that they are not likely to suffer catastrophic damage caused by intense laser radiation. A threat laser, which basically originates as a distant point source, will appear as a point spread function on the input plane. Therefore, if it is intense enough to cause material damage there, it will be manifested as a hardly noticeable pin-prick blemish in the field of field. The dynamic range of the fiber array is therefore as large as the optical system in which it is deployed would allow.

In the next few sections, we present a review of the nonlinear fiber core molecular photonic processes and the nonlinear guided wave propagation and limiting effect. We also give a summary of the limiting results obtained with picosecond -nanosecond laser pulses. We also point out recent optical limiting effects on ms - long pulse laser using thin nematic liquid crystal films where the threshold is an unprecedented 70 nanowatt.

NONLINEAR FIBER CORE MOLECULES

Among the various core liquids we have studied, we shall consider two exemplary systems. One is a commercially available isotropic liquid crystal mixture ILC [3-5], and the other is a liquid L34 synthesized at Penn State. ILC is a mixture of four organics [two nematics and two isotropic liquids], with molecular structures as shown in **fig. 2a**. The mixture is colorless, with a refractive index $n = 1.54$ [at 532 nm] and a linear loss constant of $\sim 0.1 \text{ cm}^{-1}$; owing to orientational fluctuations, ILC does incur a sizable scattering loss of $\sim 1 \text{ cm}^{-1}$. L34 is a single constituent liquid with the molecular structure shown in **figure 2b**. Its refractive index is 1.61 and its pure form is also colorless. The absorption constant at 532 nm of L34 is $< 0.5 \text{ cm}^{-1}$. **Figure 2c** shows the linear absorption spectrum of pure L34. The linear absorption band around 300 nm translates into the observed two-photon absorption in the visible spectrum [$\sim 400 \text{ nm} - 700 \text{ nm}$]. Studies of these and other similar isotropic liquid crystals [6-9] have shown that the

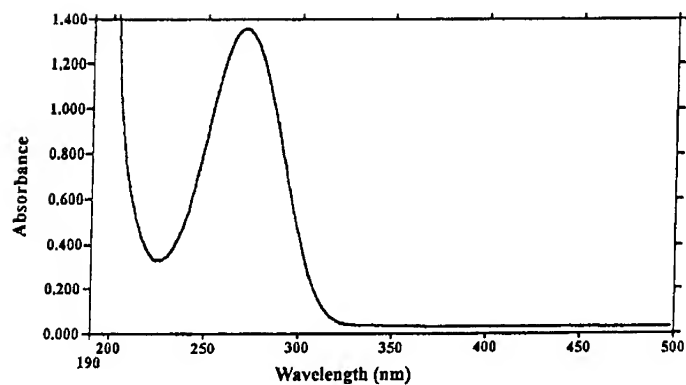
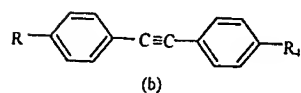
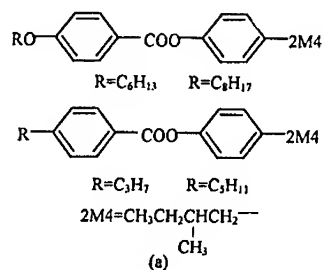


Fig. 2 (a) Molecular structures of the 4 components of ILC mixture. (b) Molecular structure of L34. (c) Linear absorption spectrum of L34.

relevant molecular photonic absorption processes may be described by a model as depicted in **Figure 3**. The ground state 1 is connected by a two-photon transition to the excited state 2. Picosecond laser pulse pump-probe studies [8] of ILC have shown that the direct two-photon accessed state rapidly relaxes, in time 1 psec, to the the excited state 2. The excited state 2, which relaxes in a time scale of about 30 ns [8], is connected to other high lying excited state manifolds by single photon absorption cross sections σ_{exc} that can be much larger than the ground state counterpart σ_g ; such Excited State Absorption [ESA] effect will enhance the optical limiting process initiated by the two-photon absorption.

The intermediate states are made up of the high lying ro-vibrational manifold of the ground state. They could enhance the two-photon transition either by providing single-photon 'resonance' or the so-called Reverse Saturable Absorption [RSA] effect. In typical RSA molecular systems such as Fullerene C_{60} [10] and Phthalocyanines [11], the single photon transition cross-section σ_i from the intermediate state to the excited two-photon state is much larger transition than the ground to intermediate state transition σ_g . To study how intermediate-state absorption may affect the optical limiting action, we also studied ILC doped with C_{60} .

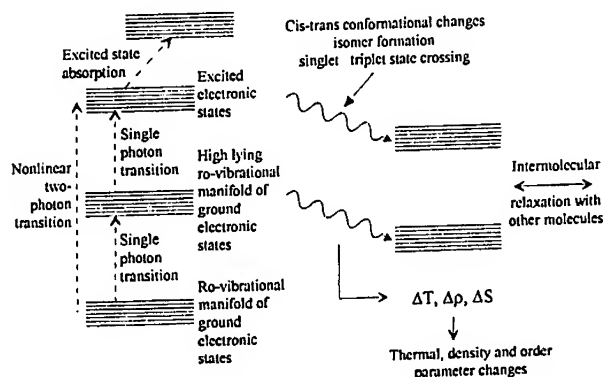


Fig. 3. Schematic depiction of two-photon, sequential-, and excited-state absorption processes, intersystem crossing, and other processes occurring in the core molecule.

The actual molecular level structures of these molecules are of course much more complex than the one depicted here. The photo-excited states, for example, could undergo intersystem crossing, cis-trans or other conformational changes, and form isomers or charge transfer complexes as in Fullerenes or Phthalocyanines. These processes become important at longer time scales, as in the case of dye-doped liquid crystalline film under ms - cw laser illumination [9,12] which we will discuss at the end of this paper; they could be neglected, however, in the nano- pico second time scale. Even with this simplification, the molecular model shown here has incorporated several highly efficient optical limiting mechanisms [TPA, RSA, ESA].

NONLINEAR ABSORPTIONS

Accounting for all the linear and nonlinear absorption processes, the rate equations for the molecular level population densities are given as follow:

$$\begin{aligned} dN_2/dt &= (\sigma^{(2)} I^2 / 2h^2 \nu^2) N_1 - N_2/\tau_{21} - N_2/\tau_{2i} - N_2 \sigma_{exc} I/h\nu + N_i \sigma_i I/h\nu \\ &= (\beta I^2 / N_0 2h\nu) N_1 - N_2/\tau_{21} - N_2/\tau_{2i} - (\alpha_{exc} / N_0 h\nu) N_2 I \\ &\quad + (\alpha_i / N_0 h\nu) N_i I \end{aligned} \quad (1)$$

$$dN_i/dt = N_1 \sigma_g I/h\nu + N_2/\tau_{21} - N_i/\tau_i - N_i \sigma_i I/h\nu \quad (2)$$

$$dN_1/dt = N_2/\tau_{21} + N_i/\tau_i - (\beta I^2 / N_0 2h\nu) N_1 - \sigma_g N_1 I/h\nu \quad (3)$$

where N_0 is the total molecular number density; $N_{1,2,i}$ are the respective level population densities; σ_g , σ_i , σ_{exc} are the ground-, intermediate and excited-state linear [one-photon] absorption cross sections, respectively; $\sigma^{(2)}$ is the ground-state two-photon absorption cross section. These σ 's are related to the corresponding single- and two-photon absorption constants α 's and β by:

$$\alpha_g = N_0 \sigma_g; \alpha_{exc} = N_0 \sigma_{exc}; \alpha_i = N_0 \sigma_i; \beta = (N_0 / h\nu) \sigma^{(2)} \quad (4)$$

NONLINEAR PROPAGATION AND LIMITING

Consider the propagation of the laser pulse through the fiber core. Because of the large index difference between the liquid crystal core and the glass cladding, and the relatively large core diameters, these fibers operate in the multimode regime, c.f. Table 1.1. The intensity distribution, and therefore the molecular level densities $N_{1,2,i}$ within the fiber core are radially uniform. i.e., they are thus functions of the propagation distance z into the

fiber.

There are two distinct types of intensity dependent propagation losses in the fibers, namely, (i) nonlinear photonic absorptions in the core liquids, and (ii) nonlinear scattering and core--> cladding loss caused by laser induced thermal and density fluctuations in the core. In the picoseconds regime, thermal/density effects are absent [3.9], and the limiting processes are caused mainly by the nonlinear absorptions. On the other hand, if the laser pulse length is in the nanoseconds or longer time scale, thermal and density effects will also be involved. The process of propagation loss from the fiber core due to the thermal/density effects has been treated previously [5]. In this paper, we shall discuss further the effects of ESA and RSA and TPA in the picosecond -nanosecond time regime.

Accordingly, the intensity of the laser in the fiber core is given by:-

$$dI/dz = -\alpha_g(N_1/N_0) I - \alpha_i(N_i/N_0) I - \beta(N_1/N_0) I^2 - \alpha_{exc}(N_2/N_0) I \quad (5)$$

Since the N's and I are both functions of time and the propagation distance z., the solutions of equations (1)-(5) are quite complicated. Nevertheless, we can obtain some analytically explicit forms for I and N's for the realistic case where the ground state is not significantly depopulated. We thus have $N_1 \sim N_0$, $N_2/N_0 \ll 1$, and $N_i/N_0 \ll 1$. We start by inserting the first order solution for $I(t;z) \sim I(z)$ into equations (1)-(4), and solve for the level population densities $N_1(t;z)$, $N_i(t;z)$ and $N_2(t;z)$. The solutions for N's are then inserted into the equation (5) to assess the effects of molecular excitations in the dynamical core transmission and limiting processes. Details are presented in reference [3]. In particular, we showed that equation (5) becomes in the case of negligible ground state depopulation:

$$dI/dz = -\alpha_g I - (\alpha_i - \alpha_g) I C t - \beta I^2 - (\alpha_{exc} - \alpha_g) I B t \quad (6)$$

where

$$B = \beta I^2 / N_0 2h\nu; \quad C = \sigma_g I / h\nu = \alpha_g I / N_0 h\nu \quad (7)$$

for $0 < t < \tau_p$, the laser pulse duration. Note that both Bt and Ct are $\ll 1$ since $N_1 \gg N_2$, N_i . Since $B \sim I^2$ and $C \sim I$, the second and fourth terms on the RHS of (8) varies as I^2 and I^3 , respectively. We can therefore rewrite equation (6) as:

$$\begin{aligned} dI/dz &= -\alpha_g I - [\beta + (\alpha_i - \alpha_g) \sigma_g t / h\nu] I^2 - (\alpha_{exc} - \alpha_g) t \beta I^3 / N_0 2h\nu \\ &= -\alpha_g I - \beta_{eff} I^2 - \gamma_{exc} I^3 \end{aligned} \quad (8)$$

This equation may be further integrated w.r.t. time to yield a similar equation in the laser fluence and the laser pulse width.

The second term on the R.H. S. of equation (8), namely, $(\alpha_i - \alpha_g)\sigma_g t/\hbar\nu$ is the contribution from the intermediate state absorption, and it gives rise to an effectively larger two-photon absorption coefficients $\beta_{\text{eff}} = \beta + (\alpha_i - \alpha_g)\sigma_g t/\hbar\nu$ if $\alpha_i > \alpha_g$. The last term, arises from the excited state absorption.

If two-photon and intermediate absorptions are the main contribution mechanisms, i.e., we have:

$$dI/dz = -\alpha_g I - \beta_{\text{eff}} I^2 \quad (9)$$

The solution for the transmitted intensity $I(L)$ in a fiber of length L is given by

$$I(L) = \alpha I(0) / [\alpha e^{\alpha L} - \beta_{\text{eff}} I(0)(1 - e^{\alpha L})] \quad (10)$$

where $I(0)$ is the input laser intensity. We have also replaced α_g by α to include other linear losses such as scattering, i.e., $\alpha_g = \alpha_g + \alpha_s + \dots$

Notice that for large I , such that $\beta_{\text{eff}} I^2 \gg \alpha I$, the transmitted intensity is held at a constant value $I_{\text{clamped}}(L)$ given by:

$$I_{\text{clamped}} = 1/\beta_{\text{eff}} L. \quad (11)$$

In ILC cored fibers, the dominant contributing mechanism is TPA and indeed the above relationship is observed [3], c.f. fig. 4. If excited absorption is significant, the $\gamma_{\text{exc}} I^3$ term in equation will come into play, the clamped transmitted intensity is further reduced. This is observed in the case of C_{60} -doped ILC fibers [3].

EXPERIMENTAL RESULTS

The experimental set up used for evaluating the optical limiting performance of the nonlinear fiber is similar to those used before [4]. Two Nd: Yag laser systems operating at $\lambda = 532$ nm were used. The FWHM pulse widths of the laser pulses from these systems are 20 ns and 66 ps, respectively. The laser is expanded to a diameter of 2 mm or 4 mm and is focused by a 1.2 cm focal length lens into the fiber. The collection optics is adjusted accordingly to match the input F#s, in this case ranging from F3 to F6. The input, transmitted laser pulse energies, and the normalized transmission are measured with a Molelectron ratiometer.

In general, the transmitted laser energy shows a typical limiting behavior, with the output clamped at an almost constant value for high input laser, c.f. Fig. 4. The thresholds and clamped transmission are all below the eye/sensor damage level, showing that the nonlinear cored fiber array is effective for protection against the picosecond laser pulses. Using equations 10, the effective nonlinear absorption constants β_{eff} for ILC and L34 are obtained. These picosecond laser pulse limiting results are summarized in Table 2.

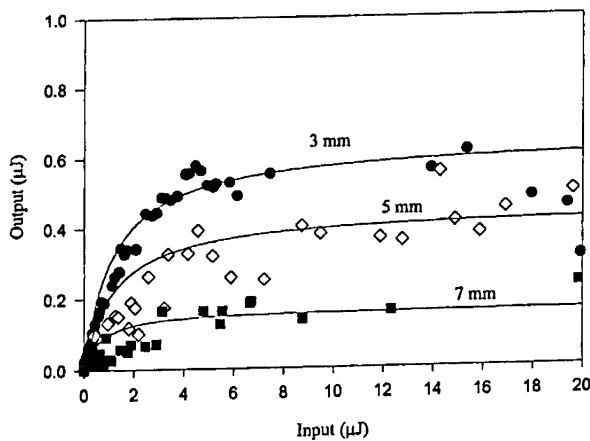


Fig. 4 Picosecond laser pulse limiting results through ILC cored fibers for various fiber lengths. F6 collection optics. Solid lines: analytical solution using equation 10.

Table 2. Optical Limiting Results-Picosecond Laser Pulses

Core Materials	ILC	ILC+C60	L34
	[Fiber length: 5 mm; Core-diameter: 30 μm ; [F3-F6 optics]		
Transmission	80%	60 %	70 %
Limiting thresholds energy fluence (at focal plane)	<0.1 μJ	<0.1 μJ [<0.12 J/cm ²]	<0.1 μJ
Clamped output energy fluence (at focal plane)	0.3 μJ 0.04 J/cm ²	0.2 μJ 0.03 J/cm ²	0.2 μJ 0.03 J/cm ²

In Table 3, we compare the β_{eff} values obtained in our study with other studies [8,13] of isotropic liquid crystals with picosecond laser pulses. Higher β_{eff} values obtained here are most likely due to the RSA effects and larger TPA absorption efficiencies as well as the longer laser pulse length [66 ps in our case] used. Among these liquids, L34 appears to be the best nonlinear fiber core liquid because of the low scattering loss and large β_{eff} , and yields exceptional optical limiting performance in the picosecond as well as the nanosecond time regime, c.f. next section.

Table 3 : Comparison of effective two-photon absorption coefficients

Materials	Effective β in cm/GW	pulse width
Fiber [this study, ref. 3]		
ILC	~ 1	[66 ps]
L34	~ 10	[66ps]
ILC + C60	~ 5	[66 ps]
Bulk [ref. 13]		
ETBBA; IPBBA; BBIPA	~ 0.55	[30 ps]
PEBBA; MEBBA		
Bulk [ref. 8]		
Mixture of 4 isotropic liquid crystals	~ 0.21	[1.5 ps]

Nanosecond Laser pulse limiting

Consider now optical limiting action in the nanosecond time scale. For a given laser fluence [energy per unit area], the corresponding laser intensity is lower if the pulse duration is longer and greatly diminishes the nonlinear absorption processes, which vary as I^2 and I^3 . For $\beta = 10$ cm/GW and a fiber length L of 5mm, for example, I_{clamp} is ~ 0.2 GW/cm², c.f. equation (11). This corresponds to a laser fluence of 4J/cm^2 for a 20 ns laser pulse, or a laser energy of $36\mu\text{J}$ over the $30\mu\text{m}$ diameter fiber. In other words, the 5 mm long fiber will not be able to provide limit nanosecond laser pulses $< 1\mu\text{J}$ with nonlinear absorption mechanisms alone. In previously reported studies [5], we show that indeed the ILC cored fiber length required to clamp the output to $\sim 1\mu\text{J}$ is over 3 cm.

If the core liquids are slightly absorbing due to intermediate absorption as in the case of L34], or possess RSA capability [the C60-doped ILC], the enhanced nonlinear absorptions and the resulting thermal/density effects will provide the needed mechanism to reduce the clamped output. Experimentally, the L34 and the C60-doped ILC cored fibers

are found to provide the lowest clamped outputs of $\sim 1 \mu\text{J}$, corresponding to a fluence value of 0.1 J/cm^2 for a fiber core diameter of $30 \mu\text{m}$, c.f. **Table 4**. These values are below the eye/sensor damage-level.

Table 4. Optical Limiting Results for 20-Nanosecond Laser Pulses

Core Liquids	ILC+C60	L34
Fiber length	5 mm	5 mm
Core-diameter	$30 \mu\text{m}$	$30 \mu\text{m}$
Transmission [corrected for reflection losses]	50%	70%
Limiting thresholds energy	1.1 μJ (F6 optics); 1.4 μJ (F3 optics)	
fluence (at focal plane)	0.12 J/cm^2 (F6) 0.15 J/cm^2 (F3)	[similar]
Clamped output energy	$\sim 1 \mu\text{J}$ (F6); 1.3 μJ (F3)	[similar]
fluence (at focal plane)	0.11 J/cm^2 (F6) 0.14 J/cm^2 (F3)	[similar]
Damage Mechanism (Frontal glass damage)	220 μJ^*	[similar]

EXTREMELY NONLINEAR NEMATIC LIQUID CRYSTAL FILM FOR LIMITING APPLICATION WITH LONG PULSE - CW LASER

For laser pulses longer than microseconds, clearly the highly intensity dependent nonlinear absorption processes will no longer be effective because of the greatly reduced intensity for a given laser energy. In this case, other limiting mechanisms such as nonlinear scattering, thermal effects and electro-optical devices have been proposed. Recently studies [12] in our laboratory suggest an interesting and highly promising alternative. We have discovered that aligned nematic liquid crystal films doped with methyl-red dye are capable of extremely large nonlinear optical refractive index changes.

The basic mechanism is analogous to the so-called photorefractive effects observed in C_{60} - or R6G-doped nematic [14,15] but occurring at a rate more than two orders of magnitude higher. This could be due to several factors such as much better solubility of methyl red dye than C_{60} in nematic liquid crystal, much higher photocharge production and large difference in the ionic mobilities contributing to much larger space charge fields. Consequently, the Methyl-red dye-doped nematic films yield a refractive index change coefficient n_2 of $> 6 \text{ cm}^2/\text{Watt}$ in 10 -25 micron thick films. Using these nematic liquid

crystal films and external self-defocusing set up, we have demonstrated the feasibility of optical limiting of long pulse - cw lasers at unprecedented low laser power on the order of 100 nWatt [16,17]. The response times range from fraction of a second to a few milliseconds, depending on the laser intensity, with the net effect that $< 1\mu\text{Joule}$ of the input laser energy will reach the detector/sensor in these long pulse-cw regime.

Since many dyes exist that will cover the entire visible spectrum, such dye-doped nematic films are highly promising candidates for application as very broadband optical limiters. Because of their thin film nature, these films can be easily integrated onto other optical limiting devices, such as the nonlinear liquid core fiber array to fabricate devices that will provide protection against frequency agile picosecond - cw lasers. New configurations involving these liquid crystalline films and the nonlinear fiber arrays are currently being investigated for such purposes.

CONCLUSION

We have successfully developed nonlinear core fiber structures for sensor protection application. We have also developed quantitative theoretical models for the device operation principle and the basic molecular photonics processes. A few fundamentally interesting and practical questions still remain. These include: quantitative characterization of all the relaxation times of the intermediate and excited states, the spectral dependence of the absorption cross-sections and complete time dependent studies of molecular excitation and fiber propagation in the high intensity limit. These questions cannot be answered with pulse limiting studies alone, and may require other techniques such as transient pump-probe absorption spectroscopy with laser pulses of various time durations, and time-delayed fluorescence spectroscopy. Studies along these lines are currently underway, in conjunction with synthesis of new nonlinear core liquids. We are also actively investigating the use of the extremely nonlinear nematic thin film for optical switching and limiting, as well as spatial light modulation, image processing and adaptive optics applications.

REFERENCES

1. See, for example L. Tutt and T. Boggess, "A review of optical limiting mechanisms and devices using organics, fullerenes, semiconductors and other materials," *Prog. Quant. Elect.*, vol. 17, pp.299-338, 1993.
2. I. C. Khoo, M. V. Wood and Brett D. Guenther, "Nonlinear Liquid Crystal Fiber Structures for Passive Optical Limiting of Short Laser Pulses". *Optics Letters* **21**, 1625-1627 (1996). I. C. Khoo, U.S. Patent no. 5,589,101; issued Dec.31, 1996]
3. I. C. Khoo et al, "Nonlinear liquid-cored fiber arrays for passive optical limiting of

short laser pulses", J. Opt. Soc. Am. **B**, 15, pp. 1533 - 1540 (1998). See also reference 16.

4. I. C. Khoo, H. Li, P. G. LoPresti and Y. Liang, Optics Letts., **19**, 530 (1994). See also I. C. Khoo, "Fullerene-doped liquid crystal fibers and fiber arrays for all-optical switching", Chapter 10, pp 271-293 in 'Novel Optical Materials and Applications', ed. I. C. Khoo, F. Simoni and C. Umeton [Wiley Interscience, NY 1996].

5. I. C. Khoo and H. Li, J. Appl. Phys. **B59**, 573 (1994).

6. F. W. Deeg and M. D. Feyer, J. Chem. Phys. **91**, 2269 (1989)

7. H. J. Eichler, R. Macdonald and B. Trosken, Mole. Cryst. Liq. Cryst. **231**, 1 (1993)

8. R. J. McEwan and R. C. Hollins, J. Nonl. Opt. Phys. and Materials **4**, 245-260 (1995).

9. I. C. Khoo "Liquid Crystals: Physical Properties and Nonlinear Optical Phenomena," [Wiley Interscience, NY 1994] and references therein. See also I. C. Khoo and S. T. Wu, "Optics and Nonlinear Optics of Liquid Crystals", World Scientific Publishing, New Jersey, 1993.

10. For Fullerene systems, see for example, K. M. Nashold and D. P. Walter, J. Opt. Soc. Am. **12**, pp 1228-1237 (1995). See also, D. G. Mclean, R. L. Sutherland, M. C. Brant, D. M. Brandelik, P. A. Fleitz and T. Pottenger, Opt. Letts., **18**, 858 (1993) and references therein.

11. For Phthalocyanine systems, see for example, Hari Singh Nalwa and James S. Shirk, "Nonlinear Optical Properties of Metallophthalocyanines" in Phthalocyanines: Properties and Applications, Vol. 4 ed. C. C. Leznoff and A. B. P. Lever [VCH Publishers, 1995]

12. I. C. Khoo, S. Slussarenko, B. D. Guenther and W. V. Wood, 'Optically Induced Space Charge Fields, DC Voltage, and Extraordinarily Large Nonlinearity in Dye-doped Nematic Liquid Crystals'. Opt. Letts. **23**, pp 253 - 255 (1998).

13. M. J. Soileau, E. W. Van Stryland, G. Guha, E. J. Sharp, G. L. Wood and J. L. W. Pohlman, Mole. Cryst. Liq. Cryst. **143**, 139-143 (1987).

14. E. V. Rudenko, A. V. Sukhov, JETP **78**, 6, pp. 875-882, 1994.

15. I. C. Khoo, H. Li, Y. Liang, Opt. Lett. **19**, pp. 1723-1725, 1994; I. C. Khoo, Optics Lett. **20**, pp. 2137-2139, 1995; I. C. Khoo, IEEE J. Quant. Elect., **32**, pp. 525-534, 1996.

16. I. C. Khoo, M. V. Wood, B. D. Guenther, Min-Yi Shih, P. H. Chen, Zhaogen Chen and Xumu Zhang, "Liquid Crystal Film and Nonlinear Optical Liquid Cored Fiber Array for ps-cw Frequency Agile Laser Optical Limiting Application" [Optics Express, Vol. 2, no. 12. (1998).

17. I. C. Khoo, B. D. Guenther, Min-Yi Shih, P. H. Chen and M. V. Wood, "Optical Limiting of sub-microwatt long pulse - cw lasers with extremely nonlinear liquid crystal films," in Conference on Lasers and Electro-Optics, Vol. 16, 1998 OSA Technical Digest Series (Optical Society of America, Washington DC, 1998), pp. 374 - 375.

ALL-OPTICAL SWITCHING OF LIGHT IN HYBRID LIQUID CRYSTAL STRUCTURES

STANISLAW BARTKIEWICZ and ANDRZEJ MINIEWICZ

Institute of Physical and Theoretical Chemistry, Wrocław University of
Technology, Wrocław, Poland

FRANÇOIS KAJZAR

LETI (CEA - Technologies Avancées) DEIN - SPE, Groupe Composants
Organiques, Gif Sur Yvette, France

MALGORZATA ZAGÓRSKA

Faculty of Chemistry, Warsaw University of Technology, Warsaw, Poland

Abstract In this paper we report the results of all-optical controlling of light obtained in a hybrid liquid crystal panel. The structure of a device, composed of two ITO covered glass plates with photoconducting polymeric layers and a nematic liquid crystal sandwiched between them, is described in detail. The intensity of the input laser beam can be modulated or limited by the presence of another beam incident onto the device. This is accomplished by the process of a strong two-beam coupling occurring via photoconductivity mediated molecular reorientations of liquid crystal molecules. The described optical device is capable of controlling the intensity of a laser beam (specially of low power cw lasers) by change in intensity of the second beam. Low dc driving voltage is used for operation of the device. Almost 100 % efficiency of all-optical beam switching has been reported.

INTRODUCTION

Dye-doped nematic liquid crystals and liquid crystal panels with photoconducting surface layers have received considerable attention due to possibility of reversible and dynamic recording of phase holograms (i.e. holograms basing on spatial modulation of a refractive index of a liquid crystal) at relatively low laser light intensities [1-7]. The principle mechanism leading to the efficient creation of these holograms has been found to be related with a formation of light induced spatially modulated electric field in a

proximity of nematic molecules followed by their reorientation due to electric and elastic torques acting on them. Such ordered molecular reorientations in a nematic lead to considerable changes of refractive index which could be seen by properly polarized light and just leading to efficient light diffraction. Diffraction of light on simple refractive index gratings depends on many factors among which the grating amplitude Δn , grating spacing Λ , grating shape, light incidence angle and light polarization are crucial for diffraction efficiency and other related performances of the optical medium. Specially interesting are the systems which can work in a transmissive regime which allows for the beam mixing: either degenerate two-wave mixing (DTWM) or degenerate four-wave mixing (DFWM) or nondegenerate wave mixing. It has been shown recently, that in specially designed liquid crystal panels, an efficient energy transfer from one beam to another in a two-beam coupling experiment is possible [8,9]. It is well known from the literature devoted to photorefractive effects [10,11] that the energy transfer is possible when there is a phase shift $\Delta\Phi$ between a light interference pattern and a refractive index grating. However, it is required that the refractive index grating mechanism is of a non-local character. Most of the mechanisms leading to formation of index gratings are local ones including photochemical reactions, photochromism, third-order optical effects etc. [12]. In these systems the energy transfer between the beams is impossible. Fortunately in the classic photorefractive effect (for example such as observed in BaTiO_3 single crystal [10]) the phase shift between a light interference pattern and a refractive index grating is a simple consequence of photoconductivity induced diffusion mechanism for photogenerated charge carriers and their subsequent trapping. The resulting space charge field is $\pi/2$ shifted with respect to the light intensity pattern and so is the refractive index which is the direct replica of space charge field modulation via the Pockels effect [10,11].

Nematic liquid crystals are centrosymmetric then they can not exhibit a classic photorefractive effect but instead one can produce gratings with much higher amplitudes Δn than in photorefractive inorganic crystals [5,6,13]. In the hybrid structures by combination of the photoconductive properties of a polymer, high amplification factor of index modulation due to molecular reorientation process in liquid crystal and suitable reading angle of the induced gratings one can achieve the desired shift $\pi/2$ between the

mentioned above gratings. Such a shift allows for a coherent light amplification i.e. one of the beams gains energy from the other which is depleted. The process of energy transfer i.e. its direction and efficiency can be controlled by an externally applied dc voltage. The construction details of the liquid crystal device in which this can be accomplished has been reported elsewhere [9].

The aim of this paper is to show that basing on the same principle and using similar liquid crystal panels as in Ref. [9] one can make an optical device (an all-optical switcher) which can either switch off one of the beams or attenuate it with no need of any external action except the change in intensity of the other beam. We will present the experimental results of the beam intensity attenuation or switching and discuss the physical mechanism responsible for the effect.

EXPERIMENTAL

A liquid crystal panel, which characteristics are studied in this work, consists of commercially available nematic liquid crystal mixture E7 (Merck KGaA, Darmstadt, Germany) sandwiched between two ITO covered glass plates and aligned homogeneously by an uniaxial rubbing of surface polymeric layers. These polymeric layers are different: at the front electrode we deposited a photoconducting polymer the Disperse Red 1 (DR1) substituted poly(3-octylthiophene) and at the rear electrode we deposited the polyimide. Both polymeric layers have thickness of the order of 100 nm as it was measured by a surface profiler Dektak³ ST. Used by us DR1 substituted poly(3-octylthiophene) allows for efficient operation at green laser lines.

The schematic structure of the hybrid polymer - liquid crystal panel is shown in detail in the inset to the Figure 1. The plates of glass are parallel to each other and are separated by the 10 μm polyester spacer (then an LC layer thickness is being set to $d_{LC} = 10 \mu\text{m}$). The parallel rubbing direction on the front and rear surfaces defines the homogenous (planar) alignment of a nematic liquid crystal mixture. The cells were filled by a capillary action with a multicomponent nematic liquid crystal mixture E7. Such an LC composition at room temperature is characterised by a positive static dielectric

anisotropy $\Delta\epsilon = +13.8$, birefringence $(n_e - n_o) = 0.2253$ at 589 nm ($n_e = 1.7464$, $n_o = 1.5211$) and viscosity $\gamma = 39 \text{ mm}^2\text{s}^{-1}$ [14]. The birefringence value at the wavelength 532 nm used in our experiments can be few percent lower than the value given above. The dc voltage delivered by a 9 V battery was sufficient to change the orientation of the long molecular axes of nematic liquid crystal from a homogenous to near homeotropic alignment (i.e. perpendicular to the glass surfaces).

All-optical control of intensity of an incident laser beam can be realized in a conventional two-beam coupling experiment. The experimental configuration is shown in Figure 1.

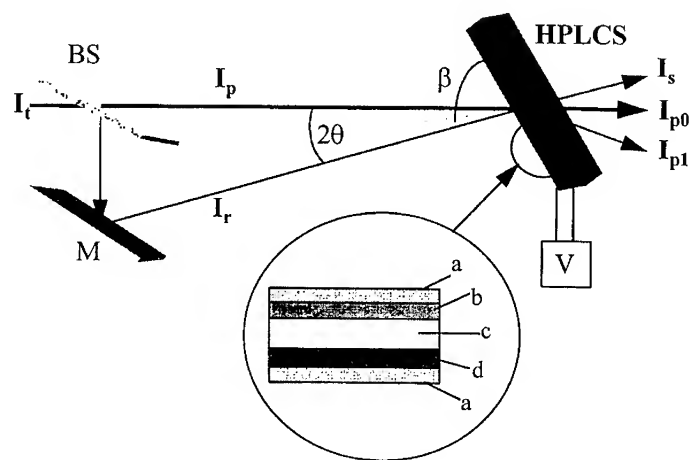


FIGURE 1. Schematic view of the two-beam coupling experiment in the hybrid polymer - liquid crystal structure (HPLCS). The sample is tilted with respect to the direction of light incidence by angle $\beta = 45^\circ$, laser beams ($\lambda_o = 532 \text{ nm}$) are crossing at the angle $2\theta = 0.6^\circ$ and are p-polarized. BS - beam splitter, M - mirror, V - dc voltage supplier. In the inset a scheme of the HPLCS is given in detail: (a) - ITO covered glass plate, (b) - a thin layer of DR1 substituted poly(3-octylthiophene) the photoconducting polymer, (c) - E7 nematic liquid crystal layer, (d) - a thin polyimide layer.

The DPSS 532 Coherent laser (cw doubled in frequency YAG) served as a coherent light source. The input laser beam I_i was split by a beam splitter into two beams: I_p and I_r . The first one (I_p) plays a role of a pumping beam (having the higher intensity than the other beam) and the second one (I_r) is a reference beam. These two beams cross inside the hybrid polymer liquid crystal structure (abbreviated hereafter as HPLCS) at the small angle 2θ ($\theta = 0.3^\circ$). In the experiment HPLCS was tilted with respect to the bisectrice of the incoming beams by a reasonably high angle $\beta = 45^\circ$. In HPLCS we observed an efficient self-diffraction process accompanied by the energy transfer between the beams. Both zero-order (I_s and I_{p0}) and first order (I_{p1}) diffracted beam powers are monitored with the use of the Labmaster Ultima (Coherent, USA) laser power meter. In order to study temporal behavior of the device a light chopper and photodiode detectors, connected to the digital oscilloscope Tektronics, were used. The optical device, shown in Figure 1, is able to control the output signal beam intensity I_s as a function of the incoming powers I_t , I_r and I_p .

ON THE SELF-DIFFRACTION OF LIGHT IN LIQUID CRYSTAL PANEL

When two coherent light beams cross inside a photoactive medium they can produce an index of refraction or absorption grating which is a replica of the interference fringes. Let us assume that incident upon the structure are the pumping wave $E_p(\mathbf{r})$ and the reference wave $E_r(\mathbf{r})$. For the sake of clarity we assume that both waves are monochromatic plane waves, both at a frequency $\omega_0 = ck_0$, write a thin phase hologram in the HPLCS. The writing field incident upon the structure can be written as

$$E(\mathbf{r}) = E_p(\mathbf{r}) + E_r(\mathbf{r}) = E_p \exp[i(\varphi_p + \mathbf{k}_p \cdot \mathbf{r})] + E_r \exp[i(\mathbf{k}_r \cdot \mathbf{r})] \quad (1)$$

where E_p and E_r are the real amplitudes of the pumping and reference wave, respectively, \mathbf{k}_p and \mathbf{k}_r are the corresponding wave vectors and φ_p is an arbitrary constant phase in the pumping wave. The validity of the assumption of thin grating can be verified by an

analysis of the value of the quality factor Q [15] :

$$Q = 2\pi d_{LC} \frac{\lambda_o}{n_e^{\text{eff}} \Lambda^2} \quad (2)$$

where d_{LC} is the liquid crystal film thickness, Λ is the grating spacing, n_e^{eff} is the effective extraordinary index of refraction of a liquid crystal. If $Q < 1$ the hologram is said to be in the thin region (the Raman-Nath regime), and if $Q > 1$ the hologram is said to be in the thick region (the Bragg regime). For relatively small angles of incidence ($< 1^\circ$) that satisfy the paraxial approximation, the grating spacing is usually several times larger than the wavelength λ_o . Therefore, the thin-hologram condition will be satisfied for thin films with thickness up to a few micrometers.

One can decompose the wavevectors \mathbf{k}_p and \mathbf{k}_r into their transverse \mathbf{k}_\perp and longitudinal components, with the z axis being the propagation axis following the theory presented in Ref. [16]:

$$\mathbf{k} = \mathbf{k}_\perp + \sqrt{|\mathbf{k}|^2 - |\mathbf{k}_\perp|^2} \mathbf{e}_z \quad (3)$$

$$\mathbf{r} = \mathbf{x} + z\mathbf{e}_z \quad (4)$$

Thin hologram which is formed inside the HPLCS can be described by a transparency $t(\mathbf{x})$ describing, at steady state, the spatially modulated phase introduced by a liquid crystal layer when illuminated by the two incident light beams:

$$t(\mathbf{x}) = \exp \left[ik_o \int_{d_{LC}} \Delta n_e^{\text{eff}}(\mathbf{x}, z) dz \right] \quad (5)$$

with

$$\Delta n_e^{\text{eff}}(x, z) = n_e n_o \left[\frac{1}{\sqrt{n_o^2 \sin^2 [\alpha(E(x, z, I_0(x)))] + n_e^2 \cos^2 [\alpha(E(x, z, I_0(x)))]}} - \frac{1}{\sqrt{n_o^2 \sin^2 [\alpha(E(x, z, I_0 = 0))] + n_e^2 \cos^2 [\alpha(E(x, z, I_0 = 0))]} \right] \quad (6)$$

where $E(x, z, I_0(x))$ is a local steady-state electric field interacting with molecular dipoles in the presence of illumination and $E(x, z, I_0(x)=0)$ is the electric field in the absence of illumination, n_e and n_o are the extraordinary and ordinary refractive indices, α is the field dependent angle between the average long molecular axis direction and the direction perpendicular to the liquid crystal cell surfaces. This formula assumes that for planarly aligned nematic the effective refractive index is measured for the extraordinary polarized light. The spatial modulation of light intensity pattern $I_0(x)$ is given by

$$I_0(x, z) = (I_p + I_r) \left(1 + \frac{2\sqrt{I_p I_r}}{I_p + I_r} \cos(\varphi_p + zK_z + \mathbf{q} \cdot \mathbf{x} + \Delta\Phi) \right) \quad (7)$$

where

$$\begin{aligned} \mathbf{q} &= \mathbf{k}_{p\perp} - \mathbf{k}_{r\perp}, \\ K_z &= k_{pz} - k_{rz}, \end{aligned} \quad (8)$$

are the perpendicular and the longitudinal components of the grating vector \mathbf{K} inside the liquid crystal layer. $\Delta\Phi$ is the phase shift between the refractive index grating and the fringe field, it can take any value between $-\pi$ and $+\pi$. Considering the thin-grating approximation we can write the transmission function as

$$t(\mathbf{x}) = \exp[i\delta \cos(\varphi_p + d_{LC}K_z + \mathbf{q} \cdot \mathbf{x} + \Delta\Phi)] \quad (9)$$

where

$$\delta = \frac{2\pi}{\lambda_o} |\Delta n_e^{\text{eff}}| d_{LC}^{\text{eff}}. \quad (10)$$

The path length in the perturbed region is d_{LC}^{eff} can be calculated from the angle of

incidence β and the index of refraction of the optical medium. Use of the expression (9) to describe the transparency of a thin phase hologram limits the theory to the paraxial region. The electric field of the reading wave diffracted on the structure is given by

$$E_S(\mathbf{x}) = t(\mathbf{x})E_R(\mathbf{x}, z=0) \quad (11)$$

where $E_R(\mathbf{x}, z=0)$ is any of the two incident waves E_p or E_r .

The output amplitude for the m th diffracted order is proportional to the square of the Bessel function $J_m(\delta)$ of an m th order ($\sim J_m^2(\delta)(-i)^m$) and may be obtained by collecting and summing all the waves diffracted on the grating in this direction. The diffraction efficiency of the m -th order diffracted wave is defined as [15]:

$$\eta_m = \left| \frac{E_S^{(m)}}{E_R(z=0)} \right|^2 \quad (12)$$

and for a single reading wave it is given by the Bessel function $J_m(\delta)$ of an m th order

$$\eta_m = J_m^2 \left(\frac{2\pi}{\lambda_o} |\Delta n_e^{\text{eff}}| d_{LC}^{\text{eff}} \right) \quad (13)$$

The zeroth order is completely quenched when $\delta = 2.4$ since $J_0(2.4) = 0$.

If this is the case one can expect, according to the theories developed for photorefractive media, that in a two-beam coupling experiment the energy transfer between the incoming beams takes place. The amount of energy transferred from one to another beam is a function of the $\Delta\Phi$ angle and is at the maximum for $\Delta\Phi = \pi/2$. In the case of the nonlinear optical medium studied in this work this shift is a result of the nature of the grating formation process. Spatially modulated light intensity pattern creates inside a photoconducting polymeric layer a distribution of photogenerated charge carriers. The space charge electric E_{sc} field is modulated according to the light intensity pattern i.e. has the same periodicity but it is shifted by $\pi/2$ with respect to the

light intensity pattern as follows from the Poisson equation [10]. The sum of the space charge field E_{sc} and the externally applied electric field E_a contributes to the electric torque τ_e [3]:

$$\tau_e = \frac{\Delta\epsilon}{4\pi} (\hat{n} \cdot (E_{sc} + E_a)) (\hat{n} \times (E_{sc} + E_a)) \quad (14)$$

where \hat{n} is a director of a small volume of a nematic liquid crystal, i.e. represents a local quantity. Pseudo vector \hat{n} is defined as an average direction of long molecular axes of a liquid crystal. Both fields are functions of a distance z measured inside the liquid crystal panel and E_{sc} depends on light intensity and the electrical properties of a photoconducting polymer (charge carrier mobilities, dark conductivity, dielectric constant, density and energetics of traps, etc.). The balance between the electric torque and elastic forces establishes the orientation of the nematic director in the bulk of the liquid crystal layer. As a result of this process the refractive index grating shifted in phase $\Delta\Phi$ with respect to the light intensity pattern is established, then the energy transfer between the beams is possible.

RESULTS AND DISCUSSION

The two-beam coupling experiment in HPLCS yielded typical multiple diffraction orders pattern in the far field on the exit side of the sample. From the experimental geometry we calculated the effective path length $d_{LC}^{eff} = 11, 2 \mu m$ and from the wave mixing angle $\theta = 0,3^\circ$ the corresponding grating constant $\Lambda = 64 \mu m$. Besides the Raman-Nath regime is fulfilled because the quality factor (cf. equation 2) $Q = 5 \times 10^{-3} \ll 1$. Well visible diffraction orders were observed for an incident laser power as weak as $\approx 1 mW$ for externally applied voltage of $V = 5 - 9 V$.

Typical experimental results showing a process of all-optical switching of light are shown in Fig. 2. In the experiment the pumping beam I_p was periodically chopped while the beam I_r was incident without interruption onto the HPLCS. At the same time the intensities of the three output beams (cf. Fig.1) were monitored and captured by a digital

oscilloscope. The trace shown at the top of Fig. 2 represents the intensity of the +0 order diffracted beam I_{p0} and is related to the intensity modulation of the input pumping beam I_p . The trace shown in the middle part of Fig. 2 represents the intensity of the -0 order diffracted beam. Notice that the intensity of this beam is in antiphase with respect to the

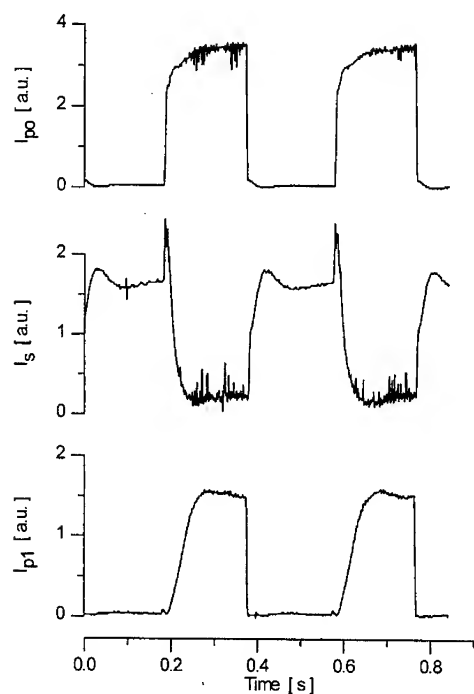


FIGURE 2. Typical experimental results showing the process of all-optical switching of light in HPLCS ($\beta = 45^\circ$, $\Lambda = 64 \mu\text{m}$). The pumping beam I_p is chopped while three output beams are monitored: I_{p0} - the zeroth order diffracted beam of I_p (at the top); I_s - the zeroth order diffracted beam of I_r (in the middle); I_{p1} - the first order diffracted beam (at the bottom).

intensity of the pumping beam I_p . Then when I_p is blocked the intensity of the I_s beam is

related to the incoming I_r beam intensity. Switching on the pumping beam I_p causes the sudden drop in intensity of the I_s beam while the intensity of the +1 order diffracted beam I_{p1} is build-up (cf. trace at the bottom of Fig. 2). This enables us to switch the power between the beams I_s and I_{p1} by an external switching of the input beam I_p . The efficiency of the energy switching can reach 100% when the input beam intensities and other experimental conditions are at optimum. Using the equation (13) one can calculate the refractive index effective grating amplitude $|\Delta n_e^{\text{eff}}|$ by putting $\delta = 2.4$ then the grating amplitude $|\Delta n_e^{\text{eff}}| = 0.018$ which constitutes near 10% of the liquid crystal birefringence value ≈ 0.2 . Several experimental parameters must be optimized in order to achieve the complete light switching. The most important are: small θ angle between the incident beams in order to obtain large grating period Λ , precise control of the mutual beam polarization (p-type polarization was employed) in respect to the rubbing direction and a suitable driving dc voltage.

Because the energy switching is a result of dynamic grating recording and erasing the time constants of signal build-up τ_B and decay τ_D will depend on the characteristic parameters of liquid crystal (its viscosity, elastic constants, thickness of a layer and grating wavevector) and polymer (quantum yield for charge carrier photogeneration, hole and electron mobilities). These parameters were already a subject of separate studies in similar systems [5,6,9]. The energy switching in the described system is typically accomplished within 50 ms. This time can be shortened by an optimization of all the parameters involved in the process of grating formation.

The efficiency of the energy switching is dependent on the total input power as well as on the ratio of powers of the beams I_p and I_r . In Figure 3 the functional dependence of intensity of the -0 order diffracted beam I_s is plotted versus the pumping beam intensity I_p . The three curves presented in this figure show the depletion of the I_s beam power for the three different values of I_r power (1000, 500 and 100 μW). Using the input beam power I_p of the order of 1000 μW one can effectively switch off the second beam with the power not exceeding half of the power of I_p , approximately. A proper choice of the ratio of the input powers I_p and I_r can yield a desired level of attenuation of the I_s beam.

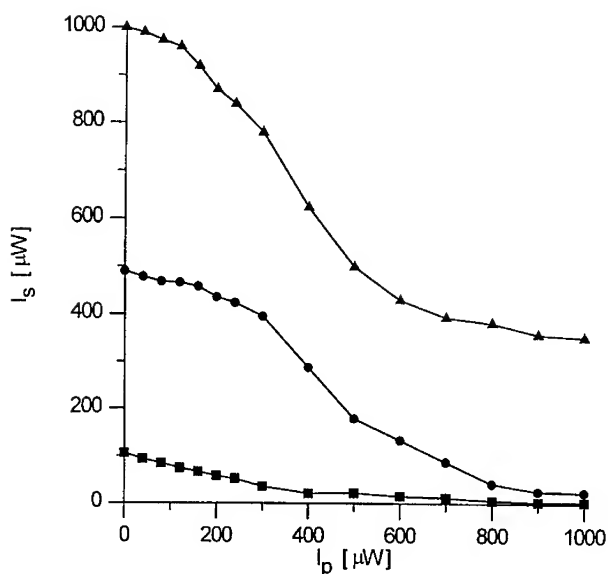


FIGURE 3. The power of the -0 order diffracted beam, the signal beam I_s , is plotted versus the pumping beam power I_p for the three values of I_r power 1000, 500 and 100 μW .

In Figure 4 we show the relation between the powers of the I_s and I_r beams for a given value of the pumping beam power $I_p = 1000 \mu W$. This dependence is highly nonlinear showing that the energy transfer is dependent on the light intensity modulation factor (cf. Equation 7) as well as on the $\Delta\Phi$ angle established in the HPLCS.

In this paper we would like to demonstrate one of the possible use of the described before effects, namely the active optical limiter based on induced scattering mechanism. Use of photorefractive effect for optical power limiting with the help of two-wave mixing techniques has been already reported [17]. The principle of the device operation is to split of the input laser beam into two-parts and recombine them in a strongly nonlinear optical medium able for producing an efficient diffraction grating. This diffraction grating will scatter the light into various direction and then will limit the

amount of light passing in the direction of observation. The amount of power transferred by the system depends on nonlinear optical characteristics of the material. Such a photoinduced scattering can be used in optical limiting for sensor protection.

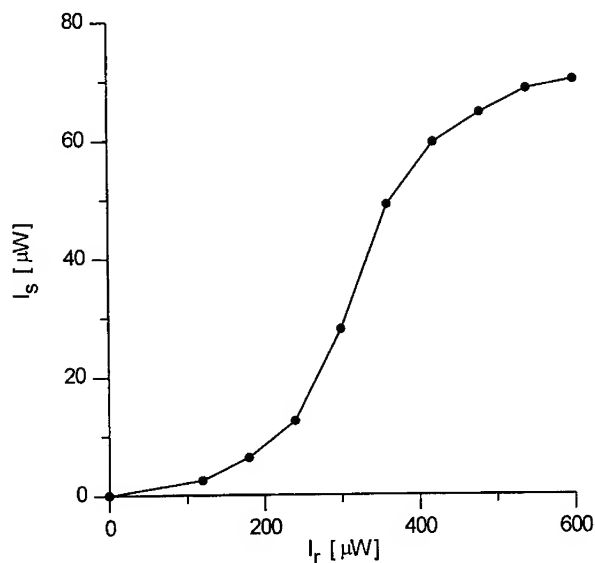


FIGURE 4. Power of the I_s signal beam versus power of the I_r beam measured at the pumping beam power $I_p = 1000 \mu W$ in a two-beam coupling experiment in HPLCS.

An optical limiter realized by us with the help of the HPLCS is able to limit the power of the input beam in the range up to 1.6 mW. As it is shown in Figure 5 the output power of the limiter I_s is attenuated with increasing strength and does not exceed the level of 80 μW . This means that only 5% of the input beam power emerges from the device. In the inset to Figure 5 we present the dependence of a ratio I_s/I_i as a function of I_i . One can notice that limiter works better at higher input powers.

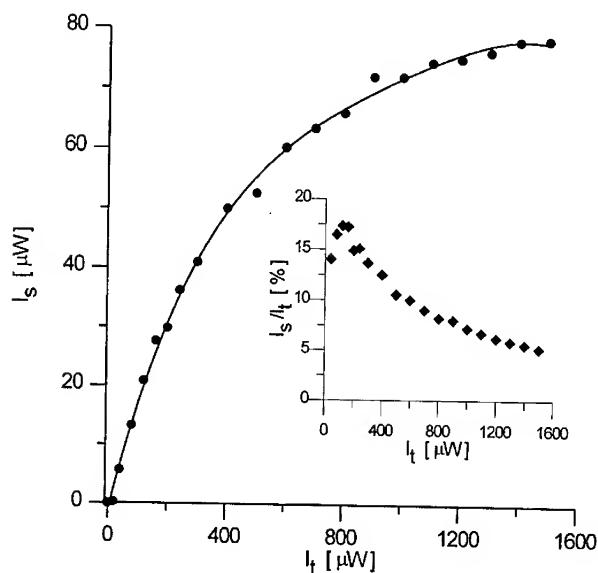


FIGURE 5. Optical limiting curve measured for cw laser radiation at $\lambda = 532$ nm for HPLCS. Plot of the signal beam power I_s versus the input beam power I_t for the two-beam coupling experiment with $I_p/I_t = 2$. Inset shows the ratio I_s/I_t in function of the input power I_t .

CONCLUSIONS

In this paper we demonstrated almost 100 % efficient all-optical beam switching device basing on light diffraction on refractive index grating induced in the hybrid polymer liquid crystal structure developed by us. This simple device can serve also as an optical limiter working at small light power levels. The switching of light, in the described above panel, can be realized in the spectral range where the polymer exhibits its photoconducting properties. Nematic liquid crystal acts as highly nonlinear optical medium due to its ability of refractive index grating recording by optically induced space

charge fields in photoconducting polymer. High optical quality of the liquid crystal panels (small light scattering and small light absorption) is the necessary conditions for the effective device operation. We also discussed the principle of the device operation in relation with the theory of two-beam coupling.

Acknowledgments

This research was supported by the Polish Committee for Scientific Research under grant no. 3T09A 133 11, and partially by Ministre des Affaires Etrangeres Direction de Relation Internationale CEA, France. We thank the Foundation For Polish Science for supporting us with scientific equipment used in this work.

REFERENCES

1. E.V. Rudenko, and A.V. Sukhov, *JETP (in Russian)*, **105**, 1621 (1994)
2. I.C. Khoo, *Optics Lett.*, **20**, 2137 (1995); I. C. Khoo, *IEEE J. Quantum Electronics*, **32**, 525 (1996)
3. I.C. Khoo, H. Li, and Y. Liang, *Optics Lett.*, **19**, 1723 (1994)
4. G.P. Wiederrecht, B.A. Yoon, M.R. Wasielewski, *Science*, **270**, 1794 (1995)
5. A. Miniewicz, S. Bartkiewicz, A. Januszko, and J. Parka, in *Photoactive Organic Materials Science and Application*, edited by F. Kajzar, V. M. Agranovich and C. Y.-C. Lee, *NATO ASI Series*, Vol. 3/9, (Kluwer Academic Publishers, Dordrecht, 1996), p. 487.
6. S. Bartkiewicz, A. Miniewicz, A. Januszko, and J. Parka, *Pure and Applied Optics*, **5**, 799 (1996)
7. H. Ono, and N. Kawatsuki, *Optics Commun.*, **147**, 237 (1998)
8. A. Miniewicz, S. Bartkiewicz, and F. Kajzar, *Nonlinear Optics*, **19**, 157 (1998)
9. S. Bartkiewicz, F. Kajzar, A. Miniewicz, and M. Zagorska, *Appl. Opt.*, sent to editor (1998)

10. P. Günter, and J.-P. Huignard J.-P. (eds.), Photorefractive Materials and their Applications, Vols. 1 and 2, (Springer Verlag, Berlin, 1988).
11. P. Yeh, Introduction to Photorefractive Nonlinear Optics, (Wiley, New York, 1993)
12. B.L. Feringa, W.F. Jager and B. de Lange, Tetrahedron, **49**, 8267 (1993)
13. I.-C. Khoo, Liquid Crystals Physical Properties and Nonlinear Optical Phenomena, (J. Wiley, New York, 1995).
14. Data supplied with E7 liquid crystal by Merck KGaA, Darmstadt, Germany.
15. H. J. Eichler, Laser-Induced Dynamic Gratings, (Springer-Verlag, Berlin, 1986)
16. R. De Vré and L. Hesselink, J. Opt. Soc. Am., **B11**, 1800 (1994)
17. M. Cronin-Golomb and A. Yariv, J. Appl. Phys., **57**, 4906 (1985)

USE OF PHOTOCHROMIC MOLECULES AS OPTICAL POWER LIMITERS

ROGER A. LESSARD AND CHRISTOPHE LAFOND

Centre d'optique, photonique et laser, Département de physique
Faculté des sciences et de génie, Université Laval
Québec, QC G1K 7P4, Canada

IVAN PETKOV

University of Sofia, Department of Organic Chemistry, Faculty of Chemistry, 1,
James Bouchier Ave., B-1164, Sofia, Bulgaria

VALERY BARACHEVSKY

Institute of Chemical Physics, Bldg 1, Photochemistry Dept., Novotorov Street 7-
A, 117421 Moscow, Russia

Abstract. Many substances, in the form of dyed and undyed plastic films, host-guest systems, LB films, mixed dynamic molecular/bimolecular crystals, modified sol-gel materials exhibit a measurable change in their properties upon exposure to UV radiation. The depth of the colour or the darkness depend on solely on the radiant exposure. The functions, sensibility, nuances of the colours or the darkness can be function of: the kind of the compounds, the host system, concentration, mono - or multilayer systems, polymers, other substrates and ingredients. On the base of the selective choice of the components can be developed multifunctional systems in what the illumination to be the initial starting moment for the work of the system. The spectral, colour or other changes the systems are function of:

- cascade evaluation of the low molecular compounds as Hcl - process of protonation of dyes
- photochromic process of individual compounds
- induced photochromic processes of two and more component systems
- induced process of orientation into host-guest systems
- induced specific interactions into organized systems

INTRODUCTION

Photostimulation of chemical or physical properties of molecules and macromolecules provides the basis for the development of future multifunctional devices. In this connection the use of different kind of irradiation for the stimulation of changes with different character, which can exercise the functions of markers for the irradiation power is too attractive. Many substances, in the form of dyed and undyed plastic films, host-guest systems, LB films, mixed dynamic molecular/bimolecular crystals, modified sol-gel materials exhibit a measurable change in their properties upon exposure to radiation. The

depth of the colour or the darkness depends on solely on the radiant exposure. The functions, sensibility, nuances of the colours or the darkness can be function of the kind of the compounds, the host system, concentration, mono- or multilayer systems, polymers, other substrates and ingredients. On the base of the selective choice of the components can be developed multifunctional systems in what the illumination to be the initial starting moment for the work of the system. The spectral, colour or other changes of the systems are function of

- The structure of the sensitive compounds
- The supramolecular architectures.
- Specific interaction between the radiation and the compounds.

The basic requirement for the mark of the illumination is bistability or multistability, i.e. the occurrence of two or more different forms of a molecule or system, which can be interconverted by means of an external source. There are many compounds and systems in the organic chemistry that have stable states which can be reversibly marked from one state to another and which states can be identified. This is illustrated schematically in Figure 1:

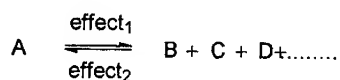


FIGURE 1. A - initial form, B,C,D... different forms of the multi functional system product of the form A and as result of the action of the effect 1.

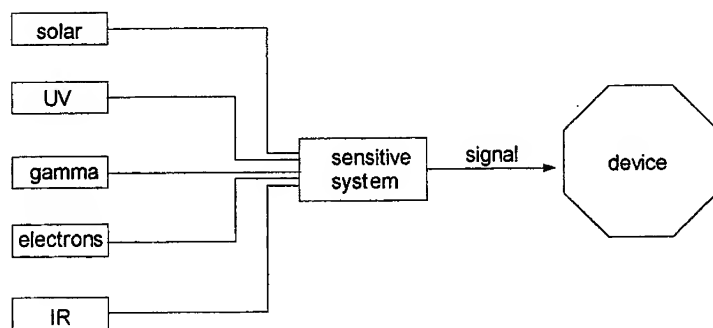
A,B,C,D represent the different forms of a multistable system, whereby *effect₁* and *effect₂* refer to different stimuli to effect the reversible marked behaviour.

The multistability might be based on various properties of molecules like electron transfer, isomerizations, and differences in complexation behaviour, photocyclizations, and photochromism. Several arguments indicate that dynamic structural changes during irradiation/compound interaction are additionally needed for the use the changes for the mark of the power limit. In order to avoid successive changes of the sensitive system with all the difficulty of controlling the energetic properties of intermediates, it may be attempted to transfer energy or electrons collectively in a co-operative way. In practice this irreversible thermodynamic approach to multielectron transfer and chemical fuel generation means that very specific electronic-dynamic conformation changes must occur

during the process. The induced illumination processes - as it occurs in sensitive systems are energetically extremely efficient process since it occurs very close to the reversible thermodynamic oxidation potential of many compounds and may thus be considered to be a phenomenon of non-linear irreversible thermodynamics. These processes might limit the steps of the changes and then they will be excellent markers for the energy level.

The problem is: is it possible to use a sensitive molecule as central part of a supermolecule system to allow energy marked from one of its different configurations into the other one and back? The radiation-induced change in optical density of a particular film depends on several factors, among them: the concentration of dye precursor, acid, and polymer in the cast film, as well as the purity of the dye precursor and the polarity of solvents used in the preparation of the polymeric solution. But those are pure chemical problems and they can be decided without problems.

The interaction of radiation with special constructed systems provides the molecular basis for the photochemical/photophysical or electrochemical/electrophysical processes, which can be of multimode type as systems for power limiters. For this reason those systems are well suited for use as sensitive materials and as building blocks for the fabrication of multifunctional devices.



SCHEME 1. Principal scheme of multi functional system.

The elements of the multifunctional systems are:

1. Light sources:

- Solar beams
- UV light

- IR light
- Gamma radiation
- α , β - Beams
- Fast electrons

2. Sensitive systems

Processes:

- Phototropism
- Electrochromism
- Halochromism
- Piezochromism
- Thermochromism

Function Change

- colour
- Fluorescence
- Electric properties
- Chemical structure

Materials

- Individual compounds
- Mixture of compounds
- Polymer composition
- Sol-gel systems
- Host - guest- systems

3. Devices

- Analytical
- Electrical
- Physical

The important moment in such systems as power limiters is the relationship between the power of the irradiation and the change of the systems to be linear (Figure 2).

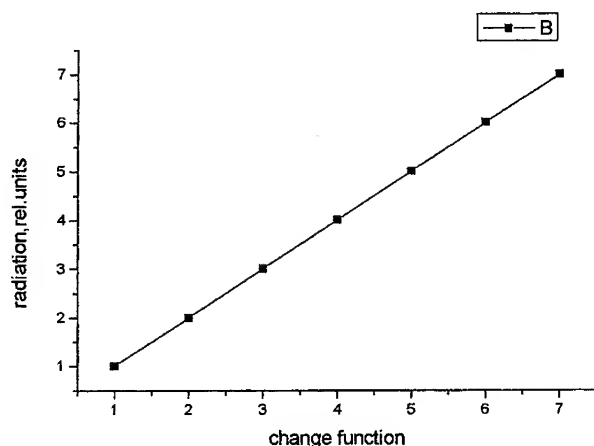


FIGURE 2. Dependence between the radiation(or other actions) in relative units and the changes of the system(color, spectral and other physical characteristics, chemical changes,conductivity).

The different characters of the illumination, the possibilities for chromism of organic dyes and compounds - photo-, termo-, electro-, halo- can be excellent candidates for the realisation of the idea for the most attractive systems for practical application.

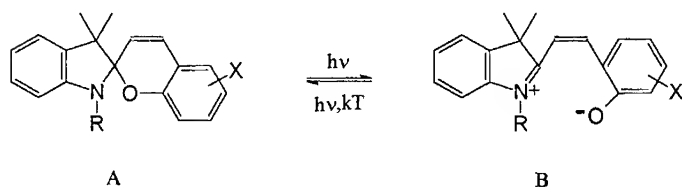
The present study is aimed at showing the photochromism as process for the using as power limiters and some its varieties as:

- Photochromic process of individual compounds
- cascade evaluation of the low molecular compounds as HCl - process of protonation of dyes
- Induced photochromic processes of two and more component systems
- Induced process of orientation into host-guest systems
- Induced specific interactions into organised systems

Promising candidates as photochromic compounds are spiropyrans, fulgides, diarylalkenes, anils and others. It is known that molecules of this class can be transformed by light in a reversible way from a configuration A into configuration B. Irradiation with UV light causes an intramolecular ring opening reaction (colouring), visible light causes a ring closure reaction (bleaching). The kinetics of such processes and the stability of educts and products during many cycles depend on the structure of the compounds. One of

most important properties of any photochromic compounds, if it is to be used in plastic lens systems, is stability against photodegradation. Good photostability, also called fatigue resistance, is required for a practical lifetime for the lens system.

An important class of photochromic molecules is the spiropyrans. They are usually colourless in one form because they are composed of two π -electron moieties that are set orthogonal to each other and therefore the molecule exhibits their individual absorption spectra rather than that of a completely conjugated system. However, upon excitation, bond cleavage takes place, which allows for the rotation of the moieties and the formation of a nearly planar structure referred to as the merocyanine form. The π -electron system extends, now, throughout the molecule and is responsible for the red shift found in the absorption spectrum of the merocyanine form. Because of the large spectral shift between the original and the merocyanine form and the fluorescence of the latter, these molecules are found to be quite promising materials for power limiters devices.



It seems to us that it is necessary to understand in depth the mechanism that is operative during the photochromic process of spiropyrans before they can be of use in any application.

The induced molecular change of the photochromic molecule can serve as an easily comprehensible output signal from a molecular device. The exciting light would act as a power supply and various structures can provide input signals. The changes that supply an output only when certain input conditions are satisfied would then behave as gates with various logic functions. The molecular logic gates have excited the imagination of the wide application because of their wide potential applications in too wide areas.

The appearance of multi-component molecular systems with increasingly focussed photofunctions is a suggestive indicator of the maturation of supramolecular photochemistry as a research field. Systems with three or more functional units, which are not all necessarily photoactive, have been particularly useful for addressing important

problems in photoscience. Some of these systems and relatives showed good selectivity for guest recognition because of the relatively fixed separation between receptor units due to the intervening fluorophore. Specifically, there will be large variations in local optical path lengths, quenching agents and degrees of sensor incorporation (and degradation) in the different microenvironments under observation. Cancelling out these variations by using fluorescent sensors that have two ratioable optical channels usually solves these problems.

The photochromic compounds are designed to contribute to the following three topics:

- Very well defined photochemical induced processes
- Relationship between the power of the illumination and the stages of the opening /closing of the forms - visual changes
- Reversible effect - multifunctional system
- Possibilities to be prepared polymer films or fibres, glass plate or glass fibres, modified papers, textile and other materials.

It is very important to be noted that from synthetic point of view the molecular architecture of the photochromic compounds can be changed and can be synthesised compounds with intelligent behaviour.

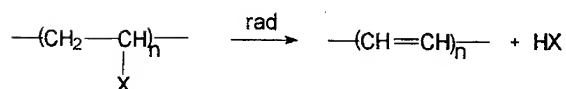
The photochromic process can give the «pump» process and the signal of the changes may serve as "mark" information. In some cases the presence of fluorescence may be utilises to examine supramolecular systems since photochromic switching, in general, is accompanied by a change of size and therefore on/off switching depends on the molecular environment.

In this connection the development of systems on the base of different kind of chromism permit the area to be enlarge the limits of the area.

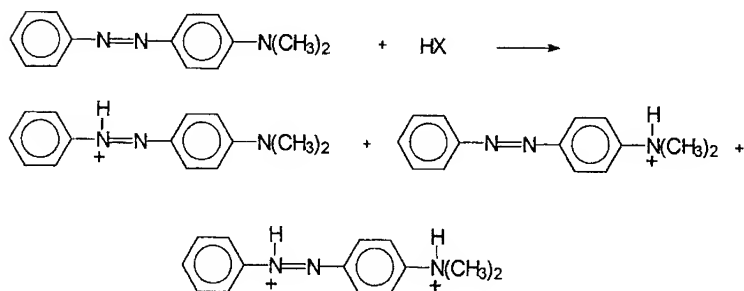
Halochromism

There are two processes.

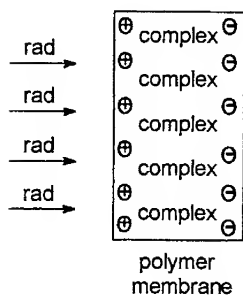
1. Processes of dehydrohalogenation - in polymers, containing halogen or polymers, solutions, host - guest systems, containing protonodonors. Under the influence of the radiation take place process of receiving of HX:



2. Process of protonation of acid sensitive dyes, for example azodyes:



The form of the different protonated form and their combination permit to be realised colours and nuances depend on the power of the irradiation. That system is very perspective because permit to be form electric potential on the polymer membranes and this fact is excellent for the realisation of devices for the registration of the changes.



Such photochromic processes can be realised under the influence of radiation, which can initiate interaction between two or more compounds in solution, polymer films, and host-guest systems.

This report present information dealing with the development of multifunctional dye systems which can be used to registration of radiation and to separate the energy levels.

CONCLUSIONS AND PERSPECTIVES.

The experimental and theoretical data on the molecular reorientation and interaction under the radiation in various systems containing light absorbing chromophores showed that the most important factors, which control the phenomenon, are chemical changes and a photoselection of the chromophores. Even in diluted dye solutions, they provide, respectively, the necessary rotational mobility of the chromophores and the consequent optical anisotropy of medium. In condensed phases (LB films, polymers, host-guest systems, sol-gel materials) the shape of the intermolecular interaction potential is also of paramount importance. Many problems concerning the physico-chemical mechanism of the phenomenon, however, are still to be solved. We can mention a few of them: to what extent the change is confined by sensitive molecules; the presence of the photoinduced processes is indicative of other possibilities. How a precise shape of the intermolecular interaction potential influence the final orientation state of the chromophores. What factors control the kinetics of the process and how reorientation of chromophores influenced the structure of the surrounding. What is a precise shape of the orientation distribution function of photooriented chromophores and how we can govern this shape. What electric and other parameters of the excited state should be taken for the measurements.

Of course, a lot of other interesting questions may arise and new experiments are in progress to elucidate the problem.

The introduction of sensitive organic molecules to radiation into a suitable site of such materials and systems will offer much more sensitive and drastic responsive multifunctional systems. Multidisciplinary approaches, based on recent advances in photonics and new organic photoactive materials will beyond doubt play a key role in future technology developments.

RÉFÉRENCES

1. Ben L. Feringa, Wolter F. Jager and ben de Lange, *Tetrahedron*, Vol. 49, No 37, 8267, 1993.
2. Itamar Willner, *Acc. Chem. Res.*, Vol. 30, No 9, 347, 1997.
3. T. W. Lewis and G. G. Wallace, *J. Chem. Educ.*, Vol. 74, No 6, 703, 1997.
4. T. Kinoshita, *J. of Photochem. and Photobiol. B: Biology* 42, 12, 1998.

-
5. J. Griffiths, *Chemistry in Britain*, November, 1986, 997.
 6. M. Shirai and M. Tsunooka, *Prog. Polym. Sci.*, Vol.21, 1-45, 1996.
 7. L.M.Blinov, *J. Nonlinear Optical Physics and Materials*, Vol. 5, No 2, 165, 1996.
 8. Z. Hao and A. Iqbal, *Chem. Soc. Revs.*, Vol. 26, 203, 1997.
 9. P. M. Blanchard, A. Gilbert and G. R. Mitchell, *J. Mater. Chem.*, 3(10), 1015, 1993.

OPTICAL PROPERTIES OF SOL-GEL FILMS

JACQUES LIVAGE AND CLEMENT SANCHEZ

Chimie de la Matière Condensée, Université Pierre et Marie Curie
4, place Jussieu, 75252 Paris, France

Abstract The sol-gel process is based on the synthesis of glasses and ceramics via the polymerization of molecular precursors. A solution of metal alkoxides is converted via hydrolysis and condensation into a sol or a gel which on drying and densification give a solid materials. This leads to the production of single or multicomponent oxide materials with high purity, novel compositions, tailored microstructures and potentially greater chemical homogeneity. Optically transparent thin films of vanadium oxide can be deposited directly from a solution of alkoxide. Moreover this low temperature process allows the synthesis of hybrid organic-inorganic materials. Organic dyes and even biomolecules can be trapped within silica films. This paper describes some new developments of the sol-gel process for the production of thin films with optical properties.

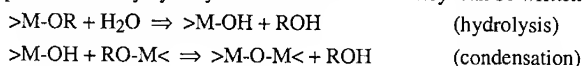
Keywords: sol-gel optics, VO₂, hybrid materials, bioencapsulation

INTRODUCTION

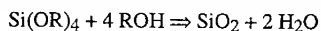
Wet chemistry has already been used for a long time for the preparation of oxide powders and the first synthesis of silica from silicon alkoxide was reported by Ebelmen more than 150 years ago.¹ He concluded that such a process could be used for the production of optical materials and as a matter of fact sol-gel optics is becoming a major field of sol-gel science.² One of the main advantage of the sol-gel process for optical applications is the easy deposition of thin films directly from the solution by techniques such as dip-coating, spin-coating or spray. The commercial production of sol-gel coatings onto flat glass was developed in the early sixties, long before academics began to be interested in this process. Sol-gel coatings are currently made of several oxide layers (SiO₂, TiO₂). More recently, hybrid organic-inorganic materials have been made via the sol-gel route. They open a wide range of possibilities and lead to the development of a new field in materials science known as "sol-gel optics".³

THE SOL-GEL PROCESS

The sol-gel synthesis of metal oxides is based on the polymerization of molecular precursors such as alkoxides $M(OR)_z$ where M is a metal, R an organic group ($Me=CH_3$, $Et=C_2H_5, \dots$) and z the oxidation state of the metal. Two chemical reactions are involved in this process, namely hydrolysis and condensation. They can be written as follows:



In the case of silica for instance the overall reaction is:



Actually alkoxides and water are generally not miscible so that a common solvent, usually the parent alcohol ROH, has to be added.

Condensed species are formed as these reactions proceed leading to the growth of oxopolymers, sols or gels which on drying under ambient conditions give a xerogel that still contains a large amount of water. Further drying and densification have to be performed in order to obtain a bulk material. The critical step in the drying of these alkoxide-derived gels is the rate of removal of water. Due to capillary forces, strains are developed between pores of different sizes when a meniscus is formed. Cracks usually appear upon drying and large monoliths are very difficult to produce. This is no longer the case with thin films ($< 1\mu m$). Strong interactions with the substrate prevent shrinkage along the parallel direction and optically transparent coatings are now currently deposited at an industrial scale via spin- or dip-coating.⁴

The morphology and optical properties of sol-gel deposited thin films strongly depend on the chemical process. Silica is formed via the hydrolysis of a silicon alkoxide such as $Si(OEt)_4$. However depending on the pH of the water different products can be obtained.⁵

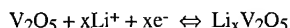
Acid or base catalyses are currently used to increase the gelation rate, however they also lead to the formation of completely different products. Acid catalysis increases hydrolysis rates and leads to the formation of chain polymers. Thin films deposited from such solutions have a fine porosity and are highly transparent. Base catalysis increases condensation rates and leads to the formation of highly branched polymers that finally give monodispersed spherical particles. Films deposited from such solutions have large pores and are usually rather translucent because of light scattering.

OPTICAL SWITCHING IN VANADIUM OXIDE FILMSElectrochromic V_2O_5 thin films.

Vanadium oxide gels can be easily made via the hydrolysis and condensation of vanadium alkoxides $VO(OR)_3$ ($R=Pr^i$, Am^t), but the final product actually depends on the hydrolysis ratio $h=[H_2O]/[V]$.

Vanadium pentoxide gels, $V_2O_5 \cdot nH_2O$ are formed in the presence of an excess of water.⁶ Acid dissociation occurs at the V_2O_5/H_2O interface leading to the formation of H_3O^+ species. The hydrated vanadium oxide then behaves as a polyvanadic acid $H_xV_2O_n \cdot nH_2O$ ($x \approx 0.3$). It exhibits fast proton conduction and the a.c. conductivity increases with the water content. When slightly reduced, vanadium pentoxide gels also exhibit electronic conduction arising from the hopping of unpaired electrons between V^{4+} and V^{5+} ions. Their electrical conductivity increases with the amount of V^{4+} ($\sigma_{300} \approx 4 \cdot 10^{-5} \Omega^{-1} cm^{-1}$ for $V^{4+}=1\%$). Such films are now used commercially for the production of antistatic coating in the photographic industry.⁷

Sol-gel deposited vanadium oxide coatings exhibit interesting electrochemical properties.⁸ Li^+ ions can be reversibly inserted within the oxide film leading to the reduction of V^{5+} ions:



The coloration of the film changes progressively during the reduction-oxidation cycles. It turns from yellow to green and blue upon reduction. The process is highly reversible and optical switching occurs within few seconds when a voltage of ± 2 V is applied. Films deposited from vanadium alkoxides could therefore be used for the realization of electrochromic devices.⁹ However their optical absorption in the visible region is rather weak when the film is very thin ($\approx 0.1 \mu m$). Amorphous tungsten oxide WO_3 thin films actually exhibit much better properties as electrochromic layers. They switch reversibly from white to blue upon electrochemical reduction and electrochromic devices using V_2O_5 as a counter electrode and WO_3 as a colored electrode have been developed in which both layers are deposited via the sol-gel process.¹⁰

Thermochromic VO_2 thin films

Vanadium dioxide VO_2 is known to undergo a reversible semiconductor-metal transition around $70^\circ C$.¹¹ This transition is associated with the formation of $V^{4+}-V^{4+}$ pairs along the c direction. This V-V pairing opens a gap at the Fermi level in the t_{2g} band leading to a change in electrical resistivity and optical properties. Above $68^\circ C$ electrical conductivity increases abruptly and vanadium dioxide becomes infrared reflecting. The switching temperature for VO_2 is nearer to room temperature than for any other compounds, which

accounts for the interest in this oxide for applications such as smart windows, thermal sensors and optical or electrical switching devices. Most fundamental studies have been performed on VO_2 single crystals, but due to the structural distortion associated with the crystallographic transition they break after few cycles. Thin films appear to be able to survive stresses during repetitive cycling and would be much more convenient for optical applications.

Optically transparent thin films can be easily deposited directly from alcoholic solutions of vanadium alkoxides to which no water is added. The alkoxide film is left in air so that partial hydrolysis occurs spontaneously due to ambient humidity.¹² The molecular precursors for condensation $\text{VO}(\text{OR})_{3-x}(\text{OH})_x$ are only partially hydroxylated and non hydrolyzed alkoxy groups prevent the formation of an oxide network, oxo-polymers $[\text{V}_2\text{O}_{5-x}(\text{OR})_x]_n$ rather than vanadium oxides are formed. Alkoxide solutions are much less viscous than vanadium oxide gels and thin films about $0.1 \mu\text{m}$ thick are obtained. Moreover, their adhesion to the substrate is much better due to the remaining alkoxy groups that can react with Si-OH groups at the surface of the silica substrate giving covalent Si-O-V bonds.

When deposited at room temperature from alkoxide solutions, vanadium oxide films are amorphous. Crystalline phases can only be obtained upon heating. V_2O_5 films are formed in air whereas reduced phases are formed in the presence of hydrogen. The pure VO_2 phase is obtained when the film is heated for two hours at 500°C under a reducing gas flow (Ar-H_2 5%). Conductivity measurements performed on these films show that their electrical resistance drops by almost three order of magnitude above 70°C . A heating-cooling hysteresis effect of about 10°C is observed.¹³

Crystalline VO_2 thin films deposited from alkoxides also exhibit good optical properties. Their optical transmission was measured in the infra-red at a wavelength $\lambda=2.5\mu\text{m}$ in the temperature range 15°C - 100°C . IR transmittance exhibits a typical hysteresis loop around the transition temperature (Fig.1). For pure VO_2 films, optical switching occurs around 80°C upon heating and below 60°C upon cooling. In the metallic state, optical transmittance drops by almost two orders of magnitude and becomes smaller than 1% suggesting that the reflectivity of VO_2 films is quite high. The shape of the hysteresis curve actually depends on the thermal treatment leading to crystalline VO_2 . It is rather large ($\Delta T=30^\circ\text{C}$) and non symmetric when the VO_2 film is made directly from the amorphous coating (Fig.1a). It is much narrower ($\Delta T=10^\circ\text{C}$) and symmetric when the thermal treatment is performed in two steps: first in the presence of oxygen giving V_2O_5 and then reduction giving VO_2 (Fig.1b). Such a difference seems to be due to the size of the crystals which are larger in the two steps procedure.

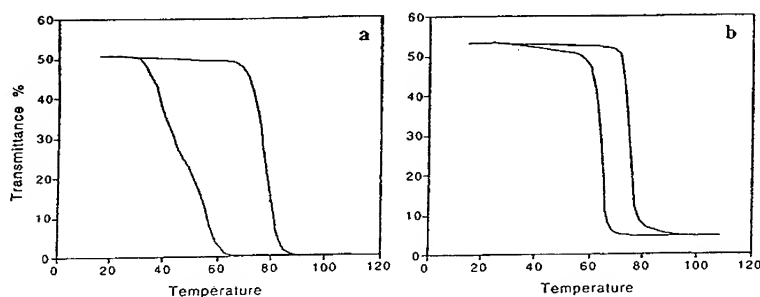


Figure 1. Optical switching of VO₂ thin films deposited from vanadium alkoxide (transmittance at $\lambda=2.5\mu\text{m}$)

(a) direct thermal treatment (b) thermal treatment in two steps

The transition temperature T_c of VO₂ can be modified by doping. It usually decreases with high-valent cations (Nb⁵⁺, Mo⁶⁺, W⁶⁺) and increases with low-valent dopants (Al³⁺). Doping can be very easily performed via the sol-gel route. Doped $M_x\text{VO}_2$ ($M = \text{W}^{6+}, \text{Al}^{3+}$) thin films are obtained by adding a given amount of molecular precursor such as WOCl₄, Ti(OPrⁱ)₄ or Al(OBu^s)₂(etac) (etac=C₆H₉O₃) to the vanadium alkoxide solution. The mixed solution is then deposited by spin-coating and heated as previously.^{14,15}

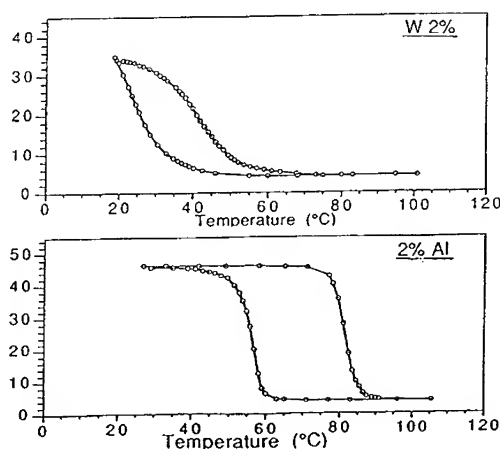


Figure 2. Optical switching in doped VO₂ thin films $M_x\text{VO}_2$

The temperature at which the optical switching occurs is significantly smaller, around 40°C upon heating, when the film is doped with 2% of W^{VI}. Transition close to ambient temperature can even be observed when the amount of W^{VI} reaches 5%. The reverse is observed with Al^{III} doped VO₂ films for which the optical switching occurs around 90°C upon heating (Fig.2). The optical decreases as the amount of doping increases. These impurities introduce defects that decrease the metallic character of the high temperature phase.

HYBRID ORGANIC-INORGANIC MATERIALS

The mild conditions of sol-gel chemistry allow to mix organic molecules with inorganic oxides.¹⁶ Inorganic and organic components can be mixed at the molecular scale in almost any ratio leading to hybrid organic-inorganic nanocomposites.¹⁷⁻²² These new hybrids materials are extremely versatile in their composition, processing and properties and represent a major advance in sol-gel processing. Such an intimate mixing at a nanoscale leads to a large interface between both organic and inorganic phases. The properties of these nanocomposites (optical, mechanical...) can be tuned via the chemical control of this interface in size and composition. Hybrids have then be classified in two classes depending on whether strong chemical bonds are between organic and inorganic components.¹⁹ Only weak interactions (van der Waals forces, hydrogen bonds or electrostatic interactions) are involved in Class I hybrids whereas many organic and inorganic components are linked through strong chemical bonds in class II hybrids.

The recent development of sol-gel optics takes advantage of the optical properties of organic dyes together with the hardness and optical transparency of silica matrices.^{2,3} A large number of organic dyes can be trapped within sol-gel glasses. They provide optical properties such as fluorescence, laser emission, photochromism, non linear optics or photochemical hole burning .

Sol-gel hybrid matrices offer several advantages for optical dyes. the mean size of organic and inorganic phases can be of the order of few nanometers. Therefore they are transparent and can be used for optical applications. Moreover, due to their improved mechanical properties, hybrid sol-gel matrices can be polished down to one nanometer in surface roughness. They fill the gap between polymers and glasses and offer new possibilities as optical matrices for organic dyes.

. Interactions between dyes and the oxide matrix prevent aggregation that could lead to the quenching of luminescence. The solubility of organic dyes can be increased significantly and larger amount of dyes can be used.

. These interactions can be tailored in order to improve the optical response of trapped dyes. Hydrophobic organic groups (alkyl, phenyl ...) can be covalently linked the hydrophilic oxide network in order to tune the hydrophilic-hydrophobic balance of the matrix. Polar solvents such as water or alcohol are not retained in the gel network. They don't have to be removed upon drying or heating avoiding shrinkage and the formation of cracks. Thick coatings ($> 10\mu\text{m}$) and even bulk materials can then be obtained without cracks.

. The physical properties of the sol-gel matrix (hardness, T_g ...) can be optimized in order to control the molecular motion of dyes and matrix relaxation, a very important problem for some applications such as second order non linear optical properties or photo chemical hole burning.

Sol-gel hybrids of class II are mainly synthesized from organo-alkoxysilane precursors, $\text{R}'_4\text{-}_x\text{Si(OR)}_x$ in which Si-C sp^3 bonds are not sensitive towards hydrolysis. The nature of the final product depends on the functionality, x , of the precursor.

- Trifunctional alkoxides such as methyltriethoxysilane, MeSi(OEt)_3 (MTES) are now commonly used to introduce organic groups within an inorganic network. These organic groups act as network modifiers bringing some new physical or chemical properties to the inorganic network (flexibility, hydrophobicity, refractive index, optical property, NLO...).

- The hydrolysis-condensation of difunctional precursors such as dimethyldiethoxysilane, $\text{Me}_2\text{Si(OEt)}_2$ (DEDMS), does not lead to gelation, only short chains polymers or cyclic species are formed. They have to be mixed with metal alkoxides M(OR)_4 ($\text{R}=\text{Si, Ti, Zr...}$). These metal alkoxides play a double role. They behave as cross-linking reagents, and could catalyze redistribution reactions of siloxane species through their Lewis acid character.¹⁹

- Even polymerizable organic groups (vinyl, epoxy,...) can be introduced. They act as network former leading to the formation of an organic network together with the oxide one.

Photochromic materials.

Photochromic glasses are limited to few inorganic dopants that can withstand the high temperature of glass melting. Organic dyes offer thousands of active molecules such as spiropyranes, spirooxazines, furylfulgydes and diarylethenes that can now be entrapped within sol-gel matrices.²³⁻²⁸ These organic molecules are known to change in color upon UV irradiation. For example, the colorless spiropyranes and spirooxazines (Fig.3) undergoes an heterolytic C-O ring cleavage, producing colored forms of merocyanines.

Their optical response actually depends on the chemical nature of the hybrid matrix and two types of photochromic behavior have been observed.^{23,26-28}

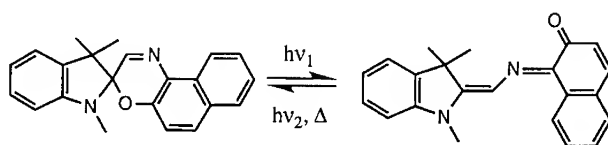


Figure 3. Molecular structure of spirooxazine

- Direct photochromism is observed when spiropyran dyes are trapped within hydrophobic hybrid matrices synthesized from $\text{MeSi}(\text{OEt})_3$. The molecule turns from colorless to colored upon irradiation.

- Reverse photochromism is observed in hydrophilic silica synthesized from $\text{Si}(\text{OCH}_3)_4$. In this case, the open zwitterionic species should form hydrogen bonds with the Si-OH groups of the silica matrix. The colored form is then stabilized and can be observed even in the absence of irradiation. Bleaching is obtained upon irradiation in the visible range. A mixture of both effects is currently observed in most hybrid matrices that contain both hydrophilic and hydrophobic nano-domains. The optical contrast is then small and thermal fading is slow (few hours). Moreover the gel matrix shrinks upon drying preventing the free rotation of trapped organic molecules and the photochromism stops when the gel is dry. Such a materials can obviously not be of any practical use.

Much better results have been obtained recently using highly hydrophobic sol-gel matrices synthesized via the hydrolysis and co-condensation of $\text{HMeSi}(\text{OEt})_2$ (DH) and $\text{HSi}(\text{OEt})_3$ (TH).²⁸ Spirooxazine (SO) doped matrices exhibit normal photochromism. All SO molecules being in the closed form before irradiation these materials are colorless. The time dependence of absorption upon repeated irradiation at 365 nm for SO doped DH70/TH30 coatings is reported in figure 4.

Upon irradiation an intense blue coloration appears in less than one second. The optical contrast between colored and bleached states is high ($\Delta\text{OD} = 1.3$). Bleaching is very fast (rate constant = 0.2 s^{-1}) and photochromism highly reversible. The photochromic response of these SO doped hybrid materials are to the best of our knowledge much faster than those reported for SO in any other matrix (sol-gel matrices, organic polymers, alcohol solution, ...).²⁸ The high reactivity of DH/TH precursors towards hydrolysis-condensation reactions (Si-OH groups are immediately consumed) and the strong hydrophobicity of the resulting matrix are both responsible for the fast and direct

photochromism that could lead to interesting applications for optical switches or optical lenses.

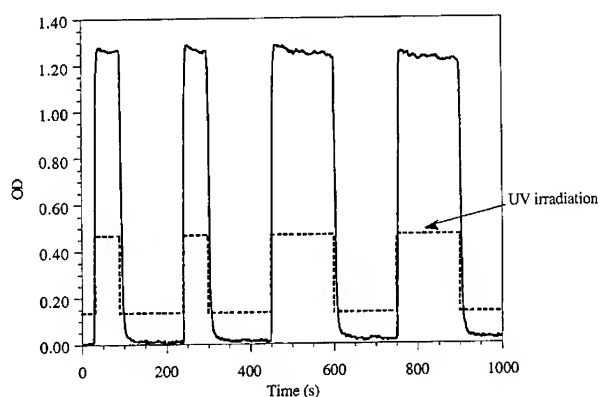


Figure 4 : Photochromic response of the SO doped DH70/TH30 matrix

The photochromism of diarylethene (DE) and furylfulgides (FF) is based on a reversible isomerization and thermal fading does not occur at room temperature. A photochemically reversible change is observed upon alternate UV/visible irradiation (Fig.5). These photochromic compounds are thermally stable and resistant to photochemical side reactions and can be used in various applications such as photo-optical switches or optical information storage.

Both DE and FF dyes exhibit a direct photochromism in solution or embedded in hybrid sol-gel matrices made via the hydrolysis of DH/TH precursors. Upon UV irradiation the hybrid matrix takes a red coloration arising from a broad absorption band around 500 nm. This absorption is blue shifted (about 10 nm) when going from a toluene solution to the DH/TH matrix. This hypsochromic shift is a confirmation of the strongly hydrophobic and non polar host media provided by these matrices.²⁵

Typical coloration-bleaching cycles were recorded at 531 nm for each dye embedded in hybrid matrices, in order to study the kinetics of ring opening and ring closing reactions. A photochemical kinetic treatment was done in order to obtain experimental quantum yields. The kinetics of coloration measured for DE dyes embedded in solid matrices are close to those of DE and FF in solution. It has also to be pointed out that the quantum yield (F) measured for DE (F=0.24) and FF (F=0.15) dyes embedded in these DH/TH hybrid matrices are quite high.²⁵ The stable and efficient photochromic properties of DE

in these DH/TH hybrid matrices opens many opportunities in the field of optical memories and patterning.

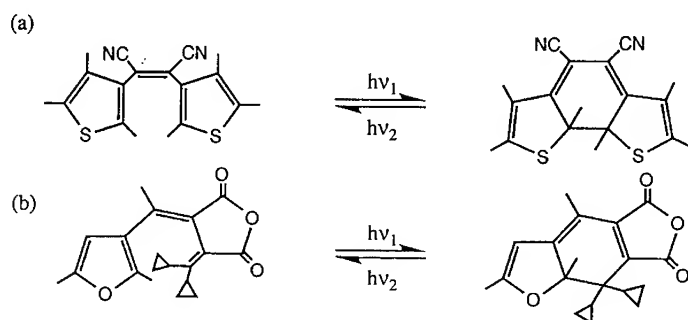


Figure 5 : Molecular structure of diarylethene DE (a) and furylfulgide FF (b)

Reverse-saturable absorption. Phthalocyanines

Reverse-saturable absorption could be used for the fabrication of optical limiting devices. Such materials are transparent at a given wavelength for low-energy pulses and become absorbent for high-energy pulses. This phenomenon is due to the fact that their excited states are more absorbent than the ground state. This phenomenon has been mainly studied in solution with dyes such as phthalocyanines, HITC and fullerenes (Fig.6).^{29,30} However solutions are not very convenient for the realization of optical devices. Solid materials or films would be more suitable and there is considerable interest in the possibility of fabricating optical limiters based on solid-state materials. Sol-gel processing could be an answer to this problem. Metallophthalocyanines MePc (Me=Al, Sn, Ge, Si...), fullerenes and HITCI molecules exhibit strong Excited State Absorption (ESA) at 532 nm.³¹ When trapped within sol-gel matrices phthalocyanines, fullerenes and HITCI molecules have been shown to retain their optical properties.³²⁻³⁹

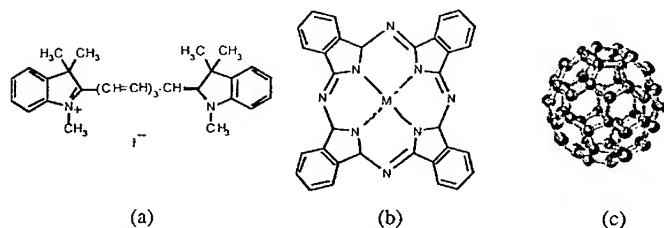


Figure 6 : Molecular structure of some dyes showing reverse-saturable absorption properties in sol-gel matrices. (a) HITCI, (b) Phthalocyanines, (c) Fullerenes

HITCI molecules embedded within sol-gel derived matrices exhibit good optical non linear properties.³⁴ However these merocyanine dyes are known to present some lack in long term stability that prevents their use in many optical devices.³² On the contrary phthalocyanines remain stable in sol-gel matrices and exhibit optical non linearities comparable to those of the solutions.³⁵⁻³⁷ However phthalocyanine dyes are poorly soluble in organic solvents and sol-gel matrices, typically about 10^{-5} to 10^{-6} mol/l. The absorption of sol-gel coatings may then be too low. Grafting dyes onto the sol-gel matrix could then provide an opportunity to overcome this problem. Silicon phthalocyanine (PcSiCl_2) was reacted with methyl-diethoxysilane ($\text{MDES}=\text{SiHMe}(\text{OEt})_2$) and the resulting solution was hydrolyzed in the presence of zirconium propoxide. Coatings in which the PcSiCl_2 concentration is of about $5 \cdot 10^{-3}$ M were deposited from the resulting sols. The absorption spectra of the coatings show an intense Q band located at 666 nm and two weak transitions located at 601 nm and 632 nm. The low energy shift of the Q band (initially located at 690 nm for PcSiCl_2) was assigned to the replacement of the two chlorine by oxygen ligands coming from silyloxy, alkoxy or hydroxy groups.³⁸ The weak transitions were assigned to a vibrational band (601 nm) and to phthalocyanine dimers (632 nm).^{37,39} The weak intensity of this latter absorption suggests that phthalocyanine dyes are well dispersed within the hybrid matrix even at such a high concentration. The solubility of phthalocyanines increases by two order of magnitude and the high dispersion of these dyes within the hybrid matrix is likely related to some grafting of PcSiCl_2 to MDES precursors through PcSi-O-Si links.

Optical limiting measurements were performed on hybrid bulk samples by using an incident radiation consisting of 10ns pulses with energy up to 8 J. The laser beam (frequency doubled Nd:YAG laser at 532 nm) was focused on the samples with a diameter of about 200 μm and the transmitted light was measured with a calibrated photodiode.

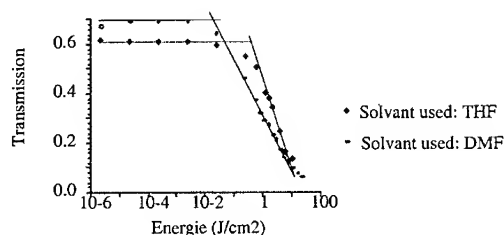


Figure 7 : Transmission of PcSiCl_2 in hybrid sol-gel matrices vs incident fluence (41)

The evolution of the transmission as a function of the incident fluence for the bulk materials is shown in figure 7. Fluence threshold as low as 0.02 J/cm² and transmission at low intensity as high as 70% have been obtained showing that these materials are efficient reverse saturable absorbers. These results are in agreement with those already obtained with phthalocyanines doped sol-gel matrices.⁴⁰

However many hybrid matrices are damaged by the high energy irradiation required to reach saturation. As a consequence the stability of these matrices or/and the efficiency of the dyes need further improvement before these new materials could be used as efficient optical limiters.

Non-linear optics

Most of the research devoted to the Non-Linear Optical (NLO) properties of hybrid materials was first related to third order processes which are compatible with the isotropy of amorphous sol-gel matrices. Organic molecules in amorphous sol-gel matrices are usually randomly oriented thus ruling out the emission of second harmonics. Second order nonlinearities can only be observed in non centrosymmetric environments. Organic chromophores can actually be oriented in hybrid sol-gel matrices via Electrical Field Induced Second Harmonic (EFISH) or corona electrical field poling techniques.⁴¹⁻⁴³ Organic molecules such N-[3-Triethoxysilyl-propyl]-2,4 Dinitrophenyl amine (TSDP) were chemically bonded to the oxide backbone of gels. The chemical bonding of the dye to the sol-gel matrix allowed to increase the dye concentration without any crystallization.⁴¹⁻⁴³

The NLO response of hybrid coatings can be improved by using organic dyes with high polarisabilities such as N-(4-nitrophenyl)-L-prolinol (NPP) or disperse red derivatives. The thermal relaxation of embedded chromophores can be controlled by increasing the matrix rigidity. This point is without no doubt the most important in order to be able to make efficient NLO devices. Promising results have been obtained via the co-condensation of polyfunctional alkoxy silane carrying an NLO dye with a high quadratic hyperpolarizability and a tetrafunctional Si(OMe)₄ precursor of silica. A difunctional Red 17, 4-(amino-N,N-diethanol)-2-methyl-4'-nitroazobenzene chromophore can bind two molecules of the alkoxy silane precursor (Fig.8). This double grafting should minimize the randomization of the oriented dyes.⁴⁴⁻⁵²

The poled hybrid coatings exhibit non resonant second-order nonlinearities as high as 150-200 pm/V, with significant long-term stability (10% of the signal is lost after 20 days).^{45,52} The thermal stability at 80°C was shown to be excellent, making the ICTES-Red 17/TMOS system a competitive candidate for nonlinear optics systems.

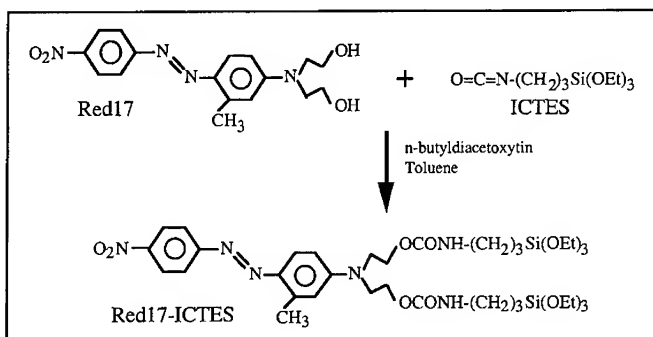


figure 8 : Reaction scheme of the coupling process between ICTES and Red 17

These reproducible high non linearities could probably be improved by using the optical poling techniques recently tested in sol-gel derived matrices.⁵³ However, as far as NLO devices are concerned these promising results must be completed by measurements of electro-optical efficiency, waveguiding properties and the evaluation of the optical losses.

Encapsulation of biomolecules

Materials based on biomolecules could be good candidate for potential applications in optical information processing. The mild conditions associated with sol-gel chemistry allows the encapsulation of fragile biomolecules such as enzymes. They have been extensively studied for the realization of bio-sensors and bio-catalysts.^{54,55} Proteins other than enzymes can also be trapped within sol-gel matrices and some of them such exhibit interesting optical properties. Bacteriorhodopsin for instance is able to transfer protons under irradiation and could be used in the design of optoelectronic devices.⁵⁶

Bacteriorhodopsin (bR) is found in the purple membrane of a bacteria called *Halobacterium halobium*. It is made of 248 amino acid residues in seven trans-membrane α helices (Fig.9). Upon light illumination, bR undergoes a conformational change that pumps protons across the membrane, from the cytoplasm inside the cell to the external environment. The resulting pH gradient is used as an energy source for the synthesis of ATP from ADP. Several steps are involved in the photocycle. The step whereby the proton is released results in a blue-shift in the absorption spectrum of more than 150 nm and is responsible for the photochromic behavior of bR. It absorbs at 410 nm and turns back to the ground state which absorbs at 570 nm with a relaxation time of 10 ms. Many attempts have been made to immobilize this protein on solid substrates in order to use its properties in the design of optoelectronic devices. Actually bR has been encapsulated

along with its membrane lipids within sol-gel glass and it has been shown that the protein retains its light-sensitive properties and proton pumping function.⁵⁷⁻⁵⁹ When excited by a He-Ne laser at 632.8 nm, entrapped samples show a decrease in absorbance at 570 nm and an increase at 410 nm as long as the laser irradiation is maintained. These results are quite reproducible and the optical activity of the protein remains for many cycles. The average half-time to maximum change even shorter in the sol-gel glass than in an aqueous suspension.

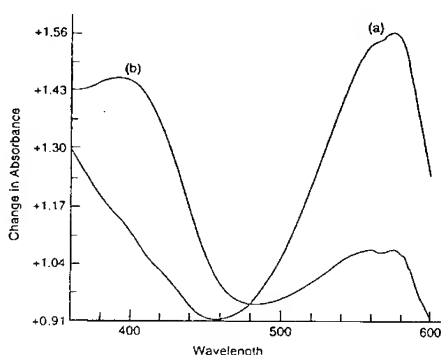


Figure 9. Optical absorption of Bacteriorhodopsin in a sol-gel matrix
(a) in the absence of light excitation, (b) under laser irradiation (from ref.57)

Phycocerythrin (PE) is another light-transducing protein. It absorbs light at 495 and 565 nm and display very intense fluorescence with high quantum yield at 575 nm. It could be a promising candidate for signal transduction and biosensor applications. The light receptors of this protein are open-chain tetrapyrroles coupled to the protein residues through thioether linkages. As for bR, phycocerythrin retains its optical activity when encapsulated within sol-gel glasses and the biomolecule even exhibits enhanced stability toward photodegradation. PE in solution degrades approximately 60% faster than PE encapsulated in sol-gel.⁶⁰ A strong two-photon induced fluorescence is even observed, suggesting that this material could be used for 3-D optical memories.

CONCLUSION

The sol-gel process actually offers unique opportunities for the synthesis of optical materials.

. The sol-gel route is ideally suited for the production of shaped materials in the form of thin films, fibers, fine powders and even monoliths.

. The homogeneous mixing of several components at a molecular level makes it possible to vary the chemical nature of optical materials over a wide range of compositions in order to tailor their optical properties such as the refractive index.

. The low temperature synthesis of metal oxides in organic solvents opens the possibility to add organic and even bio-molecules to the alkoxide solution. Hydrolysis and condensation then lead to the formation of an oxide network around the encapsulated species.

. Novel hybrid organic-inorganic materials can be synthesized via the sol-gel route. They fill the gap between polymers and glasses and offer new possibilities as matrices for many optical devices.

REFERENCES.

1. M. Ebelmen, Comptes Rendus Acad. Sci. Fr. 21, 502 (1845)
2. Sol-Gel Optics, processing and applications, L.C. Klein Ed., Kluwer Pub.(1994)
3. Sol-Gel Optics, SPIE Proceedings, Vol. 1328 (1990), Vol. 1758 (1992), Vol. 2288 (1994), Vol. 3136 (1997)
4. Sol-Gel Technology, L.C. Klein Ed., Noyes Pub. Park Ridge (1988)
5. C.J. Brinker, G.W. Scherer, Sol-Gel Science, Academic press, new York (1990)
6. J. Livage, Chem. Mater. 3, 578 (1991)
7. C. Gestaux, J. Leauté, C. Virey, J. Vial, US Patent 3 658 573 (april 1972)
8. J. Livage, Solid State Ionics, 86-88, 935 (1996)
9. J. Livage, G. Guzman, F. Beteille, P. Davidson, J. Sol-Gel Sci. Techn. 8, 857 (1997)
10. Z.A.E.P. Vroon, C.I.M.A. Spee, J. Non-Cryst. Solids, 218, 189 (1997)
11. F.G. Morin, Phys. Rev. Lett. 3, 34 (1959)
12. G. Guzman, R. Morineau, J. Livage, Mat. Res. Bull. 29, 509 (1994)
13. G. Guzman, F. Beteille, R. Morineau, J. Livage, J. Mater. Chem. 6, 505 (1996)
14. G. Guzman, F. Beteille, R. Morineau, J. Livage, Eur. J. Solid State and Inorg. Chem. 32, 851 (1995)
15. F. Beteille, R. Morineau, J. Livage, M. Nagano, Mat. Res. Bull. 32, 1109 (1997)

16. J. Livage, C. Sanchez, F. Babonneau in Chemistry of Advanced Materials, 9, 389, Wiley-VCH (1998)
17. H. Schmidt and B. Seiferling, Mat. Res. Soc. Symp. Proc. 73, 739 (1986)
18. B.M. Novak, Adv. Mater. 5, 422 (1993)
19. C. Sanchez, F. Ribot, New J. Chem. 18, 1007 (1994)
20. U. Schubert, N. Hüsing, A. Lorenz, Chem. Mater. 7, 2010 (1995)
21. D.A. Loy, K.J. Shea, Chem. Rev. 95, 1431 (1995)
22. P. Judenstein, C. Sanchez, J. Mater. Chem. 6, 511 (1996)
23. D. Levy, Chem. Mater. 9, 2666 (1997)
24. J. Biteau, G. M. Tsvigoulis, F. Chaput, J. P. Boilot, S. Gilat, S. Kawai, J. M. Lehn, B. Darracq, F. Martin, Y. Levy, Mol. Cryst. Liq. Cryst., 297, 65 (1997)
25. C. Sanchez, A. Lafuma, L. Rozes, K. Nakatani, J. A. Delaire, E. Cordocillo, B. Viana, P. Escribano in Inorganic-Organic Hybrids For Photonics, L. Hubert, S. Najafi Eds., Proc. SPIE, Washington (1998)
26. D. Levy, S. Einhorn and D. Avnir, J. Non-Cryst. Solids, 113, 137 (1989)
27. J. Biteau, F. Chaput, J. P. Boilot, J. Phys. Chem. 100, 9024 (1996)
28. B. Schaudel, C. Guermeur, C. Sanchez, K. Nakatani, J. Delaire, J. Mater. Chem. 7, 61 (1997)]
29. W. Blau, H. Byrne, W.M. Dennis, Opt. Commun. 56, 25 (1985)
30. R.C. Hoffman, K.A. Stetyick, R.S. Potemberg, D.G. McLean, J. Opt. Soc. Am. B6, 772 (1989)
31. J.W. Perry, L.R. Khundakar, D.R. Coulter, D. Alvarez, S.R. Marder, T-H Wei, M.J. Sence, E.W. Van Stryland, D.J. Hagan, Proc. NATO Conf. Organic Molecules for Nonlinear Optics and Photonics, J. Messier, F. Kajzar, P. Prasad Eds. Kluwer Pub. London (1991) pp.369
32. B. Lebeau, N. Herlet, J. Livage, C. Sanchez, Chem. Phys. Lett., 15, 206 (1993)
33. F. Delmonte, D. Levy, Chem. Mater., 7, 292 (1995)
34. C. Sanchez, P. Griesmar, E. Toussaere, G. Puccetti, I. Ledoux and J. Zyss, Non Linear Optics, 4, 245 (1992)
35. F. Bentivegna, M. Canva, P. Georges, A. Brun, F. Chaput, L. Malier, J.P. Boilot, Appl. Phys. Lett. 62, 1721 (1993)
36. M. Brunel, F. Le Luyer, M. Canva, A. Brun, F. Chaput, L. Malier, J.P. Boilot, Appl. Phys. B58, 443 (1994)
37. P.D. Fuqua, K. Mansour, D. Alvarez, S.R. Marder, J.W. Perry, B. Dunn, SPIE Sol-Gel Optics II, 1758, 499 (1992)
38. A.B.P. Lever, Adv. Inorg. Chem. Radiochem. 7, 27 (1965)
39. L.C. Gruen, Aust. J. Chem. 25, 1661 (1972)

40. B. Lebeau, C. Guermeur, C. Sanchez, Mater. Res. Soc. Proc., 345, 315, (1994)
41. G. Pucetti, I. Ledoux, J. Zyss, P. Griesmar and C. Sanchez, Polymer Preprint, 32, 61 (1991)
42. E. Toussaere, J. Zyss, P. Griesmar, C. Sanchez, Non Linear Optics, 1, 349 (1991)
43. P. Griesmar, C. Sanchez, G. Pucetti, I. Ledoux and J. Zyss, Mol. Eng. 1, 205 (1991)
44. J. Kim, J. L. Plawsky, E. Van Wagenen and G. M. Korenowski, Chem. Mater., 5, 1118 (1993)
45. B. Lebeau, C. Sanchez, S. Brasselet, J. Zyss, Chem. Mater. 9, 1012 (1997)
46. B. Lebeau, J. Maquet, C. Sanchez, F. Beaume, F. Lauprêtre, J. Mater. Chem. 7, 989 (1997)
47. C. Sanchez, and B. Lebeau, Pure Appl. Opt., 5, 689, (1996)
48. (a) F. Chaput, . Reihl, Y. Levy, J.P. Boilot, Chem. Mater., 5, 589, (1993). (b) D. Reihl, F. Chaput, Y. Levy, J.P. Boilot, F. Kajzar, P.A. Chollet, Chem. Phys. Lett., 245, 36, (1995)
49. H.W. Oviatt, K.J. Shea, S. Kalluri, Y. Shi, W. Steier L.R. Dalton, Chem. Mater., 7, 493, (1995).
50. Y. Zhang, P.N. Prasad, and R. Burzynski, Chem. Mater., 4, 851, (1992)
51. S. Marturunkakul, J. I. Chen, R. J. Jeng, S. Sengupta, J. Kumar and S. K. Tripathy, Chem. Mater., 5(6), 743, (1993)
52. D. Blanc, P. Peyrot, C. Sanchez, C. Gonnet, Optical Engineering on Integrated Optics, 37, 1203 (1998)
53. C. Fiorini, F. Charra, J.M. Nunzi, I.D.W. Samuel, J. Zyss, Opt. Lett. 20, 1, 2469 (1995)
54. D. Avnir, S. Braun, O. Lev, M. Ottolenghi, Chem. Mater. 6, 1605 (1994)
55. B.C. Dave, J.S. Valentine, J. Zink, Anal. Chem. 66, 1120A (1994)
56. R.R. Birge, Ann. Rev. Phys. Chem. 41, 683 (1990)
57. H.H. Weetall, B. Robertson, D. Cullin, J. Brown, M. Walch, Biochim. et Biophys. Acta, 1142, 211 (1993)
58. W. Shuguang, L.M. Ellerby, J.S. Cohan, B. Dunn, M.A. Elsayed, J.S. Valentine, J.I. Zink, Chem. Mater. 5, 115 (1993)
59. H.H. Weetall, Biosensors & Bioelectronics, 11, 327 (1996)
60. Z. Chen, L.A. Samuelson, J. Akkara, D.L. Kaplan, H. Gao, J.K. Jumar, K.A. Marx, S.K. Tripathy, Chem. Mater. 7, 1779 (1995)

HYBRID SOL-GEL GLASSES CONTAINING FULLERENE DERIVATIVES FOR BOTTLENECK OPTICAL LIMITING WITH MULTILAYER STRUCTURES

R. SIGNORINI¹, S. SARTORI¹, M. MENEGHETTI¹, R. BOZIO¹, M. MAGGINI²,
G. SCORRANO², M. PRATO³, G. BRUSATIN⁴, M. GUGLIELMI⁴

¹Department of Physical Chemistry, University of Padua, Via Loredan 2, I-35131
Padua, Italy; ²Centro Meccanismi Reazioni Organiche - CNR, Department of

Organic Chemistry, University of Padua, Via Marzolo 1, I-35131 Padua, Italy;

³Department of Pharmaceutical Sciences, University of Trieste, Piazzale Europa 1,
I-34127 Trieste, Italy; ⁴Department of Mechanical Engineering, Materials Division,
University of Padua, Via Marzolo 9, I-35131 Padua, Italy

Abstract Functionalized pyrrolidino-fullerenes are investigated as candidates for optical limiting (OL) applications based on a reverse saturable absorption mechanism. NL transmission data and their wavelength dispersion measured on solution samples are analyzed theoretically and it is concluded that the pyrrolidino-fullerenes fulfill the requirements for practical devices in a spectral region ca. 100 + 150 nm wide centered around the triplet absorption peak at 700 nm. Solid materials suitable for OL devices are produced by incorporation in organically modified sol-gel glasses and their NL transmission properties are compared with those of solution samples. It is shown that structural factor that may negatively affect the OL properties of disordered solids with comparatively high dye concentration do not play a major role in the present case. Multilayer structures following a bottleneck design are prepared and their NL transmission properties are characterized. Discrepancies with the predictions of a simple model are reported and discussed in view of further development work.

Keywords: Fullerene derivatives, Optical limiting, Reverse saturable absorption, Sol-gel glasses

INTRODUCTION

Among the many possible optical processes suitable for implementation into optical limiters,¹ nonlinear (NL) absorption appears to ideally respond to the main requirement of a passively protecting device in that the energy of the laser field is converted mostly into thermal energy and to a lesser extent into incoherent emission (fluorescence or

phosphorescence). Depending on more specific requirements, either a coherent multiphoton process (two- or three-photon absorption) or one in which an incoherent radiationless step intervenes between the interactions with the laser field may be preferable. In general, limitation of pico- or femtosecond pulses with very high peak powers can be accomplished by means of coherent multiphoton absorption whereas the cumulative character of incoherent processes such as reverse saturable absorption (RSA) makes them more apt for limitation of pulses of nanosecond or longer duration. An RSA process initiated by a one-photon absorption is likely to be characterized by a low threshold for NL transmittance whereas one involving an initial two-photon absorption presents the advantage of a higher transparency of the device under ordinary illumination.

The initial interest in the fullerenes² as potential optical limiting materials was motivated by their high quantum yield for singlet to triplet population transfer and by their almost flat weak absorption extending over almost all the visible spectral range. Combined together, these two features make fullerenes promising as low-threshold, broad band optical limiting materials based on a one-photon-induced RSA process. With pulses of duration from nanoseconds to microseconds, the active species in the RSA is the strongly absorbing triplet state.

The C₆₀ fullerene is an attractive molecule not only for its potentially useful optical properties but also because of its flexible chemistry.³ The ingenious combination of these two features opens the way to the preparation of novel materials endowed with the combination of physical and chemical properties needed to exploit them in practical optical limiters. In particular, the implementation of design principles^{4,5} which have been developed for the optimization of these devices, demands for processible solid materials that incorporate the active molecules at a suitably high concentration yielding optically clear materials that are thermally, photochemically and environmentally stable. Early attempts⁶ have been made by incorporating C₆₀ into a polymer (PMMA) matrix but the threshold fluence for laser damage of these materials is possibly too low for practical applications.

In the last few years, we have been involved⁷ in solving some of the material's issues related to the exploitation of the optical limiting (OL) properties of C₆₀ in practical

passive devices for the protection of optical detectors against laser damage. Our approach has been to prepare organically modified sol-gel glassy materials incorporating pyrrolidino-fullerenes highly soluble in polar solvents and functionalized with silicon alkoxide groups enabling them to covalently link the sol-gel matrix.

In this paper, the wavelength dispersion of the NLO transmission of functionalized fullerenes in solution is compared with that of C_{60} ^{2,8} and discussed in terms of the perspectives for the preparation of practical OL devices based on a multilayer structure composed of alternating silica and organically modified sol-gel glasses. After some general consideration on structural factors that may affect the performance of reverse saturable absorbers in a glassy matrix, the NL transmittance data of our sol-gel samples is compared with that of solutions and it is shown that inclusion in the glassy matrix does not affect appreciably the OL properties of the pyrrolidino-fullerenes.

The OL performances of multilayer structures prepared according to the prescriptions for bottleneck optical limiters,⁴ measured with *f*/5 optics, are reported and discussed in view of possible further improvements.

OPTICAL LIMITING PROPERTIES OF PYRROLIDINO-FULLERENES

Investigating the NL transmission properties of isolated molecules in dilute solutions is the first obvious step in assessing the practical usefulness of an OL material based on RSA. The OL properties of C_{60} have been the subject of several reports. More recently, we have reported OL data^{7,9} for some C_{60} -derivatives which have been purposefully synthesized in order to increase the solubility of C_{60} in polar solvents and to endow the fullerenes with a silicon alkoxide group able to covalently link the silica network of sol-gel glasses. Here we focus on one of these derivatives, hereafter denoted as FULP2, whose structure is shown in Fig. 1. FULP2 was generated by thermal ring-opening of an aziridine bearing both an electron-attracting $-COOCH_3$ group and the silicon alkoxide functionality in the presence of C_{60} .¹⁰ The solubility of FULP2 in THF, a polar solvent suitable for the processing of sol-gel glasses, is 43 mg/ml.

The electronic absorption spectrum of FULP2 is similar to that of other 1,2-dihydrofullerenes.^{11,12} The main differences with respect to that of the parent C_{60} is a typical narrow peak around 430 nm, a slow decrease of absorption intensity in the visible

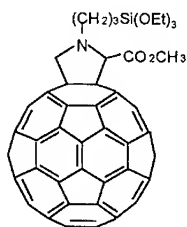


FIGURE 1 Chemical structure of FULP2.

and, most notable, a weak band around 700 nm, that is at wavelengths where C_{60} practically does not absorb.¹³ Combined with a shift of the main peak of the triplet absorption spectrum from 750 nm in C_{60} to about 700 nm in FULP2 and with a still high (almost unitary) quantum efficiency for intersystem crossing,^{11,12} the change in the ground state absorption leads one to expect a higher OL efficiency for FULP2 than for C_{60} in the deep red region of the spectrum. This is ascribed to an RSA process in which the higher ground state absorptivity of FULP2 around the peak wavelength of the triplet absorption spectrum (700 nm) makes it easier to pump the derivative into the strongly absorbing triplet state.

This expectation has been confirmed experimentally by measuring and comparing the NL transmittance of toluene solutions of pyrrolidino-fullerenes and of C_{60} at various wavelengths.^{7,9} These data, as well as those reported here for solution samples, have been measured using ca. 15 ns pulses delivered by an excimer pumped dye laser focused with a 200 mm focal length lens into 10 mm liquid cells.

RSA model analysis of the NL transmission

A quantitative analysis of the NL transmission data based on a suitable model for the RSA process can provide us with useful insights on the role of a number of system parameters such as concentration and thickness of the solution samples, wavelength, energy and beam properties of the laser, possible concurrent phenomena that may enhance or depress the OL performance.

The model we have adopted considers six levels, sketched in Fig. 2, to mimic the electronic structure of fullerenes.

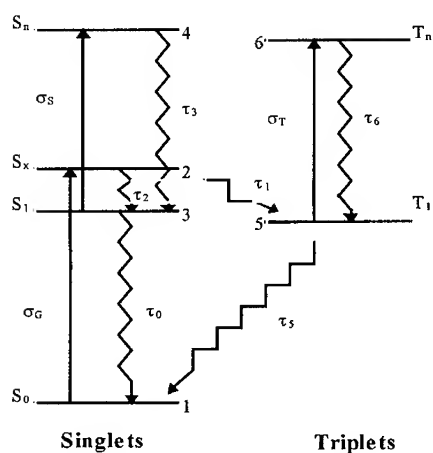


FIGURE 2. Six level system used to model the RSA phenomenon.

The population dynamics is described by the coupled rate equations

$$\dot{\mathbf{n}} = \mathbf{X}\mathbf{n} \quad (1.a)$$

with

$$\mathbf{X} = \begin{pmatrix} -\frac{\sigma_G I_L}{h\nu} & \frac{\sigma_G I_L}{h\nu} & \frac{1}{\tau_0} & 0 & \frac{1}{\tau_5} & 0 \\ \frac{\sigma_G I_L}{h\nu} & -\frac{\sigma_G I_L}{h\nu} - \frac{1}{\tau_2} & 0 & 0 & 0 & 0 \\ 0 & \frac{1}{\tau_2} & -\frac{\sigma_S I_L}{h\nu} - \frac{1}{\tau_0} - \frac{1}{\tau_1} & \frac{\sigma_S I_L}{h\nu} + \frac{1}{\tau_3} & 0 & 0 \\ 0 & 0 & \frac{\sigma_S I_L}{h\nu} & -\frac{\sigma_S I_L}{h\nu} - \frac{1}{\tau_3} & 0 & 0 \\ 0 & 0 & \frac{1}{\tau_1} & 0 & -\frac{\sigma_T I_L}{h\nu} - \frac{1}{\tau_5} & \frac{\sigma_T I_L}{h\nu} + \frac{1}{\tau_6} \\ 0 & 0 & 0 & 0 & \frac{\sigma_T I_L}{h\nu} & -\frac{\sigma_T I_L}{h\nu} - \frac{1}{\tau_6} \end{pmatrix} \quad (1.b)$$

and the transmission properties are calculated from the propagation equation

$$\frac{dI_L}{dz} = -I_L N [\sigma_G (n_1 - n_2) + \sigma_S (n_3 - n_4) + \sigma_T (n_5 - n_6)] \quad (2)$$

In Eq. 1, \mathbf{n} and $\dot{\mathbf{n}}$ are column vectors of the fractional populations n_i of the six levels and their time derivatives, respectively. The meaning of the absorption cross sections (σ) and of the decay times (τ) is given in Fig. 2; I_L is the intensity of the laser radiation at the frequency ν and, in Eq. (2), N is the number density of fullerene molecules.

For thick samples, solutions of the above equations can be calculated numerically by dividing the samples into thin slices and using the intensity obtained by integration of Eq. (2) in one slice as the input for the rate equations in the next slice. For a 10 mm sample, convergence of the results was obtained after reducing to 1 mm the thickness of each slice. Assuming a Gaussian temporal profile of the incoming pulses, that means integrating over 8,000 time intervals of about 5 ps each to get a complete crossing of the sample by the laser pulse. The transmitted energy is then calculated by integrating the emerging pulse. A top-hat spacial beam profile has been assumed for simplicity.

Accounting for the propagation geometry of the focused beam turned out to be critical for the success of our model calculations. This is because with our optics and with a 3 mm diameter of the collimated beam entering the focusing lens, the thickness of the solution samples is well above the confocal region. Initial attempts at using the geometry for propagation of a Gaussian beam did not produce satisfactory results. The likely reasons of this difficulty are (i) the deviation from a Gaussian intensity profile of our laser beam and (ii) the intensity dependent refractive index changes induced by the propagating beam. A satisfactory fitting of the experimental data could only be obtained by considering a beam geometry in which the diameter of the confocal region was considered as an adjustable parameter while all the other parameter values were kept fixed (the rate constants and absorption cross sections were literature values^{11,12,14}).

Figure 3, upper panel, shows the NL transmission data for a toluene solution of FULP2 with a linear transmission of 78 % measured at 532 nm and plotted against the logarithm of the incident fluence. Note that the reported fluences are nominal values obtained by simply dividing the incident pulse energy by the cross sectional area at the beam waist. The full curve is the calculated NL transmission according to our RSA model using a diameter of 250 μm at the beam waist. The data were measured up to a nominal fluence of 0.8 J/cm². Already at this moderate fluence the data show a deviation

towards reduced NL transmittance compared to the RSA model which is likely due to a contribution from NL scattering and thermal effects.

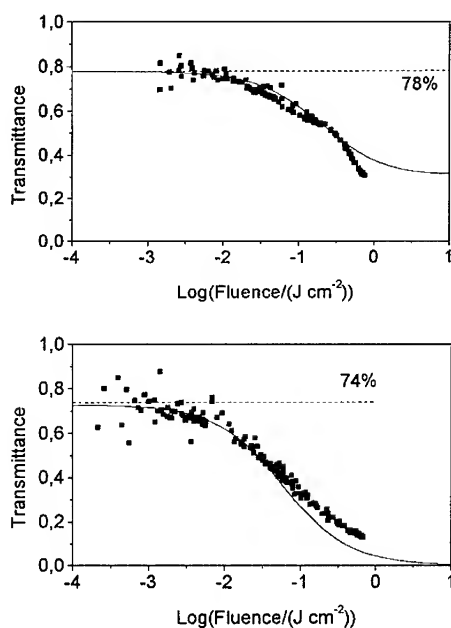


FIGURE 3. Measured and calculated nonlinear transmission of FULP2 solutions in toluene measured at 532 nm (upper panel) and 690 nm (lower panel).

Figure 3, lower panel, shows corresponding data measured and calculated at 690 nm. Note that the calculated NL transmission drop is larger at this wavelength than at 530 nm owing the larger ratio σ_T / σ_G at this wavelength which is close to the peak wavelength of the triplet absorption spectrum. The negative slope of the measured data is less than that predicted by the RSA model. A possible origin of this discrepancy is related to the intensity dependent refractive index of the fullerene solution due to both the electronic contribution of the solute molecules and the local heating of the solvent. There is enough evidence¹⁵ to suggest that the NL refractive index is negative for these

solutions and this leads to a fluence dependence of the beam propagation geometry that is not accounted for in our RSA model calculations.

Further insight into the microscopic mechanism of the NL transmission of our samples is gained by analyzing the time evolution of the populations at different points in the solution samples as deduced from the RSA calculations. Figure 4 shows the relative populations of the ground state S_0 (full curve), of the first excited singlet state S_1 (dotted curve) and of the triplet state T_1 (dashed curve). These curves are shown for each of the ten slices in which our sample was divided by shifting the time scale by ca. 20 ns for each successive slice. All the data were calculated for a nominal fluence of 0.5 J/cm^2 . Panels a) and b) give the results for C_{60} and for FULP2, respectively, when the laser wavelength is at 652 nm. The lower OL efficiency of C_{60} with respect to FULP2 at this wavelength is clearly understood as a result of both the smaller absorption cross section of the triplet state and the higher fluence required for transferring population from the ground to the excited triplet state. The effect of the latter is clearly evident in the data of Fig. 4 where the maximum achieved triplet state population is significantly lower for C_{60} than for

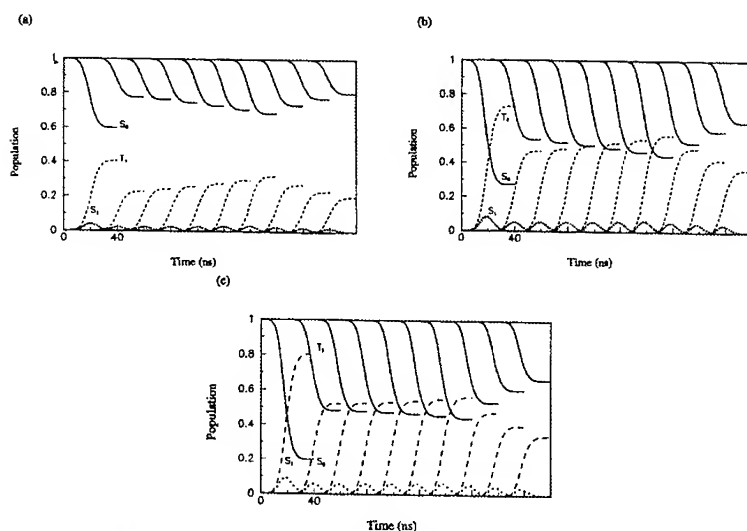


FIGURE 4. Calculated time evolution of the ground (S_0 , full curve), excited singlet (S_1 , dotted curve) and triplet (T_1 , dashed curve) states along the beam path in 10 nm thick solution samples excited with 10 ns pulses of 0.5 J/cm^2 nominal fluence. (a): C_{60} at 652 nm; (b) FULP2 at 652 nm; (c) FULP2 at 690 nm.

FULP2 and can be accounted for in simple terms by considering the different values of the saturation fluence $F_s = h\nu/\Phi\sigma_G$. At 652 nm this amounts to 0.96 J/cm² for C₆₀ and 0.37 J/cm² for FULP2. The data in panel c) of Fig. 4 give the population dynamics for FULP2 pumped at 690 nm, close to the triplet absorption peak, with a nominal fluence of 0.5 J/cm². Consider that at this wavelength the saturation fluence for C₆₀ would reach the prohibitively large value of about 5 J/cm².

It is worth considering the envelope of the maximum achieved triplet state population over the ten slices taking into account that for this case $F_s = 0.32$ J/cm². The envelope is the result of the balance between the pulse attenuation while the beam crosses the sample and the enhancement of the fluence in the confocal region yielding a plateau at about 0.5 of the relative triplet state population. Note that for slices beyond the confocal region the population transfer is rather inefficient thus reducing their contribution to the overall OL performance.

The wavelength dispersion of the OL properties of FULP2 solutions is shown in Fig. 5. The data points are measured NL transmittance values for a 10 mm thick solution sample at 0.5 J/cm² nominal fluence. The full curve gives calculated values according to our RSA model for the same nominal fluence using literature data^{11,12} for the ground state, excited singlet and triplet state absorption cross sections as fixed input data. The good agreement with the measured NL transmission data indicates that RSA is the

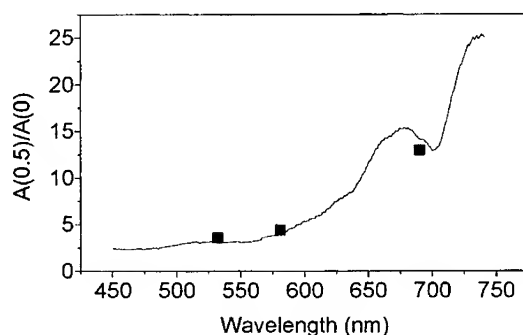


FIGURE 5. Measured and calculated wavelength dispersion of the optical limiting properties of FULP2.

dominant mechanism for OL at all the investigated laser wavelengths. It also gives us confidence in using the literature data for absorption cross sections in assessing the potential usefulness of pyrrolidino-fullerenes as NL materials for practical passive devices for the protection of optical detectors. The maximum achievable efficiency of these devices is attained when, during each pulse, the laser beam excites practically all the molecules to the triplet state from which it is efficiently absorbed. It has been frequently reported that an OL device suitable for protection of the human eye against typical 10 mJ laser pulses of ns to μ s duration should exhibit a linear transmission around 70 % and limit the transmitted pulse to below 1 μ J, that is it should be capable of an attenuation exceeding 10^4 . It is easily seen that, for this to be possible based on RSA, the ratio of the absorption cross section of the triplet to that of the ground state should be at least 25.8.⁴ Based on this, if other mechanisms such as NL scattering, multi-photon absorption, etc. do not add their contribution to the RSA one, the pyrrolidino-fullerenes can be considered as good candidates for practical devices in a spectral region ca. 100 \div 150 nm wide centered around the triplet absorption peak at 700 nm. Note that this does not hold for C₆₀ itself since it cannot be efficiently pumped at wavelengths longer than 700 nm whereas the triplet absorption peaks at 750 nm.

DOPED SOL-GEL GLASSES FOR OPTICAL LIMITING

Structural factors that may affect RSA

We have recently developed processing techniques for preparing hybrid (organic-inorganic) sol-gel glasses doped with C₆₀ derivatives at high concentrations which are chemically, mechanically and thermally stable.⁷ They possess other properties which are highly desirable in view of their use in OL devices with multilayer structures, namely they can be deposited as thick (from tens to a few hundreds μ m) films, they have high optical quality and they can withstand prolonged irradiation with laser pulses at fluence of some tens J/cm².

Only recently has the issue of comparing the OL performance of RSA materials in glassy matrices with the same materials in solution been addressed. In their work on C₆₀-doped PMMA, Kost and collaborators³ noted that the OL performance of the polymer was poorer than that of solution samples, a fact that they attributed to a less efficient NL

scattering in PMMA. More recently, McBranch and coworkers¹⁶ carried out an investigation of the excited state dynamics of fullerene by comparing solutions, evaporated thin films and doped sol-gel glasses. The decay of the excited state absorption was much faster in the evaporated films than in solution and the sol-gel glasses exhibited a behavior intermediate between the two. A faster decay of the excited state absorption would mean a less efficient OL and this was in fact verified by comparing the fluence dependent NL transmittance of their sol-gel samples with that of solution samples. The microscopic origin of the faster decay in the solid samples was ascribed to exciton-exciton annihilation in the microcrystalline C₆₀ composing the evaporated films or in C₆₀ aggregates which were supposed to be present in the sol-gel samples.

The tendency of C₆₀ to form clusters and eventually to phase-separate in sol-gel glasses is well known. The addition of a reactive, easily hydrolizable silicon alkoxide group in our pyrrolidino-fullerenes is just meant to favor a molecular dispersion of the NL chromophores by way of their stable linking to the silica network in the early stage of densification of the sol-gel materials. Preliminary results¹⁷ of investigations of the excited state dynamics of our sol-gel samples have shown a long lived component of the transient absorption with decay time in the microsecond range, comparable to that of the triplet state in solution samples.

Another factor that may cause a lower OL efficiency in glassy matrices than in solution is related to the structural disorder of these materials. Disorder causes inhomogeneous broadening of optical transitions. In accounting for its possible effects on an RSA process one must consider the possibility that the inhomogeneous distributions of the transition from ground to singlet excited state and that of the transition from lowest triplet to higher triplet states are uncorrelated. When narrow band laser pumping is used, the spectral distribution of singlet excited molecules can be described by the product

$$n_s(x) = H(x)Ng_s(x). \quad (3)$$

The factor

$$H(x) = \frac{I_L \sigma_G \gamma_s \tau_0 \tau_1 / (\tau_0 + \tau_1)}{2\pi \left[x^2 + \left(\frac{\gamma_s}{2} \right)^2 \left(1 + \frac{2I_L \sigma_G \tau_0 \tau_1}{\pi \gamma_s (\tau_0 + \tau_1)} \right) \right]} \quad (4)$$

accounts for the (quasi) steady-state pumping probability for molecules whose homogeneous absorption bandshape is centered at a frequency x relative to the center of the inhomogeneous distribution.¹⁸ For simplicity we assume $\nu_L = 0$, i.e., the laser frequency is resonant with the center of the inhomogeneously broadened absorption bandshape. In Eq. (4), γ_s is the homogeneous width of the transition from the ground to the lowest excited singlet state, the term $2I_L \sigma_G \tau_0 \tau_1 / \pi \gamma_s (\tau_0 + \tau_1)$ accounts for intensity-dependent broadening effects.

The factor

$$g_s(x) = \frac{1}{\sqrt{2\pi}\sigma_x} \exp\left(-\frac{x^2}{2\sigma_x^2}\right) = \int_{-\infty}^{+\infty} G(x, y) dy \quad (5)$$

is the inhomogeneous distribution of the singlet transition, assumed to be a normalized Gaussian of width σ_x . The integrand function

$$G(x, y) = \frac{1}{2\pi\sigma_x\sigma_y} \exp\left[-\frac{1}{2(1-r^2)}\left(\frac{x^2}{\sigma_x^2} + \frac{y^2}{\sigma_y^2} + \frac{2rxy}{\sigma_x\sigma_y}\right)\right] \quad (6)$$

is a bivariate Gaussian distribution function accounting for the degree of correlation between the inhomogeneous distributions of the ground-singlet and of the triplet-triplet transitions through the correlation factor $r = \langle xy \rangle / (\langle x^2 \rangle \langle y^2 \rangle)^{1/2}$.

The spectral distribution of molecules transferred from the excited singlet to the triplet state is

$$n_t(y) = N \int_{-\infty}^{+\infty} H(x) G(x, y) dx \quad (7)$$

where y is the frequency of the homogeneous triplet-triplet transition relative to the center of the inhomogeneous distribution located at some distance Δ from the laser

frequency. The absorbance at the laser frequency of the molecules excited to the triplet state is calculated as

$$\alpha_T(0) = \frac{\sigma_T \gamma_T}{2\pi} \int_{-\infty}^{+\infty} \frac{n_T(y) dy}{y^2 + \left(\frac{\gamma_T}{2}\right)^2} \quad (8)$$

with γ_T the homogeneous broadening of the triplet-triplet transition.

Figure 6 shows that the ratio $\alpha_T(0)/\alpha_G(0)$ depends on the ratio σ_x/γ_s and on the correlation coefficient r of the bivariate distribution function. The model calculations¹⁸ have been performed assuming $\gamma_s = 1$, $\sigma_T/\sigma_G = 100$, $\sigma_x = \sigma_y$ and a laser intensity 100 times the saturation value. It is seen that there is a decrease in the RSA efficiency as the ratio σ_x/γ_s increases and as the correlation coefficient r between the inhomogeneous distributions of the ground-singlet and triplet-triplet transitions decreases.

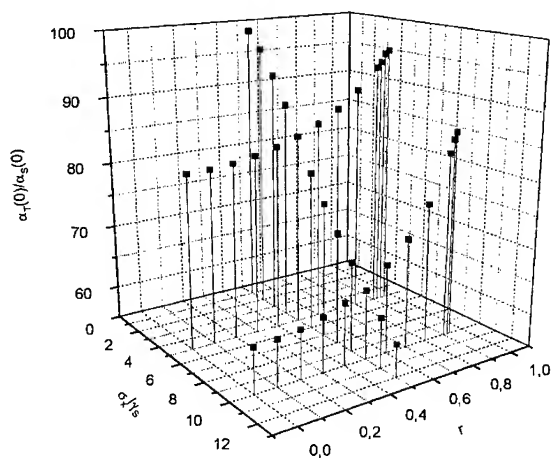


FIGURE 6. Dependence of the absorbance ratio on the features of the inhomogeneous broadening.

Optical limiting measurements

As mentioned above, the tendency of fullerenes to form clusters may have a negative effect on the OL properties. It has been reported¹⁹ that the formation of clusters in polar

solvents is signaled by a change in the absorption spectrum of fullerene into a broad or even structureless shape.

The great majority of our sol-gel samples exhibited spectra quite similar to those of pyrrolidino-fullerenes in solution. However, depending on the fullerene concentration and on details of the sol-gel processing (hydrolysis and condensation time, thermal treatment, etc.), a few of our samples showed an absorption spectrum where all the structures characterizing the C_{60} derivatives, including the sharp band at 430 nm, were smoothed out. Despite this, the measured absorbance levels were those expected from Beer's law based on the concentration and on the thickness of the samples and there was no clear sign of scattering from inhomogeneities. Comparison of the NL transmission properties of the two types of samples supports the idea that the formation of clusters of nanoscopic size was the origin of the anomalous absorption spectrum. In fact, two samples having the same linear transmittance of 77 %, one with a structureless spectrum the other with a solution-like spectrum, exhibited quite different nonlinear absorption values. The ratio $A_{NL}(0.5)/A_L$ between the nonlinear absorbance measured at 0.5 J/cm^2 and the linear absorbance was 1.86 and 3.89, respectively.

To compare OL data of sol-gel samples and of solutions under conditions as similar as possible we have prepared a multilayer structure of total thickness 2.15 mm composed of ten fullerene-doped sol-gel layers, each $50 \mu\text{m}$ thick, interleaved with soda

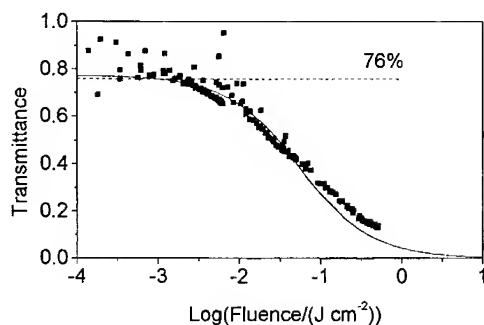


FIGURE 7. Measured and calculated nonlinear transmission at 690 nm of a ten-layers structure of sol-gel films containing FULP2

lime glass layers of thickness 150 μm each. The processing, thickness and fullerene concentration of the sol-gel films were similar to those used for the preparation of "bottleneck" structures (see below). The total transmittance of the multilayer structure was 76 %. The NL transmittance of this sample measured at 690 nm with $f/66$ optics (the same used for solution samples) is shown in Fig. 7. The full curve is a fitting to the data according to our RSA model obtained by using the same parameter values used for solution samples. Only the beam waist diameter was adjusted to 500 μm . This result shows that the inclusion in the sol-gel glassy matrix does not affect appreciably the OL properties of pyrrolidino-fullerene. In particular, our sol-gel materials should fulfill the requirements for achieving the desired attenuation factor based on the RSA mechanism according to the conclusion drawn in the previous section. What remains to be developed is an appropriate strategy to attain complete saturation of the active fullerene molecules along all the beam path in the sample, thus reaching an optimal OL performance.

MULTILAYER OPTICAL LIMITERS

Design strategies that should enable one to optimize the attenuation capabilities of an optical limiter based on the RSA mechanism have been reported and discussed in recent papers.^{4,5} Miles⁴ noted that, to keep the laser fluence at a constant level that warrants a full saturation over the entire beam path, the beam attenuation due to excited state absorption can be balanced by the use of a fast focusing optics (typically $f/5$), provided the concentration of the absorbers varies continuously with an hyperbolic profile, i.e. $C_A(z) \propto |z|^{-1}$ where z is the distance from the focus and the exit surface of the sample is at the plane $z = z_{\text{min}}$ upstream from the focal plane. The constant fluence value should be set well above the saturation fluence (typically at $2.5 \times F_s$) but below the threshold fluence F_{max} for damage of the absorbing material or of the matrix.

The processing of solid samples with a continuously varying concentration of absorbers is however impractical and a finite element version of the above design can be a suitable replacement. In this design the thickness and location of a finite number of absorbing layers of suitable constant concentration is chosen so that the beam enters the

front surface of each layer with a fluence kept below F_{max} and exits the layer at a fluence $2.5 \times F_s$. After leaving one absorbing layer and before entering the next the fluence increases as $|z|^{-2}$ while traversing a non absorbing medium. Close to the focus, such an increase is fast enough that in the last absorbing layer the fluence, after going through a minimum greater than $2.5 \times F_s$, reaches the upper fluence limit both at the entrance and at the exit plane. Note that assuming a $|z|^{-2}$ dependence of the fluence (neglecting absorption) over all the sample must imply that the final exit surface be well upstream (above a Rayleigh range) from the beam focus. It further neglects any possible effect of propagating in a nonlinear medium.

Model calculation of an optimized multilayer structure following the bottleneck principle have been carried out using parameters appropriate for a pyrrolidino-fullerene at concentration 8×10^{-3} M in a hybrid sol-gel matrix, a laser wavelength at 690 nm for which $\sigma_T/\sigma_G = 56$ and $f/5$ focusing optics. A conservative value of 3.8 J/cm^2 was adopted for the damage threshold fluence. The calculated structure and performance of this "ideal" model are reported in Table I.

TABLE I Calculated structure and performance at 690 nm of multilayer optical limiters based on pyrrolidino-fullerene

Layer	Thickness (mm)	Dist. from focus (mm)	Attenuation	Transmittance
"Ideal" model^a				
1	0.184	1.2×10^{-2}	249.8	0.91
2	0.066	0.466	1.84×10^3	0.87
3	0.061	1.267	1.14×10^4	0.85
"Test" model^b				
1	0.1	0.05	9.0	0.96
2	0.1	0.25	82	0.91
3	0.05	0.95	250	0.90

^a Input pulse energy: 2 mJ.

^b Input pulse energy: 5.3 mJ.

The "ideal" model would reach an attenuation factor that fulfils the minimum requirement (10^4) and the total thickness of 1.3 mm would be quite acceptable for a practical device. However, the exit surface of the first layer should be located at $12\text{ }\mu\text{m}$ from the focal plane and the assumption of a spherical wave front would be questionable there.

To simplify the initial testing of the performance enhancement with the bottleneck design we have prepared a three layer structure according to the pattern described in the lower part of Table I, hereafter denoted as "test" model. The calculated attenuation factor and linear transmittance are given in the last two columns and will be used for comparison with the experimental data measured with $f/5$ optics. Figure 8, upper panel, shows z-scan data measured on the "test" sample prior to measuring the NL

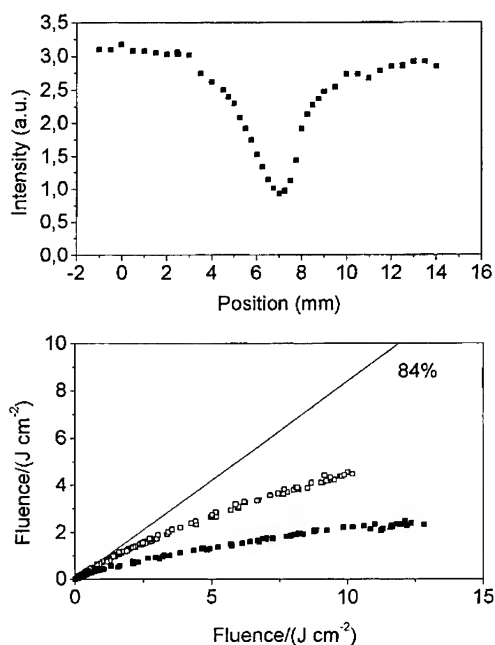


FIGURE 8. Z-scan (upper panel) and optical limiting (lower panel) data of a three-layers bottleneck structure composed of sol-gel films containing FULP2 measured at 690 nm with $f/5$ focusing optics. Full and open squares are used for data taken with the sample positioned at the minimum of the z-scan and 1.5 mm backward, respectively.

transmission in order to locate, in an empirical way, the optimal positioning of the sample. The data were measured in the open-aperture mode and the dip structure is a typical signature of the NL absorption, rather than of NL scattering and thermal effects. The asymmetric dip shape is inherent in the bottleneck concept since once the first active layer crosses the focal plane the loss of fluence due to absorption ceases to be compensated by the beam focusing. The measured OL curves shown in the lower panel of Fig. 8 exhibit the expected critical dependence on the positioning of the sample. However the observed attenuation factor of ≤ 10 fall short of the model result of Table I (250). Possible origins of this discrepancy are likely to be found in the oversimplified propagation geometry adopted for the model calculations which does not take into account of the finite size of the beam waist at the focal plane nor of the intensity dependent refraction effects related to the electronic NL susceptibility and to the thermal and density effects on the matrix. As a result of the nonlinear propagation properties, the beam geometry and the cross sectional intensity distribution might strongly deviate from the simple classical optics model with top-hat intensity distribution used for the calculations. It should be further considered that during the sol-gel processing and in the preparation of the multilayer structure it is difficult to exert a rigorous control on the thickness of the sol-gel films and on the molar concentration of dye molecules since they are dependent on the degree of densification, adhesion and surface tension phenomena, etc.. From the foregoing arguments it is clear that the quantitative comparison attempted here is only preliminary and that more systematic work on the experimental side and a more realistic model from the viewpoint of theory are needed before a sound meaning can be attached to such comparisons.

CONCLUSIONS

From the experimental results and the theoretical analyses presented in this paper it appears that FULP2-doped sol-gel materials do possess the requisites (RSA properties, mechanical, thermal and photochemical stability) for the preparation of solid state OL devices operating in the red spectral region (from about 650 to 750 nm) with the specifications required for the protection of optical detectors including the eye. The adoption of a bottleneck structure appears to be mandatory to reach this goal but the

reported design rules⁴ for multilayer devices are too simplified to yield a meaningful quantitative comparison with experimental data.

One final note concerns the interplay between different mechanisms that may potentially contribute to the OL properties such as the RSA and NL scattering ones. From measurements on fullerenes in solution, it has been reported that the contributions from these two mechanisms substantially add up.²⁰ The situation with solid samples when fast focusing optics is employed is not as clear and it may well be that, as suggested by our preliminary results on a multilayer sample, they interfere with each other reducing the resulting OL performance.

Acknowledgments

This work was supported by the Italian National Research Council (C.N.R.) through the program "Materiali Innovativi (legge 95/95)" and by the European Commission (DG XII) through Brite-Euram III Contract BRPR-CT97-0564.

REFERENCES

- ¹ (a) R. Crane, K. Lewis, E. Van Stryland, M. Khoshnevisan (eds.), *Materials for Optical Limiting*, M. R. S. Symp. Proc. Vol. 374 (Materials Research Society, Pittsburgh, 1995); (b) Ch.M. Lawson (ed.), *Nonlinear Optical Liquids and Power Limiters*, SPIE Vol. 3146 (1997).
- ² L.W. Tutt and A. Kost, *Nature* **356**, 225 (1992).
- ³ A. Hirsch, *The Chemistry of the Fullerenes*, (Thieme, Stuttgart, 1994).
- ⁴ P. A. Miles, *Appl. Opt.* **33**, 6965 (1994).
- ⁵ D.J. Hagan, T. Xia, A. Dogariu, A.A. Said, and E.W. Van Stryland, in Ref. 1(a), p. 161; G.J. Kowalski and R.A. Whalen, in Ref. 1 (b), p. 81.
- ⁶ A. Kost, L. Tutt, M. B. Klein, T. K. Dougherty, and W. E. Elias, *Opt. Lett.* **18**, 334 (1993).
- ⁷ R. Signorini, M. Zerbetto, M. Meneghetti, R. Bozio, M. Maggini, G. Scorrano, M. Prato, G. Brusatin, E. Menegazzo, and M. Guglielmi, SPIE Vol. 2854, *Fullerene and Photonics III*, 130-139 (1996); M. Prato et al., to be published.
- ⁸ D.G. Mc Lean, L.R. Sutherland, M.C. Brant, D.M. Brandelik, P.A. Fleitz, and T. Pottenger, *Opt. Lett.* **18**, 858 (1993); B.L. Justus, Z.H. Kafafi, and A.L. Huston, *Opt. Lett.* **18**, 1603 (1993); S. Couris, E. Koudoumas, A.A. Ruth, and S. Leach, *J. Phys. B: At. Mol. Opt. Phys.* **28**, 4537, (1995).
- ⁹ R. Signorini, M. Zerbetto, M. Meneghetti, R. Bozio, M. Maggini, C. De Faveri, M. Prato, and G. Scorrano, *J. Chem. Soc., Chem. Comm.*, 1891 (1996).

- ¹⁰ M. Maggini, C. De Faveri, G. Scorrano, M. Prato, G. Brustain, M. Guglielmi, M. Meneghetti, R. Signorini and R. Bozio, to be published; M. Prato, M. Maggini, G. Giacometti, G. Scorrano, G. Sandonà, and G. Farnia, *Tetrahedron* **52**, 5221 (1996).
- ¹¹ R. V. Bensasson, E. Bienvenue, J.-M. Janot, S. Leach, P. Seta, D.I. Schuster, S.R. Wilson, and H. Zhao, *Chem. Phys. Lett.* **245**, 566 (1995).
- ¹² R. M. Williams, J.M. Zwier, and J.W. Verhoeven, *J. Am. Chem. Soc.* **117**, 4093 (1995).
- ¹³ S. Leach, M. Vervloet, A. Desprès, E. Bréheret, J.P. Hare, T.J. Dennis, H.W. Kroto, R. Taylor, and D.R.M. Walton, *Chem. Phys.* **160**, 451 (1992).
- ¹⁴ J.L. Anderson, Y.-Z. An, Y. Rubin, and C.S. Foote, *J Am Chem. Soc.* **116**, 9763 (1994); Y. Nakamura, T. Minowa, S. Tobita, H. Shizuka, J. Nishimura, *J. Chem. Soc., Prekin Trans. 2*, 2351 (1995).
- ¹⁵ F.Z. Henari, S. MacNamara, O. Stevenson, J. Callaghan, D. Weldon, and W.J. Blau, *Adv. Mater.* **5**, 930 (1993).
- ¹⁶ V. Klimov, L. Smilowitz, H. Wang, M. Grigorova, J.M. Robinson, A. Koskelo, B.R. Mattes, F. Wudl, and D.W. McBranch, *Res. Chemical Intermediates* **23**, 587 (1997).
- ¹⁷ D. Guldi *et al.*, private communication.
- ¹⁸ R. Bozio and F. Fantinel, to be published.
- ¹⁹ Y.-P. Sun, B. Ma, Ch.E. Bunker, and B. Liu, *J. Am. Chem. Soc.* **117**, 12705 (1995).
- ²⁰ K.M. Nashold and D.P. Walter, *J.Opt. Soc. Am. B* **12**, 1228 (1995).

REVERSE SATURABLE ABSORPTION USING PHOTOINDUCED
INTRAMOLECULAR ELECTRON TRANSFER IN PORPHYRIN-VIOLOGEN
DYADS AND PORPHYRIN-TETRAVIOLOGEN ARRAY.

BRUNO DUPUIS, ISABELLE JOUANIN, CLAUDE BIED-CHARRETON AND
JACQUES DELAIRE
PPSM, URA 1906 of CNRS, Ecole Normale Supérieure de Cachan, 61 avenue du
Prdt Wilson, 94235 Cachan Cedex, France,
PHILIPPE ROBIN, PATRICK FENEYROU and VERONIQUE DENTAN
Laboratoire Central de Recherches, Thomson-CSF, Domaine de Corbeville, 91404
Orsay cedex, France.

Abstract Reverse saturable absorption based on photoinduced intramolecular electron transfer (PIET) has been investigated for optical limiting in the nanosecond range. Solutions of porphyrin-viologen dyads and porphyrin-tetraviologen array were studied by picosecond time-resolved fluorescent measurements and nanosecond time-resolved transient absorption spectroscopy. With the first method, we have studied the fluorescence quenching mechanism by PIET, and the transient absorption spectroscopy studied by the second method, has given clear evidence of efficient photoinduced charge separation. Nevertheless, we have observed for the different kinds of dyads differences in photoinduced charge separation efficiency and consequently in optical limiting effect which are due to the conformation of the donor-acceptor pair. Nonlinear transmission measurements at several wavelengths in the visible with nanosecond laser pulses have shown that PIET can induce more optical limiting than the model porphyrin in solution (especially for the porphyrin-tetraviologen array). Moreover, dyads and porphyrin-tetraviologen solutions are more efficient than a similar solution made of porphyrin and viologen at such a concentration that the quenching is the same in both solutions.

INTRODUCTION

Among all the non linear optical phenomena that can be used to build an optical limiter, reverse saturable absorption (RSA) seems very promising.¹ RSA is due to chromophores which have a larger excited-state absorption cross-section than in the ground state, over a large spectral range in the visible. In the nanosecond time range, non linear absorption is due to the first excited singlet state ($S_1 \rightarrow S_n$) and/or triplet state ($T_1 \rightarrow T_n$), and the so-called "five-level model" which takes absorption cross sections and rate parameters for all these species into account, correctly describes the nonlinear behavior. Different families of chromophores have been studied, which belong to this kind, among which free base and metallated porphyrins, metallated phthalocyanines, naphthalocyanines, cyanines, fullerenes and metal cluster compounds.

However, all these systems suffer from at least one substantial limitation, as it is impossible to choose independantly the absorption cross sections of the ground and of the excited states, or the absorption spectra and the dynamics of a given chromophore in order to enhance the nonlinear effect. To overcome this limitation, a general approach consists in using a mixture of two or several chromophores astutely chosen in such a way that their ground state absorbs over a broad domain in the visible and their excited states lead to the formation of strongly absorbing species after charge or energy transfer.² Keeping with these ideas, photoinduced intermolecular charge transfer in simple binary donor/acceptor systems has been studied in solution and applied to optical limiting.^{3,4} Chromophores such as tricyanocyanines and porphyrins have been added with viologen derivatives which are strong electron acceptors. In all the systems studied, a RSA phenomenon was observed which was attributed to photoinduced radical-ion absorption. Indeed, it is well known that reduced viologen radical cation absorbs in the visible with a maximum near 600 nm⁵ and porphyrin cation has also a significant absorption throughout the visible.⁶ The authors described the conditions that must be fulfilled by RSA systems based on photoinduced charge transfer^{3,4}: (a) the ratio of radical-ion absorption cross section to the chromophore ground state value must be greater than unity; (b) the rate of charge transfer should be fast compared to the laser pulse duration (a few nanoseconds in our case) and (c) the rate of radical ion separation out of the solvent cage must exceed or be comparable to the rate of charge recombination (k_{cr}) in the solvent cage in order to obtain a high yield of the radical-ions. We could add a fourth condition: charge recombination should quickly give back the original system, without any photochemical degradation.

In the work described here, we present the first demonstration of optical limiting with a system based on photoinduced intramolecular charge transfer: we studied two kinds of porphyrin-viologen dyads, which differ in the nature of the viologen derivative: the first is a free base 5-(4-hydroxyphenyl)-10,15,20-tritolylporphyrin with a viologen attached to it through a methylene bridge made of three methylene groups ($TTPC_3V^{2+}$) or six methylene groups ($TTPC_6V^{2+}$) (Fig. 1). This viologen has a long aliphatic chain (C_{16}) linked to the two pyridinium rings. The second is the same free base tritolylporphyrin with a methylviologen attached to it through a methylene bridge made of three methyl groups ($TTPC_3MV^{2+}$). The porphyrin-tetraviologen molecule ($TPP(C_3MV^{2+})_4$) is a free base 5,10,15,20-tetra-(4-hydroxyphenyl) porphyrin appended to four methylviologen through a methylene bridge made of three methyl groups. Preliminary fluorescence studies on the dyads $TTPC_3V^{2+}$ and $TTPC_6V^{2+}$ have already been described.⁷ In this work first, we analyse in more details the fluorescence quenching mechanism. Then, we put into

evidence photoinduced radical ions by nanosecond transient absorption spectroscopy. Finally, we compare optical limiting of these dyads and the porphyrin-tetraviologen in solution with solutions of the model tetraphenylporphyrin (TPP) and of a mixture of TPP with free methylviologen at a concentration giving the same fluorescence quenching.

EXPERIMENTAL

The photophysics of $\text{TTPC}_3\text{V}^{2+}$, $\text{TTPC}_6\text{V}^{2+}$, $\text{TTPC}_3\text{MV}^{2+}$ has been studied in solution in acetonitrile, and compared with the photophysics of TPP as a reference molecule. The photophysics of $(\text{TPP}(\text{C}_3\text{MV}^{2+}))_4$ has been studied in solution in methanol and compared with the photophysics of TPP too. TPP containing less than 0.1 % chlorin is commercially available (Aldrich). The dyad synthesis was carried out according to the classical procedure already described in the literature.⁷ Acetonitrile (Prolabo RP Normapur) was freshly distilled over alumina and dried over molecular sieves (3 Å, 8-12 mesh). Benzyl alcohol (Aldrich 99 %) was used as received.

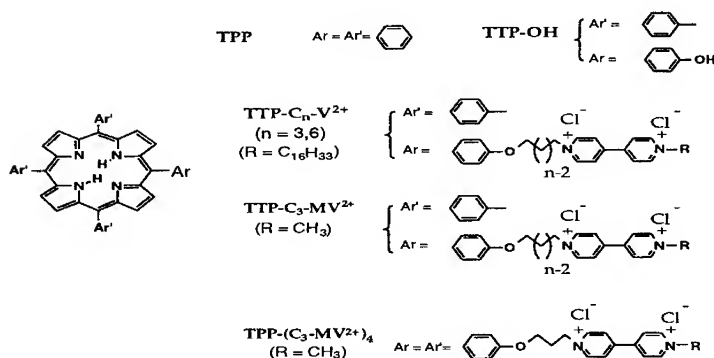


FIGURE 1 Structure of the studied molecules

Ground-state absorption spectra were taken on a Cary 5E Varian spectrophotometer. Steady-state fluorescence spectra were taken on a Spex Fluorolog spectrofluorimeter. Fluorescence decay kinetics for the dyads $\text{TTPC}_3\text{V}^{2+}$ and $\text{TTPC}_6\text{V}^{2+}$ were measured on a time correlated single photon counting set-up coupled with a titanium-saphyre picosecond laser, delivering pulses of 1.3 ps (FWHM) at a frequency of 82 MHz lowered down to 4 MHz by a Bragg cell put in the frequency doubling module.⁸ This module allows to select excitation wavelength from 360 to 450 nm, and the porphyrin solutions were excited at 430 nm, the emission wavelength being chosen at 654

nm. The fluorescence lifetimes were obtained by deconvoluting the fluorescence decay curves against the profile of the laser pulse. For $\text{TTPC}_3\text{MV}^{2+}$ and $\text{TPP}(\text{C}_3\text{MV}^{2+})_4$, fluorescence decay kinetics were measured on a streak camera set-up coupled with a mode-locked Nd:YAG (BM Industries) picosecond laser, delivering pulses of 30ps (FWHM) at a frequency of 10 Hz. The porphyrin solutions were excited with the third harmonics of the Nd:YAG (355nm) and the emission wavelength was chosen at 650 nm.

Transient absorption measurements were made by nanosecond laser flash photolysis. This set-up which uses the third harmonics of a Q-switched Nd:YAG (BM Industries) laser has already been described.⁹ Optical limiting measurements were performed with a wavelength-tunable laser source, consisting of a tripled Q-switch Nd:YAG laser (BM Industries), whose third harmonics is pumping an Optical Parametric Oscillator (BBO Crystal). The pulse length is 7 ns (FWHM) with energy between 13 and 20 mJ in the visible. The experimental set-up for measuring the nonlinear transmission (NATO type) has already been described.¹⁰ The incident and transmitted laser energies were measured either with two RJP 735 Laser Precision pyroelectric detectors, or with two RJP765 Laser Precision silicon detectors.

RESULTS AND DISCUSSION

Steady-state photophysics results

Absorption spectra of solutions of TPP, $\text{TTPC}_3\text{V}^{2+}$, $\text{TTPC}_6\text{V}^{2+}$, $\text{TTPC}_3\text{MV}^{2+}$ and $\text{TPP}(\text{C}_3\text{MV}^{2+})_4$ are very similar and show no evidence for the ground-state formation of charge transfer complexes between viologen and porphyrin macrocycle. So we may consider that irradiation of the dyads in the visible leads to excitation localized on the porphyrin macrocycle. Steady-state fluorescence spectra of these molecules in acetonitrile solution put into evidence fluorescence quenching for the three dyads and for porphyrin-tetraviologen array, compared to TPP, the stronger quenching being observed for the shorter spacer (see Table 1).

Time-resolved fluorescence results

Fluorescence decay profiles of TPP, $\text{TTPC}_3\text{V}^{2+}$, and $\text{TTPC}_6\text{V}^{2+}$ in acetonitrile solution are shown in Figure 2. As usual, the fluorescence decay curve of TPP obeyed single-exponential decay and the fluorescence lifetime (τ_f) was 9.4 ± 0.1 ns. For both dyads, the fluorescence decay profile was found to be bi-exponential (see Table 1). The long lifetime (τ_L) is close to that of viologen-free porphyrin (TPP) and the short one (τ_S) varies with the length of the spacer; the longer the spacer, the larger τ_S . Similarly, the ratio of fast component (A_S) is stronger for the short spacer. In agreement with previous

works on other viologen¹¹⁻¹³ or quinone-linked¹⁴ porphyrins, we suppose that one must consider two conformations of molecules : one is a folded conformer and the other one is extended. The viologen lies close to the porphyrin ring in the former and remote in the latter, which makes the quenching inefficient in this case. Furthermore, from the above lifetimes τ_S , the rate constant k_{et} for the electron transfer in the folded conformation can be deduced according to:

$$k_{et} = \frac{1}{\tau_S} - \frac{1}{\tau_0}$$

Values of k_{et} , also shown in Table 1, put into evidence a slight decrease of the rate of electron transfer as the length of the spacer chain increases. For both lengths of the spacer, quenching by electron transfer occurs on the same time-scale as the laser pulse duration.

For the dyad $TTPC_3MV^{2+}$ and the porphyrin tetraviologen $TPP(C_3MV^{2+})_4$, we observe also a bi-exponential decay, but the short and the long components, compared to the previous dyads $TTPC_3V^{2+}$ and $TTPC_6V^{2+}$, are shortened. So even for the long component, which corresponds to the extended conformer, the quenching by PIET is efficient. We observe the effect of the methyl group at the end of the viologen, which makes quenching by PIET more efficient than the hexadecyl group (C_{16}). We can assume that, compared to the dyads $TTPC_3V^{2+}$ and $TTPC_6V^{2+}$, in both conformations, viologen lies closer to the porphyrin ring, which increases PIET rate (see values in Table 1).

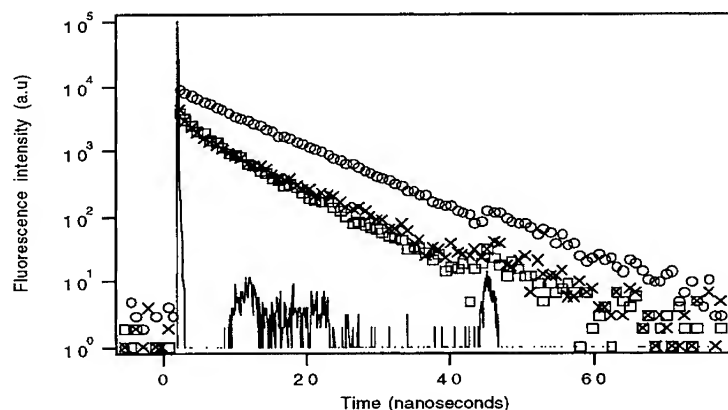


FIGURE 2 Fluorescence decays of ○ TPP in toluene, □ $TTPC_3V^{2+}$ in acetonitrile, X $TTPC_6V^{2+}$ in acetonitrile. Full line : apparatus response function. The porphyrin concentration was around 10^{-5} mol.L⁻¹ in every solution.

Compound	I/I_0 a)	Φ_q b)	τ_s ns	A_s	τ_L ns	A_L	k_{et} c) $10^9 s^{-1}$	Φ_{ion} d)	β_{CS} e)
TPP	1.00	0	--	--	9.4	1.00	--	--	--
TTPC ₃ V ²⁺	0.35	0.65	1.4	0.59	9.8	0.41	0.61	0.16	0.25
TTPC ₆ V ²⁺	0.73	0.27	1.7	0.38	8.0	0.62	0.47	0.17	0.63
TTPC ₃ MV ²⁺	0.35	0.65	0.7	0.71	1.8	0.29	1.27		
TPP(C ₃ MV ²⁺) ₄	0.3	0.7	0.2	0.79	0.7	0.21	4.82		

TABLE 1 Photophysical properties of porphyrins and viologen-linked porphyrins in solution in acetonitrile (except for TPP(C₃MV²⁺)₄ in Methanol)

a) Relative fluorescence intensity calculated from the ratio of integrated fluorescence spectra.

b) Quenching yield ($\Phi_q = 1 - I/I_0$)

c) $k_{et} = \frac{1}{\tau_s} - \frac{1}{\tau_0}$

d) Φ_{ion} is measured taking $\epsilon_{(ion)} = 20000 \text{ L.mol}^{-1}.\text{cm}^{-1}$ at 605 nm.

e) β_{CS} is the charge separation efficiency ($\beta_{CS} = \Phi_{ion}/\Phi_q$)

Transient absorption spectroscopy results

The transient absorption spectrum of TPP in acetonitrile recorded after a nanosecond pulse excitation on a time scale of 1 microsecond per division and extrapolated to the end of the pulse looks like the one attributed to TPP first excited triplet state.^{15,16} The differential absorbance (ΔOD) of this solution has a positive maximum at 440 nm, it is strongly negative below 430 nm due to the strong absorption of the Soret band which is

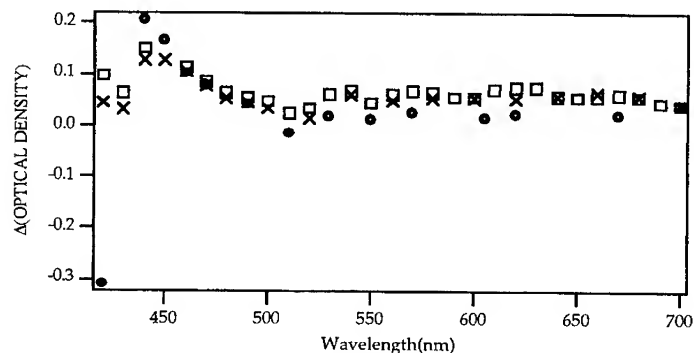


FIGURE 3 Transient absorption spectra of \circ TPP, \square TTPC₃V²⁺, \times TTPC₆V²⁺ in acetonitrile ($c = 1.1 \times 10^{-5} \text{ mol.L}^{-1}$) observed 200 ns after the end of a nanosecond laser pulse excitation (355 nm, $\tau = 8\text{ns}$)

partly bleached, slightly negative at 510 nm which corresponds to the first peak of the Q band and it is positive and weak between 530 nm and 700 nm. The lifetime of this triplet state is 120 microseconds in degassed acetonitrile solution. For $\text{TTPC}_3\text{V}^{2+}$ and $\text{TTPC}_6\text{V}^{2+}$ solutions in acetonitrile, the nanosecond transient spectra are very similar in shape and amplitude, but completely different from the TPP one (Fig. 3): first, there is no more negative ΔOD neither between 400 and 430 nm and nor around 510 nm, and there is a larger absorption between 550 and 700 nm. This absorption is attributed, at least in part, to the reduced viologen radical-cation and to the oxydized porphyrin radical-cation. The first one is known to absorb with a maximum at 400 nm and a secondary maximum at 605 nm⁵, and the porphyrin cation is also known to absorb between 400 nm and 750 nm. The extinction coefficient of TPP radical cation was estimated by pulse radiolysis of TPP in dichloromethane solvent¹⁷ and was found to be around $20000 \text{ L.mol}^{-1}\text{cm}^{-1}$ at 605 nm. In deaerated solutions, the decay kinetics of the absorbance of $\text{TTPC}_3\text{V}^{2+}$ and $\text{TTPC}_6\text{V}^{2+}$ shows two components, a fast one which lasts over one microsecond and a much longer one, lasting a few tens of microseconds (see Figure 4). The long-lived component is attributed to the triplet state according to its resemblance with the $\text{T}_1 \rightarrow \text{T}_n$ absorption spectrum of free base TPP, and the short-lived one is attributed to the ion pair recombination.

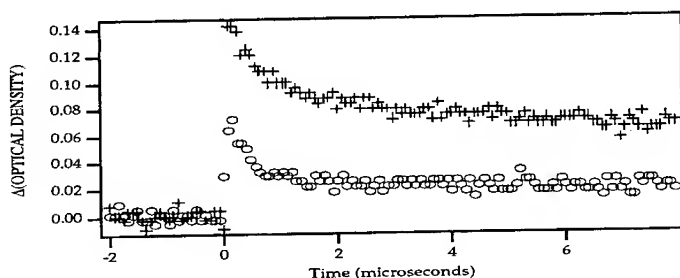


FIGURE 4 Transient differential absorbance decays after a 8 nanosecond laser pulse excitation (355 nm) of a $\text{TTPC}_6\text{V}^{2+}$ solution in acetonitrile ($c = 1.1 \times 10^{-5} \text{ mol.l}^{-1}$). Upper curve : analysing wavelength at 450 nm; lower curve : analysing light at 600 nm

The values of the radical-ion formation quantum yield (Φ_{ion}) obtained for both dyads $\text{TTPC}_3\text{V}^{2+}$ and $\text{TTPC}_6\text{V}^{2+}$ (see table 1) are very closed. From these values and supposing that the photoinduced ions originate from the excited singlet state, it is possible to estimate the charge separation efficiency β_{CS} , defined by the ratio $\Phi_{\text{ion}} / \Phi_{\text{Q}}$, where Φ_{Q} is the quenching quantum yield ($\Phi_{\text{Q}} = 1 - I/I_0$, I and I_0 being the fluorescence intensities of the dyad and the model porphyrin respectively). In photoinduced electron transfer, β_{CS} is

always less than unity because of charge recombination of the radical-ion pair within the solvent cage. The values of β_{CS} obtained here tend to show that the longer the chain, the easier the charge separation. So the increase in methylene chain length acts in two opposite directions : first, it prevents efficient quenching, mainly by decreasing the fraction of dyads which are in a folded conformation, and second it helps charge separation out of the solvent cage.

Contrarily to the previous dyads with a long aliphatic chain at the end of the viologen, the transient absorption spectra of $TTPC_3MV^{2+}$ and $TPP(C_3MV^{2+})_4$, compared to the spectrum of TPP, have a weaker amplitude (see figure 5). So, we have a less efficient radical-ion formation, although the replacement of the long C_{16} alkyl chain by a methyl group leads to an increase of the electron-transfer rate. This methyl group at the end of the acceptor acts in two opposite directions. First, it increases PIET rate and second, it prevents efficient charge separation because the reverse PIET rate within the solvent cage is increased.

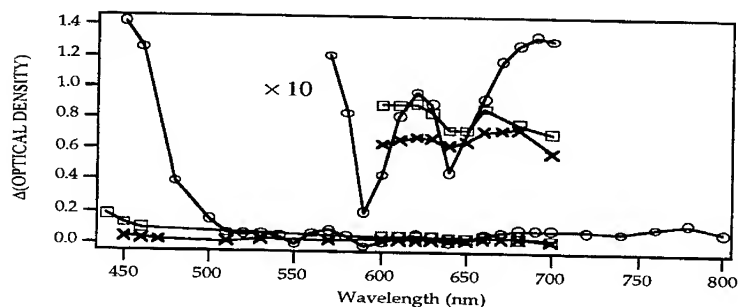


FIGURE 5 Transient absorption spectra of solutions of solutions of \bigcirc TPP in Toluene, \square $TTPC_3MV^{2+}$ in acetonitrile, \times $TPP(C_3MV^{2+})_4$ in methanol observed at the end of a nanosecond laser pulse excitation (355 nm, $\tau = 8$ ns)

Optical-limiting measurements

Measurements of the energy dependent nonlinear transmission were made with solutions of $TTPC_6V^{2+}$, $TTPC_3MV^{2+}$ in acetonitrile and $TPP(C_3MV^{2+})_4$ in methanol. The concentration of these solutions was chosen in order to have an integrated photopic transmission of 70 % over 1 cm of optical length for $TTPC_6V^{2+}$ and 2 mm for $TTPC_3MV^{2+}$ and $TPP(C_3MV^{2+})_4$. Nonlinear transmission was also measured for a reference solution of TPP in benzyl alcohol having the same photopic transmission, and for the same solution added with methylviologen chloride at a concentration leading to the

same quenching efficiency as our three systems. ($\Phi_q = 0.27$ for $\text{TPPC}_6\text{V}^{2+}$, $\Phi_q = 0.7$ for $\text{TPPC}_3\text{MV}^{2+}$ and $\text{TPP}(\text{C}_3\text{MV}^{2+})_4$). The normalized nonlinear transmittance curves of the dyad $\text{TPPC}_6\text{V}^{2+}$, the model porphyrin TPP and $\text{TPP}/\text{MV}^{2+}$ measured at 600 nm are shown in Figure 6. The same curve profiles have also been observed at 620 nm. Both wavelengths are located in the vicinity of the maximum of the transient spectrum beyond 500 nm (see Fig 3). All three solutions (TPP, TPP added with MV^{2+} , $\text{TPPC}_6\text{V}^{2+}$) present a reverse saturable absorption with a threshold near 10 mJ.cm^{-2} (waist radius $w_0 = 70 \mu\text{m}$). Both TPP and TPP added with methylviologen chloride behave similarly, and the nonlinear effect is attributed mainly to $\text{S}_1 \rightarrow \text{S}_n$ and $\text{T}_1 \rightarrow \text{T}_n$ absorptions, the transient differential absorbance being positive at the end of a nanosecond pulse in this wavelength domain for the model compound. The dyad behaves differently and shows a lower transmission with no saturation at high fluences. For the highest fluence available (6 J.cm^{-2}), the maximum photoinduced transmittance at 600 nm equals 0.7 for TPP and $\text{TPP}/\text{MV}^{2+}$ solutions, and 0.45 for $\text{TPPC}_6\text{V}^{2+}$ dyad. This lower transmission at high fluences of the dyad $\text{TPPC}_6\text{V}^{2+}$ is attributed to the efficient photoinduced charge separation ($\beta_{\text{SC}} = 0.63$).

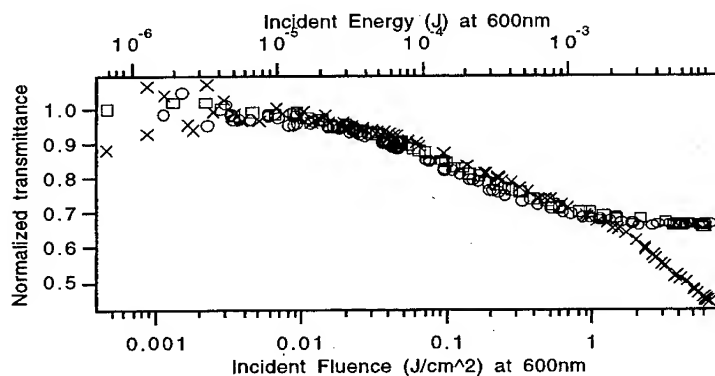


FIGURE 6 Normalized nonlinear transmittance curves as a function of incident energy at $\lambda = 600 \text{ nm}$ for different porphyrin solutions: \circ TPP in benzyl alcohol; \square TPP added with methyl viologen ($c = 2 \times 10^{-2} \text{ mol.L}^{-1}$) in benzyl alcohol; \times $\text{TPPC}_6\text{V}^{2+}$ in acetonitrile. All the solutions have the same linear photopic transmission of 70% in 1 cm thick cell. The methyl viologen concentration in the second solution was chosen in order to give the same fluorescence quenching as in the dyad (27 %).

The nonlinear transmittance curves of $\text{TPPC}_3\text{MV}^{2+}$ and $\text{TPP}(\text{C}_3\text{MV}^{2+})_4$, measured at 610 nm are shown in figure 7, together with the curves for reference TPP and TPP added with MV^{2+} . Contrarily to the results obtained for the $\text{TPPC}_6\text{V}^{2+}$ dyad, the $\text{TPPC}_3\text{MV}^{2+}$ dyad is equivalent to TPP with a threshold near 1 J.cm^{-2} ($w_0 = 10 \mu\text{m}$) and

less efficient than the free donor-acceptor system. This is a consequence of the effect of the methyl group at the end of the viologen, which leads to a fast charge recombination within the solvent cage. The same behavior for $\text{TPPC}_3\text{MV}^{2+}$ has been observed at other wavelengths (570, 530, 510 and 450 nm). Concerning $\text{TPP}(\text{C}_3\text{MV}^{2+})_4$, optical limiting measurements at several wavelengths (610, 570, 530, 510 and 450 nm) have shown that it is the most efficient system compared to TPP, $\text{TPPC}_3\text{MV}^{2+}$, TPP + MV^{2+} , with a nonlinear transmittance at 610 nm of 0.23 for the highest fluence available (100 J.cm^{-2}) (see fig 7). This greatest efficiency of the porphyrin-tetraviologen, in spite of the low radical-ion formation yield, is probably due to highest PIET rate obtained by picosecond time-resolved fluorescence analysis (see Table 1). Furthermore, a "seven-level" model which takes $\text{S}_1 \rightarrow \text{S}_n$, $\text{T}_1 \rightarrow \text{T}_n$ and radical-ion cross section absorption into account is under study to describe differences in optical-limiting behavior of these systems (spacer-chain length effect, conformations effect). Finally, as a last remark, after several hundred of pulses of 1 J.cm^{-2} , these solutions did not present any photodegradation.

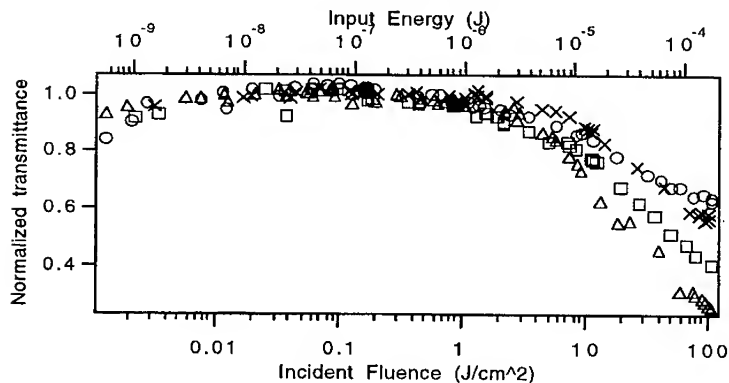


FIGURE 7 Normalized nonlinear transmittance curves as a function of incident energy at $\lambda = 610$ nm for different porphyrin solutions: \circ TPP in Toluene; \blacksquare TPP added with methyl viologen ($c = 1.3 \times 10^{-4} \text{ mol.L}^{-1}$) in benzyl alcohol; \times $\text{TPPC}_3\text{MV}^{2+}$ in acetonitrile, \triangle $\text{TPP}(\text{C}_3\text{MV}^{2+})_4$ in methanol. All the solutions have the same linear photopic transmission of 70% in 2 mm thick cell. The methyl viologen concentration in the second solution was chosen in order to give the same fluorescence quenching as $\text{TPPC}_3\text{MV}^{2+}$ and $\text{TPP}(\text{C}_3\text{MV}^{2+})_4$ (70 %).

CONCLUSION

Measurements of the normalized nonlinear transmittance, the electron transfer rates, and photoinduced radical ion spectra of covalently-linked porphyrin viologen dyads and porphyrin-tetraviologen molecule have shown that PIET can induce more optical limiting

than singlet and triplet state. The other main interest of these covalently-linked donor-acceptor systems is the possibility to improve optical limiting by changing the spacer-chain length and by changing the nature of the acceptor. With this end of view, it is possible to adjust the extent of transient absorption due to the unquenched excited singlet and triplet states and that due to photoinduced ion-radicals. As a consequence, these systems may lead to optical limiting over a wide spectral range.

ACKNOWLEDGEMENTS

We thank Jean-François Delouis (PPSM) for running the nanosecond laser photolysis experiment and Robert Pansu for fluorescence lifetimes measurements. Support from the DGA (Délégation Générale pour l'Armement) and from the Ministère de la Recherche et de la Technologie is gratefully acknowledged.

REFERENCES

1. J.W. Perry, Nonlinear Optics of Organic Molecules and Polymers, (H.S. Nalwa and S. Miyata Eds, CRC Press Inc., Boca Raton, Florida, 1997), p. 813.
2. M. Cha, N.S. Sariciftci, A.J. Heeger, J.C. Hummelen and F. Wudl, Appl. Phys. Lett., **67**, 26 3850 (1995).
3. J.W. Perry, I.-Y.S. Lee, M. Bohorquez and X.-L. Wu, Polymer Preprints, **37**, 1 99 (1996).
4. X.-L. Wu, A.A. Heikal, I.-Y.S. Lee, M. Bohorquez and J.W. Perry, Mat. Res. Symp. Proc., 479 (1997).
5. T. Watanabe and K. Honda, J. Phys. Chem., **86**, 2617 (1982).
6. T. Asahi, M. Ohkohchi, R. Matsusaka, N. Mataga, R.P. Zhang, A. Osuka and K. Maruyama, J. Am. Chem. Soc., **115**, 5665 (1993).
7. X. D. Wang, B.W. Zhang, J.W. Bai, Y. Cao, X.R. Xiao and J.M. Xu, J. Phys. Chem., **96**, 2886 (1992).
8. L. Schouteten, P. Denjean and R.B. Pansu, Journal of Fluorescence, **7**, 155 (1997).
9. L.P. Ermolenko, J.A. Delaire and C. Giannotti, J. Chem. Soc., Perkin Trans., **2**, 25 (1997).
10. P. Le Barny, V. Dentan, P. Robin, F. Soyer and M. Vergnolle, SPIE Proceedings, (Denver, August 1996).
11. V. Y. Shafirovich, E. Amouyal and J. Delaire, Chem. Phys. Lett., **178**, 24 (1991).
12. J.D. Batteas, A. Harriman, Y. Kanda, N. Mataga and A.K. Novak, J. Am. Chem. Soc., **112**, 126 (1990).
13. J. Hirota and I. Okura, J. Phys. Chem., **97**, 6867 (1993).
14. T. Asahi, M. Ohkhchi, R. Matsusaka, N. Mataga, R.P. Zhang, A. Osuka and K. Maruyama, J. Am. Chem. Soc., **115**, 5665 (1993).
15. A. Harriman, J. Chem. Soc. Faraday Trans. 2, **77**, 1281 (1981).
16. J. Rodriguez, J. Am. Chem. Soc., **111**, 6500 (1989).
17. B. Dupuis and J.A. Delaire, unpublished results.

MODELING OF PULSED LASER IRRADIATION OF VO₂ THIN FILMS

J.P. SEGAUD, B. DILLEMANN, O. GIRAUDO
ONERA, DOTA, 91761 Palaiseau Cedex, France

Abstract During a pulsed laser irradiation, the energy absorption in a multilayer structure modifies the temperature distribution in the stack. Materials exhibiting a phase transition controlled by temperature can be introduced to realize optical limiting devices. A thermal and optical conjugated model has been developed to investigate and control the induced phenomena and their relevant parameters. Results are presented for the specific case of VO₂ thin films under YAG and TEA CO₂ laser irradiation.

INTRODUCTION

In recent years, pulsed laser heating of thin films has gained importance for different problems as annealing, damage of optical coatings and optical recording [1-3]. So, the absorption of optical energy by a multilayer structure and the consequent temperature rise within the structure span a wide range of applications. Since the optical properties of materials in thin films depend generally on the temperature and the wavelength of the laser source, they induced a thermally optical nonlinearity. Materials exhibiting a phase transition controlled by temperature can then be used to realize optical limiting devices. Therefore, the analysis of thermal conductive and optical distributions is important to describe the interaction of a pulsed laser beam with multilayered thin films presenting temperature dependent properties. To the knowledge of the authors, a deep analysis of the conjugated optical and thermal fields for phase transition materials has not been presented. In this paper, a full spatial (3D restricted to axisymmetric beam) and temporal analysis has been conducted [4]. The optical treatment uses thin film optics theory. The thermal problem is considered following the classical conductive Fourier hypothesis. Results are presented for the semi-conductor to

metallic phase transition in VO₂ thin films deposited on different substrates for application with YAG and TEA CO₂ pulsed lasers.

THEORY

A sketch of the basic structure is shown in Figure 1. A VO₂ thin film of thickness d (a few 100nm) is deposited on a thick substrate considered as semi-infinite. The VO₂ layer is illuminated by a pulsed laser beam. A part of the electromagnetic energy is dissipated into the film, generating a volumic flow of heat in the stack. Meanwhile, the coherent nature of electromagnetic field generates a complex interferential scheme within the interfaces. After a while, an overheating of the material leads, in the case of VO₂, to a phase transition and thus to a change of propagation. The thermal distribution induces an inhomogeneous profile for the optical and thermal characteristics in the VO₂ layer.

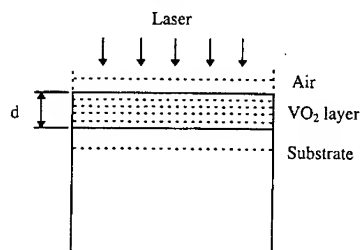


FIGURE 1 Sketch of a VO₂ layer of thickness d deposited on a semi-infinite substrate

Compared to the photons time of flight inside the layer ($\sim 10^{-14}$ s), the thermal relaxation time ($\sim 10^{-11}$ s) is much longer. Thus, we can consider that the interferential electromagnetic state takes place before any thermal response. And the wave propagation can be described with a linear but parametrized relationship. At any moment and for time short enough compared to the flash duration, light travels in an inhomogeneous but stationary absorbing medium. The temporal evolution is then described step by step. The thermal and optical characteristics profile in the whole medium at some moment is rescaled with the help of optical losses calculated at a

previous moment. We then calculate the new electromagnetic distribution in the modified medium and use these new values to predict the thermal profile of the next step. This procedure is repeated for the flash duration. At this temporal grid corresponds a spatial one : the stationary inhomogeneous medium is cut into superposed slices which are sufficiently thin to be considered as homogeneous and defined by their respective complex index and thermal properties. This leads, at the optical level, to a classical formulation using thin film optics theory and, at a thermal level, to a discrete scheme compatible with a finite difference analysis. The complete calculation procedure is given in Figure 2.

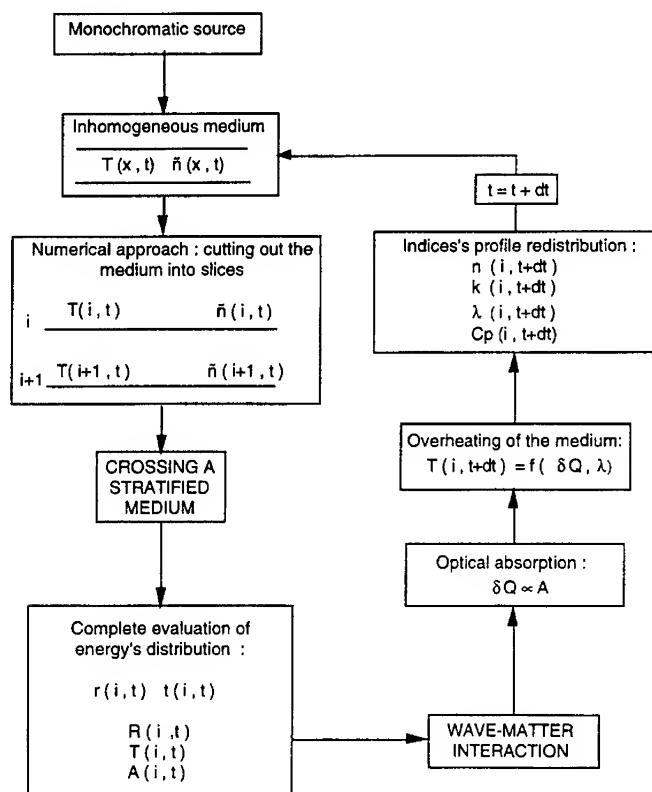


FIGURE 2 System diagram of the laser excitation simulation for VO₂ film

Two kinds of incident spatial profiles have been studied : the planar one (1D model) and the gaussian one (2D axisymmetric model). The incidence is taken normal and, in the gaussian case, the waves are supposed to be planar inside the layer. This later hypothesis imposes that the layer thickness must be much shorter than the depth of profile. It allows to choose a planar mesh to describe the electromagnetic wave propagation and the thermal diffusion . When the lateral thermal diffusion remains small, the problem does not require the use of the full spatial model (2D gaussian) but can be treated as several 1D problems which restore the gaussian spatial profile. That was the case for all the examples presented below (non diffusing or impulse regime). So the theoretical presentation will be restricted to the 1D configuration model.

The 1D heat conduction equation is :

$$\text{div}(\lambda \cdot \text{grad } T(x, t) - \rho \cdot C_p \cdot \frac{\partial T}{\partial t}) = -S(x, t) \quad (1)$$

with λ : thermal conductivity ($\text{W} \cdot \text{K}^{-1} \cdot \text{m}^{-1}$)

ρ : density ($\text{kg} \cdot \text{m}^{-3}$)

C_p : specific heat ($\text{J} \cdot \text{kg}^{-1} \cdot \text{K}^{-1}$)

In this work the thermophysical properties are considered as temperature dependent. The initial and boundary conditions are :

$T(x, t=0) = T_e$ T_e : external temperature

Heat flow continuity and convection at surface : $\lambda_1 \cdot \frac{\partial T}{\partial x}(0, t) = h_e \cdot (T - T_e)$ (2)

Heat flow continuity at interfaces : $\lambda_i \cdot \frac{\partial T}{\partial x}(d_i, t) = \lambda_{i+1} \cdot \frac{\partial T}{\partial x}(d_i, t)$ (3)

Temperature discontinuity at interfaces : $T_{i+1} - T_i = R_c \cdot \lambda_i \cdot \frac{\partial T}{\partial x}(d_i, t)$ (4)

with R_c : thermal resistance at the interface between the two media.

For a few 10 ns pulse, the energy loss due to convection to the ambient can be considered as negligible compared to the energy absorbed in the films.

The internal heat source term $S(x,t)$ is related to the optical losses by the following equation :

$$S(x,t) = -\text{div}(F_o) \quad (5)$$

where F_o is the optical flux and S is the power density absorbed.

When a monochromatic wave irradiates the stratified medium at normal incidence, an interferential scheme occurs in each layer. The optical interference simulation can be obtained by solving Maxwell's equations [4]. Two stationary modes are trapped in each slice : one going up and one going down. Generally , the electromagnetic field in the i th layer of the stratified medium can be expressed with the help of a transfer matrix representation :

$$\begin{bmatrix} E_i \\ \mu_0 \cdot c \cdot H_i \end{bmatrix} = [\tilde{M}_i] \begin{bmatrix} E_{i+1} \\ \mu_0 \cdot c \cdot H_{i+1} \end{bmatrix} = \begin{bmatrix} \cos \tilde{\beta}_i & \frac{j}{\tilde{n}_i} \cdot \sin \tilde{\beta}_i \\ j \cdot \tilde{n}_i \cdot \sin \tilde{\beta}_i & \cos \tilde{\beta}_i \end{bmatrix} \begin{bmatrix} E_{i+1} \\ \mu_0 \cdot c \cdot H_{i+1} \end{bmatrix} \quad (6)$$

$$\text{with } \tilde{\beta}_i = \frac{2 \cdot \pi \cdot d}{\lambda} \cdot \tilde{n}_i \cdot \cos \tilde{\theta}_i$$

The existing fields at the extreme interfaces are related together by the matrix product :

$$[\tilde{M}] = \prod_{i=1}^N [\tilde{M}_i] = \begin{bmatrix} \tilde{A} & \tilde{B} \\ \tilde{C} & \tilde{D} \end{bmatrix} \quad (7)$$

The coefficients of the product matrix allow to calculate the electromagnetic reflected E_r and transmitted E_t fields. The global energetic factors R , T and A are deduced from them:

$$r = \frac{n_0 \cdot \tilde{A} - n_s \cdot \tilde{D} + n_0 \cdot n_s \cdot \tilde{B} - \tilde{C}}{n_0 \cdot \tilde{A} + n_s \cdot \tilde{D} + n_0 \cdot n_s \cdot \tilde{B} + \tilde{C}} \quad t = \frac{2 \cdot n_0}{n_0 \cdot \tilde{A} + n_s \cdot \tilde{D} + n_0 \cdot n_s \cdot \tilde{B} + \tilde{C}} \quad (8)$$

$$R = |r|^2 \quad T = \left(\frac{n_s}{n_0}\right) |t|^2 \quad A = 1 - R - T \quad (9)$$

The energy flux along the direction of propagation is given by the time averaged magnitude of the Poynting vector :

$$\langle \vec{\Pi} \rangle = \langle \text{Re}(\vec{E} \wedge \vec{H}) \rangle \quad (10)$$

The global energy balance is calculated by taking the divergence of the Poynting vector in each layer. With the planar configuration considered, the electromagnetic energy lost inside each slice is simply the difference between the normal components of the Poynting vector at each interface.

Equation (1) was solved by a finite difference method. It appears while making a Taylor development of the thermal relations, at the second order on the space variables and at the first order on the time. Its resolution depends on several algorithms developed specially for the evolution problems. We have chosen the Crank-Nicholson's one in its semi-implicit form for its great stability. However we had to respect the Fourier convergence criterion:

$$\Delta t \leq \frac{\Delta x^2}{2.a} \quad \text{with } a = \frac{\lambda}{\rho \cdot C_p} : \text{thermal diffusivity} \quad (11)$$

This condition insures to correctly represent the thermal heterogeneity. Spatial sampling must be fixed within this relation to insure sufficient accuracy.

RESULTS AND DISCUSSION

Thermodynamical data of phase transition

Temperature dependent parameters are introduced with an analytic description. Their evolution in temperature must be slowly variable for numerical treatment. The following relation has been used to describe the physical behavior of the VO₂ during the phase transition :

$$X(T) = X_{sc} + \frac{(X_m - X_{sc})}{2} \cdot [1 + \tanh(\frac{T - T_c}{10})] \quad (12)$$

where X_{sc} is any parameter value in semi-conductor state

X_m is any parameter value in metallic state

T_c is fixed at 60°C

To integrate the latent heat given out during the phase transition, we introduce an enthalpy equal to near 51 kJ.kg⁻¹ in a integral form (Figure 3) :

$$C_{p\text{ eff}} = C_p + dL/dT \quad \text{with} \quad \int \frac{dL}{dT} . dT = 51 \text{ kJ.kg}^{-1} \quad (13)$$

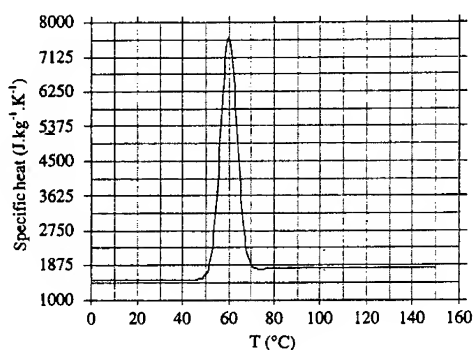


FIGURE 3 VO₂ specific heat with phase transition latent heat

YAG excitation

A VO₂ layer of thickness $d = 0.5 \mu\text{m}$ deposited on glass substrate is irradiated by a YAG laser flash ($\lambda = 1.06 \mu\text{m}$). The initial layer temperature is set to 20°C. Spatial mesh retained is 50 slices in VO₂ layer and substrate. The thermal and optical data used for simulations are given in Table 1.

	VO ₂ (semiconductor)	VO ₂ (metallic)	SiO ₂
Thermal conductivity (W.K ⁻¹ .m ⁻¹)	4.0	5.0	1.63
Density (kg.m ⁻³)	4300	4300	2200
Specific heat (J.kg ⁻¹ .K ⁻¹)	1500	1800	1100
Refraction index n	2.1	2.5	1.5
Extinction index k	0.06	0.7	0

Table 1 VO₂ thermal and optical data used for YAG excitation

Uniform spatial and temporal lightning

The pulse length is 10 ns. The time sampling is fixed to 0.1 ns (i.e. 100 iterations during the pulse). The fluence is equal to 600 J/m^2 . Figures 4 (a) and (b) shows the temperature profile in the VO_2 layer with and without the introduction of the latent heat in the specific heat. On the first one, one can see the oscillating behaviour, mark of the interference scheme occurring in the VO_2 layer before the phase transition, and the drastic temperature increase after it. The absorption is essentially limited to the VO_2 surface ($0.2 \mu\text{m}$ after 5 ns) after the phase transition leading to the occultation of the deepest slices. The introduction of the enthalpy of latent heat induces a general decrease of temperature level with the accentuation of a temperature limitation in depth. This result leads to greater commutation thresholds.

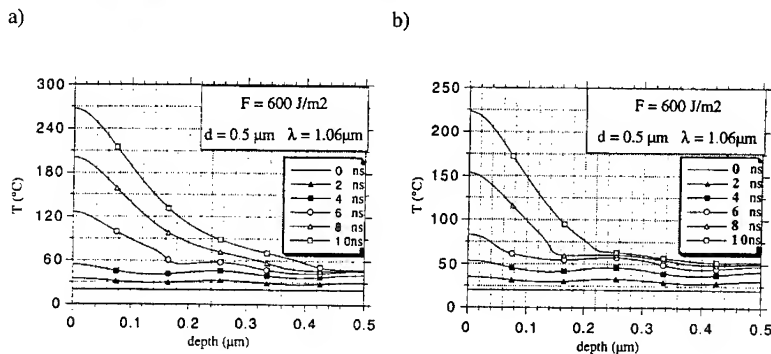


FIGURE 4 Temperature profiles without (a) and with (b) the latent heat introduction

The developed modeling may be used to optimize the multilayered architecture. As seen before, the occultation of deep slices within the phase transition suggests the concept of a matched thickness for switching performances. Figure 5 presents the transmitted energies before and after the commutation threshold, and their ratio as a function of the VO_2 layer thickness. The contrast variation indicates a maximum useful thickness around $0.4 \mu\text{m}$. Under this value, the VO_2 layer does not cut off completely. Above this value, it is too thick to be entirely switched off. So, an optimal thickness appears which is dependent of the pulse characteristics (time and energy).

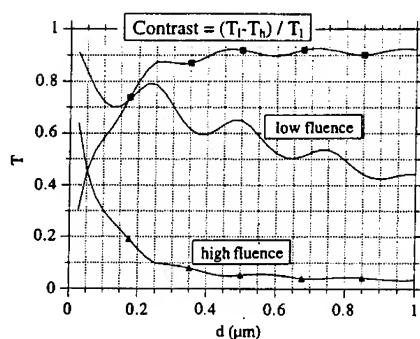


FIGURE 5 Transmissions for low and high fluences and their ratio vs VO₂ thickness

Uniform spatial and gaussian temporal illumination

The temporal pulse has now a gaussian shape with a 30 ns width at $1/e^2$. The time sampling is fixed to 1 ns (i.e. 100 iterations during the pulse). The total fluence is equal to 2000 J/m². The incident and the transmitted power densities as a function of time are presented in Figure 6. One can distinguish two working fields. Before the phase transition, the transmitted signal recopies the incident one with respect to the linear transmission coefficient. After it, the transmitted signal is greatly reduced but presents a second maximum corresponding to the center of the incoming gaussian signal peak.

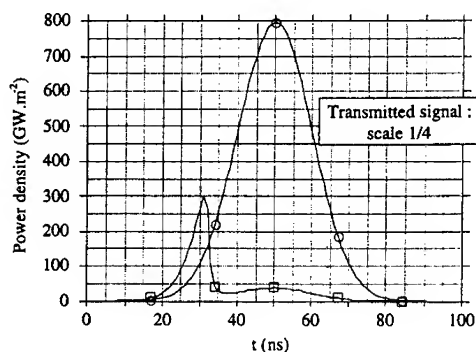


FIGURE 6 Incident and transmitted power densities vs time

TEA CO₂ excitation

A VO₂ layer of thickness d deposited on germanium substrate is irradiated by a TEA CO₂ laser flash ($\lambda = 10.6\mu\text{m}$). The initial layer temperature is set to 20°C. Spatial mesh retained is 40 slices in VO₂ layer and substrate. The thermal and optical data used for simulations are given in Table 2.

	VO ₂ (semiconductor)	VO ₂ (metallic)	Ge
Thermal conductivity ($\text{W.K}^{-1}.\text{m}^{-1}$)	4.0	5.0	64
Density (kg.m^{-3})	4300	4300	5323
Specific heat ($\text{J.kg}^{-1}.\text{K}^{-1}$)	1500	1800	321.9
Refraction index n	4.1	4.2	4
Extinction index \bar{k}	0.04	7	0

Table 2 VO₂ thermal and optical data used for TEA CO₂ laser excitation

The temporal shape of the pulse, corresponding with the 10P20 ray, is shown in Figure 7. The time sampling is fixed to 1 ns (i.e. 500 iterations during the pulse)

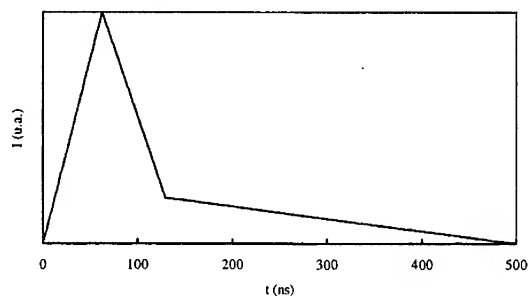


FIGURE 7 Pulse temporal shape for the 10P20 ray of a TEA CO₂ laser.

Uniform spatial illumination

The developed modeling may be used to investigate the influence of the VO₂ thermal and optical data upon the commutation and damage thresholds. Figure 8 shows the global transmission (integrated over the pulse time) for different values of the

extinction coefficient k_{sc} as a function of input fluence. The commutation threshold defined at 3 dB can be reduced by a factor of 3 when k_{sc} is multiplied by a factor of 5. This drift leads rapidly to an asymptotical behaviour while the linear transmission decreases.

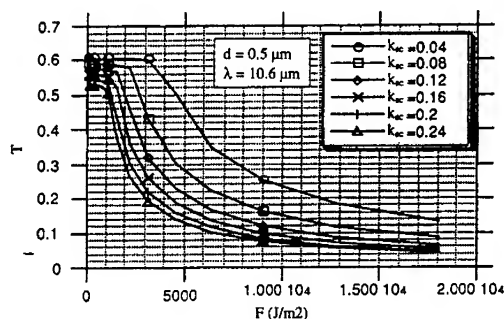


FIGURE 8 Time averaged transmission for different VO₂ k_{sc} vs input fluence

In the same time, the damage threshold, set for an maximum temperature in the VO₂ layer equal to 1000°C, does not greatly change. The ratio of these both thresholds is given in Figure 9.

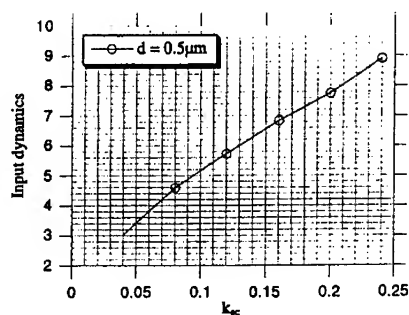


FIGURE 9 Input dynamics as a function of extinction coefficient of VO₂

So, the input dynamics can then increased by a factor of 3 if one knows how to lightly modify the extinction coefficient of VO₂. This can be done by introducing metallic particles in a VO₂ host matrix. Then, the absorption increase before the phase transition leads effectively to an input dynamics gain which has been observed [5].

Gaussian spatial illumination

The spatial pulse has now a gaussian shape. The incident and the transmitted fluences as a function of lateral position are presented in Figure 10. One can distinguish two working regions. The central part of the pulse contains sufficient energy to switch the film. The transmission characteristics are reduced for this region of the film while a large external ring is not participating to the optical limiting performances. This rigorous simulation leads to the saturation of the transmission from the pulse center to a defined radius and beyond it to the duplication of the incident pulse with the respect to the linear transmission coefficient. No overshooting behaviour is observed [6].

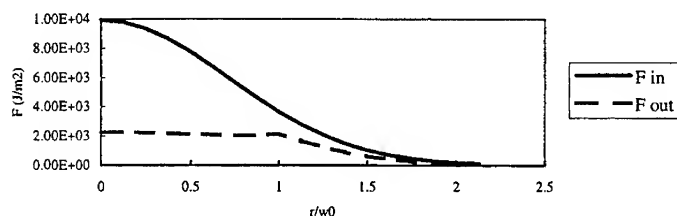


FIGURE 10 Spatial intensity profiles of laser beam transmitted by VO_2

This type of simulation allows by spatial integration to determine the optical limitation curve. Figure 11 shows the induced optical density as a function of input energy for two sets of specific and latent heats.

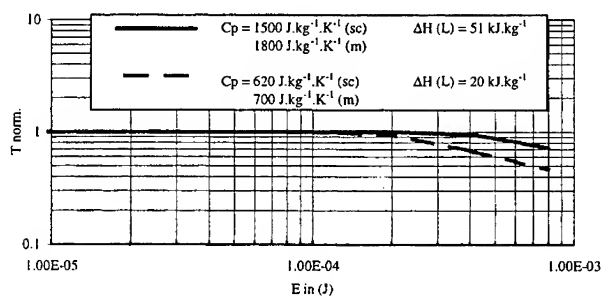


FIGURE 11 Optical density induced by a VO_2 thin film vs input energy for two sets of specific and latent heats

With the extinction coefficient, these data are other parameters that greatly influence the commutation threshold. So, the commutation threshold is reduced by a factor of 2 while the specific and latent heats are reduced by a factor of 2.5.

CONCLUSION

The transient evolution of a VO₂ thin film under a laser irradiation has been numerically evaluated to examine dynamical characteristics of such phase transition material devices. This tool allows to study the influence of the intrinsic properties of VO₂ and the extrinsic device architecture, for different conditions of threat, on the optical limitation performances. Design optimizations which increase them are possible.

ACKNOWLEDGMENTS

This work was partially performed under contracts from the DGA through the DRET and STTC departments.

REFERENCES

1. S. Nakano et al., Japanese Journal of Applied Physics, 25,12 (1986)
2. G. Chen and C.L. Tien, Journal of Heat Transfer, 116,313 (1994)
3. N. Angelucci, N. Bianco and O. Manca, Int. J. Heat Mass Transfer, 40,18 (1997)
4. B. Dillemann, Ph. D thesis, Univ. Of Paris VII, (1995)
5. M. Born and E. Wolf, Principles of Optics, Ed. Pergamon Press
6. J.P. Segaud, O. Giraudo, C. Indrigo, E. Cavanna and J. Livage, these proceedings
7. M. Corbett, K.L. Lewis and A.M Pitt, private communication

OPTICAL LIMITING IN C_{60} DOPED SOLID SOL-GEL GLASSES

BERND HÖNERLAGE, JOCHEN SCHELL and ROLAND LEVY
Institut de Physique et Chimie des Matériaux de Strasbourg, (IPCMS)
UMR 46 CNRS-ULP-ECPM, 23, rue du Loess, 67037 Strasbourg Cedex, France

Abstract We compare the nonlinear absorption properties and their dynamics in C_{60} -solutions and C_{60} -doped solid xerogel matrices. The measurements are performed in a pump-test geometry using ps pulses generated from a frequency doubled mode locked Nd:YAG laser at 532 nm. In both kinds of samples we observe an induced absorption leading to optical limiting. In the doped porous glasses, we observe a decrease of the initial laser-induced absorption with a time constant of 150 ps, down to a very long-living constant level. We attribute this dynamics to a transition of a substantial part of the C_{60} molecules from excited singlet to triplet electronic states. This shows that contrary to thin films where no long lasting induced absorption can be observed, the doped porous glasses can act as efficient solid state optical limiters against ns laser pulses.

Keywords C_{60} , fullerenes, optical limiting, induced absorption, dynamics

1. INTRODUCTION

The fullerene C_{60} shows a strong, spectrally broad induced absorption, which makes this material to be an interesting candidate for an application in optical power limiting. Several studies have been performed on induced absorption properties of the C_{60} molecules diluted in solutions¹⁻⁷ or deposited in the form of thin films on substrates⁸⁻¹⁵. Only a few measurements of optical limiting properties have been carried out on C_{60} embedded in solid matrices¹⁶⁻²⁰. In this article, we present a comparative study of the dynamics and saturation of induced absorption of C_{60} in solutions and porous glasses. We also investigate the potential of C_{60} embedded in solid xerogel matrices for optical power limiting purposes.

In our porous sol-gel glasses, the fullerene molecules are trapped in the pores. Due to the close contact of the C_{60} molecules and the surrounding silica, heat can be effectively evacuated through this matrix. Compared to C_{60} in liquid solutions or

crystalline films, the use of these glass matrices presents a number of advantages as there are: ease of handling, excellent optical quality, mechanical stability and a considerably higher damage threshold against laser irradiation when compared to crystalline C_{60} -films and even to solutions in thin glass cells. Finally, the doping concentration can be varied throughout the sample. This last point is important for the elaboration of so-called bottle-neck limiting devices. These devices show a concentration of active material adjusted to keep the internal fluence constant within the Rayleigh-length when the sample is placed in the focus of a gaussian beam. Such a device is expected to improve considerably the limiting effectiveness. These properties, combined with the spectrally broad excited state absorption of the C_{60} molecule makes fullerene-doped xerogel matrices a promising candidate for optical power limiting devices. From the point of view of possible applications, it is therefore very interesting to know if the favourable properties of C_{60} for optical limiting as observed in solutions remain the same after the molecules being embedded in these matrices.

2. PREPARATION OF THE SOL-GEL SAMPLE

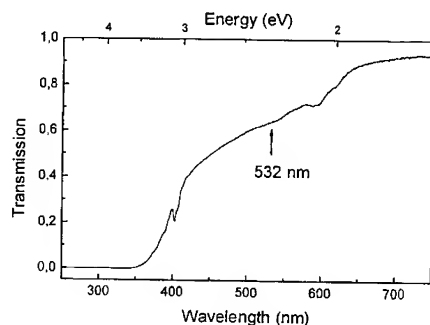


Figure 1 : Linear transmission spectrum

Sol-gel methods were used to prepare porous bulk xerogels. The preparation process is described in detail in Ref. 20. We obtain porous xerogels after a drying process and heat treatments. The resulting porous samples were sodden with saturated C_{60} chlorobenzene

solution. As a final step the samples are dried to eliminate the solvent. The linear transmission spectrum for the dried sample is shown in Fig. 1. The spectrum changed only slightly during the evaporation process. According to Bensasson et al.²¹ the vibronic features at 410 nm and the absence of strong absorption around 450 nm indicate well dispersed C₆₀ molecules in our samples.

3. NONLINEAR ABSORPTION IN ISOLATED MOLECULES.

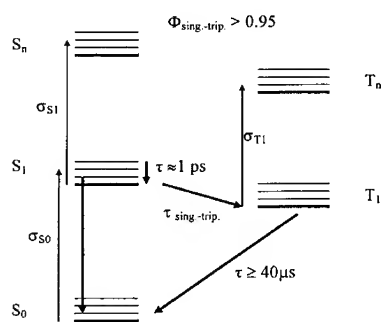


FIGURE 2 5-level model

In order to describe the induced absorption properties of an isolated C₆₀ molecule, many authors^{5,6,17,22} propose Reverse Saturable Absorption (RSA) within a five-level-model, depicted in Fig. 2. C₆₀ shows singlet and triplet excited electronic states. The first triplet state T₁ is lying energetically below the first

excited singlet state S₁ and is populated very efficiently (Φ close to unity)²³ via intersystem crossing from S₁. The radiative decay of the lowest triplet state is spin-forbidden, the corresponding lifetime is therefore very long (≥ 40 μs)²³. The origin of the increase in absorption with light intensity (RSA) is due to the fact that the absorption cross sections σ_{S1} or σ_{T1} of the excited states S₁ and T₁ are higher than σ_{S0}, i.e. the cross section for absorption from the ground state. Consequently, the total absorption of the sample grows with increasing excited state populations. At a wavelength of 532 nm, used throughout our measurements, the linear absorption is very weak. It is due to a transition derived from the parity-forbidden HOMO-LUMO transition which becomes only weakly allowed due to coupling to vibrations²⁴. As a consequence, both the excited singlet and the triplet states have higher absorption cross sections (σ_{S1}, σ_{T1}) than the

ground state and induced absorption takes place. Since the singlet excited state has a considerably shorter life time than the metastable triplet state, different excited state populations are prepared if different laser pulse lengths are used. For pulses shorter than the intersystem crossing time, singlet state absorption will dominate, for increasing pulse length the triplet state, where the excited molecules accumulate due to its longer lifetime, will become more and more important. Therefore, for the efficient limiting of ns pulses, the existence of a long-living triplet state is of crucial importance.

4. EXPERIMENTAL

Our measurements of the dynamics of induced absorption and of the intensity dependant transmission of singlet and triplet state excited molecules are performed in a pump-test geometry. This evaluation method uses two laser pulses with different intensities. The first laser pulse (pump) is of high intensity and creates an important excited state population. The second pulse is of very low intensity and monitors the changes in transmission created by the first one. When delaying this test pulse, the temporal evolution of the excited state populations can be determined. In varying the pump intensity at a given delay, the intensity dependant transmission of molecules in different excited states can be measured.

In our experiment we create test and pump pulses by a beam splitter from the same beam. We derive both pump and probe pulses from the same frequency doubled Nd :YAG laser, providing pulses of 32 ps duration and an average energy of 2 mJ per pulse at a wavelength of 532 nm. At this wavelength, the linear transmission of the sample is about 60%. We use a half-wavelength-plate to achieve crossed polarisations of pump and test beams and a polarisation filter before the acquisition system to avoid coherent coupling effects and to reject scattered light from the pump beam. To minimise the experimental error due to intensity fluctuations of the laser source, we measure the intensity of a reference beam and we use a discrimination system which enables us to consider only laser shots within a certain energy window. The two beams are focused onto the sample by the same lens of $f = 20$ cm, into a spot of approximately $160 \mu\text{m} \times$

110 μm . The transmitted light of the test pulse is sent onto an optical multichannel analyser and averaged over 200 laser shots.

The delay of the test pulses with respect to the pump pulses can be adjusted by using a variable delay line. Hence the temporal evolution of the transmission can be measured. Great care is taken that the spatial coincidence of the two beams stays fixed when the delay between test and pump pulses is varied.

The intensity variation of the pump pulse during the measurement of the intensity dependant transmission is achieved by inserting two polarisers in the pump beam. By turning one of them, the transmitted intensity can be varied.

5. SOLUTIONS: DYNAMICS OF INDUCED ABSORPTION

To study the dynamics of induced absorption in C_{60} solutions we perform a pump-probe experiment. In varying the delay between probe and pump pulse, we can monitor the temporal evolution of the excited states at the origin of induced absorption. The excitation density is 34 mJ/cm^2 . The result is shown in Fig. 3. We observe a rapid, laser-

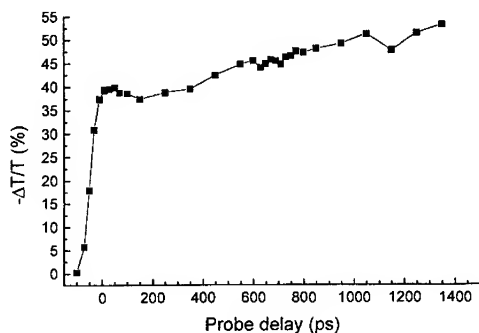


FIGURE 3 Dynamics of induced absorption in solutions

limited rise of absorption, followed by a slowly continuing rise of weaker amplitude. We interpret this result by a fast directly laser-induced population in the first excited singlet state, followed by intersystem crossing to the first excited triplet state. The time

constant for this exponential relaxation to the triplet state has been determined by different groups to be either 650^{2,19} or 1200 ps⁷. The observed slow rise is compatible with these values. We therefore state that for our experimental conditions, the induced absorption created by the triplet state molecules is stronger than the one created by singlet state excited molecules. We come back to this result in the next section.

6. SOLUTIONS : INTENSITY DEPENDANT TRANSMISSION OF SINGLET AND TRIPLET STATE EXCITED MOLECULES

To study the induced absorption of singlet and triplet excited states, we measure the intensity dependant transmission using the same pump-probe configuration as described above. In difference to the last section, we measure at two fixed delay values, the first one at 20 ps where only singlet excited molecules contribute, the second one at 1 ns where the triplet state excited molecules dominate. In varying the pump intensity, we can therefore determine the intensity dependant transmission created by singlet and triplet excited molecules. The result is shown in Fig. 4. Up to an energy density of about

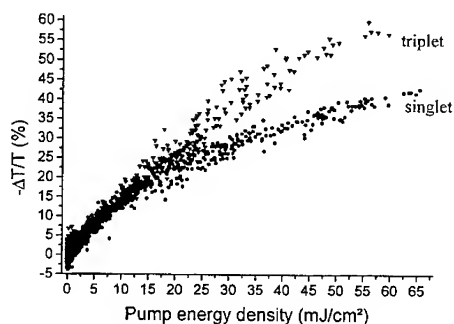


FIGURE 4 Induced absorption created by singlet and triplet state excited molecules

15 mJ/cm², singlet and triplet state excited molecules produce a comparable effect. For higher energies, the triplet state molecules create a stronger effect. As the intersystem crossing rate is assumed to be close to 100%, we find that the absorption cross sections

for the first excited singlet and triplet states are close to one another at low excitation density. This result is in reasonably good agreement with published values^{2,7,19}. As the singlet state induced effect is found to saturate at lower intensities, the triplet state effect is larger at energy densities exceeding 15 mJ/cm². This explains the slow increase in the dynamics of induced absorption as the molecules relax to the triplet state.

7. DOPED POROUS GLASSES : DYNAMICS OF INDUCED ABSORPTION

In this section, we study the temporal evolution of the induced absorption in the fullerene-doped xerogel matrices. We use again the above cited pump-probe technique with a variable delay between pump and probe pulses. The result is shown in Fig. 5.

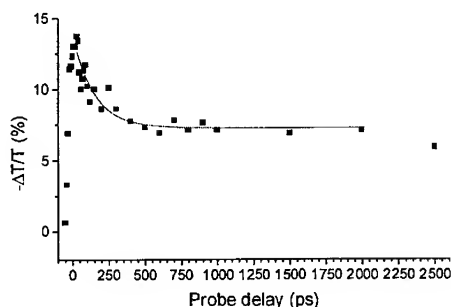


FIGURE 5 Dynamics of induced absorption in porous glasses

We observe a fast increase of absorption due to population of the first excited singlet state. This laser limited rise is followed by a slower and roughly exponential decay to a plateau which lasts, as in the solution case, much longer than the ns time scale of our experiment. Again we identify the long-lived component as the absorption of a triplet state population, created by some intersystem crossing processes. An exponential fit to the initial decay gives us a time constant of 150 ps for the depopulation of S₁. When we compare this lifetime to the findings in C₆₀ solutions, we observe a time constant which is shorter than the lifetime of S₁ in solutions, exclusively determined by intersystem

crossing. Nevertheless, the lifetime of S_1 in porous glass samples is still long enough to allow a considerable fraction of intersystem crossing to occur. This is in contrast to the very rapid relaxation in C_{60} thin films which is explained by interaction of neighbouring C_{60} molecules. This fast relaxation allows no intersystem crossing to occur and excludes therefore an application of thin films for optical limiting of ns pulses as no long-lived induced absorption can occur. The observed time constant being closer to the one in solutions than the one in thin films, we state that our porous glass samples contain relatively well dispersed fullerene molecules, as already indicated by the vibronic features in the transmission spectrum. If we assume the same physical mechanism for intersystem crossing as in solutions, the shorter time constant for the depopulation of S_1 in the porous glasses could indicate that an increased interaction between the C_{60} molecules and the surrounding glass matrix takes place as compared to the case of solutions. To decide if this latter conclusion is justified, a detailed investigation of the intersystem crossing dynamics in our samples is needed which is currently under way.

8. POROUS GLASSES : INTENSITY DEPENDANT TRANSMISSION OF SINGLET AND TRIPLET STATE EXCITED MOLECULES

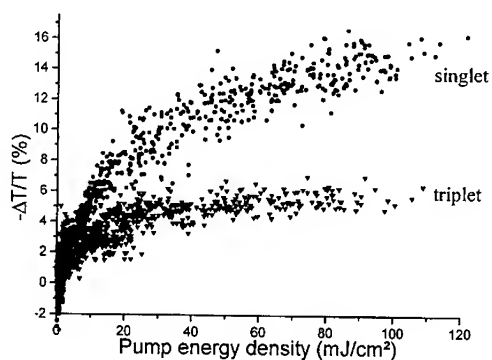


FIGURE 6 Intensity dependant transmission of singlet and triplet state excited molecules

To study the behaviour of singlet and triplet state induced absorption, we perform a similar measurement as described in Sec. 6. on our porous glass samples. The result is shown in Fig. 6. We observe a stronger effect due to singlet state excited molecules already at low excitation density. This difference to the solution case can easily be explained by an incomplete intersystem crossing, the relaxation S_1-S_0 being too rapid for reaching intersystem crossing rates close to 100% as in solutions. Furthermore, the triplet state induced effect saturates very rapidly and with great efficiency. We interpret this behaviour by a complete filling of the triplet state. Therefore, the intersystem crossing rate is found to be strongly intensity dependant in the porous glass samples.

9. OPTICAL LIMITING PROPERTIES

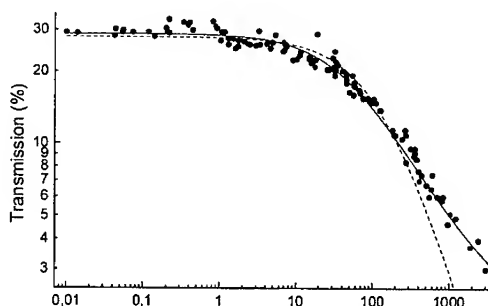
To evaluate the potential of our samples for optical limiting, we determine their transmission as a function of the excitation intensity. The excitation source is again the frequency doubled Nd:YAG laser at 532 nm with a pulse length of 32 ps and a repetition rate of 5 Hz. This pulse length being considerably shorter than the intersystem crossing time, the increase in absorption will be dominated by the singlet excited state population, the triplet state playing only a minor role.

Single pulses

To ensure that we always excite a non-degraded area of the sample, we move it after each single laser shot in the focal plane. The sample being homogeneous, we minimise by this means the effect of laser induced irreversible changes. Fig. 7 shows the transmission as a function of the energy of the laser pulses. When the pulse energy increases, the effect of induced absorption is evident. The transmission remains nearly constant up to a threshold energy of approximately 10 mJ/cm², from which on it diminishes rapidly down to 10% of the linear transmission value. To get more quantitative information about the limiting behaviour, we fit the experimental transmission results by a model for (sequential) two photon absorption. The theoretical curves are obtained by solving the following differential equation :

$$\frac{\partial I}{\partial z} = -(\alpha_0 + \alpha_2 I)I \quad \text{with} \quad \alpha_2 = \frac{\alpha_2^0}{1 + \frac{I}{I_{\text{sat}}}}$$

where α_0 describes the linear absorption and α_2^0 the sequential two photon absorption which is at the origin of the limiting action. We further take into account a saturation effect where I_{sat} is a phenomenological saturation intensity. The result of this adjustment is plotted as the solid line in Fig. 7.



We find a two photon absorption coefficient of $\alpha_2^0 = 11 \text{ cm/GW}$, and a saturation energy density of about 100 mJ/cm^2 . For comparison we also show the result when neglecting saturation which clearly fails at high energy densities. We attribute the observed saturation effect to the depopulation of the ground state, which becomes important at these high excitation densities.

Care must be taken concerning the very last points of the measured curve, because we found the damage threshold of the xerogel matrices located between 1.5 and 2 J/cm^2 . Nevertheless, the sample continues its limiting action even above this value.

Repetitive pulses

Here, the sample is not moved during the whole series of measurements. We also

observe a constant part of the transmission for small excitation energies, followed by a pronounced decrease at a threshold value of the same order of magnitude as for single pulses. Above an energy density of about 200 mJ/cm² we find an irreversible bleaching effect. We even observe a steep re-increase of transmission for excitation energies exceeding 400 mJ/cm². We attribute this behaviour to an irreversible degradation of the C₆₀-silica glass system²⁰. It should nevertheless be noticed, that these fluences correspond to extremely high peak intensities (200 mJ/cm² gives 6.7 GW/cm²) as the excitation source is a ps-laser. The so-observed damage threshold for repetitive ps-excitation is considerably higher than the one found for C₆₀ thin films or solutions in glass cells.

10. Conclusion

We investigate the induced absorption dynamics of C₆₀-doped solid xerogel matrices as well as the influence of singlet and triplet state excited molecules and we compare it to the results for C₆₀ solutions. Performing time-resolved pump-probe experiments, we find in both samples an induced absorption which is governed by either singlet or triplet excited state populations, depending on the time delay of the probe pulse with respect to the pump pulse. For the porous glass sample, the depopulation of S₁ is governed by a time constant of 150 ps, shorter than the reported values for intersystem crossing for C₆₀ in liquid solutions. Nevertheless, this relaxation is sufficiently slow for a considerable amount of intersystem crossing to occur. Therefore, in both cases we observe a very long living plateau in the induced absorption due to the triplet state population resulting from intersystem crossing. This indicates that contrary to C₆₀ thin films, porous glasses can act as efficient optical limiters against ns pulses. This shows the importance of well dispersed molecules as the rapid relaxation in films is due to an interaction of neighbouring C₆₀ molecules.

REFERENCES

- ¹ M. P. Joshi, R. Mishira, H. S. Ravat, C. Mehendale and K. C. Rustagi, *Appl. Phys. Lett.* Vol. **62** No. 15, 1763 (1993).
- ² R. J. Sension C. M. Phillips, A. A. Szarka, W. J. Romanow, A. R. McGhie, J. P. McCauley Jr., A. B. Smith and R. M. Hochstrasser, *J. Phys. Chem.* **95**, 6075 (1991).
- ³ K. M. Nashold and D. Powell Walter, *J. Opt. Soc. Am. B* Vol. **12** No. 7, 1228 (1995).
- ⁴ S. Couris, E. Koudoumas, A. A. Ruth and S. Leach, *J. Phys. B: At. Mol. Opt. Phys.* **28**, 4537 (1995).
- ⁵ M. Lee, O. Song, J. Seo, D. Kim, Y. D. Suh, S. M. Jin and S. K. Kim, *Chem. Phys. Letters* **196** No. 3, 4 325 (1992).
- ⁶ C. Li, L. Zhang, R. Wang, Y. Song and Y. Wang, *J. Opt. Soc. Am. B* Vol. **11** No. 8, 1356 (1994).
- ⁷ T. W. Ebbesen, K. Tanigaki and S. Karoshima, *Chem. Phys. Lett.* **181**, 6, 501 (1992).
- ⁸ J. V. Bezel, S. V. Chekalin, Y. A. Matveets, A. G. Stepanov, A. P. Yartsev and V. S. Letokhov, *Chem. Phys. Letters* **218**, 475 (1994).
- ⁹ S. L. Dexheimer, W. A. Vareka, D. Mittleman, A. Zettl and C. V. Shank, *Chem. Phys. Letters* **235**, 552 (1995).
- ¹⁰ S. D. Brorson, M. K. Kelly, U. Wenschuh, R. Buhleier and J. Kuhl, *Phys. Rev. B*, Vol. **46** No.11, 7329 (1992).
- ¹¹ T. N. Thomas, R. A. Taylor, J. F. Ryan, D. Mihailovic and R. Zamboni, *Europhys. Lett.* **25** (6), 403 (1994).
- ¹² R. A. Cheville and N. J. Halas, *Phys. Rev. B*, Vol. **45** No. 8, 4548 (1992).
- ¹³ V. M. Farztdinov, Y. E. Lozovik, Y. A. Matveets, A. G. Stepanov and Y. S. Letokhov, *J. Phys. Chem.* **98**, 3290 (1994).
- ¹⁴ T. Juhasz, X. H. Hu, C. Suarez, W. E. Bron, E. Maiken and P. Taborek, *Phys. Rev. B*, Vol. **48** No. 7, 4929 (1993).
- ¹⁵ S. R. Flom, F. J. Bartoli, H. W. Sarkas, C. D. Merrit and Z. H. Kafafi, *Phys. Rev. B*, Vol. **51** No. 17, 11376 (1994).
- ¹⁶ F. Bentivegna, M. Canva, P. Georges, A. Brun, F. Chaput, L. Malier and J. Boilot, *Appl. Phys. Lett.*, Vol. **62** No. 15, 1721 (1993).
- ¹⁷ A. Kost, L. Tutt, M. B. Klein, T. K. Dougherty and W. E. Elias, *Optics Letters* Vol. **18** No. 5, 335 (1993).
- ¹⁸ R. Gvishi, J. D. Bhawalkar, N. D. Kumar, G. Ruland, U. Narang, P. N. Prasad and B. A. Reinhardt, *Chem. Mater.* **7**, 2199 (1995).
- ¹⁹ V. Klimov, L. Smilowitz, H. Wang, M. Grigorowa, J. M. Robinson, A. Koskelo, B. R. Mattes, F. Wudl and D. W. McBranch, *Res. Chem. Intermed.* **23**, 7, 587-600 (1997).
- ²⁰ J. Schell, D. Brinkmann, D. Ohlmann, B. Hönerlage, R. Levy, M. Joucla, J. L. Rehspringer, J. Serughetti and C. Bovier, *J. Chem. Phys.* **108**, 20, 8599-8604 (1998).
- ²¹ R. Bensasson, E. Bienvenue, M. Dellinger, S. Leach and P. Seta, *J. Phys. Chem.* **98**, 3492 (1994).
- ²² F. Z. Henari, K. H. Cazzini, D. N. Weldon and W. J. Blau, *Appl. Phys. Lett.* **68** (5), 619 (1996).
- ²³ J. W. Arbogast, A. P. Darmanyan, C. S. Foote, Y. Rubin, F. N. Diederich, M. N. Alvarez, S. J. Anz and R. L. Whetten, *J. Phys. Chem.* **95**, 11 (1991).
- ²⁴ G. Gensterblum, *Journal of Electron Spectroscopy and Rel. Phenom.* **81**, 89 (1996).

THERMALLY INDUCED LENS IN NIGROSIN DOPED XEROGELS

BENJAMIN CAMPAGNE, ANTOINE COURJAUD, ALAIN BRUN
Laboratoire Charles Fabry de l'Institut d'Optique, CNRS URA 14, Orsay, France

FREDERIC CHAPUT, JEAN-PIERRE BOILOT
Physique de la Matière Condensée, CNRS UMR 7643, Ecole Polytechnique,
Palaiseau, France

Abstract Nonlinear refraction was investigated in nigrosin doped xerogels and in solutions of nigrosin in methanol in nanosecond timescale. Using classical Z-scan experiments at 532 nm, we characterized a series of doped samples. We present a qualitative study and determine the influence of the matrix (whether solid or liquid), as well as the concentration and the incident energy on the dynamic peak-valley. Liquid samples exhibit large dynamic compared to the xerogels. But at high energy and/or for high concentration, xerogels tend to behave similarly to liquids. A modelization using the beam propagation method is presented to analyse the Z-scan curves. Optical limiting experiments were also performed using an aperture of 90% linear transmittance. The activation threshold was of some J/cm^2 in xerogels and liquids. Finally, we present a two-wavelength pump-probe experiment to measure the lifetime of the nonlinear effect. The timescale of the recovering time is about some milliseconds, which corresponds typically to a thermal effect.

INTRODUCTION

The sol-gel process allows the trapping of organic molecules in a solid matrix¹. Once trapped in the solid glass, when no modification of the absorption spectrum is observed, the optical properties of the molecule are generally preserved. This process is also a good method to keep molecules safe in time, the ones sheltered from oxygen inside the medium. For optical limiting applications, molecules exhibiting reverse saturable absorption have been trapped successfully in gel matrices and nonlinear absorption was observed.²⁻³

Nonlinear absorption (NLA) is generally accompanied by nonlinear refraction (NLR). The contribution of the NLR is often neglected compared to the NLA effects. This consideration is realistic when no aperture stops the border of the beam. When the sample is integrated in a complex optical system, the presence of an iris is quite common. In this case, the contribution of the NLR must be taken into account. The interaction mechanisms responsible for the NLR effects have different origins.⁴⁻⁶ First, the intrinsic coefficient n_2 of NLR which is proportional to the $\text{Re}(\chi_3)$, is due to electronic effects. The response

time is ultrafast, on picosecond or shorter timescales. This coefficient n_2 depends on the nature of the matrix (xerogel or solvent). A refraction index change (Δn) can also be associated with the contribution of the excited state population introducing a nonlinear refraction cross section σ_n .⁷⁻⁸ The Δn can be caused by a thermal effect⁹, whose risetime is in the nanosecond timescale. The thermal effects induce larger values of Δn compared to electronic effects.

In this paper, we present a comparative study concerning the induced NLR effects in nigrosin doped xerogels and in solutions of nigrosin in methanol. Classical Z-scan experiments are performed at 532 nm with nanosecond pulse duration. For this timescale, the induced Δn is expected to be dominated by the thermal effect. Several comparisons are made between solids and liquids. We shall discuss the influence of the matrix, the influence of the concentration and the incident energy on the dynamic peak-valley ΔT_{pv} . A model¹⁰⁻¹¹ based on the Beam Propagation Method (BPM) which takes into account the NLR is proposed to interpret Z-scan measurements. Some optical limiting experiments are presented with the same samples, followed by discussions and comparisons. Additional experiments of two-wavelength pump-probe are also performed to measure the lifetime of the nonlinear effect.

EXPERIMENTS:

The behavior of the samples was observed in a given geometrical configuration and we did not study the dependence of Z-scan measurements versus focus strength. We focused a doubled frequency 532 nm Nd:YAG of pulse duration 5ns (half width at $1/e$) with a spot diameter of 35 μm (full width at $1/e^2$). The maximum energy available on the sample was about 1.3 mJ. The spatial profile can be approximated to a closely TEM00 gaussian curve, so that we can define the fluence as :

$$DE = \frac{2E}{\pi w^2} \quad (1)$$

where E is the incident energy, and w is the radius of the beam.

Each acquisition was performed using one single shot to avoid cumulative damage. The light was collected through an aperture situated 0.4m beyond the sample on a silicium photodiode. A set of optical densities was used to change the value of the incident energy. The data points were directly recorded on a computer using an IEEE interface.

We made three nigrosin doped xerogels of different concentration and prepared three equivalent solutions. The linear transmissions were respectively 64%, 42% and 20%. The thickness of the samples was 2mm. The Rayleigh range was longer than the thickness, so

the beam was nearly collimated inside the samples. The optical quality in volume and surface of the solid matrices had to be sufficient to avoid the deformation of the wavefront in a linear regime Z-scan experiment. The trapping of the nigrosin molecules in solid matrix was obtained successfully with a good homogeneity, but it was necessary to polish the two surfaces so as to obtain an acceptable planicity.

In this study, we are only interested in a nonlinear refraction mechanism, therefore we had to eliminate all the others. Thus, we chose a chromophore, absorbing in the visible spectrum, which did not exhibit NLA: the nigrosin molecule. An open aperture Z-scan was performed to check this property. Furthermore, neither fluorescence nor phosphorescence was observed under UV excitation: the desexcitation of this molecule is nonradiative. The whole absorbed energy is converted into thermal energy to heat up the medium.

Z-scan experiments:

To decrease the noise due to the fluctuation of the intensity of the laser, the beam was separated into two paths, one for a reference and the other one for the measurement.

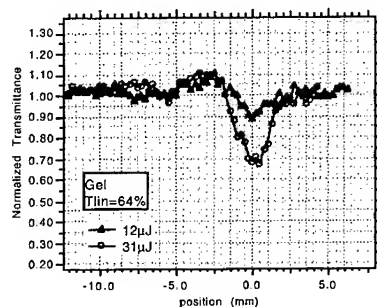


FIGURE 1 Gel, $T_{lin}=64\%$

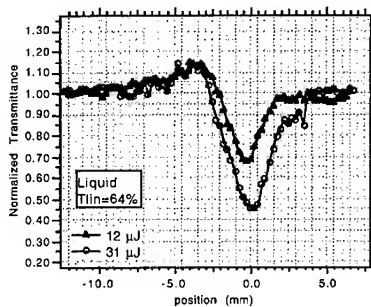


FIGURE 2 Liquid, $T_{lin}=64\%$

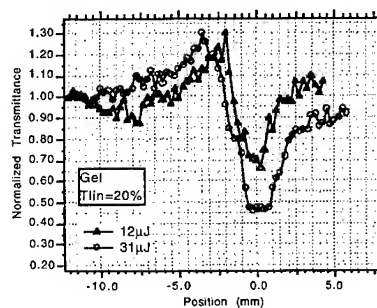


FIGURE 3 Gel, $T_{lin}=20\%$

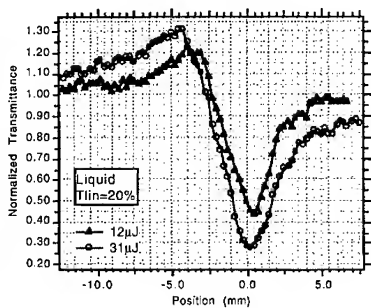


FIGURE 4 Liquid, $T_{lin}=20\%$

We collected about 3% of the linear transmission through an iris which was centered on the beam profile. The samples were moved from $-Z$ to $+Z$. The six samples (three solids and three liquids) were tested with two incident energies :12 μ J (2.5J/cm²) and 31 μ J (6.5J/cm²). Typical normalized Z-scan curves are presented in Figures 1-4 with the 64 and 20% linear transmission samples using one single shot.

The sign of the nonlinearity is negative, which is significative of an induced diverging lens. We can note a strong dissymmetry of the curves along the horizontal and vertical axes. The dynamic of the valley is more important than the dynamic of the peak. And this effect occurs for a position of the sample very close to the focus point- inside the Rayleigh range (4 mm). We report on Tables I and II the measured ΔT_{pv} obtained for each sample in any experimental condition:

TABLE I Z-scan results in doped xerogels

Linear Transmission	DE (J/cm2)	Peak value	Valley value	ΔT_{pv}
64%	2.5	1.10	0.90	0.20
64%	6.5	1.10	0.70	0.40
42%	2.5	1.15	0.85	0.30
42%	6.5	1.25	0.55	0.70
20%	2.5	1.25	0.70	0.55
20%	6.5	1.30	0.45	0.85

TABLE II Z-scan results in doped liquids

Linear Transmission	DE (J/cm2)	Peak value	Valley value	ΔT_{pv}
64%	2.5	1.13	0.68	0.45
64%	6.5	1.13	0.45	0.68
42%	2.5	1.15	0.55	0.60
42%	6.5	1.23	0.35	0.88
20%	2.5	1.20	0.45	0.75
20%	6.5	1.30	0.27	1.03

We remark that the ΔT_{pv} is always larger in liquid than in solid matrices considering one configuration. This behavior depends on the experimental conditions (fluence) and also depends on the properties of the medium (concentration and nature of the matrix). We compared the different results and determined how a modification of one parameter influences ΔT_{pv} .

Influence of energy

Whatever the type of the matrix, ΔT_{pv} increased with the incident energy. In any configuration, the results obtained with liquids are always dominant. But the differences between liquids and solid matrices decrease when the concentration is high and/or when

they are illuminated at high energy. For instance, considering the samples of linear transmittance 64% excited with the fluence of 2.5 J/cm², ΔT_{pv} in liquid is 2.25 times larger than in solid. This ratio is just 1.2 if we illuminate the samples of 20% linear transmittance with a fluence of 6.5 J/cm². In this last case ($\alpha_0=8 \text{ cm}^{-1}$ and $F_0=6.5 \text{ J/cm}^2$) the temperature rising ΔT is estimated at 30°C using the Equation (2)⁹. This computation assumes that the thermal properties of the xerogel are close to the ones of the fused silica¹³. The specific heat C_p is 0.76 J.g⁻¹.°C⁻¹ and the density ρ_0 is 2.2 g.cm⁻³. The heating of the medium is thus not high enough to significantly modify the xerogel structure.

$$\Delta T = \frac{\alpha_0 F_0}{\rho_0 C_p} \quad (2)$$

We observed that a variation of incident energy had a more significant impact on the modification of ΔT_{pv} in xerogels. These comparisons reveal that NLR effect is achieved earlier in liquids than in solids at low concentration. In highest concentrated xerogels, it may be possible that several dye molecules are located in a same pore, modifying the xerogel structure. This could explain the similar behavior of high doped xerogels and solutions.

Simulations

We developed a simulation based on the Beam Propagation Method taking into account the NLR. In our model, the index variation Δn expressed in Equation (3) is a combination of two mechanisms. The first one $n_2 I$ is relative to the instantaneous Kerr effect using the nonlinear index n_2 , and the second one is the result of a cumulative effect associated to the build-up of the excited state.

$$\Delta n = n_2 I + \sigma_r N, \quad \text{with } \sigma_r = \frac{\lambda}{2\pi} \quad (3)$$

σ_r is defined as the nonlinear cross section refraction, and N is the density population of the excited state.

Two preliminary Z-scan experiments using picosecond and nanosecond duration pulses were performed to estimate the value of the nonlinear index n_2 in one undoped xerogel. No transmittance change was observed, therefore we can consider the contribution of the Kerr effect in solid matrix as negligible.

A simulated Z-scan curve is reported in Figure 5. We can note that the model does not exactly predict the experimental result. This model assumes that lifetime of the excited state is longer than the pulse duration. The molecule nigrosin is excited on a metastable state so that nonradiative desexcitation time is fast compared to the pulse width.

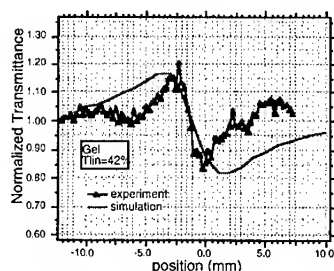
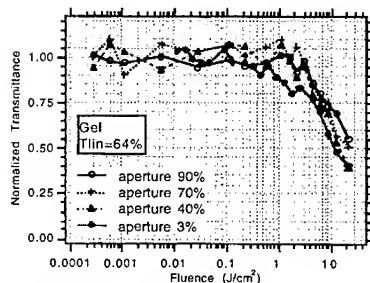
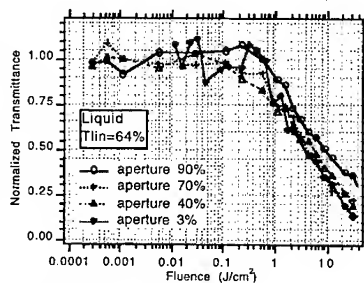


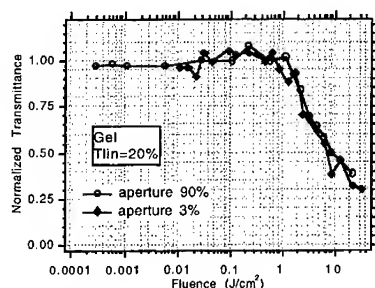
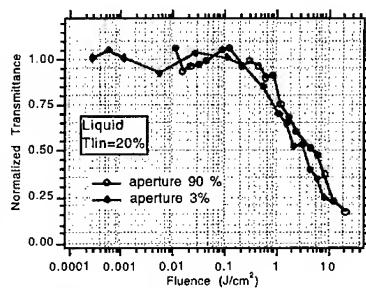
FIGURE 5 Simulation and experiment.

Considering a larger strength of the RNL near the focus point, a model taking into account the thermal diffusion and acoustic wave propagation should be more suitable for this investigation.⁹ But, the lack of information about the exact values of thermodynamic properties of xerogel, such as the calorific capacity or the temperature dependence of the refractive index (dn/dT), has not allowed us to carry out further investigation. Nevertheless, we present in the last part of this paper some complementary pump-probe results showing a manifestation of thermal effects.

Optical limiting experiments

The preliminary Z-scan results showed a strong defocusing effect. When the sample was placed around the focus, a decrease of transmittance through an aperture as a function of the incident energy was expected. We performed a series of limiting experiments with each sample, and we measured how the diameter of the aperture can modify the transmitted light. The diameter was adjusted to transmit 90%, 70%, 40% and 3% of the energy. For a convenient display, we normalized the curves (see Figures 6-9).

FIGURE 6 Gel, $T_{lin}=64\%$ FIGURE 7 Liquid, $T_{lin}=64\%$

FIGURE 8 Gel, $T_{lin}=20\%$ FIGURE 9 Liquid, $T_{lin}=20\%$

We define the activation threshold as the sufficient fluence to transmit 70% of the linear transmission. We report these values in Table III. They are generally weaker in liquids than in solids. And the higher the absorption is, the lower the threshold. We note one more time, that solid matrices tend to behave more like liquids with increasing absorption. Effectively, with 64% linear transmission samples, the threshold is 4.6 times smaller in liquid. And it is just twice smaller with 20% linear transmission samples.

TABLE III Activation threshold (J/cm^2) versus diameter iris

Linear Transmission	sample	90%	70%	40%	3%
64%	xerogel	12	9	8	6
64%	liquid	2.6	2	1.8	1.4
42%	xerogel	4	4	4	2.6
42%	liquid	2.4	x	x	1.6
20%	xerogel	3.2	x	x	2.4
20%	liquid	1.6	x	x	1.2

Influence of the iris diameter

With the low concentrated samples (liquids and solids), the modification of the iris diameter seems to affect the threshold value. For instance, we divided by two this value if the aperture was reduced from 90% to 3%. On the contrary, a weak change (division by 1.33 of the threshold value) was only observed with high concentrated samples. For a given concentration, the change of the iris diameter acted in the same proportion on liquids and solids. Therefore, the mechanism occurring in the medium is the same in the two matrices.

Two-wavelength pump-probe experiments

We used a cw HeNe at 633nm to measure the lifetime of the induced lens occurring in the medium. The two beams were colinear, and the pump beam could be shifted on each side

of the probe beam. The spot diameters were likely the same in the sample, so that there is a good spatial overlapping between the two beams. An iris collected a part of the cw probe, and a photomultiplier detector collects the energy passing through the aperture. The response time of the combined photomultiplier and oscilloscope was about 20 ns. In this experiment, all the measurements were not limited by the passband of the instruments. The risetime of the induced lens was about 100 ns which was relatively short (Figure 10). A stationary state was reached and was maintained during some microseconds. Then, the signal decreased with a characteristic time of some milliseconds (Figure 11). A translation of the pump beam induced a temporal shift of the transient response that we interpreted as a manifestation of an acoustic wave propagating through the medium. Therefore, we can measure the velocity of this wave, knowing the displacement of the pump beam in relation to the probe beam. In solutions, we measured a velocity of 1000 ± 200 m/s. This value is in good agreement with the literature¹² (vs methanol 1103 m/s). Using the same technique, we also measured the acoustic wave velocity in xerogel: 2000 ± 300 m/s. This interesting result suggests that the xerogel has an intermediate behavior between a solid and a liquid. In fused silica, the velocity¹² is reported to be 5968 m/s.

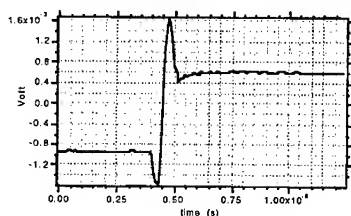


FIGURE 10 Transient regime

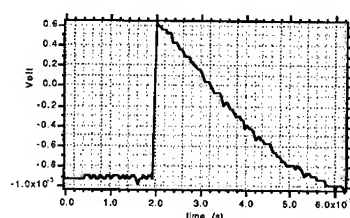


FIGURE 11 Thermal diffusion

CONCLUSION

The various stages of the experiment attest some nonlinear refraction effects in doped xerogels. Although these effects are stronger in liquids, the difference between solid and liquids matrices tends to disappear with high concentration and/or high illumination.

Beyond some J/cm², the nonlinear effect is well-established, and the presence of an iris adapted to the beam diameter improves the optical limiting fonction.

The proposed simulation does not give evidence of the strong dissymmetry which can be observed in experimental Z-scan curves. A model taking into account the propagation of the acoustic waves in the medium could improve the agreement between experimental and theoretical curves.

REFERENCES

1. J-P. Boilot, COLOO 4, Quatrième Colloque sur les Lasers et l'Optique Quantique, Ecole Polytechnique (6-8 Nov. 1995)
2. M. Brunel, M. Canva, A. Brun, F. Chaput, L. Malier and J.P. Boilot, Materials for optical limiting, Mat. Res. Soc. Symp. Proc. 374, p.281 (1995)
3. M. Brunel, F. Le Luyer, M. Canva, A. Brun, F. Chaput, L. Malier, J.P. Boilot, Appl. Phys. B, 58, 443 (1994)
4. E.W. Van Stryland, D.J. Hagan, T. Xia and A.A. Said, Nonlinear Optics of Organic Molecules and Polymers, Chap. 13, p. 841, Eds Nalwa & Miyata, CRC Press (1997)
5. Mansoor Sheik-Bahae, Ali A. Said, Tai-Hue Wei, D. J. Hagan and Eric W. Van Stryland, IEEE Journal of Quantum Electronics, 26, No. 4 (1990)
6. T.H. Wei, D.J. Hagan, M.J. Sence, E.W. Van Stryland, J.W. Perry, D.R. Coulter, Appl. Phys. B 54, 46-51 (1992)
7. A.A. Said, T. Xia, D.J. Hagan, and E.W. Van Stryland, M. Sheik-Bahae, J. Opt. Soc. Am. B/ vol.14, No. 4 (1997)
8. E.W. Van Stryland, M. Sheik-Bahae, A.A. Said and D.J. Hagan, Proc. Soc. Photo-Opt. Instrum. Eng. 1852, 135 (1993)
9. P. Brochard, V. Grolier-Mazza, R. Cabanel, J. Opt. Soc. Am. B/ vol.14, No. 2 (1997)
10. J.M Burzler, S. Hughes and B.S. Wherret, Appl. Phys. B 62, 389-397 (1996)
11. S. Hughes, J.M Burzler, G. Spruce and B.S. Wherret, J. Opt. Soc. Am. B/ vol.12, No. 10 (1995)
12. Handbook of Chemistry and Physics, 59th Edition 1978-1979, E 47
13. Melles Griot 1995/1996 Catalogue

VO₂ AND AU-VO₂ THIN FILMS PREPARED BY SPUTTERING AND SOL-GEL FOR INFRARED OPTICAL POWER LIMITING

J.P. SEGAUD^a, O. GIRAUDO^a, C. INDRIGO^b, E. CAVANNA^c, J. LIVAGE*
ONERA, DOTA^a/DMMP^b/DMSC^c, 91761 Palaiseau Cedex, France
* LCMC, Univ. P. et M. Curie, 4, place Jussieu, 75252 Paris Cedex 05, France

Abstract VO₂ and Au-VO₂ thin films were produced by reactive sputtering and sol-gel techniques. They were characterized by X-ray diffraction, scanning electron microscopy, nuclear probe microanalysis and spectrophotometry. Their optical switching performances were performed using a TEA CO₂ laser working at 10.6 μ m. The influence of the introduction of gold upon the commutation and damage threshold was investigated.

INTRODUCTION

The oxygen-vanadium system is a complicated one involving as many as 13 distinct phases [1]. Moreover, the stoichiometry can greatly vary for the same structure like, for example, in the case of the rutile one [2]. A semiconductor to metal transition has been reported in at least 8 vanadium oxides at temperature ranging from -147°C to 68 °C [3]. It is accompanied by large changes in electrical and optical properties [4]. This can be exploited as part of a designed thin film stack to exhibit fast and effective optical power limiting characteristics when exposed to a pulsed infrared laser irradiation. The performances of such a device depend on the quality of deposited materials. A number of methods have been used to prepare VO₂ thin films, such as vacuum evaporation [5], RF sputtering [6], chemical vapor deposition and the sol-gel process [7]. However, most of the published work focused on the phase transition itself and the optical and electrical quasi-static changes. Few dynamic investigations using pulsed laser irradiation have been related. In this paper, we report the preparation of VO₂ and Au-VO₂ thin films by reactive sputtering and sol-gel techniques. The influence of several process parameters was studied in the both cases. The optical power limiting

characteristics were investigated for VO_2 and Au-VO_2 thin films in order to show the absorption part in the semiconductor (cold) state on the commutation and damage performances.

EXPERIMENTAL PROCEDURE

Sputtering

Thin films of various vanadium oxides and Au-VO_2 mixtures were produced using a DC triode sputtering set-up shown schematically in Figure 1. It includes :

- a cryogenic pumping system,
- an electron gun with its opposite anode,
- two metallic targets (cathodes) which can work independantly,
- a micro-furnace which encloses the sample,
- a mass spectrometer which drives a double gas mass flow control system to keep the partial pressure of oxygen constant during the growth,
- a flat valve between the chamber and the pump to drive the working pressure.

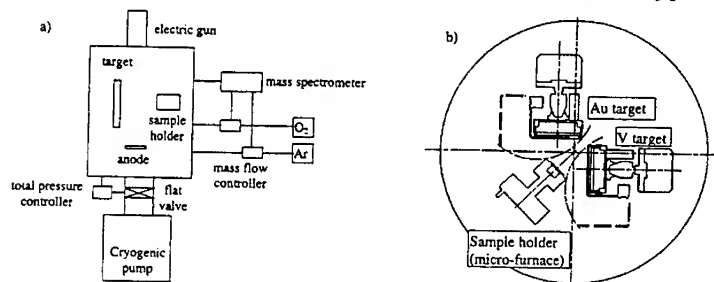


FIGURE 1 Schematic diagram of DC triode sputtering set-up :
a) general view b) targets & microfurnace (sample holder)

Germanium wafer ($\phi=1''$) were used as the substrate material for the purpose of infrared measurements. Sputtering of the V (and Au) metal target was performed in a mixture of argon and oxygen gases to form vanadium oxide. The partial pressure of oxygen was explored to find the right conditions to produce pure stoichiometric VO_2 . In another connection, it was kept constant during deposition by mass spectrometer driving. The total gas pressure was kept constant at 3 mT. Substrates were heated during deposition up to 500°C .

Sol-Gel

Vanadium dioxide thin films are synthesised from a vanadium oxo-alkoxide precursor, the tri-isopropoxyvanadyl VO(OPrⁱ)₃. The gold solution precursor is prepared by diluting tetrakis chloroauric acid (H(AuCl₄)) in the appropriate alcohol PrⁱOH. The final precursor solutions used for the deposition of Au doped VO₂ films are prepared by simply adding the gold solution precursor to the vanadium oxo-alkoxide solution.

The alkoxide solution is deposited on a precleaned double side monocrystalline (100) silicon polished substrate. Spin coating is performed in air with a Karl Suss RC5 spin coater (2000 rpm, 30s) and hydrolysis occurs spontaneously via ambient humidity. The coating is then heated around 60°C with an infrared heater in order to prevent the dissolution of previous layers. Three coatings are usually deposited one after the other and lead to a 0,3 µm film in thickness. Some attempts were made to increase the film thickness but most of films appear to crack beyond three coatings. This is probably due to the high internal stress resulting of the thermal crystallisation treatment.

After the spin coating deposition process, not all the alkoxy groups are hydrolysed and amorphous oxo-polymers [V₂O_{5-x}(OR)_x]_n films are formed. The reduction of the amorphous film to the monoclinic crystalline VO₂ state is based on the method of Greenberg and al [8]: the samples are heated in reducing aromatic hydrocarbon atmosphere at 400°C during 1 mn. Guzman and al [7] improved the process by using an Ar-H₂ 5% mixture which is a less reducing atmosphere that enables a better control of the thermal treatment parameters. Following the same process, amorphous films were annealed under flowing atmosphere (Ar-H₂ 5%, Noxal 3, Air Liquide Product) in a tubular furnace to achieve complete dehydration, residual solvent removal and crystallization. Some samples were heated at temperatures between 350 and 500°C for 2 minutes. Another set is maintained at 500°C for different duration between 2 minutes and 10 hours.

Measurements of films properties

Several standard techniques were employed to evaluate the properties of the fabricated films. The morphology and the thickness of the films were evaluated by

scanning electron microscopy on a Zeiss DSM 982 Gemini model. The crystal structure was studied by X ray diffraction by the way of a Philips PW 1877 diffractometer (sputtering samples) or a Philips PW 1820 diffractometer (sol-gel samples). The stoichiometry was studied by nuclear probe micro-analysis. It includes Rutherford backscattering spectrometry (RBS), nuclear reaction analysis (NRA) and deuteron induced X-ray emission (DIXE) with bombardment of 2.1 MeV deuterons. The oxygen composition was determined by NRA. The vanadium and gold ones were fixed by the combinations of RBS and DIXE results. The hysteresis loop of optical transmission was recorded at $\lambda=2.5\ \mu\text{m}$ as a function of temperature between 20°C and 90°C on a Nicolet 550 FTIR spectrophotometer equipped with a temperature controlled chamber. Experiments were performed at heating and cooling rates of 1°C/mn.

RESULTS

Sputtering

VO₂ films

Polycrystalline VO_x films were deposited on germanium substrates heated to a temperature of 500°C. Deposition rate was of the order of 1 $\mu\text{m}/\text{h}$. The microstructure of a VO₂ film is shown in Figure 2 which indicates a fine and dense granular structure. Films were composed of microcrystallites with a size ranging from 0.2 μm to 0.4 μm . The cross-section view displays the typical sputtering columnar regime of growth.

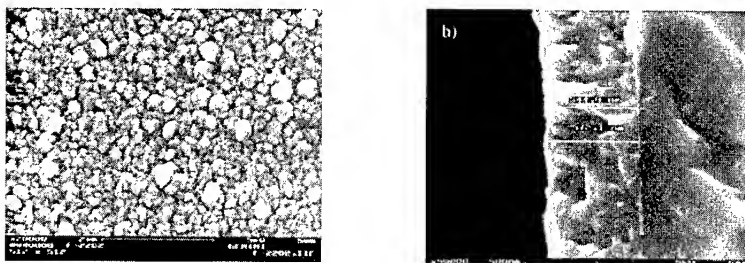


FIGURE 2 Scanning electron micrograph of a VO₂ film :
a) top view b) cross -section view

Figure 3 shows X-ray diffraction patterns from VO_x films deposited with different partial pressure of oxygen ranging from 0.038 mT to 0.084 mT. The film deposited at P_{O₂} = 0.038 mT is identified as a V₂O₃ single phase as shown in (a). The film deposited at P_{O₂} = 0.047 mT yields a diffraction pattern (b) that corresponds to monoclinic VO₂ phase with a strong (011) orientation. The film in (c) deposited at P_{O₂} = 0.084 mT is a mixture of orthorhombic V₂O₅ phase and monoclinic VO₂ phase. Repeated experiments proved that VO₂ single phase film could only be formed at a very narrow range of P_{O₂} and a small deviation from it would result in the formation of mixed phases. This fact is not surprising considering the complexity of the vanadium-oxygen system. From which, the interest and the necessity of the partial pressure control system stands out to prepare effective good VO₂ films.

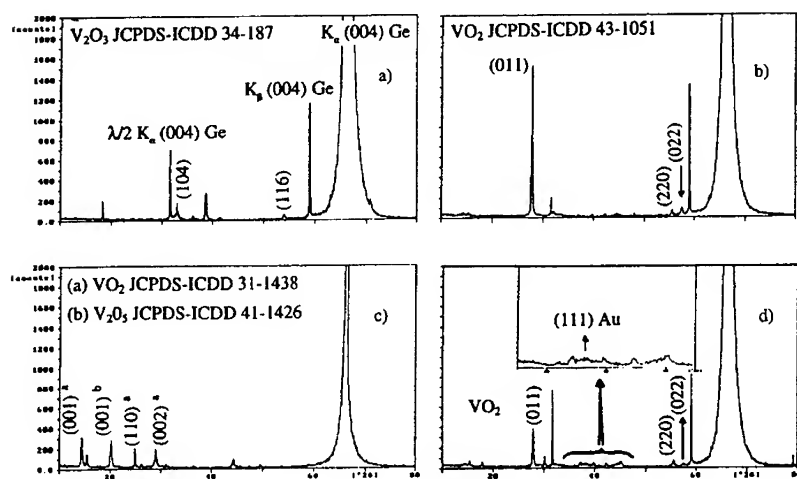
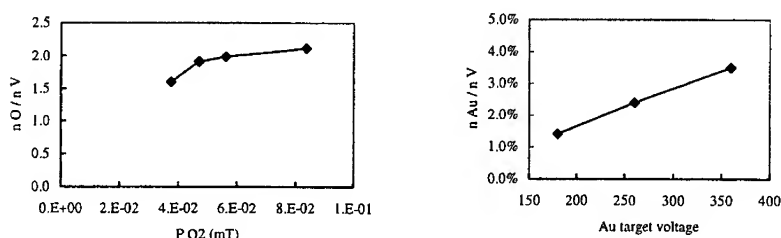


FIGURE 3 X-ray diffraction patterns for VO_x films deposited at different P_{O₂} :
a) 0.038 mT b) 0.047 mT c) 0.084 mT and a Au-VO₂ film (d)

Nuclear probe quantitative microanalysis showed that the stoichiometry of films depends strongly on the P_{O_2} . No impurities were detected in the deposited films. Figure 4 (a) displays the oxygen ratio as a function of the partial pressure of oxygen. It indicates the difficulty to obtain high level of vanadium oxydation by sputtering. Even at high P_{O_2} , films are not a V_2O_5 single phase but a mixture of V_2O_5 and other sub-oxides of vanadium.

FIGURE 4 a) oxygen ratio vs P_{O_2}

b) gold ratio vs Au target voltage

Au-VO₂ films

Polycrystalline Au-VO₂ films were deposited using a second metallic target made of gold. The voltage applied to the gold target was explored to modify the sputtering yield and so the gold quantity incorporated in the films. Figure 3 (d) shows an X-ray diffraction pattern from the Au-VO₂ film deposited with $V=300V$ and $P_{O_2} \approx 0.047$ mT. It exhibits that the vanadium oxide formed is still the VO₂ monoclinic phase. There is no interaction due to the gold target use on the working process parameters determined to obtain good effective VO₂ films. But the gold quantity introduced remains quite small. The inset in figure 3 (d) shows the broadening of the peak corresponding to (111) planes of metallic gold. It proves that gold is added in metallic form and the peak width suggests that the particles size is about 4 nm. Figure 4 (b) gives the gold ratio as a function of gold target voltage determined by RBS. In this range of small filling factor, the gold ratio is proportional to the voltage applied to the gold target. For all these samples, there is no significant decrease of the transmission level recorded by infrared spectrophotometry.

Sol-Gel

VO₂ films

The influence of thermal treatments on the structure and optical switching properties of thin films was followed. The kinetic of the VO₂ crystallized phase formation is shown in figure 5 which represents the optical hysteresis loop of sample annealed at a heating rate of 5°C/min to 400°C, 450°C and 500°C. As no other phase except VO₂ is detected by x-ray diffraction for the sample treated at 400°C, the crystallization is not completely performed and the film presents a mixture of crystallized VO₂ and amorphous phase.

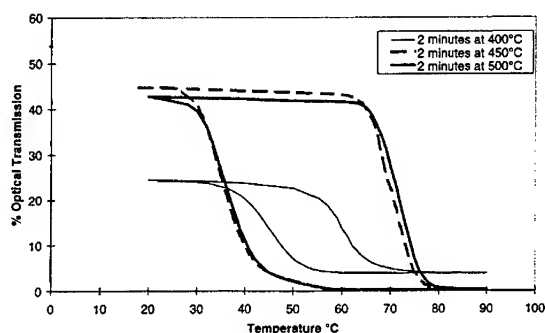


FIGURE 5 Temperature dependence of the infrared transmittance of VO₂ thin films treated at different temperature at $\lambda=2.5\mu\text{m}$.

As described in literature the vanadium oxygen system [1] exhibits a complex phase due to the multivalent vanadium ion and the large number of oxides that can be formed. The VO₂ phase occurs within a very small domain only. It may therefore be difficult to adjust the thermal treatment parameters. The reducing atmosphere flow control is critical since insufficient flow may induce the formation of a VO₂-V₆O₁₃ mixed phase and strongly affects the optical switching properties. Indeed, V₆O₁₃ is formed first during the early stages of reduction. The x-ray diffraction pattern, recorded at room temperature, of the corresponding samples are shown in figure 6. For both VO₂ pure and VO₂-V₆O₁₃ mixed films, the x-ray diffractograms exhibits all the peaks corresponding to the low temperature α -VO₂ phase [JCPDS 43-1051] and the intensity of the peaks

suggests a preferred (011) orientation for the α -VO₂ phase. The presence of a V₆O₁₃ phase in the film treated under the lower reducing gas flow is revealed by the x-ray diffractogram which presents the peaks of a (011) preferential orientation for V₆O₁₃ [JCPDS 27-1318].

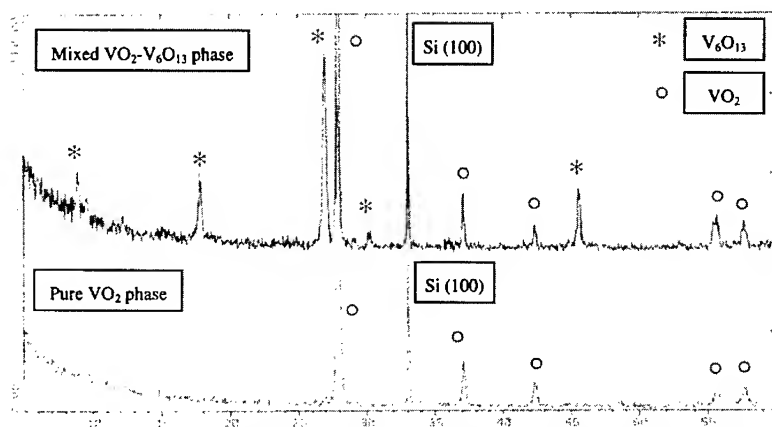


FIGURE 6 X-ray diffraction pattern of VO₂ coating film and mixed VO₂-V₆O₁₃ film.

Switching behaviours of VO₂ thin films annealed at 500°C between 2 minutes and 10 hours are very similar and present a sharp optical switching upon heating. The transition temperature is around 72°C and when the temperature decreases, switching process is not so sharp and occurs at a temperature between 60°C and 30°C. The microstructures of the VO₂ films pyrolyzed at 500°C for 2 minutes and 10 hours are presented in figure 7 for both cross and top views. The surface microstructure displays a granular structure with many cracks due to thermal stresses induced by the annealing treatment. The films seem to be porous with a nominal thickness around 300 nm. As the heat treatment duration increases, the dimension of some grain is growing and the film exhibits a two population grain size of 300-600 nm and 100-200 nm. In comparison, the grain size population of the film treated for only 2 minutes at 500°C is relatively homogeneous and much smaller 40-150 nm.

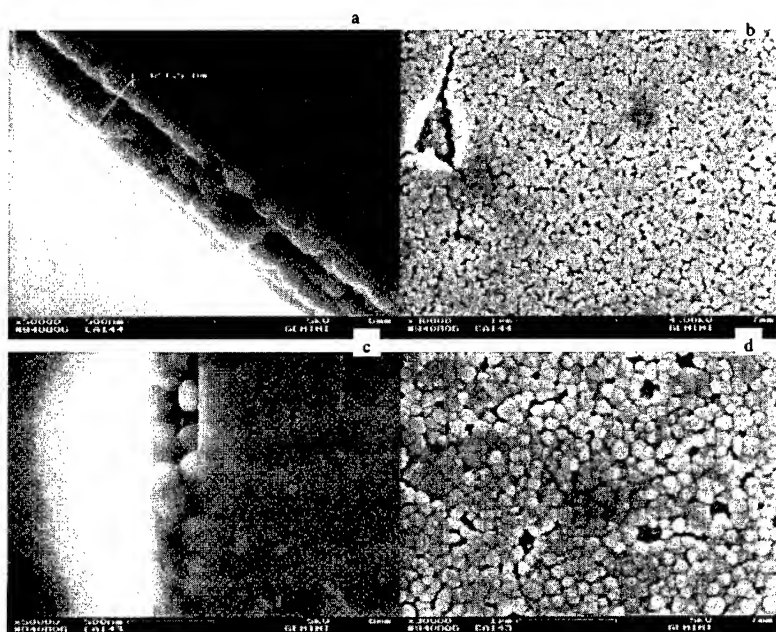


FIGURE 7 Scanning electron micrographs of transverse and surface VO₂ films treated at 500°C. a) and b) : 2 minutes treatment duration. c) and d) : 10 hours treatment duration.

Au-VO₂ films

Thin films containing 0,25%, 0,50% and 1,25% at Au (n_{Au} / n_V) have been made following the process described previously. Several attempts were made to increase the Au content up to 5% atomic but all the films crack during the crystallisation treatment. The addition of gold as dopant seems to be harmful to the formation of a perfectly crystallised α -VO₂ phase. So the deposition process should be improved for higher gold doping content.

The high magnitude microscopy observation on the surface of a 1,25% at Au doped film annealed at 500°C during 2 hours shows a non homogeneous collection of 65-130 nm grain size disposed on the surface of the film. This result leads us to consider the migration of gold particles to the surface of the coating as a possible fact, but EDX

analyses did not lead us to conclude about the presence of gold particles on top of the film surface. Otherwise, the results provided by analyses performed successively on the first and the third film layer, clearly corroborate the hypothesis of gold colloid migration towards the film surface.

The X-ray diffraction pattern of crystalline $V_{1-x}Au_xO_2$ films, recorded at room temperature, confirms the formation of the α - VO_2 phase with a (011) preferred orientation. This orientation progressively disappears as the Au content increases, and $V_{0,9875}Au_{0,0125}O_2$ film appears to be more randomly oriented (figure 8). Very small peaks at $2\theta = 38,1^\circ$, corresponding to (111) planes of metallic gold can be seen on the X-ray diffractograms of 0,50% at Au and 1,25% at Au doped films. The sharper the peaks are, the larger the grain particles are. So the crystallite size of gold is very thin and this result seems to be agree with the fact that it is not possible to see gold particles by scanning electron microscopy.

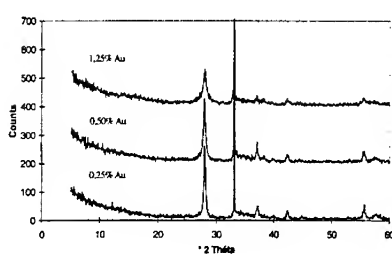


FIGURE 8 X-ray diffraction pattern of $V_{1-x}Au_xO_2$ films at room temperature with $x=0,0025$; $0,0050$; $0,0125$.

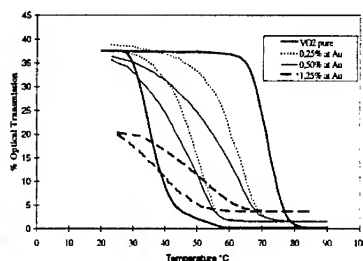


FIGURE 9 Gold doping influence upon switching of $V_{1-x}Au_xO_2$ films at $\lambda=2,5\mu m$.

The effect of gold addition upon film optical properties is displayed in figure 9. As pure VO_2 film becomes metallic and infrared reflecting above the transition temperature ($72^\circ C$), a small amount of Au (0,25% at) leads to the improvement of the thermochromic behaviour of the films. The transition temperature upon heating drastically decreases ($61^\circ C$ for 0,25% at Au), and the hysteresis curve is narrower ($T=12^\circ C$). As the amount of Au increases, this behaviour goes on and the hysteresis curves become narrower ($T=10^\circ C$ for 0,50% at Au and $T=8^\circ C$ for 1,25% at Au). The transition temperature upon heating reaches $57^\circ C$ for 0,5% at Au and $49^\circ C$ for 1,25% at

Au but optical transitions become medium at the low temperature phase and the high temperature state simultaneously becomes less and less reflecting.

DISCUSSION

The optical power limiting characteristics were determined at 10.6 μm using a cavity TEA CO₂ laser (500 ns pulse width) with incident and transmitted pulses measured using pyroelectric detectors operating at room temperature. The set-up used for the work is shown in Figure 10. Alternatively, a thermal camera could be used to image the local plane and so to allow spatial effects to be explored.

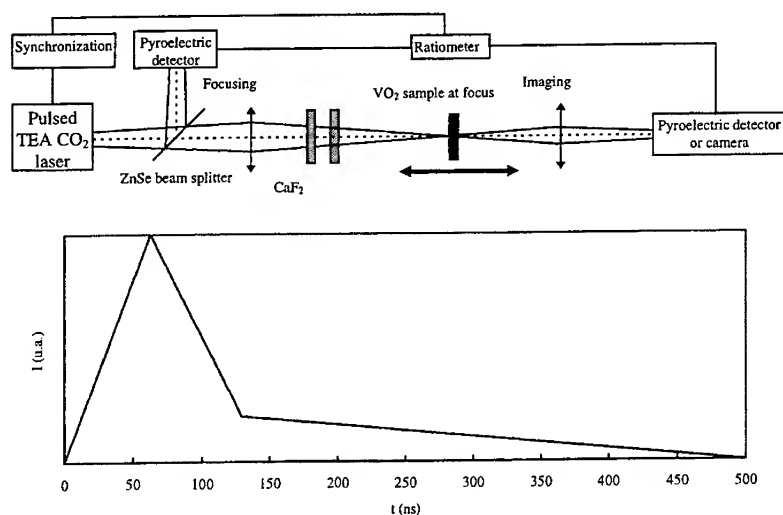


FIGURE 10 a) Schematic diagram showing configuration used for measuring characteristics of VO₂ and Au-VO₂ films at 10.6 μm
b) Temporal profile of the TEA CO₂ laser beam

In the experiments, the spatial profile of the beam was very close to gaussian and the temporal one is given in Figure 10 (b). VO₂ and different Au-VO₂ thin films were measured to investigate the influence of the absorption in the semi-conductor (cold) state on the commutation and damage thresholds. It deals with the extinction coefficient k_{sc} of the optical constant which is connected to the gold filling factor in the Au-VO₂ mixtures. The optical power limiting characteristics recorded for a VO₂ and a Au-VO₂ films are shown in Figure 11 (resp. 12) in the case of sputtering (resp. sol-gel) process.

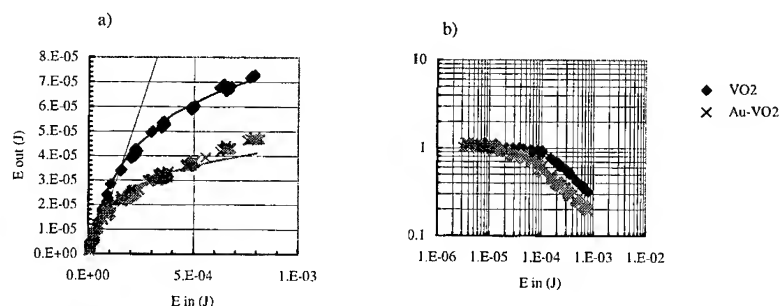


FIGURE 11 Optical power limiting curve for sputtering VO₂ and Au-VO₂ ($V_{Au} = 260V$) samples in terms of a) energy and b) induced optical density

The commutation threshold (measured at 3 dB from the induced optical density data) decreases from 0.35 mJ to 0.15 mJ. The damage threshold, fixed at the first optical flash recorded during experiments, remains of the same order. The input dynamics, defined as the ratio of the commutation over the damage thresholds, is so multiplied by a factor of 2. In the case of sputtering, all the Au-VO₂ samples produced the same typical shifted limitation curve in comparison with the VO₂ sample one. This result could be explained by a too high gold ratio explored range. At that point, the commutation threshold decrease is limited by the drastic linear transmission level decrease which does not allow effective measurements. The both limitation curves are compared with calculations issued from a conjugated thermal and optical model presented otherwise [9]. The thermal and optical data used are summarized in Table 1.

	Semi-conductor state	Metallic state
Specific heat C_p ($J.kg^{-1}.K^{-1}$)	600	720
Thermal conductivity ($W.K^{-1}.m^{-1}$) λ	4	5
Refraction index n	4.2	4.3
Extinction index k	VO ₂ : 0.05 Au-VO ₂ : 0.25	7

Table 1 Thermal and optical data used to fit VO₂ and Au-VO₂ optical limiting curves

Only the k_{sc} value has been changed by a factor of 5 between the two sets. The specific heat determined is 2.5 smaller than bulk value accepted in the literature. This result is in agreement with recent measurements performed on different oxide thin films [10].

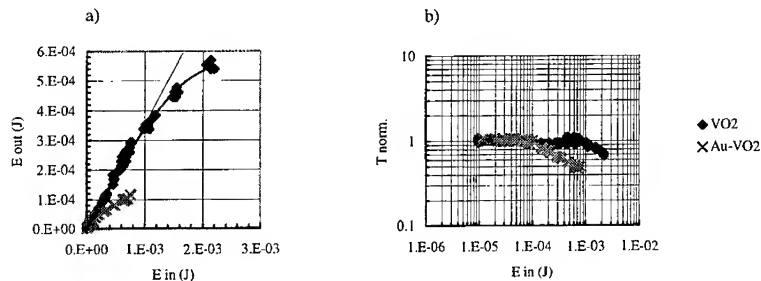


FIGURE 12 Optical power limiting curve for sol-gel VO₂ and (1.25%)Au-VO₂ samples in terms of a) energy and b) induced optical density

In the case of sol-gel process, the same shift is observed with higher thresholds. This is certainly due to less dense and thick films which do not allow to obtain better performances. Moreover, as displayed on the X-ray diffractograms corresponding, the addition of gold particles seems to disturb the α -VO₂ phase formation.

CONCLUSION

VO₂ and Au-VO₂ mixtures thin films have been successfully deposited by reactive sputtering and sol-gel spin-coating process. In the case of sputtering, stoichiometric VO₂ is produced with the help of a partial pressure control system. And the gold ratio is accurately controlled by the voltage applied to the Au target. The introduction of metallic clusters in VO₂ increases the extinction coefficient k_{sc} and so the absorption part in the semiconductor state. This involves a fall of the commutation threshold without greatly changing the damage threshold. The input dynamics is so increased by a factor of 2. In the case of sol-gel, pure VO₂ optically transparent films about 300 nm in thickness can be easily formed upon heating at 500°C under a reducing atmosphere (Ar-H₂ 5%). In the same experimental conditions, gold addition disrupts the film formation and only low Au content films have been successfully made.

ACKNOWLEDGMENTS

J.P. Segaud would like to acknowledge D. Boutard and P. Berger for nuclear probe microanalysis at the CNRS/CEA P. Süe laboratory in Saclay, C. Diot for XRD experiments and Y. Pioche for SEM images.

This work was partially performed under contracts from the DGA through the DRET and STTC departments.

REFERENCES

1. Massalski, Binary alloys phase diagrams, Ed. ASM Int., (1990)
2. J. Stinger, *J. Less-common Mat.*, 8, 1 (1965)
3. D. Adler, *Rev. Mod. Phys.*, 40, 714 (1968)
4. H. Jeronimek, F. Picard and D. Vincent, *Optical Engineering*, 32, 9 (1993)
5. G.A. Nyberg and R.A. Buurhman, *J.V.S.T.* A2, 301 (1984)
6. J.A. Theil, E. Kusano and A. Rochett, *Thin Solid Films*, 298, 122 (1997)
7. G. Guzman, R. Morineau and J. Livage, *Mat. Res. Bull.*, 29,5,(1994)
8. C.B.Greenberg, *Thin Solid Films*, 110, 73-82 (1983)
9. J.P. Segaud, B. Dilleman and O. Giraudo, these proceedings
10. S. Orain, Y. Scudeller and T. Brousse, Journées d'automne 1997, SFM

TWO-PHOTON AND HIGHER-ORDER ABSORPTIONS AND OPTICAL LIMITING PROPERTIES OF BIS-DONOR SUBSTITUTED CONJUGATED ORGANIC CHROMOPHORES

J. W. PERRY,*†§ S. BARLOW,§ J. E. EHRLICH,† A. A. HEIKAL,§ Z.-Y. HU,§
I.-Y. S. LEE,§ K. MANSOUR,§ S. R. MARDER,*†§ H. RÖCKEL,§ M. RUMI,§
S. THAYUMANAVAN,§ X. L. WU§

† Jet Propulsion Laboratory, California Institute of Technology, Pasadena, CA
91109

§ Beckman Institute, California Institute of Technology, Pasadena, CA 91125

‡ Department of Chemistry, The University of Arizona, Tucson, AZ 85721

Abstract Two-photon absorption spectra have been measured for bis-donor diphenylpolyene derivatives with varying conjugation lengths and end groups. Large two-photon absorptivities are observed via nanosecond nonlinear transmission measurements in comparison to picosecond nonlinear transmission and two-photon excited fluorescence methods, which suggests a large contribution of excited-state absorption to the nanosecond nonlinear transmission results. These results are reasonably well modeled as a combined two-photon and two-photon induced excited-state absorption process. Strong nonlinear absorption of nanosecond pulses is observed for bis(diarylamino)biphenyl derivatives at 525 nm. This blue shifted nonlinear absorption, relative to bis(dialkylamino)stilbene, makes possible the design of broadband optical limiting materials based on a combination of derivatives with varying conjugation lengths and end groups. We have demonstrated the feasibility of achieving broadband response using a tandem combination of cells containing three such compounds.

INTRODUCTION

Considerable interest has recently arisen in organic materials possessing large two-photon absorptivities, because they can foster the development of new nonlinear optical devices and 3-D technologies. They can be used in optical limiters,¹⁻⁴ to control the intensity of laser beams for eye or sensor protection, or for intensity stabilization or pulse shaping in laser sources and devices. Other applications of current interest include microscopic fluorescence imaging,⁵ 3-D optical data storage and 3-D microfabrication.^{6,7}

* To whom correspondence should be addressed.

Two-photon absorbers offer the advantage for optical limiting over reverse saturable absorbers of having a very high transmittance in the low intensity regime. On the other hand, until recently^{8,9} the magnitudes of two-photon absorption cross sections known for organic chromophores have been too small for use in optical limiting of nanosecond (ns) laser pulses. We have recently shown that bis(di-*n*-butylamino)stilbene (**1** in Figure 1) exhibits a large effective two-photon absorptivity at 600 nm: a value of the effective two-photon absorption cross section, δ , of about 1.7×10^{-46} cm⁴ s/photon-molecule was obtained by way of a nonlinear transmission (NLT) experiment using ns pulses.⁸ However, a strong dependence of this effective nonlinearity on pulse duration was observed⁴ and this result has raised questions regarding the origin of the large apparent two-photon response on the ns timescale for **1** and related molecules.

We have also reported⁸ that there is a significant red shift (~90 nm) in the peak position of the effective two-photon absorption on going from **1** to bis(diphenylamino)stilbene, **6**, whereas there is only a small shift of the one-photon absorption maximum. A solution containing both molecules was shown to exhibit a nonlinear response that was additive in the contributions of the individual components, and indicated the potential for broadband optical limiting over 170 nm with high linear transmission over this range. However, the superposition of the responses of **1** and **6** does not extend to wavelengths between 450 and 550 nm, and as a result we were interested in the design of molecules with shorter wavelength two-photon absorptivity.

In this paper, we report on: 1) two-photon absorption spectra obtained on a series of bis-donor substituted diphenyl-polyenes and the correlation of molecular structure (conjugation length and alkylamino *versus* arylamino end groups) with the position and strength of the two-photon absorption bands; 2) results obtained using two different experimental techniques (namely nonlinear transmission and two-photon excited fluorescence measurements) and different pulse durations (ns and picosecond, ps), in order to gain insight into the mechanism responsible for the large two-photon cross section observed in ns nonlinear transmission experiments; 3) the dispersion of the two-photon absorptivity of bis-donor biphenyls, which are candidates for achieving two-photon absorption near 530 nm; 4) the performance of these molecules as optical limiting materials in an f/5 optical system, and 5) a demonstration of optical limiting over a wide wavelength range in the visible based on a tandem cell arrangement involving three different bis-donor compounds.

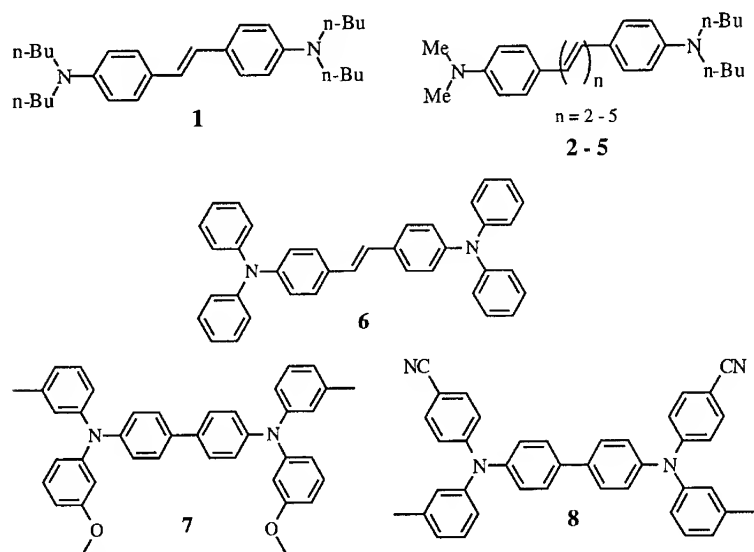


FIGURE 1 Structures of the compounds studied in this work.

EXPERIMENTAL

Figure 1 shows the molecular structure of the compounds studied in this work. All of these compounds are D- π -D molecules in which the end electron donor groups (D) are dialkylamino (compounds 1 through 5) or diarylamino groups (compounds 6, 7 and 8) and the conjugated bridge (π) is a diphenyl-polyene (1-6) or biphenyl (7, 8). Compounds 1-5 were prepared using Wittig reactions.¹⁰ Compound 6 was prepared from 4-(diphenylamino)benzaldehyde using the McMurray coupling.¹¹ The syntheses of compounds 7 and 8 have been described elsewhere.¹² The molecules were studied in toluene or acetone solution at concentrations of about 10^{-4} M for the two-photon excited fluorescence (TPF) measurements and from 10^{-3} to 10^{-2} M for the nonlinear transmission experiments. Concentrations as high as 0.14 M were used for the optical limiting measurements. For all measurements, optical cells of 1 cm pathlength were used.

Nonlinear transmission measurements were carried out using two laser systems. For nanosecond measurements a Nd:YAG-pumped dye laser with ~ 5 ns pulse duration and a relatively uniform "top-hat" spatial profile was used. For picosecond

measurements, an amplified synchronously-pumped cavity-dumped dye laser with a 4 ps pulse duration was used. A two-lens telescope was used to collimate the beam and to reduce the beam diameter to give a cross sectional area of 0.0025 cm² for the nanosecond measurements, while various lens combinations were used to produce areas of 0.009 - 0.11 cm² for the picosecond measurements. For these experiments the beam was essentially collimated over the 1 cm pathlength of the sample. Nanosecond optical limiting measurements were done in an *f*/5 optical system at 600 nm and 532 nm. The calculated beam waist radius ($HW1/e^2M$) was about 3.5 μ m for the 600 nm measurements and 8 μ m for the 532 nm measurements, the difference being due to different beam sizes on the focusing lens. The beam waist was located ~2 mm from the exit window of the sample cell. The incident laser intensity was controlled using neutral density filters and a half-wave plate/polarizer combination. A beam splitter was used to provide an intensity reference beam. The beams in the signal and reference arms were detected with 1-cm² area silicon photodiodes. In all ns NLT measurements the uncertainty in the effective absorptivities was about $\pm 15\%$.

For two-photon excited fluorescence measurements, we used a Nd:YAG-pumped optical parametric oscillator/amplifier system that produces 5 ns pulses (repetition rate: 10 Hz) and is tunable over a wide range in the visible and near infrared. Determination of δ is performed using compounds of known two-photon absorptivity (namely bis(methylstyryl)benzene in cyclohexane and fluorescein in pH 11 water solution)^{13,14} as reference standards and using a two arm set-up to obtain an intensity calibration. In each arm the fluorescence emission from the solution is collected at 90° from the exciting beam by a lens and imaged onto a photomultiplier tube. The signal is then amplified and directed to an integrator. Proper short-pass filters are used to suppress any scattered laser light.

If the linear absorption at wavelength λ and saturation effects are negligible, the fluorescence signal, F , is proportional to the square of the incident intensity and the two-photon absorptivity, δ :

$$F \propto \frac{1}{2} \delta C \phi \eta \langle I \rangle^2 g^{(2)} \quad (1)$$

where C is the molar concentration, η is the quantum yield of the fluorescence, ϕ is the collection efficiency (that takes into account the geometry of the collection system, the wavelength dependence of the instrumental response over the range of the fluorescence spectrum and the refractive index of the solvent), $g^{(2)}$ is the second-order coherence coefficient of the laser beam¹⁵ and $\langle I \rangle$ is the average over the pulse duration of the

instantaneous intensity. The coefficient of 1/2 in Equation (1) is due to the fact that two photons must be absorbed to produce one fluorescent photon. Following measurement of the fluorescence signals for a sample, $F_{\text{sam.}}$, and a reference solution, $F_{\text{ref.}}$, the two-photon absorption cross section for the sample, $\delta_{\text{sam.}}$, was calculated using the following expression:

$$\delta_{\text{sam.}} = \frac{F_{\text{sam.}}}{F_{\text{ref.}}} \frac{\phi_{\text{ref.}} \eta_{\text{ref.}} C_{\text{ref.}}}{\phi_{\text{sam.}} \eta_{\text{sam.}} C_{\text{sam.}}} \delta_{\text{ref.}} \quad (2)$$

The uncertainty in determination of δ_{sam} values were in range of ± 10 to 15%

ANALYSIS OF NONLINEAR TRANSMISSION DATA

A nonlinear transmission experiment consists of the measurement of the transmittance $T = I/I_0$ of the sample (I_0 is the intensity of the incident beam, I the intensity of the transmitted beam) as a function of I_0 . In the case of a material with single and two-photon absorption, the intensity of the beam propagating through the sample is given by the following equation:

$$\frac{dI}{dz} = -\alpha I - \beta g^{(2)} I^2 \quad (3)$$

where z is the position in the propagation direction, α is the linear absorption coefficient and β is the two-photon absorption coefficient. The solution of this equation, expressed in terms of I/T , is:

$$\frac{1}{T} = \frac{1}{T_0} + \beta g^{(2)} I_0 L_{\text{eff}} \quad (4)$$

where $T_0 = \exp(-\alpha L)$ is the linear transmission, and $L_{\text{eff}} = (1 - \exp(-\alpha L))/\alpha$ is the effective sample pathlength. Generally, the results reported in this paper will be confined to measurements in the transparent spectral regions of the compounds where the linear absorption is negligible and the intercepts of the $1/T$ versus I_0 plots are very close to 1. From the slope of linear fit to the $1/T$ data as a function of I_0 we derive an estimate of $\beta g^{(2)}$.

The above solution is appropriate for the case where the beam is collimated across the length of the sample, the pulse intensity is a "top-hat" shape in time and transverse distribution, and the ground-state population is not significantly depleted

during the pulse. Since our pulses are not "top-hat" shaped in time, the two-photon absorption coefficient we obtain using Equation (4) must be viewed as a rough time average over the pulse. We have not measured $g^{(2)}$ of our laser pulses directly. Our nanosecond pulses are short coherence length, multimode pulses, whereas our mode-locked picosecond pulses are nearly transform limited. The two-photon absorptivities from nonlinear transmission measurements reported in this paper implicitly contain the factor of $g^{(2)}$.

The molecular two-photon absorption cross section, δ , is related to the two-photon absorption coefficient through the following expression:

$$\delta = \frac{h\nu\beta}{N_A C} \quad (5)$$

where N_A is Avogadro's number and $h\nu$ is the photon energy. We apply the above analysis to both nanosecond and picosecond measurements, although there may be contributions from higher-order nonlinearities, especially in the case of nanosecond pulses, as will be discussed below. Thus, the two-photon absorptivities which have been derived from NLT measurements are denoted as effective parameters, δ_{eff} .

RESULTS AND DISCUSSION

Effective Two-Photon Absorptivity from Nanosecond Experiments

In Figure 2, we show typical nonlinear transmission data for compounds **1** and **2** in acetone and in toluene at 605 nm. According to Equation (4), $1/T$ depends linearly on I_0 and from the slope of the straight line, δ_{eff} values of 1.6×10^{-46} in acetone and $7.5 \times 10^{-47} \text{ cm}^4 \text{ s/photon-molecule}$ in toluene are obtained for **1**. The δ_{eff} values for **2** are 6.3×10^{-47} in acetone and $2.1 \times 10^{-47} \text{ cm}^4 \text{ s/photon-molecule}$ in toluene. As can be seen in the figure, there is some upward curvature of the data, suggesting that there may be contributions of higher-order nonlinearities to the response, as will be discussed below.

The nonlinear transmission measurements have been extended for compounds **1-6** to cover the wavelength range from 550 to 850 nm. Figure 3 shows the effective two-photon absorption spectra obtained for compounds **1**, **2** and **4**.⁴ We have previously reported that **1** gives a peak value of $\beta = 3.2 \text{ cm/GW}$ at 0.01 M and $\delta_{\text{eff}} = 1.77 \times 10^{-46} \text{ cm}^4 \text{ s/photon-molecule}$ in acetone,⁸ which is one of the largest values reported for organic molecules.^{9,13,16}

In Figures 4a and 4b, we show the spectra of **1-5** as obtained from two-photon excited fluorescence measurements. It is evident from the comparison of Figure 3 and

Figures 4a and 4b, that the values of the absorptivity derived from the two different methods differ by more than an order of magnitude, but that the position of the peak

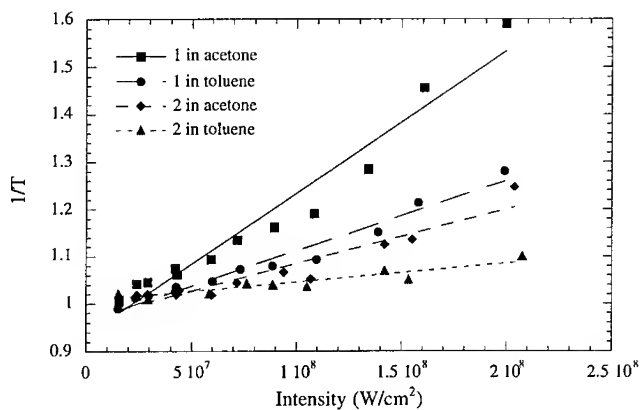


FIGURE 2 Intensity dependent transmission of **1** and **2** in acetone and toluene at 0.01 M using 5-ns pulses at a wavelength of 605 nm.

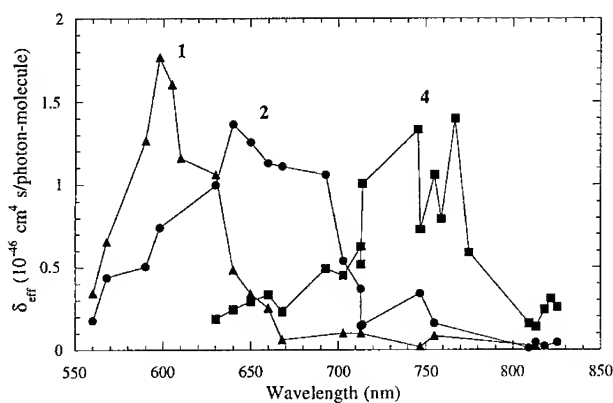


FIGURE 3 Dispersion of the effective two-photon absorptivity for **1** in acetone (\blacktriangle), **2** in toluene (\bullet) and **4** in toluene (\blacksquare), as measured by nonlinear transmission using 5-ns laser pulses. The connecting lines are provided as a guide to the eye.

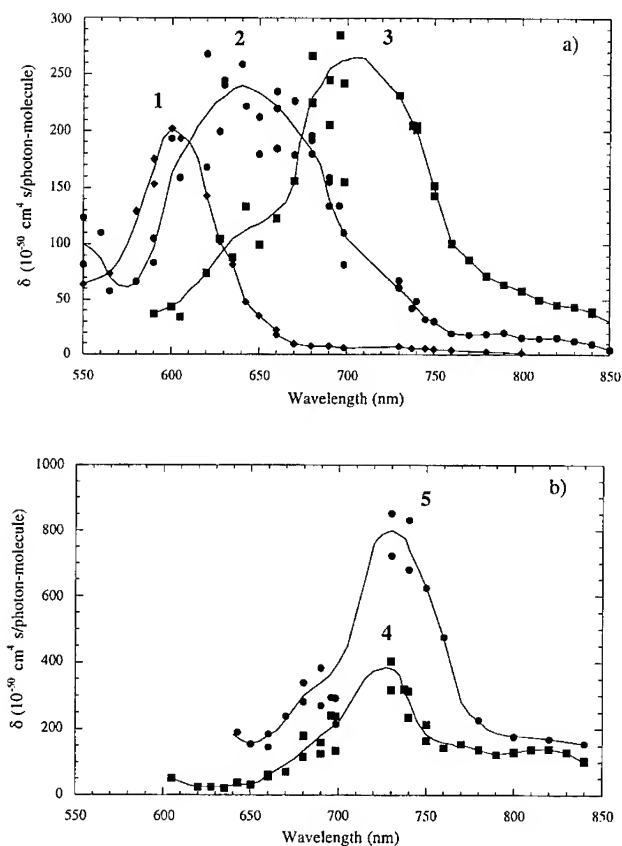


FIGURE 4 Two-photon absorption spectra of a) 1 (\diamond), 2 (\bullet), 3 (\blacksquare) and b) 4 (\blacksquare) and 5 (\bullet) as derived from two-photon excited fluorescence measurements. All molecules were dissolved in toluene at a concentration of about 10^{-4} M. The curves are provided as a guide to the eye.

and the overall shape of the spectra are very similar. As illustrated in Figure 5 for compound 1, the peak position and shape of the spectra obtained by ns NLT and ns TPF methods are in very good agreement. As will be discussed below, the effect of excited-state absorption can explain the large effective two-photon cross sections obtained in the NLT measurements.

The increase in the conjugation length in the series **1-5** results in a red shift of the peak position of the two-photon absorption band, $\lambda_{\max}^{(2)}$, from 600 nm for **1** to 730 nm for **5**, as observed for the TPF data (see Table I). From the last column of Table I an increase in the maximum δ , δ_{\max} , that is almost linear with chain length in the series **1-4**, is evident.

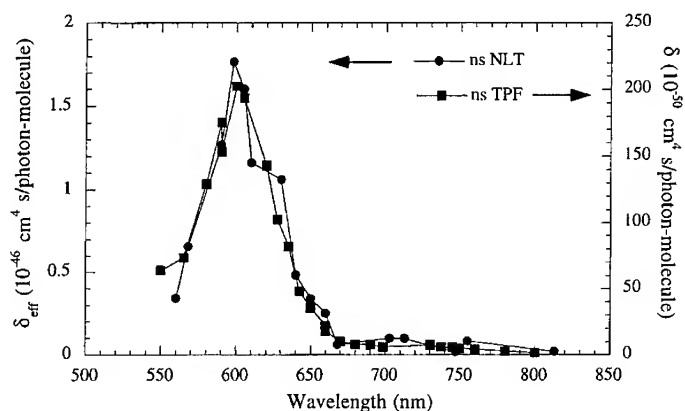


FIGURE 5 Comparison between the ns nonlinear transmission, NLT, (●) and two-photon excited fluorescence, TPF, (■) measurements for compound **1** (solvents: acetone for NLT, toluene for TPF).

TABLE I Peak two-photon absorptivity for compounds **1-6** for ns NLT and ns TPF¹⁷ measurements (solvent: toluene). δ is in units of $10^{-50} \text{ cm}^4 \text{ s/photon-molecule}$.

	NLT		TPF	
	$\lambda_{\max}^{(2)}$ (nm)	$\delta_{\text{eff}}^{\max}$	$\lambda_{\max}^{(2)}$ (nm)	δ_{\max}
1	600	9300	600	210
2	640	13600	645	260
3	745	7800	710	310
4	750	14000	720	360
5	755	17000	730	790

In all these compounds, the origin of the large two-photon absorptivity is ascribable to the ability of the terminal groups to donate electronic charge to the center of the molecule. This intramolecular charge transfer creates states with an appreciable quadrupole moment and gives rise to large transition dipole moments between the ground state and the lowest excited singlet state, as well as between the first and second excited singlet states.¹⁸ The position and magnitude of the two-photon absorption peak are related to the strength of the electron donor groups and the distance over which the charge is transferred (length of the conjugated bridge). δ_{\max} can be further increased if acceptor groups are substituted in the central part of the conjugated skeleton. We have shown¹⁸ that a charge transfer from the center to the end of the molecule (obtained with acceptor substituents on the ends and donor substituents in the center) is also effective in increasing δ_{\max} .

Pulse Width Dependence and Role of Excited-State Absorption

To study the effect of the pulse duration on the observed two-photon absorptivities, the NLT measurements have also been performed with ps pulses. In Table II we compare the values of δ_{eff} from ns NLT and ps NLT as well as δ from ns TPF for **1-6** at selected

TABLE II Two-photon absorption cross section as obtained from ns NLT, ps NLT and ns TPF experiments. (Solvent: toluene).

	λ (nm)	δ_{eff} or δ (10^{-50} cm ⁴ s/photon-molecule)		
		ns NLT	ps NLT	ns TPF
1	600	9300	310	210
2	600	6100	230	220
3	600	1500	-	40
1	700	1000	-	6 ^(a)
2	700	6000	60	110 ^(a)
3	700	7000	160	240 ^(a)
4	700	6700	200	240 ^(a)
5	700	10000	290	300 ^(a)
6	700	10000	110	-

(a) δ value measured at 698 nm.

wavelengths. It is clear that the ps NLT results are more than an order of magnitude lower than their ns NLT counterparts, whereas they are in reasonable agreement with the results of the TPF technique.

If the mechanism responsible for the nonlinear transmission is a pure two-photon process, one would expect δ to be pulse-width independent, providing that there is not a substantial depletion of the ground state population during the excitation. However, as population builds up in the lower excited states, S_2 or S_1 , as would be the case under the prolonged excitation from a ns laser pulse, absorption from these states to higher lying excited states, S_n (excited-state absorption), can take place (see Figure 6) and contribute to the overall nonlinear loss.

To describe the response of the system in the case when excited-state absorption is significant, we use the equation for the propagation of light taking into account both two-photon absorption and three-photon absorption:

$$\frac{dI}{dz} = -\beta I^2 - \gamma I^3. \quad (6)$$

γ is the three-photon absorption coefficient (the three-photon absorption cross section σ_3 is related to γ through: $\sigma_3 = (h\nu)^2 \gamma / N$, where N is the number density). In Equation (6) we have neglected the linear term and the coherence coefficients have not

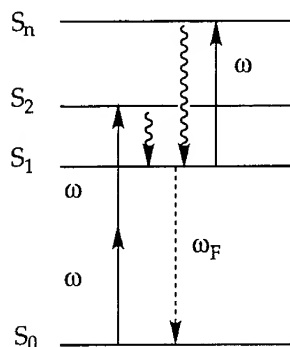


FIGURE 6 Schematic representation of the energy levels involved in two-photon absorption and two-photon induced excited-state absorption processes. S_0 is the ground state, S_1 is the first-excited state, S_2 is the second-excited state (two-photon allowed), and S_n is a generic, higher energy, excited state. ω is the frequency of the exciting photons, ω_F is the frequency of the fluorescent photons.

been explicitly indicated. It should be recognized that, in general, the three photon process can be a simultaneous absorption of three photons, but in the context that we are considering, it is viewed as a doubly resonant three-photon absorption, i.e. two-photon absorption followed by excited-state absorption. The solution of Equation (6) is:

$$\frac{1}{T} = 1 + \beta L I_0 - \frac{\gamma I_0}{\beta} \ln T + \frac{\gamma I_0}{\beta} \left[\ln \left(1 + \frac{\gamma T I_0}{\beta} \right) - \ln \left(1 + \frac{\gamma I_0}{\beta} \right) \right]. \quad (7)$$

An approximate solution of Equation (6) is:

$$\frac{1}{T} = 1 + \beta L I_0 + \frac{\gamma}{\beta} I_0 \ln(1 + \beta L I_0) \quad (8)$$

in the case of a spatially and temporally uniform beam, negligible ground-state depletion, and where the γI term is small compared to β . On the other hand, in the case in which the three-photon term in Equation (6) dominates, the solution for the transmittance is:

$$\frac{1}{T} = \sqrt{1 + 2\gamma L I_0^2}. \quad (9)$$

Equations (8) and (9) show that higher-order effects manifest themselves as upward deviations from the linear dependence of $1/T$ on I_0 predicted by Equation (4). This can explain the curvature observed in the data shown in Figure 2. In the case of **1** in acetone, fitting of the ns NLT data to Equation (8) gives $\gamma = 1.6 \times 10^{-17} \text{ cm}^3/\text{W}^2$ ($\sigma_3 = 3 \times 10^{-73} \text{ cm}^6 \text{ s}^2/\text{photon}^2\text{-molecule}$), where a fixed value of the parameter β ($4.1 \times 10^{-11} \text{ cm/W}$), as obtained from the TPF measurements, was used. On the other hand, using Equation (9) we obtained $\gamma = 2.0 \times 10^{-17} \text{ cm}^3/\text{W}^2$ ($\sigma_3 = 3.8 \times 10^{-73} \text{ cm}^6 \text{ s}^2/\text{photon}^2\text{-molecule}$). Similarly for **1** in toluene we have from Equation (8) $\gamma = 7.5 \times 10^{-18} \text{ cm}^3/\text{W}^2$ (same β for fitting as above) and from Equation (9) $\gamma = 8.7 \times 10^{-18} \text{ cm}^3/\text{W}^2$ ($\sigma_3 = 1.3$ and $1.5 \times 10^{-73} \text{ cm}^6 \text{ s}^2/\text{photon}^2\text{-molecule}$, for fitting with Equations (8) and (9), respectively). The values of γ obtained from either of the above models are within a factor of 1.5 and are in good agreement with the value of γ of about $2.5 \times 10^{-17} \text{ cm}^3/\text{W}^2$ that is obtained from a numerical solution of Equation (7). The effective three-photon cross section obtained in the above analysis is proportional to σ_e , the excited-state absorption cross section, and the relationship between these two quantities for a steady-state pumping condition is:

$$\sigma_3 = \frac{1}{2} \frac{\sigma_e \delta}{k_f} \quad (10)$$

(k_f is the rate of fluorescence emission). From Equation (10), a σ_e value of about $8 \times 10^{-17} \text{ cm}^2$ is obtained for **1** in toluene. Our analysis indicates that for molecules with such a large σ_e , and a moderately large δ , of the order of $10^{-48} \text{ cm}^4 \text{ s/photon-molecule}$, the two-photon induced excited-state absorption process can make a significant contribution to the overall nonlinear loss in a ns nonlinear transmission measurement. Similar third- and fifth-order phenomena have been observed for bis(benzothiazoyl)-didecyloxy-thiophene (BBTDOT) and didecyloxy-septiphenyl (DDOS) by Said *et al.*¹⁹ and the fifth-order part corresponds to two-photon absorption followed by excited-state absorption. In the case of BBTDOT, the excited-state absorption cross section is $6.2 \times 10^{-18} \text{ cm}^2$.¹⁹

We will show in the next section that ns NLT data for bis-donor biphenyl molecules also show this kind of behavior in the high intensity range and that these molecules are characterized by even larger effective three-photon cross sections.

In contrast, the values of δ obtained from a TPF experiment are independent of the pulse duration, as long as the population of the ground state S_0 is not substantially depleted. In fact, in this type of measurement, the overall fluorescence emission from the S_1 state is collected over a time scale that is longer than the typical lifetime of the excited states. So, even if excited-state absorption is induced by the two-photon absorption, a fast nonradiative relaxation from S_n follows, bringing the system to the lowest lying excited-state, S_1 , from which the molecule can fluoresce. A TPF experiment thus gives information on the number of molecules that have reached the S_2 state by absorbing two-photons from the incident laser beam (a number that is directly proportional to the two-photon absorption cross section), while NLT measures the total number of photons that are absorbed by the system and is not selective for a particular process. We have verified the independence on pulse duration of TPF measurements for a series of bis(styryl)benzene compounds using both ns and fs pulses.¹⁸ Nonetheless, for the series of molecules examined, the shape of the NLT spectrum is essentially the same as the TPF spectrum (Figure 5). This observation suggests that the contribution from excited-state absorption is not strongly dependent on wavelength over the range of the two-photon absorption.

Design of Broadband Optical Limiting Materials

For optical limiting applications, very large nonlinearities over a wide bandwidth are typically needed. In the case of eye protection, response over the range of 400–700 nm is required. We previously reported⁸ an approach to obtain relatively broadband nonlinear absorption, simultaneously with high transparency, based on bis-donor stilbenes. Replacement of the dialkylamino groups in **1** with diphenylamino groups, leading to **6**, resulted in a 90 nm red-shift in the effective two-photon absorption peak, but little loss of transparency at wavelengths > 450 nm.⁸ Thus a mixture of **1** and **6** gave rise to a nonlinear absorption bandwidth of ~170 nm and high linear transmission. However, superposition of the nonlinear response of **1** and **6** leaves the spectral region ranging from 500 to 550 nm, where the linear transmission is very high, with negligible nonlinear absorption. In order to fill this gap, we considered the design of molecules with smaller conjugation length and bis(diaryl-amino) substitution. As shown above, the peak two-photon absorptivity can be tuned to longer wavelength by increasing the conjugation length. For example, for compound **5**, the effective two-photon absorption peak is at 730 nm, as compared to 600 nm for **1**. As we will show below, on going to a biphenyl bridge the two-photon absorption peak blue-shifts to ~525 nm. The molecular structures for bis(diaryl-amino)biphenyls with methoxy and cyano groups, **7** and **8**, respectively, are shown in Figure 1.

We examined the magnitude and dispersion of the two-photon absorptivity for **7** and **8** using ns NLT and ns TPF measurements. We found that having methoxy *versus* cyano substitution on the phenyltolylamine has only a small effect on the magnitude of the two-photon absorptivity: δ for compounds **7** and **8**, as determined by ns TPF measurements, were 260×10^{-50} and 250×10^{-50} cm⁴ s/photon-molecule, respectively. However, this variation in end groups has a significant effect on the nonlinear transmission response. Figure 7 shows plots of $1/T$ as a function of incident intensity for **7** and **8**, as measured using 532-nm, 9-ns laser pulses. Whereas we observed a moderate curvature of the $1/T$ *versus* I_0 plots for **1**, as discussed above, **7** and **8** show a pronounced curvature. This observation indicates that there is a strong two-photon induced excited-state absorption contribution to the NLT response.

The ns NLT data for **7** and **8** were analyzed using the pure three-photon absorption model (Equation (9)) and the model based on combined two- and three-photon absorption (Equation (8)). The values obtained for σ_3 for **7** and **8** were 2.8×10^{-73} and 0.7×10^{-73} cm⁶ s²/photon²-molecule, respectively. The fitted curves shown in Figure 7 are those for the two- and three-photon absorption model, obtained by fixing β at the value derived from ns TPF measurements and varying the value of γ to

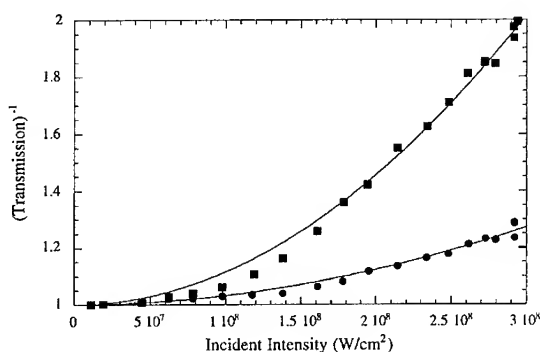


FIGURE 7 Intensity dependent transmission of **7** (■) and **8** (●) in toluene (concentration = 10^{-2} M), using 9-ns, 532-nm laser pulses. Solid lines are the fit to data using Equation (8) with β obtained from ns TPF measurement.

get the best fit. We note that a better fit is obtained with the two- and three-photon absorption model than with the three-photon absorption model alone, although the validity of Equation (8) at the higher intensities is questionable; this issue is currently under investigation. Nonetheless, we obtain values for the effective γ from fitting to the two models which are in reasonably good agreement with each other. Furthermore, a numerical solution of Equation (7) gives $\sigma_3 = 3.1 \times 10^{-73} \text{ cm}^6 \text{ s}^2/\text{photon}^2\text{-molecule}$ for compound **7**. These results show that for **7**, which possesses electron donating methoxy groups, there is a larger effective γ than for **8**, which has electron accepting cyano groups. Since the two-photon absorption cross sections and peak positions of **7** and **8** are nearly identical, the larger effective γ for **7** is likely due to a larger excited-state absorption cross section ($\sigma_e \approx 1.3 \times 10^{-16} \text{ cm}^2$ for **7**). This increase in excited-state absorption cross section may result from a shift of peak position or a change in overall magnitude of the cross section itself; transient absorption spectroscopy experiments are needed to determine which is the case.

In order to assess the utility of the bis(diarylamino)biphenyl compounds for use in a broadband optical limiter, we compared the nanosecond-pulse optical limiting response of **7** at 532 nm to that obtained previously for **1** at 600 nm.⁸ The experiments were performed in an $f/5$ optical system and the transmitted laser beam was collected with a matching $f/5$ lens. Figure 8 shows the optical limiting responses of **1** and **7**. For

a concentration of 0.14 M, the strong signal suppression ($1/T$) at an incident energy of 160 μJ was ~ 9 and ~ 6 for **1** and **7**, respectively; the linear transmission for the solutions of both compounds was 0.95. These values are of comparable magnitude and indicate potential utility of the bis(diarylamino)biphenyl compound for broadband limiter devices. At high incident energies we observed the formation of a nonlinear refractive ring pattern on the transmitted wavefront, likely due to thermal and possibly excited-state refractive index changes. Although there was certainly a contribution to the observed limiting response from this effect, most of the transmitted energy was collected by the output lens and detected.

We measured the dispersion of the two-photon absorption for **7**, which is shown in Figure 9, along with the data for **1** and **6**, reported previously.⁸ The two-photon absorption spectrum for **7** was measured using ns TPF and the δ values were then scaled to match the δ_{eff} values derived from ns NLT at 532 nm. The center wavelength of the two-photon absorption band for **7** occurs at 525 nm. The band position is in the range to partially fill the gap in the spectral range of the nonlinear absorption dispersion for **1** and **6**. Accordingly, a limiting material based on an additive combination of the response of all three molecules would provide nonlinear absorptivity over an extremely broad spectral range (~ 250 nm), and maintain high linear transmission, $>90\%$, over the same range.

As a simple demonstration of the broadband limiting response, we examined the optical limiting of solutions of **1**, **6** and **7** in a triple-stacked tandem cell geometry, at

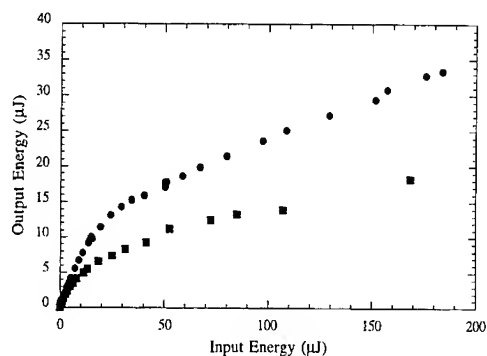


FIGURE 8 The $f/5$ optical limiting response of **1** (■) for 600 nm, 5-ns laser pulses and **7** (●) for 532 nm, 9 ns laser pulses. Samples were dissolved in toluene at a concentration of 0.14 M.

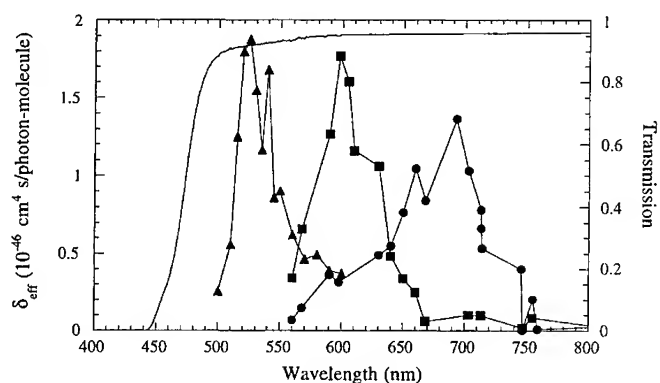


FIGURE 9 Spectrum of effective two-photon absorptivity for **1** (■), **6** (●) and **7** (▲), in toluene at 0.01 M concentration. The solid curve without points is the linear transmission spectrum for a triple-stacked arrangement of cells containing toluene solutions of **1**, **6** and **7** at 0.1 M.

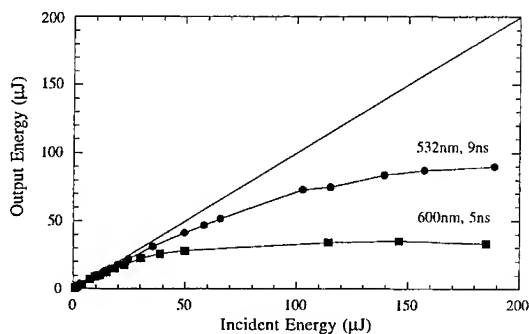


FIGURE 10 Optical limiting response of triple-stack tandem cell: 600-nm, 5-ns pulses (■) and 532-nm, 9-ns pulses (●). The straight line is the linear transmission of the triple-stack tandem limiter.

600 nm and 532 nm in a collimated beam ($f/23$) optical system. The triple-stack tandem cell contained three compartments, each with a 1-mm optical pathlength. Figure 10 shows the optical limiting response of the triple-stack tandem sample, wherein the concentration for each solution, in toluene solvent, was 0.1 M. The results shows that the triple-stack tandem sample performs well at the two wavelengths used in the test.

CONCLUSIONS

Our studies provide strong evidence that two-photon induced excited-state absorption can make a significant contribution to the effective nonlinearity in ns nonlinear transmission measurements. We have shown that bis-donor substituted diphenylpolyenes exhibit large effective two- and three-photon cross sections, which can be tuned by varying the length of the polyene bridge and modifying the substituents on the terminal amino groups. We have also shown that this control over the strength and position of the effective nonlinear absorption cross sections allows the design of materials for broadband optical limiting and high linear transparency. A demonstration of this strategy, that makes use of a simple triple cell tandem geometry, has been described.

ACKNOWLEDGMENTS

This work was performed in part at the Jet Propulsion Laboratory, California Institute of Technology and was supported by the Air Force Office of Scientific Research. Support at Caltech from the National Science Foundation, the Office of Naval Research and the Air Force Office of Scientific Research, is gratefully acknowledged.

REFERENCES

1. J. W. Perry, K. Mansour, I.-Y. S. Lee, X.-L. Wu, P. V. Bedworth, C.-T. Cheng, D. Ng, S. R. Marder, P. Miles, T. Wada, M. Tian, and H. Sasabe, *Science*, **273**, 1533 (1996).
2. J. D. Bhawalkar, G. S. He, and P. N. Prasad, *Rep. Prog. Phys.*, **59**, 1041 (1996).
3. L. W. Tutt and T. F. Boggess, *Prog. Quant. Electr.*, **17**, 299 (1993).
4. J. E. Ehrlich, X.-L. Wu, I.-Y. S. Lee, Z.-Y. Hu, H. Röckel, S. R. Marder and J. W. Perry, in *Mat. Res. Soc. Symp. Proc., Materials for Optical Limiting II*, edited by R. Sutherland, R. Pachter, P. Hood, D. Hagan, K. Lewis and J. W. Perry, (MRS, Pittsburgh, 1997) Vol. 479, p. 9.
5. W. Denk, J. H. Strickler and W. W. Webb, *Science*, **248**, 73 (1990).
6. J. H. Strickler and W. W. Webb, *SPIE Proceedings*, **1398**, 107 (1990).
7. S. Maruo, O. Nakamura, and S. Katawa, *Optics Letters*, **22**, 132 (1997).
8. J. E. Ehrlich, X.-L. Wu, I.-Y. S. Lee, Z.-Y. Hu, H. Röckel, S. R. Marder, and J. W. Perry, *Optics Letters*, **22**, 1843 (1997).
9. G. S. He, G. C. Xu, P. N. Prasad, B. A. Reinhardt, J. C. Bhatt, and A. G. Dillard, *Opt. Lett.*, **20**, 435 (1995).
10. B. E. Maryanoff and A. B. Reitz, *Chem. Rev.*, **89**, 863 (1989).
11. J. E. McMurray, *Acc. Chem. Res.*, **16**, 405 (1983).
12. S. Thayumanavan, S. Barlow, and S. R. Marder, *Chem. Mater.*, **9**, 3231 (1997).
13. C. Xu and W. W. Webb, *J. Opt. Soc. Am. B*, **13**, 481 (1996).
14. S. M. Kennedy and F. E. Lytle, *Analit. Chem.*, **58**, 2643 (1986).
15. R. Loudon, *The Quantum Theory of Light* (Oxford Univ. Press, London, 1973).

16. G. S. He, J. D. Bhawalkar, C. F. Zhao, and P. N. Prasad, Appl. Phys. Lett., **67**, 2433 (1995).
17. B. H. Cumpston, A. A. Heikal, J. E. Ehrlich, L. Erskine, I.-Y. S. Lee, M. Rumi, X.-L. Wu, J. W. Perry, H. Röckel, D. McCord-Maughon, G. Subramanian, S. R. Marder, M. Albota, C. Xu, and W. W. Webb, submitted.
18. M. Albota, D. Beljonne, J.-L. Brédas, J. E. Ehrlich, J.-Y. Fu, A. A. Heikal, S. Hess, T. Kogej, M. D. Levin, S. R. Marder, D. McCord-Maughon, J. W. Perry, H. Röckel, M. Rumi, G. Subramanian, W. W. Webb, and C. Xu, Science, accepted for publication.
19. A. A. Said, C. Wamsley, D. J. Hagan, E. W. Van Stryland, B. A. Reinhardt, P. Roderer, and A. G. Dillard, Chem. Phys. Letters, **228**, 646 (1994).

MEASUREMENT OF TWO-PHOTON ABSORPTION COEFFICIENTS EMPLOYING FEMTOSECOND, PHASE-MISMATCHED DFWM AND nDFWM SPECTROSCOPY

LARRY R. DALTON, RULON J. LARSEN, AND FRITZ STROHKENDL
Loker Hydrocarbon Research Institute, University of Southern California, Los
Angeles, California, USA and Department of Chemistry, University of
Washington, Seattle, Washington, USA

Abstract The real and imaginary components of the third order nonlinear optical susceptibility for the fullerenes (C60, C70) and for N,N-diphenyl-7-[2-(4-pyridinyl) ethenyl]-9,9-di-n-decyl-fluoren-2-amine (AF50) were measured over the wavelength range from 0.5 to 2.0 microns by a variety of techniques (including newly developed techniques of nDFWM and THG/DFWM) based on four wave mixing employing 100 femtosecond pulses. Results are compared with related data obtained by third harmonic generation, electro-absorption, and direct two-photon absorption measurements. The magnitudes of two photon absorption for these materials are found to be comparable to that of GaAs (0.020 cm/MW).

INTRODUCTION

The use of Degenerate Four Wave Mixing (DFWM) for exploration of electronic structure has been restricted in the past to a few select wavelengths. This is due to the strict requirements on spatial and temporal beam qualities as well as the perceived complexity of a multibeam experiment with fickle laser systems. Also the distinction between electronic and nonelectronic contributions to the nonlinear signal is often a serious problem.¹ Signals from DFWM with long, nanosecond pulses are essentially unrelated to the electronic $\chi^{(3)}$. In contrast, third harmonic generation (THG) has traditionally been the technique of choice for the exploration of the purely electronic $\chi^{(3)}$ and the underlying electronic structure which gives rise to it. The THG signal is naturally related to the purely electronic nonlinearity due to the large frequency shift between input and signal beams and the interpretation of THG data is, therefore, essentially independent of pulse duration.

We have been able to convert recent advancements in laser technology into a reliable tool for fully tunable, frequency (or wavelength) agile DFWM spectroscopy.

We overcame the described problems of DFWM through the use of short, femtosecond pulses and demonstrated in C60¹ and C70² between 0.74 and 1.7 μm (below the optical band-gap) the clear advantages which femtosecond DFWM has over third harmonic generation (THG) for the detection of two-photon states. Briefly, while DFWM exhibits only one and two-photon resonances, THG exhibits in addition predictable (from the one-photon spectrum) three-photon resonances which interfere unpredictably with the two-photon spectrum. Denoting the optical band-gap by E_g , one finds that THG is able to detect two-photon states free of interference from one- and three-photon resonances only for excited state energies up to $2/3 E_g$ whereas DFWM can do so up to $2 E_g$. Therefore, the "free spectral range" for two photon spectroscopy is for DFWM three times that of THG.² Similarly, electro-absorption which measures the imaginary part of $\chi^{(3)}$ can detect two-photon states interference free only up to E_g .² The ability of DFWM to measure unambiguously two-photon spectra for excited state energies above E_g and up to $2E_g$ makes it the technique of choice for the exploration of noncentrosymmetric molecules. The ambiguity associated with the interpretation of THG data was amply demonstrated in the case of C60. Fig.1 shows a comparison of DFWM,¹ THG^{3,4} and direct two-photon absorption measurements.⁵ While our DFWM results clearly indicate a two-photon state, this resonance is apparently absent from the THG data which are

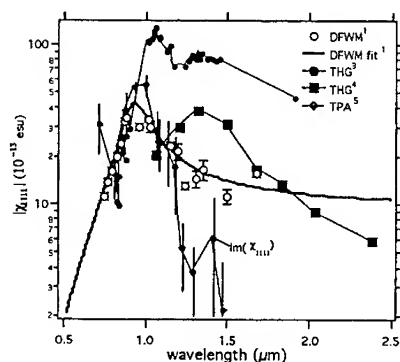


Fig. 1. Comparison of DFWM, third harmonic generation (THG), and direct two-photon absorption (TPA) measurements in C60 films.

dominated by predictable three-photon resonances. We have modeled these data and have shown that interference of a higher lying three-photon resonance is the likely cause for the non-observation of the two-photon resonance which can be seen so clearly in DFWM. The more recent results from direct two-photon absorption⁵ clearly confirm our findings.

In addition to our instrumental efforts, we have developed a DFWM technique which allows in a straight forward manner the measurement of not only the amplitude but also the phase of all elements of the third order nonlinear optical susceptibility tensors for solid and liquid thin-film samples.⁶ Briefly, our technique is based on the measurement of phase-matched and non phase-matched signals, see Fig. 2. Three input beams denoted by 1, 2, and 3 generate nine DFWM signal beams. Only one of the

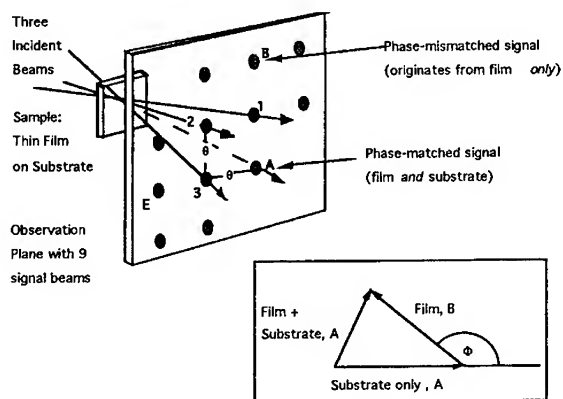


Fig. 2. Geometry for phase-mismatched degenerate four-wave mixing. Three input beams generate nine signal beams. The phase-matched signal at point A arises from a superposition of the thin-film and the substrate signals. The remaining eight signals are all phase-mismatched and arise essentially from the thin film only. The inset shows the phasor diagram for the addition of the signal-field amplitudes in the phase-matched direction when all beam polarizations are parallel. The phase, Φ , of the thin film χ_{1111} can be derived from three amplitude measurements, as indicated.

signal beams, denoted by A, is phase-matched. This phase-matched signal involves thin-film and thick-substrate contributions while the phase-mismatched signals arise essentially only from the thin film. The phase-matched signal is of the form $|E_s + E_f e^{i\phi}|^2$ while the phase-mismatched signals are of the form $|E_f|^2$; here E_s is the electric field amplitude of the substrate signal, E_f that of the thin film signal, and ϕ is the relative phase between substrate and film $\chi^{(3)}$. Through comparison of thin film and substrate measurements the phase can be determined. Since the substrate phase is typically zero (e.g. for fused silica or CaF_2 at visible or near IR wavelengths) one finds that in the phase-matched signal the superposition of substrate and thin film signals emphasizes the real part of the thin-film $\chi^{(3)}$. Therefore, an accurate determination of the real part of $\chi^{(3)}$ can be performed even in the presence of a strongly resonant signal. This is in contrast to the z-scan technique, which is the commonly used technique for phase measurements on solid state samples.⁷ Also, the z-scan technique would be unable to separate thin-film and substrate contributions and is inherently less sensitive than DFWM.⁷

The two-photon absorption cross-section is proportional to the imaginary part of the DFWM $\chi^{(3)}$ for frequencies below the optical gap, i.e. knowledge of the phase and amplitude is required for its accurate determination. Above the optical gap knowledge of the phase is required for the deconvolution of superimposed one- and two-photon spectral features. Based on the phase measurements one can positively identify the zero-frequency limit of the electronic $\chi^{(3)}$ which is an important parameter for all optical switching as well as for comparison to theoretical computations. The interpretation of experimental data concerning this zero-frequency limit without knowledge of the phase is often quite speculative as has been amply demonstrated in the case of C60.⁸

A severe short-coming of DFWM is its inability to measure the "instantaneous" electronic $\chi^{(3)}$ under one-photon resonant conditions.⁹ Here the change in the linear susceptibility of the exposed material, due to accumulation of excited state population during the pulse duration, gives rise to signals which usually overwhelm the instantaneous signal contributions. Even if short, femtosecond pulses are used one observes signal contributions from excited state population which is evident from the

tails of time delayed signals.¹⁰ Even nonintrinsic absorption tails which extend into the intrinsic optical bandgap pose problems.^{9,10} Here we propose a novel and frequency agile implementation of nDFWM to overcome these problems. In nDFWM, the participating input beams are offset by a small frequency shift $\Delta\omega$ relative to each other. Nearly degenerate four wave mixing (nDFWM) combines the advantages of THG and DFWM. This leads to frequency shifted signal beams, similar to THG, but maintains the "free spectral range" for two photon spectroscopy up to $2 E_g$. The fact that the gratings involved in nDFWM are moving limits the effective accumulation time for excited state gratings to about $(\Delta\omega)^{-1}$. The shortest effective accumulation times in our implementation of nDFWM are, depending on wavelength, about 5 to 15 femtoseconds. Maximum obtainable frequency shifts result in $\hbar\Delta\omega$ values of about 0.05 to 0.13 eV. While the THG signal suffers from severe signal reduction due to the large refractive index difference between fundamental and third harmonic, we find in nDFWM only very mild effects of phase-mismatch. Under the nDFWM conditions proposed here the phase-mismatch induced signal reduction in thin film samples is negligible. Even in a 1 mm thick fused silica sample we find that phase-mismatch effects are very small. For example, if we employ a frequency offset corresponding to four times the bandwidth of 100 fs transform limited sech^2 pulses near $0.5 \mu\text{m}$ in the beam configuration of Fig. 7 c) we find a signal loss due to phase-mismatch of about 1% and a corresponding phase-change of about 13° .

IMPLEMENTATION OF nDFWM

We have constructed a reliable and ultrastable femtosecond pulse source with performance concerning pulse-to-pulse and beam-pointing stability presently not commercially available.¹¹ This source is continuously tunable from below $0.5 \mu\text{m}$ to beyond $2 \mu\text{m}$ and meets the beam quality requirements necessary for DFWM. The system is based on a highly stable regenerative Ti:sapphire amplifier (1 mJ, $\pm 0.4\%$ rms pulse to pulse stability at 20 Hz) and a Type I optical parametric amplifier (OPA) which is pumped by the frequency doubled output of the Ti:sapphire amplifier. The OPA delivers over most of its tuning range signal-plus-idler energies near $60 \mu\text{J}$ at $\pm 1\%$ rms stability which is better than any commercial system can deliver at this time. Type I

optical parametric devices suffer from large bandwidth increases in the generated beams near the degeneracy point which is in our case $0.79\ \mu\text{m}$. Through original design modifications we have been able to obtain near transform limited pulses (time bandwidth products of ≤ 0.5) at pulse durations between 100 to 120 fs throughout our tuning range except for an interval of $\pm 30\ \text{nm}$ which occurs at the degeneracy point. (This interval is covered by the tuning range of our Ti:sapphire amplifier.) The optical parametric device is computer controlled which allows access of the full tuning range without manual adjustments. We have demonstrated the frequency agility of our system as well as our phase sensitive DFWM technique in the wavelength range 0.74 to $1.7\ \mu\text{m}$ on thin solid (C60 and C70)^{1,2} and liquid (AF-50)¹² films, see Fig. 3, 4, 5.

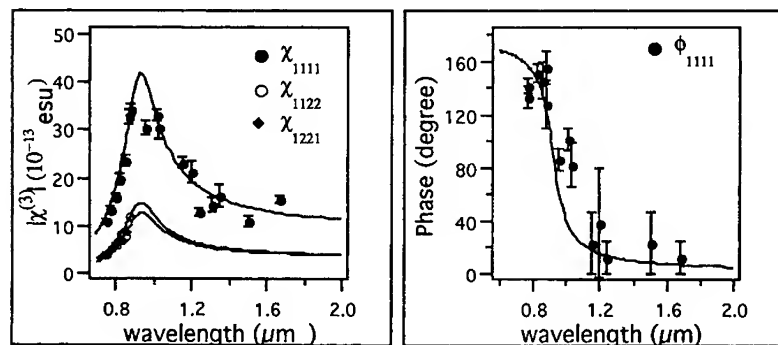


Fig. 3. Amplitude and phase of $\chi^{(3)}$ tensor elements of C60 film from DFWM.

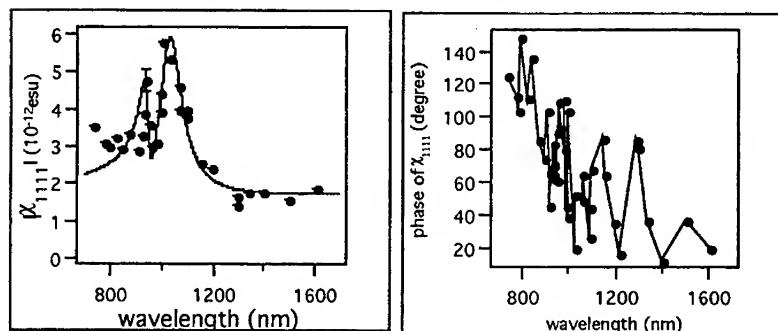


Fig. 4. Amplitude and phase of χ_{1111} of C70 film from DFWM.

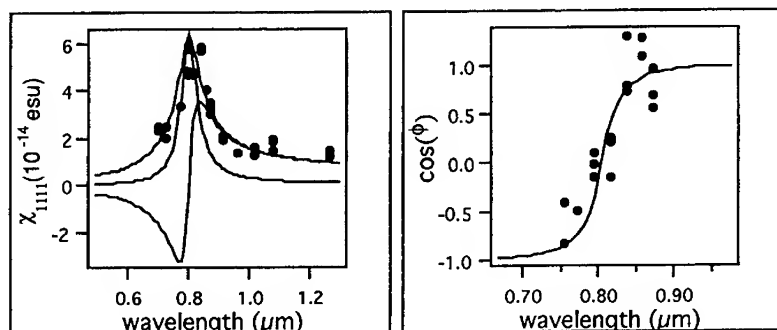


Fig. 5: Amplitude and $\cos(\phi)$ of χ_{1111} for the AF50 chromophore in 100 μm thick sample benzene solution. Additional measurements indicate a second peak at shorter wavelength with the two-photon spectrum mirroring the one-photon.

Our optical parametric amplifier is a two stage device based on thin, submillimeter thick BBO crystals. A schematic is given in Fig. 6. It is pumped by a 395 nm femtosecond pulse and seeded by a white light continuum which is generated

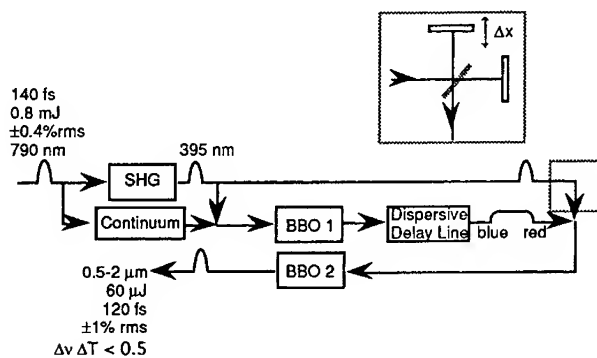


Fig. 6, Schematic of existing two-stage optical parametric amplifier (OPA) with typical operating parameters. The inset shows its modification in order to create a double pump pulse for the second OPA stage which results in a double pulse at the OPA output. The two output pulses are offset in wavelength. This offset is adjusted through the variable delay Δx .

through focussing in fused silica. The maximum bandwidth which can be amplified through a parametric process in a given crystal is, among other parameters, determined by the effective interaction length. The shorter the interaction length is, the broader is the generated spectrum. The crystal thickness in our OPA was chosen such that it matches approximately the group-velocity walk-off length, i.e. the length after which one of the participating pulses (signal, idler or pump) has separated from any of the other pulses by more than a pulse width in time. Tuning of the OPA requires adjustment of the tilts of the BBO crystals as well as adjustments of the two pump beam delays relative to the "color" in the continuum beam which one wants to amplify. The bandwidth emerging from the first stage is large. Depending on the center wavelength in our tuning range it can support from less than 10 to about 25 fs pulses. After the first stage we send the amplified pulse through a dispersive delay line. Due to this we find in the second OPA stage that we can, within the bandwidth emerging from the first stage, determine the color of the pulse after the second stage simply by adjusting the second pump-beam delay. Here the wavelength which is amplified is determined by the temporal overlap of the short pump pulse with the "chirped" long pulse arriving from the first stage. The amplification in the second stage is about a factor one hundred such that good discrimination is achieved against the unamplified parts of the bandwidth arriving from the first stage. Under our present operating conditions tuning the signal wavelength from 0.5 to 0.79 μm requires a delay of the pump of the second stage by about 3 ps. The pulses emerging from our OPA are moderately chirped due to the described generation process. We find from autocorrelation measurements time bandwidth products of ≤ 0.5 , i.e. our pulses are still close to transform limited. These pulses are well suited for DFWM experiments.

Based on the operational characteristics of our OPA, we are implementing the use of two time-delayed but collinear pump pulses for the second amplification stage. Such a double pulse can be achieved through a "Michelson interferometer" like arrangement as is indicated in the inset of Fig. 6. This results in two time and frequency separated pulses of about 100 fs duration each. The maximum achievable frequency shift between these pulses varies, depending on center frequency, between 4 to more than 10 pulse bandwidths. We have, for example, tuned our OPA from 0.90 to 1.05 μm simply through the delay of the second stage pump beam with only little degradation in

output energy. We are able to compensate for the the loss in pump energy of the second OPA stage through appropriate pump collimation optics. The generated double pulse, whose pulses are at frequencies ω and $\omega+\Delta\omega$, is injected into our existing four-wave mixing setup. One of the two pulses can be switched off through use of a shutter in the "Michelson interferometer," if necessary. Depending on the relative delay of the three incident write pulses, we can measure $\chi^{(3)}[-(\omega-\Delta\omega),\omega,\omega,-(\omega+\Delta\omega)]$ and $\chi^{(3)}[-\omega,\omega,\omega,-\omega]$. As usual, the sum of the frequency arguments of $\chi^{(3)}$ is zero; the first of the frequency arguments gives the frequency of the generated signal. Measurements where one would measure the degenerate and nondegenerate signal in a single computer controlled run are easily implemented. Comparison of these measurements is facilitated through an already implemented reference branch where a four-wave mixing experiment is performed on a fused silica plate simultaneously with the actual sample measurement. Different cases for write beam and resulting signal beam frequencies based on the beam geometry from Fig. 2 are shown in Fig. 7. Photon echoes could, in principle, contribute

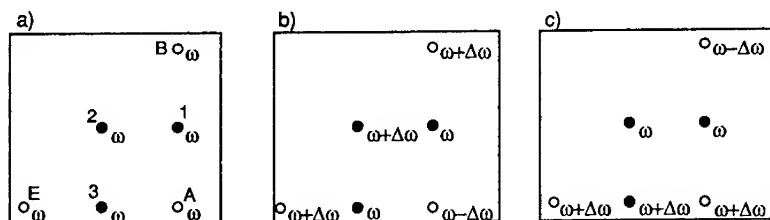


Fig. 7. Observation plane of Fig. 2 is shown for different frequency configurations of the input beams. The solid dots signify the input beams 1, 2, and 3, the hollow dots signal beams A, B, E. The beams are also labeled with their frequencies. Configuration a) corresponds to DFWM and configurations b) and c) to nDFWM.

to the observed signals due to the double pulse arrangement proposed by us. Even so this appears to be extremely unlikely, such signals could be observed in simple single-pulse DFWM experiments (i.e., one pump-pulse of the second OPA stage is blocked) or through frequency resolved signal detection (imaging spectrometer with CCD camera) which has already been implemented in our laboratory.

C60 AS A TEST SYSTEM FOR nDFWM

Our present interest in C60 is twofold: (1) exploration of the two-photon spectrum of C60 and in particular the lowest lying two-photon state of symmetry A_g , which has been theoretically predicted,¹³ and promises a high resonant nonlinearity; (2) C60 is an ideal test model for nDFWM.

Two intersecting optical beams with orthogonal polarizations and uniform intensity profile create a polarization grating, i.e. a grating where the polarization of the optical field varies as a function of position while the intensity remains constant. The optical absorption cross-section of molecules depends generally on their relative orientation to the polarization of the exciting optical field. The interaction of a polarization grating with an ensemble of molecules will therefore result in the accumulation of an excited-state population grating which leads to signal beams which are not related to the instantaneous $\chi^{(3)}$. The absorption cross-section of the C60 molecule, however, has due to its high symmetry no dependence on the polarization of the optical field. The use of DFWM in conjunction with polarization gratings in C60 samples allows, therefore, the measurement of the instantaneous electronic $\chi^{(3)}$. For example, if beam 3 in Fig. 2 is cross-polarized to beams 1 and 2 then the signal B arises from polarization gratings only. Moderate detuning of the frequency of any of the beams, e.g. by two pulse band-widths (≈ 0.08 eV), should cause only little variation in the strength of the signal. (E. g., the Lorentzian half-width of the lowest lying two-photon resonance was 0.2 eV, i.e. larger than such a shift.) The complications due to the excitation of Raman modes may arise even so we do not expect it to play a significant role due to the shortness of our pulses. Observations to the contrary could, however, be interesting by themselves.

Let us consider the two photon spectrum of C60. The general $\chi^{(3)}$ tensor is of the form¹⁴ where ω_1, ω_2 , and ω_3 are the input frequencies whose sum equals the signal

$$\begin{aligned} \ddot{\chi}^{(3)}(-\omega_4, \omega_3, \omega_2, \omega_1) = \\ \frac{F}{\hbar^3} \sum_{a,b,c} N \left(\frac{\langle g|\epsilon\tilde{r}|c\rangle\langle c|\epsilon\tilde{r}|b\rangle\langle b|\epsilon\tilde{r}|a\rangle\langle a|\epsilon\tilde{r}|g\rangle}{[(\omega_{cg}-\omega_3-\omega_2-\omega_1)-i\gamma_{cg}][(\omega_{bg}-\omega_3-\omega_2)-i\gamma_{bg}][(\omega_{ag}-\omega_3)-i\gamma_{ag}]} + \dots \right) \quad (1) \end{aligned}$$

frequency ω_4 ; $|g\rangle$ is the ground state ket, $\langle a|e\vec{r}|b\rangle$ a transition dipole moment, ω_{ag} a molecular transition frequency, γ_{ag} a transition line-width, and N the number density of molecules. The factor F summarizes local field factors¹⁴ which are not important for the present discussion. The $\chi^{(3)}$ tensor is an average over all dipole-allowed transition pathways which begin and end in the ground state $|g\rangle$. These transition pathways are represented by the quadruple transition-dipole-moment products in eq. (1). The sequence of transitions is ground state to one-photon state to two-photon state to one-photon-state to ground state. The last excited state in such excitation pathways must be one-photon in nature as a single transition-dipole moment connects it to the ground state. Even though these allowed transition pathways do not depend on the input frequencies their relative weight in the summation of eq. (1) does due to the resonance-frequency terms in the denominator. The expansion of $\chi^{(3)}$ in eq. (1) is symmetrized such that it is invariant under permutations of the three input frequencies. Whenever the sum of some combination of the input frequencies equals an allowed molecular transition frequency a resonance occurs which emphasizes a particular transition pathway and leads to a strong frequency dependent variation in $\chi^{(3)}$. In DFWM all signal beams shown in Fig. 2 are generated by $\chi^{(3)}[-\omega, \omega, \omega, -\omega]$. The terms in the denominator give rise to one- and two-photon resonances as can be recognized in the sample term in eq. (1). One- and two-photon states are revealed through resonances when $\hbar\omega$ and $2\hbar\omega$ equal their respective excitation energies. Using nDFWM in the beam configuration (c) of Fig. 7 we can observe a signal at the phase-mismatched point B, which is generated by

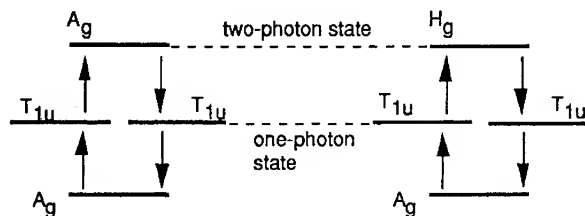


Fig. 8. The two types of excitation pathways which contribute to $\chi^{(3)}$ in C60. States are labeled with their symmetries. The chosen sequence of photon "absorption" and "emission" is specific to DFWM.

$\chi^{(3)}[-(\omega-\Delta\omega), \omega, \omega, -(\omega+\Delta\omega)]$. Inspection of the full expression indicated by eq. (1) shows, two-photon resonances occur again at the same resonance frequency as in DFWM.

The symmetries of the excited states of C60 are classified in terms of the irreducible representations of its molecular point group, I_h . A large number of these states cannot be excited through electric-dipole allowed one- or two-photon excitation. The ground state is a singlet of A_g symmetry. Excitations from the ground state through one-photon transitions are allowed only into singlet states of T_{1u} symmetry. From this intermediate T_{1u} state only transitions into states of A_g and H_g symmetry are allowed, i. e. two-photon states are of symmetry A_g or H_g . There are, therefore, two possible transition pathways which contribute to $\chi^{(3)}$, see Fig. 8. The quadruple transition-dipole-moment products in eq. (1) are of the form

$$\langle A_g | e\vec{r} | T_{1u} \rangle \langle T_{1u} | e\vec{r} | H_g \rangle \langle H_g | e\vec{r} | T_{1u} \rangle \langle T_{1u} | e\vec{r} | A_g \rangle \quad (2)$$

or

$$\langle A_g | e\vec{r} | T_{1u} \rangle \langle T_{1u} | e\vec{r} | A_g \rangle \langle A_g | e\vec{r} | T_{1u} \rangle \langle T_{1u} | e\vec{r} | A_g \rangle, \quad (3)$$

where the states are labeled with their symmetries.

The early calculations by Laszlo and Udvardi predict the excitation energy of the lowest excited A_g state at 7.1 eV, somewhat below their value for $2E_g=8.0\text{eV}$.¹³ Here again E_g refers to the optical gap. They also predict five H_g states below $2E_g$ of which we have already located the lowest one at 2.7 eV in a C60 film.¹ Overall their predictions tend to overestimate the actual excited state energies by about 10 to 20 percent.^{1,13,15} Of all the state symmetries only A_g reflects the full symmetry of the C60 ground state. We expect that an excitation of this kind is a collective excitation of a large number of electrons which gives rise to a correspondingly large optical nonlinearity. Exploration of the full energy interval up to the lowest A_g level may require frequency doubling of our OPA output which should be easily possible given the large amount of energy available.

The research discussed here is clearly still work in progress although all preliminary indications indicate that the proposed objectives will be attainable.

Measurements on the H_g two photon state of the fullerenes by DFWM and nDFWM have likely lead to quite reliable values of $\chi^{(3)}$ for these materials and permits a quantitative comparison of these materials with GaAs.

CORRELATION OF DFWM AND THG DATA

From our DFWM and nDFWM data, together with linear susceptibility, we can calculate THG spectra. We illustrated this process below for C70. In Fig. 9, we show data obtained from DFWM and nDFWM experiments utilizing signal lattice concepts discussed earlier. Real and imaginary components, as well as the amplitude, of various susceptibility components are shown and compared with the data of other workers.

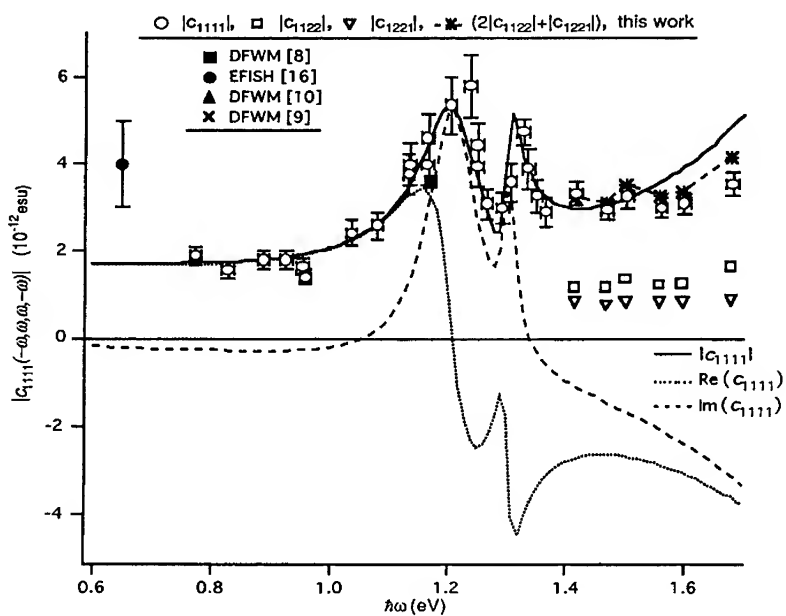


Fig. 9. The amplitude, real, and imaginary components of the third order susceptibility measured in this work are shown (indicated by lines). Results are compared with data of other workers.

We have also developed a scheme for the direct measurement of THG employing a forward DFWM mixing configuration illustrated in Fig. 10. Although the low number of exciting photons available with femtosecond pulses create certain signal-to-noise issues, these are readily addressed by single photon counting. The signal lattice approach also has the advantage of separating contributions from sources other than the thin film sample.

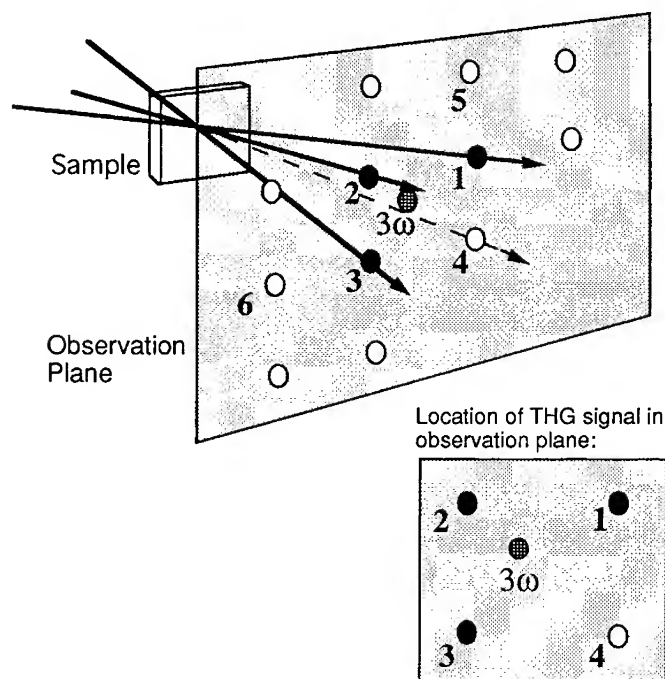


Fig. 10. $\chi^{(3)}$ signal lattice. Solid circles show the intersection of write beams with an observation plane. Open circles indicate beams generated by degenerate four wave mixing, $\chi^{(3)}(-\omega, \omega, \omega, -\omega)$. The hashed circle indicates the third harmonic signal generated by beams 1, 2, and 3 consistent with wave vector

conservation. This scheme affords several advantages relative to conventional THG and is complementary to such measurements.

In Fig. 12, we compare $c_{1111}(-3\omega, \omega, \omega, \omega)$ amplitude, real, and imaginary component values determined from our DFWM-based measurements with conventional THG data recorded by other investigators.^{17,18} Note it is particularly interesting that our data agree with the measurement of a negative imaginary component near 800 nm.

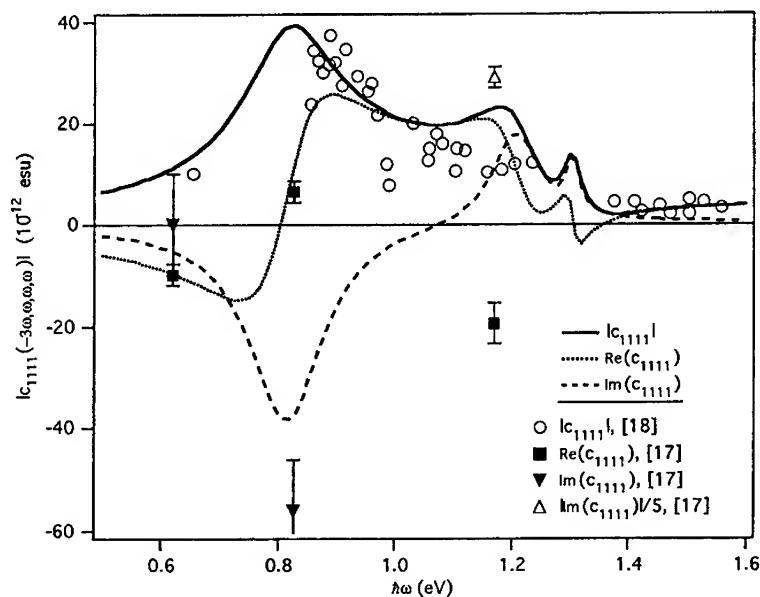


Fig. 11. The frequency dependence of "THG data" is determined from "DFWM-based data". Comparison with the THG measurements of others is also given.

CORRELATION OF TWO PHOTON ABSORPTION COEFFICIENTS AND $\chi^{(3)}$

The two photon absorption coefficient α_2 (where α_2 is defined by the relationship $\alpha = \alpha_0 + \alpha_2 I$; I = light intensity) is related to the third order susceptibility by

$$\alpha_2 = (192\pi^3/n^2\lambda c)\{\text{Im}\chi_{1111}(-\omega, \omega, \omega, -\omega)\} \quad (4)$$

DFWM and nDFWM experiments establish the following energy level structures for the fullerenes and values for the fullerenes and values for nonlinear optical parameters:

TABLE I Two photon state energies and nonlinear optical parameters

Parameter	C60	C70	Reference
H_g State Energy	2.67 eV	2.61, 2.41 eV	
$\chi_{1111}(0,0,0,0)$	$250 \times \chi_{1111}^{\text{FS}}$	$500 \times \chi_{1111}^{\text{FS}}$	$\chi_{1111}^{\text{FS}} = 4.0 \times 10^{-15}$ esu
$ \chi_{1111} ^{\text{max}}$	4.0×10^{-12} esu	6.0×10^{-12} esu	where $\alpha_2^{\text{GaAs}} = 20$ cm/GW
π phaseshift	2 mm	1 mm	@ 10 GW/cm ² , 1.5 μ m

It is interesting that the two photon absorption coefficients for C60 and GaAs are essentially identical while the value for C70 is 1.5 times that of GaAs. The value for AF50 is also comparable to that of GaAs.

ACKNOWLEDGMENTS

The authors wish to thank Professor P. N. Prasad and Dr. Z. H. Kafafi for providing several of the samples examined in this study and for helpful discussions. This research was supported by the National Science Foundation (DMR-9527021).

REFERENCES

1. F. P. Strohkendl, T. J. Axenson, R. J. Larsen, L. R. Dalton, R. W. Hellwarth, and Z. H. Kafafi, *J. Phys. Chem.*, **101**, 8802 (1997).
2. F. P. Strohkendl, T. J. Axenson, R. J. Larsen, L. R. Dalton, R. W. Hellwarth, and Z. H. Kafafi, *Proc. SPIE*, **3142**, 2 (1997).
3. F. Kajzar, C. Taliani, R. Zamboni, S. Rossini, and R. Danieli, *Synthetic Metals*, **54**, 21 (1993).
4. J. S. Meth, H. Vanherzeele, Y. Wang, *Chem. Phys. Lett.*, **197**, 26 (1992).
5. G. P. Banfi, D. Fortusini, M. Bellini, and P. Milani, *Phys. Rev. B*, **56**, 10075 (1997).

6. F. P. Strohkendl, L. R. Dalton, R. W. Hellwarth, H. W. Sarkas and Z. H. Kafafi, J. Opt. Soc. Am. B, **14**, 92 (1997).
7. M. Sheik-Bahae, D. C. Hutchings, D. J. Hagan, and E. W. Van Stryland, IEEE J. Quantum. Electron., **27**, 1296 (1991).
8. J. R. Lindle, P. G. S. Pong, F. J. Bartoli, and Z. H. Kafafi, Phys. Rev. B, **48**, 9447 (1993).
9. S. R. Flom, R. G. S. Pong, F. J. Bartoli, and Z. H. Kafafi, Phys. Rev. B, **46**, 15598 (1992).
10. M. J. Rosker, H. O. Marcy, T. Y. Chang, J. T. Khoury, K. Hansen, and R. L. Whetten, Chem. Phys. Lett., **196**, 427 (1992).
11. F. P. Strohkendl, D. J. Files, and L. R. Dalton, J. Opt. Soc. Am. B, **11**, 742 (1994).
12. G. S. He, L. Yuan, N. Chen, J. D. Bhawalkar, P. N. Prasad, L. L. Brott, S. J. Clarson, and B. A. Reinhardt, J. Opt. Soc. Am. B, **14**, 1079 (1997).
13. I. László and L. Udvardi, J. Molec. Struct., **183**, 271 (1989).
14. Robert W. Boyd, Nonlinear Optics (Academic Press, San Diego, 1992).
15. S. Leach, M. Vervloet, A. Despres, E. Breheret, J. P. Hare, T. J. Dennis, H. W. Kroto, R. Taylor, and D. R. M. Walton, Chem. Phys., **160**, 451 (1992).
16. Y. Wang and L.-T. Cheng, J. Phys. Chem., **96**, 1530 (1992).
17. D. Neher, G. I. Stegeman, F. A. Tinker, and N. Peyghambarian, Opt. Lett., **17**, 1491 (1992).
18. F. Kajzar, C. Taliani, R. Danieli, S. Rossini, and R. Zamboni, Phys. Rev. Lett., **73**, 1617 (1994).

THE OPTICAL BEHAVIOR OF NEW TPA DYES IN NANOPOROUS GLASSES

M.K. CASSTEVENS, D. KUMAR, S. GHOSAL, R. BURZYNSKI
Laser Photonics Technology, Inc., 1576 Sweet Home Rd., Amherst, NY 14228
and

C.W. SPANGLER AND EL HADJ ELANDALOUSSI
Department of Chemistry and Biochemistry and Optical Technology Center Montana State
University, Bozeman, MT, 59717 USA

Abstract The optical power limiting response of several new two photon absorption dyes is presented. Specific effort has been made to characterize the wavelength dispersion of these dyes in various environments. Of particular interest is the use of nanoporous glass hosts which can be used to create nanocomposites offering broadband performance arising from different active components. The preparation and characterization of these material systems are discussed followed by a discussion of how these material systems can be used in practical systems to protect against broadband threats.

INTRODUCTION

There are a number of applications that require the use of optical power limiters to protect human vision and optical sensors from intense laser radiation. In those instances where a known narrowly-defined threat exists, notch and cut-off filters can be effectively employed. In contrast, where laser threats can occur over a wide range of wavelengths and pulse durations (even cw), it is impossible for a single active compound to provide complete protection. The relatively recent development of solid-state frequency agile (tunable) laser sources dramatically illustrates the need for broadband performance. There are a myriad of organic compounds that have been investigated for this application operating through several different mechanisms.^{1,2} The obvious solution to multiple threats is the use of complementary active species placed into a common host.³ The simplest example of this type of system is when several organic compounds are dissolved in a common solvent. A very serious limitation for these systems is finding a common solvent for molecules that

may have very different structures and hence have very different solubilities. Further, one must also consider the effect of the solvent and the presence of the other species on overall performance. Even for those cases where there are available common solvents, there are applications where solution filled cells are less preferable than solid materials.

In all cases where multiple materials are used cooperatively, there is a real need to minimize linear absorption; there is little use for a material that transmits negligible ambient illumination. A nominal value of 70% broadband transmission is generally given as a practical goal. Many optical power limiting materials have sizeable linear absorption necessitating serious compromises regarding the active species' concentration. In contrast, materials operating by Two Photon Absorption (TPA) typically have negligible linear absorption at the wavelength where they are most likely to have the greatest TPA cross-sections and are therefore ideal for use in practical systems.

TPA (as discussed here) is a process wherein two photons of identical energy are simultaneously absorbed by a molecular species which is then promoted to some singlet excited state. It is important to understand that the molecule has only a virtual excited state corresponding the absorption of a single photon and, therefore, TPA should not be confused with sequential absorption. TPA is a nonlinear process and is therefore strongly dependent upon the intensity of light. The change (decrease) in intensity (I) of a beam as it propagates through a medium with linear and two photon absorption is given by

$$\delta I / \delta z = -(\alpha_1 I + \alpha_2 I^2) \quad (1)$$

where α_1 is the linear absorption coefficient, α_2 is the TPA absorption coefficient (in units of cm MW^{-1}) and I is the incident intensity. Making some assumptions about the ideality of a flat topped incident beam and neglecting the linear absorption, the transmitted intensity can be shown to be

$$I(L) = I_0 / (1 + I_0 L \alpha_2) \quad (2)$$

and slightly different for a Gaussian beam⁴:

$$I(L) = (1/L\beta) [\ln(1 + I_0 L \beta)] \quad (3)$$

where I_0 is the incident intensity in MW/cm², $I(L)$ is the intensity at distance L , and L is the path length. To make quantitative comparisons between different materials, it is necessary to develop a set of equations that take the concentration of the TPA compounds into account. The simplest and most useful expression that yields a coefficient for a specific molecule is

$$h\nu\alpha_2 = \sigma_2 N_0 \quad (4)$$

where σ_2 is the molecular two photon absorption cross-section in units of cm⁴/photon and N_0 is the number density (number of TPA molecules per unit volume). This expression can be reexpressed as

$$h\nu\alpha_2 = \sigma_2 N_A d_0 10^{-3} \quad (5)$$

where N_A is Advogadro's number and d_0 is the molar concentration. Equation 5 enables the determination of molecular cross-sections from experimental results.

Multiphoton absorption was one of the first nonlinear phenomena to be observed following the development of short pulse lasers.⁵ Recently, TPA materials have received greater attention owing to the higher, than previously observed, effective cross-sections.⁶ A recent review of TPA processes has provided an extensive list of values for many organic compounds.⁷ Reinhardt in collaboration with Prasad have synthesized and measured an extensive series of systematically derived structures to better establish the structure-property relationship.⁸ There are a number of other groups that have also explored this relationship.^{7,9}

This work discusses the use of two nanoporous glass matrices as hosts for complementary optical power limiting compounds. The first of these hosts is a pure silica glass monolith made in our laboratories using sol-gel techniques. The second of these glasses is purchased from Corning® and is sold under the name of "thirsty" or porous Vycor®. The diameter of the pores is sufficiently small in both materials such that visible light is not effectively scattered and the glass has reasonable optical quality. When the pores are filled with substances whose refractive index is close to that of SiO₂, the optical quality of the materials is extremely good.

Porous glasses can be used to combine dissimilar materials into a single solid host. Three distinct phases can be prepared within an optical quality glass.³ Optical power limiting materials can be placed within the glass phase itself (in the case of sol-gel materials) by adding nanoparticles or even thermally stable ormosils to a sol-gel preparation in its earliest stages. A second phase can be prepared at the pore walls by infiltrating the host material with solutions containing an organic compound(s) known to have optical power limiting action. Allowing the sample to dry under ambient temperatures causes the remaining dye(s) to form nanocrystallites on the pore walls; the size of these crystallites will depend upon the concentration of the original solution and the diameter of the pores. To the extent that subsequent solvents do not dissolve previously deposited nanocrystallites, this process can be repeated a number of times with different solutions. A third possible phase is created by mixing a compound(s) and polymerizable monomer which can then be placed in the pores to form a completely nonporous final material of exceptional optical quality.

It is clear that porous glasses can be used to form nanocomposites of several materials which do not have to share common solubilities. To the extent that solid-state properties need to be retained, it is possible to have nanoparticles and nanocrystalites small enough not to introduce optical scattering. The final materials are easily handled and are hard enough to be polished. The nanocomposite approach offers an exciting opportunity to develop broadband performance from a single optical power limiting material.

EXPERIMENTAL

Synthesis of TPA Materials

There are effectively two classes of compounds that are presented in this work. The first is a series of symmetric compounds that have triphenylamine groups joined by conjugated chains. The second class of compounds are variations of 4-diethanolamino-4'-(6"-hydroxyhexylsulfinyl)stilbene (THS) - a conjugated donor- acceptor compound.

DTPAF6,12 is a 9,9 dialkyl derivatized fluorene with diphenylamino groups at positions 2 and 7 (see Figure 1 for structures). DTPADVP6,6 and DTPADVP are two

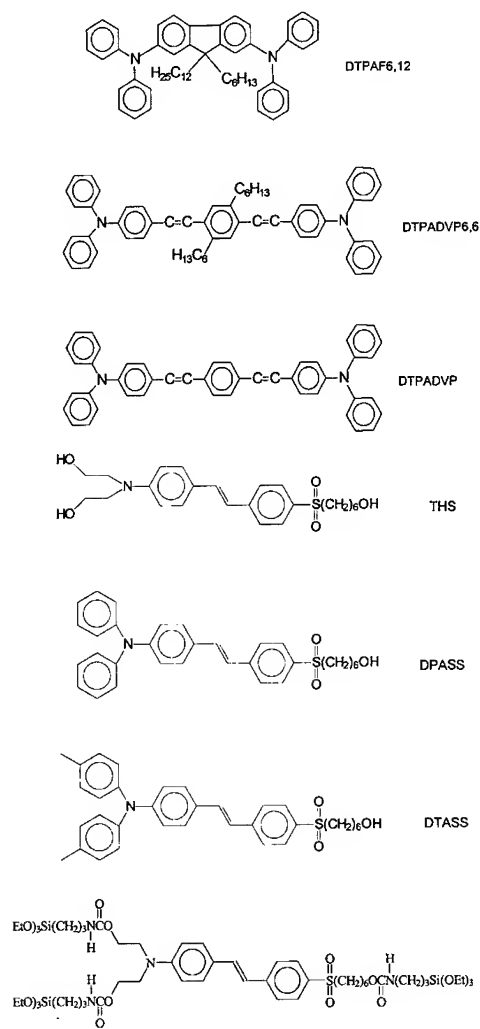


Figure 1. Organic TPA compounds synthesized

triphenylamine groups joined by a conjugated molecular bridge consisting of p-divinylbenzene; DTPADVP6,6 has its central phenyl ring substituted by hexyl chains in positions 2 and 5 to enhance solubility and reduce intermolecular energy transfer. Equivalent compounds without the center phenyl ring did not show as impressive TPA in earlier screening studies and were not pursued. The alkyl substituents improved solubility, but results from Reinhardt's earlier work suggest that the alkyl chains can also play an important role in modifying the value of the TPA cross-sections.¹⁰ DTPADVP6,6 and DTPADVP were both prepared via Wittig condensation of triphenylamine carboxaldehyde with the appropriate bis-Wittig salts in good yield.

THS is a compound that has a classical donor-acceptor structure. Our research group has found it to be an electrooptical chromophore useful in such applications as electrooptic modulation. The central portion of the compound is a stilbene structure which was synthesized using a Wittig reaction. THS, DPASS and DTASS have sulfonyl electron withdrawing groups. The amine donor portion of THS contains two hydroxyethyl groups whereas DPASS contains phenyl rings and DTASS has two tolyl groups.

An ormosil is an organically modified silane that can be used in the preparation of sol-gel materials.¹¹ An ormosil typically has one or more of the alkoxy groups replaced by an alkyl or aromatic group which does not participate in the hydrolysis or condensation reactions. A THS based ormosil (THSORM1) has been prepared from THS and 3 equivalents of triethoxysilylpropyl isocyanate yielding a compound containing three urethane linkages and nine alkoxy groups which can participate in hydrolysis and condensation reactions. A complete description of the synthetic chemical reactions for these compounds will be available in a subsequent publication.¹²

Preparation of Solutions and Ormosil Films

Several different samples were prepared and are discussed in this work. Compounds were studied in solutions at the concentrations indicated. All of the samples were prepared using solvents available from the Aldrich Chemical Company. Each solution was filtered using Teflon® filters with 0.5 μm pores and placed into clean quartz cuvettes with a 1 cm path length. THSORM1 was studied both as butanol solution as well as a solid film prepared by spincoating and solution casting. In each case, 450 mg of 88% formic acid is added to 2.37 g of THSORM1 and sonicated for 1 hour

immediately prior to film preparation.

Spincoating yields thin films deposited on microscope slides and which are processed by heating at 100 °C for 18 hours. Solution cast films were dried at room temperature for three days and heated at 100 °C for 18 hours. Both methods yield hard glassy films that are conveniently handled.

Preparation of nanoporous silica hosts

Glass polymer composites containing TPA chromophores for optical power limiting was made from two different types of porous glass: sol-gel glass and porous Vycor® glass. Two different approaches for making sol-gel glass were employed (A and B) along with the use of a commercially available product (C) as described below:

(A) Two step acid hydrolysis

Tetraethyl orthosilicate (TEOS), water and ethyl alcohol in the ratio 1:4:4 was used to make sol-gel glass. 10 g of TEOS was mixed with 3.456 g water and 8.845 ethanol and 6 drops of HNO₃ was added to the solution and stirred for 1 hour. The partially hydrolyzed solution thus obtained was fully hydrolyzed by adding 4 drops of 49% HF to the solution and mixing it for 15 minutes. The final clear filtered solution (sol) was cast in polystyrene cuvettes for gelation and covered with perforated aluminum foil. The cuvettes containing the sol were then kept in an oven at 45 °C for two weeks resulting in a stiff gel. The gel samples were removed from the oven and heated slowly to 500 °C and cooled to room temperature to form porous sol-gel glass. The porosity of sol-gel glass made using this approach determined by nitrogen adsorption is about 65% and the average pore diameter is known to be approximately 4 nm.

(B) Base catalyzed hydrolysis

TEOS was mixed with 0.1 N ammonium hydroxide in 1:10 ratio for 24 hours at room temperature to form a hazy and viscous solution. The solution is cast in polystyrene dishes and covered with perforated aluminum foil. The samples were then kept in an oven at 45 °C for two weeks to form an opaque gel. The opaque gel was then heated slowly up to 1050 °C in a furnace and cooled to room temperature. The porosity of the glasses made using this approach was about 70% and was more stable than the two-step acid hydrolyzed sol-gel samples. We have elected to use sol-gel glasses made using the base catalysis method for making composite glasses for this work due to their

better overall stability. The average pore diameter for these samples is slightly larger (6-8 nm) as evidenced by increased light scattering of the porous glass and diffusion times.

(C) Porous Vycor® glass

Porous Vycor® was purchased from Corning® and was cleaned in boiling hydrogen peroxide followed by thorough rinsing in de-ionized water before further use. Vycor® glass is known to have a 28% pore volume with an average pore diameter of 5 nm.

Preparation of Nanocomposites

Incorporation of TPA dyes into a porous glass matrix was done in two different ways. TPA dyes soluble in methyl methacrylate (MMA) were introduced in the glass pores by immersing the samples in saturated solution of the dye in MMA which was later polymerized within the pores using radical polymerization to form a composite glass. Dyes that are insoluble in MMA were incorporated into the pores by solution infiltration of the dyes using an appropriate solvent. The solvent is then removed from the pores by evaporation. After drying, the samples were placed in MMA solution and polymerized *in-situ* to form the final glass-polymer composite. The composites of sol-gel glass and Vycor® glass with PMMA containing the active chromophore were polished to an optical finish before characterization. Table I describes how each material was prepared.

TABLE I. Dyes, solubility and processing methods

Compound	Solubility	Sample Preparation
DTPAF6,12	DMF	DMF soln
DTPADVP6,6	CHCl ₃ , MMA	CHCl ₃ soln; MMA solution infiltr. (solid)
DTPADVP	CHCl ₃	CHCl ₃ soln
THS	DMF	DMF soln; DMF soln infiltr./dried/MMA infiltr. (solid)
DPASS	DMF	DMF soln
DTASS	DMF	DMF soln
THSORM1	butanol	butanol soln; 100 µm films

Optical Characterization Techniques

Measurements of TPA cross-sections were determined from nonlinear transmission experiments utilizing 10 Hz, 8 ns, 800 nm pulses. Optical power limiting measurements were performed using an OPO laser (OPOTEK Magic Prism) pumped by a frequency doubled Quanta Ray (Brilliant) NdYAG. The laser was run at the highest output power where the energy per pulse was stable. The incident energy was controlled using a combination of cross polarizers and neutral density filters and monitored using a beam splitter/calibrated photodetector combination. A 7 mm diameter collimated beam was focused onto the center of all samples using a 10 cm focal length lens. The transmitted energy was collected using a pyroelectric detector (open aperture). In all cases, data were obtained where there was no visible evidence of refractive phenomena. All data points represent the average of 20 pulses. Liquid samples showed no evidence of bubble formation at the energies used and (obviously) no evidence of damage. The solid samples are more prone to damage since any damaged materials can not diffuse away. Repeated exposure of solid samples to high intensity pulses could be seen to leave a permanent mark. Care was taken to lower the energy and to use a fresh sample area for each data point.

RESULTS AND DISCUSSION

The UV-Vis spectra of all the compounds described in this paper have strong absorptions in the blue and virtually no linear absorption beyond 450 nm. This observation is good proof that we can load TPA optical limiters to high concentrations without compromising linear transmission. TPA occurs nominally at wavelengths that are twice λ_{max} which is well beyond where linear absorption occurs.

Effective TPA cross-sections at 800 nm were obtained for a number of compounds presented in Figure 1. Preliminary measurements on several compounds have yielded the following results: DTPAF6,12 : 5×10^{-50} cm⁴/s/photon, DTPADVP6,6: 8180×10^{-50} cm⁴/s/photon, DTPADVP: 6670×10^{-50} cm⁴/s/photon. It is clear that DTPAF6,12 is orders of magnitude inferior to the others measured. At this point we became seriously interested in the dispersion of the TPA cross-section since this value was so low inspite of the fact that similar structures had much better TPA cross-

sections.¹⁰ The absorption maximum for this compound is at 373 nm - some 20 nm lower than that of the other two compounds. If the dispersion was great over this limited range then it might explain the low value at 800 nm. The dispersion curves that we have since obtained are quite broad (~100 nm) which imply that aside from dispersion effects, the TPA cross-section for DTPAF6,12 is inferior. This result is in the process of being confirmed experimentally. The other two compounds DTPADVP6,6 and DTPADVP have cross-section values that are comparable to some of the best materials produced in recent years.^{8,9}

It is important to point out that the effective cross-sections discussed here were obtained with 10 ns pulses and there is almost certainly a strong excited state absorption component. This is consistent with recent studies that show there is a 10-30 times effective improvement in the value of the measured cross-sections when one goes from using ps to ns pulses.⁹ It is now widely recognized that there is a significant contribution to optical power limiting from the excited state absorption which is more pronounced during nanosecond pulse widths.⁹ The excited state absorption is initiated by a TPA event and is therefore a very useful way to get amplification of optical power limiting performance. Recognition of the fact that there are processes other than simple TPA complicates our understanding of these events and suggests that increasing the effective cross-sections further may have more to do with optimizing excited state absorption and less with the inherent ability of the compounds to experience multiphoton absorption. Ultimately, however, both will need to be optimized to render compounds with the greatest effective TPA cross-sections.

Each of the compounds in Figure 1 were evaluated for optical power limiting at wavelengths from 675 and 840 nm although there were limitations in the output power of the laser at wavelengths near the extremes of this range. The focal arrangement was not optimized for obtaining the best limiting performance, but rather was selected because there was little chance of bubble formation, lensing, and other effects that would have confounded the interpretation of our results. In all cases, the power limiting curves are directly comparable except for the fact that it was difficult to precisely determine or control the amount of material that was placed in the pores of the hosts owing to the differences in how the materials were introduced. Nonetheless, the wavelength dispersion of each of the dyes was of great interest as well as the shift of effective TPA maxima as a function of environment (sol-gel, Vycor[®], solution, etc.).

Figure 2 is representative of the data collected in this study. The lines drawn are a reasonable fit to the experimental points and are intended to assist the reader to extrapolate between measured values. Figure 2 illustrates the output intensity (open aperture) as a function of input intensity for several wavelengths between 675 and 840 nm. It should be clear from this data that there is a definite dispersion effect. Similar curves were obtained for each of the samples in Figure 1 in a variety of environments in an attempt to study the effect of local environments for each of the systems (solution, sol-gel, Vycor®, etc.).

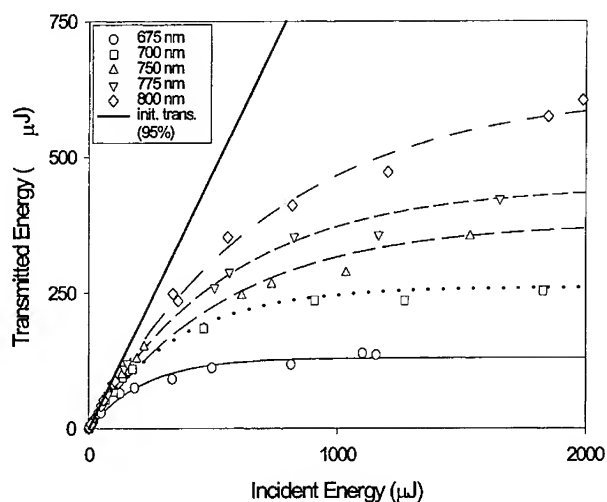


Figure 2. Wavelength dispersion in optical power limiting of DTPADVP6,6 in CHCl_3 (50 mg/g). Optical arrangement used a 7 mm diameter collimated beam, 10 cm focal length lens, and open aperture detection. Data points represent the average of 20 pulses.

Figure 3 is a compilation of the data for several systems. In light of the fact that different systems had different amount of active substance, the data have been normalized for comparison purposes. For a given sample, the fraction of transmitted light at 2 mJ input energy was extrapolated and noted. All values for a particular sample were multiplied by a constant that would make the lowest transmitted/incident intensity value equal to one - the others are all larger than 1 depending upon the amount of dispersion. These values are plotted for several THS and THS derivative systems.

There is clear evidence of dispersion in all systems. THS in DMF exhibits a maximum optical

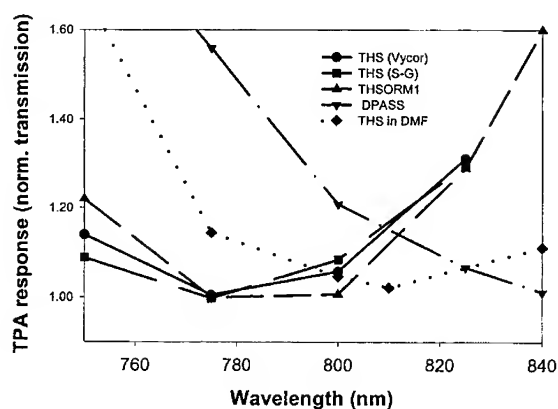


Figure 3. Wavelength dispersion of THS and related systems in different host media. The data have been normalized for comparison purposes. Each data point represents transmitted/input intensity at 2 mJ multiplied by a constant. This constant is the value that makes the minimum transmitted/incident value for any sample equal to 1.0.

power limiting at 810 nm. Both nanoporous glass host systems (sol-gel and Vycor®) have their maxima 35 nm shifted to the blue to 775 nm. This observation is consistent with and due in part to the fact that the maximum linear absorption for the sol-gel and Vycor® samples is blue shifted

approximately 10 nm from 391 nm in DMF to 382 nm. THSORM1's effective TPA cross-section maximum is similar to that of the nanoporous glass samples. All three of these samples have the presence of Si-O linkages which may also be partly responsible for this shift. Further studies will need to be performed to elucidate the exact nature of this effect. The DPASS sample is far red shifted from that of any of the THS systems demonstrating how effectively the TPA cross-sections can be shifted by small changes in molecular structure. The DTASS sample (not shown) demonstrates very similar performance as that of DPASS.

Similar to Figure 3, Figure 4 is a normalized representation for three different samples containing the dye DTPADVP6,6. From this data and the data found in Figure 2, the maximum effective TPA cross-section is at or below 675 nm. The fact that this compound is operable in the red indicates that we may have the opportunity to develop similar structures covering a broader spectrum in the

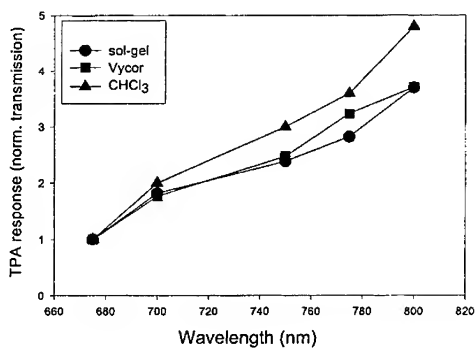


Figure 4. Wavelength dispersion of TPA for DTPADVP6,6 in different host media. The data have been normalized for comparison purposes. Each data point represents transmitted intensity/input intensity at 2 mJ multiplied by a constant. The constant for any sample is the value that makes the minimum transmitted intensity/incident intensity value equal to 1.0.

visible. This is a real challenge for TPA materials since even the best ones normally have their linear absorption in the 300-400 nm range. There are no clear differences in the dispersion for samples in Figure 4 since the DTPADVP6,6 molecules are dispersed in the PMMA when the material is placed in the pores of sol-gel and Vycor® samples.

In conclusion, we have described several new TPA dyes which have potential for optical power limiting. TPA materials have been described as ideal candidates for optical power limiting since their linear absorption is negligible at the wavelength of operation. Sol-gel and Vycor® solid monoliths have been shown to be effective hosts for TPA dyes and it has been shown that they can be used as nanocomposites offering broadband protection. The optical quality of these materials is exceptional. The optical damage mechanisms in these materials vary depending upon the relative amounts of polymer or glass that are present; glass rich materials tend to shatter while polymer rich material fail in ways characteristic of pure polymers.

Derivatives of THS were shown to have their maximum cross-sections red-shifted by almost 100 nm with respect to THS. THS itself has TPA activity in the NIR whereas DTPADVP6,6 has its maximum TPA activity in the red. Within the limits of our measurements performed thus far, we have determined that the maximum effective TPA cross-section is as low as 675 nm. Further studies will ascertain whether it is even further toward the blue. There appears to be an approximately 35 nm blue shift associated with having THS in the form of nanocrystallites along the pore walls in both sol-gel and Vycor® samples. A similar effect is seen with an ormosil of THS (THSORM1) though it may be due to entirely different processes since it is in fact a different molecular structure. Further experimentation will continue to elucidate these mechanisms.

ACKNOWLEDGEMENTS

The authors would like to thank the members of LPT's staff, Andrew Mott of Army Research Laboratory and Bruce Reinhardt of the Air Force Research Laboratory for valuable discussions, Mohammad Al Nouri for assistance with DTASS, and various other members of the Photonics Research Laboratory for their assistance, cooperation and discussions. LPT gratefully acknowledges

financial support from the United States Army under contract number DAAL01-97-C-0092.

REFERENCES

1. Papers found within Materials for Optical Limiting, Eds. R. Crane, K. Lewis, E. Van Stryland, and M. Khoshnevisan, MRS Symp. Proc. Vol. 374, MRS Pittsburgh PA (1995).
2. Papers found within Materials for Optical Limiting II, Eds. R. Sutherland, R. Pachter, P. Hood, D. Hagan, K. Lewis, J. Perry, MRS Symp. Proc. Vol. 479, MRS Pittsburgh PA (1997).
3. R. Gvishi, J.D. Bhawalkar, N.D. Kumar, G. Ruland, U. Narang, and P.N. Prasad, B.A. Reinhardt, Chem. of Materials, 7, 2199 (1995).
4. T.F. Boggess, K. Bohnert, K. Mansour, S.C. Moss, I.W. Boyd, and A.L. Smirl, IEEE J. Quantum Electron., 22, 360 (1986).
5. R.J. Collins, D.F. Nelson, A.L. Schawlow, W.L. Bond, C.G.B. Garrett, and W.K. Kaiser, Phys. Rev. Lett., 5, 303 (1960).
6. J.D. Bhawalkar, G.S. He, and P.N. Prasad, Rep. Prog. Phys., 59, 1041 (1996).
7. S. Kershaw in Characterization Techniques and Tabulations for Organic Nonlinear Optical Materials, Chapter 7, 515-654, Marcel-Dekker, Inc New York (1998).
8. B.A. Reinhart, L.L. Brott, S.J. Carlson, R. Kannan and A.G. Dillard, SPIE Vol. 3146, 2 (1997).
9. J.E. Ehrlich, X.L. Wu, I-Y. S. Lee, A.A. Heikal, Z-Y. Hu, H. Rockel, S.R. Marder, and J.W. Perry, in Materials for Optical Limiting II, Eds. R. Sutherland, R. Pachter, P. Hood, D. Hagan, K. Lewis, J. Perry, MRS Symp. Proc. Vol. 479, 9, MRS Pittsburgh PA (1997).
10. B.A. Reinhardt, L.L. Brott, S.J. Carlson, R. Kannan, and A.G. Dillard in Materials for Optical Limiting II, Eds. R. Sutherland, R. Pachter, P. Hood, D. Hagan, K. Lewis, J. Perry, MRS Symp. Proc. Vol. 479, 3, MRS Pittsburgh PA (1997).
11. C.J. Brinker and G.W. Scherer, The Physics of Sol-Gel Processing, Academic Press, New York (1990).
12. *in preparation*

NONLINEAR TRANSMISSION OF OPTICALLY THICK TWO-PHOTON ABSORPTIVE MATERIALS

P. FENEYROU^a, D. BLOCK^a, M. PIERRE^a, A. IBANEZ^b, P. L. BALDECK^a

^aLaboratoire de Spectrométrie Physique, Université J. Fourier Grenoble 1,
CNRS (UMR 5588), BP 87, 38402 Saint Martin d'Hères Cedex, France.

^bLaboratoire de Cristallographie, BP 166, 38042 Grenoble Cedex 09, France.

Abstract: We study the influence of incident beam focusing and sample thickness on the nonlinear absorption. To discuss the optimization of the thickness, we introduce a nonlinear length which describes the length of the sample part in which the nonlinear interaction is efficient. A simple model for the weak nonlinear regime is derived and compared to experimental results on 2-Amino-5-Nitro-Pyridinium-Chloride crystal. Then, computations based on the beam propagation method are used in order to discuss the strong nonlinear regime.

INTRODUCTION

Various applications involve the protection of sensors from optical stresses. For example, the optical limiting can be performed by two-photon absorption in semiconductors¹ and in organic crystals² or by reverse saturable absorption in dyes.³ For thin samples, the nonlinear absorption increases as a function of the thickness, but saturates for thick samples. Thus, there is no need to considerably enlarge the sample. The optimization of the thickness in view of the maximal sensor protection has to take into account a large number of parameters such as the beam properties, the damage threshold of the nonlinear material, and the thermal conductivity. The first step is to determine the optimal thickness for a given material, and a given optical configuration.

Analytic and numerical descriptions of the optical beam propagation in nonlinear media have been investigated by a number of authors. Particular works have been carried

out on the beam propagation in Z-scan measurements on thick and thin samples,^{4,5,6,7} but there are few descriptions of the nonlinear absorption of thick samples.⁸

To discuss the role of the thickness, for a given gaussian (in time and space) incident beam focused at the center of the sample we define a nonlinear thickness L_{nl} for the sample using the nonlinear transmission for an optically thin medium: for a measured or calculated nonlinear transmission of a sample, the corresponding nonlinear length is given by the expression :

$$T_{nl} = \frac{1}{\sqrt{\pi} \beta L_{nl} I_0} \int_0^\infty \ln(1 + \beta L_{nl} I_0 e^{-t^2}) dt \quad (1)$$

where T_{nl} is the nonlinear transmission of the sample, β is the two-photon absorption coefficient, I is the input peak intensity on the axis at the waist. In this paper we do not take into account any linear absorption.

Once the nonlinear transmission is measured or calculated, the nonlinear length is obtained by inverting Eq. 1. The physical meaning of this nonlinear thickness is the length of the sample part in which the nonlinear interaction is efficient (see Fig.1). For a thin sample the nonlinear length is its thickness. Using the nonlinear length, the comparison between results corresponding to different beam configurations becomes easier.

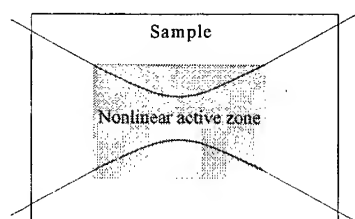


FIGURE 1 Schematic description of the nonlinear interaction length

In the first section of this paper, we present experimental results on the nonlinear transmission of 2-Amino 5-Nitropyridinium Chloride (2A5NPCI) crystal⁹ as a function of the thickness. In the second part of this paper, a simple model is derived for the attenuation of light on the optical axis in a weak nonlinear absorptive material. In the third section, a

numerical simulation based on the well-known beam propagation method¹⁰ (BPM) is done to fit the experimental data, and to study the strong nonlinear regime.

MEASUREMENT OF THE NONLINEAR THICKNESS

In this section, we present measurements of the nonlinear transmissions of 2A5NPCl crystals. The transmission was measured as a function of the sample thickness using a frequency-doubled Nd:YAG laser ($\lambda=532$ nm). The pulse duration was 250 ps and the input intensity are less than 1 GW cm^{-2} . The beam was focused by a lens of 5 cm focal length. The beam waist was measured to be $6 \pm 0.8 \text{ }\mu\text{m}$ using the knife edge technique.

With a linear index of refraction of 1.89 ± 0.02 on the crystallographic plane (100), the Rayleigh length inside the sample is equal to $400 \pm 110 \text{ }\mu\text{m}$. For thin samples, the measurement of the nonlinear transmission leads to a nonlinear absorption coefficient of 5 cm GW^{-1} .

The experimental results on the nonlinear thickness (deduced from the slope of the nonlinear transmission at low intensity) are presented in figure 2. For thin samples, the nonlinear thickness is equal to the sample length. Theoretically, this approximation remains correct within the 10% uncertainty up to 0.6 mm which corresponds to $1.5 z_0$ where z_0 is the Rayleigh length inside the sample. Beyond this limit, the nonlinear length saturates.

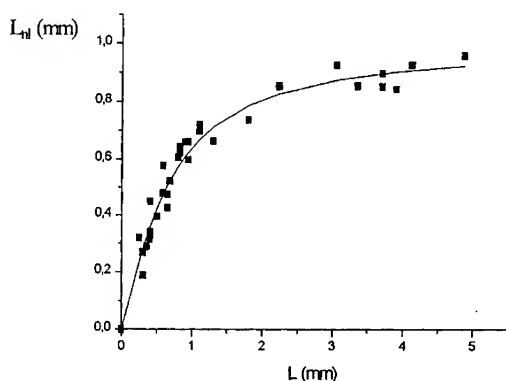


FIGURE 2: Experimental nonlinear thicknesses of 2A5NPCl crystals. The full line represents the best fit using Eq. 8.

ANALYTIC MODEL FOR THE NONLINEAR THICKNESS

Model

In the model the beam is described as a sum of tubes of light. The topology of each tube is assumed to be insensitive to the non-linearity, but the carried energy is attenuated through the nonlinear absorption. This approach is only valid within the weak nonlinear regime. The effects of the nonlinear index of refraction are also neglected. The energy dissipation for the tube around the optical axis can be written as:

$$I(z,t) S(z) - I(z+dz,t) S(z+dz) = -\beta I^2(z,t) S(z) dz \quad (2)$$

where $I(z,t)$ is the intensity on the optical axis at the location z and time t , $S(z)$ is the area of the cross-section of this tube.

$S(z)$ is given by:

$$S(z) = S(0) \left(1 + \frac{z^2}{z_0^2} \right) \quad (3)$$

where $z=0$ corresponds to the waist, and z_0 is the Rayleigh length inside the medium. This expression is related to the properties of a gaussian beam.

Then, we find :

$$\frac{\partial I(z,t)}{\partial z} = -\beta I^2(z,t) - \frac{2z}{z_0^2} I(z,t) \quad (4)$$

Using Eq. (4) and the fact that the incident beam is focused at the center of the sample, we can calculate the nonlinear transmission $T_{oa}(t)$ on the optical axis:

$$T_{oa}(t) = \frac{1}{1 + 2\beta z_0 I_i(t) \arctan\left(\frac{L}{2z_0}\right)} \quad (5)$$

where $I_i(t)$ is the input intensity at time t on the optical axis at the waist, and L is the thickness of the sample. It is worth comparing Eq. 5 with the expression for the corresponding nonlinear transmission, $T'_{oa}(t)$, in the case of a thin sample with thickness L' :

$$T'_{oa}(t) = \frac{1}{1 + \beta I_i(t) L'} \quad (6)$$

The comparison suggests that the nonlinear thickness is given by:

$$L_{nl} = 2 z_0 \arctan\left(\frac{L}{2 z_0}\right) \quad (7)$$

This formula is coherent with the results obtained through a different formalism by Hermann.⁸

Comparison with experimental results

As shown in Fig. 2, a good agreement is observed at low intensity with the expression :

$$L_{nl}(L) = 2 z_{0fit} \arctan\left(\frac{L}{2 z_{0fit}}\right) \quad (8)$$

where z_{0fit} is the fitted Rayleigh length equal to 320 μm compared to the measured 400 μm . This 20 % correction is within the experimental uncertainty on the Rayleigh length.

COMPUTATION OF THE NONLINEAR THICKNESS (BEAM PROPAGATION METHOD)

We used the beam propagation method^{10,11,12} (BPM) to compute the nonlinear thickness as a function of the sample length and the nonlinear absorption. Early publications on the BPM showed its efficiency to compute the solution of the scalar paraxial wave equation by means of fast Fourier transform (FFT). This method which has been described and completed in an extensive way for anisotropic materials, consists in sampling the electric field on a transverse lattice, and to describe the incident wave as a superposition of plane waves that are propagated in the reciprocal space through fast Fourier transform. The absorption and refraction are then taken into account. An extensive description of this method is given in reference 10-12.

The nonlinear refractive index of the crystal was neglected to be consistent with the proposed analytic model. Thus, the crystal was supposed to be a pure nonlinear absorptive homogeneous medium. In our case, the linear absorption at 532 nm can be neglected.

In this paragraph, we give the values of the parameters used in our computations. The temporal shape of the incident pulse is assumed to be gaussian. As cumulative nonlinear effects (such as thermal lens) are neglected, the gaussian pulse can be divided into independent temporal equal parts where the intensities are assumed to be constant. In our

case, the pulse is divided into 50 temporal parts. The electric field is sampled on a 256×256 grid points on a sampling area calculated to describe correctly the beam waist and the electric field at the entrance and exit interfaces. The longitudinal steps are $25 \mu\text{m}$ long. To compute the nonlinear length we used a nonlinear absorption coefficient β of 5 cm GW^{-1} and compute the nonlinear transmission as a function of the incident beam intensity.

At a given wavelength, the computation of the nonlinear thickness normalized by the Rayleigh length only depends on two parameters : the product of the sample thickness by the nonlinear absorption coefficient and by the input intensity ($\beta L I$), and the sample thickness normalized by the Rayleigh length (L/z_0). The first parameter characterizes the nonlinear properties of the sample at a given intensity and the second one characterizes the focusing into the sample. The results of the computation of the nonlinear length as a function of these two parameters are given in figure 3.

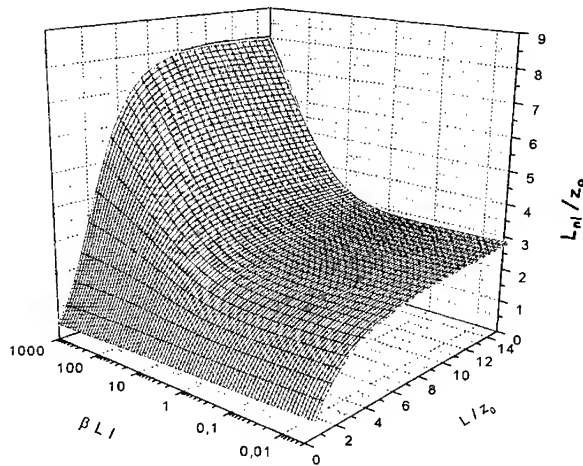


FIGURE 3 : Nonlinear thickness as a function of the sample thickness and the nonlinear absorption.

At low intensity, the beam propagation method gives the same result as the analytic expression for the nonlinear length. In the analytic description, due to the approximation of low non-linearity, the nonlinear length does not depend on the input intensity. In figure 3, the dependency of the nonlinear length as a function of the input intensity, computed by BPM, is shown: for low intensity, the nonlinear length remains constant but increases as the input intensity increases. At given focusing and sample thickness, the active zone of the sample increases when the input intensity increases: the nonlinear absorption becomes more efficient even near the entrance and exit interface of the sample.

The numerical simulation shows that the analytic expression is valid within 10 % up to a value of βIL of 2 which clearly shows the limit of this simple analytic model. Hermann has extended this analytic result to higher non-linearity (or intensities) in terms of transmission loss. But, in this regime the meaning of the nonlinear length becomes questionable particularly because of the refractive non-linearity that arises from acoustic wave and thermal diffusion into the sample.

CONCLUSION

In conclusion, we have measured the nonlinear thickness that should be taken into account to calculate the nonlinear transmission at relatively low intensity. This measurement is in good agreement with BPM simulation, and with an analytic model. The main limitation of this analytic model is its relatively low intensity domain of validity.

REFERENCES

- ¹ T.H. Wei, D.J. Hagan, M.J. Sence, E.W. Van Stryland, J.W. Perry, D.R. Coulter, *Appl. Phys. B* **54**, 46 (1992)
- ² P. Feneyrou, O. Doclot, D. Block, P.L. Baldeck, *J. Nonlin. Opt. Phys. Mat.* **5** n° 4 (1996)
- ³ J.W. Perry in *Nonlinear Optics of organic molecules and polymers* CRC Press (1996)
- ⁴ P.P. Banerjee, R.M. Misra, M. Maghraoui, *J. Opt. Soc. Am. B* **8**, n°5, 1072 (1991)
- ⁵ M. Sheik-bahae, A.A. Said, D.J. Hagan, M.J. Soileau, E.W. Van Stryland, *Opt. Eng.* **30**, n°8, 1228 (1991)
- ⁶ J.A. Hermann, R.G. McDuff, *J. Opt. Soc. Am. B* **10** n° 11, 2056 (1993)
- ⁷ P.B. Chapple, J. Staromlynska, R.G. McDuff, *J. Opt. Soc. Am. B* **11** n° 6, 975 (1994)
- ⁸ J.A. Hermann, *J. Opt. Soc. B* **14**, n°4, 814 (1997)

⁹ A. Ibanez, J.P. Levy, C. Mouget, *J. Solid State Chem.* **129**, n°1 (1997)

¹⁰ M.D. Feit, J. A. Fleck, Jr., *Appl. Opt.* **17** n°24, 3990 (1978)

¹¹ S. Hughes, J. M. Burzler, G. Spruce, B. S. Wherrett, *J. Opt. Soc. Am. B* **12** n° 10, 1888 (1995)

¹² J.M. Burzler, S. Hughes, B. S. Wherrett, *Appl. Phys. B* **62**, 389 (1996)

TWO PHOTON ABSORPTION IN REGIO-REGULAR POLY(3-ALKYL THIOPHENES)

S. DELYSSE^a, F. KAJZAR^a, J.-M. NUNZI^a, M. TRZANDEL^b AND
M. ZAGORSKA^c

^aLETI (CEA - Technologies Avancées), DEIN/SPE, CEA/Saclay, 91191 GIF-SUR-YVETTE CEDEX, France

^bCEA - DSM, Laboratoire de Physique des Metaux Synthétiques, 17 Rue des Martyrs, 38054 GRENOBLE, France

^cFaculty of Chemistry, Warsaw Technical University, ul. Noakowskiego 3 00-664 WARSZAWA, Poland

Abstract: Wave dispersed Kerr ellipsometry technique is used for the determination of real n_2' and imaginary κ_2 parts of nonlinear index of absorption n_2 of regio-regular poly(3-octylthiophene) in solution. A strong two photon absorption is observed at pump and probe energy, corresponding to a two photon state lying at 3.4 eV above the fundamental level. The measured two photon absorption coefficient is quite large. For an 11.2 g/l solution a two photon absorption coefficient $\beta = 0.85$ cm/GW is observed, corresponding to the bulk material value of 76 cm/GW. Corrected for polymer chain disorder it gives a large value of $\beta_{\text{corr}} = 380$ cm/GW. The results are compared with those obtained for a statistical poly(3-octyl thiophene) and by third harmonic generation technique.

Keywords: two photon absorption, nonlinear index of refraction, Kerr ellipsometry, poly(octyl thiophene) regioregular, third harmonic generation

INTRODUCTION

Conjugated, quasi one dimensional polymers exhibit large third order nonlinear optical response due to the π electron delocalization. Moreover, the strong electron-electron correlations in these systems shift the two photon allowed states below the one photon states. The presence of a two photon state in the optical gap of these materials is interesting from the point of view of application of these materials in optical limiting via two photon - and excited state absorption. These materials are transparent at low light intensity and become absorbing at high fluences.

In this paper we present the two photon absorption characterization of a regio-regular poly(3-alkylthiophene) (PAT) studied by the wave dispersed Kerr ellipsometry technique in solution. The measurements are compared with the results of third harmonic generation on solution cast thin films and with two photon absorption measurements on a statistical counterpart.

POLYMER SYNTHESIS

Several methods of the synthesis of poly(3-alkylthiophenes) have been developed in the last 15 years, the majority of them being non-regiospecific¹⁻³. However recently two methods leading to regiochemically defined poly(3-alkylthiophenes) have been proposed. Chen *et al*⁴⁻⁶ obtained PATs with 98% regioregularity via polycondensation of 2,5-dibromo-3-alkylthiophene in the presence of active zinc. Alternatively McCullough *et al*⁷⁻⁹ used 2-bromo-3-alkylthiophenes which after lithiation at the 5 position and the transformation into the Grignard reagent condensed regiospecifically to P3ATs.

In this research we have used a modification of the method developed by McCullough and coworkers. The reaction sequence leading to regioregular poly(3-octylthiophene) is schematically shown below (Scheme 1).

3-octylthiophene was obtained from 3-bromothiophene (97 % Aldrich) by Grignard coupling in the presence of Ni(dppp)Cl₂ (Aldrich)⁴. Then it was brominated in the 2 position using N-bromosuccinimide (NBS) (Merck) in DMF as the brominating agent. In this step we have slightly modified the original procedure of McCullough since the bromination with NBS gives better yields⁵ than the bromination with Br₂ in acetic acid⁴. In the next step 2-bromo-3-octylthiophene was lithiated in the 5 position using lithium diisopropylamide (LDA). The lithiation with this reagent carried out at low temperatures is very selective⁷⁻⁸. Lithium was then substituted with the MgBr group and the resulting Grignard reagent condensed regiospecifically to P3HT. The detailed description of the polymerization can be found in Ref. 8.

The resulting polymer showed number average molecular weight $M_n=18700$ and the polydispersity index $P_i=1.68$. Its optical absorption spectrum in THF solution is shown in Fig. 1. With respect to the usual poly(3-alkylthiophenes) the maximum

absorption wavelength is red shifted indicating a larger π electron conjugation in the present case.

OPTICAL KERR EFFECT

Under the action of the external electric field the medium nonlinear index of refraction varies linearly with the light intensity I :

$$n = n_0 + n_2 I \quad (1)$$

where n_0 and n_2 are the medium linear and nonlinear indices of refraction, respectively. The nonlinear index of refraction n_2 is linked to the medium optical Kerr susceptibility $\chi^{(3)}(-\omega; \omega, -\omega, \omega)$ through the following relation

$$n_2 = \frac{3\chi^{(3)}(-\omega; \omega, -\omega, \omega)}{4\varepsilon_0 n^2 c} \quad (2)$$

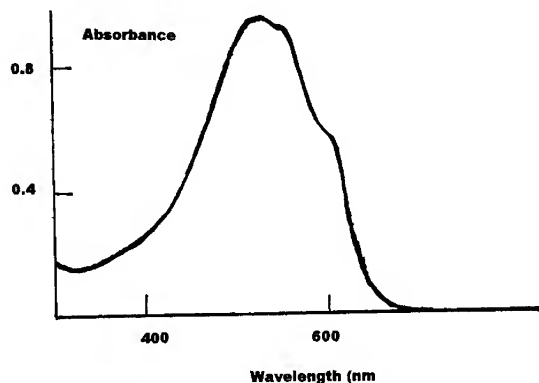
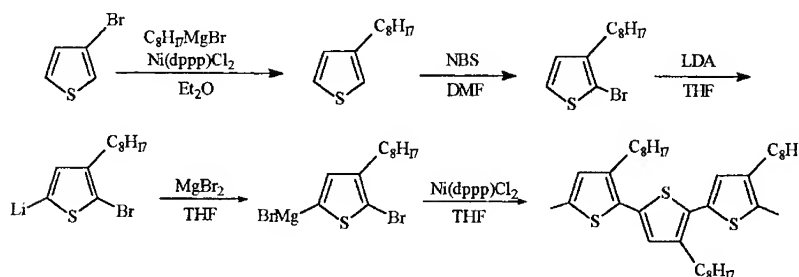


FIGURE 1. Optical absorption spectrum of regioregular poly(3-octylthiophene) in THF solution.

As the Kerr susceptibility $\chi^{(3)}(-\omega; \omega, -\omega, \omega)$ and the linear index of refraction are, in general, complex, the nonlinear index of refraction n_2 will be complex too. Consequently it can be

written in the following form $n_2 = n_2' + i\kappa_2$, where n_2' is the real part and κ_2 is the imaginary part of the nonlinear index of refraction. The presence of an imaginary part in n_2 leads to the incident light absorption, called two photon absorption which is described by the imaginary part of coefficient β given by

$$\beta = \frac{2\pi\kappa_2}{\lambda_0} \quad (3)$$



SCHEME 1.

Consequently the output light intensity is given by

$$I_{out} = I_{inc} e^{-(\alpha + 2\beta' I)x} \quad (4)$$

where α , is linear absorption coefficient, x is the medium thickness and I_{out} is the actual light intensity (at point x).

KERR ELLIPSOMETRY

Several experimental techniques have been developed for the measurements of the nonlinear index of refraction. One of the is the Kerr Ellipsometry technique¹⁰⁻¹⁴, which is a useful tool to measure the medium nonlinear index of refraction n_2 and its frequency dependence. It is a Pump-Probe experiment. It permits temporal and spectral resolution of dichroism and birefringence induced by high intensity fields. Delays up to about 1.5 ns and spectral resolution covering the 450-1500 nm range are possible.

The experimental set-up used in Kerr ellipsometry technique is shown schematically in Fig. 2. It consists of a 1064 nm-Nd:YAG laser with pulse duration of 33 ps and repetition rate of 8 Hz. The beam with pulse energy of about 10 mJ is split into two equal parts. One, the pump, is attenuated with neutral filters, horizontally polarised and send onto the sample with an angle of approximately 20° of the probe beam. The other one, the probe, is focused into a 10-cm long cell filled with a D_2O - D_3PO_4 solution and giving a broad light emission spectrum in near-IR and visible by self-phase modulation and Raman effects. Subsequently the probe passes through a Kerr gate. The sample is oriented along

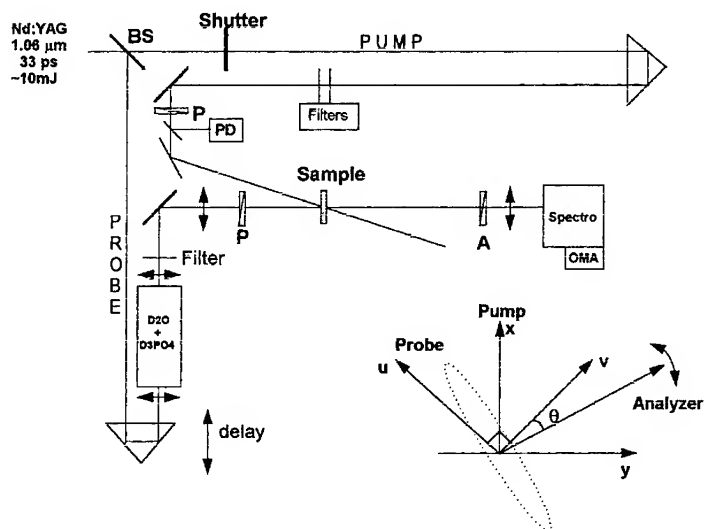


FIGURE 2. Experimental set-up for Kerr ellipsometry. Inset shows the probe polarisation at 45° of the pump polarisation before passing through the sample and after (dotted ellipse).

neutral axis of the cell between the polariser and the analyser. The polarisation of the probe is at 45° of the pump at the entrance of the gate.

The probe signal is analysed around the extinction angle and sent into an Optical Multichannel Analyser (OMA) which amplifies the visible part of the spectrum. Spectral resolution is 0.52 nm/pixel in 450-900 nm range and 3.2 nm/pixel in 950-1500nm range. A variable delay line on the trajectory of the probe, analyser and shutters are computer controlled. Intensity measurements are averaged over 100 shots for each angle.

The pump of intensity I_p , polarised at 45° of the probe, instigates a transient optical anisotropy which induces a depolarisation of the probe beam. The intensity of transmitted signal I_t for small angles θ around the extinction is given by, for each probe wavelength λ_t :

$$I_t \approx I_{inc} e^{-\alpha l} e^{-2\phi_0''} \left((\theta - \phi')^2 + \phi'^2 \right) \quad (5)$$

where ϕ_0'' is the imaginary part of the mean induced absorption and ϕ'' (resp. ϕ') is the imaginary (resp. real) part of the induced anisotropy.

$$\phi = \frac{3\pi}{2\varepsilon_0 \lambda_t n_t n_p c} \text{Im} \left(\chi_{yyyy}^{(3)}(-\omega_t; \omega_p, -\omega_p, \omega_t) - \chi_{yyxx}^{(3)}(-\omega_t; \omega_p, -\omega_p, \omega_t) \right) \quad (6)$$

where the imaginary part of ϕ is the induced dichroism, expressed as a difference of absorption in two perpendicular directions and real part of ϕ is the induced birefringence. These are linked to the third-order susceptibility tensor $\chi_{yyyy}^{(3)}(\omega_t, \omega_p, -\omega_p, \omega_t)$ ($i=x$ or y).

$I_{inc} e^{-\alpha l} e^{-2\phi_0''}$ is the transmitted probe intensity through the sample with thickness l , n_t and n_p are indices of solution at probe (t) and pump (p) wavelengths, respectively.

In the case of a pump and probe parallel experiment, the absorption α is expressed as $\alpha = \alpha_0 + 2\beta'' I_p$ where α_0 is the linear absorption and

$$\beta'' = \frac{3\pi}{\varepsilon_0 \lambda_t n_t n_p c} \text{Im}(\chi_{xxxx}^{(3)}) \quad (7)$$

If we assume that our molecules are quasi-one dimensional then

$$\chi_{xxxx}^{(3)} = 3\chi_{yyxx}^{(3)} \quad (8)$$

From equations (6) - (8) one gets

$$\beta^* = \frac{3\varphi}{l \cdot I_p} \quad (9)$$

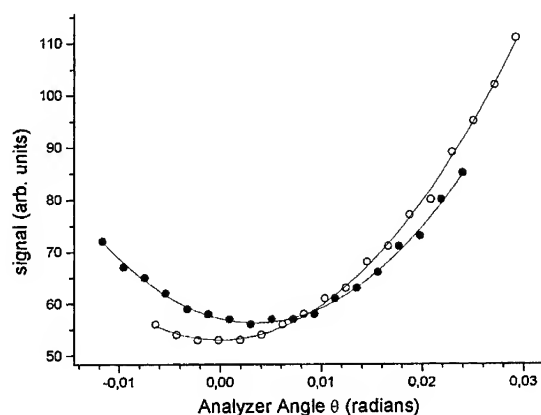


FIGURE 3. Typical signal intensity dependence versus analyser angle at the pixel corresponding to 900 nm wavelength for the DBANS molecule. Open circles (resp. solid circles) correspond to signal without (resp. with) the pump beam. Solid lines are fits, calculated with Equation 5.

Figure 3 shows the dependence of transmitted intensity with analyser angle around extinction. Smooth parabolas are obtained after many shots. The minima of parabolas for each wavelength is extracted from fits of experimental points. It gives an accurate and absolute determination of $\langle \text{Im}(\varphi) \rangle$ as function of wavelength λ . The average of the transmission of expression (5) over many shots is given by:

$$\langle T \rangle = \left(\langle \text{Im}(\varphi) \rangle - \alpha \right)^2 + \langle \text{Re}(\varphi)^2 \rangle + \sigma^2 \left(\langle \text{Im}(\varphi) \rangle \right) \quad (10)$$

where σ is the standard deviation.

Introducing a quarter-wave plate in the Kerr gate inverts $\text{Im}(\varphi)$ and $\text{Re}(\varphi)$ in Equation (5). Consequently one can measure the sign of both real and imaginary parts of

nonlinear index of refraction n_2 . The wave dispersed real and imaginary parts of two photon absorption coefficients as function of the probe beam energy (pump wavelength $\lambda_p = 1064$ nm) are shown in Fig. 4 for the studied regioregular poly(3-octylthiophene).

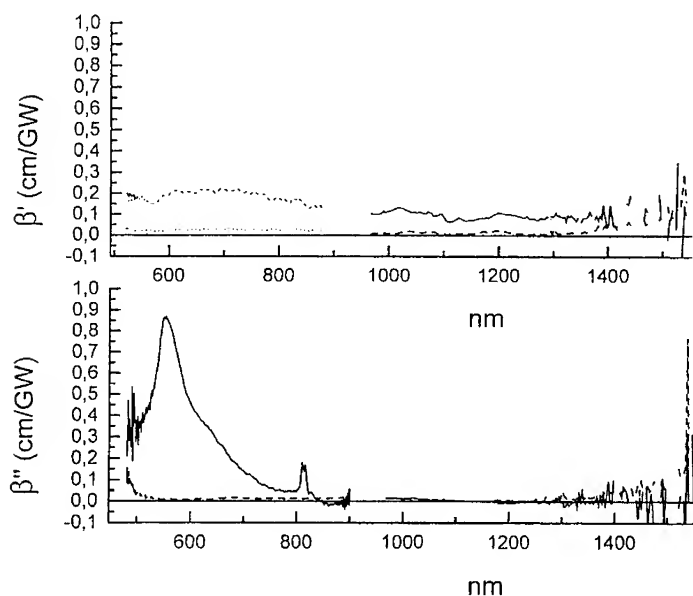


Figure 4. Wavelength dependence of real (a) and imaginary (b) parts of two photon absorption coefficient versus the probe energy (bottom axis) in 11.2 g/l solution of regioregular poly(3-octyl thiophene) in THF.

RESULTS AND DISCUSSION

The regioregular poly(3-octylthiophene) was dissolved in tetrahydrofuran (index $n=1.4$) with the concentration of 11.2 g/l. The solution was contained in 1 mm thick spectroscopic quality liquid cell. The maximum of optical absorption wavelength in THF (cf. Fig. 1) is 550 nm.

The wave dispersed spectra of measured real and imaginary parts of two-photon absorption coefficient β (real and imaginary parts), displayed in Fig. 4, show a strong

enhancement of β'' at 730 nm of pump + probe wavelengths. It corresponds to a tw photon level lying at 365 nm above the fundamental state, thus above the one photon allowed excited state (cf. Fig. 1). The observed maximum value is $\beta''_{\max} = 0.85$ cm/GW (cf. Fig. 4) is compared with those obtained for another conjugated molecules in Table 1. The real part β' undergoes also an oscillation around the 730 nm pump+probe wavelengths, characteristic for a resonance. A shoulder in β' spectrum is seen at 620 nm, which may be a printout of another two photon state, lying closer to the one photon state, or a vibronic contribution. The second peak in β'' at 805 nm is a Raman resonance.

TABLE 1. Two photon absorption coefficients for different molecules and extrapolated bulk values.

Molecule	β' (cm/GW)	λ_{\max} nm	λ_{β} nm	concent. g/l	solvent	bulk value (cm/GW)	Ref.
DR 1	0.8	490	835	70	THF	11.4	15
DBANS	1.1	450	808	70	THF	15.7	15
DCNP	0.06	460	920	30	THF	2.3	16
DEANST	0.64	440	920	105	THF	6.1	17
DCM	0.1	480	950	11	DMSO	9.1	17
PDA-PTS	80	620	1064 not max of λ_{β}	bulk	single crystal	80	18
PDA-PTS	800	620	925	bulk	single crystal	800	19
poly(octyl thiophene)	0.27	435 (142)	720 (94)	25	THF	9.6	13
poly(octyl thiophene) regioregular	0.85	550 (170)	730 (70)	11.2	THF	76	pres. study

λ_{\max} corresponds to the maximum linear and λ_{β} to the maximum nonlinear absorption wavelengths, respectively.

The solution value may be easily extrapolated to the bulk material value by using the following relationship:

$$\beta = N_p F_p \beta_p + N_s F_s \beta_s \quad (12)$$

where N_p and N_s are number density of solute (p) and solvent (s), respectively and F_p and F_s are corresponding local field factors. These can be expressed in terms of average molecule density $d(C)$, solvent (M_s) and solute (M_p) molecular masses giving for the solution cubic susceptibility the following expression

$$\beta(C) = \frac{F(C)d(C)N_A}{1+C} \left\{ \frac{C(\delta'_p + i\delta''_p)}{M_p} + \frac{\delta'_s}{M_s} \right\} = \beta' + i\beta'' \quad (13)$$

where C is the mass concentration ($C = m_p/(m_p + m_s)$) and δ is the two photon absorption coefficient at molecular level. F is the local field factor

$$F = \left[\frac{(n_s^2 + 2)}{3} \right]^2 \left[\frac{(n_p^2 + 2)}{3} \right]^2 \quad (14)$$

where n is the solution refractive index at pump (n_p) and probe (n_s) wavelengths, respectively

In Equation 13 we have assumed *a priori*, that the two photon absorption coefficient of solvent is real, as it is expected in the measurement wavelength range. Moreover, for the studied concentration δ_s can be neglected with respect to δ'_p . Consequently the bulk material value for the two photon absorption coefficient is given by

$$\beta(C = \infty) = \frac{1+C}{C} \beta(C) \quad (15)$$

with

$$C = C_v d_s \quad (16)$$

where C_v is the usually used concentration of solute mass per solvent volume (g/cm^3 in esu). Thus it follows from equation (15) that the bulk value $\beta(C = \infty) = 76 \text{ cm/GW}$. This is a very large value, as it is seen from comparison with other molecules (cf. Table 1). Moreover, if we take into account the fact that in solution polymer chains are randomly oriented and from 81 components of δ tensor only those in polymer chain direction $\times \delta_{xxx}$ is enhanced and the other can be neglected we obtain from the following relation $\langle \delta \rangle = 0.2 \delta_{xxx}$ where $\langle \rangle$ denotes orientational average over all chain orientations. Correcting for orientation disorder we obtain a huge two photon absorption coefficient for

a single crystal (or monooriented structure): $\beta_{xxxx} = 380$ cm/GW in the polymer chain direction X in the laboratory reference frame XYZ. This value is half of that reported by Stegeman et al¹⁹ for a PTS single crystal and also in the polymer chain direction. It shows that the conjugated polymers represent a great potential for applications in optical limiting.

CONCLUSIONS

The Kerr ellipsometry technique is a useful tool for the study of wavelength variation of two (and/or excited state) absorption coefficients of molecules in solutions, but it may be also used for thin films. Contrary to harmonic generation process no nonlinear interference is used in Kerr ellipsometry technique. Consequently the signs of both real and imaginary parts can be determined. In harmonic generation experiments usually the sign of imaginary part is undetermined, as the reference is characterized usually by real and positive cubic susceptibility. The knowledge of the frequency variation of nonlinear optical coefficients gives insight to the electronic structure of molecules as well as transition dipolar moments. It allows to determine the sequence of excited states, transition dipolar moments between fundamental and excited states as well as between excited states.

For the studied regioregular poly(3-octylthiophene) we observe a large two photon absorption coefficient of 0.85 cm/GW for a 11.2 g/l solution in THF. Extrapolated to bulk material and corrected for chain disorder it leads to a huge two photon absorption coefficient $\beta'' = 380$ cm/GW for a monooriented structure, comparable to that observed in PTS single crystal. Although obtaining of monooriented structures is not very simple, even in the case, much easier to realize and not needing a use of polarizer for protection of a planar disorder (all polymer chains parallel to a plain) we can expect a still large two photon absorption coefficient $\beta''_p = 140$ cm/GW as in that case the orientational average (cf. Equation (17)) is given by $\langle \delta \rangle = \frac{3}{8} \delta_{xxx}$. We note also about one order of magnitude larger value of β'' for poly(3-octylthiophene) regioregular with respect to the statistical one (cf. Table 1). This increase is not only due to the larger conjugation in the first one, but also to the narrowing of β'' spectrum (cf. Table 1). Third harmonic generation measurements performed at 1907 nm fundamental wavelength on solution cast thin films give also a larger $\chi^{(3)}(-3\omega; \omega, \omega, \omega)$ susceptibility for poly(3-octylthiophene) regioregular

($\chi^{(3)}(-3\omega; \omega, \omega, \omega) = 4.9 \times 10^{-11}$ esu compared to $\chi^{(3)}(-3\omega; \omega, \omega, \omega) = 0.8 \times 10^{-11}$ esu for a statistical poly(3-decylthiophene). Although we expect a stronger 3 photon resonance enhancement in the first case, surely larger π electron conjugation in regioregular poly(3-alkylthiophenes) leads to higher $\chi^{(3)}$ values too. A more detailed analysis of these two experiments via multilevel quantum models is in progress.

ACKNOWLEDGEMENTS

A part of this study was funded by French Embassy in Warsaw and Komitet Badan Naukowych (KBN). Financial contribution of both institutions is kindly acknowledged.

REFERENCES

1. J. Roncali, *Chem. Rev.*, **711**(1992).
2. R. Sugimoto, S. Takeda M. B. Gu and K. Yoshino *Chem. Express*, **1**, 635(1986).
3. K. Y. Jen, G. G. Miller and R. L. Elsenbaumer *J. Chem. Soc., Chem. Commun.*, 1346(1986).
4. T.-A. Chen and R. D. Rieke, *J. Am. Chem. Soc.*, **114**, 1087(1992).
5. T.-A. Chen and R. D. Rieke; *Synth. Met.*, **60**, 175(1993).
6. T.-A. Chen, A O'Brien; and R. D. Rieke, *Macromolecules*, **26**, 3462(1993).
7. R. D. McCullough, S. P. Williams, S. Tristram-Nagle, M. Jayaraman, P. C. Ewbank and L. Miller; *Synth. Met.*, **69**, 279(1995).
8. R. D. McCullough, R. D. Lowe, M. Jayaraman and D. L. Anderson, *J. Org. Chem.*, **58**, 904(1993).
9. R. D. McCullough and R. D. Lowe; *J. Chem. Soc., Chem. Commun.*, 70(1992).
10. C. Soucy-Breau, A. MacEachern, L. C. Leitch, T. Arnason and P. Morand; *J. Heterocycl. Chem.*, **28**, 411(1991).
11. N. Pfeffer, F. Charra and J. M. Nunzi, *Opt. Lett.*, **16**, 1987(1991).
12. N. Pfeffer, P. Raimond, F. Charra and J. M. Nunzi, *Chem. Phys. Lett.*, **201**, 357(1993).
13. Pfeffer N., Variations de l'indice de réfraction complexe induites optiquement dans les composés organiques, Thesis, University Paris-Nord, Villetanneuse 1994.
14. Pang Y., M. Samoc and P. N. Prasad, *J. Chem. Phys.*, **94**, 5282(1991).
15. S. Delysse, J. M. Nunzi, P. Raimond and F. Kajzar, *Nonlinear Spectroscopy in Conjugated Molecules, in Electrical and Related Properties of Organic Solids*, R. W. Munn, B. Kuchta and A. Miniewicz, Eds, NATO ASI Series, vol. 24, Kluwer Academic Publishers, pp. 339-358.
16. A. Miniewicz, S. Delysse, J.-M. Nunzi and F. Kajzar, *Chem. Phys. Lett.*, **287**, 17(1998).
17. S. Delysse, Thesis, Université Orsay, 1997.
18. J. M. Nunzi and F. Charra, *Pure Appl. Opt.*, **7**, 501(1998).
19. W.E. Torruellas, B.L. Lawrence, G.I. Stegeman and G. Baker, *Opt. Lett.*, **21**, 1777(1996).

DISPERSION OF OPTICAL POWER LIMITING IN STILBENE 3 SOLUTIONS

PIERRE-A. CHOLLET, VINCENT DUMARCHER, JEAN-M. NUNZI
CEA (LETI-Technologies Avancées), DEIN/SPE, 91191 GIF Cedex (France)

PATRICK FENEYROU*, PATRICE BALDECK
Laboratoire de Spectrométrie Physique, Université J. Fourier, CNRS (UMR 5588),
BP 87, 38402 Saint Martin d'Hères, Cedex (France)

Abstract Optical power limitation has been determined in concentrated stilbene3 solutions in the visible range. The measurements were made using nanosecond laser pulses in the visible range. It appears that the dominant nonlinear absorption was the cubic one $\beta_3 I^3$. The chromatic dispersion of β_3 reveals a strong resonance centered around 600 nm ($\beta_3^{\max} = 1800 \text{ cm}^3/\text{GW}^2$) and a weaker one around 500 nm. A simulation of a device using this molecule in a bottle neck configuration shows that limitation for eye protection (0.5 μJ) can be achieved.

INTRODUCTION

Considerable interest has arisen during the last years in materials which possess optical limiting properties, to control the intensity or the pulse energy of laser beams for eye and photo-detector protection.¹ This is the reason for seeking for colorless materials which are transparent at low energy, and absorbing in the whole visible range for microjoule pulse energy. Materials with two-photon absorption meet this first requirement, but the nonlinear absorption is rather low. By combining two-photon absorption with re-absorption toward excited states of higher energy, it has been possible to approach the above specifications in the nanoseconde regime,² but in a restricted wavelength range. Broadband limiting can be obtained in principle by mixing several kinds of molecules having efficient limiting properties in one part of the visible range.³

*Present address : Laboratoire Central de Recherches, THOMSON CSF,
Domaine de Corbeville 91404 ORSAY Cedex (FRANCE)

An alternative is to look for molecules possessing broadband limiting properties, since the blend of molecules is not always achievable in a solvent or solid matrix.

In this paper we report on preliminary results on the optical limiting properties of a conjugated molecule (stilbene 3) dissolved at high concentration (300 g/l). Intensity-dependent transmission spectra are characterized in the 450-650 nm wavelength range with a nanoseconde tunable laser system. The dispersion of nonlinear absorption coefficients is obtained in the framework of gaussian collimated beam propagation in thin nonlinear sample. Then, the nonlinear transmission of this molecule is evaluated for a high focusing geometry that simulates a realistic device.

EXPERIMENTAL SETUP AND PROCEDURE

Molecule studied

The Stilbene 3 molecule structure is represented in Figure 1. Stilbene3 molecules (purchased from LambdaPhysik) were dissolved in spectroscopic DMSO (300 g/l), and the solution filtered successively on PTFE 5 μm and 0.5 μm .

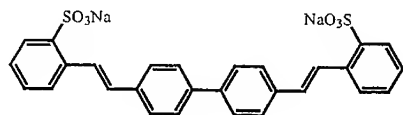


FIGURE 1 Scheme of the Stilbene 3 molecule

The transmission spectrum of a stilbene 3 solution (300g/l in DMSO) is represented in Figure 4).

Optical power limiting experimental setup and procedure

The power limiting measurements were made in the visible range with the experimental setup represented in Figure 2. A nanosecond pulsed Nd:YAG laser (Quantel Brilliant B) is tripled to pump an OPO single path laser using 2 BBO crystals (OPOTEK), which delivers at 10 Hz repetition rate pulses in the wavelength range 450-650 nm. The pulse

energy is typically 10 mJ. The beam is focused in a liquid cell (thickness : 2 or 10 mm) with a 50 or 100 mm focal lens. The beam waist w_0 (typically $\sim 500 \mu\text{m}$) was measured at the sample location by the razor blade edge method. The time dependence of the pulses (2.6 ns FWHM) was determined using a fast photodiode. The energy of the incident and transmitted pulses were continuously recorded by calibrated pyroelectric detectors. The incident pulse energy could be varied from 0 to 10 mJ (with 50 μJ steps) by rotating a broad band half-wave plate between two polarizers. The whole experiment was computer controlled with a data acquisition board for recording the energies.

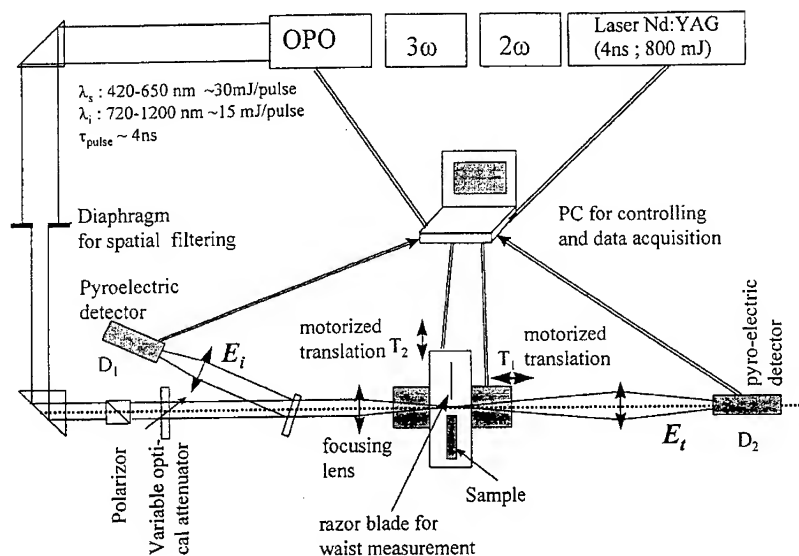


FIGURE 2 Experimental setup for optical power limiting measurements

Optical power limiting in stilbene3 solutions

A typical variation of the transmitted pulse energy E_t versus incident energy E_i is reported in Figure 3 for a 2 mm thick cell, inside which the beam is collimated.

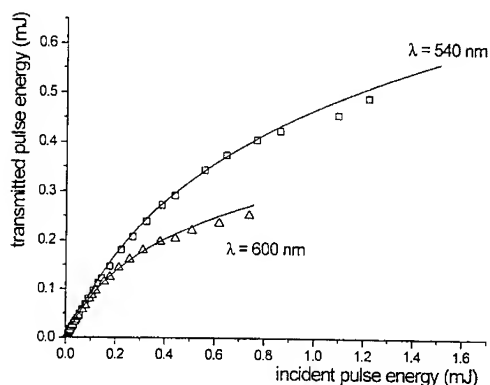


FIGURE 3 Optical power limiting in a 2 mm thick sample of stilbene3 solution (300 g/l), at two different wavelength. Waist ($HW1/e^2M$): 200 μm . Pulse FWHM: 2.6 ns. The fits (continuous curves) are calculated with the following parameters : $\lambda = 540$ nm $\beta_2 = 395$ cm³/GW² ; $\lambda = 600$ nm $\beta_2 = 1730$ cm³/GW² ; The dependence in β_1 is not detectable if β_1 smaller than 10 cm/GW.

In Figure 4 is shown the transmission in a thicker cell (10 mm), as a function of wavelength, for different incident pulse energies.

OPTICAL LIMITING FOR A GAUSSIAN COLLIMATED BEAM

When submitted to intense laser pulses lasting some nanoseconds in their transparent domain, molecules are excited via two-photon absorption and then the two photon state absorbs to higher excited levels. This is a complex process which involves state populations and transition probability between different levels, including triplet states. When the processes are much faster than the pulse duration, they can be described from a phenomenological point of view by introducing effective two- and three-photon absorption coefficients β_1 and β_2 . In the case of samples thinner than the Rayleigh length, the beam can be considered as collimated inside the sample and the calculation of the absorption is rather straightforward. When the beam is focusing inside the sample, the calculation is much more complicate and can only be performed by using beam propagation methods.⁴⁻⁶

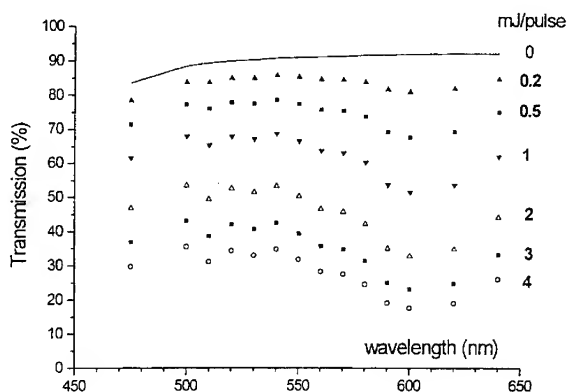


FIGURE 4 Transmission of a 1cm thick cell of stilbene3 (300 g/l in DMSO) for different pulse energy. (beam waist $\sim 500 \mu\text{m}$). The continuous line is the linear transmission.

If we assume that the laser beam has an axial symmetry around the propagation direction z , the optical limiting can be described from a phenomenological point by the following equation :

$$\frac{dI}{dz} = -\beta_1 I^2(r, z, t) - \beta_2 I^3(r, z, t) \quad (1)$$

where z is the propagating direction and r the distance to the center of the beam. In the case where the different level populations do not change (ps time domain), β_1 and β_2 can be connected with the two and three photon absorptions. In the cases where either β_2 or β_1 are equal to zero, the solutions of Equation (1) are respectively :

$$\frac{1}{I(r, L, t)} - \frac{1}{I(r, 0, t)} = \beta_1 L \quad (2)$$

$$\text{and} \quad \frac{1}{I^2(r, L, t)} - \frac{1}{I^2(r, 0, t)} = 2\beta_2 L \quad (3)$$

The general solution of Equation (1) is given by :

$$\left(\frac{1}{I(r,L,t)} - \frac{1}{I(r,0,t)} \right) + \frac{\beta_2}{\beta_1} \text{Log}_e \frac{I(r,L,t)}{I(r,0,t)} - \frac{\beta_2}{\beta_1} \text{Log}_e \frac{\beta_1 + \beta_2 I(r,L,t)}{\beta_1 + \beta_2 I(r,0,t)} = \beta_1 L \quad (4)$$

where L is the sample thickness.

In our experiments we detect the energy of the incident and transmitted pulses, namely:

$$E(z) = \int_{-\infty}^{+\infty} dt \int_0^{\infty} 2\pi r I(r,z,t) dr \quad (5)$$

with $z = 0$ for the incident energy E_i and $z = L$ for the transmitted one E_t . Experimental determination of the transverse map of the beam (by the razor blade method) and time variation by a fast photodiode show that the pulses have a gaussian space and time variations :

$$I(r,t) = \frac{2}{\pi w^2} e^{-\frac{2r^2}{w^2}} \times \frac{2\sqrt{\text{Log}_e 2}}{\sqrt{\pi \Delta t}} e^{-4(\text{Log}_e)(\sqrt{\Delta t})^2} E_i \quad (6)$$

In the two above equation, w is the beam waist ($\text{HW1/e}^2 M$, $\sim 200 \mu\text{m}$ in our case), Δt the temporal FWHM (2.6 ns in our case) and r the distance from beam axis. The other symbols have their usual meanings.

Since $I(r,0,t)$ is linearly connected with the incident energy E_i at the entrance face (cf. Equation (6), and that E_t is linearly connected with $I(r,z,t)$ at the exit face (cf. Equation(5)), the dependence, at low energy the dependence of E_t versus E_i is similar as the dependence of $I(r,z,t)$ versus $I(r,0,t)$. In that case the energy transmission coefficient

$$T_E = \frac{E_t}{E_i} \text{ has the same behavior as the intensity transmission coefficient } T_I = \frac{I(r,z,t)}{I(r,0,t)}$$

whose values are respectively given by :

$$\text{for only } \beta_1 \neq 0: \quad T_I = 1 - \beta_1 L I(r,0,t) \quad \text{or} \quad \frac{1}{T_I} = 1 + \beta_1 L I(r,0,t) \quad (7)$$

$$\text{for only } \beta_2 \neq 0: \quad T_I = 1 - \beta_2 L I^2(r,0,t) \quad \text{or} \quad \frac{1}{T_I} = 1 + \beta_2 L I^2(r,0,t) \quad (8)$$

Consequently the transmission variation at low energy is completely different according to the kind of non-linear absorption : it is quadratic with a derivative close to zero, the absorption is essentially governed by β_2 and of course with increasing energy this behavior will become more pronounced ; the variation is linear if β_1 dominates. However

in this latter case it is not possible to draw conclusion for higher energies, since the behavior depends on the relative values of β_1 and $\beta_2 I$.

DETERMINATION OF THE NON-LINEAR ABSORPTION COEFFICIENTS

The non-linear absorption coefficients β_1 and β_2 were determined at different wavelength by a least square procedure performed on the experimental curves $E_t = f(E_i)$ using the equations (4-6). This was done on 2 mm thick cell in order to ensure the collimation of the beam inside the cell. The beam parameters are given in the caption of figure 3. It proved that the convergence of the least square procedure did not depend upon β_1 provided its value was smaller than 10 cm/GW, but was very dependent on β_2 . We can only give an upper limit of β_1 (10 cm/GW). A confirmation of this behavior is given by the variation of $1/T$ versus E_i which is clearly quadratic as shown in figure(5), in accordance with equation(8).

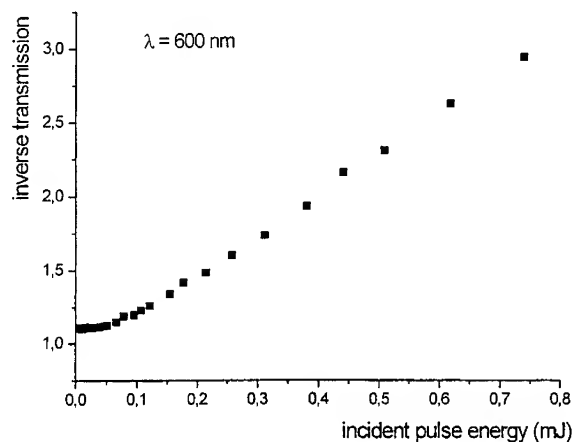


FIGURE 5 Inverse transmission versus incident pulse energy

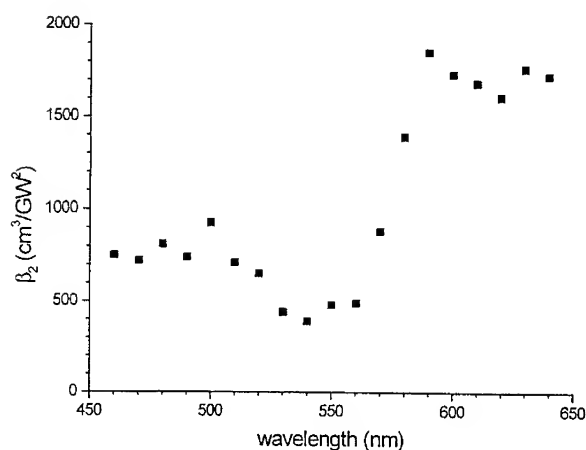


FIGURE 6 Dispersion of β_2 in a stilbene3 solution (300 g/l) in DMSO.

The chromatic dispersion of β_2 is represented in figure 6. It reveals a strong resonance in the red range and a weaker one in the blue one. This results in a large band optical power limiting, as already shown in figure 4. The microscopic origin determination at the molecular scale is in progress

Calculation of nonlinear transmission for a realistic device geometry

The above experiments enable the determination of the nonlinear absorption coefficients. For this purpose the laser beam was collimated or weakly focused as in figure 3. We have calculated using a Beam Propagation Code⁶ the limitation in the case of tight focusing (waist : 6 μm) in a thick cell (10 mm) using the following parameters: $\beta_1 = 10 \text{ cm/GW}$ and $\beta_2 = 5000 \text{ cm}^3/\text{GW}^2$. These values imply that the molecules are at the maximum concentration, for instance in a liquid phase, for instance by grafting small lateral aliphatic chains. This curve (figure 7) shows that the eye protection (0.5 μJ) can be obtained.

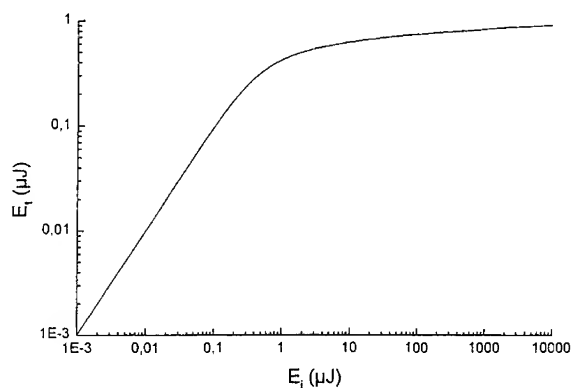


FIGURE 7 Optical limitation in a tight focusing configuration : waist 6 μm ;
 $\beta_1 = 10 \text{ cm/GW}$; $\beta_2 = 5000 \text{ cm}^3/\text{GW}^2$

CONCLUSION

We have determined the nonlinear absorption coefficients of stilbene 3 molecules in the visible range in the nanosecond regime. The fits have revealed that the nonlinear absorption is dominated by the cubic term $\beta_2 I^3$ which is likely to originate from a two photon absorption followed by a reabsorption of the excited states. Experiments are in progress to study more closely this mechanism. We have observed a strong resonance around 600 nm and a weaker around 500 nm. A model extrapolated to a liquid phase of stilbene 3 molecules has shown that eye protection (0.5 μJ) can be achieved with this molecule.

ACKNOWLEDGMENTS

This work was partially supported by DGA (Délégation Générale pour l'Armement, Contrat DGA n°95 417). Thanks are due to S. Lameau for experimental assistance.

REFERENCES

1. Materials for Optical Limiting II, San Francisco, Ca, U.S.A. 03.31-04.02, 1997, edited by R. Sutherland et al., Material Research Society, Symposium Proceedings vol.479, Pittsburgh PA 1997.
2. J. Perry, Opt. Lett., 22, 1843 (1997).
3. X.L. Wu et al., Material Research Society, 479 (ref.1), 103 (1997).
4. J.A. Hermann, R.G. McDuff, J.Opt.Soc.Am. B, 10, 2056 (1993).
5. J.A. Hermann, J.Opt.Soc.Am.B, 14, 814 (1997).
6. P. Feneyrou, this issue (1998).

ENGINEERING OF TRANSPARENT DIPHENYLPOLYENE DERIVATIVES FOR OPTICAL POWER LIMITING AT VISIBLE WAVELENGTHS

CHRISTELLE NGUEFACK,[†] THOMAS ZABULON,[†] RÉMI
ANÉMIAN,[†] CHANTAL ANDRAUD,[†] ANDRÉ COLLET,[†]
SUAT TOPÇU,[#] AND PATRICE L. BALDECK[#]

[†] École Normale Supérieure de Lyon, Stéréochimie et Interactions moléculaires,
UMR CNRS n° 117, 69364 Lyon cedex 07, France

[#] Spectrométrie Physique, Université Joseph Fourier, CNRS (UMR 5588), B.P.
87, 38402 St Martin d'Hères, France

Abstract. Enhancement of two-photon absorption (TPA) by excited-state absorption (ESA) has been studied for seven diphenylpolyene derivatives at visible wavelengths. Semi-empirical calculations indicate that these molecules have wide-band TPA and ESA, hence enhanced nonlinear absorption, at visible wavelengths. In addition, giant nonlinear absorption can be obtained for push-pull and bis-donor symmetrical molecules if their strong TPA and ESA resonances overlap. As predicted, the nonlinear absorption of these compounds, characterized with nanosecond laser pulses at $\lambda = 600$ nm, is dominated by ESA. The nonlinear coefficients a_3 are in the range 25 to 7200 cm³ GW⁻² for concentrations normalized at 1 kg L⁻¹. These results confirm that several orders of magnitude in nonlinear absorption can be gained by an appropriate molecular design.

Keywords: Two-photon absorption; optical power limiting; excited state absorption

INTRODUCTION

Photoactive materials are of great interest for the protection of sensors and eyes from intense laser radiation.¹⁻³ For nanosecond time-duration pulses, optical power limiting can be obtained by nonlinear absorption processes, such as reverse saturable absorption (RSA) and two-photon absorption (TPA). TPA offers several advantages: it uses colorless materials, allowing high transmission at low incident intensities, and presents no absorption saturation at the highest intensities. However, TPA still has a power-limiting threshold significantly higher than RSA.

Recently, several papers have proposed new organic systems with improved TPA properties.⁴⁻¹³ Bis-donor diphenylpolyene derivatives are presently the transparent organic molecules showing the best TPA response. Following the TPA step, the molecules may have additional transient absorption during their excited-state lifetime. Thus, excited-state absorption (ESA), such as singlet-singlet absorption or triplet-triplet absorption, may also be used to enhance the nonlinear absorption of molecules in the nanosecond time regime.¹⁴⁻¹⁹

In the case of TPA followed by a singlet absorption S_1 - S_n , and when the laser pulse lasts longer than the excited-state lifetime τ_{10} , the material nonlinear absorption is given by:

$$\alpha(I) = \alpha_2 I + \alpha_3 I^2 = \alpha_2 I + \frac{\alpha_2 \tau_{10} \sigma_{1n}}{\hbar \omega} I^2 \quad (1)$$

where α_2 is the two-photon absorption coefficient, α_3 is the three-photon absorption coefficient, σ_{1n} is the excited-state absorption cross-section, τ_{10} is the excited-state lifetime, ω is the laser pulsation, and I is the laser intensity in the sample.

The role of the molecular structure on both TPA and ESA has not been investigated yet. In this work, we propose to develop a molecular engineering approach to optimize not only the TPA initiating step, but also the subsequent induced absorption process, within transparency requirements. In the first part of this paper, we consider theoretical TPA and ESA spectra, obtained by semi-empirical and sum-over-states calculations, to discuss the property-structure relationship of some diphenylpolyene derivatives (weak push-pull, bis-donor symmetrical, and octupolar molecules). In the second part, we present preliminary measurements of nonlinear absorption at $\lambda = 600$ nm using nanosecond time-duration pulses.

THEORETICAL TPA AND ESA SPECTRA OF DIPHENYLPOLYENESTheoretical Method

The investigated model molecules are displayed on Figure 1: weak push-pull **1-3**, bis-donor symmetrical **4-5**, and octupolar molecules **6-7**.

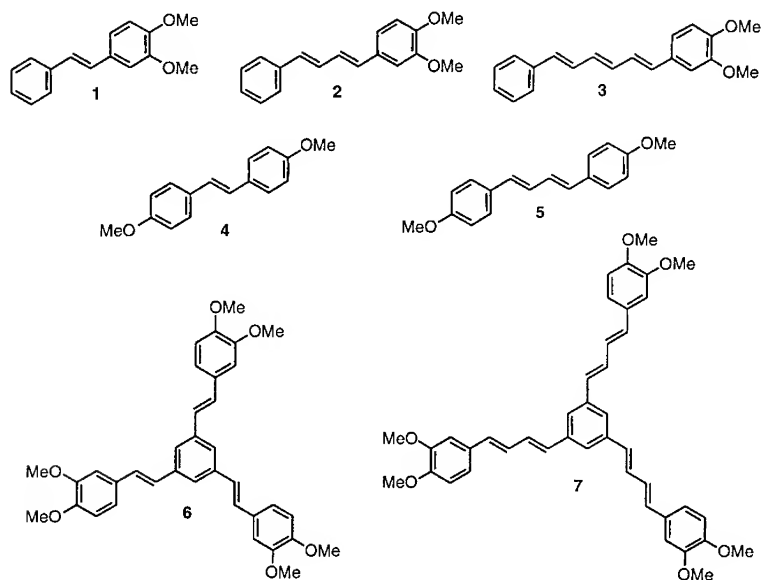


FIGURE 1 Structures of model molecules 1-7.

For each molecule, the electronic state parameters, i.e. singlet state energies, and dipole moments, were obtained by a configuration interaction (CI) procedure based on the CNDO/S method using the QCPE program #333. The CI calculations included 100 singly (SCI), and 100 doubly (DCI) excited π -configurations. The geometry of the molecules was optimized by using Sybyl, i.e. Tripos force field and PM3 from the MOPAC package.²⁰

TPA is a third-order nonlinear process, in which the TPA coefficient α_2 is proportional to the imaginary part of the mean second hyperpolarizability $\langle\chi(-\omega;\omega,-\omega,\omega)\rangle$. The imaginary parts of χ_{ijkl} components were computed using Orr

and Ward's equation based on time-dependent perturbation theory.²¹ ESA spectra were computed using the energies and oscillator strengths of transitions from the first excited singlet state. TPA and ESA spectra were evaluated by using the parameters of the 19 lowest excited states. Damping factors for all states were taken to be 1000 cm^{-1} .

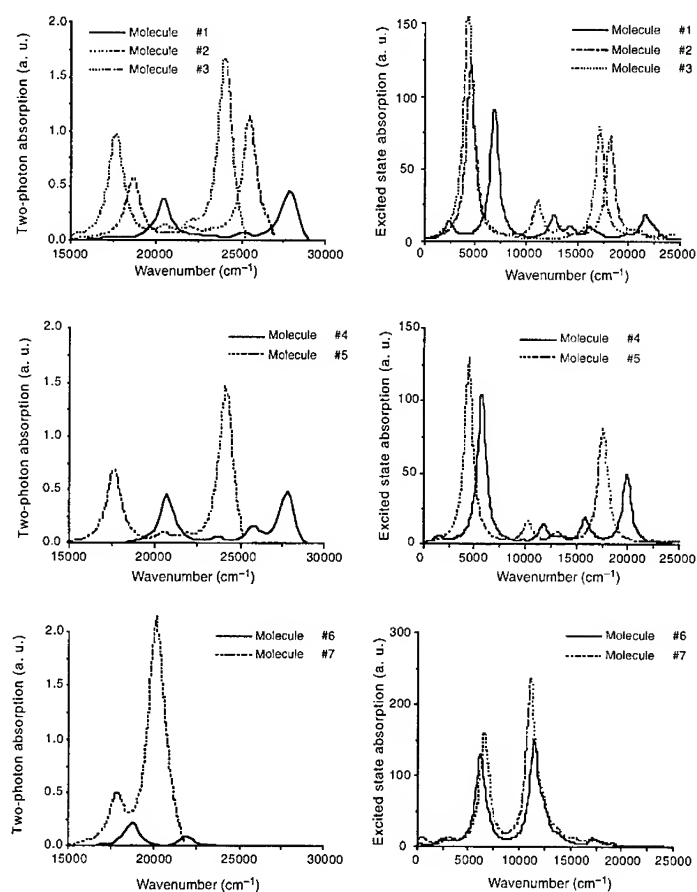


FIGURE 2 Theoretical TPA and ESA spectra of model molecules 1-7.

Theoretical Results

The theoretical TPA and ESA spectra of compounds **1–7** are displayed in Figure 2. Surprisingly, all TPA spectra have features similar to their corresponding ESA spectra. They span a wide spectral range, and are bounded by two strong resonances. For all compounds, these resonances correspond to one-photon forbidden transitions. They are enhanced and shifted toward red frequencies when the number of double bonds is increased. While the spectra of push-pull and bis-donor symmetrical molecules look alike, spectra of octupoles differ: their TPA and ESA oscillator strengths are more concentrated on low energy transitions.

The nonlinear absorption initiated by TPA is enhanced when there is an ESA at the laser frequency. It is generally the case for diphenylpolyene derivatives **1–7** due to the wide-band of their TPA and ESA spectra. The enhancement is maximal, and a giant nonlinear absorption may be obtained, when strong TPA and ESA resonances occur at the same energy. Uncertainties on calculated transition energies do not allow for a direct comparison of TPA and ESA spectra. However, Figure 2 shows that this optimized overlap is possible for symmetrical and push-pull molecules, but cannot occur for octupolar molecules. It is also more likely to occur at red frequencies than at blue frequencies.

PRELIMINARY MEASUREMENTS OF NONLINEAR ABSORPTION

Experimental Method

In this section we report on the nanosecond nonlinear absorption of molecules **1'–7'** at $\lambda = 600$ nm. These molecules have previously been synthesized in a different context, and their preparation will be described elsewhere.²² Molecules **1'**, **2'**, **3'**, **6'**, **7'** and **4'**, **5'** differ from their model parents by their donor end groups R' and R'' , respectively (see Fig. 3). Because their conjugation and charge transfer are similar, their optical properties are assumed to be comparable. They were studied at high concentrations (0.5 to 1 mol L^{-1}) in chloroform solvent.

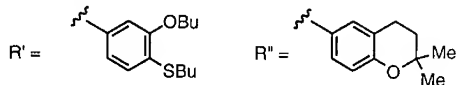


FIGURE 3 Donor end groups of experimentally investigated molecules. R' for molecules **1'**, **2'**, **3'**, **6'**, **7'** and R'' for molecules **4'**, **5'**

The nonlinear absorption of molecules was characterized using an Optical Parametric Oscillator pumped by a Q-switched Nd:YAG (laser system from Quantel laser company). The laser wavelength was set at $\lambda = 600$ nm for convenience as these results are part of a large screening test. The FWHM pulse duration was 2.6 ns. The length of the optical cell was one centimeter. The cell was centered at the 200- μm waist of the beam. The input pulse energy was adjusted in the 1 μJ –10 mJ range by rotating a half-waveplate between cross-polarizers. Reference and transmitted signal were measured with Molelectron pyroelectric detectors.

Nonlinear absorption coefficients were obtained by analyzing optical power limiting curves in the framework of temporal and spatial Gaussian beam propagation.¹¹ For convenience, the excited-state absorption initiated by TPA was taken into account by the phenomenological coefficient α_3 . In fact, the $\alpha_3 I^2$ contribution was always dominant, and the $\alpha_2 I$ contribution could be neglected in the analysis. In the followings, normalized α_3 coefficients are reported for 1 kg L⁻¹ of solvated molecules in order to compare the nonlinear response of molecules that are very different in molecular weights and volumes.

Experimental results

All molecules **1'**–**7'** display an optical limiting response. For example, curves obtained for **1'**, **3'**, **4'** and **7'** are shown on Fig. 4. Values of nonlinear absorption coefficient α_3 are summarized in Table I.

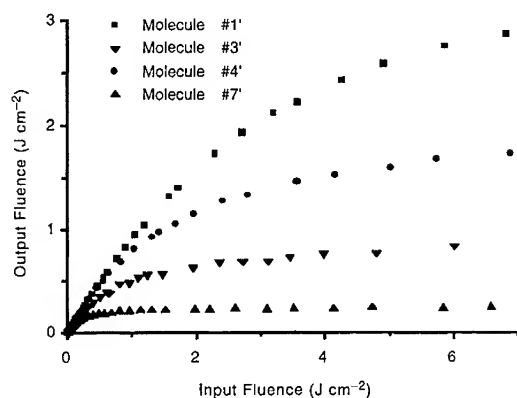


FIGURE 4 Optical limiting curves of molecules **1'**, **3'**, **4'**, **7'** in chloroform at $\lambda = 600$ nm. Concentrations are 317, 300, 310 and 587 g L⁻¹, respectively.

TABLE 1 Nanosecond α_3 values for molecules 1'-7' in chloroform at $\lambda = 600$ nm. Normalized values are for a theoretical concentration of 1 kg L⁻¹.

MOLECULE #	Measured α_3 (cm ³ GW ⁻²)	Concentration (g L ⁻¹)	Normalized α_3 (cm ³ GW ⁻²)	Color of 1 cm-thick sample
1'	8	317	25	colorless
2'	1150	426	2700	light yellow
3'	1170	300	3900	yellow
4'	650	310	2100	light yellow
5'	1210	168	7200	yellow
6'	440	550	800	light yellow
7'	1700	587	2900	yellow

The theoretical analysis predicts a large wavelength dispersion of nonlinear coefficients. For this reason, the experimental results at one wavelength ($\lambda = 600$ nm) are not sufficient to derive a relationship between molecular structure and optical property. However, these data are qualitatively in agreement with the calculated spectra (Fig. 2): (i) α_3 increases with the number of double bonds (1'-3', 4'-5', and 6'-7'). This phenomenon corresponds to increased resonances of TPA and ESA with conjugation, and to their red shifts towards the laser frequency; (ii) symmetric molecules 4'-5' are more efficient than their push-pull analogs 1'-2', which have similar TPA resonances. This arises from the larger amplitude and lower energy of RSA resonance for 4'-5'; (iii) octupolar molecules 6'-7' have higher nonlinear absorption than their rod-like parents 1'-2'. This is due to a better matching of TPA resonances with the laser frequency for 6'-7'.

CONCLUSION

The nonlinear optical absorption of diphenylpolyene derivatives has been studied theoretically and experimentally (at $\lambda = 600$ nm). These molecules display wide-band TPA and ESA, hence present enhanced nonlinear absorption at visible wavelengths. Strong ESA and TPA resonances occur in the same spectral range for push-pull and bis-donor symmetrical derivatives. This indicates that one could find derivatives with giant nonlinear absorption due to overlapping resonances. These resonances involve high-level excited-states that cannot be computed accurately. Thus, calculations cannot determine the best derivatives, but they can be helpful to suggest molecular engineering criteria.

These experimental results confirm that several orders of magnitude in nonlinear

absorption at a given wavelength can be gained by an appropriate choice of molecules. This work is a first step towards a strategy to optimize simultaneously the TPA and ESA of optical limiting molecules. Others model molecules are being investigated, and further wavelength-dispersion measurements of TPA and ESA are in progress.

Acknowledgements. We are grateful to DGA / DSP / STTC (n° 96-116) and to MENESR for financial support.

REFERENCES

1. L. W. Tuff, T. F. Bogess, *Prog. Quant. Electron.*, **17**, 299 (1993).
2. E. W. Van Stryland, D. Hagan, T. Xia, and A. Said, in *Nonlinear Optics of Organic Molecular and Polymeric Materials*, edited by H. S. NALWA and S. Miyata (CRC Press, Boca Raton, 1997), pp. 841-860.
3. J. W. Perry, in *Nonlinear Optics of Organic Molecular and Polymeric Materials*, edited by H. S. NALWA and S. Miyata (CRC Press, Boca Raton, 1997), p. 813.
4. G.S. He, G.C. Xu, P.N. Prasad, B.A. Reinhardt, J.C. Blatt, and A.G. Dillard, *Optics Lett.*, **20**, 435 (1995).
5. G.S. He, R. Gvishi, P.N. Prasad, B.A. Reinhardt, *Opt. Commun.*, **117**, 133 (1995).
6. G.S. He, J.D. Bhawalkar, C.F. Zhao, P. Prasad, *Appl. Phys. Lett.*, **67**, 2433, (1995).
7. G.S. He, L. Yuan, N. Cheng, J.D. Bhawalkar, C.F. Zhao, and P. Prasad, *J. Opt. Soc. Am. B*, **14**, 1079 (1997).
8. B.A. Reinhardt, L.L. Brott, S. J. Clarkson, R. Kannan, and A.G. Dillard, *Proc. SPIE 3146*, **2** (1997).
9. P.A. Fleitz, and R.L. Sutherland, *Proc. SPIE 3146*, **24** (1997).
10. J.E. Ehrlich, X.L. Wu, I.-Y. S. Lee, H. H. Röckel, S. R. Marder, and J. W. Perry, *Optics Lett.*, **24**, 435 (1997).
11. P.A. Chollet, V. Dumarcher, J.-M. Nunzi, and P.L. Baldeck, *Nonlinear Optics*, this issue.
12. P. Feneyrou, O. Doclot, D. Block, and P. L. Baldeck, *J. Nonlin. Opt. Phys. Mat.*, **5**, 767 (1996).
13. P. L. Baldeck, Y. Morel, M. Plazanet, P. Feneyrou, C. Andraud, T. Brotin, C. Nguefack, A. Collet, J. F. Nicoud, and A. Ibanez, *Proc. SPIE 3147*, **112** (1997).
14. J. Kleinschmidt, S. Rentsch, W. Tottleben, and B. Wilhelmi, *Chem. Phys. Letters*, **15**, 309 (1974).
15. A.A. Said, C. Wamsley, D. J. Hagan, E. W. Van Stryland, B. A. Reinhardt, P. Roderer, A. G. Dillard, *Chem. Phys. Lett.*, **228**, 646 (1994).
16. K. McEwan, and R. Hollins, *Proc. SPIE 2229*, **122** (1994).
17. W. Zhao, J. H. Kim, and P. Palfy-Muhoray, *Proc. SPIE 2229*, **131** (1994).
18. G. R. J. Williams, *Appl. Phys. B*, **63**, 47 (1996).
19. J.E. Ehrlich, X.L. Wu, I.-Y. S. Lee, H. H. Röckel, S. R. Marder, and J. W. Perry, *Mat. Res. Soc. Symp. Proc.*, **479**, (1997).
20. SYBYL, from Tripos, 1699 S. Hanley Road, St Louis, MO 63144-2913.
21. B. J. Orr, and J. F. Ward, *Mol. Phys.*, **20**, 513 (1971).
22. Crystal of bis-donor symmetrical molecule **4'** exhibits a high nonlinear absorption : C. Nguefack, C. Andraud, A. Collet, A. Ibanez, B. Suchod, P.L. Baldeck (to be published). Octupoles **6'**, **7'** and their rods push-pull **1'**, **2'** are efficient quadratic nonlinear molecules: T. Zabulon, R. Anémian, C. Andraud, A. Collet, S. Brasselet, J. Zyss (to be published).

MEASUREMENTS OF MULTIPHOTON ABSORPTION COEFFICIENTS IN ZnSe/ZnS_xSe_{1-x} STRAINED-LAYER SUPERLATTICES

A. ADINOLFI, M.C. NETTI, M. LEPORE*, R. TOMMASI**, AND I.M. CATALANO

Dipartimento Interateneo di Fisica, Università degli Studi di Bari and Istituto Nazionale per la Fisica della Materia, Unità di Bari, ITALY

Abstract We report on an experimental investigation of nonlinear losses in ZnSe/ZnS_{0.18}Se_{0.82} strained-layer superlattices. Two- and three-photon absorption coefficients have been measured at different excitation energies corresponding to the allowed excitonic transitions in the TE polarization. Clear experimental evidence of three-photon absorption at the exciton resonances near the band gap is reported. The experimental results for two-photon absorption have been compared with the theoretical predictions of an analytical model on third-order nonlinear processes in quantum well systems including excitonic effects, showing a fairly good quantitative agreement.

Keywords: ZnSe/ZnS_xSe_{1-x} superlattices, multiphoton absorption, nonlinear comparative photoluminescence technique, optical limiting.

Low-dimensional synthetic materials have shown great potentialities in the photonic and optoelectronic fields. In particular, two-dimensional semiconductor multi-quantum wells and superlattices have been extensively investigated leading to a good knowledge of their excitonic nonlinearities.¹⁻⁴ Nonlinear absorption is assuming an increasing importance from a technological perspective, especially for sensor protection applications like multiphoton absorption-induced optical power limiting (OPL). The use of a quantum confined system as an OPL device could allow to tune its operating wavelengths by a proper choice of system parameters, such as well width, strain, and composition. Large exciton binding energies and oscillator strengths in II-VI systems allow the observation of distinct excitonic features even at room temperature. Among

* Unità di Napoli, Dipartimento di Scienze Fisiche, Università Federico II (Italy)

** Also with: Istituto di Fisica Medica, Università degli Studi di Bari (Italy)

wide band gap II-VI heterostructures, much interest has been devoted to ZnSe/ZnS_xSe_{1-x} strained layer superlattices (SLSs). In view of the potential implementation of optical limiters using ZnSe/ZnS_xSe_{1-x} SLSs, the quantitative determination of their nonlinear losses is required.

Here we report on the experimental determination of two- and three-photon absorption (TPA and ThPA) coefficients $\alpha^{(2)}$ and $\alpha^{(3)}$ in two symmetric ZnSe/ZnS_xSe_{1-x} SLSs grown by metallorganic chemical vapor deposition (MOCVD) on (100)-oriented GaAs substrates. The investigated samples had a fixed sulphur content $x=0.18$ and well/barrier thickness equal to 100 Å/100 Å (S100) and 37 Å/37 Å (S37), respectively. The sulphur content was chosen to minimize misfit dislocation.⁵ The strain was determined to be $\tau=0.24\%$ for S100 and $\tau=0.08\%$ for S37 by independent Raman measurements. For both the samples the total thickness was $\approx 0.8 \mu\text{m}$ which is expected to be comparable to or slightly larger than the critical relaxation thickness.⁶ In order to accurately characterize the excitonic states in the S100 and S37 samples one- and two-photon absorption-induced photoluminescence excitation (OPA-PLE and TPA-PLE) measurements were performed for both of them (see Figures 1 and 2, respectively). The interpretation of the excitonic features of these spectra has been previously reported in detail.^{2,3}

The $\alpha^{(2)}$ and $\alpha^{(3)}$ values have been measured by means of the comparative nonlinear luminescence (CNL) technique.⁷ Although this method is indirect, it is particularly reliable for measuring nonlinear absorption coefficients in the case of small active volumes. The CNL technique allows to deduce the nonlinear absorption coefficients from the ratio of two quantities of the same type, measured using the same experimental configuration and from parameters which can be easily determined by other techniques such as linear absorption coefficients. The luminescence signals $L^{(1)}$, $L^{(2)}$ and $L^{(3)}$ at the frequency ω_L of the photoluminescence peak, induced by one-, two- and three-photon excitation respectively, are given by:

$$L^{(1)} = C_1 \xi_1 T_L \alpha_1 I_{01} e^{-\alpha_L \ell} \frac{1 - e^{-(\alpha_1 - \alpha_L) \ell}}{\alpha_1 - \alpha_L} \quad (1)$$

$$L^{(i)} = C_i \xi_i T_L \alpha^{(i)} I_{0i}^i \frac{1 - e^{-\alpha_L \ell}}{\alpha_L} \quad i = 2, 3 \quad (2)$$

where I_{01} , I_{02} , I_{03} are the exciting intensities at $\hbar\omega_1$, $\hbar\omega_2$ and $\hbar\omega_3$, respectively; ξ_i ($i=1,2,3$) are the recombination quantum efficiencies relative to i -photon absorption; C_i ($i=1,2,3$) are the calibrating factors taking into account the geometry of the optical arrangement for the luminescence detection. T_L is the transmission coefficient at ω_L frequency; α_i (α_L) is the linear absorption coefficient at the excitation (detection) energy, and ℓ is the active thickness of the sample. The above equations are valid provided that the OPA coefficients at $\hbar\omega_2$ and $\hbar\omega_3$ and TPA coefficient at $\hbar\omega_3$ are negligible.

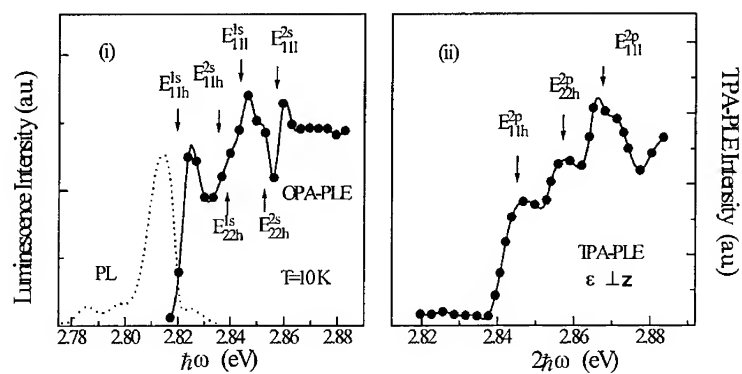


FIGURE 1 (i) Photoluminescence (PL) and one-photon absorption-induced photoluminescence (OPA-PL) spectra of the S100 sample at $T=10$ K. The arrows indicate the theoretical exciton transition energies calculated taking into account strain and confinement effects.² (ii) Two-photon absorption photoluminescence excitation (TPA-PL) spectrum of the same sample at $T=10$ K obtained in the TE polarization ($\epsilon \perp z$). The arrows indicate the TPA-allowed transitions.

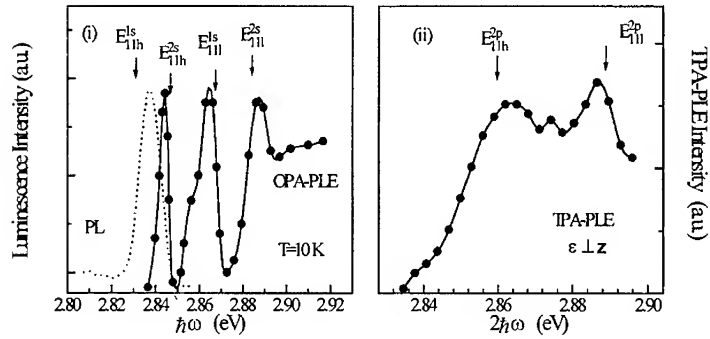


FIGURE 2 The same as Figure 1 for the S37 sample.

By assuming a quantum efficiency independent on the pumping mechanisms in the case that $\hbar\omega_1 \approx 2\hbar\omega_2 \approx 3\hbar\omega_3$, and by arranging the same detection configuration ($C_1=C_2=C_3$), $\alpha^{(2)}$ and $\alpha^{(3)}$ values can be directly derived by the ratios $L^{(2)}/L^{(1)}$ and $L^{(3)}/L^{(1)}$ respectively, obtaining:

$$\alpha^{(i)} = \frac{L^{(i)} I_{01}}{L^{(1)} I_{0i}} \frac{\alpha_1 \alpha_L}{e^{\alpha_L \ell} - 1} \frac{1 - e^{-(\alpha_1 - \alpha_L) \ell}}{\alpha_1 - \alpha_L} \quad i = 2, 3 \quad (3)$$

It can be observed that for 2D structures the TPA-induced exciton transitions involve p-type states instead of the s-type states allowed in OPA and ThPA processes. For this reason the quantum efficiency ξ_2 could be different from ξ_1 and ξ_3 because quantum confinement and interface roughness may differently act on p excitons, owing to their larger Bohr radius. Nevertheless, it is reasonable to guess that such difference is not considerable if the three absorption processes induce optical exciton transitions having final states at almost the same energy, since the carrier relaxation toward the emitting state might be considered similar in this case.

We measured $\alpha^{(2)}$ values for the S100 and the S37 sample at $T=10$ K in the $\epsilon \perp z$ polarization configuration, where $\underline{\epsilon}$ is the polarization vector of the incident electromagnetic field and \underline{z} is the growth axis of the SLs. The detection energy was set

at the peak energy of the luminescence $\hbar\omega_L=2.814$ eV for the S100 sample and $\hbar\omega_L=2.837$ eV for the S37 sample, independently determined by the PL measurements.² We excited resonantly with 2p exciton transitions associated with subbands having the same principal quantum number as allowed by the parity selection rules for TPA processes in the TE polarization.^{2, 3} Such energies were determined by means of the TPA-PLE spectra shown in Ref. 2.

As detuning from the half band gap increases, ThPA absorption can become the dominant nonlinear loss mechanism. Nevertheless, there are few experimental investigations on such fifth-order nonlinear process because of its very small cross section. We determined the $\alpha^{(3)}$ coefficient at different energies on the S37 sample. Measurements were performed at $T=10$ K at the exciton transition energies allowed by the parity selection rules for processes involving an odd photon number.⁸ Such energy values, corresponding to 1s heavy- and light-hole excitons associated to subbands with the same principal quantum number, were determined by means of OPA-PLE measurements, as reported in Ref. 2.

The source of one, two- and three-photon absorption measurements was a dye laser (9 ns pulse duration, 10 Hz repetition rate, 2 Å tuning accuracy) pumped by the third (second) harmonic of a Nd:YAG laser for linear (nonlinear) excitation. The light intensity after focusing reached up to 50 MW/cm². The near infrared light for multiphoton absorption was produced by the first- and the second-order Stokes, Raman shifted output of a cell containing H₂ gas. The emitted luminescence was detected by an S20 extended-response photomultiplier tube while the incident beam was monitored by a fast-response photodiode. Both signals were sent to a digital oscilloscope for data acquisition. The signal-to-noise ratio was better than 200:1 for each run.

Our experimental results on third-order nonlinear losses in the S100 and the S37 samples are summarized in Tables I and II, respectively. For designating the exciton transitions we employed the standard notation defined in Ref. 2. The linear absorption coefficients α_1 and α_L , to be used in eq. (3), have been evaluated from optical density measurements independently performed and reported in Tables I, II and in their captions. The larger magnitude magnitude of the $\alpha^{(2)}$ values measured for the S37 sample with

respect to the ones of the S100 sample, can be probably due to the presence of a non-negligible component parallel to the z axis of the polarization vector projected by the laser beam. This component, which was observed in Ref. 2, would enhance two-photon absorption because of the continuum contribution that becomes significant in the $\underline{E} // \underline{z}$ polarization.⁹

We compared our experimental results with the theoretical predictions relative to TPA in quasi-two-dimensional semiconductors. Simple analytical expressions developed for $\alpha^{(2)}$ in the energy range near the half band gap and including excitonic effects have been proposed in the literature.^{10, 11} In particular, one of these¹⁰ gives the values reported in Table I and II.

TABLE I Linear absorption coefficients α_1 , experimental and theoretical results of $\alpha^{(2)}$ values for the S100 sample. For the physical parameter values used in the calculations see Ref. 12. $\alpha_L = 7.92 \times 10^4 \text{ cm}^{-1}$ at $\hbar\omega_L = 2.814 \text{ eV}$.

TRANSITION	$2\hbar\omega_2$ (eV)	$\alpha_1 (\times 10^4)$ (cm^{-1})	$\alpha_{\text{exp}}^{(2)} (\times 10^{-3})$ (cm/MW)	$\alpha_{\text{th}}^{(2)} (\times 10^{-3})$ (cm/MW)
E_{11h}^{2p}	2.846	16.09 ± 1.61	1.3 ± 0.3	1.30
E_{22h}^{2p}	2.858	16.09 ± 1.61	2.1 ± 0.5	1.95
E_{11l}^{2p}	2.867	16.09 ± 1.61	2.8 ± 0.7	2.91

TABLE II The same as Table I for the S37 sample. $\alpha_L = 8.83 \times 10^4 \text{ cm}^{-1}$ at $\hbar\omega_L = 2.837 \text{ eV}$

TRANSITION	$2\hbar\omega_2$ (eV)	$\alpha_1 (\times 10^4)$ (cm^{-1})	$\alpha_{\text{exp}}^{(2)} (\times 10^{-3})$ (cm/MW)	$\alpha_{\text{th}}^{(2)} (\times 10^{-3})$ (cm/MW)
E_{11h}^{2p}	2.865	9.78 ± 0.98	5.9 ± 1.5	4.1
E_{22h}^{2p}	2.888	10.35 ± 1.03	7.2 ± 1.8	6.2

It is worth noting that in such calculation the excitonic contribution was described by a Gaussian function. We assigned to this function the experimentally determined FWHM

values of the excitonic peaks, ranging from 4 to 10 meV for both samples. The $\alpha^{(2)}$ theoretical values show a satisfactory agreement with our experimental results, especially for the S100 sample. This finding comforts our assumption of equal recombination quantum efficiencies in TPA and OPA processes. However, this topic deserves further experimental and theoretical investigations for a more accurate extension of the NLC technique to reduced dimensionality systems.

The results of photoluminescence measurements relative to the $\alpha^{(3)}$ determination in the S37 sample are presented in Figure 3 (i) and (ii).

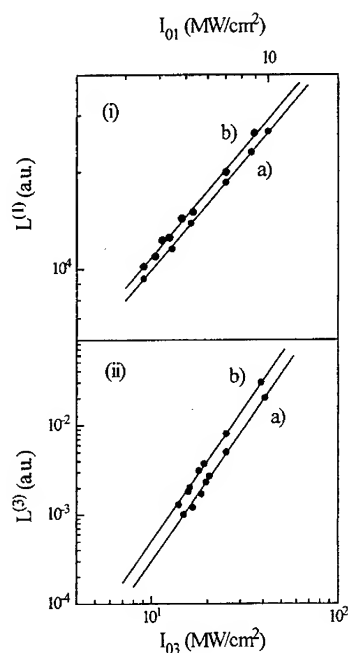


FIGURE 3 i) OPA and (ii) ThPA luminescence intensity from the S37 sample at $\hbar\omega_L=2.837$ eV versus I_{01} and I_{03} laser power density respectively, at (a) $\hbar\omega_1=3\hbar\omega_3=2.843$ eV (E_{11h}^{1s}), (b) $\hbar\omega_1=3\hbar\omega_3=2.866$ eV (E_{11l}^{1s}).

It can be observed that for the $3\hbar\omega_3$ excitation energies the cubic behavior of the luminescence emission as a function of the incident intensity indicates a process in which three photons are simultaneously absorbed. The $\alpha^{(3)}$ values for the S37 sample, shown in Table III, were calculated by eq. (3) for $i=3$, using the α_1 and α_L values reported in the same Table and in its caption.

TABLE III Linear absorption coefficients α_1 and experimental results of $\alpha^{(3)}$ values for the S37 sample.

TRANSITION	$3\hbar\omega_3$ (eV)	$\alpha_1(\times 10^4)$ (cm ⁻¹)	$\alpha_{\text{exp}}^{(3)}(\times 10^{-8})$ (cm ³ /MW ²)
$E_{\text{Ih}}^{\text{Is}}$	2.843	10.54 ± 1.05	3.8 ± 0.9
$E_{\text{Il}}^{\text{Is}}$	2.866	9.84 ± 0.98	7.0 ± 1.7

For the other sample it was not possible to perform the ThPA coefficient determination, owing to its very low luminescence signal. The higher ThPA-induced radiative efficiency shown by the S37 sample could be probably due to its smaller well width and/or to a larger concentration of nonradiative recombination centers.

In conclusion two- and three-photon absorption coefficients have been measured in ZnSe/ZnS_{0.18}Se_{0.82} SLSs by a high sensitivity experimental technique. For $\alpha^{(2)}$ values a comparison with a theoretical model shows a good numerical agreement and a correct dependence on the thickness of the well and barrier. The observation of significative third- and fifth-order responses in ZnSe/ZnS_{0.18}Se_{0.82} SLSs suggests that in these multilayer structures both TPA and ThPA could, in principle, be used for optical power limiting in the near-infrared spectral range.

ACKNOWLEDGMENTS

The authors wish to thank I. Suemune (Research Institute for Electronics Science, Hokkaido University, Sapporo, Japan) for providing the samples. This work was partially supported by INFN (Istituto Nazionale per la Fisica della Materia).

REFERENCES

1. I.M. Catalano, A. Cingolani, and M. Lepore, *Phys. Rev B*, **41**, 12937 (1990).
2. R. Tommasi, M. Lepore, M.C. Netti, and I.M. Catalano, *Phys. Rev B*, **49**, 14367 (1994).
3. M. Lepore, M.C. Netti, R. Tommasi, and I.M. Catalano, *Solid State Commun.*, **92**, 695 (1994).
4. M.C. Netti, M. Lepore, A. Adinolfi, R. Tommasi, I.M. Catalano, L. Vanzetti, L. Sorba and A. Franciosi, *J. Appl. Phys.*, **80**, 2908 (1996).
5. I. Suemune, H. Masato, K. Nakanishi, Y. Kuroda, and M. Yamanishi, *J. Cryst. Growth*, **107**, 679 (1991).
6. K. Shahzad, D.J. Olego, and C.G. Van de Walle, *Phys. Rev B*, **38**, 1417 (1988).
7. I.M. Catalano, A. Cingolani, M. Ferrara, and M. Lugarà, *Opt. Acta*, **27**, 625 (1980).
8. L.C. Andreani and F. Bassani, *Symmetry in Nature* (Quaderni della Scuola Normale Superiore di Pisa)
9. A. Pasquarello and A. Quattropani, *Phys. Rev. B*, **41**, 12728 (1990).
10. A. Shimizu, *Phys. Rev. B*, **40**, 1403 (1989).
11. A. Shimizu, T. Ogawa, and H. Sakaki, *Phys. Rev B*, **45**, 11338 (1992).
12. A. Obeidat and J. Khurgin, *J. Opt. Soc. Am B*, **12**, 1222 (1995).
13. *Landolt-Börnstein New Series Group III*, vol. **17**, edited by O. Madelung (Berlin: Springer), pp. 61-157 (1982).

Z-SCAN MEASUREMENTS OF OPTICAL NONLINEARITIES IN BULK LiNbO₃

A. ADINOLFI, T. CASSANO, R. TOMMASI*, AND M. FERRARA
Dipartimento Interateneo di Fisica, Università degli Studi di Bari and Istituto
Nazionale per la Fisica della Materia, Unità di Bari, ITALY

Abstract Third-order nonlinear optical measurements have been performed on bulk LiNbO₃ at 532 and 1064 nm by using picosecond single-beam Z-scan technique. Both in the visible and in the infrared regions the sign of the bound electronic refractive nonlinearity is found to be positive, showing a self-focusing effect. The quantitative determination of $\text{Re}\chi^{(3)}$ and $\text{Im}\chi^{(3)}$ provides the basis for the potential use of this type of material in nonlinear optical devices such as optical limiters and switches.

Keywords: lithium niobate, Z-scan, optical Kerr nonlinearity, two-photon absorption, optical power limiting.

Bulk lithium niobate (LiNbO₃) has attracted a great deal of attention for a wide variety of applications using nonlinear optical, ferroelectric and fotorefractive effects.¹ Its large use in active optical devices, like integrated optic modulators, is chiefly motivated by the manufacture of sizable crystals with low defect densities and by the effective methods for realizing low-loss optical waveguides.² Most of the research studies on this wide-gap non-centrosymmetric crystal concerned its second-order nonlinear properties for the implementation of infrared parametric oscillators and second-harmonic generators.³ Nowadays an increasing interest is focused also on its cubic nonlinearities. Several devices, based on third-order effects, have been suggested to limit the optical power below critical thresholds, operating as protective elements to restrict the irradiance of a light pulse upon a sensitive component, or as regulators to smooth optical transient. The behavior of a laser beam which passes through a third-order nonlinear optical material depends strongly on the real and imaginary parts of $\chi^{(3)}$

* Also with: Istituto di Fisica Medica, Università degli Studi di Bari, (Italy)

and, in particular, on the ratio $\text{Re}\chi^{(3)} / \text{Im}\chi^{(3)}$. A large ratio can lead to a significant power-limiting action at relatively low input laser power with respect to the ones required by pure nonlinear absorption.⁴ In order to assess the actual feasibility of exploiting LiNbO₃ in the field of optical power limiting and other irradiance-dependent phenomena, the knowledge of the absorption coefficients and refractive indexes of crystal under high excitation is required. LiNbO₃ is relatively well characterized in the visible region,^{5,6} but there are only few information concerning the nonlinear optical behavior of this material in the infrared domain which deserves further investigations.

In the present work we report on the experimental determination of bound electronic nonlinear refraction index n_2 and two-photon absorption coefficient β of a pure LiNbO₃ crystal both in the visible ($\lambda=532$ nm) and in the infrared ($\lambda=1064$ nm) ranges. It is worth noting that β and n_2 parameters are defined here according to the relations: $\alpha=\alpha_0+\beta I$ and $n=n_0+n_2 I$, where α_0 and n_0 are the linear parts of the total absorption coefficient α and the refraction index n , respectively. Our measurements were performed at room temperature by means of the single-beam Z-scan technique, whose high sensitivity was demonstrated both for thermal and conventional Kerr nonlinearities.^{7,8} The optical nonlinear medium is illuminated by a focused laser beam and it is scanned along the propagation axis (z-axis) while the transmitted power is monitored in the far-field. The intensity dependent absorption can be measured as a change of the transmission through the sample (open-aperture). The nonlinear refraction is determined by the spot size variation at the plane of a finite aperture placed in front of the detector, by which the phase distortion of the laser beam during its propagation is transformed into amplitude distortion (closed-aperture). Absorptive and refractive nonlinearities reflect in characteristic features in the associated Z-scan traces which provide information not only on the magnitude of the real and imaginary parts of $\chi^{(3)}$ ($n_2 \propto \text{Re}\chi^{(3)}$; $\beta \propto \text{Im}\chi^{(3)}$), but also on the sign of the real part.

The experimental arrangement was a classical Z-scan set-up. The excitation source was a Q-switched, mode-locked Nd:YAG laser with single-pulse selector delivering ~ 35 ps (FWHM) at a 10Hz repetition rate and at $\lambda=1064$ nm. For measurements in the visible the fundamental radiation was frequency doubled by means of a KDP crystal. The temporal profile of the beam was nearly Gaussian and its spatial mode was close to

TEM₀₀. A small part of the laser radiation was sent by a beam splitter to a photodiode to monitor the input energy. The laser beam was focused onto the sample by a 15-mm focal length lens. The measured waists ω_0 of the fundamental and second-harmonic laser beams were $\sim 32 \mu\text{m}$ and $\sim 16 \mu\text{m}$, respectively. The crystal position was scanned by a 50-mm motor driven translation stage and the transmittance was recorded in the far field as a function of the sample position with respect to the focal plane (z) both in the open- and closed-aperture configurations. Data acquisition was performed with a personal computer by averaging over several pulses. We calibrated our experimental set-up by performing a Z-scan measurement with a 32% aperture for a 1mm-thick cell filled with carbon disulphide (CS₂). This liquid is a good lossless Kerr medium which is often used as a standard reference nonlinear material because of its well known nonlinear parameters.

For our measurements we used a 1mm-thick, [001]-cut, undoped LiNbO₃ single crystal with polished surfaces. The sample satisfied the "thin" sample condition $L < n_0 z_0$, where L is the sample thickness, n_0 the linear refraction index and z_0 the diffraction length of the focused beam.

In Figure 1, open- and closed-aperture Z-scan measurements at $\lambda=532 \text{ nm}$ are reported. At room temperature LiNbO₃ behaves as a two-photon absorber at this wavelength, being its gap $\sim 3.9 \text{ eV}$. This is confirmed by the open-aperture Z-scan trace reported in Figure 1(a), which shows a symmetric behavior with respect to the beam waist ($z=0 \text{ mm}$), where the transmittance reaches the minimum value. This curve was obtained for an intensity $I_0=17.4 \text{ GW/cm}^2$, being I_0 the peak irradiance. To quantify the nonlinear absorption we fitted the experimental data in Figure 1(a) (closed circles) by applying the model of Sheik-Bahae et al.⁷ and treating the irradiance-dependent component as pure two photon absorption (2PA). The solid curve in Figure 1(a) has been calculated using $\beta=4.5 \cdot 10^{-10} \text{ cm/W}$. We checked that the absorption resulting from the free carries produced by 2PA was actually negligible, by performing open-aperture Z-scan at lower input irradiances. The absolute uncertainty on β value was estimated to be $\pm 20\%$. The closed-aperture Z-scan curve at the same wavelength is shown in Figure 1(b) for an aperture linear transmission $S=0.12$ and a peak irradiance $I_0=17.4 \text{ GW/cm}^2$.

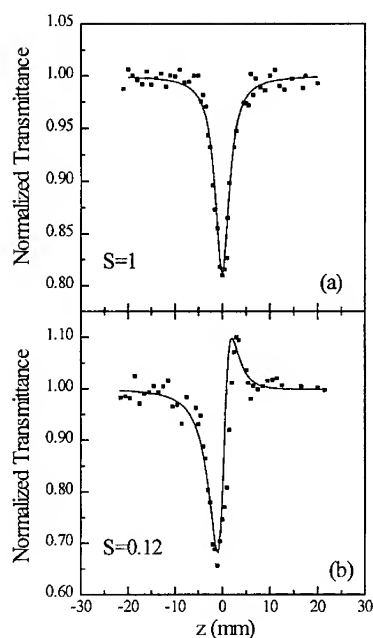


FIGURE 1 Normalized open-aperture (a) and closed-aperture (b) Z-scan measurements (closed squares) for LiNbO₃ at $\lambda=532$ nm and $I_0=17.4$ GW/cm². Theoretical fits are represented by the solid curves.

From these data a positive refractive nonlinearity is evident, since the transmission dip precedes the peak. The nonlinear absorption produces the effect to suppress the peak and enhance the valley. The separation between the maximum and the minimum of the curve is ~ 3 mm, i.e. $\sim 1.7 z_0$, indicating a third-order nonlinear contribution to the transmission change.⁸ The observed self-focusing effect can be attributed to the bound electronic Kerr nonlinearity, being nonlocal nonlinearities such as thermal or photorefractive negligible with ultrashort pulses at low repetition rate. Using the fitting procedure outlined in Ref. 9, we obtained the solid curve in Figure 1(b) by setting $\beta=4.5 \cdot 10^{-10}$ cm/W and extracting

a n_2 value of $8.7 \cdot 10^{-15} \text{ cm}^2/\text{W}$ with an experimental accuracy of $\pm 20\%$. Our experimental values of β and n_2 at $\lambda=532 \text{ nm}$ are in good agreement with the ones reported in Ref. 5.

Z-scan measurements were also performed on the same sample by exciting it with the fundamental of the Nd:YAG. For $I_0=20.0 \text{ GW/cm}^2$, the open-aperture transmission does not show any discernible intensity-dependent absorption and it has not been reported here. However, the corresponding closed-aperture Z-scan with $S=0.15$ indicates a positive nonlinear refraction, as seen in Figure 2, revealing a self-focusing effect which is particularly desirable for the realization of optical switches, modulators, and memories.¹⁰ Also in this case the distance between peak and valley of the normalized transmittance indicates a cubic nonlinear contribution to the pure refractive nonlinearity.

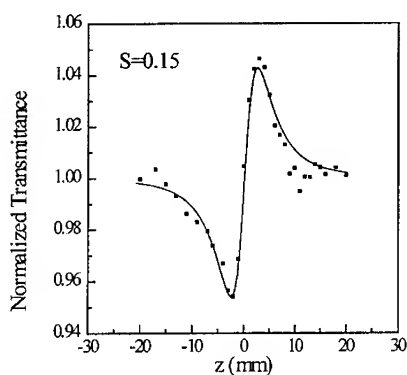


FIGURE 2 Normalized closed-aperture Z-scan measurements (closed squares) and simulation (solid line) for LiNbO₃ at $\lambda=1064 \text{ nm}$ and $I_0=20 \text{ GW/cm}^2$.

The best theoretical fit to the data, represented by the solid line in Figure 2, gives $n_2=2.7 \cdot 10^{-15} \text{ cm}^2/\text{W}$, with an experimental uncertainty of $\pm 20\%$. This value is three times larger than that reported in Ref. 5. Although the magnitude of the Kerr coefficient n_2 at $\lambda=1064 \text{ nm}$ results to be smaller than in the green by a factor of ~ 3 , the null nonlinear absorption coefficient gives a particular importance to this result making possible the realization of nonlinear optical devices with negligible losses and ultrafast response time.

The knowledge of both n_2 and β experimental values allowed us to determine the real and imaginary parts of the third-order susceptibility $\chi^{(3)}$ according to the following relations¹¹:

$$\text{Re } \chi^{(3)} = \frac{4}{3} \varepsilon_0 c n_0^2 n_2 \quad (1)$$

$$\text{Im } \chi^{(3)} = \frac{2 \varepsilon_0 c^2 n_0^2 \beta}{3 \omega} \quad (2)$$

where ε_0 is the permittivity in vacuum, ω and c are the angular frequency and the vacuum speed of the incident light, respectively. All the quantities in (1) and (2) are expressed in MKS units. With $n_0=2.33$ for $\lambda=532$ nm and $n_0=2.21$ for $\lambda=1064$ nm, as reported in Ref. 12, we obtained the $\text{Re } \chi^{(3)}$ and $\text{Im } \chi^{(3)}$ values reported in Table I.

In addition, we compared our experimental findings with a simple two-parabolic band model describing both semiconductor and dielectric materials.^{13,14} This model predicts a scaling relation for the degenerate 2PA coefficient given by:

$$\beta(\omega) = K \frac{\sqrt{E_p}}{n_0^2 E_g^3} F_2 \left(\frac{\hbar \omega}{E_g} \right)$$

where $F_2=(2x-1)^{3/2}/(2x)^5$ is the dispersion function for the 2PA, E_p is the Kane momentum parameter, E_g the band-gap energy of the material, and K is a material-independent constant. With $E_p=21$ eV, $K=1940$ cm eV^{5/2}/GW and $E_g=3.9$ eV, we obtained at $\lambda=532$ nm the β value shown in Table 1, which is consistent with our experimental result. The theoretical calculation of the Kerr coefficient n_2 was performed by applying the following Kramers-Krönig transformation of the 2PA dispersion:¹³

$$n_2(\omega) = K' \frac{\sqrt{E_p}}{n_0 E_g^4} G_2 \left(\frac{\hbar \omega}{E_g} \right)$$

where K' is a material-independent constant and $G_2(\hbar\omega/E_g)$ is proportional to the Kramers-Krönig transformation of the F_2 function. By taking $K'=0.94 \cdot 10^{-8}$ esu eV^{7/2},

$G_2=0.042$ (0.018) for $\lambda=532$ nm (1064 nm), we found the values reported in Table 1. The overall agreement appears to be quite good.

TABLE I Experimental and theoretical results from n_2 and β measurements in LiNbO₃ for the two excitation wavelengths.

λ (nm)	532	1064
$n_2^{\text{exp}} (\times 10^{-15} \text{ cm}^2/\text{W})$	8.7 ± 1.7	2.7 ± 0.5
$\beta^{\text{exp}} (\times 10^{-10} \text{ cm/W})$	4.5 ± 0.9	~ 0
$n_2^{\text{th}} (\times 10^{-15} \text{ cm}^2/\text{W})$	6.0	2.9
$\beta^{\text{th}} (\times 10^{-10} \text{ cm/W})$	9.7	~ 0
$\text{Re}\chi^{(3)} (\times 10^{-20} \text{ m}^2\text{V}^{-1})$	1.67 ± 0.33	0.47 ± 0.09
$\text{Im}\chi^{(3)} (\times 10^{-21} \text{ m}^2\text{V}^{-1})$	3.65 ± 0.91	~ 0

In conclusion, we measured the two-photon absorption coefficient β and the nonlinear refraction index n_2 in a bulk LiNbO₃ crystal at two wavelengths in the visible and infrared domains, by using the picosecond Z-scan experimental technique. In both cases the laser beam propagating into the crystal undergoes a self focusing process due to bound electronic Kerr nonlinearity, while only in the green an intensity dependent absorption was observed and attributed to a two-photon process. At $\lambda=532$ nm our result are in close agreement with the findings of R. De Salvo et al.⁵ In contrast, at $\lambda=1064$ nm our experimental value of n_2 is three times larger than the one previously reported,⁵ but it shows an excellent agreement with well established theoretical predictions. From the experimental data the values of the real and imaginary parts of the third-order nonlinear susceptibility $\chi^{(3)}$ were derived. The quantitative determination of $\chi^{(3)}$ in the infrared is particular useful for the development of efficient ultrafast devices operating in a region of interest for waveguides and optical fibers.

ACKNOWLEDGMENTS

This work has been partially supported by the National Research Council of Italy (under Special Project "Materiali e Dispositivi per l'Elettronica a Stato Solido").

REFERENCES

1. B. Sturman, M. Anguilar, F. Agullo Lopez, V. Pruneri, and P.G. Kazansky, *J. Opt. Soc. Am. B*, **14**, 2641 (1997).
2. M. Thompson, *Laser Focus World*, **34**, 105 (1998).
3. G.J. Dixon, *Laser Focus World*, **33**, 105, 1997.
4. J.A. Hermann, *J. Opt. Soc. Am. B*, **1**, 729 (1984).
5. R. De Salvo, A.A. Said, D.J. Hagan, E.W. Van Stryland, and M. Sheik-Bahae, *IEEE J. Quantum Electron.*, **32**, 1324 (1996).
6. H. Li, F. Zhou, X. Zhang, and W. Ji, *Appl. Phys. B*, **64**, 659 (1997).
7. L.C. Oliveira and S.C. Zilio, *Appl. Phys. Lett.*, **65**, 2121 (1994).
8. J. Wang, M. Sheik-Bahae, A.A. Said, D.J. Hagan, and E.W. Stryland, *J. Opt. Soc. Am. B*, **11**, 1009 (1994).
9. A.A. Said, M. Sheik-Bahae, D.J. Hagan, T.H. Wei, J. Wang, J. Young, and E.W. Van Stryland, *J. Opt. Soc. Am. B*, **9**, 405 (1992).
10. H. Nasu and J. D. Mackenzie, *Optical Engineering*, **26**, 102 (1987).
11. R. De Salvo, M. Sheik-Bahae, A.A. Said, D.J. Hagan, and E.W. Van Stryland, *Opt. Lett.*, **18**, 194 (1993).
12. G.D. Boyd, R.C. Miller, K. Nassau, W.L. Bond and A. Savage, *Appl. Phys. Lett.*, **5**, 234 (1964).
13. M. Sheik-Bahae, D.C. Hutchings, D.J. Hagan, and E.W. Van Stryland, *IEEE J. Quantum Electron.*, **27**, 1296 (1991).
14. D.C. Hutchings and E.W. Van Stryland, *J. Opt. Soc. Am. B*, **9**, 2065 (1992).

Coherent Dip in Optical Kerr Measurement Arising from Grating Formation in Weakly Absorptive Media

ASHISH AGARWAL^a, KENJI KAMADA^{*a}, YO SHIMIZU^b, and KOJI OHTA^a

^aDepartment of Optical Materials, Osaka National Research Institute, Ikeda, Osaka 563-8577, Japan

^bDepartment of Organic Materials, Osaka National Research Institute, Ikeda, Osaka 563-8577, Japan

Abstract An unusual narrow dip was observed in optical heterodyne detection (OHD) optical Kerr effect (OKE) measurement of tetraphenylporphyrin derivative solution in CCl₄ under a non-resonant condition. It was found that the width of the dip increases as the coherent time of the incident laser pulse increases while it does not depend on intensity nor chirp of the laser pulse. The negative dip is considered to be associated with formation of a transient grating within the coherence time. The formation of the grating can be attributed to residual linear absorption of tetraphenylporphyrin at the wavelength of the laser pulse.

Keywords: optical Kerr effect; optical heterodyne detection; tetraphenylporphyrin; transient grating; coherent time

INTRODUCTION

Optical Kerr effect (OKE) method, or also often mentioned as optical Kerr gate (OKG), has been widely performed to investigate third-order nonlinearity of variety of isotropic materials since the early stage of nonlinear optics [1]. With the advancement of pulsed laser technology in the last three decades, temporal resolution of the method has been drastically improved and reaches in the order of several tens femtoseconds with commercially available Ti:sapphire lasers. The ability of OKE method is also enhanced by

* Corresponding author

combining with optical heterodyne detection (OHD) technique, which allows one to measure the amplitude and phase of third-order susceptibility [2]. For example, phase-tuned OHD-OKG, a variation of this method, has been used for determining both the real and imaginary parts of the third-order susceptibilities of dye solutions [3].

We have performed femtosecond OHD-OKE experiments on a number of molecular liquids under non-resonance condition and reported instantaneous and causal responses, which correspond to pure electronic and nuclear contributions, respectively, of molecular third-order nonlinearity [4]. In the course of the experiments, we found an intense dip around zero delay time in the OHD-OKE signal for the solution of a tetraphenylporphyrin (TPP) derivative under non-resonant condition. The width of the dip is narrower than that of the autocorrelation of the incident laser pulse, which is hard to understand with ordinary OKE formulation. In this paper we report such dips observed in OHD-OKE experiment and evidence that this dip is due to formation of transient grating during coherence time of the incident laser pulse. Understanding of the origin of this dip and distinguishing it from ordinary OKE process are of importance for precise determination of the susceptibility and avoiding the confusion of this process with the fifth- and higher-order processes due to nonlinear optical absorption.

THEORETICAL BASIS AND EXPERIMENTAL SCHEME OF OKE

First we describe the ordinary OKE process briefly. Let us consider the interaction between a strong pump beam and a weak probe beam inside an isotropic and transparent nonlinear optical medium. The both two beams are linearly polarized but are different from each other in the direction of the polarization by 45° . The ordinary OKE process can be understood by two sequential processes: the pump pulse induces the anisotropic refractive index change in the medium and then the activated medium can change the polarization direction of the probe pulse. In general, the third-order nonlinear refractive index change of an isotropic medium due to interaction with the pump pulse is expressed as [5]

$$\delta n(t) = \int_{-\infty}^t dt' R(t-t') I_p(t'), \quad (1)$$

where $R(t)$ is the material response function due to the pump pulse, and the $I_p(t)$ is the light intensity of the pump pulse.

In the optical configuration of OHD, a weak replica of the probe pulse is generated by a quarter-wave plate. The replica is called local oscillator pulse, whose phase is delayed by $\pi/2$ and polarization direction is orthogonal to those of the pump pulse. This local oscillator interferes with the polarization component generated from the probe pulse by interacting with the activated medium. The interference component between the local oscillator pulse and the interacted probe pulse is detected as OHD-OKE signal.

The material response function can be expressed by the sum of the instantaneous component σ and the casual component $N(t)$. Considering such a configuration, the intensity of the OHD-OKE signal at delay τ is given by

$$S_{OHD}(\tau) \propto \sigma \langle I_r(t-\tau) I_p(t) \rangle_t + \int_0^\infty dt' N(t') \langle I_r(t-\tau) I_p(t-t') \rangle_t, \quad (2)$$

where $\langle \rangle_t$ denotes temporal average and $I_r(t-\tau)$ is the light intensity of the probe pulse. Here $\langle I_r(t-\tau) I_p(t) \rangle_t$ corresponds to the autocorrelation of the incident laser pulse because the pump and probe pulses are replica of each other. So Equation 2 readily indicates that OHD-OKE signal is proportional to the autocorrelation function of the incident laser pulses if the media responds instantaneously, i. e. $\sigma \neq 0$ and $N(t) = 0$. This is why the OHD-OKE signal of CCl_4 , whose third-order nonlinearity almost arises from pure electronic nonlinearity, has the same width as that of the autocorrelation.

The experimental arrangement for our femtosecond OHD-OKE measurement is described previously [4]. Pulses of about 10 nJ in energy, obtained from a femtosecond Ti:sapphire laser pumped by an argon-ion laser, were used. A pair of fused silica prisms were placed in the path of the beam for dispersion compensation to provide transform limited and chirped pulses. The incident pulses were divided by a beam splitter into weak (probe) and strong (pump) pulses and were focused by an 8-cm fused-silica plano-convex lens and spatially overlapped in a 1-mm quartz cell. The intensity ratio of the pump and probe beams at the position of overlap was around 10:1. In the

optical path of the probe beam, two Glan-laser prisms rotated orthogonally to each other to act as a polarizer and an analyzer were placed before and after the sample cell. A quarter-wave plate, which provides local oscillator light for OHD, was installed just after the first polarizer. We perform $\pi/2$ out-of-phase OHD by a slight rotation ($< 1^\circ$) of the first polarizer, to detect refractive index change induced by the pump pulse.

We prepared the samples of tetrakis(*p*-pentylphenyl)porphyrin in CCl_4 in various concentrations. Before the samples were poured into the cell, the solution was filtered with a 0.2- μm polytetrafluoroethylene filter to remove residual dust particles.

RESULTS AND DISCUSSION

We measured the OHD-OKE signal of 3.2×10^{-3} M solution of TPP in CCl_4 and compared it with that of the CCl_4 measured under the same experimental condition. CCl_4 has an instantaneous electronic response to the incident pulse [5], so its OKE signal has the same shape as the autocorrelation of the incident pulse. The OHD-OKE signal from TPP solution (Figure 1A) shows a narrow and negative dip near the zero delay time with temporal width (in full

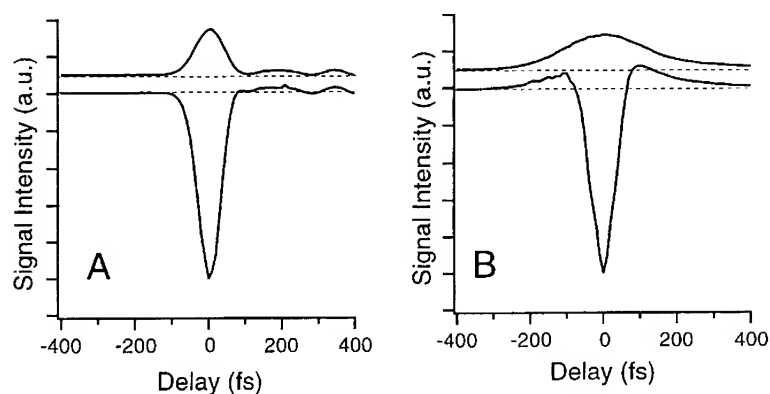


FIGURE 1 OHD-OKE signal from CCl_4 (upper curve) and 3.2×10^{-3} M solution of TPP in CCl_4 (lower curve) with a near transform limited pulse (A) and a chirped pulse (B). The baselines of the curves are shifted for readability.

width at half maximum, FWHM) of about 80% of that from CCl_4 . The long time response from TPP almost follows the CCl_4 response.

One plausible reason for the negative and narrow signal was the fifth- or higher-order nonlinear processes including the effect due to excited state generation by two-photon absorption [6]. To test the possibility, we gradually decreased the pumping intensity down to the half of its original value. We found the amount of narrowing of TPP signal to be almost independent of the pumping intensity. We also tried to measure the imaginary part of the susceptibility by removing the quarter-wave plate from the path of the probe beam. However, no signal was detected, implying the two-photon absorption is negligible under the present experimental condition. These results rule out the possibility of the higher-order processes.

Another evidence ruling out the higher-order processes was obtained by the experiments with chirped pulses. The chirped incident pulses were introduced by slightly shifting a prism used for dispersion compensation. By introducing chirped pulses, the intensity autocorrelation of the incident pulses became broader (data not shown) and the signal from pure CCl_4 also became broader (upper curve in Figure 1B). We found that the signal (lower curve in Figure 1B) almost follows the CCl_4 response except that it shows a sharp negative dip near the zero delay time. The amount of chirp does not effect the width of the negative signal, so the TPP response is independent of the chirp of the incident pulse.

The chirped pulse experiments suggest that the negative dip is related to the coherence of the incident pulse because the coherence is independent of the amount of chirp of the pulse. In order to see the relation with the coherence, we estimated the coherence time of the incident light assuming it to be a Gaussian envelope transform limited pulse. Here we use the intensity correlation width, $\Delta\tau_i$, as a measure of coherent time. The intensity coherent width can be obtained as

$$\Delta\tau_i = \frac{2\sqrt{2} \ln 2}{\pi c \Delta\lambda} \lambda^2, \quad (3)$$

where λ is the center wavelength of the incident pulse and $\Delta\lambda$ is its band-

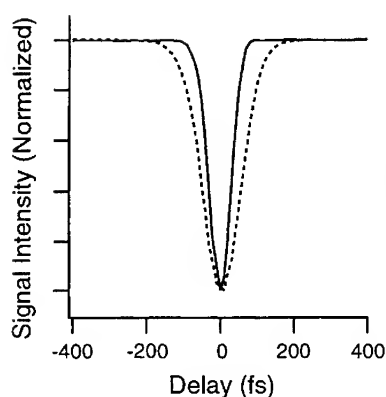


FIGURE 2 The interference signal extracted by the subtraction of the OKE signal of CCl_4 from that of TPP. The intensity correlation time of the incident pulse is 73 fs for solid curve and 130 fs for dotted curve.

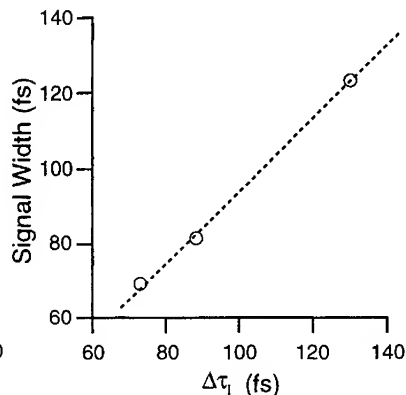


FIGURE 3 Plot of OKE signal width of TPP versus intensity correlation time of the incident pulse for 3.2×10^{-3} M solution of TPP in CCl_4 .

width. We changed the coherence time of the incident pulse by tuning mode-locking condition of the laser and found the width of negative dip to be dependent on the coherence time of the incident pulse (Figure 2). For longer coherence times, the width of the dip from TPP solution was larger. Figure 3 shows the variation of the width of the signal dip from TPP solution is in linear relation to $\Delta\tau_1$.

The fact that the width of the negative dip does not depend on chirp but on coherence time, clearly indicates that the negative dip is due to additional process that occurs during the coherence overlap of the pump and probe pulses. So we can explain that the dip is due to the contribution of self-diffraction by a transient grating formed in the sample. From this point of view, the reason why the width of the negative dip is narrower than that of the autocorrelation width even with near transform limited pulses as shown in Figure 1, can be explained; i.e., as the incident pulses are near to transform limit but not exactly, so the width of the signal for CCl_4 is slightly broader than that for transform limit pulse while the width of the dip for TPP solution

keeps to be the coherence time of the incident pulse.

Recently, Kinoshita et al. have also reported a similar negative dip in OHD-OKE signal for pure alcoholic solvents such as methanol and ethanol. They concluded that the negative dip is caused by a grating produced due to overtones of vibrational absorption of the solvents [7]. We observed that magnitude of the negative dip decreases as the concentration of TPP is lowered, indicating the grating formation is not related to solvent but to solute in our case. Then, what kind of material response does induce the transient grating? These experiments can be considered to be performed under non-resonant condition in usual sense because the absorption of the TPP solution at the wavelength of incident laser pulse (800 nm) was no more than 0.002 in absorbance. However, though this amount of absorption is very small, it is sufficient to compete with the ordinary Kerr process.

CONCLUSIONS

A narrow dip was observed in OHD-OKE signal for the solutions of TPP in CCl_4 . The width of the dip is narrower than that of the autocorrelation of the incident pulse, which cannot be explained solely from the ordinary formulation for OHD-OKE process. The width of the negative dip is independent of intensity of the incident pulse, ruling out the possibility of the fifth- and higher-order nonlinear optical processes associated with excited state formation by two-photon absorption. The width of the negative dip also depends not on the amount of chirp, but on the coherent time of the incident pulses.

The dip depending on the coherence time can be explained if the additional process due to coherent coupling between pump and probe beams is considered. The additional process is the formation of a transient grating and self-diffraction by it, which are not considered in the ordinary OHD-OKE formulation. The transient grating is considered to be formed due to absorption of TPP along the interference pattern of two pulses, though the absorption of TPP is nearly negligible.

We have shown that the grating effect due to the interference of the pump and probe beams should also be considered even for weakly absorptive

media. From this result it is concluded that attentions should be paid for OHD-OKE experiment even for weakly or almost no absorptive media. Because OHD-OKE responses of different materials may be distorted due to the interference effect. However, there is a criterion for confirming the observed signal to be undistorted. The grating effect can be distinguished from ordinary OKE signal using the chirped pulse excitation. This criterion will be important when OHD-OKE experiment is used for the studies of nonlinear absorption.

ACKNOWLEDGMENT

We sincerely thank Professor S. Kinoshita for helpful discussion.

REFERENCES

1. P. D. Maker, R. W. Terhune and C. M. Savage, Phys. Rev. Lett., **12**, 507 (1964) .,
2. G. L. Eelsley, M. D. Levenson, and W. M. Tolles, IEEE J. Quantum. Electron., **QE-14**, 45 (1978).
3. M. E. Orczyk, M. Samoc, J. Swiatkiewicz, Guolin Huang, and P. N. Prasad, J. Phys. Chem., **98** , 7307(1994).
4. K. Kamada, M. Ueda, T. Sakaguchi, K. Ohta, and T. Fukumi, Chem. Phys. Lett., **263**, 215 (1996); K. Kamada, M. Ueda, T. Sakaguchi, K. Ohta, and T. Fukumi, J. Opt. Soc. Am. B, **15**, 838 (1998).
5. D. McMorow, W. T. Lotshaw, and G. A. Kenney-Wallace, IEEE J. Quant. Electron., **24**, 443 (1988).
6. R. Morita, H. Yanagisawa, and M. Yamashita, Abstracts of International Workshop on Femtosecond Technology, Tsukuba, Japan, 1996, p. 73.
7. S. Kinoshita, T. Ariyoshi, and Y. Kai, Chem. Phys. Lett., **257**, 303 (1996); S. Kinoshita, Y. Kai, T. Ariyoshi, and Y. Shimada, Int. J. Mod. Phys. B, **10**, 1229 (1996).

CRYSTALLINE COLLOIDAL ARRAY OPTICAL SWITCHES AND LIMITERS

SANFORD A. ASHER, GUISHENG PAN AND RASU KESAVAMOORTHY*

Department of Chemistry, University of Pittsburgh, Pittsburgh, PA 15260,

*Materials Research Division, Indira Ghandi Center for Atomic Research,
Kalpakkam 603 102, Tamil Nada, India

Abstract We fabricated nsec optical switches and optical limiters by utilizing polymerized crystalline colloidal arrays (CCA). CCA are face centered cubic or body centered cubic arrays of colloidal particles with lattice constants of 200-300 nm. These structures efficiently Bragg diffract visible light. We polymerized a CCA of absorbing colloidal particle in a hydrogel matrix and refractive indexed matched the particles to the surrounding medium. Thus, these CCA show a modulation in the only the imaginary part of their refractive index and show little or no diffraction of light. Nsec pulses of visible light absorbed by the colloidal particles increase their temperature which decreases the particle refractive index. This creates a periodic modulation in the real part of the refractive index which pops up in 3 nsec to diffract light. Theoretical calculations indicate that the array should diffract essentially all light meeting the Bragg condition. At present we observe a smaller diffraction efficiency, which is due to disorder in the CCA. We are improving the CCA array ordering to increase the diffraction efficiency.

INTRODUCTION

Dispersions of highly charged, monodisperse, submicrometer size colloidal particles can self-assemble into body centered cubic (bcc) or face centered cubic (fcc) crystalline colloidal arrays (CCA) due to the presence of interparticle screened Coulombic repulsions.¹⁻⁶ The refractive index of these particles generally differs from that of the surrounding medium, which results in a periodic variation in the CCA refractive index. This modulation in the refractive index results in Bragg diffraction, similar to the diffraction of x-rays from atomic and molecular crystals. A major difference occurs, however, in that the periodicity in the refractive index for the CCA is much larger than that found for atomic and molecular crystals; it occurs in the 10 nm-3 μ m length scale. Thus, the CCA efficiently diffracts electromagnetic radiation in the UV, visible and near-IR spectral regions.^{4,6} This unique property can be used to make devices such as narrow band optical rejection filters^{4,7-11} and chemical sensing devices.¹²

We demonstrated recently that the CCA periodicity can also be used to fabricate nanosecond nonlinear optical switching and limiting devices.¹³⁻¹⁶ The idea is to match the real part of the refractive index of dyed CCA particles to that of the medium. Thus, at low light intensities, no modulation occurs in the real part of the refractive index and light freely transmits. However, since the dyed particles have a thermal nonlinear dependence of their refractive index on the incident light intensity, at high light intensities the particle refractive index diverges from that of the medium, and the periodic modulation of the real part of the refractive index will „pop up“ to diffract the high intensity incident light. For a 5 nsec pulsed laser beam of 10 MW/cm^2 , our calculations¹⁵ showed that the refractive index of the particles would diverge sufficiently from that of the medium that a perfectly ordered CCA would diffract $> 90\%$ of the incident light within 5 ns (Fig. 1).

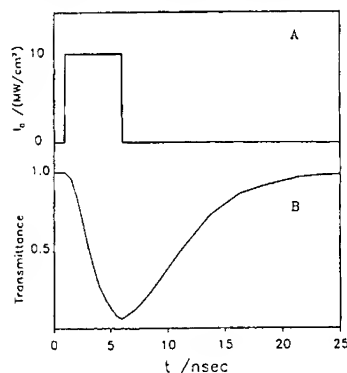


Fig. 1 Calculated time dependence of transmittance through a nonlinear CCA. (A) Temporal dependence of incident heating laser beam. (B) Transmission of probe beam of wavelength 514.5 nm incident at $\theta_B = 75^\circ$ on an indexed matched CCA of 81 nm particles.

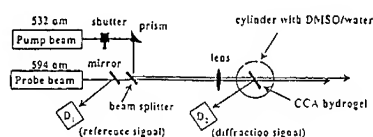


Fig. 2 Experimental setup of nonlinear optical diffraction switching. A PCCA sample was mounted on an aluminum frame, which was placed in a glass cylinder containing a mixture of water and DMSO. The 532 nm pump and 594 nm probe beams ($\sim 3.5 \text{ ns}$ duration) were collinear and focused onto the PCCA sample. The Bragg diffracted probe intensities were measured by photodiode D_2 and normalized to the incident probe intensity measured by photodiode D_1 . R_{off} and R_{on} , the normalized diffracted probe beam, were measured in the absence and presence of the pump beam, respectively. The diffraction switching ratio, $R_{\text{on}}/R_{\text{off}}$, was monitored as a function of pump energy.

We developed a synthetic method to fabricate monodisperse, low refractive index, dyed, highly charged colloidal particles consisting of poly(1H,1H-heptafluorobutyl methacrylate)¹³. These particles, have a sufficiently low refractive index ($n_D = 1.3860$) that they can be easily matched to a predominantly aqueous medium. We also covalently attached to these particles the dye Oil Blue N which strongly absorbs light in the 500-540 nm spectral region.

We induced the self assembly of these dyed particles into a CCA which we then polymerized into a polyacrylamide hydrogel matrix (PCCA). We then adjusted the refractive index difference between the particles and the medium by replacing the aqueous medium within the hydrogel. This system allows us to easily fine tune the refractive index mismatch between the particles and the medium.

EXPERIMENTAL

A circular PCCA disc of 1.6 cm diameter was cut and immersed in a water/DMSO solution contained in a cylindrical glass tank. Figure 2 shows the experimental setup used to monitor the diffraction switching. The PCCA surface was tilted from the normal by $\sim 20^\circ$ in order to Bragg diffract a 594 nm probe beam from a dye laser, which was pumped by a 532 nm, 3.5 nsec pulsewidth YAG laser (Coherent Inc. Infinity). The 532 nm YAG pump beam was used to switch on the PCCA diffraction. The pump and the probe beams were collinear and focused onto a 100 μ m radius spot on the PCCA sample. The probe beam was delayed with respect to the pump by 2.5 ns. The diffracted probe energy (I_2), as measured by photodiode D_2 , was normalized to the incident probe energy (I_1), as measured by photodiode D_1 , because the dye laser output fluctuates from one pulse to another by ca. 6%. R_{off} and R_{on} , the normalized diffracted probe beam intensities in the absence and presence of the pump beam, respectively, are defined as:

$$R_{off} = (I_2/I_1)_{off} - (I_2/I_1)_{bck}, \quad R_{on} = (I_2/I_1)_{on} - (I_2/I_1)_{leakage} - (I_2/I_1)_{bck} \quad (1)$$

where $(I_2/I_1)_{off}$ and $(I_2/I_1)_{on}$ are the normalized signals in the absence and presence of the pump beam, respectively. $(I_2/I_1)_{leakage}$ is the normalized leakage pump beam signal in the absence of the probe beam, $(I_2/I_1)_{bck}$ is the normalized background signal in the absence of

both the probe and the pump beams. Each measurement (R_{on}/R_{off}) was averaged over 20 pulses and the standard deviation was calculated. An absorbing filter placed in front of D_2 removed most of the 532 nm scattered pump beam. The remaining leakage of the scattered pump beam into D_2 was numerically removed from the measured R_{on} as shown in Equation (1).

RESULTS and DISCUSSION

Figure 3A shows the extinction spectrum of the PCCA in a DMSO/water solution at normal incidence, while Figure 3B shows the dependence of the maximum value of this extinction at 656 nm, as a function of the hydrogel medium refractive index(n_m). The 530 nm peak results from the dye absorption band. The diffraction of the incident beam almost follows Bragg law:

$$M \lambda_0 = 2 n d_{hkl} \sin \theta_B \quad (2)$$

where M is the diffraction order, λ_0 is the Bragg diffracted wavelength in air. d_{hkl} is the interplanar spacing of the lattice plane with Miller indices (hkl). θ_B is the Bragg glancing

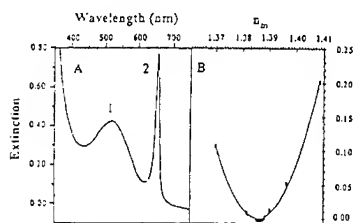


Fig. 3 (A): Extinction spectrum of 138 nm diameter dyed poly(1H,1H-heptafluorobutyl methacrylate) PCCA in water. Peak 1 derives from absorption of acylated Oil Blue N dye covalently bound to the particles. Peak 2 is the PCCA Bragg diffraction. The spectrum was measured with the PCCA surface normal to the incident light. (B): Extinction of dyed PCCA (sample A) as a function of medium refractive index. The data (filled circles) are best fit to: $A = 405.85(n_m - 1.3860)^2 + 0.0063$, where n_m is the medium refractive index and 1.3860 is the particle refractive index.

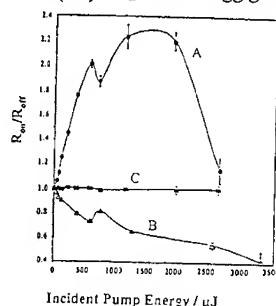


Fig. 4 Pump beam energy dependence of R_{on}/R_{off} for the case of over- and under-index matching conditions. The probe beam was delayed by 2.5 ns compared to the pump beam. The pump beam spot size on the sample had a 100 μ m radius. Curve A and B were measured for a dyed PCCA with n_m adjusted to 1.3902 and 1.3817, respectively; Curve C was measured for an undyed PCCA at $n_m = 1.38$

angle between the incident beam and the (hkl) plane inside the crystal. n is the average refractive index of the PCCA:

$$n = n_p \Phi_p + n_m(1 - \Phi_p) \quad (3)$$

where n_p is the particle refractive index (1.3860). Φ_p is the particle volume fraction in the PCCA. n_m is the hydrogel medium refractive index given by

$$n_m = 1.543x + n_{\text{mix}}(1 - x) \quad (4)$$

where 1.543 is the refractive index of polyacrylamide. x is the volume fraction occupied by the polyacrylamide hydrogel network in the medium, and n_{mix} is the measured refractive index of the DMSO/water solution. n_{mix} can be varied by varying the fraction, y , of DMSO in water,

$$n_{\text{mix}} = 1.479y + 1.333(1 - y) \quad (5)$$

where 1.479 and 1.333 are the refractive indices of DMSO and water, respectively. The extinction is defined by:

$$E = -\log\left(1 - \frac{I_D}{I_0}\right) \quad (6)$$

where I_0 is the incident light intensity, I_D is the diffracted intensity. The extinction was best fit to a parabola:

$$E = a_1(n_m - n_p)^2 + b_1 \quad (7)$$

We found $x = 0.0301$, $a_1 = 405.85$, $b_1 = 0.0063$. The minimum value of E occurs when $n_m = n_p$.

We placed the PCCA in the sample chamber, adjusted the medium to the appropriate refractive index and made the pump and probe beams coincident on the sample. Figure 4 shows the measured ratio of the diffraction of the probe beam in the presence and absence of the pump beam. Curve A was obtained for an over-index matched ($n_m(1.3902) > n_p(1.3860)$) PCCA, while curve B was obtained for an under-index matched ($n_m(1.3817) < n_p(1.3860)$) PCCA, and curve C was obtained for an undyed PCCA with $n_m = 1.3817$. The signal, $R_{\text{on}}/R_{\text{off}}$, is independent of the pump energy for the undyed PCCA, since the undyed colloidal spheres do not absorb the pump. Thus, their temperature and n_p do not change; hence, no change occurs in the diffraction efficiency with increasing pump energy.

Curves A and B clearly indicate an optically nonlinear response of the dyed PCCA. As the pump beam heats the CCA, the diffraction efficiency increases when it is over-index matched ($n_m > n_p$), but decreases when it is under index-matched ($n_m < n_p$). The dyed CCA particles absorb the pump energy and heat up to decrease n_p , since $dn_p/dT < 0$. The over-index matched particles show an increasing refractive index mismatch as the pump pulse energy increases, and the particle refractive index decreases; this results in increased diffraction. In contrast, the under index-matched CCA becomes more matched on pump beam heating, which causes the diffraction to decrease.

A measurement of the transmitted pump energy indicates that the particles in the PCCA absorb 34% of the incident pump energy, which is identical to that calculated from the dye absorption at $\lambda=532$ nm shown in Figure 3A. Assuming that this energy was absorbed uniformly by the CCA particles in the volume illuminated by the pump beam, the temperature increase (ΔT) can be calculated:

$$\Delta T = f_1 f_2 \Delta E / m C_p \quad (8)$$

where ΔE is the average pump pulse energy. f_1 is the fraction of the incident light energy that enters and is absorbed by the PCCA (34%). f_2 is the energy loss coefficient due to the reflection from the front surface of the container wall (96%). C_p is the heat capacity of the polymer making up the particles. Since the PCCA was tilted from normal by $\sim 20^\circ$, the illuminated total mass of particles by the pump beam is:

$$m = N (\pi r^2 l_0 / \cos 20^\circ) (\pi d_0^3 / 6) \quad (9)$$

where r is the pump beam radius at normal incidence on the PCCA and l_0 is the PCCA thickness. d_0 is the particle diameter. There is insignificant refraction of light within the sample due to the close matching of the refractive index of the surrounding DMSO/water solution and the PCCA sample. N , the particle concentration ($6.11 \times 10^{13}/\text{cm}^3$) was obtained from the calculated value of d_{th} , using Equation (2), given the 648 nm measured diffraction wavelength, and that $n = 1.3926$. By inserting $\Delta E = 570 \mu\text{J}$, $C_p = 1.15 \text{ J/K/g}$, $r = 100 \mu\text{m}$, $l_0 = 800 \mu\text{m}$, and $d_0 = 138 \text{ nm}$ into Equations (8) and (9), the particle temperature increase at an incident pump pulse energy of 570 μJ , which corresponds to the first dip (peak) in curve A (B) of Figure 4, was calculated to be 46 $^\circ\text{C}$. Hence, the calculated particle temperature was 69 $^\circ\text{C}$. Both the dip in A, and the peak in B of the diffracted probe energy ratio, $R_{\text{on}}/R_{\text{off}}$ occurs at 570 μJ . This calculated particle temperature of 69 $^\circ\text{C}$ is close to the 62 $^\circ\text{C}$ measured T_g value for these particles¹³.

n_p should continuously decrease with increasing particle temperature. Thus, we interpret the dip (peak) in the Figure 3A (B) curve in the over- (under-) refractive index matched sample at pump energies of $\sim 570 \mu\text{J}$ to indicate a region where the pump heating does not continuously increase with increasing pump energy. The fact that this pump energy corresponds to the T_g of the particles, suggests that this phase transition is associated with the phenomenon.

As the pump energy continues to increase the diffracted intensity continues to increase (decrease) after the T_g dip (peak), due to further increases in particle temperature, and further decreases in particle refractive index, up to pump energies of $\sim 1500 \mu\text{J}$. As long as the pump energy is maintained below $\sim 1500 \mu\text{J}$, the PCCA response is fully reproducible and there is no evidence of degradation. However, for pump energies above $1500 \mu\text{J}$, the PCCA undergoes irreversibly damage, which results in irreversible diffraction efficiency decreases for both curves A and B of Figure 3. This irreversible PCCA damage appears to result from damage to the array of particles, since we observe damage to a liquid dispersion of these particles if they are illuminated with 1000 pulses of $2000 \mu\text{J}$ pump energy focused to a $100 \mu\text{m}$ spot radius.

Although we calculated that essentially all of the incident light should be diffracted at pump energies of $10 \text{ MW}/\text{cm}^2$, we observe that the biggest $R_{\text{on}}/R_{\text{off}}$ achieved is only 3.0 at T_g . Without the pump the system is poised to diffract $\sim 0.6\%$ of the probe beam. Thus, only $\sim 2\%$ of the probe beam is diffracted in the presence of the pump.

Figure 5 shows the pump delay time dependence of the diffraction efficiency at a pump beam energy which heats the particles to T_g . If the probe precedes the pump by 2.5 nsec , no change in diffraction occurs compared to that in the absence of the pump beam. If the probe and pump coincide in time, the diffraction increases and continues to increase until the probe is delayed by 2.5 nsec relative to the pump. Further delays cause the diffraction efficiency to decrease, and by a 10 nsec delay little impact of pump heating is observed. The maximum diffraction is observed for a probe delay where there is a maximum temporal overlap between the heating and probe pulses. This $\sim 5 \text{ nsec}$ observed time dependence is very similar to that we theoretically predicted.¹⁵

Thus, we have observed nanosecond optical switching for these mesoscopically periodic arrays. We expect that this switching phenomenon can be used for optical limiting if the dye absorption is coincident with the diffracted wavelength, or for optical switching where a pump beam would control the diffraction and transmission of one or more probe beams. In fact this device could be used for parallel optical switching since small areas of the PCCA could be individually addressed to permit parallel processing. We expect that the pixel density could be quite high.

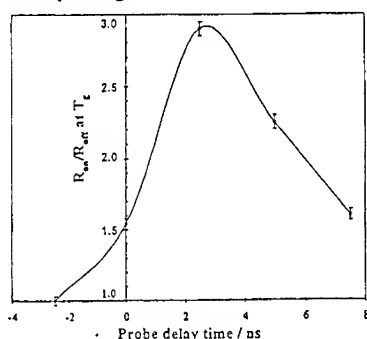


Fig. 5 Dependence of R_{on}/R_{off} on the delay time between the probe and pump beams. The pump beam energy was set to heat the spheres to a temperature of T_g .

At present, however, the device switches only 2% of the probe beam, which is far below that theoretically expected. We calculated using Dynamical Diffraction Theory^{9,15,18,19} that the diffraction efficiency for a perfect PCCA lattice should be 97% for the 600 μ J pump excitation that transiently heats the spheres to 60 °C. Since we independently verified¹⁴ that our temperature and refractive index changes conform to our theoretical conditions, we ascribe the decreased Bragg diffraction efficiency to disorder in the PCCA lattice.

We are developing methods to prepare more perfect PCCA films. In addition, we recently discovered that we can increase the sphere scattering power by over 10-fold by using second order diffraction.²⁰ Further optimization of these PCCA should lead to efficient optical switching devices and limiters. The unique potential efficiency of these devices results from the fact that this mesoscopically period array concentrates the scattering power of the particles into a narrow solid angle which fulfills the Bragg condition.

ACKNOWLEDGMENTS

Supported by the Office of Naval Research through Grant No. N00014-94-0592 and by the National Science Foundation through Grant No. CHE 9633561.

REFERENCES

1. (a): I. M. Krieger and F. M. O'Neill, J. Am. Chem. Soc. **90**, 3114-3120; (b): P. A. Hiltner and I. M. Krieger, J. Phys. Chem. **73**, 2386-2389 (1969).
2. N. A. Clark, A. J. Hurd, and B. J. Ackerson, Nature **281**, 57-60 (1979).
3. P. Pieranski, Contemp. Phys. **24**, 25-73 (1983).
4. P. L. Flaugh, S. E. O'Donnell, and S. A. Asher, Appl. Spectrosc. **38**, 847-850 (1984).
5. A. K. Sood, in Solid State Physics, ed. by H. Ehrenreich and D. Turnbull, Academic Press, New York, **45**, 1-73 (1991).
6. R. J. Carlson and S. A. Asher, Appl. Spectrosc. **38**, 297-304 (1984).
7. S. A. Asher, P. L. Flaugh, and G. Washinger, Spectroscopy **1**, 26-31 (1986).
8. S. A. Asher, U.S. Patents No. 4,627,689 and 4,632,517 (1986).
9. R. J. Spry and D. J. Kosan, Appl. Spec. **40**, 782-784 (1986).
10. H. B. Sankara, J. M. Jethmalani, and W. T. Ford, Chem. Matter. **6**, 362 (1994).
11. J. M. Weissman, H. B. Sunkara, A. S. Tse, and S. A. Asher, Science **274**, 959-960 (1996).
12. J. H. Holtz and S. A. Asher, Nature **389**, 829-832 (1997).
13. G. Pan, A. S. Tse, R. Kasavamoorthy and S. A. Asher, J. Am. Chem. Soc., in press (1998).
14. G. Pan, R. Kasavamoorthy and S. A. Asher, J. Am. Chem. Soc., in press (1998).
15. R. Kesavamoorthy, M. S. Super, and S. A. Asher, J. Appl. Phys. **71**, 1116-1123 (1992).
16. G. Pan, R. Kesavamoorthy, and S. Asher, Phys. Rev. Lett. **78**, 3860-3863 (1997).
17. P. A. Runquist, S. Jagannathan, R. Kesavamoorthy, C. Brnardic, S. Xu, and S. A. Asher, J. Chem. Phys. **94**, 711-717 (1991). R. Kesavamoorthy, S. Jagannathan, P. A. Rundquist, and S. A. Asher, J. Chem. Phys. **94**, 5172-5179 (1991).

18. W. H. Zachariasen, Theory of X-ray Diffraction in Crystals, John Wiley and Sons, New York (1946).
19. P. A. Rundquist, P. Photinos, S. Jagannathan and S. A. Asher, *J. Chem. Phys.* 91, 4932-4941 (1989).
20. L. Liu, P. Li, and S. A. Asher, *J. Am. Chem. Soc.* 119, 2729-2732 (1997).

COMPARING THE SCATTERING PROCESS IN PARTICLE SUSPENSIONS IN LIQUIDS AND GASES FOR USE AS OPTICAL LIMITERS

KAREN M. NASHOLD, DIANE P. WALTER, JEFF M. VOSS,
GLENN S. FRYINGER,* AND ROBERT L. SHARPLESS
SRI International, 333 Ravenswood Avenue, Menlo Park, California, USA

Abstract SRI has been investigating the optical limiting properties of suspensions of small particles. A strong contributor to optical limiting is the scattering of light that occurs when the energy absorbed by the carbon particles in a tightly focused laser beam is sufficient to trigger optical breakdown in the media. The limiting seen in the carbon suspensions is similar to that seen as a result of optical breakdown in gases, particularly when particulates are present in the gas.

In gases, the limiting is attributed to plasma buildup initiated by the absorption of laser energy. Small particulates in the gas seed the breakdown process, causing breakdown to occur at much lower fluence levels than if the gas is kept free of particulates. This is analogous to what occurs in liquids. Liquids that are free of particulates also break down given a high enough fluence level. Particulates in liquids lower the breakdown threshold as they do in gases.

INTRODUCTION

A cell filled with a suspension of small absorbing particles and placed in the focal plane of an optical system will limit the transmission of pulsed laser light.¹⁻⁸ This limiting is caused by optical breakdown of the fluid in the focal volume of the limiter cell. The absorbing particles act as initiation sites for lowering the threshold for optical breakdown in the liquid. During the optical breakdown process, a white flash is created in the focal volume of the liquid. This is assumed^{2,3} to be due to plasma generation similar to that created during optical breakdown in gases,⁴ but could also be due to blackbody radiation caused by the heating of the particles. Measurements of the duration of the attenuation created when a Q-switched pulse is focused into a limiter cell show that the attenuation lasts 450 ns or longer after the laser pulse has passed. Additional attenuation is created by the shock wave generated by the rapid heating and vaporization of carbon particles, and, in some cases, by the creation of macroscopic bubbles, which can remain in the optical path for hundreds of microseconds.²

* Dr. Fryinger is currently at the US Coast Guard Academy, Dept. of Science (ds-1), 15 Mohegan Avenue, New London, CT 06320-4195.

In 1990 we performed an experiment⁶ in which we removed the liquid from the suspension to see if the liquid was important in the limiting process. We did this by suspending particles between two oppositely charged electrodes. The particles are repelled from one electrode to the other as they acquire the charge of the electrode with which they are in contact. The particles travel at a rate of about 10 m/s, depending on the particle type, electrode spacing, and applied voltage.⁹ At this speed the particles are suspended in the timeframe of a short (nanoseconds to microseconds) laser pulse. Unfortunately, in this experiment the particles were large compared with the wavelength of light, and concentrations were not sufficient to achieve consistent breakdown for limiting visible radiation. Our results do fit, however, with data collected for varying particle sizes in liquids which showed that sufficient concentrations were required to get consistent limiting. This technique of suspending particles in gas did work well for infrared radiation, and most of the data presented here for the gas suspensions were taken at $\lambda = 10.6 \mu\text{m}$.

LIMITING AS A RESULT OF SCATTER CREATED IN SUSPENSIONS OF CARBON IN LIQUIDS

In this paper we will review the scatter in liquids, describe results obtained with particles suspended in gases, and show that many aspects of the limiting process are the same. In both, the pulse duration gets shortened as enough energy is absorbed to trigger the breakdown process and the remainder of the pulse is scattered and absorbed by the change in the medium. Lowering the ionization potential of the suspending medium results in a lower breakdown fluence threshold for both liquids and gases. However, the presence of particles lowers the threshold beyond that of the neat liquid or gas, and the lower ionization potential of the liquid or higher gas pressures does not provide further benefit over that of the particles. Particle size is a factor in that using smaller particles allows for higher concentrations of particles with the same insertion loss prior to breakdown. Sufficient concentration of particles is required to ensure that enough particles will be present in the focal volume to help trigger the breakdown process. In the following section we discuss the nonlinear scattering process with liquids.

Scattered vs. Absorbed Energy

The standard suspension studied in this work consists of carbon black (obtained from india ink) in ethanol. Carbon is used for the absorbing particles because of its high and uniform absorption over a large spectral range. The uniform absorption makes the suspension useful as an optical limiter over the entire transmission band of the liquid in which the particles are suspended.

Since the particle sizes in the standard suspension are for the most part all smaller than $0.02\text{ }\mu\text{m}$ (measured with a Horiba CAPA-700 Particle Size Distribution Analyzer), there is essentially no scattered energy until the transmission becomes nonlinear as a result of the optical breakdown. In an experiment to measure the relative contribution of scatter and absorption in the limiting process,⁵ scatter was not seen until input energies reached $1\text{ }\mu\text{J}$. This corresponds to a fluence level at a focus of $25\text{ to }30\text{ mJ/cm}^2$. In Reference 5, three different particle concentrations of the carbon black suspensions were tested at $\lambda = 532\text{ nm}$ in a relatively long pathlength cell (1 cm). As the input energy (and hence the fluence in the focal volume) increases, the transmission decreases and both the scattered and absorbed energy increase. The ratio of scattered to absorbed energy decreases for higher concentrations, possibly due to the fact that more of the scattered light gets absorbed before it leaves the cell with the higher concentration suspensions. Therefore, although light is initially scattered, it eventually gets absorbed.

Tests made including the energy from the white flash in the scattered energy indicated that the white flash is negligible compared with the light that is scattered.

Scattered Energy as a Function of Angle

The amount of light collected from the suspension depends on the f -numbers of the optics used to focus the light into the cell containing the suspension, and the f -number of the lenses used to collect the light after it leaves the cell. Before breakdown, the light rays are refracted by the lens used to focus the light into the cell. For $F/4$, for example, collimated rays from an infinite conjugate point are bent into a 14° cone. This can be

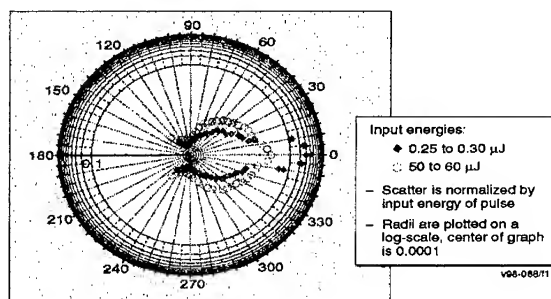


FIGURE 1 Distribution of scattered energy for 1-cm pathlength cell with 81% transmitting carbon suspension and $F/4$ input beam.

seen in low input energy data in Figure 1. These data show the relative energy (normalized to the input energy) as a function of angle around the limiter cell. (These data were collected with the optical setup shown in Figure A1 in the appendix.) The majority of the light is in the forward direction determined by the lens used to focus it. If the acceptance angle of the output lens is less than that of the input lens, not all of the energy input into the cell will be collected by the output lens even if breakdown does not occur.

After breakdown, the energy decreases in the forward direction and increases throughout the entire sphere surrounding the focus. However, the energy is still greatest in the forward direction. In Figure 1, the average ratio of the scattered energy to input energy is 3×10^{-2} for input energies between 50 and 60 μJ . At $\pm 10^\circ$ the value is 10^{-2} . By $\pm 30^\circ$ the ratio is down to between 5×10^{-3} and 8×10^{-3} , and it continues to decrease with a minimum at around 90° of about 3×10^{-4} . Even in Reference 5, where the input optics were $f/48$, the majority of the scattered light was also within $\pm 30^\circ$ of the transmitted direction for energies when optical breakdown occurred.

Limiting as a Function of Particle Size

To see if particle size played a significant role in limiting, we measured scattering as a function of particle size using three different sizes of black polystyrene monodisperse particles from Seradyn. Because of the small sizes in the standard carbon suspension (less than $0.02 \mu\text{m}$ in diameter), it would have been difficult to filter the standard suspension to significantly different size distributions. We therefore decided to purchase from Seradyn, Inc., some well-defined size distributions of polystyrene spheres that had been dyed black. The particles were 0.805, 0.420, 0.299, and $0.075 \mu\text{m}$ in diameter. According to Seradyn, the particles were all within $\pm 10\%$ of the specified diameter, and in many cases the distribution had a standard deviation of less than 1% of the specified diameter.

The samples were diluted with water to provide an 81% transmission relative to water at $\lambda = 532 \text{ nm}$. Water was used since the particles are shipped suspended in water. The samples were tested for limiting using the setup shown in Figure A2. The laser used for these tests was a Q-switched, frequency-doubled Nd:YAG laser. The full-width half-maximum (FWHM) pulse duration was 6 ns.

Figure 2 shows the limiting as a function of particle size for the four different polystyrene samples compared with the standard carbon in ethanol suspension. None of the polystyrene samples limited as well as the carbon suspension. The carbon suspension has particle sizes of less than $0.02 \mu\text{m}$, which is smaller than any of the available polystyrene spheres. Limiting measurements (not shown here) with the $0.075 \mu\text{m}$ polystyrene sphere

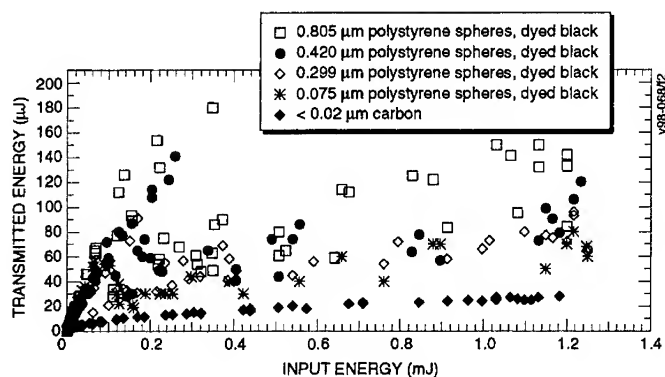


FIGURE 2 Limiting as a function of particle size (all suspensions 81% transmission over 1 cm, $\lambda = 532$ nm).

suspension with a concentration that provided 47% transmission over a 1 cm pathlength also did not limit as consistently as the carbon suspension. Using Beer's law and assuming that the dyed polystyrene spheres have the same refractive index as the carbon (which may be a poor approximation), and that the initial focal volume is 10^{-9} cm³ (the $1/e^2$ spot diameter was 6 μ m), we estimated that there were approximately 14 polystyrene particles in the focal volume for the 47% transmitting suspension. This compares with approximately 3035 particles in the 81% transmitting carbon suspension. The poor limiting with the larger (and hence less concentrated) particles indicates that the small size of the carbon particles is important in achieving the desired limiting levels if a reasonable low-level transmission is desired. This will also be seen in the sections discussing limiting in particle suspensions in gases.

The scattered light distributions for three different sized particles collected with $\lambda = 532$ nm are shown in Figure 3. Below the threshold for breakdown, the radiation patterns are different for the three different particle sizes. Above the threshold, the scattering distributions for all three particle sizes are very similar, falling just outside the distributions for the non-breakdown distributions for the 0.02 μ m and the 0.3 μ m particle. This indicates that the scattering centers are reaching roughly the same size and composition regardless of the starting size and type of particle.

The transmission dropped in the forward direction with input energies above threshold for all of the particles, but not as much for the larger particles. This is likely due to the fact that there are not as many of them in the focal volume to contribute to the breakdown and subsequent change in scatter.

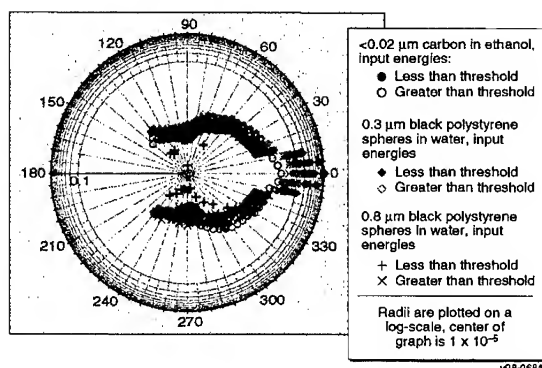


FIGURE 3 Scattered energy/input energy as a function of angle for different sized particles.

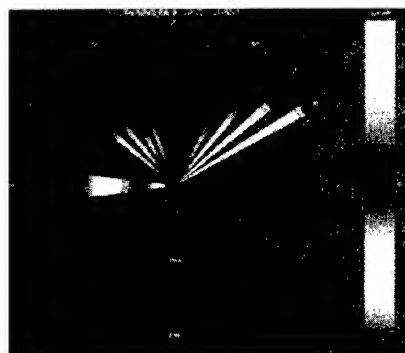
Scatter as a Function of Time

Figure 4 shows scatter from the carbon suspension limiter as a function of time and angle for two input energy ranges. Optical breakdown occurred for both input energy ranges shown here. The intensity of the pulse, plotted as a function of time along the radial direction for each of the angles measured, is displayed as color changes according to the linear color maps shown at the side of each plot. Since the scattered power levels are so much lower than the levels for the input and transmitted pulse, a different color map was used for the scattered levels. The upper half of the color bar shows the color scale for the scattered levels, and the lower half shows the color map for the input and transmitted pulse. The input pulse is plotted on the 180° axis and the transmitted pulse on the 0° axis. In all cases, time $t = 0$ is at the center of the plot. The data were collected as described in the appendix (Figure A3).

In Figures 4a and 4b, the maximum of the scale for the scattered power is the peak of the scattered power, which in both cases was at the 30° measurement (angles less than 30° could not be measured in our experimental setup because of hardware constraints on where we could place the detectors). The maximum for the input and output scale is the maximum of the input pulse. Figure 4c shows the scattered power clipped to 82.6 mW, so that the lower scattering intensities could be seen for the data taken with input energies around 200 μJ . This value of 83.6 mW is equal to the peak of the scattered power in Figure 4a, which was collected with pulses with lower input energies. Figure 4c shows that there is significantly more scattered energy for angles outside of $\pm 30^\circ$ for the higher



(a) 8 to 10 μJ input.



(b) 194 to 231 μJ input.



(c) 194 to 231 μJ input,
scatter clipped at 82.6 mW.

FIGURE 4 Scatter as a function of time and angle (36 shots for input and output)

input energies than for lower input energies. It is just still much smaller than the amount within $\pm 30^\circ$. The fact that breakdown is occurring can be seen by comparing the transmitted pulse to the input pulse. For all except the beginning of the pulse, the transmission is lower than the 81% of the carbon suspension. The output pulses are shortened with increasing input energy. This is because the time to accumulate the fluence needed for breakdown is shorter with higher energy pulses. The scattered energy increases as the transmission decreases. Looking at the scatter as a function of time in Figure 4c, one can see that early in the pulse the scatter is more symmetric in the forward and backward directions, which indicates small particle scattering. Within 20 ns the scatter is stronger in the forward direction out to about $\pm 50^\circ$. After another 20 ns it is within $\pm 30^\circ$. This is indicative of the growth of the scattering centers with time.

The peak instantaneous power of the output pulse as a function of the peak instantaneous power of the input pulse is shown in Figure 5. The data points follow the shape of a typical limiter curve. The ratio of the peak scattered power to peak input power for the different angles (Figure 6) is flat for input levels measurable above the detector noise. This is consistent with earlier data⁷ that showed that the total energy at different scattering angles is a constant fraction of the input energy after the input energies are high enough to cause breakdown. This indicates that the scattering centers are not getting larger with increasing input energies after they reach a critical point. This lack of growth could be due to the fact that as the input energies increase, the fluence levels closer to the cell wall reach the threshold level required to produce optical breakdown, attenuating the pulse before it reaches the focus. The fluence right at focus, then, does not exceed the threshold level. The size of the scatter center does not grow because the fluence at focus does not grow. Mansour *et al.*⁷ saw evidence of the plasma centers growing with input intensity for short pathlength cells. This might indicate that one should use a longer pathlength cell,

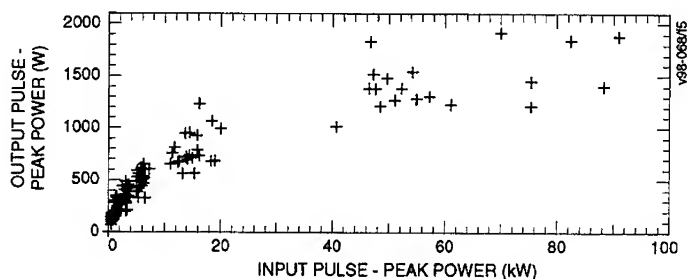


FIGURE 5 Peak instantaneous output power vs. peak instantaneous input power.

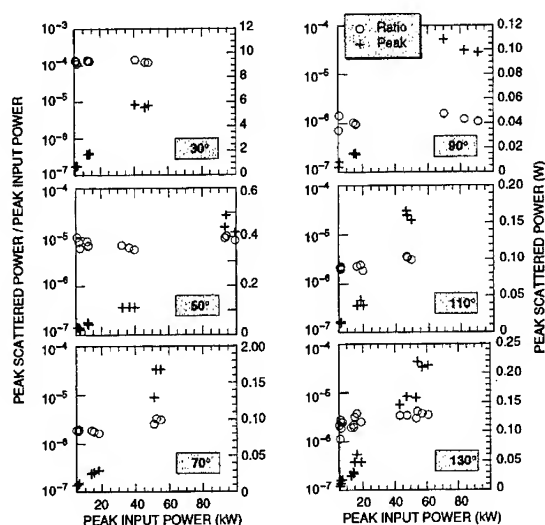


FIGURE 6 Peak scattered power as a function of peak input power.

since larger scattering centers would give rise to more of the scattered energy in the forward direction, which is the reverse of what is desired.

Lowering the Limiting Threshold by Lowering the Ionization Potential of the Liquid

If plasmas are being created, then the ionization potential of the medium should have an effect on the threshold level for breakdown. We investigated the effect of liquid ionization potential on limiting with Tetrakis(dimethylamino)ethylene (TMAE). TMAE has a low gas-phase first ionization potential of 5.36 eV.¹⁰ This is about half the ionization potential of ethanol (10.49 eV), and less than half that of water (12.6 eV).¹¹ Data taken with the same optical setup without a cell, with a cell filled with ethanol, and with a cell filled with TMAE, are shown in Figure 7a. The TMAE breaks down approximately an order of magnitude sooner than the ethanol. The air (no cell case) did not break down at all for these input energies with this optical arrangement (Figure A4).

Since water is not miscible in TMAE, we were not able to use liquid india ink as the source of carbon in producing TMAE suspensions. Several other sources of small particulate carbon were tried, and we were eventually able to produce a suspension that settled with time but stayed in suspension long enough, after sonification, for us to perform some limiting tests. The settling was due to the agglomeration of particles, which caused them to be much larger than their nominal size of 28 nm. Tests on this

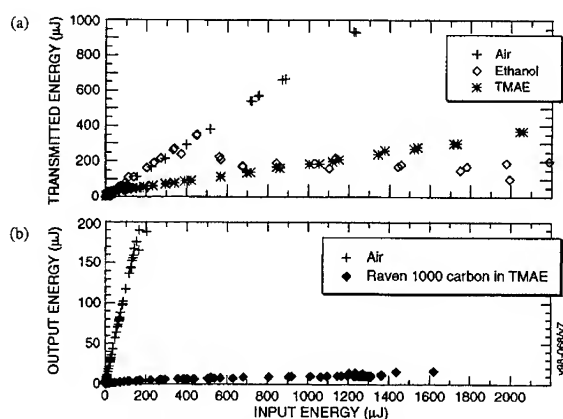


FIGURE 7 Transmission for Q-switched, frequency-doubled Nd:YAG pulses ($\lambda = 532$ nm; $\tau = 6$ ns).

suspension showed no signs of improved limiting over that seen in other solvents. A cell made out of Delrin for another application was used because less agglomeration was seen in this cell. The suspension used to collect the data in Figure 7b was very concentrated (only 26% transmission over a 1 cm pathlength), so throughput was already low without limiting. The Delrin cell had a long liquid pathlength (2.5 cm), which reduced the linear transmission even further than the 1 cm pathlength. The data in Figure 7b appear to limit reasonably well, reaching an optical density (OD) of 2 at an input energy of 1.6 mJ, but the linear transmittance of this sample is only 3.8%. If the linear transmittance is backed out (by dividing by 0.038), the nonlinear absorption provided by the suspension produces an OD of only 0.6. The output versus input curve does not break away from linear until about 40 μ J, or at an average fluence over the focused spot of 27 J/cm² (spot size is defined at the point where the intensity is down to 40% of its peak value, and transmission to the focus is assumed to be 0.195).

Comparison of the data taken with the TMAE with data in Figure 2 shows that limiting in the TMAE suspension is more consistent than that obtained with the larger, black-dyed polystyrene spheres, but the levels (when adjusted for the low energy transmission) are not as low as obtained with the small (less than 0.02 μ m diameter) carbon in water. Care should be taken in comparing these data, since the collection optics were faster with the TMAE suspension than for the ink suspension in Figure 2, so more scattered light is likely to have been collected with the TMAE and TMAE suspension. However, we still believe that the presence of the particles lowers the breakdown threshold

more than does lowering the ionization potential of the liquid. Data collected at a later time with a more dilute suspension of carbon in TMAE (86% transmitting over 1 cm) and F/2.8 collection optics still showed slightly lower output levels with the carbon suspension than with the TMAE alone. At $\lambda = 532$ nm, the threshold input energy for the transmission to break away from the linear transmission for low input energies was about 5 μ J for the TMAE and 3 μ J for the suspension (the $1/e^2$ spot diameter was measured to be 13 μ m at focus). At $\lambda = 1064$ nm, the threshold was about 700 μ J for TMAE and 500 μ J for the TMAE and carbon suspension.

In summary, scattering is important to the limiting process in liquids. The scattering centers grow with time once the breakdown occurs, but for the optical configurations we tested, the scattering centers did not grow further for higher-energy input pulses. The presence of a high enough concentration of particles has a greater effect on limiting than the ionization potential of the liquid.

LIMITING AS A RESULT OF SCATTER CREATED IN A SUSPENSION OF PARTICLES IN GASES

As stated earlier, we removed the liquid from the suspension by suspending particles between two oppositely charged electrodes. The particles were repelled from each electrode as they acquired the charge of that electrode, and were thus continually moving back and forth between the two electrodes at a rate of about 10 m/s, but were suspended in the time frame—nanoseconds to microseconds—of the laser pulses used.

In this experiment the particles were large, between 1 and 40 μ m. The limiting at $\lambda = 532$ nm was not consistent (Figure 8) due to the large particle sizes and low concentrations similar to the 0.8 μ m particles in Figure 2. We did, however, observe that a white flash occurred every time the output energy dropped, indicating that optical breakdown was occurring.

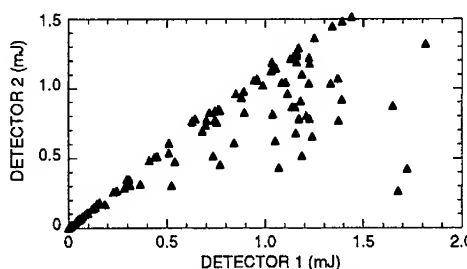


FIGURE 8 Output energy vs. relative input energy for superior graphite.

We were unable to suspend particles small enough with the electrostatic device to be useful for limiting visible light, but we were able to demonstrate its usefulness for infrared applications using a TEA CO₂ laser at $\lambda = 10.6 \mu\text{m}$. Results from some of these experiments are presented below. Many similarities can be seen between the data obtained in the gases with the data obtained with the liquid suspensions.

Limiting as a Function of Particle Concentration

For the infrared experiments we mostly used silver-coated hollow glass spheres (Potters Industries, No. C302-4) sieved to a 10 to 20 μm diameter. These particles were easier to suspend than different forms of carbon that we tried, and studies performed on many different types of particles showed that the particle type did not have a strong effect on the limiting. The particles were suspended between the electrodes via electrostatic charging and repulsion or by a method of aerodynamic mixing.⁸ For the electrostatic method of suspension, the electrode potential ranged from 500 to 1000 V. (High gas pressure operation requires higher electrode potential for equal particle suspension.)

The concentration of the glass sphere cloud was monitored with a HeNe laser and a silicon detector. Based on the particle size, HeNe extinction, and detector field of view, we calculated a particle concentration of 6.5×10^4 particles/cm³ when the HeNe transmission of the particle cloud was 75%.

Data collected with different cloud concentrations showed that 90% transmission did not provide a high enough concentration⁸ to provide consistent limiting. A transmission of 80%, however, was sufficient.

Limiting Measurements for Particles with Different Size Distributions

Particle size did not have a significant effect on the limiting with the silver-coated glass spheres we used, which consisted of the following size distributions (d = particle diameter), obtained using a graded screen instrument:

- $d < 10 \mu\text{m}$
- $10 \mu\text{m} < d < 20 \mu\text{m}$
- $20 \mu\text{m} < d < 32 \mu\text{m}$
- $32 \mu\text{m} < d < 38 \mu\text{m}$
- $38 \mu\text{m} < d < 45 \mu\text{m}$
- $d > 45 \mu\text{m}$

In the limiting tests (Figure A5), the particle density was kept constant by monitoring the transmission of a HeNe laser beam through the particle cloud and adjusting the applied voltage on the electrodes to maintain a transmission of 80%. The IR transmission was 7% greater. Over this range of particle sizes, a HeNe transmission of 80% was sufficient to maintain sufficient particles in the focal volume to trigger breakdown (Figure 9). Changes in particle size had no significant effect on the limiting efficiency.

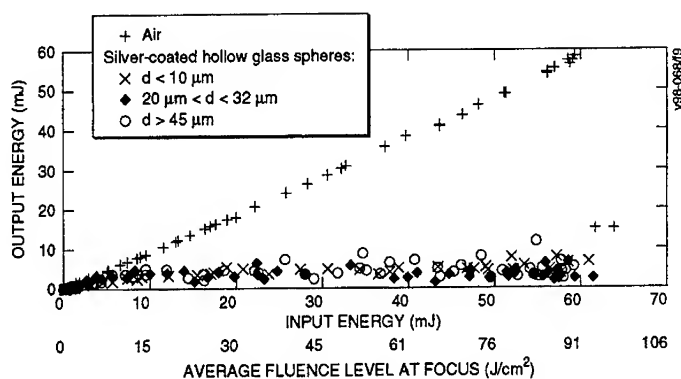


FIGURE 9 Limiting curves for three test sphere sizes and air using the F/6 optical system (laser spot size, $D = 290 \mu\text{m}$).

Distribution of Scattered Radiation Produced by IR Breakdown with the Particle Devices

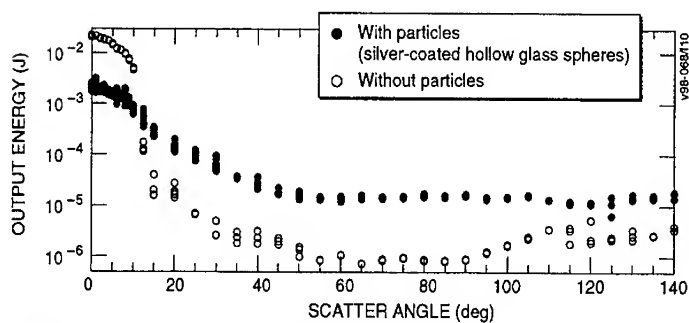
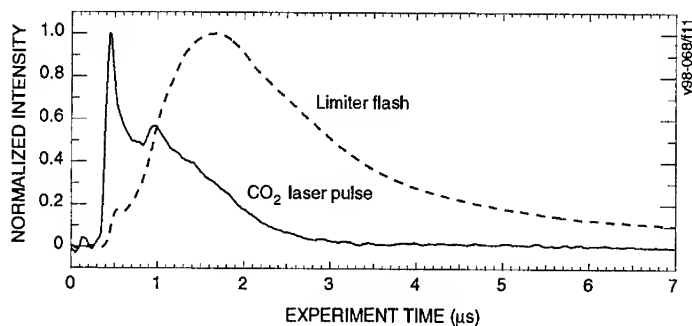
The scattered energy during breakdown is distributed throughout the 2π steradians for the particles in gas, reducing the transmitted radiation in a manner similar to that of particles in liquid. For the F/3.8 system in Figure A6, the majority of the scattered energy is within $\pm 20^\circ$ of the optic axis, but the scattered radiation at 90° is over an order of magnitude higher than it is if there are no particles present (Figure 10).

Temporal Response of Limiter Flash

In standard operation, the TEA CO_2 laser that we used for the IR limiting tests has a main spike on the order of 100 ns, followed by a 3 to 5 μs tail. When a limiting event occurs, a bright white flash is visible. The flash begins at the focal point and expands both outward and backward toward the input laser pulse. The temporal evolution of the limiter flash is related to the intensity of the input CO_2 laser pulse. Figure 11 shows a typical pulse and the duration of the white flash that occurs at breakdown. The CO_2 laser pulse lasts a total of 3 μs . The white flash is delayed about 0.1 μs from the laser pulse and lasts for about 10 μs . Thus, the white flash lasts long after the input pulse is gone. This has also been noticed with breakdown in liquids.^{2,7,12}

Effect of Pulse Duration on Limiting

To evaluate the performance of the particle limiters with shorter pulses, we built a pulse clipper to remove the 5 μs tail. The pulse clipper was installed directly after the laser in the optical path and worked by electrically triggering air breakdown immediately after the main spike of the pulse. The electrical breakdown had to be synced with the laser

FIGURE 10 Scattered energy as a function of angle (input energy ≈ 140 mJ).FIGURE 11 Temporal response of CO₂ laser pulse and limiter flash.

pulse. Since maximum laser power was required for best pulse clipping, the intracavity aperture in the CO₂ laser was removed. As a result, the beam was no longer Gaussian. The diameter of the beam entering the focusing lens to the cell was restricted by the aperture of the polarizer to 1.5 cm. This represents an F/5 system. The non-Gaussian beam produced a greater than diffraction-limited beam diameter measured with a translated knife edge to be approximately 580 μm in the focal plane of the limiter cell, defined from the point where the beam was first blocked by the knife-edge to the point where no measurable energy was left unblocked.

Breakdown occurred for lower input energies with the shorter pulses than it did for the long pulses. For the long, 5 μs , CO₂ laser pulses, the particles had a limiting threshold of 2.2 J/cm² and an OD of 0.6 at 100 mJ input energy (fluence at focus = 38 J/cm²). The OD increased to 1.1 at 350 mJ input energy (fluence at focus = 132 J/cm²). For the shortened CO₂ laser pulse, with the nitrogen tail removed, the limiting threshold was lowered to 0.75 J/cm² and the OD was 0.9 at 100 mJ input energy. This represents roughly a factor of two increase in limiting over the unclipped pulses.

Effect of Limiting on Output Pulse Shape

Figure 12a shows the effect of the optical breakdown on an unclipped pulse as a function of time. For the unclipped CO_2 pulses, the breakdown strongly attenuates both the initial peak and the nitrogen tail. Figure 12b shows the effect of the breakdown on a clipped pulse, where the tail was removed prior to entering the cell by the pulse clipper. The output pulse for the clipped input pulse looks the same as the output pulse for the unclipped pulse. This is again consistent with breakdown in liquids. The first part of the pulse is transmitted only slightly attenuated. When enough energy is absorbed to trigger breakdown, the remainder of the pulse is attenuated. This happens sooner for higher energy pulses, or when the majority of the pulse energy is at the beginning of the pulse.

Reducing the Limiting Threshold by Replacing Nitrogen with Argon and Increasing the Gas Pressure

For the gas suspensions, the equivalent experiment to lowering the ionization potential of the liquid in the liquid suspensions is to increase the electrons available in the gas for plasma production in the gas suspension. It is known that optical breakdown thresholds are lower in the rare gases (e.g.) argon, than in air, which is mostly nitrogen.¹³

We demonstrated⁸ that a suspension of particles in argon had a lower limiting threshold than an identical suspension in nitrogen. The tests were conducted with a limiter cell where silver-coated, hollow-glass spheres were suspended in a flowing gas stream. When nitrogen was the carrier gas in the limiter cell, the limiting threshold was 0.020 J (7.6 J/cm^2). When argon was substituted, the limiting threshold decreased to 0.010 J (3.8 J/cm^2). We measured similar thresholds with the electrostatic suspension method. For the nitrogen/particle test, the limiting threshold was 0.013 J (7.5 J/cm^2). For the argon/particle test, the limiting threshold was 0.004 J (2.3 J/cm^2).

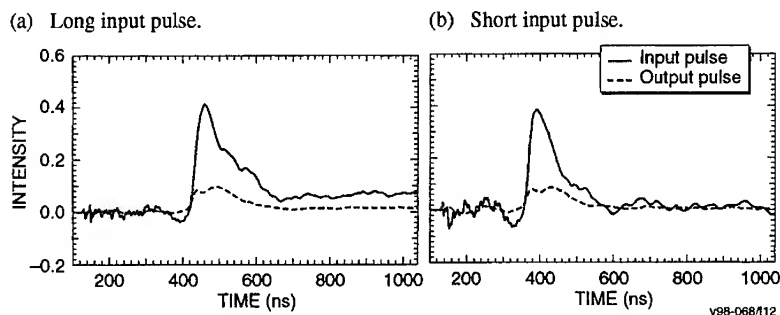


FIGURE 12 Electrostatic limiter.

We also demonstrated that small particles in argon provide lower breakdown thresholds and lower limiting levels than do particles in standard air, and provide optical breakdown thresholds 10 times lower than clean argon.⁸ This was demonstrated with the gases at atmospheric pressure. The work of other investigators has indicated that optical breakdown in argon can be lowered by increasing the gas pressure to between 10 and 20 atm.¹³ Although the particle-induced breakdown at atmospheric pressure observed in the tests at SRI was already lower than that reported for clean argon at 10 or 20 atm, we thought that it might be possible to reduce the threshold further by increasing the gas pressure in addition to adding particles. To investigate this, we built a pressure cell and tested the performance of the particle suspension at different gas pressures from 1 to 18 atm. The absorbing particles used were silver-coated hollow glass spheres sieved to 10 to 20 μm .

The limiter response curves for 1.0, 5.1, 7.8, and 12.9 atm argon gas are displayed in Figure 13. The observed limiter threshold was 0.046 J (2.6 J/cm²), 0.037 J (2.1 J/cm²), 0.020 J (1.1 J/cm²), and 0.010 J (0.6 J/cm²) for the argon limiter cell pressures of 1.0, 5.1, 7.8, and 12.9 atm, respectively. These numbers were obtained by finding the energy level on the plots in Figure 13 where the output energy first drops off of the linear region of the curve. Breakdown is not guaranteed yet at these input energies, since some points with input energies near this energy and higher still maintain the original transmission. The last set of data plotted on Figure 13 is that for the 10 to 20 μm silver-coated glass spheres at atmospheric pressure. Breakdown with the particles occurs at 0.004 J (0.24 J/cm²), lower than the highest gas pressure with the clean argon. Figure 14 shows limiting with the silver-coated glass spheres with various argon gas pressures. The overall trend of the argon/particle limiter threshold energy was to decrease slightly with increases in argon pressure. The percent decrease in limiting threshold for the 14.6 atm argon was about 25% to 30% of that for the 2.7 atm argon. The limiting curves for energies above threshold were virtually identical for the four different argon pressures. The particles thus aid the limiting more than increasing the gas pressure does.

These results are similar to those obtained with TMAE. The breakdown threshold of TMAE was lower than that of ethanol, but the suspension of TMAE and carbon did not perform better than the suspension of carbon in ethanol. For gases, increasing the gas pressure lowers the breakdown threshold, but this does not contribute more to reducing the output energy than adding particles does.

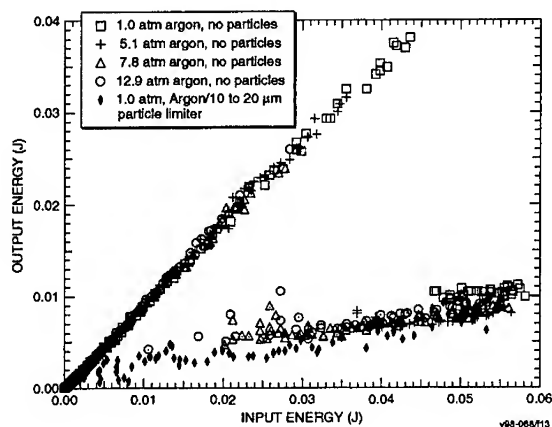


FIGURE 13 Limiting in argon as a function of pressure.

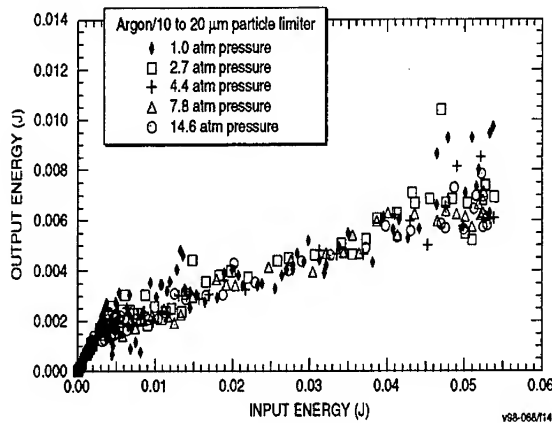


FIGURE 14 Particle suspension limiting as a function of argon pressure.

SUMMARY

For liquids, the long-pathlength (1 cm) cells we used, in which the length of the cell is longer than the Rayleigh length of the focused beam, the ratio of scattered to absorbed energy grows with increasing input energy to a point where the scatter is equal to or greater than the absorbed energy. The ratio does depend on particle concentration. (If the low energy transmission is greater than 70%, scatter is more dominant than absorption for high-input energies.⁵)

Measurements of the angular distribution of the scattered radiation for carbon suspensions in liquids show that the scattering centers grow with time for input energies above breakdown. For the limiting configurations we tested, increasing the input energy significantly above threshold did not cause the scattering centers to grow larger.

Comparing the limiting in the liquid suspensions with that in the suspensions in gases shows that their behaviors are very similar, including the fact that the limiting is not improved for either by increasing the electrons available for plasma production in the suspending media over that obtained by the addition of the particles. In both cases, sufficient particles were required to ensure that breakdown would be triggered. Smaller particles allow for higher concentrations, with higher non-breakdown transmissions, and improved limiting performance.

ACKNOWLEDGMENTS

This work was funded by the Naval Air Warfare Center – Aircraft Division. We would like to express our appreciation to the Naval Air Warfare Center and the rest of the Joint Services Review Committee for their support of this work.

APPENDIX A: EXPERIMENTAL TESTBEDS USED TO COLLECT DATA

Distribution of Scattered Energy (Figure A1)

An attenuator consisting of two rotating glass plates was used to vary the input energy to the cell. A polarizer was placed after the attenuator to maintain a constant polarization throughout the tests. (The polarization was in the vertical direction for these tests.) The 50 mm focal length lens was used to produce a magnified image of the spot at the focal region at a CCD camera which was used to measure the spot size at the focus in the cell. The focused spot was 6 μm in diameter (defined at the point where the intensity level was down to 40% of the peak intensity) in the limiter cell. The 50 mm focal length lens was removed during the angular distribution measurements so that the distribution in the forward direction could be measured. Either a Molelectron J3-09 pyroelectric detector or a Molelectron J3S-10 silicon detector was placed on a rotating arm to measure the scattered light at various angles. Which detector was used depended on the energy levels being measured. The J3S-10 detector is three orders of magnitude more sensitive than the J3-09 detector. The J3-09 detector subtended a solid angle of 0.036 sr (12.2° full angle), and the J3S-10 detector subtended a solid angle of 0.054 sr (15° full angle). Measurements were made every 5° in the horizontal plane. Ten laser shots were fired at each location and the results averaged.

Limiting for Liquids with Different Particle Sizes (Figure A2)

The laser used for these tests was a Q-switched, frequency-doubled Nd:YAG laser. The FWHM pulse duration was 6 ns. We changed the input energy by varying the angle of the linear polarizer. The input polarization was fixed, with a second polarizer kept fixed to transmit horizontally polarized light.

Scattered Energy as a Function of Time (Figure A3)

We used a Tektronix TDS 684A four-channel digitizing oscilloscope with a 1 GHz analog bandwidth, 5 GHz sampling rate, and four internally biased silicon detectors from Electro-Optics Technology, Inc. The detectors were rated to have rise times less than 0.2 ns, fall times less than 0.35 ns, and dynamic ranges of 60 dB. The ability to synchronize the four channels to the same trigger signal allowed us to simultaneously measure the input and transmitted pulses and scattered energy at two angles. Long, thin tubes, blackened on the inside, were used to limit the acceptance angle for light reaching the detectors to $\pm 5^\circ$. Pyroelectric detectors were used to calibrate the energy levels in the pulses. The fact that the energy is scattered symmetrically about the optic axis allowed us to place the energy detectors used to calibrate the instantaneous power levels in the pulses 180° from the silicon detectors used to measure the time response of the pulses. The input optical system was $f/4$. The cell was a 1 cm pathlength cuvette filled with carbon in ethanol diluted to 81% transmission relative to ethanol at $\lambda = 532$ nm. The transmitted energy was collected with an $f/3.3$ system. The angular extent of the scattered light collected by the detectors is ultimately limited by the collection aperture of the detectors. The approximate angular extents seen by the different detectors are given in Table AI. The field of view of the detectors varied slightly due to space requirements on the optical table. (Distances to the detectors varied by up to a centimeter and a half at the different angular positions. The data were corrected for the delay caused by the slightly different path lengths, even though it was small, less than 5×10^{-11} seconds.) Also, the detectors see scattered light from different angles for the different angular positions, because the scattering volume is not a point source (it is actually closer to a line source, especially for higher input energies.) The values given in Table AI assume a point source for the scattered light.

We collected a set of data for six input energy ranges (8 to 10 μJ , 15 to 23 μJ , 36 to 51 μJ , 67 to 96 μJ , 194 and 231 μJ , and 620 to 1113 μJ) with the detectors fixed to measure the instantaneous scattered power at two angles, as well as the instantaneous input and output power. The detectors used to measure the scattered power were then

TABLE AI Approximate angular extents seen by different detectors.

Input		Output		Scatter Angle 1		Scatter Angle 2	
Energy	Response Time	Energy	Response Time	Energy	Response Time	Energy	Response Time
$\pm 7.1^\circ$	$\pm 1.35^\circ$	8.5°	$\pm 0.15^\circ$	2.0°	1.2°	2.0°	1.2°

moved to measure the instantaneous power at two other angles for the same ranges of input energies. Three shots were fired at each input energy level with the detectors in each of the different angular positions.

Limiting with TMAE (Figure A4)

The optical setup shown in Figure A4 was used to collect the data in Figure 7. For the data with no carbon in TMAE, the distance from the last lens to the detector was 57 cm instead of 65 cm. The cell also had a 1 cm liquid pathlength rather than 2.5 cm.

Limiting with Different Particle Size Distributions at $\lambda = 10.6 \mu\text{m}$ (Figure A5)

A TEA CO_2 laser at $\lambda = 10.6 \mu\text{m}$ was used to measure IR limiting as a function of particle size distribution. The pulses had a main spike with duration of the order of 100 ns, followed by a 3 to 5 μs tail. A variable polarizer followed by a fixed polarization analyzer was used to adjust the input energy to the electrostatic suspension. A HeNe laser beam was used to monitor and maintain particle concentration. The input system was F/6. The collection lens was used at approximately F/14. Two pyroelectric detectors were used to monitor the input and output energy.

Distribution of Scattered Energy Produced by IR Breakdown with the Particle Devices (Figure A6)

The input energy was set to about 140 mJ with a variable polarizer and fixed polarizer analyzer and focused into the center of the electrostatic device. The output energy was measured at angles (shown as θ in Figure A6) ranging from 0 to 140° . For angles between 10 and 140° , θ was varied in 5° increments. A Molelectron J3-09 pyroelectric detector was used to measure the scattered energy. The 9 mm diameter of the detector surface and the 160 mm distance to the detector from the breakdown site gave the detector a FOV of $\pm 1.6^\circ$. For θ less than 10° we used a Molelectron J25 pyroelectric detector because of its higher energy measurement capabilities. A 10 mm aperture was placed on the front of the detector to approximately maintain the same FOV. For θ less than 10° the measurements were made at 1° increments. (Because of the FOV of the detector there is overlap in the energies measured at each of these increments.)

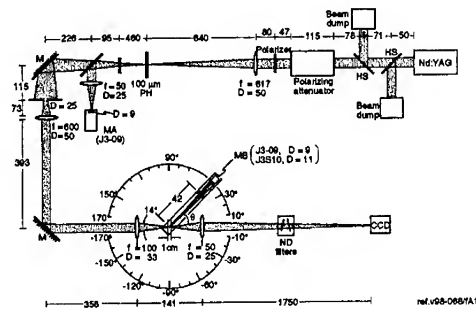


FIGURE A1 Testbed to measure distribution of scattered energy

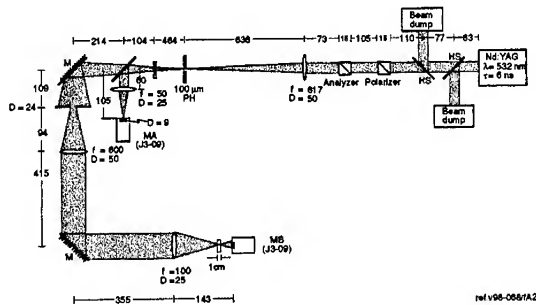


FIGURE A2 Testbed to measure limiting for liquids with different particle sizes

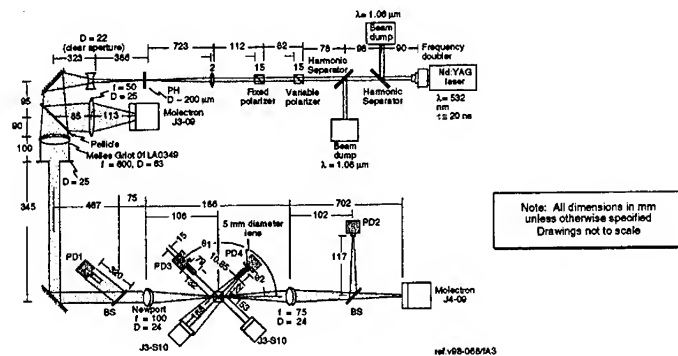


FIGURE A3 Optical setup for measuring scattered energy as a function of time

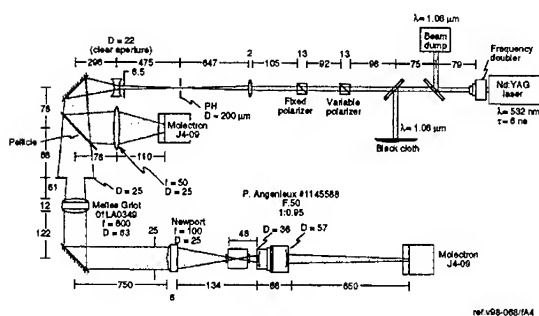


FIGURE A4 Optical setup for measuring limiting in a suspension of carbon in TMAE

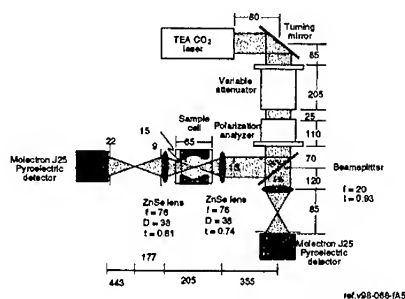


FIGURE A5 F/6 system for comparing limiting with different particle size distributions at $\lambda = 10.6 \mu\text{m}$

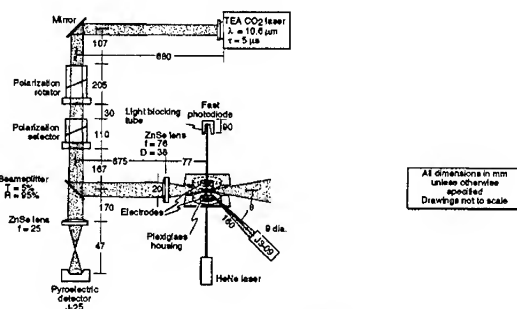


FIGURE A6 Optical testbed for measuring distribution of scattered energy during limiting with electrostatic device

Effect of Pulse Duration on Limiting

To characterize the short pulses, two fast-response (<1 ns rise time), $10.6\text{ }\mu\text{m}$, HgCdTe photodetectors were added to the optical layout of Figure A6 to monitor the pre- and post-limiting CO_2 laser pulses. The detector for monitoring the input pulse looked at a reflection from the polarizer used to attenuate the intensity of the input pulse. The detector monitoring the output pulse viewed scattered light from the pyroelectric detector after the limiter cell. The HgCdTe photodetectors were connected to 500 MHz oscilloscopes with PC-controlled screen capture cameras.

The electrostatic cell was filled with 10 to $20\text{ }\mu\text{m}$ silver-coated hollow glass spheres and adjusted to 80% transmission (measured with a CW HeNe beam). The standard electrostatic device was modified for this particular experiment to include a cylindrical sleeve of clear plastic wrapped between the top and bottom electrodes. This was to further prevent air currents from disturbing the particle flow. Four small holes, separated by 90° , were punched in the sleeve for orthogonal passage of the CO_2 pulses and HeNe laser beam. The addition of the sleeve retained the particles between the electrodes and allowed increased operation time before refilling.

Effect of Gas Pressure on Limiting

A limiter cell was designed to combine electrostatic suspension methods with high gas pressure operation. The electrostatic suspension method was chosen for these tests because it operates as a closed system. The aluminum electrodes were 2.54 cm diameter, 3.49 cm radius of curvature, positioned 1.25 cm apart in a top/bottom configuration. The electrodes were enclosed in a one-piece polycarbonate pressure housing. The polycarbonate served as an electrical insulator between the charged electrodes. The CO_2 laser beam passed through two 2.54 cm diameter, 0.508 cm thick ZnSe windows mounted against O-rings. These windows had an unobstructed aperture of 1.75 cm located 2.67 cm from the center of the cell, allowing a minimum f-number of F/1.5. Argon gas was supplied to the limiter cell via a pressure regulator and calibrated pressure gauge. The limiter cell was filled with 10 to $20\text{ }\mu\text{m}$ silver-coated, hollow glass spheres and argon at 1.0, 2.7, 4.4, 7.8, and 14.6 atm. The cell was tested in the optical system shown in Figure A5, with the exception that the distance from the last lens to the pyroelectric detector was 368 mm, and the distance from the focus in the electrostatic cell to the lens was 76 mm.

REFERENCES

1. J.L.W. Pohlmann, R.C. Honey, and J.L. Guagliardo, "Optical radiation limiter," U.S. Patent 4,890,075 (December 26, 1989).
2. K.M. Nashold, R.A. Brown, R.C. Honey, and D.P. Walter, "Temporal and spatial characterization of optical breakdown in a suspension of small absorbing particles," in Materials for Optical Switches, Isolators, and Limiters, M.J. Soileau, ed., Proc. Soc. Photo-Opt. Instrum. Eng. 1105, 78 (1989).
3. K. Monsour, M.J. Soileau, and E.W. Van Stryland, J. Opt. Soc. Am., **9**, 1100 (1992).
4. K.M. Nashold, "Particle Suspension for Infrared Limiting," Proceedings of the Second DoD Workshop on Visible/NIR Optical Limiters, 15-17 February 1994, Wright Laboratory Materials Directorate, Wright Patterson Air Force Base, Ohio.
5. K.M. Nashold and D.P. Walter, JOSA-B, **12**, No. 7, pp. 1228-1237 (July 1995).
6. K.M. Nashold, "Eye Protection Against Multiple-Wavelength and Frequency-Agile Lasers," Contract N62269-90-R-0207, Report NAWCADWAR-92061-60 (Code 8131), prepared for Air Vehicle and Crew Systems Technology Department (Code 6023), Warminster, PA (1993).
7. K. Mansour, M.J. Soileau, and E.W. Van Stryland, "Nonlinear Optical Properties of Ink", Proceedings of the First DoD Workshop on Liquid Cell Power Limiters, **1**, NRL/MR/6650-92-7139, George P. Mueller, Editor (November 1992).
8. K.M. Nashold and G.S. Frysinger, "Advanced Limiter Techniques," Final Report, SRI Project 2295, Contract F33615-91-C-5620 (March 1993).
9. R.C. Adamo and J.E. Nanevich, "Parametric Study of Electrostatic Techniques for Aerosol Dispersion," Final Report for Massachusetts Institute of Technology, Contract BB-266, under Prime Contract F19628-73-C-002 (March 1975).
10. R.A. Holroyd, S. Ehrenson, and J.M. Preses, J. Phys. Chem., **89**, pp. 4244-4249 (1985).
11. Wheast, CRC Handbook of Chemistry and Physics, 53rd Edition, (CRC Press, 1972-1973).
12. F. Fougere and J. Fabre, "Nonlinear Mechanisms in Carbon Black Suspensions in a Limiting Geometry," Materials for Optical Limiting II, MRS Symposium Proceedings, 479 (1997).
13. G.M. Weyl, "Physics of Laser-Induced Breakdown: An Update," Laser-Induced Plasmas and Applications, L.J. Radziemski and D.A. Cremers, Editors (Marcel Dekker, Inc., New York and Basel, 1989).

BUBBLE AND REFRACTIVE PROCESSES IN CARBON SUSPENSIONS

D B JAMES AND K J McEWAN

Electronics Sector, DERA Malvern, St Andrews Road, Malvern, Worcs., WR14 3PS,
UK.

Abstract Attenuation of pulsed lasers in suspensions of carbon particles is attributed to absorption by particles producing heating of the fluid. A scattering vapour bubble forms around the particle as the fluid boils. At high input fluences a micro-plasma may form which cools to form a bubble. Results will be presented which compare the attenuation of ns and μ s laser pulses. Indications are that the variations in the responses are due to different nonlinear mechanisms operating on different time scales and that the response can be improved by the choice of host fluid. Work using a pump / cw-probe configuration reveals that by the use of suitable host fluids a strongly time dependent scattering bubble can be formed which is the primary mechanism for limiting μ s laser radiation. New carbon suspensions have been developed and attenuation of a μ s laser reveals that the surface tension of the host fluid is of crucial importance to the limiting performance.

Key words: carbon suspension, bubble, laser, nonlinear optics.

INTRODUCTION

Nonlinear optical effects in suspensions of carbon particles were first studied in the 1980s. Three effects were used to explain their nonlinear characteristics:

- plasma formation producing nonlinear absorption and scatter. This was believed to be important since a visible flash could be observed within the fluid.

- nonlinear scatter from micro-bubbles formed by the vaporisation of carbon and water was suggested since macro-bubbles were observed at high input fluences.
- scattering and refraction from acoustic shock waves emanating from the expanding bubble was suggested since an audible "click" could be heard.

The relative strength of these effects is dependent upon the experimental conditions.

Nashold et al.¹ studied the temporal and spatial characteristics and proposed that all three processes play a role and that their relative strengths are dependent upon timescale. Mansour et al.^{2,3} performed detailed measurements on the nonlinear transmission characteristics and demonstrated that the threshold was fluence dependent and concluded that nonlinear scatter due to expanding micro-plasmas was the dominant mechanism on the nanosecond timescale. An activation threshold of 160 mJcm^{-2} was measured at 532 nm and it was shown, through angular scattering measurements, that the scattering centre can grow from 100 nm to at least 400 nm within a 20 ns pulse. Concurrently, McEwan et al.⁴ used a degenerate four-wave mixing experiment to show that bubble formation occurs at an input fluence well below that required to detect a change in the linear transmission using a simple single beam experimental configuration. In this case the particles were not vaporised and a bubble formed by the growth of a vapour layer of fluid surrounding the particles. Bubble generation is also required to explain the operation of the laser induced total-internal reflection device demonstrated by Lawson^{5,6,7}.

Micro-plasma generation is often associated with nonlinear absorption and two measurements have been performed to characterise the induced absorption. Nashold et al.⁸ used an integrating sphere to show that absorption is slightly larger than linear absorption at all input fluences but that nonlinear scattering is mainly responsible for the induced transmission loss. Mansour et al.³ observed a slight increase in the absorption near threshold using a photoacoustic detector. Diebold⁹ performed a similar experiment and showed that the photoacoustic effect in carbon suspensions has an amplitude approximately 2000 times greater than that produced in a dye solution of equivalent linear absorption, which adds credence to the shock wave theory.

Goedert and Becker et al.^{10,11} have developed a powerful time-resolved imaging technique and used it to study the response of carbon particle suspensions and nonlinear

fluid media. the results obtained with carbon suspensions in toluene show that: bubbles are always formed at all input fluences above threshold and that shock waves are formed. Time resolved studies by Fougéanet et al ¹² have also shown that with suspensions in carbon disulphide bubbles form at a level below that at which a white "plasma" flash is observed. The results from Goedert and Becker ^{10,11} has lead to the conclusion that bubbles are formed and grow explosively following the vaporisation of the carbon particles. The nonlinear attenuation close to threshold is due to scatter from these expanding bubbles and no micro-plasma is required. At high input fluences a plasma will form at the input face where the fluence is the highest but the plasma develops in the ionised liquid rather than at each carbon particle.

Recent work has emphasised the importance of the bubble scattering effect and indicated that it may be possible to select an optimum host fluid to maximise the nonlinear effect. In this paper the nonlinear behaviour of carbon suspensions in water using a short pulse length and a long pulse length laser is compared. The results obtained are used to suggest a means of improving device performance. A pump / cw-probe technique is used to study the nonlinear response of a carbon suspension and it is shown that the primary nonlinear mechanism operating on the μs time scale is bubble formation. Several new carbon suspensions in different host fluids are evaluated and the physical fluid parameters which determine the nonlinear performance of the suspension are discussed.

ATTENUATION OF LASER RADIATION

Experimental Configuration

A suspension of carbon particles was prepared by the dilution of India ink (Rotring) in deionised water. The sample was placed in a cuvette of optical path length 2 mm to a transmission of 40% at 532 nm. This device was then incorporated into a test bed as shown in figure 1. The lenses L1 and L2 form a $\times 2.5$, $f/5$ imaging system. The carbon suspension was placed at the common focus of L1 and L2 such that focus was formed at the centre of the fluid. Lens L3 ($f = 1000$ mm) was used to reimage transmitted light. In

the image plane formed by L3 an aperture, A, of diameter 1.5 mm was placed so as to transmit the maximum amount of laser light.

Laser light was then directed through the system using either a Q-switched Nd:YAG laser ($\lambda = 532$ nm, $\tau = 12$ ns (*fwhm*)) or a flash lamp-pumped dye laser ($\lambda_{\text{peak}} = 590$ nm, $\tau = 2.5$ μ s (*fwhm*)). The flash lamp-pumped dye laser cavity was non-selective and the peak wavelength was dictated by the dye in use; in this case rhodamine 6G in deionised water and methanol.

Incident laser energy was monitored using the beam splitter, BS, and the calibrated detector, D1 (Laser Probe, RJP735). Laser light transmitted by the aperture, A, was measured by the pyro-electric detector, D2. Attenuation of the incident laser energy was performed by the use of a waveplate / polariser / waveplate combination in the case of the Nd:YAG source, or calibrated neutral-density glass filters in the case of the flash lamp-pumped dye laser. Using the experimental configuration described the laser energy transmitted by the system was measured as a function of the incident laser energy.

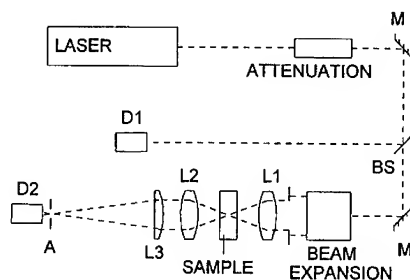


Figure 1. Experimental configuration.

Results

In figure 2 the energy transmitted by the 1.5 mm aperture, A, is plotted as a function of incident energy for the ns and μ s laser sources. The output energy is shown in arbitrary units. The results clearly show the nonlinear response of the carbon suspension to the ns pulses. The input threshold for the onset of attenuation is ~ 0.6 μ J. This response is attributed to bubble and micro-plasma formation during the laser pulse scattering the laser light which then cannot be collected by the imaging system used. When the μ s data is studied it is clear that the nonlinear response of the suspension is much weaker. The

threshold is now higher at $\sim 30 \mu\text{J}$. The output reaches a peak value and then decreases for input energies above 1 mJ.

These results indicate that the mechanisms which are available to limit the ns pulses are not present, or have not formed in time, to limit the lower peak intensity μs pulses. For input energies above 1 mJ the nonlinear response of the system improves, indicating the onset of an additional mechanism at a second, higher, input threshold. These two mechanisms are ascribed to an initial thermally induced change in the refractive index of the host fluid (due to absorption by the particles and heating of the fluid) which above the higher threshold is combined with scattering bubbles when the heating may be sufficient to cause boiling of the fluid.

If effective attenuation of μs pulses is to be achieved it is necessary to select host fluids whose physical parameters are such that bubble formation more readily occurs than in water. Hence, it is desirable to select fluids with low boiling points and low surface tensions (to ease bubble formation) and low thermal conductivity (to reduce thermal diffusion during the laser pulse).

IMPROVEMENTS IN PERFORMANCE

Attenuation of μs laser pulses by water based carbon suspensions indicates that improvements may be achieved by the use of a different host fluid. Bubble formation during the period of the laser pulse may be improved by the selection of a host fluid with low surface tension and boiling point. Water boils at 100°C , and has a surface tension of 72.7 Nm^{-1} . Chloroform boils at 61.2°C and has a surface tension of 26.7 Nm^{-1} making it a potentially more suitable host fluid.

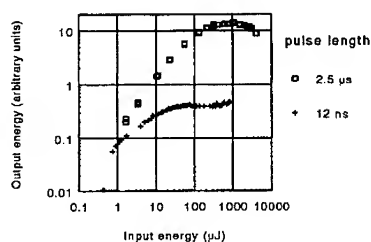


Figure 2. Attenuation of μs and ns laser pulses by carbon particles in water.

A suspension of carbon particles was prepared in chloroform in a cuvette of optical path length 2 mm to a transmission of 40% at 532 nm. This device was then incorporated into the testbed shown in figure 1 (described above). The experiment was carried out in exactly the same way as for the water based suspension.

The transmitted energy (arbitrary units) is plotted as a function of input energy in figure 3 for the Q-switched Nd:YAG laser. Data is shown for both the water and chloroform based suspensions. The results show an improvement in the performance of the suspension against the ns laser. For the chloroform suspension the threshold is $\sim 0.6 \mu\text{J}$ (as with the water suspension). However, the nonlinear attenuation is much stronger. If this improvement is attributed to enhanced bubble formation then it can be assumed that more significant improvements will be observed in the case of the μs laser where the bubble is available for longer during the laser pulse.

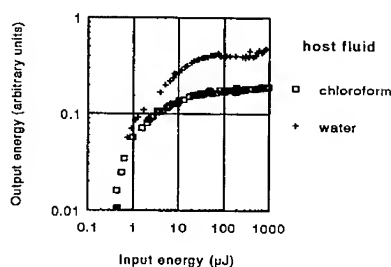


Figure 3. Attenuation of ns laser pulses by carbon particles in water and chloroform.

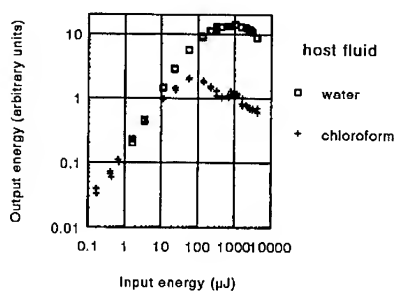


Figure 4. Attenuation of μs laser pulses by carbon particles in water and chloroform.

In figure 4 the transmitted is plotted as a function of input energy for the μs laser source ($\lambda_{\text{peak}} = 590 \text{ nm}$, $\tau = 2.5 \mu\text{s}(fwhm)$). Results are shown for both the water based

and chloroform based suspensions. The results show that the chloroform based suspension exhibits a significant improvement over the water based suspension. The threshold for nonlinear attenuation is now only $8 \mu\text{J}$ compared to $30 \mu\text{J}$ previously, while the maximum output is significantly lower. It should be noted that the curve shows the turn down seen previously but this occurs at lower input energies. The lower threshold is attributed to the lower boiling point of the chloroform compared to water while the lower peak output is attributed to more rapidly forming and longer lived scattering bubbles which attenuate the laser pulse.

These results confirm that bubble formation is the dominant nonlinear mechanism operating on the μs timescale.

PUMP / CW-PROBE STUDIES

Experimental configuration

Results presented above have shown that bubble formation is critical to the effectiveness of a carbon suspension to attenuate a μs laser pulse. To examine the bubble formation mechanism in more detail a pump / cw-probe experimental configuration was constructed. This is shown in figure 5. The pump comprises a pulsed Nd:YAG laser ($\lambda = 532$

nm , $\tau = 12 \text{ ns}$ (*fwhm*)) which is focused by the lens L1 ($f = 700 \text{ mm}$) through the carbon suspension. The cw probe beam comprises a HeNe laser ($\lambda = 543 \text{ nm}$) which is focused by the lens L2 (identical to L1). The beam paths were adjusted such that they were spatially coincident within the carbon suspension sample near to the input face. The

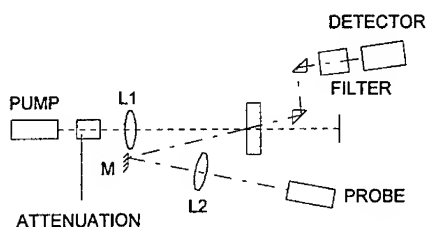


Figure 5. Pump / cw-probe experimental configuration.

beams intersected at an angle of $\sim 15^\circ$. The size of the two beams was such that the probe beam was smaller than the pump beam at the sample ($250\ \mu\text{m}$ and $300\ \mu\text{m}$ respectively). The probe beam was separated and isolated from the scattered light of the pump beam using a polariser and a notch filter centred at $543\ \text{nm}$. The probe beam was then passed through an aperture (which attenuated the nonlinear scattered and refracted light) and was monitored using a fast detector (New Focus, 1601).

Results

The response of a carbon suspension in water is shown in figure 6. The graph shows the variation in the probe power level for pump fluences of 170 , 340 and $2270\ \text{mJcm}^{-2}$. At $170\ \text{mJcm}^{-2}$ only a very slight response in the device transmission is observed. The transmission falls to a minimum of $\sim 35\%$ after the laser pulse and then fully recovers. This slow response is attributed to vapour bubbles forming as the particles are vaporised. At a

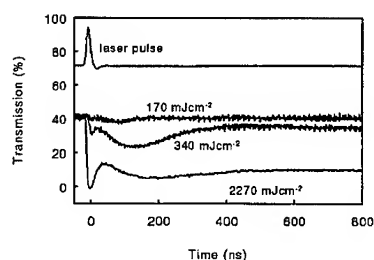


Figure 6. Response of a carbon suspension in water.

pump fluence of $340\ \text{mJcm}^{-2}$ a more dramatic response is observed. A sharp reduction in the transmission during the laser pulse is now apparent. This lasts for approximately $20\ \text{ns}$ and is attributed to either acoustic waves causing a change in the density of the fluid due to expanding bubbles, or a micro-plasma. The effect subsides on the ns timescale. A second effect begins to form at the same time as the acoustic wave / micro-plasma. This is attributed to scatter from bubbles. The effect is most significant approximately $100\ \text{ns}$ after the laser pulse is incident. The fact that the acoustic wave and the scattering bubble can be resolved shows that the two effects grow at different speeds within the fluid, i.e. the bubbles are expanding slowly. The results show that after $\sim 150\ \text{ns}$ the bubble size reaches a maximum and then reduces to a steady state after a further $200\ \text{ns}$. At the

highest input fluence studied (2270 mJcm^{-2}) the same effects are observed and are more pronounced and of longer lifetime. A steady state is reached after 500 ns at a level of only $\sim 10\%$ linear transmission. This is attributed to the bubbles reaching a steady state size. Full recovery of the device transmission takes approximately $150 \mu\text{s}$. This long recovery time compared to the bubble formation and acoustic wave / micro-plasma time scales is attributed to a thermally induced change in the refractive index of the host fluid.

The response of a carbon suspension in chloroform is shown in figure 7. Pump laser fluences of 34, 170, 340 and 2270 mJcm^{-2} are shown. It can be seen that the two separable phenomena observed in the water based suspension are no longer apparent. This is attributed to the lower surface tension of chloroform allowing bubbles to form more rapidly. If the bubble wall expands on a time scale comparable to the velocity of sound then it is reasonable to assume that it will not be

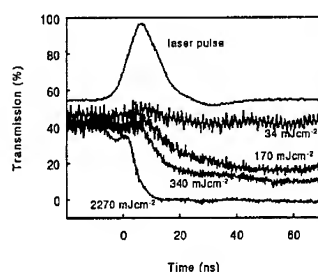


Figure 7. Response of a carbon suspension in chloroform.

distinguishable from an acoustic wave - as is the case. It is interesting to note that the bubbles form earlier in the pulse as the pump fluence is increased. The rapid bubble formation in the chloroform based suspension explains why chloroform is a better host fluid than water for attenuating μs laser pulses and also confirms bubble formation as the primary nonlinear mechanism. During the rising edge of the pump pulse a slight transient reduction in the device transmission is observed. This is attributed to a vapour layer forming around the particles. The pressure within the layer is not sufficient to sustain a bubble and the layer collapses back after a few ns.

If scattering from bubbles is the primary mechanism for attenuating the laser pulses then it is expected that the bubbles will grow to a size where the pressure of the fluid is greater than the pressure within the bubble and the bubble will collapse. Similarly, as the bubble reduces in size the pressure within the bubble may become greater than the pressure of the fluid hence the bubble will expand again. If the pressure

in the initial bubble is sufficiently large then it is possible to cause the bubble to oscillate, each oscillation will be smaller than the previous as thermal energy is given to the host fluid. These predictions are in accordance with the Rayleigh-Plesset equation.

Bubble oscillations are observed when longer

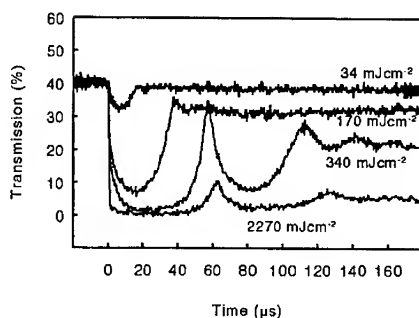


Figure 8. Long timescale response of a carbon suspension in chloroform.

timescales are studied. In figure 8 transmission is plotted as a function of time (pump pulse incident at $t=0$). It can be seen that for a pump fluence of 34 mJcm^{-2} the energy of the bubble is sufficient for only one excursion which lasts for $\sim 20 \mu\text{s}$. The device transmission does not fully recover due to the thermal energy of the bubble producing an index change in the host fluid. At an input fluence of 170 mJcm^{-2} the same effect is observed but is much more pronounced. For an input fluence of 340 mJcm^{-2} there is sufficient energy in the bubbles to allow for three distinct oscillations. As the fluence is increased the period of the oscillations increases and the thermally induced change in the refractive index becomes stronger. For an input fluence of 2270 mJcm^{-2} the thermal effect is strong compared to the scatter caused by the bubbles. Since the two effects are superimposed it becomes difficult to distinguish the individual bubble oscillations.

In the next section the factors which determine bubble growth rate and size are exploited to develop a new range of improved carbon suspensions.

SIGNIFICANCE OF THE HOST FLUID

Results presented show that the host fluid can have a significant effect upon the nonlinear performance of a carbon suspension when subjected to μs laser pulses. It is

instructive to consider the parameters of the host fluid which might effect a scattering bubble. The surface tension is proportional to the pressure that a bubble must attain before it can expand. The energy of vaporisation is proportional to the laser fluence required to create a vapour bubble. The viscosity controls the rate at which a bubble can grow. Hence, to improve the rate of formation and life time of the scattering bubbles it is desirable to select a host fluid with low surface tension, low energy of vaporisation and a low viscosity.

A wide range of carbon suspensions were prepared in different host fluids and tested using the experimental configuration of figure 1 and a flash lamp pumped dye laser ($\lambda_{\text{peak}} = 590 \text{ nm}$, $\tau = 2.5 \text{ } \mu\text{s (fwhm)}$). A summary of the results is shown in table 1. Fluids are listed in order of decreasing maximum transmitted laser energy (arbitrary units).

TABLE 1. Physical parameters of host fluids and measured output energies.

Fluid	Surface tension (N.m^{-1})	Viscosity (mPa.s)	Vaporisation energy at 25°C (kJ.cm^{-3})	Maximum transmitted energy (arb. units)
water	72	0.89	2.61	16
water / methanol (4:1)	62	0.87	2.28	11
O-xylene	30	0.76	0.927	4.9
tetrahydrofuran	24	0.46	0.873	3.2
chloroform	27	0.54	0.735	2
carbon - disulphide	32	0.35	0.666	1.7
ethanol	22	1.07	0.965	1.7
toluene	28	0.56	0.859	1.7
acetone	23	0.39	0.843	1.5
methanol	22	0.52	0.963	1.2
iodomethane	30	0.47	0.997	1.0
ether	17	0.22	0.61	1.0

These results suggest that there is a strong correlation between the surface tension and the transmitted fluence. This is confirmed in figure 9 where the maximum transmitted energy is plotted as a function of surface tension. The relationship is expected to be more complex, depending upon more parameters than just surface tension alone. However, the results suggest that surface tension is the dominant parameter in the relationship. An exponential curve has been overlaid for guidance only. It is believed that o-xylene deviates strongly from the line due to its high energy of vaporisation and high viscosity. In contrast, iodomethane is much better than expected.

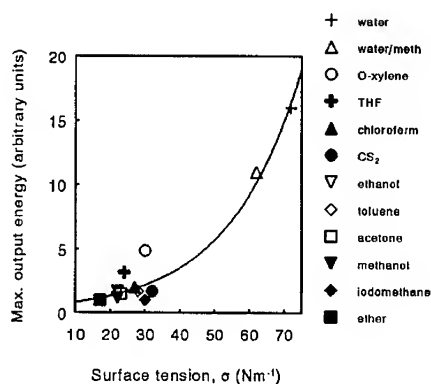


Figure 9. Maximum output energy as a function of host fluid surface tension.

CONCLUSIONS

Results have been presented which show that suspensions of carbon particles in water only weakly attenuate μs laser pulses when compared to ns pulses. This reduction in performance is attributed to the relatively low peak intensity of the μs pulses. If bubble formation is the main source of the nonlinear performance on the μs timescale then it is desirable to select a host fluid in which scattering bubbles will form more readily. Results taken using a carbon suspension in chloroform show a significant improvement in the ability of the device to attenuate a μs laser pulse. This improvement is ascribed to more rapid bubble formation.

Using a pump / cw-probe experimental configuration the optical attenuation of laser pulses in a water based suspension is ascribed to an acoustic wave propagating through the laser beam followed by a slowly growing bubble reaching a maximum size 150 ns after the pulse was incident. Hence, the bubble is the primary source of attenuation on the μs timescale. Using a carbon suspension in chloroform the acoustic wave and bubble formation cannot be separately resolved indicating that the bubble wall

is expanding at approximately the speed of sound. The more rapidly forming bubble explains why chloroform is a better host fluid for attenuating μs pulses and confirms bubbles as the primary limiting mechanism operating on the μs timescale.

To achieve rapid and useful bubble formation it is desirable to select a host fluid with several features. These are: low surface tension, low energy of vaporisation and a low viscosity. New carbon suspensions have been developed in a wide range of host fluids and evaluated using a long pulse length laser. The results indicate that there is a strong correlation between the surface tension and the transmitted fluence. The actual relationship is expected to be more complex but the results suggest that surface tension is the dominant parameter.

REFERENCES

1. K M Nashold, R A Brown, D P Walter and R C Honey, SPIE Vol 1105, 78, (1989).
2. K Mansour, E W Van Stryland and M J Soileau, SPIE Vol 1105, 91, (1989).
3. K Mansour M J Soileau and E W Van Stryland, J.Opt.Soc.Am.B, 9, 1100, (1992).
4. K J McEwan and P J Madden, J.Chem.Phys., 97, 8748, (1992).
5. C M Lawson, G W Euliss and R R Michael, Appl. Phys.Lett., 58, 2195, (1991).
6. R R Michael and C M Lawson, SPIE Vol 1692, 44, (1992).
7. C M Lawson and R R Michael, SPIE Vol 2229, 112, (1994).
8. K M Nashold and D P Walter, J.Opt.Soc.Am.B, 12, 1228, (1995).
9. H Chen and G Diebold, Science, 270, 963, (1995).
10. R Goedert, R Becker, A Clements and T Whittaker, SPIE Vol 2853, 54, (1996).
11. R Goedert, R Becker, A Clements and T Whittaker, MRS Vol 479, 285, (1997).

THERMODYNAMIC MODELING OF OPTICAL LIMITING MECHANISMS IN CARBON-BLACK SUSPENSIONS (CBS)

DIDIER RIEHL and FRANCOIS FOUGEANET
Centre Technique d'Arcueil - DGA/DCE/CTA/LOT
16 bis, avenue Prieur de la Côte d'Or - 91114 Arcueil Cédex

Abstract

We propose a simple thermodynamic model, using finite difference method, to analyse the limiting properties of carbon-black suspensions (CBS) and the different behaviours observed in water and carbon disulfide, and to distinguish the influential thermodynamic parameters. A good agreement with experimental data is obtained for the sublimation threshold of carbon particles.

1. INTRODUCTION

In the last ten years, laser-induced nonlinear scattering in carbon-black suspensions (CBS) has been extensively studied for optical limiting applications. It was demonstrated that the phenomenon is initiated by phase changes in the inhomogeneous medium, resulting from the intense heating caused by light absorption. Two distinct microscopic mechanisms were proposed. First, microplasma formation, due to the sublimation of CB particles and breakdown-induced ionization of the hot carbon vapour^{1,2}, and related to broadband emission of the medium. The threshold fluence for that effect seems to be weakly dependent of the liquid^{3,4}. However, sublimation of carbon and growth of hot carbon vapour bubbles are sufficient to account for the observed behaviour^{5,6}. Moreover, we performed spectroscopic measurements of the broadband emission, in order to detect spectral lines resulting from plasma emission. We obtained continuous blackbody spectra which did not reveal, for moderate incident laser fluences (below 20 J.cm⁻² at $\lambda = 1.064$ μm), any spectral line characteristic of ionized carbon. To our opinion, the emission observed is an incandescence signal^{5,6}, even if plasma formation occurs at much higher fluences⁵.

The second mechanism arises from heat transfer from the absorbing particles to the surrounding liquid and results in a fast growth of vapour bubbles^{3,4,7}, that effect being strongly solvent dependant^{3,4,8}. In the most favourable cases, the threshold fluence for that mechanism is nearly one order of magnitude lower than the particle sublimation threshold, resulting in considerably improved limiting performance^{3,4,8}. That behaviour is clearly related to the thermodynamic properties of the liquid used for the suspension. The limiting curves of Figure 1, obtained with CB/water and CB/carbon disulfide (CS₂) at $\lambda = 1.064 \mu\text{m}$ with 10 ns laser pulses, show a nearly identical sublimation threshold of 0.7 J.cm^{-2} for both liquids and a lower threshold for bubble formation of 0.12 J.cm^{-2} , appearing only in the case of carbon disulfide.

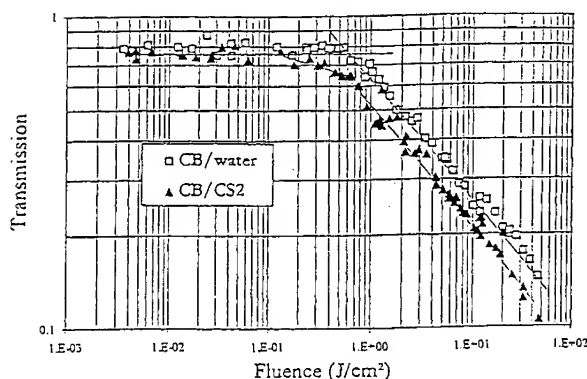


FIGURE 1 Limiting curves of CB/water and CB/CS₂
($\lambda = 1.064 \mu\text{m}$, 10 ns pulse duration)

Based on the known thermodynamic characteristics of the carbon-black particles and of different liquids, several models were developed in order to describe the evolution of the temperature field and the kinetics of bubble growth^{4,7,9}, with relative qualitative agreement with experimental data. We propose here a finite difference-based model which allows to calculate the evolution of the temperature field in the particles and in the surrounding liquid, taking into account the temperature dependence of thermodynamic properties.

II. HYPOTHESES AND FIRST APPROACH OF HEAT TRANSFER

The CB particles used in our experiments ^{3,8} were extracted from indian ink. Electron micrographs showed that the particules are spherical, with an average radius $R = 85$ nm. The microscopic structure of CB particles consists in a small amount of nano crystallites of graphite, including only a few reticular planes, embedded in an amorphous carbon host ¹⁰. The optical and thermodynamic properties are close to those of amorphous carbon. To calculate the absorption cross sections using Mie theory ¹¹, we extrapolated the values of refractive index from measurements performed on soot particles ¹². For $n=2.139 - i 0.583$ at $\lambda = 1.064 \mu\text{m}$ we found $\sigma_{\text{abs}} = 1,033 \cdot 10^{-14} \text{ m}^2$ for CB in water ($n=1,325$) and $\sigma_{\text{abs}} = 9,84 \cdot 10^{-15} \text{ m}^2$ for CB/CS₂ ($n=1,62$). These values are close to those calculated using Rayleigh theory, allowing us to consider the particle as a volumic absorber. The problem of heat transfert, taking into account the symetry of the problem, is therefore reduced to one dimension, assuming a purely radial flow of heat.

The volumic density of power absorbed by the particule is then given by:

$$W(t) = \frac{3\sigma_{\text{abs}} I(t)}{4\pi R^3}, \quad (1)$$

where $I(t)$ is the incident laser intensity. The heat transfer equations for the two media, expressed in spherical coordinates and considering purely radial flow and thermodynamic properties independent of temperature and position, are ¹³:

$$\begin{cases} \partial U_1 / \partial t - \kappa_1 \partial^2 U_1 / \partial r^2 = rW(t) / (\rho_1 C_{p1}) & (r < R) \\ \partial U_2 / \partial t - \kappa_2 \partial^2 U_2 / \partial r^2 = 0 & (r > R) \end{cases} \quad (2)$$

where $U(r, t) = r T(r, t)$ and the indices 1 and 2 refer to the particle and to the liquid, respectively. ρ , C_p and κ are the density, specific heat and thermal diffusivity, defined by $\kappa = K/(\rho C_p)$, where K is the thermal conductivity of the substance. The boundary conditions are then:

$$\begin{cases} T(\infty, t) = T(t=0) \\ T_1(R, t) = T_2(R, t) & (\text{continuity of temperatures at the surface}) \\ K_1 \partial T_1 / \partial r|_{r=R} = K_2 \partial T_2 / \partial r|_{r=R} & (\text{continuity of flow}) \end{cases} \quad (3)$$

In all cases, the reliability of the model depends strongly on that of the parameters used. We assumed for the carbon particles a density $\rho_1 = 1.8 \text{ g.cm}^{-3}$ and a conductivity $K_1 = 1.59 \text{ W.m}^{-1}\text{.K}^{-1}$, assumed to be constant.

On the other hand the specific heat of amorphous carbon is strongly temperature dependent, but there is a lack of data concerning amorphous carbon at high temperatures. However, the specific heats of amorphous carbon and graphite are close below 1000K, so we took for C_p the values of graphite¹⁰. The values for water and CS_2 are available in appropriate handbooks¹⁴, at ambient temperature $K_2 = 0.6 \text{ W.m}^{-1}\text{.K}^{-1}$ for water and $0.164 \text{ W.m}^{-1}\text{.K}^{-1}$ for CS_2 , which specific heat is $1 \text{ J.g}^{-1}\text{.K}^{-1}$.

Pump-probe experiments showed that, at the sublimation threshold of 0.7 J.cm^{-2} (for a 10 ns pulse at $\lambda = 1.064 \text{ }\mu\text{m}$), the perturbation appears at the top of the incident pulse⁸. The first (and very crude) approach consists in neglecting heat transfer to the surrounding liquid, which conductivity and diffusivity are much lower than those of the particle, and to calculate the temperature evolution of an isolated particle:

$$T(t) = T_0 + \int_0^{(W_{\text{max}})} \frac{W(t)}{\rho C_p} dt, \quad (4)$$

the integral being discretized in order to take into account the temperature dependance of C_p . The calculated fluence threshold, corresponding to a temperature at the top of the pulse equal to the sublimation temperature of 3770K, is about 0.62 J.cm^{-2} .

The Laplace transformation method¹³ allows to obtain analytical solutions: the transformation of the heat transfer equations gives ordinary differential equations instead of partial differential equations. The transformed equations (called subsidiary equations) are easily solved using initial and boundary transformed boundary conditions. The temperatures are then calculated by inverse Laplace transformation of the subsidiary solution. However, it is not possible to take into account the temporal dependence of the laser intensity and variable thermodynamic properties simultaneously. Moreover, our problem gives exact solutions only for simplified subsidiary solutions, involving media of identical thermodynamic properties or perfectly conducting particles⁴. As shown by our finite difference calculations, that last assumption made in ref. 4 is not valid for carbon black particles. In the general case, we can obtain only approximate solutions for short times ($t \ll \tau$) and long times ($t \gg \tau$), and unfortunately the critical time τ is of the order of the nanosecond. Consequently, numerical methods are the only practicable way.

III. FINITE DIFFERENCE CALCULATIONS

The finite difference method consists in replacing the partial differential equations describing the evolution of the system by difference equations on a fixed spatial grid. Starting from initial conditions, the time is increased step by step, the temperature field being updated at each time step using the difference equations. For the variable $U(r,t)$, the space-and-time discretization with steps Δr and Δt will be noted $U(r,t) \equiv U(m,n)$, with $r = m\Delta r$ and $t = n\Delta t$. The partial derivatives become:

$$\begin{cases} \frac{\partial U(m,n)}{\partial t} = \frac{U(m,n+1) - U(m,n)}{\Delta t} & \text{(forward difference)} \\ \frac{\partial^2 U(m,n)}{\partial r^2} = \frac{U(m-1,n) - 2U(m,n) + U(m+1,n)}{\Delta r^2} \end{cases} \quad (5)$$

and the heat transfer equations (2) become:

$$\begin{cases} \frac{U_1(m,n+1) - U_1(m,n)}{\Delta t} - \kappa_1 \frac{U_1(m-1,n) - 2U_1(m,n) + U_1(m+1,n)}{\Delta r^2} = \frac{m\Delta r W(n\Delta t)}{\rho_1 C_{p1}} \\ \frac{U_2(m,n+1) - U_2(m,n)}{\Delta t} - \kappa_2 \frac{U_2(m-1,n) - 2U_2(m,n) + U_2(m+1,n)}{\Delta r^2} = 0 \end{cases} \quad (6)$$

These equations, corresponding to an explicit scheme insofar as $U(m,n+1)$ depends only on the temperature field calculated at the precedent time step, are second-order accurate in space and first-order in time. To avoid the growth of errors with increasing number of time steps, Δr and Δt must verify the stability condition: $\kappa \Delta t / \Delta r^2 \leq 1/2$. Clearly, the maximum time step for a given spatial step is determined by the diffusivity of carbon, which is much larger than that of the liquid. The difference equations (6) allow us to calculate the temperature at each point of the two media, except at the surface ($m=M$), but unfortunately the condition of continuity of flow given in (3) is not directly applicable due to the inaccuracy of the difference calculations. The problem is solved using a global energy conservation condition: from the variations of temperature between the steps n and $(n+1)$, calculated in the spatial intervals $(0, M-1)$ and $(M+1, m_{\max})$, we deduce the gain of energy in that domain. By subtraction of that quantity from the total energy absorbed by the particle during the interval in consideration, we determine the surface temperature at time $(n+1)\Delta t$.

In order to take into account variable thermodynamic properties, we started from more general heat transfer equations, the expressions becoming rather more complicated than those given in (2). The procedure will not be detailed here, we mention only that this implies to recalculate the thermodynamic properties at each time step on the full spatial domain. Figure 2 shows CB/water temperature fields, calculated for an illumination of 1 ns duration, at $\lambda = 1.064 \mu\text{m}$ and at constant incident intensity of $10^8 \text{ W}\cdot\text{cm}^{-2}$, with and without variable thermodynamic properties, evidencing the large error made when the temperature dependence of the thermodynamic properties is neglected.

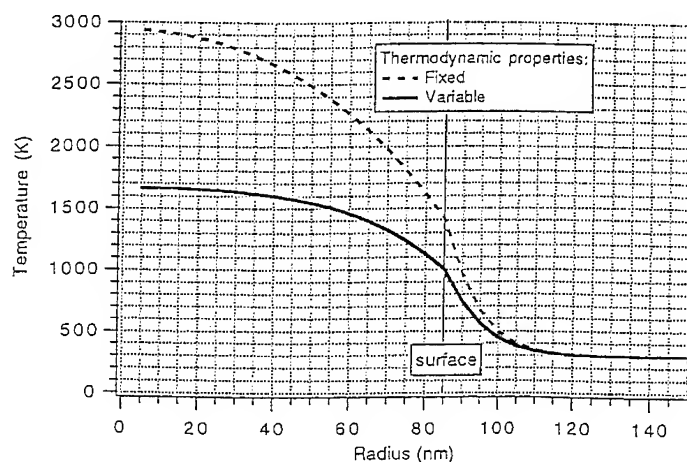


FIGURE 2 Temperature fields for CB/water, calculated with and without variable thermodynamic properties

IV RESULTS AND DISCUSSION

Figure 3 shows the temperature fields calculated for CB/water and CB/CS₂, with variable thermodynamic properties and with the same conditions as for Figure 2. The particle temperature obtained is smaller in the case of water due to its relatively high conductivity and diffusivity compared to CS₂. Moreover, the very high specific heat of water (four times that of CS₂) minimizes the heating of the liquid and is unfavourable to bubble formation.

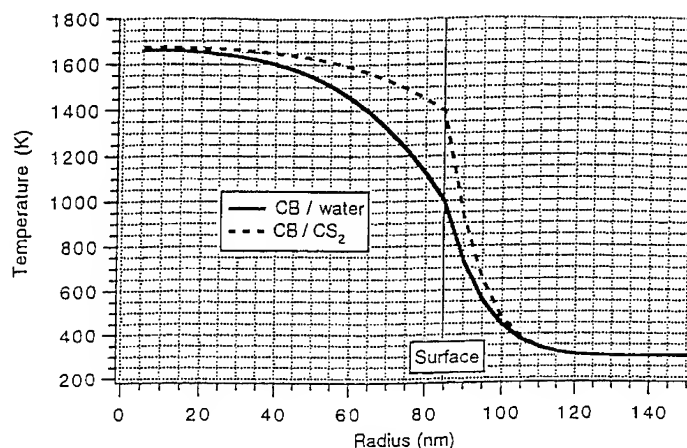
FIGURE 3 Temperature fields for CB/water and CB/CS₂

Figure 4 shows the evolution of temperature at the center of the particle, calculated with variable thermodynamic properties for CB in water and in carbon disulfide and compared to the simple isolated particle model exposed above. The calculations were made for a gaussian pulse of 10ns duration ($\lambda = 1.064 \mu\text{m}$), with a total fluence of $0.7 \text{ J}\cdot\text{cm}^{-2}$, corresponding to the experimental limiting threshold.

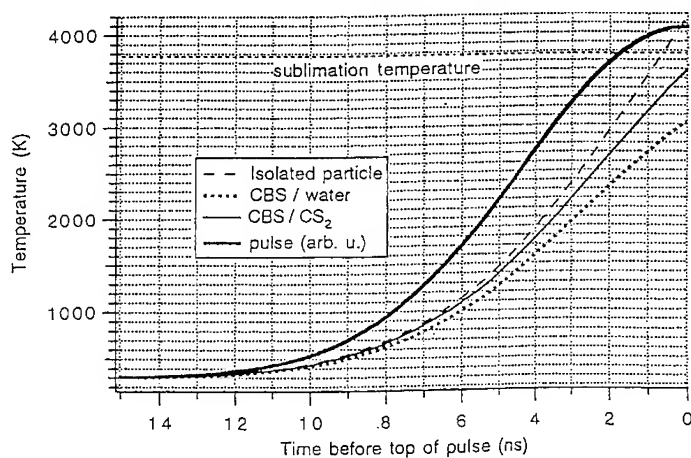


FIGURE 4 Evolution of temperature at the center of the particle

The temperatures obtained at the top of the pulse are slightly lower than the sublimation temperature. As a matter of fact, the model considers only heat transfer to a superheated liquid, without phase change (bubble formation). The heat losses from the particle to its surrounding medium are then overestimated insofar as the conductivities of the vapour phases are much lower than those of the liquids and as the losses diminish during bubble growth. To obtain the sublimation temperature of carbon at the top of the pulse, fluences of 0.74 J.cm^{-2} for carbon disulfide and 0.84 J.cm^{-2} for water are needed, corresponding to a small overevaluation of the sublimation threshold, as expected.

Concerning bubble formation, it is clear that the growth of bubbles is much faster in CS_2 than in water. The initial stage is essentially governed by heat conduction¹⁵, and the latent heat of vaporization of CS_2 is 6 times lower than that of water (372 J.g^{-1} and 2261 J.g^{-1} , respectively). Effectively, the experiments show that in the case of water the particles sublime as the size of the bubbles is not yet sufficient to increase the extinction cross section significantly. However, the modeling of bubble formation is a very difficult problem insofar as the growth depends simultaneously on heat transfer and on inertia^{4,15}. Further developments of the model are needed to describe the phase change of the liquid and bubble growth.

REFERENCES

1. K. Mansour, M. J. Soileau and E. W. Van Stryland, *J. Opt. Soc. Am. B*, **9** (7), 1100 (1992).
2. K. M. Nashold and D. Powell Walter, *J. Opt. Soc. Am. B*, **12**(7), 1228 (1995).
3. F. Fougéanet and J.-C. Fabre, *Mat. Res. Soc. Symp. Proc.*, **479**, 293 (1997).
4. A. Fein, Z. Kotler, J. Bar-Sagi, S. Jackel, P. Shaier and B. Zinger, *Nonlinear Optics*, **11**, 277 (1995).
5. R. Goedert, R. Becker, A. Clements and T. Whittaker III, *J. Opt. Soc. Am. B*, **15**(5), 1442 (1998).
6. R. L. Vander Wal and K. J. Weiland, *Appl. Phys. B*, **59**, 445 (1994).
7. K. J. Mc Ewan and P. A. Madden, *J. Chem. Phys.*, **97** (11), 8748 (1992).
8. F. Fougéanet and D. Riehl, that issue of *Nonlinear Optics*.
9. H. Löwen and P. A. Madden, *J. Chem. Phys.*, **97** (11), 8760 (1992).
10. P. Pascal (ed.), *Nouveau traité de chimie minérale*, vol. 8: carbone (Masson, Paris, 1968).
11. C. F. Bohren and D. R. Huffman, *Absorption and scattering of light by small particles* (Wiley, New York, 1983).
12. T. P. Ackermann and O. B. Toon, *Appl. Opt.*, **20** (20), 3661 (1981).
13. H. S. Carslaw and J. C. Jaeger, *Conduction of heat in solids* (Oxford University Press, 1959).
14. *Handbook of chemistry and physics* (CRC Press, Cleveland).
15. N. H. Afgan, *Boiling Liquid Superheat*, in *Advances in heat transfer*, vol. **11**, chap. 1 (Academic Press, New York, ed. T. F. Irvine Jr. and J. P. Hartnett, 1975).

SPATIOTEMPORAL EFFECTS IN NONLINEAR DISPERSIVE AND DIFFRACTIVE MEDIA USING ULTRASHORT OPTICAL PULSES

M. J. POTASEK
Air Force Research Laboratory/HEDB
2503 Gillingham Dr., BLDG 175E
Brooks AFB
San Antonio, TX 78235
And
Department of Applied Physics
Columbia University
New York, NY 10027

Abstract We investigate the relative importance of radial diffraction and material dispersion for a wide range of wavelengths for femtosecond laser pulse propagation. Furthermore, we study the significance of the various physical parameters, including the laser's temporal and radial pulse width, intensity and wavelength and the relevant nonlinear and dispersive material properties. Because no analytical solution exists which can fully explain the laser-material interaction, we use numerical techniques. We present certain numerical results for various incident laser and material parameters associated with the laser-ocular media interaction.

INTRODUCTION

The study of spatiotemporal effects of laser propagation is of considerable current interest.¹⁻²⁰ For the case of intense continuous wave (cw) light beams, the interaction of the nonlinearity and diffraction can lead to self-focusing and, in certain cases, to critical collapse. In the case of temporally pulsed optical beams, the nonlinearity couples the spatial and temporal behavior, resulting in richly complex dynamical results.

The dynamics of nonlinear, dispersive optical pulses combining the effects of diffraction, Kerr nonlinearity and group velocity dispersion (GVD) have been studied^{4,5,8,9,11,20}. Very different behavior occurs depending upon the relative sign of the Kerr nonlinearity and the GVD. In most studies, a positive Kerr nonlinearity is assumed and combined with either a negative (anomalous dispersion) or a positive GVD (normal dispersion). For the anomalous dispersion region, it is suggested that a stable light bullet forms³. The situation in the normal dispersion region is more complex.

In the normal GVD region, the pulse is broadened along the time axis but compressed (positive Kerr effect) in the transverse direction. This complex interplay leads to the splitting of the pulse in both space and time. For weak GVD, the pulse can be observed numerically to achieve a high degree of spatial compression before splitting into sub-pulses (a result of the dispersion).

Nonlinear effects, such as self-focusing, may be responsible for some of the experimental observations for laser eye damage¹⁴⁻²⁰. To determine the possible effect of self-focusing on laser propagation in the eye, the ABCD matrix method was used in a calculation of the spot size as the beam propagated in ocular media¹⁵. The nonlinearity is included using the experimental values for the nonlinear refractive indices for ocular components. It was observed that self-focusing can substantially decrease the spot size and increase laser irradiance at the retina.

It was recently proposed² that normal group velocity dispersion (GVD) increases the peak input power required for two-dimensional self-focusing of ultrashort pulses. Several researchers have examined the effects of weak GVD on self-focusing for picosecond (ps) pulses^{4,5,7,8,9}. Normal GVD affects self-focusing by spreading the pulse along the propagation direction. Because cross sections of the light pulse differ in power, those possessing powers that exceed the critical power self-focus at different rates. In the absence of GVD, assuming critical power, the self-focusing leads to a singularity with critical collapse¹⁰.

The recent advent of new lasers in the visible and near infrared spectral regions, with pulse durations down to several femtoseconds (fs), requires the extension of the study of spatiotemporal dynamics to new realms. As pulse durations become shorter, the dispersive effects of the light-matter interaction will grow in importance^{12,13,21}. Most studies assumed an instantaneous (electronic) Kerr nonlinearity. In many materials, the Kerr nonlinearity consists of both instantaneous as well as time-delayed component (i.e. Raman term). The time-delayed component becomes significant for ultrashort temporal pulses and has been experimentally observed in optical fibers where it manifests itself as a frequency downshifting of the pulse spectrum²².

As the temporal pulse width shortens, higher-order dispersive effects, beyond the GVD, can also contribute to the interplay of spatiotemporal dynamics. These effects include self-steepening in addition to the time-delayed response. In this paper we include

these effects, in addition to GVD and diffraction in a nonlinear Kerr medium, and investigate the relative influence and dependence on physical parameters, such as the laser temporal and spatial width, and material dispersion. These effects can play a role in ultrashort laser propagation in biological media, such as the eye, two-dimensional waveguides, and in bulk media, including solids, liquids and gases.

THEORY

The propagating electromagnetic field is given by

$$\nabla \times \nabla \times E + \frac{1}{c^2} \frac{\partial^2 E}{\partial t^2} + \frac{1}{\epsilon_0 c^2} \frac{\partial^2 (P_L + P_{NL})}{\partial t^2} = 0, \quad (1)$$

where

$$P_{NL}(r, t) = \epsilon_0 \epsilon_{NL} E(r, t), \quad \epsilon_{NL} = \frac{3}{4} \chi^{(3)}_{xxxx} |E|^2$$

and E is the electromagnetic field, P_L (P_{NL}) is the linear (nonlinear) part of the polarization vector, and ϵ_{NL} is the nonlinear contribution to the dielectric constant. In this case the nonlinearity is due to the third order nonlinear susceptibility, $\chi^{(3)}$. The real and imaginary parts of the frequency dependent dielectric, $\epsilon(\omega)$, are related to the refractive index $n(\omega)$ and the absorption coefficient $\hat{\alpha}(\omega)$ by the expression,

$$\epsilon(\omega) = (n(\omega) + i\hat{\alpha}(\omega)c/2\omega)^2. \quad \text{We define the operator } \nabla^2 = \frac{\partial^2}{\partial z^2} + \frac{\partial^2}{\partial r^2} + \frac{1}{r} \frac{\partial}{\partial r}.$$

In the frequency domain, the propagation of the field is given by

$$\begin{aligned} \nabla^2 \tilde{E} + \epsilon(\omega) \frac{\omega^2}{c} \tilde{E} \\ + \frac{3\chi^{(3)}_{xxxx}}{4c^2} \omega^2 \iint \tilde{E}(\omega_1) \tilde{E}(\omega_2) \tilde{E}^*(\omega_1 + \omega_2 - \omega) \tilde{R}(\omega - \omega_1) e^{i\Delta k z} d\omega_1 d\omega_2 = 0 \end{aligned} \quad (2)$$

where $\Delta k = k(\omega_1) + k(\omega_2) - k(\omega_1 + \omega_2 - \omega) - k(\omega)$ and $\tilde{R}(\omega - \omega_1)$ is the Fourier transform of $R(t-t_1)$, a response function describing the Raman effect. We expand $k(\omega)$

in a Taylor series about ω_0 , and write the n -th derivative as $k_n = \frac{\partial^n k}{\partial \omega^n} \big|_{\omega_0}$. The normal

dispersion region corresponds to $k_2 > 0$ and the anomalous dispersion region corresponds to $k_2 < 0$. In many cases the absorption is small compared to the index of refraction. In this case, $\hat{\alpha}(\omega) \ll 1$, $\varepsilon(\omega) \cong n(\omega)^2$ and we obtain,

$$\begin{aligned} & \left[i \frac{\partial}{\partial z} + \frac{1}{2k_0} \left(1 - \frac{k_1}{k_0} \Delta\omega \right) \Delta_\perp + k_1 \Delta\omega + \frac{k_2}{2} \Delta\omega^2 + \frac{k_3}{6} \Delta\omega^3 \right] \tilde{A}(r, z, \Delta\omega) \\ & + \frac{3\chi_{xxx}^{(3)}}{8cn_0} \omega_0 (1 + q_0 \Delta\omega) \\ & \times \iint \tilde{A}(r, z, \Delta\omega_1) \tilde{A}(r, z, \Delta\omega_2) \tilde{A}^*(r, z, \Delta\omega_1 + \Delta\omega_2 - \Delta\omega) \tilde{R}(\Delta\omega - \Delta\omega_1) d\omega_1 d\omega_2 \\ & = 0 \end{aligned} \quad (3)$$

where $\Delta\omega = \omega - \omega_0$, $q_0 = 1 - \frac{n_1 \omega_0}{n_0}$, and $n_1 = \frac{\partial n}{\partial \omega} \Big|_{\omega_0}$, \tilde{A} is the Fourier transform of the envelope of the field, and we use the approximations

$$\frac{\partial^2}{\partial z^2} \ll k_0 \frac{\partial}{\partial z}, \quad \left(1 + \frac{k_1}{k_0} \Delta\omega \right)^{-1} \sim 1 - \frac{k_1}{k_0} \Delta\omega, \quad \left(1 + \frac{n_1}{n_0} \Delta\omega \right)^{-1} \sim 1 - \frac{n_1}{n_0} \Delta\omega$$

The time domain expression is obtained using the inverse Fourier transform; recalling

that $\Im \left(\frac{\partial^n}{\partial t^n} \right) \Rightarrow (-i\Delta\omega)^n$, and using the convolution theorem, $f * g = \int g(y) f(x-y) dy$.

The third order susceptibility $\chi^{(3)}$ is complex and can be written in terms of its real and imaginary parts; $n_2 = \frac{3}{8n_0} \text{Re}(\chi_{xxx}^{(3)})$, $\alpha_2 = \frac{3\omega_0}{4n_0 c} \text{Im}(\chi_{xxx}^{(3)})$ where n_2 is the coefficient

of the nonlinear index of refraction¹³ and α_2 is the coefficient for two photon absorption. In many cases the two-photon absorption is small compared to the nonlinear index of refraction and we will neglect it. (It can be easily incorporated.¹³)

Using these parameters Eq (3) becomes

$$\begin{aligned} & \left[i \left(\frac{\partial}{\partial z} + k_1 \frac{\partial}{\partial t} \right) + \frac{1}{2k_0} \nabla_\perp^2 - \frac{k_2}{2} \frac{\partial^2}{\partial t^2} - i \frac{k_3}{6} \frac{\partial^3}{\partial t^3} - i \frac{k_1}{2k_0^2} \frac{\partial}{\partial t} \nabla_\perp^2 \right] A(r, z, t) \\ & + \gamma_0 \left[1 + i \left(\frac{1}{\omega_0} - \frac{n_1}{n_0} \right) \frac{\partial}{\partial t} \right] A(r, z, t) \int |A(r, z, t-t')|^2 R(t') dt' = 0 \end{aligned} \quad (4)$$

where $\gamma_0 = \frac{n_2 \omega_0}{c}$. The response function, $R(t) = f \delta(t) + (1-f)h(t)$ includes both the electronic (instantaneous) and vibrational (time-delayed) terms, where f is the fraction of the response that is instantaneous and $h(t)$ is the time delayed response function.. The nonlinear term, NLT is given by

$$\begin{aligned} NLT = & \gamma_0 f \left(1 + i \frac{q_0}{\omega_0} \frac{\partial}{\partial t} \right) A(r, z, t) |A(r, z, t)|^2 \\ & + \gamma_0 (1-f) \left(1 + i \frac{q_0}{\omega_0} \frac{\partial}{\partial t} \right) A(r, z, t) \int h(t') |A(r, z, t-t')|^2 dt' \end{aligned} \quad (5)$$

In many physical cases of interest, the incident temporal pulse width is such that $A(t-t')$ does not differ much from $A(t)$ on the time scale of the response function, so we can expand $|A(t-t')|^2$ in a Taylor series about t . Then the nonlinear term becomes

$$NLT = \gamma_0 \left(1 + i \frac{q_0}{\omega_0} \frac{\partial}{\partial t} \right) A(r, z, t) \int_0^\infty R(t') \left[|A(r, z, t)|^2 - t' \frac{\partial}{\partial t} |A(r, z, t)|^2 \right] dt' \quad (6)$$

using $T_R = \int_0^\infty t' R(t') dt'$, and neglecting second-order derivatives in t , Eq. (6) becomes

$$NLT = \gamma_0 A |A|^2 + i \frac{\gamma_0 q_0}{\omega_0} \frac{\partial}{\partial t} (A |A|^2) - \gamma_0 T_R A \frac{\partial}{\partial t} |A|^2 \quad (7)$$

where $A=A(r, z, t)$. Combining Eqs. (4) and (7) we obtain

$$\begin{aligned} & i \left(\frac{\partial}{\partial z} + k_1 \frac{\partial}{\partial t} \right) A + \frac{1}{2k_0} \nabla_\perp^2 A - \frac{k_2}{2} \frac{\partial^2 A}{\partial t^2} + \gamma_0 |A|^2 A - i \frac{k_3}{6} \frac{\partial^3 A}{\partial t^3} \\ & - i \frac{k_1}{2k_0^2} \frac{\partial}{\partial t} \nabla_\perp^2 A + 2i \frac{\gamma_0 q_0}{\omega_0} |A|^2 \frac{\partial A}{\partial t} + i \frac{\gamma_0 q_0}{\omega_0} A^2 \frac{\partial A^*}{\partial t} - \gamma_0 T_R A \frac{\partial |A|^2}{\partial t} = 0 \end{aligned} \quad (8)$$

We assume an incident pulse of the form, $A(r, 0, t) = A_0 \exp(\frac{-r^2}{2a_0^2}) \exp(\frac{-t^2}{2T_0^2})$ where a_0 is the spatial beam waist, T_0 is the temporal half-width of the pulse intensity and A_0^2 is the peak incident pulse intensity. Assuming the nonlinear diffraction effect is dominant,

we define the transformation, $Q = \frac{A}{A_0}$, $\rho = \frac{r}{a_0}$, $\xi = \frac{z\lambda_0}{\pi n_0 a_0^2}$, $\tau = \frac{(t - k_1 z)}{T_0}$, to

obtain the non-dimensioned equation

$$\begin{aligned} i \frac{\partial Q}{\partial \xi} + \frac{1}{4} \nabla_\rho^2 Q - \frac{1}{2} \bar{\alpha} \frac{\partial^2 Q}{\partial \tau^2} + \bar{\beta} |Q|^2 Q - \frac{i}{6} \bar{\gamma} \frac{\partial^3 Q}{\partial \tau^3} \\ - i \bar{\delta} \nabla_\rho^2 \frac{\partial Q}{\partial \tau} + i \bar{\varepsilon} |Q|^2 \frac{\partial Q}{\partial \tau} + i \bar{\mu} Q^2 \frac{\partial Q^*}{\partial \tau} - \bar{\sigma} Q \frac{\partial |Q|^2}{\partial \tau} = 0 \end{aligned} \quad (9)$$

where

$$\begin{aligned} \bar{\alpha} = \frac{\pi n_0 a_0^2 k_2}{\lambda_0 T_0^2}, \bar{\beta} = \frac{2\pi^2 a_0^2 n_0 n_2 A_0^2}{\lambda_0^2}, \bar{\gamma} = \frac{\pi n_0 a_0^2 k_3}{\lambda_0 T_0^3}, \tau_R = \frac{T_R}{T_0}, \\ \bar{\delta} = \frac{k_1 \lambda_0}{8\pi n_0 T_0}, \bar{\varepsilon} = \frac{4\pi n_0 n_2 a_0^2 A_0^2}{c \lambda_0 T_0}, \bar{\mu} = \frac{2\pi n_0 n_2 a_0^2 A_0^2}{c \lambda_0 T_0}, \bar{\sigma} = \frac{2\pi^2 n_0 n_2 a_0^2 A_0^2 T_R}{\lambda_0^2 T_0} \end{aligned}$$

Each coefficient is dimensionless and its magnitude determines the relative importance of its effect. The coefficients $\bar{\alpha}, \bar{\gamma}, \bar{\delta}$ correspond to linear terms and are coupled to various dispersion coefficients (i.e. k_2, k_3, k_1 , respectively). The coefficients $\bar{\beta}, \bar{\varepsilon}, \bar{\mu}, \bar{\sigma}$ correspond to nonlinear terms and depend upon the initial pulse intensity, A_0^2 . For $\bar{\beta} > 1$, we have nonlinearity; however, for a given intensity and wavelength the situation can become linear if the spatial beam waist, a_0 , gets so small that $\bar{\beta} < 1$. Numerical methods must be used to investigate the nonlinear propagation.

NUMERICAL PROCEDURE

We use the non-dimensioned equation given by

$$\begin{aligned} \left[i \frac{\partial}{\partial \xi} + \frac{1}{4} \left(1 - i\sigma \frac{\partial}{\partial \tau} \right) \nabla_\rho^2 - \frac{\gamma}{2} \frac{\partial^2}{\partial \tau^2} - i \frac{\delta}{6} \frac{\partial^3}{\partial \tau^3} \right] Q \\ + a \rho \{ |Q|^2 + i\sigma \left(2Q^* \frac{\partial Q}{\partial \tau} + Q \frac{\partial Q^*}{\partial \tau} \right) - \tau_R \left(\frac{\partial |Q|^2}{\partial \tau} \right) \} Q = 0 \end{aligned} \quad (10)$$

where

$$a = \left(\frac{1.22\pi}{4} \right)^2, \gamma = \frac{a_0^2 k_0 k_2}{2T_0^2}, \delta = \frac{a_0^2 k_0 k_3}{2T_0^3}, \sigma = \frac{1}{\omega_0 T_0}$$

The numerical solution is solved in the form²⁰

$$\begin{aligned}\frac{\partial Q}{\partial \xi} &= (D_{DS} + D_{DF} + N)Q, \\ D_{DS} &= -\frac{i\gamma}{2} \frac{\partial^2}{\partial \tau^2} + \frac{\delta}{6} \frac{\partial^3}{\partial \tau^3}, D_{DF} = \frac{i}{4} \left(1 - i\sigma \frac{\partial}{\partial \tau}\right) \nabla_{\perp}^2 \\ N &= ap \left\{ i|Q|^2 - \sigma \left[2Q^* \frac{\partial Q}{\partial \tau} + Q \frac{\partial Q^*}{\partial \tau} \right] - i\tau_R \frac{\partial |Q|^2}{\partial \tau} \right\}\end{aligned}\quad (11)$$

Equation (11) can be solved using the symmetric split-step method where the exponential operators are defined by their Taylor series expansion. The terms are evaluated using a discrete space and time grid given by $\tau \rightarrow \tau_i$, $\xi \rightarrow \xi_n$, $\rho \rightarrow \rho_j$; therefore, $Q(\xi, \rho, \tau) \rightarrow Q(\xi_n, \rho_j, \tau_i) = Q_{ij}^n$. Then the nonlinear operator can be written as

$$\begin{aligned}N(\xi_n) &= ap \left\{ |Q_{ij}^n|^2 - \sigma \left[2Q_{ij}^{n*} \left(\frac{Q_{i+1,j}^n - Q_{i-1,j}^n}{2\Delta\tau} \right) + Q_{ij}^n \left(\frac{Q_{i+1,j}^n - Q_{i-1,j}^n}{2\Delta\tau} \right)^* \right] \right\} \\ &\quad - iap\tau_R \left\{ Q_{ij}^{n*} \left(\frac{Q_{i+1,j}^n - Q_{i-1,j}^n}{2\Delta\tau} \right) + Q_{ij}^n \left(\frac{Q_{i+1,j}^n - Q_{i-1,j}^n}{2\Delta\tau} \right)^* \right\}\end{aligned}\quad (12)$$

where the "leap frog" method is used to evaluate the derivatives. The linear diffraction operator D_{DF} is equivalent to

$$\frac{\partial Q}{\partial \xi} = \kappa(\omega) \nabla_{\perp}^2 Q(\xi, \rho, \omega), \quad \kappa(\omega) = \frac{i}{4} (1 - \sigma\omega). \quad (13)$$

Equation (13) is solved using the finite difference scheme,

$$\frac{\partial Q}{\partial \xi} = \frac{Q_{ij}^{n+1} - Q_{ij}^n}{\Delta \xi}, \quad (14)$$

and the Crank-Nicholson scheme, assuming equal spacing in ρ ,

$$\frac{\partial^2 Q}{\partial \rho^2} = \frac{1}{2} \left\{ \frac{Q_{i,j+1}^{n+1} - 2Q_{i,j}^{n+1} + Q_{i,j-1}^{n+1}}{(\Delta \rho)^2} + \frac{Q_{i,j+1}^n - 2Q_{i,j}^n + Q_{i,j-1}^n}{(\Delta \rho)^2} \right\} \quad (15)$$

Equations (14)-(15) are used in Eq. (13) for $0 < \rho_j < \rho_{\max}$. Assuming a cylindrically symmetric system, $\frac{\partial Q}{\partial \rho} = 0$ at $\rho = 0$. Eq (13) becomes (i.e. $j=0$)

$$\begin{aligned} (1 + \phi(\omega_i))Q_{i,0}^{n+1} - \phi(\omega_i)Q_{i,1}^{n+1} - (1 - \phi(\omega_i))Q_{i,0}^n - \phi(\omega_i)Q_{i,1}^n &= 0, \\ \phi(\omega_i) &= \frac{2\Delta\xi\kappa(\omega_i)}{\rho_1^2} \end{aligned} \quad (16)$$

For the maximum radial value, ie $\rho = \rho_{\max} = \rho_N$, Eq. (13) becomes

$$\begin{aligned} \theta(\omega_i)Q_{i,N-1}^{n+1} + [1 - \theta(\omega_i)]Q_{i,N}^{n+1} + \theta(\omega_i)Q_{i,N-1}^n - [1 + \theta(\omega_i)]Q_{i,N}^n &= 0, \\ \theta(\omega_i) &= \frac{\Delta\xi\kappa(\omega_i)}{2\rho_N(\rho_N - \rho_{N-1})} \end{aligned} \quad (17)$$

Using Eqs. (14)-(17), Eq. (13) can be written in the form

$$\begin{aligned} \Xi_1(\omega_i) \bullet \bar{q}_i^{n+1} &= \Xi_2(\omega_i) \bullet \bar{q}_i^n, \\ \bar{q}_i^n &= (Q_{i,0}^n, \dots, Q_{i,j}^n, \dots, Q_{i,N}^n) \end{aligned} \quad (18)$$

and Ξ_1 and Ξ_2 are tridiagonal matrices. The matrix Ξ_1 is composed of the subdiagonal, diagonal and superdiagonal elements. Using these methods, Eq. (11) is used to numerically propagate the electromagnetic field in the nonlinear dispersive medium. In the limiting case of the nonlinear Schroedinger equation, the numerical results agree well with analytic solutions.

RESULTS AND DISCUSSION

We calculate the spatiotemporal propagation and the spectra for self-focusing with normal GVD and find good agreement with previous results⁴⁻⁹. However as the pulse width decreases higher-order terms can become important. One of these higher-order terms is the time-delayed Raman (SRS) response that has been shown to have considerable impact in guided-wave nonlinear pulse propagation in optical fibers²². We present new results for the influence of SRS on spatiotemporal propagation.

$$p=2.95, \gamma=0.0755, \tau_R=\delta=\sigma=0$$

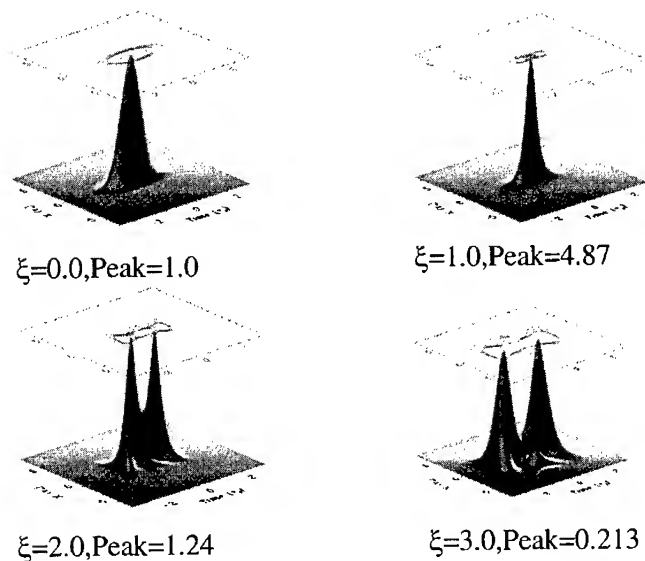


FIGURE 1 Propagation for self-focusing and dispersion.

The case of self-focusing alone has been well studied and, in the absence of other effects, leads to a singularity^{1-3,10}. However, the presence of normal GVD significantly alters this behavior⁴⁻⁹. Figure 1 (2) shows the propagation (spectra) of an incident

Gaussian pulse at four normalized distances for self-focusing with normal GVD. The figures show the incident pulse at $\xi=0$ with a normalized on-axis peak intensity (P), $P=1.0$. As the pulse propagates, it initially self-focuses (Fig. 1) with the peak intensity increasing $P \approx 5$ at $\xi=1$. However, the self-focusing is arrested and the pulse splits temporally into two sub-pulses (Fig. 1) at $\xi=2$ due to GVD, and further propagation leads to both spatial and temporal splitting (Fig. 1) at $\xi=3$ with a significant reduction in the peak intensity, $P \approx 0.2$.

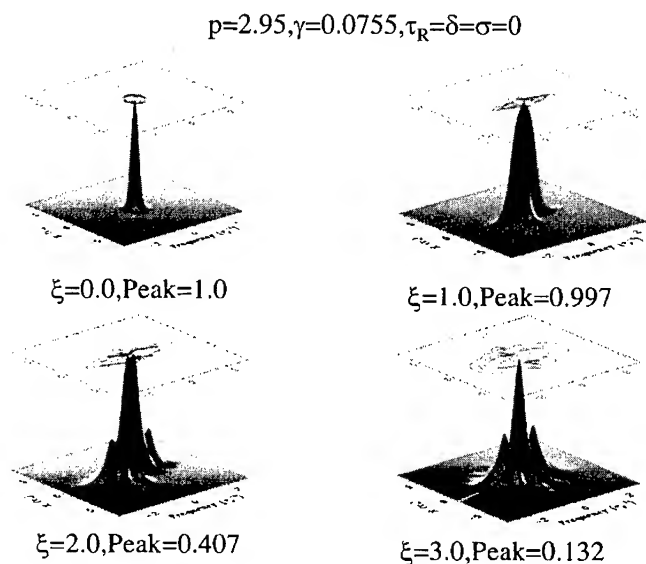


FIGURE 2 Spectra for the case shown in Fig. 1.

The spectra provide additional insight into the splitting behavior. As the pulse self-focuses, the peak intensity increases and the central portion of the pulse undergoes the most self-phase modulation (SPM). Because of normal GVD, the SPM portion of the pulse broadens temporally with energy distributed away from the pulse center. From Fig. 2 we see that as the pulse splits temporally, the spectrum broadens and develops

spectral sub-pulses. The period of this modulation in the frequency domain is inversely related to the temporal sub-pulse separation in Fig. 1.

As the temporal pulse narrows the slowly varying envelope approximation begins to break down and higher order terms can play a significant role^{12,13,21}. One of these terms, important in optical fiber systems²², is SRS and we examine its influence on dispersive self-focusing. Figure 3 (4) shows the propagation (spectra) for this case. The SRS significantly alters the spatiotemporal behavior by reducing both the self-focusing and the temporal splitting. The incident pulse is again shown at $\xi=0$. However as it propagates the pulse begins to self-focus (Fig.3) but the magnitude of the self-focusing is reduced by the SRS, as can be seen from Figs. 1 and 3 by comparing the peak intensities at $\xi=1$ (i.e. $P \approx 5$ in Fig. 1 and $P \approx 3$ in Fig. 3). Additionally, the spectra in the two cases are significantly different as shown in Figs. 2 and 4. As shown in Fig. 4 with SRS, the spectra become asymmetric with initial downshifting of the frequency at $\xi=1$. As the pulse propagates further, it does not split because the SRS interferes with the SPM generated by GVD.

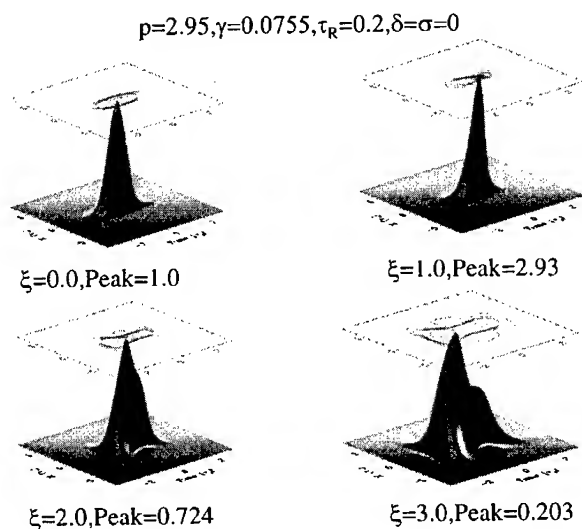


FIGURE 3 Propagation for self-focusing, dispersion and time-delayed Raman response.

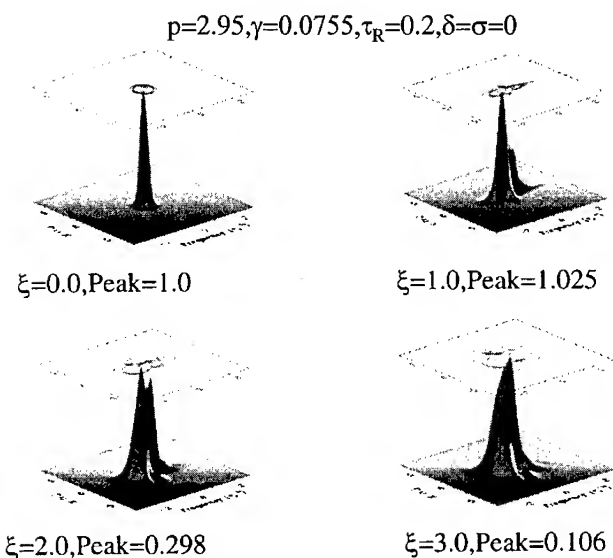


FIGURE 4 Spectra for the case shown in Fig. 3.

In conclusion, we have found that SRS reduces self-focusing more than GVD alone and arrests the splitting associated with SPM.

ACKNOWLEDGMENTS

This research was supported in part by the AFOSR, AFRL and ONR. Dr A. Paul contributed the radial part of the code. Dr. S. Kim contributed to the graphics. Profs. McLaughlin and Shelley, New York University, made suggestions in the early stages of the mathematical formulation. Dr. G. Wilson, Lucent Bell Labs, contributed to SRS.

REFERENCES

1. J. H. Marburger, "Self-focusing: Theory", Prog. Quant. Electr. **4**, 35 (1975).
2. D. Strickland and P.B. Corkum, "Short pulse self-focusing" Proc. Soc. Photo-Opt. Instrum. Eng. **1413**, 54 (1991).
3. Y. Silberberg, "Collapse of optical pulses", Opt. Lett. **15**, 1282 (1990).

4. P. Chernov and V. Petrov, "Self-focusing of light pulses in the presence of normal group velocity dispersion", *Opt. Lett.* **17**, 172 (1992).
5. J. Rothenburg, "Pulse splitting during self-focusing in normally dispersive media", *Opt. Lett.* **17**, 583 (1992).
6. A.B. Aceves and C. DeAngelis, "Spatiotemporal pulse dynamics in a periodic nonlinear waveguide", *Opt. Lett.* **18**, 110 (1993).
7. G. Luther, J.V. Moloney, A. Newell and E. Wright, "Self-focusing threshold in normally dispersive media", *Opt. Lett.* **19**, 862 (1994).
8. G. Luther, A. Newell and J. Moloney, "The effects of normal dispersion on collapse events", *Physica D* **74**, 59 (1994).
9. G. Fibich, V. Malkin, G. Papanicolaou, "Beam self-focusing in the presence of small normal time dispersion", *Phys. Rev. A* **52**, 4218 (1995).
10. M. Landman, G. Papanicolaou, C. Sulem and P. Sulem, "Rate of blowup for solutions of the nonlinear Schroedinger equation at critical dimension", *Phys. Rev. A* **38**, 3837 (1988); and references therein.
11. Q. Feng, J.V. Moloney, A.C. Newell, E.M. Wright, K. Cook, P.K. Kennedy, D.X. Hammer and C.R. Thompson, "Theory and simulation of laser-induced breakdown and self-focusing of ultrashort focused laser pulses in water", preprint.
12. M.J. Potasek, "Femtosecond solitons in optical fibers", *J. Appl. Phys.* **65**, 941 (1989); and references therein.
13. G.P. Agrawal, *Nonlinear Fiber Optics* (Academic Press, NY, 1989); and references therein.
14. P. K. Kennedy, S.A. Boppart, D.X. Hammer, B.A. Rockwell, G.D. Noojin and W.P. Roach, "A First-Order model for computation of laser induced breakdown thresholds in ocular and aqueous media: Part II-code description and comparison to experiment", *IEEE J. Quant. Electron.*, **31**, 2250 (1995).
15. B.A. Rockwell, W.P. Roach and M.E. Rogers, "Determination of self-focusing effects for light propagating in the eye", *Laser-Tissue Interaction V* **2134**, 2 (1994).
16. P.W. Lappin, "Ocular damage thresholds for the helium-neon laser", *Arch. Environ. Health* **20**, 17 (1970).
17. G.H. Bresnick, et.al., "Ocular effects of argon laser radiation I. Retinal damage threshold studies", *Invest. Ophthalmol.* **9**, 901 (1970).
18. R.G. Allen, S. J. Thomas, R.F. Harrison, J.A. Zuclich, and M.F. Blankenstein, "Ocular effects of pulsed Nd laser radiation: variation of threshold with pulsewidth", *Health Phys.* **49**, 685 (1985).
19. W. P. Roach, C.A. Toth, C.D. Stein, G. D. Noojin, D. J. Stolarski and C. P. Cain, "Minimum visible lesions from pico- and femtosecond laser pulses", *Proc. SPIE, Laser-Tissue Interaction V*, **2134**, 10 (1994).
20. M. J. Potasek and A. E. Paul, "Investigation of nonlinear ocular media using femtosecond laser pulses", *Proc. Laser and Noncoherent Ocular Effects: Epidemiology, Prevention, and Treatment*, SPIE, vol **2974**, 66 (1997).
21. P.V. Mamyshev and S.V. Chernikov, "Ultrashort-pulse propagation in optical fibers", *Opt. Lett.* **15**, 1077 (1990).
22. F.M. Mitchke and L.F. Mollenauer, "Discovery of the soliton self-frequency shift", *Opt. Lett.* **11**, 659 (1986); J.P. Gordon, "Theory of the soliton self-frequency shift", *Opt. Lett.* **11**, 662 (1986).

HIGH-PERFORMANCE OPTICAL LIMITER BASED ON FINE CARBON PARTICLES SUSPENDED IN AN ORGANIC SOLVENT

DENIS VINCENT

Defence Research Establishment Valcartier, 2459 Pie-XI Blvd North,
Val-Bélair, Qc, Canada, G3J 1X5

Abstract The limiting performances of two suspensions of fine carbon particles are compared with those of C_{60} at different wavelengths, pulselengths and repetition rates. The effects of particle size and laser spot size are discussed. Also, a few examples of integration into optical sights are included.

Key Words: Optical limiting, nonlinear optics, carbon suspension.

INTRODUCTION

Since 1989, DREV has been experimenting with different materials in liquid or solid form to develop an optical limiter covering the visible and near-IR band. Such a limiter could help to protect eyes and electro-optical sensors against multiwavelength or unknown laser radiation. The results of this research are two suspensions of fine carbon particles, DREV CBS-100 and CBS-200, whose limiting properties compare favourably to those of known materials such as C_{60} ,¹ CAP and SiNC,² over the visible and near-IR spectrum while retaining high luminous transmission (see Figure 1). This paper presents the results obtained with these suspensions.

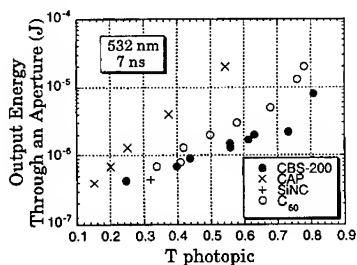


FIGURE 1 DREV CBS-200 compared with known materials.

OPTICAL CONFIGURATION AND FAR-FIELD BEAM SPREADING

Most of the time, an optical limiter is used in an optical configuration as shown in Figure 2. Lens L1 focusses the incoming radiation in the material being tested and lens L2 recollimates the transmitted radiation, then a last lens L3

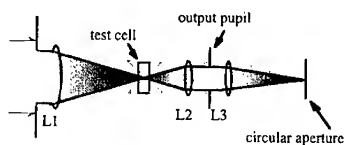


FIGURE 2 Optical arrangement used for limiter measurements.

focusses it onto an analysis plane where a series of circular apertures can be used to measure the distribution of energy on what could be a sensor surface. Figure 3 shows what happens in the analysis plane when a limiting material (in this case, a carbon suspension) is inserted at the common focus of L1 and L2 (which must be readjusted after

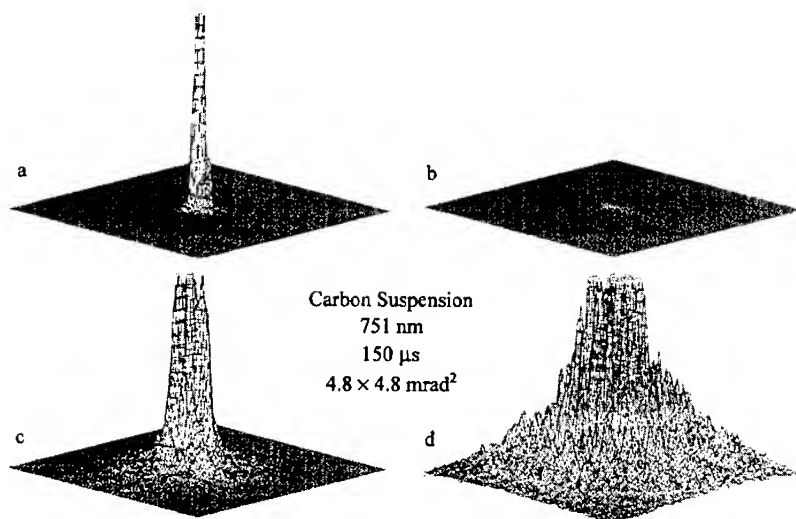


FIGURE 3 Laser spot in the focal plane of L1 as imaged on the LBA: a) cell out of focus; b) cell in focus; c) camera sensitivity increased; d) higher input energy; LBA intentionally overexposed to allow observation of the lobe in b.

insertion). When the cell is out of focus, the laser spot is small and well defined. When the limiter is brought to focus, the central lobe appears highly attenuated and enlarged. At a higher input energy, the spot becomes very large and a significant portion of the output energy appears in the wings. Therefore, a single aperture measurement does not fully characterize the changes induced by the limiter on the distribution of energy. However, by comparing materials we found that an aperture's size 5 to 10 times the size of the unaffected spot is a good compromise between ease of alignment and sharp clamping effect useful to evaluate materials. For an 8-mm output pupil, it corresponds to an aperture angular diameter near 1 mrad for wavelengths across the visible and near-IR spectrum. Since 1.5 mrad is an interesting FOV angle for laser safety purposes,³ most of the measurements presented below have been taken with an analysis aperture subtending this angle, as seen from L3.

PREPARATION AND MEASUREMENT METHODS

Since the solutions of C_{60} are easily compared between laboratories, the cells containing this material have been made as a reference. Great care has been taken during the preparation of the materials in order to obtain reproducible results.

Carbon 60

The 99.9% pure C_{60} was procured either from SES Research Inc. (Houston, Texas) or Pyrogenesis Inc. (Montréal, Québec). Saturated solutions in chlorobenzene were stirred during a full day, then filtered through 220 nm pores and diluted to the required concentration. The prepared material is kept sealed in darkness.

CBS-200

This proprietary recipe starts with a commercial ink which is then dispersed into an organic solvent with the appropriate surfactant. After being stirred for one day, the

suspension is filtered through 220 nm pores and diluted to the required concentration. The prepared material is kept sealed in darkness.

CBS-100

This proprietary recipe starts from a mixture of carbon powder and surfactant disrupted ultrasonically at high power. The resulting paste is dispersed into an organic solvent with the appropriate surfactant, filtered through 100 nm pores and diluted to the required concentration. The prepared material is also kept sealed in darkness.

Cells

Figure 4 shows the standard DREV's cell design. Some variants were used but they were basically of the same design. The liquid pathlength has been varied between 1 and 4 mm, but the results presented below come from cells with a 2-mm pathlength. The ordinary glass windows have a refractive index near 1.5. All the cells were sealed under vacuum with a vapour space left in it to absorb the laser-induced shock waves and to ease the formation of laser-induced bubbles.

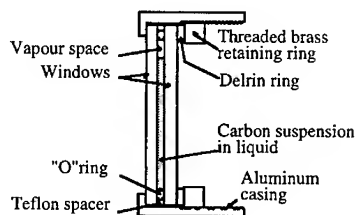


FIGURE 4 DREV's standard cell

Measurement Setup

The measurement setup shown in Figure 5 has been described elsewhere.¹ The only difference resides in the use of several laser sources: a Q-switched Nd:YAG laser emitting 7-ns pulses at 532 nm and 8-ns pulses at 1064 nm, an Rh6G-dye laser emitting 0.8 μ s-pulses at 590 nm and an alexandrite laser emitting 100-ns pulses in Q-switched mode and 1- μ s or 100 to 150- μ s pulses (depending on the pumping and cavity configuration) in relaxation mode at 751 nm. Figure 6 shows the measured normalized transmission when a

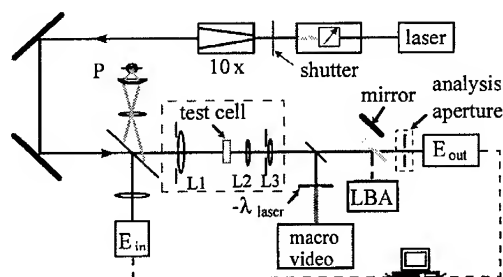


FIGURE 5 Measurement setup: L1-L2 forms an $f/5$ afocal system, L2-L3 re-images the focal spot with a linear magnification of $25\times$.

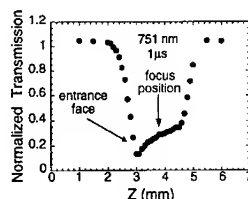


FIGURE 6 Z-scan and the position for measurements

cell containing a carbon suspension is moved across the common focal plane of L1 and L2. Nonlinear refraction appears clearly for the spot's position near the windows. The measurements reported below were always taken with the focus in the center of the cell, not at the minimum. This provides more reproducible results and makes it possible to use higher input energy without damaging the entrance window.

COMPARISON CBS- C_{60}

The performances of CBS-100, CBS-200 and C_{60} have been evaluated at different wavelengths and pulselengths, as shown in Figure 7 where single pulse data for clamped output levels are plotted. In all cases, CBS-100 limits better than CBS-200 and C_{60} , CBS-200 being second in performance.

CBS-100 was not developed yet when the data at 590 and 1064 nm were collected. Clearly, C_{60} does not limit well in the red and near IR,⁴ at least for the cells having a photopic transmission larger than 0.3. On the other hand, the

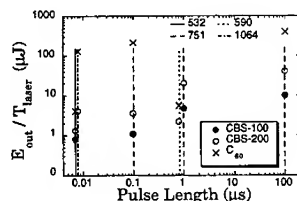


FIGURE 7 Comparison CBS- C_{60}

output energy with CBS-100 increases by an order-of-magnitude when the pulselength varies from 7 ns to 100 μ s. However, the output remains clamped at this higher value.

COMPARISON OF THE TWO SUSPENSIONS

Figure 8 shows the normalized transmission ($E_{out} / T_{lin} E_{in}$) of CBS-100 and CBS-200 as a function of the input energy for 7-ns pulses. Different symbols in the plot represent cells with different linear transmission (T_{lin}) at the selected laser wavelength. These data indicate that the values of E_{out} / T_{lin} for the two materials are in a constant ratio for $E_{in} > 10^{-5}$ J. Furthermore, each curve goes as E_{in}^{-1} for $E_{in} > 10^{-4}$ J, which means that $E_{out} / T_{lin} = \text{constant}$ in this range of values of input energy.

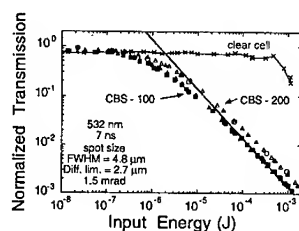


FIGURE 8 Nonlinear transmission of CBS for $T_{lin} < 0.7$

The effects of particle size and laser spot size for 7-ns pulses at 532 nm are illustrated in Figure 9 where the normalized transmission at a fixed $E_{in} > 10^{-4}$ J is plotted

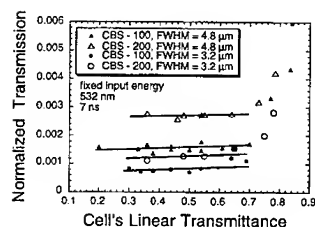


FIGURE 9 Effects of focussed spot size and particle size

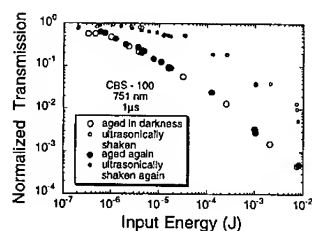


FIGURE 10 Conditioning of CBS-100

as a function of T_{lin} . Smaller particles limit better than large ones and a smaller spot size (or a larger energy density) is preferable. However, the conclusion about particle size

does not apply directly to the long pulse case. As shown in Figure 10, aged cells of CBS-100 limit the long red pulses better than ultrasonically shaken cells. The two photographs of Figure 11 show the appearance of fresh and aged cells. Clearly, in an aged suspension, the carbon particles are arranged in small clusters where the particles are so

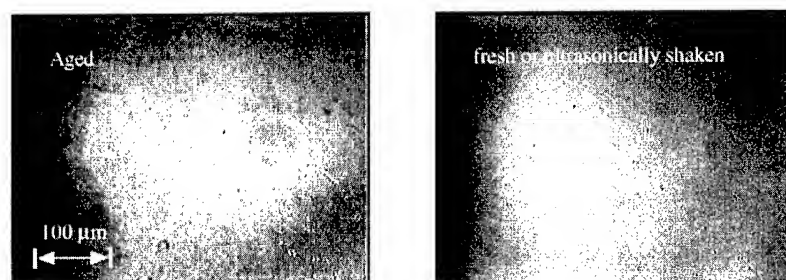


FIGURE 11 Views of particles in the suspension CBS-100

loosely bound that low-power ultrasounds can break them. Usually, carbon agglomerates cannot be broken at such low power. Ageing does not change appreciably the response to short pulses. It seems that pulses a few ns long interact primarily with the particles, and that longer pulses interact with the clusters. The effect of ageing is much less apparent in CBS-200.

BEHAVIOUR OF CBS AT HIGH REPETITION RATE

It is well known that CBS performance degrades at high repetition rates, as opposed to C₆₀. Carbon disappears gradually from the interaction site and, finally, the laser beam passes through the cell almost unaffected. By choosing a liquid with better thermal properties, it is possible to produce laser-induced convection currents in the cell (see Figure 12). With such currents present in the cell, the interaction site is replenished with carbon particles and, after a certain recovery time, the output energy value comes back to



FIGURE 12 Laser-induced convection currents in CBS cells. The two photographs, taken at different times, show the propagation of the clarified portion of the suspension. The laser spot is at the center of each photograph. The large black spots were dust particles on the vidicon tube open to air.

the initial energy value, as illustrated by the oscilloscope traces in Figures 13a and 13b for progressively faster liquids. With CBS-100 at 6 pps, the maximum output energy is smaller than 3 times the single pulse value for $T_{lin} < 0.55$ as shown in Figure 13c.

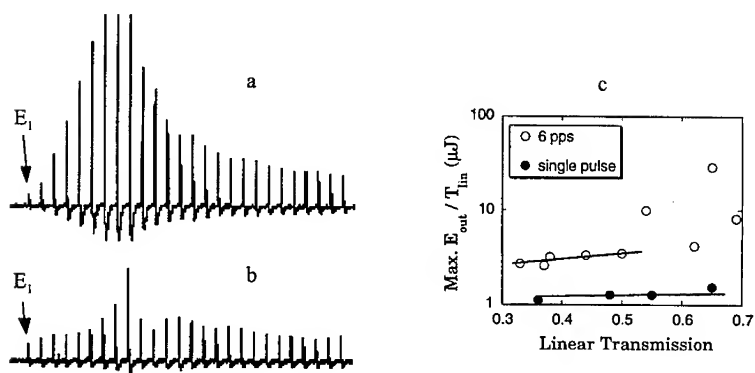


FIGURE 13 Transmission of a pulse train at 6 pps: a) oscilloscope trace of the pulse train after the limiter for a fast liquid; b) same as a) but in a faster liquid; c) maximum E_{out} as a function of T_{lin} . Data taken with 7-ns pulses at 532 nm.

To minimize the recovery time, $M_r = \alpha_v / \rho C_p$ must be maximized, and to maximize the current speed, $M_c = \alpha_v / \eta C_p$ must be maximized. In these relations, α_v is the volumic expansion coefficient (K^{-1}), ρ , the density (kg/m^3), C_p , the specific heat at constant pressure ($J/kg-K$) and η , the viscosity coefficient ($kg/m-s$).

INTEGRATION IN OPTICAL SIGHTS

The carbon suspension CBS-200 has been tested extensively in two optical sights: an elbow sight (Figure 14) and binoculars (Figure 15). With this latter piece of equipment

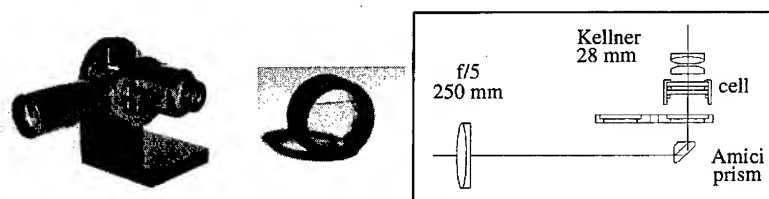


FIGURE 14 Integration in an elbow sight: the sight, the standard cell and the optical diagram

1 km away from the laser source, it has been found that air turbulence affects the performance of CBS at low input energy but not the performance of C_{60} (Figure 16). That could be due to the presence of many spots in the focal plane (Figure 17) at high level of turbulence. However, this point requires further investigation.

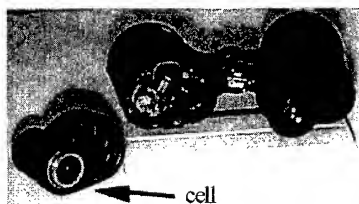


FIGURE 15 Integration in binoculars

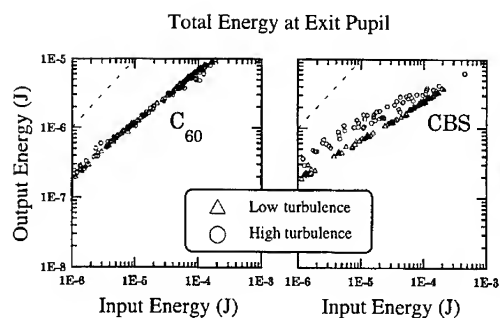


FIGURE 16 Effects of air turbulence in a 1-km country range



FIGURE 17 Spots present at the focal plane when there is turbulence (data with binoculars).

CONCLUSION

From the results reported here, it appears clearly that DREV CBS-100 is a very effective broadband optical limiter for pulselengths between 7 ns and 150 μ s. The output energy measured through the analysis aperture does not increase by more than a factor of 3 at 6 pps for $T_{lin} < 0.55$. To be effective against long pulses, CBS-100 must be properly aged. These results come from both fresh cells and cells several years old.

REFERENCES

1. D. Vincent and J. Cruickshank, *Applied Optics*, **36**, 7794-7798 (1997).
2. L.W. Tutt and T. Boggess, *Prog. Quant. Electr.*, **17**, 299-338 (1993).
3. ANSI Z136.1, American National Standard Institute, Safe Use of Lasers (1993).
4. A. Kost, J.E. Jensen, M.B. Klein, S.W. McCahon, M.B. Haeri and M.E. Ehrhitz, in Nonlinear Optical Materials for Switching and Limiting, edited by M.J. Soileau (Proc. SPIE 2229), pp.78-90 (1994).

NONLINEAR LIGHT SCATTERING IN A TWO-COMPONENT MEDIUM : OPTICAL LIMITING APPLICATION

V. JOUDRIER⁽¹⁾, P. BOURDON⁽¹⁾, F. HACHE⁽²⁾, C. FLYTZANIS⁽²⁾

⁽¹⁾Centre Technique d'Arcueil, DGA / DCE, Arcueil, France

⁽²⁾Laboratoire d'Optique Quantique, Ecole Polytechnique, Palaiseau, France

Abstract We present an experimental investigation of an optical limiting device based on nonlinear light scattering due to a photoinduced refractive index mismatch in a colloidal suspension. Several experiments performed at 532 nm with nanosecond laser pulses are described and the origins of the optical limiting effect are discussed.

INTRODUCTION

Scattering is a fundamental manifestation of the interaction between matter and radiation, resulting from inhomogeneities in the refractive index, which decrease transmission. This phenomenon is then especially attractive for sensor protection from laser light by optical limiting. One of the methods to induce scattering at high incident energy is to make use of the Kerr effect where the index of refraction is intensity dependent. The idea is then to use a two component medium with a good index matching between the two components at low intensity, resulting in the medium transparency, and to modify it at high intensity due to the non linearity of one component, making the medium highly scattering. The limitation principle is illustrated in FIGURE 1.

In this paper, some of the experimental and theoretical investigations concerning nonlinear light scattering are presented in the visible domain ($\lambda = 532$ nm) for protection against nanosecond pulses.

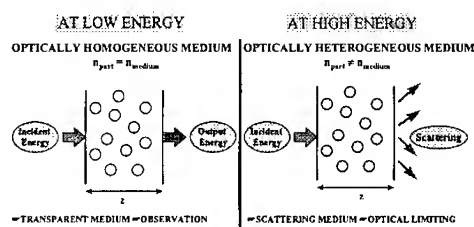


FIGURE 1 Limitation principle based on non linear light scattering.

MATERIALS AND EXPERIMENTAL SETUPS

In this study, the two-component composite is a colloidal suspension of spherical silica particles in toluene, a nonlinear medium which must produce the index mismatch at high fluences. The Stöber method¹ is used to grow small silica particles homogeneous in size, which are then embedded in toluene with alcohol chain grafting on the surface to keep them in suspension and prevent cluster formation. With this method, one gets a very uniform distribution of spherical particles. In our sample, the diameter of the silica spheres is $0.11 \mu\text{m} \pm 0.03$ and the volume fraction about 5 percent. Finally, the index matching between silica and toluene is achieved adding a linear liquid (hexane) and the linear transmission approaches 80 %. The photon mean free path (equal to 40 mm) is much larger than the cell thickness (5 mm) and thus we are in a single scattering regime. After the sample preparation phase, different experimental investigations concerning this material are made in the nonlinear regime with a frequency-doubled, injection-seeded, Q-switched Nd:YAG laser delivering 10 ns pulses ($\lambda = 532$ nm). The first optical experiment is a classical setup², used to perform optical limiting and Z-scan experiments³ with different aperture. From these experiments, it is possible to discriminate between several nonlinear effects such as nonlinear refraction, absorption and scattering. And after this simple experimental approach, two complementary

experiments are made to characterize more precisely the detected nonlinear scattering : measurement of the angular distribution of scattered energy generated in the limiting process and an estimation of the total scattered energy by using an integrating sphere. These two experimental setups will not be described in this paper but similar optical test-beds have already been used in the work of K. Nashold et al⁴. Finally, another experimental setup² based on a pump-probe technique is also presented to investigate the dynamics of the optical nonlinearities. This time-resolved study provides an efficient means to measure and distinguish fast and slow nonlinear mechanisms and leads to a better understanding of the nonlinear scattering effect.

OPTICAL LIMITING RESULTS

Our sample consisting of toluene, hexan and 0.1 μm silica particles in suspension was tested in different ways with the classical test-bed, and every time, the optical limiting characteristics were clearly exhibited. FIGURE 2 shows the limiting behaviour of this material, when different apertures are used. It is evident here that the output energy drop increases with decreasing diaphragm size. As it can be observed in the right insert graph of FIGURE 2, a closed aperture Z-scan of the solution shows only a strong decrease of the sample transmission, ruling out the contribution of nonlinear refraction in our experiment. Two photon absorption (TPA) cannot explain the observed results. First of all, we have checked that the solvent alone does not give any signal in a Z-scan experiment, which means that TPA is very weak in toluene at 532 nm, in accordance with reference 5. This shows that the phenomenon comes from the silica particles. However, one would need a TPA coefficient of the silica spheres of at least 1 cm/GW to explain the experimental curves, which is not supported by bibliographical data⁶. As a further indication, the aperture dependence of limitation effect (FIGURE 2) is not compatible with nonlinear absorption, but confirms the presence of nonlinear scattering. The nonlinear scattering is then clearly the dominant mechanism originated in the optical limiting behaviour of this sample. A direct examination of scattered light with naked eye confirms at first this conclusion, as well as the experiments involving the measurement

of the angular distribution of scattered energy and the integrating sphere measurement. The principal results will be given briefly now.

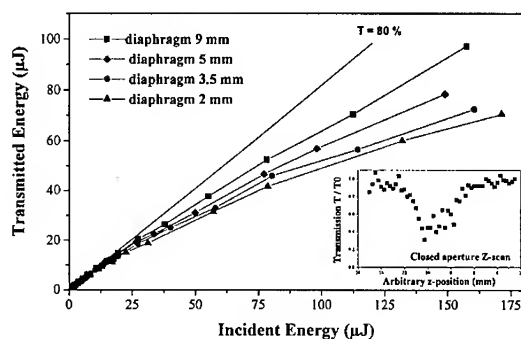


FIGURE 2 Optical limiting curve of a solution containing toluene, hexan and 0.1 diameter silica particles illustrating the dependence and the presence of non linear scattering. Closed aperture Zscan in insert.

FIGURE 3 presents the ratio of scattered to input energy as a function of angle θ when a sensitive detector is moved around the cell containing the sample. Three values of the incident energy (2, 121 and 300 μJ) were sent on our material, with a 300 mm focal length lens, the purpose being to observe the difference of behaviour between the linear and nonlinear regime. A logarithm representation was necessary here to make the signal observable, given that the laser energy is still very strong along the optical axis (located here for $\theta = 0^\circ$). On this graph however, it is clear that the detected scattered light increases with incident intensity, showing the presence of nonlinear scattering effects at high energy. But due to the specific setup used in this configuration and to the strong influence of the laser beam along the optical axis, the collected energy results from pure scattering only within a small angular area ($20^\circ < \theta < 40^\circ$). On the other hand, no backscattering has been detected in a significant way to be represented on FIGURE 3. It is clear that the scattering is mainly in the forward direction. It can nevertheless be efficient in an optical limiting device through the use of a diaphragm (see FIGURE 2).

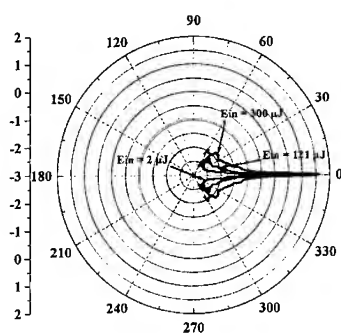


FIGURE 3 Logarithmic representation of the ratio of scattered to input energy as a function of angle θ for three different values of incident energy.

In the same way, the total scattered energy integrated over all scattering angles can be estimated to complete the characterization of the nonlinear scattering from our sample. To perform this experiment, a 25-cm diameter integrating sphere was used at the center of which the material was placed. The interior of the sphere was coated with Spectralon, a Lambertian scattering coating which has an overall efficiency of 0.99 at $\lambda = 532$ nm. The sphere has three ports: two ports by which the laser beam is at first collimated by a 300 mm focal length lens into the sample and then exits from the sphere. The last port is used to collect the scattered energy. And after a complete calibration of this experimental setup and the optimisation of the focused lens position to ensure a sufficient fluence in the sample, a measurement of the total scattered energy is possible, even if the signal versus noise ratio is low due to the weak effective efficiency of the integrating sphere (2.3 %). However, the results of this experiment show a fairly good coherence with the optical limiting curves as it can be observed on FIGURE 4, where the scattered energy is represented as a function of the incident one. The curve is similar (with reverse slope) to a classical limiting curve and the total scattered energy (38 μ J for an incident energy of 190 μ J) estimated from this experiment agrees well with the previous optical limiting experiments.

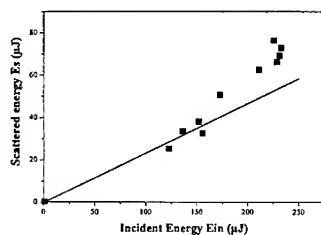


FIGURE 4 Representation of the total scattered light measured with the integrating sphere versus the incident energy.

THEORETICAL APPROACH

The previous experimental data can now be analyzed with some simple theoretical methods to evaluate the nonlinearity of the material from the optical limiting, the angular scattering and the total scattering energy measurements. The Rayleigh-Gans regime is used in this theoretical approach, as the material parameters fulfill its specific requirement : $ka|m-1| \ll 1$ (k is the wavevector, a is the average radius of the spherical particles, m the ratio between the refractive indices of these particles and the surrounding medium).

The first numerical analysis uses a model of nonlinear propagation in a medium with spatially random refractive index. It is based on the flux theory of light scattering, where the two-component medium is considered as a composite showing effective scattering and absorption losses along the optical axis (the z -direction) :

$$\frac{dI}{dz} = -\alpha_a \cdot I - \alpha_s \cdot I,$$

where α_a is the linear absorption coefficient, α_s the effective scattering coefficient. The latter is given by Rayleigh-Gans relations and is proportional to the square of the difference in the effective refractive indices of the two components $\Delta \tilde{n}$: $\alpha_s = g_s (\Delta \tilde{n})^2$.

The g_s parameter is independent of intensities but depends on the size, shape and

concentration of the particles and the wavelength of light. Its linear variation with the particles concentration, in the weak scattering regime, has been checked experimentally in the limitation measurements. The Δn expression is then splitted into its linear and nonlinear parts : $\Delta n = \Delta n_L + \Delta n_{NL}$ where the nonlinear part is function of the intensity inside the medium by : $\Delta n_{NL} = \Delta n_2 I$ with Δn_2 the nonlinear coefficient. Moreover the relaxation of light-induced changes in the refractive indices of the components can be taken into account by introducing a Debye-type equation. Finally, the equations are solved numerically for an initial Gaussian pulse. Using the model, optical limiting curves can be simulated for different values of Δn_2 . The best fit is given in FIGURE 5.

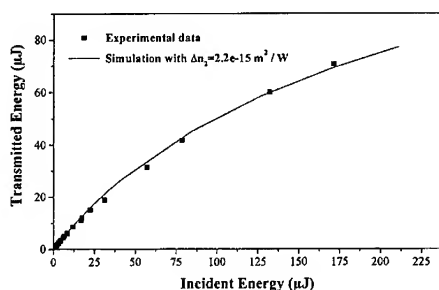


FIGURE 5 Simulation of the experimental results (diaphragm 2 mm) giving an estimation of Δn_2 .

The second theoretical analysis is a quantitative study of the angular and total scattered energy measurements. From the well-known expressions of the Rayleigh-Gans regime, scattered intensity can be linked with the incident one by : $I_s = NL\Delta\Omega \frac{dC_{sca}}{d\Omega} I$ (*). In this equation, N is the particles concentration per volume units, L the sample length, $\Delta\Omega$ the solid angle under which the scattering light is measured. $\frac{dC_{sca}}{d\Omega}$ is the differential scattering cross section, also called the phase function, which will be useful in the study of the angular scattering measurement where it is specific to a measurement angle. Then the integrated form of the previous expression (*) will be then used for the integrating

sphere data interpretation. Indeed, in this case, it gives the scattering cross section C_{sca} , itself proportional to the square of the difference in the effective refractive indices of the both sample components (this is connected to the previous calculation by: $\alpha_s = g_s(\Delta n)^2 = NC_{sca}$). Finally, from the equation (*) in its integrated form or not, the two experiments (giving angular scattering and total scattering measurements) can be analyzed. In both cases, the difference in the effective refractive indices Δn exhibits a linear variation with the incident intensity I , allowing an estimation of the linear and nonlinear coefficients Δn_L and Δn_2 . The next table gathers the Δn_L and Δn_2 values obtained from the experimental data analysis of the optical limiting, the angular scattering and the integrating sphere experiments.

Experiments	Δn_L	Δn_2 (en m^2/W)
limiting curve	$1,24 \cdot 10^{-2}$	$2,2 \cdot 10^{-15}$
angular scattering	$1,54 \cdot 10^{-2}$	$1,56 \cdot 10^{-15}$
integrating sphere	$1,33 \cdot 10^{-2}$	$1,3 \cdot 10^{-15}$

TABLE 1 Summary of simulation results for Δn_L and Δn_2 from optical limiting, angular scattering and integrating sphere experiments.

These three different experiments give very close results with an average value of the Δn_L coefficient around $1.37 \cdot 10^{-2}$ and of the nonlinear coefficient around $1.68 \cdot 10^{-15} m^2/W$. However, this value for Δn_2 , which is very strong, is not in agreement with bibliographic data^{7,8} ($\Delta n_2 = -7.10^{-19} m^2/W$ for the toluene). It cannot come from the surrounding medium nor from the silica particles, according to previous Z-scan experiments. Several other mechanisms can be invoked to explain this large effective Kerr nonlinearity and more particularly nonlocal processes such as thermal^{3,7} or electrostrictive⁹ ones or whispering gallery modes phenomena¹⁰. But after appropriate calculations, none of these properties can explain the observed refraction index variation.

One is therefore left with another possibility, namely that the index mismatch comes from the interface of the silica spheres with the surrounding medium. The observed phenomena could be connected to a photoinduced modification of the interface since, as stated above, the particles are surrounded by long-chain molecules to prevent

aggregation. These chains certainly play a role in the index matching of the solution. This is confirmed by the ratio of 1:0.8 necessary to achieve perfect index matching for the toluene: hexane mixing, corresponding to an index of 1.444, sensibly different from the value for bulk silica (1.458). The present experimental observation would be consistent with a photoinduced rearrangement or a photodegradation of the long molecules in the adsorbed layer, which would modify the index matching condition. Some new experimental investigations must be carried out to ascertain this hypothesis, for example using a solution where no alcohol chains will be grafted on the particles surface, as long as their suspension is also maintained in this case. These new investigations will be addressed now.

COMPLEMENTARY ANALYSES

The new sample, synthesized without alcohol chains grafting on the particles surface, must also obey several conditions to permit an easier comparison with the previous sample limiting behaviour. For instance, it must have similar particles size and concentration. However, the surrounding medium can not be the same in this configuration, because the silica particles are polar (due to their fabrication process), which is not the case of the toluene and hexan mixing. A direct transfer of particles without grafted chains in such a medium induces a fast particles aggregation, as nothing prevents their sticking. One way to solve this problem is to use a polar surrounding medium. From this condition, the glycerol and the ethylen glycol have been chosen, on account of their respective polarity, their strong viscosity (maintaining the particles in suspension), and their weak non-linearities (which are similar to those of toluene and hexan).

This new sample of glycerol, ethylen glycol and 0.1 μm silica particles in suspension without grafted chains has been tested in the same way as for the first sample. And unexpectedly, optical limiting characteristics have been demonstrated. Here again, only the nonlinear scattering property has been proved to be at the origin of this effect. As previously, this conclusion has been established after having ruled out all the other

possible nonlinear mechanisms. Moreover, when a direct comparison between the first and new sample is made, as in FIGURE 6, a strong optical limiting effect could be clearly seen in the second one, revealing that the grafted chains don't have the properties that were expected. The threshold, defined for a decreasing transmission of 20 %, is even lower : near $1 \text{ J} / \text{cm}^2$ for the new material, versus $10 \text{ J} / \text{cm}^2$ for the first one.

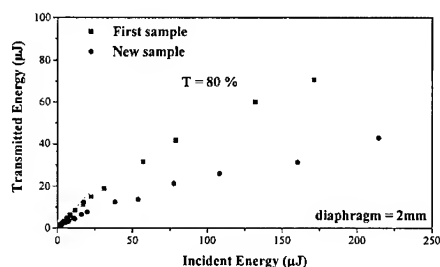


FIGURE 6 Comparison between optical limiting curve of first sample (with alcohol chain grafting on the silica particles surface) and new sample (without alcohol chain grafting).

In conclusion, the origin of the strong refraction index variation seems to be a complex phenomenon, which certainly involves simultaneously several mechanisms. Further information about the nonlinear scattering effect can be gained by studying the time response of the optical nonlinearities with a dual-beam (pused-pump, cw probe) technique². Monitoring of probe transmission after pump excitation permits the determination of response and relaxation times for the nonlinear properties. The fast and slow nonlinear mechanisms of both samples can be measured and distinguished by continuous time resolution¹¹. Figures 7 and 8 show an example of typical curves with a millisecond time scale for the first sample and second time scale for the new one. In both cases, a very strong and fast transmission change is induced by the excitation pulse. However, in spite of short response times in both samples, the recorded signals reveal strong difference in their relaxation times (the decay times are close to 3 ms for the first sample and 2s for the new one).

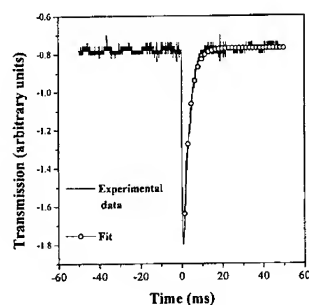


Figure 7

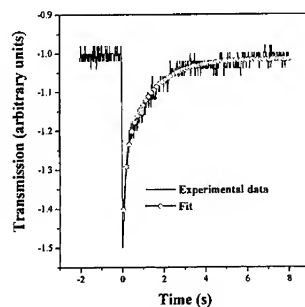


Figure 8

FIGURE 7 and FIGURE 8 : Transmission time trace after one laser pulse in first and new samples. A single exponential fit ($y_0 + A_1 \exp [-(x-x_0)/t_1]$) gives a relaxation time t_1 around 3 ms for the first sample (Figure 7) and around 2 s for the new one (Figure 8).

These two kinds of results confirm that the nonlinear scattering effect is completely due to the interaction between the particles and the surrounding medium. The short activation times (not shown in figures 7 and 8) could be connected in the two cases to the rearrangement phenomenon itself which is expected to perturb locally the pressure. It could be consistent with the hypothesis of a photoinduced rearrangement of the molecule layer surrounding the particles. In that case, the phenomenon will be reversible. On the other hand, it could be connected to a photodegradation of the particles surface, which would be an irreversible phenomenon and would last as long as the particles stay in the laser beam. As for the long decay times, the stronger viscosity in the surrounding medium of the new material can certainly explain the slower mechanism in comparison with the previous sample (this viscosity is closed to 880 centipoises for the new sample, against 0.48 for the first one). These long decay times could be connected to the time required by a photodegraded (or not) particle to get out of the probe beam or come back to its initial equilibrium state.

Moreover, the polarity of the surrounding medium seems to be at the origin of the better limiting effect observed in the new sample. In any case, the choice of this specific characteristic is necessary to induce a sufficient nonlinear scattering.

CONCLUSION

In summary, optical limiting of nanosecond laser pulses in a medium containing spherical silica particles in suspension in a liquid surrounding medium is reported. The limiting mechanism is shown to be mainly due to nonlinear scattering in accordance with what was expected. This one leans on mismatch of the refraction indices by optical nonlinear effects at high fluence. The precise origin of this effect is not easy to understand but it seems to be closely connected to the nature of the surrounding medium (more precisely, its polarity). Further work should be undertaken to improve this nonlinear scattering effect, for example by increasing the particles concentration to go to the multiple scattering regime. A promising application could be the utilization of this effect in association with other optical limiting mechanisms (such as reverse saturable absorption). This could lead to improved behaviour of existing devices, especially at high intensity.

REFERENCES

- ¹ W. Stöber, A. Fink :J.of Colloid and Interface Science, **26**, 62 (1968)
- ² V. Joudrier, P. Bourdon, F. Hache, C. Flytzanis, Appl. Phys. B (to be published)
- ³ M. Sheik-Bahae, A. A. Said, T-H. Wei, D. J. Hagan, E. W. Van Stryland, IEEE J. Quant. Electr., **26**, 760 (1990)
- ⁴ K. Nashold, D. P. Walter, J. Opt. Soc. Am B, **12**, 1228 (1995)
- ⁵ J. Castillo, V. P. Kozich, A. Marciano O., Opt. Lett., **19**, 171 (1994)
- ⁶ T. Mizunani, K. Takaji, Opt. Commun., **68**, 223 (1988)
- ⁷ P. Brochard, V. Grolier-Mazza, R. Cabanel, J. Opt. Soc. Am B, **14**, 405 (1997)
- ⁸ R. Adair, L. L. Chase, S. A. Payne, Phys. Rev. B, **39**, 3337 (1989)
- ⁹ P.W. Smith, A. Ashkin, W. J. Tomlinson, Opt. Lett., **6**, 284 (1981)
- ¹⁰ H. -B. Lin, A. L. Huston. B. L. justus, A. L. Campillo, Opt. Lett. **11**, 614 (1986)
- ¹¹ D. O. Caplan, G. S. Kanter, P. Kumar, Opt. Lett., **21**, 1342 (1996)

INVESTIGATION OF OPTICAL LIMITING MECHANISMS IN CARBON-BLACK SUSPENSIONS

FRANCOIS FOUGEANET, DIDIER RIEHL
DGA/DCE/CTA/LOT, 16 bis Av. Prieur de la Côte d'Or 94114 Arcueil Cedex France

Abstract Optical limiting mechanisms respectively related to particles and to surrounding liquid phase changes are evidenced in the case of carbon-black in water and in CS₂ via a pump-probe experiment and via limiting measurements. A simple thermal model is presented to extract influential parameters on the phase change of both particles and liquid and to explain the different limiting behaviour of carbon-black particles in water and in CS₂.

INTRODUCTION

Carbon-black suspensions (CBS) are of great interest for optical limiting in view of their strong nonlinearity, sensitivity, and broadband transmission. The two mechanisms previously observed in these suspensions have been attributed to microplasmas scattering and absorption^{1, 2}, and to scattering by vapour bubbles formed around the intensely heated carbon particles^{3, 4, 5}. In order to determine the influential mechanism on limiting performance we have performed a collinear time-resolved pump-probe experiment coupled with a measurement of the emission generated in the CBS cell. Measurements were done using carbon-black particles diluted in water and in CS₂. The study of carbon black in these two different liquids allowed us to distinguish two limiting mechanisms and to compare their limiting features in terms of threshold and efficiency. The first limiting mechanism is related to a phase change of particles although the second one is due to the growth of bubbles in the liquid. A simple model of thermal conduction from particles to the liquid is proposed to explain the different behaviours of carbon-black in water and in CS₂ (CB/water, CB/CS₂). The influential parameters on limiting mechanisms are extracted from this model for the two different limiting mechanisms observed.

PUMP PROBE MEASUREMENTS

The pump probe set-up is shown in Figure 1. The pump beam was a Q-switched injected Nd:Yag laser emitting temporally gaussian pulses of duration $\tau_{\text{las}} = 9$ ns (FWHM) and wavelength $\lambda = 1.064$ μm . It passed through a waveplate/polariser pair which controlled the incident energy on the sample. The incident pulse energy was measured on a pyroelectric detector and the temporal profile using a fast photocathode (rise time = 270 ps). The pump beam was focused in the sample using a 200 mm focal length achromatic doublet and generated the nonlinearity in the CBS cell. The measured beam waist was $w_{(1/e^2)} = 22$ μm . This nonlinearity was read by a continuous He-Ne laser emitting at $\lambda = 632.8$ nm. This continuous probe was inserted on the optical path of the pump beam using a polarizing cube, and extracted by the same way. A fast photomultiplier (rise time 0.6 ns) connected to a digital oscilloscope was used to analyze the probe signal. Time resolved measurements of the emission of CBS were simultaneously performed using the same type of photomultiplier in the sensitivity range (300-800 nm) of the detector.

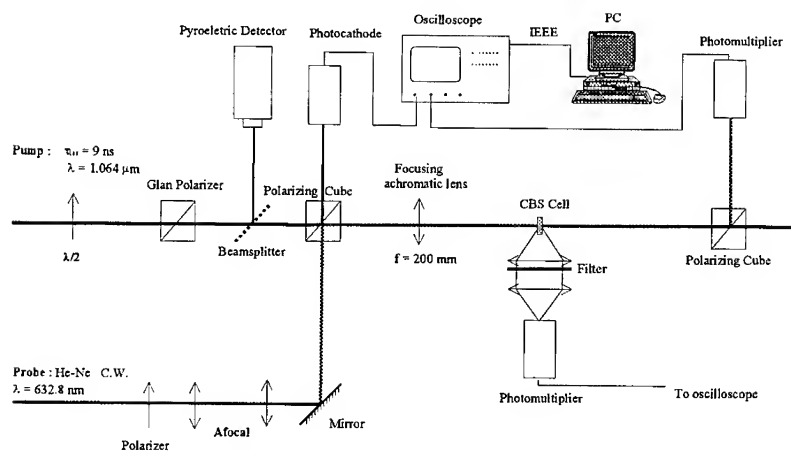


FIGURE 1. Pump-Probe set up

Case of Carbon-Black in water

The probe intensity variation for carbon black in water is shown in Figure 2 at incident fluence above the limiting threshold. As it will be shown thereafter, the measured limiting threshold defined as the intersection of the linear and nonlinear parts of a limiting curve is in the case of carbon-black in water $E_{th} = 0.7 \text{ J/cm}^2$ for the pump wavelength $\lambda = 1.064 \text{ }\mu\text{m}$. Temporal measurements of the white light emission from the medium show that the lifetime of the emission is about twice as long as laser duration. In contrast probe perturbation lifetime is much longer than laser duration.

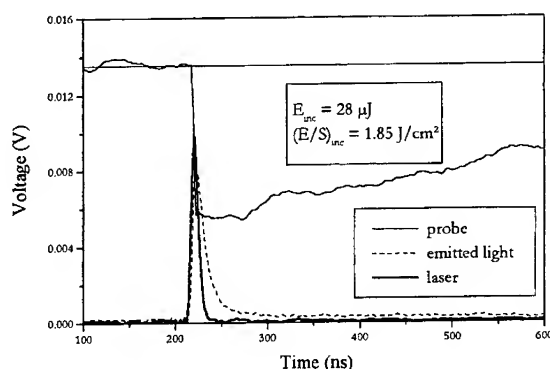


FIGURE 2. Probe intensity variation for Carbon-Black in water

The emitted signal seems to be linked to the probe variation during the laser pulse for at least two reasons. The first one, as it will be shown thereafter, is that the appearance of these two signals arises for comparable fluences. The second reason concerns the temporal behaviour of probe variation and of emitted signal which both appears earlier when the incident fluence is increased. The limiting properties of CBS are due to a phase change of the particle characterized by the broadband emission of the medium. After the laser pulse the perturbation of the probe is caused by the scattering from the cavities filled with the hot carbon vapour. In order to determine the nature of the white light emitted by the medium, the relative intensity of the emission have been measured as a function of the incident fluence on the CBS cell (Figure 3). The emitted intensity increases linearly with

incident fluence below 0.7 J/cm^2 , which corresponds to the limiting threshold. Above this threshold, a saturation is observed and the signal increases slowly with incident fluence.

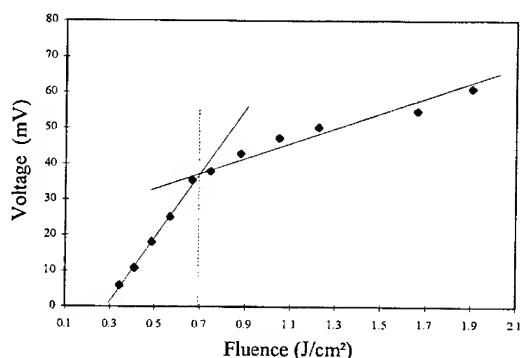


FIGURE 3. Relative intensity of the emitted light as a function of incident fluence

The behaviour of the emitted signal and the level of intensities involved in Figure 3 are characteristics of an incandescence signal of the carbon-black particles, frequently reported by researchers in the field of combustion in diesel engine ^{6, 7, 8}. According to the blackbody radiation law the incandescence signal increases with temperature, and the saturation threshold in Figure 3 corresponds to the sublimation of particles. When the sublimation begins, the incident energy is consumed by the latent heat of sublimation and the temperature remains almost constant as well as the incandescence signal. In the case of carbon-black in water the limiting process is thus triggered by the sublimation of the carbon particles since the limiting threshold corresponds to the sublimation threshold of particles.

Case of Carbon-Black in CS_2 with surfactant

In order to lower the limiting threshold of CBS, a more appropriate liquid than water was tested: the carbon disulfide (CS_2). CS_2 has lower specific heat capacity, thermal conductivity and latent heat of vaporization than water and should be more efficient than water for bubbles growth. Since particles are extracted from indian ink, the first suspension used with CS_2 was composed of a mixture of carbon-black particles and

surfactant which contains no water. The probe signal is reported in the figure 4 for an incident fluence of 8.10^{-2} J/cm^2 . At this weak fluence no incandescence signal is observed.

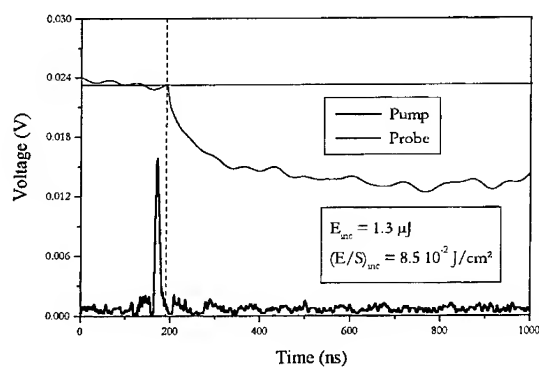


FIGURE 4. Probe intensity variation in the case of carbon-Black in CS_2 with a surfactant

Unfortunately for limiting efficiency, in this case, the probe perturbation due to bubbles growth appears after the laser pulse. Figure 5 illustrates the limiting curve of CB/CS_2 with surfactant compared to CB/water .

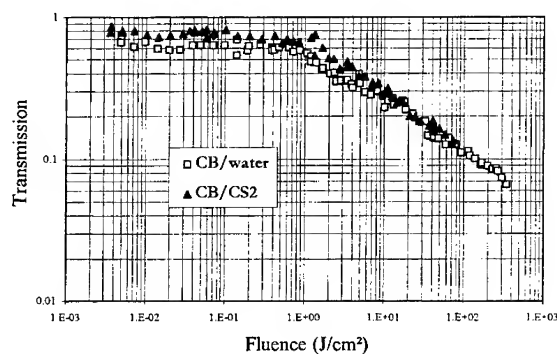


FIGURE 5. Limiting curves of CB/Water and CB/CS_2 with surfactant

No significant difference could be observed in the response of the two suspensions during the laser pulse. The delayed response of CB/CS₂ may be explained by a contact resistance between particles and liquid. This resistance could be attributed to the surfactant itself or to the bad quality of contact between the surfactant and the surrounding liquid.

Case of Carbon-Black in CS₂ without surfactant.

The precedent initial mixture was centrifuged to obtain carbon particles cleared from any surfactant. The probe perturbation for this sample of CB/CS₂ without surfactant is illustrated in Figure 6 for a weak incident fluence for which no incandescence is observed. In this case the perturbation appears during the pump pulse and is thus efficient for optical limiting application.

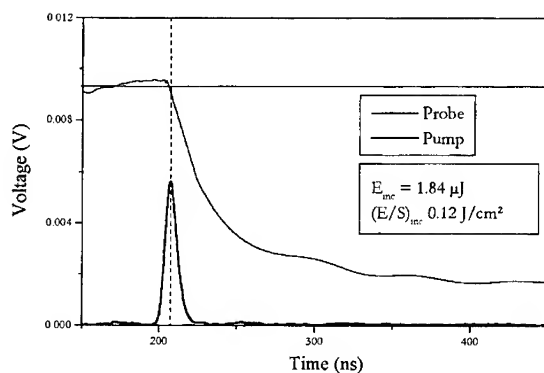


FIGURE 6. Probe intensity variation in the case of carbon-Black in CS₂ without surfactant.

Figure 7 illustrates the limiting curve of CB/CS₂ without surfactant. This curve has two different slopes which correspond to the two different limiting mechanisms that are the sublimation of the carbon particles and bubbles growth. The first threshold corresponding to bubbles growth appears for an incident fluence of about 0.12 J/cm², although the second one due to carbon sublimation appears near 0.7 J/cm² as in the case of CB/water. Compared to CB/water the effect of bubbles reduced the limiting threshold by a factor of 7.

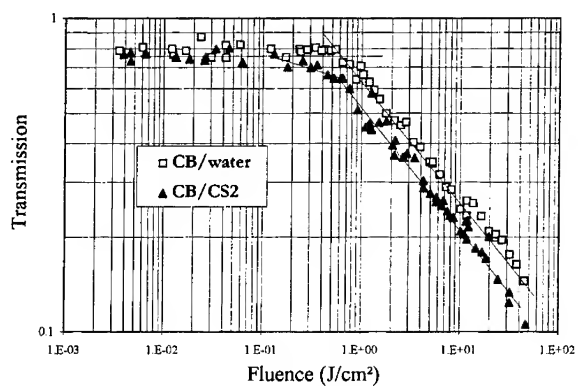


FIGURE 7. Limiting curves of CB/Water and CB/CS₂ without surfactant

Case of pulse of 100 ns duration at $\lambda = 694$ nm

Figure 8 shows limiting curves of CB/Water and CB/CS₂ without surfactant, in the case of an incident Ruby laser of pulsewidth, $\tau_{\text{las}} = 100$ ns emitting at $\lambda = 694$ nm. In this case the limiting threshold in CB/water corresponding to particles sublimation is of about 0.22 J/cm².

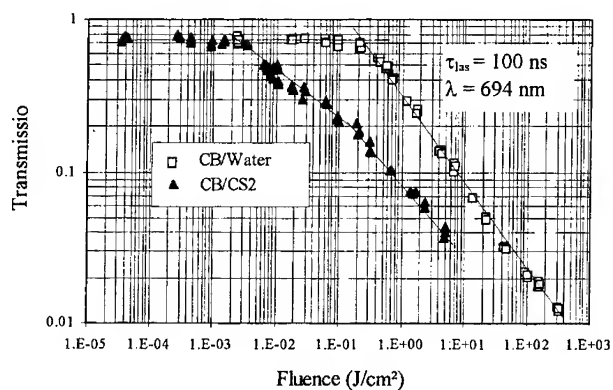


FIGURE 8. Limiting curves of CB/Water and CB/CS₂ without surfactant for $\tau_{\text{las}} = 100$ ns

In CB/CS₂ the limiting threshold corresponding to bubbles growth is $E_{th} = 2.2 \cdot 10^{-3} \text{ J/cm}^2$. It's thus reduced by a factor 100 compared to CB/water. In this case of a 100 ns pulsewidth, bubbles have enough time to growth during the pulse and to strongly lower the limiting threshold. As for $\tau_{las} = 9\text{ns}$, the second mechanism corresponding to carbon particles sublimation appears for the same fluence in water and in CS₂.

THERMODYNAMICAL CONSIDERATIONS

The pump probe experiment demonstrates that the limiting behaviour of carbon black suspension is first triggered by a phase change in the liquid surrounding the intensely heated carbon particles and for higher incident fluences by the sublimation of carbon particles. In this section, thermodynamical considerations are presented in order to estimate sublimation threshold of carbon particles and heating of the liquid.

Hypothesis and parameters used

The absorption of carbon particles is considered on their whole volume, which corresponds to a size parameter $x \leq 1$ with $x = 2\pi a/\lambda$, where a is the radius of the particle. The average radius of the particles used is $a = 85 \text{ nm}$, corresponding to $x = 0.5$ at $\lambda = 1.064 \text{ nm}$. The absorption cross section of carbon particles is calculated using Mie theory associated with refractive indices of soot that is $\tilde{n}_p = 2.139 - i0.583$ interpolated at $\lambda = 1.064 \text{ nm}$ from Ackermann measurements from 400 to 1000 nm⁹. Variation of thermodynamical parameters with temperature as specific heat capacity and thermal conductivity are taken into account¹⁰.

Case of isolated particle

The precedent measurement shows that the sublimation threshold of particles does not depend on surrounding liquid in spite of differences in thermodynamical parameters of water and CS₂. This threshold is 0.7 J/cm^2 for both CB/water and CB/CS₂. When incident temporally gaussian pulse is absorbed by the carbon particle, the first layer of liquid in contact with the particle is vaporized very early in the pulse. The weak thermal

conductivity of vapour makes that as a first approach, the carbon particles can be considered as isolated.

Experimentally the limiting threshold measured on the limiting curve corresponds to a perturbation which appears at the top of the gaussian incident pulse. In consequence, the calculated thermal threshold is taken as the energy of the incident pulse which increases the temperature of the particles up to the sublimation temperature of graphite at the top of the pulse. The temperature T_i at the top of the pulse ($t = 0$) is calculated by :

$$T_i = T_0 + \int_{-3\tau_{las}}^0 \frac{C_{abs}}{mC_p(T)} I(t) dt,$$

where T_0 is the room temperature, $I(t)$ the gaussian incident intensity, C_{abs} , the absorption cross section of a carbon particle, $C_p(T)$ the time dependant specific heat capacity of carbon, and m the mass of the particle. The pulse energy corresponding to $T_i = T_{sub}$ is $E_{th} = 0.62 \text{ J/cm}^2$ although the measured limiting threshold is 0.7 J/cm^2 . This calculated threshold minimize the real energy since the losses to the medium were neglected. This result confirm the sublimation of carbon particles as the mechanism responsible for the limiting threshold observed.

Thermal transfer

In order to estimate the heating of the liquid, the thermal transfer from particle to the surrounding liquid has to be taken into account. In spherical coordinates, the temperature T as a function of position r from the center of the particle and time t is determined by the equation :

$$\begin{cases} \frac{\partial u_1}{\partial t} - \kappa_1 \frac{\partial^2 u_1}{\partial r^2} = r \frac{A(t)}{\rho_1 C_{p1}} & 0 \leq r < a, \quad \text{with } u(r,t) = r.T(r,t) \\ \frac{\partial u_2}{\partial t} - \kappa_2 \frac{\partial^2 u_2}{\partial r^2} = 0 & r > a \end{cases}$$

where the subscript 1 and 2 refer respectively to the particle and to the liquid, κ ($\text{cm}^2 \cdot \text{s}^{-1}$) is the thermal diffusivity, ρ the volumic mass ($\text{g} \cdot \text{cm}^{-3}$), C_p the specific heat capacity ($\text{J} \cdot \text{K}^{-1} \cdot \text{kg}^{-1}$), a the radius of the particle, and $A(t)$ the volumic power density absorbed by the

particle (W.m^{-3}). This equation is resolved numerically using a finite difference method associated with an explicite scheme.

The temperature at the boundary layer is calculated using a global condition of energy conservation in the total volume of the particle and liquid which is much more accurate than local boundary conditions as temperature and heat flow conservation at the boundary. As a first approach figure 9 presents the effect of the surrounding liquid on the evolution of particle's temperature at the center, and at the surface submitted to an incident fluence of 0.7 J/cm^2 , corresponding to the sublimation threshold. The thermodynamical parameters considered are those of the liquid phase, and no phase changes are taken into account.

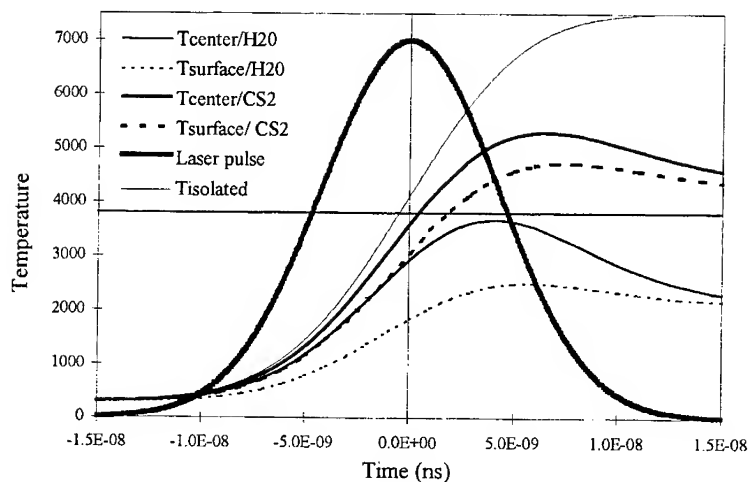


FIGURE 9. Evolution of the temperature of a carbon particle in water and in CS_2 , submitted to an incident gaussian pulse of total fluence 0.7 J/cm^2 .

The sublimation temperature of carbon $T_{\text{sub}} = 3800 \text{ K}$ and the top of the pulse are also located in figure 9. Compared to the case of an isolated particle, thermal conduction from particle to liquid diminish particle temperature. In this case, the incident fluence necessary to increase particle's temperature up to T_{sub} is respectively $E_{\text{th}}(\text{CS}_2) = 0.74 \text{ J/cm}^2$, and $E_{\text{th}}(\text{H}_2\text{O}) = 0.84 \text{ J/cm}^2$. These values maximize the particle's sublimation threshold since thermal conductivity of liquids is much larger than that of gases.

Figure 10 illustrates the temperature variation as a function of the distance from particle's center in both particle and liquid for an incident fluence of 0.12 J/cm^2 at the top of the pulse corresponding to bubbles threshold in CB/CS₂. It simply illustrates, the higher temperatures obtain in CS₂ due to its lower specific heat capacity and thermal conductivity.

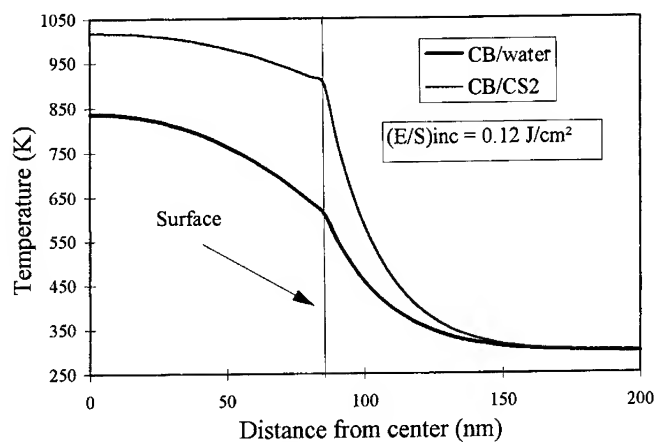


FIGURE 10. : Evolution of temperature as a function of distance from center.

Bubbles growth description involves consideration of phase changes and of gaz expansion that are not taken into account in this paper. For instance latent heat of vaporization that is 6 time higher in water than in CS₂ has to be considered. These consideration will be soon included in the present calculation to estimate bubbles growth rates.

CONCLUSION

Time resolved measurements have been perform using a pump-probe experiment in CB/Water and in CB/CS₂. In the case of water, the limiting threshold has been shown to be due to sublimation of carbon particle. By the use of an appropriate liquid as CS₂, bubbles growth has been shown to be an effective mechanism for optical limiting below the sublimation threshold of particles. A simple model of thermal heating of particle and liquid

has been presented. Further improvement of this model will include phase change in the liquid.

REFERENCES

1. K. Mansour, M. J. Soileau, and E.W. Van Stryland J. Opt. Soc. Am. B9, 1100, (1992)
2. Karen M. Nashold and Diane Powell Walter, J. Opt. Soc. Am. B12, 1228 (1995)
3. K. J. McEwan, Paul A. Madden, J. Chem. Phys. 97 (11), 8748 (1992)
4. A. Fein, Z. Kotler, J. Bar-Sagi, S. Jackel, P. Shaier and B. Zinger Nonlinear optics, 11, 277 (1995)
5. F. Fougéanet, J.C. Fabre, Mat., Res., Soc. Proc., Vol. 479, 1997.
6. R.L. Vander Wal, K.J. Weiland, Appl. Phys. B 59, pp 445-452, 1994,
7. P.E. Bentgsson, M. Aldén, Appl. Phys. B 60, pp. 51-59, 1995.
8. L.A. Melton, Appl. Opt., Vol. 23, N°13, July 1984, pp 2201-2207.
9. T.P. Ackerman, O.B. Toon, Appl. Opt., Vol. 20, N°20, oct. 1981, pp 3661-3667.
10. P. Pascal, « Nouveau Traité de Chimie minérale », Tome VIII - Carbone, Editions Masson, 1968.

MODELLING OF PARAMETRIC BEAM CONVERSION: APPLICATION TO IMAGE AMPLIFICATION WITH OPTICAL SELF-LIMITING

JEAN-PAUL FAURE * and OLIVIER GIRAUDO

ONERA - Département d'Optique Théorique et Appliquée
Fort de Palaiseau - F 91761 Palaiseau

Abstract: Optical Self-limited imaging capabilities of down-conversion processes are investigated both theoretically and experimentally. We use parametric gain at low level to get image amplification and pump depletion at high level to achieve optical limiting. We derive a formulation for the angular acceptance, which is confirmed by experimental results. Theoretical investigations are done on this mixing process to understand how three continuum sets of plane waves propagate in a highly nonlinear regime. The model considers all anisotropic effects as well as diffraction, pump depletion and absorption. A code has been developed to solve numerically the propagating equations. Numerical results are shown to be in accordance with the experiments and lead to clear interpretation of the different phenomena involved.

INTRODUCTION:

Since the early of non linear optics, parametric interactions in quadratic media have been used for optical imaging applications.^{1,2} Up and downconversion processes can be used to transfer an image from a signal wave on an idler wave, which is eventually shifted to another frequency range.¹ Unlike upconversion, downconversion allows amplification of both signal and idler images.³⁻⁶ In both cases, the parametric nature of the interaction allows intensity limitation of the idler, by controlling the pump intensity, whatever the signal level is. In the following, we demonstrate the possibility to achieve optically self-limited parametric image amplification within a specific configuration.

At first, we use a standard model based on plane waves to investigate the

*email: faure@onera.fr

different requirements to get image amplification from a down-converter in the parametric regime. The imaging capabilities at non critical phase-matching are derived from angular acceptance in a biaxial cristal.

In a second step, we study the saturation of the gain in the highly non linear regime. For this purpose, we develop each beam as a continuum of plane waves to derive the general propagation equations in the Fourier space. This eigen mode expansion allows us to take into consideration all anisotropic effects such as inhomogeneous diffraction including walk-off and phase-mismatch. The coupled equations are then numerically integrated, in the Fourier space using a Cash-Karp adaptive step-size control algorithm to get required accuracy. The modelisation retrieves signal and idler amplification in the parametric regime, and shows a strong pump depletion and back-conversion in the highly nonlinear regime. Numerical calculations are found to be in good agreement with the experimental results.

THEORY:

Configuration of interaction:

An optically limited parametric image amplifier is characterized by two main requirements.

At first, the angular acceptance which is limited by phase-mismatch has to be large enough for imaging. One way to increase it is to choose an angular *one beam non critical phase-matching* configuration⁷⁻⁹ in a principal plane. In this case, phase-matching becomes insensitive to small angulations of the signal around the non critical direction, whereas the pump, which is the *critical beam*, needs to be highly collimated. This kind of phase-matching can be either collinear or not and concerns both type I or II as well as degenerate/non degenerate configurations.

Secondly, the idler beam is intrinsically optically limited by the pump intensity, but one needs to separate efficiently the signal beam from the idler at the output of the system. This can be achieved by three different ways:

- *spatial* separation is possible only for non colinear phase-matching ($\vec{k}_s \nparallel \vec{k}_i$), but the separation angles between the signal and the idler are usually small and might be lower than the total angular acceptance of the system.

- *spectral* separation implies the use of a non degenerate configuration ($\lambda_s \neq \lambda_i$).
- *polarisation* separation can be achieved only for type II configurations ($\hat{e}_i \perp \hat{e}_s$), but is easy to perform for both degenerate/non degenerate configurations.

For practical reasons, we have worked in a *degenerate configuration* ($\lambda_s = \lambda_i = \lambda_p/2$), excluding spectral separation. As a non critical phase-matching is always collinear for a type I degenerate configuration,¹⁰ spatial separation is also excluded. We have used indeed a type II, non critical non collinear scheme together with a polarisation separation. The signal beam is chosen as the *ordinary* one, whereas the idler is *extraordinary*. Our choice does not limit the generality of the formalism and conclusions could be generalized to a non degenerate configuration.

Phase-matching considerations:

In the following, we consider three *monochromatic* beams propagating in a quadratic biaxial cristal around central directions \vec{k}_{p0} , \vec{k}_{s0} , \vec{k}_{i0} (with \vec{k}_{p0} aligned with the z direction of propagation). Their frequencies are supposed to verify the energy conservation $\omega_s + \omega_i = \omega_p$ and no idler wave is present at the input of the cristal.

Suppose that these central directions are phase-matched in a principal plane, into a non collinear configuration which is *non critical for the signal*⁷ beam whereas the *pump is the critical one* *. \vec{k}_{p0} , \vec{k}_{s0} , \vec{k}_{i0} are referenced by their spherical angles (θ_p, ϕ_p) , (θ_s, ϕ_s) , (θ_i, ϕ_i) in the dielectric referential as shown in figure (1). Other angular frequencies can be referenced by their angular deviations $\delta\phi_s$ and $\delta\theta_s$ (respectively *in* and *out* of the principal plane) from the central frequency and will undergo phase-mismatches $\Delta k_z(\theta_s, \phi_s + \delta\phi_s)$ and $\Delta k_z(\theta_s + \delta\theta_s, \phi_s)$.

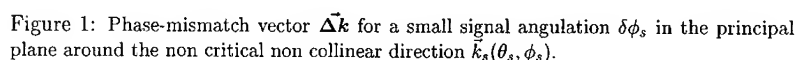
In the special case of a non critical phase-matching in a principal plane, the phase-mismatch is of second order in $\delta\theta_s$, $\delta\phi_s$ and it can be shown^{10,11} that:

$$\Delta k_z(\theta_s, \phi_s + \delta\phi_s) \sim \frac{\pi n_p}{\lambda_p} (\delta\phi_s)^2 \quad \text{and} \quad \Delta k_z(\theta_s + \delta\theta_s, \phi_s) \sim \frac{\pi n_p}{\lambda_p} (\delta\theta_s)^2 \quad (1)$$

Hence, for imaging applications, the total conical acceptance will be:

$$\Delta\Omega_s = \delta\phi_s \times \delta\theta_s \approx \frac{\lambda_p}{\pi n_p} \Delta k_z$$

*the phase-matching we consider is in the $[XY]$ plane, so that the non-critical angle will be ϕ_s .



Parametric gain in the plane wave limit (imaging):

At first the beams are approximated as linearly polarized plane waves:

where the subscripts $j = p, s, i$ refer to the pump, signal and idler beams, and \hat{e}_j are the polarisation directions. In this case, the solution of the propagation equations for zero input idler beam are the well known¹² hyperbolic functions. They lead to a net parametric gain on the idler wave (defined as the ratio between signal input and idler output intensities) that can be written as:

where $\Delta k_z = [\vec{k}_{p_0} - (\vec{k}_{s_0} + \vec{k}_{i_0})] \cdot \hat{z}$ is the projection of the phase-mismatch vector onto the propagation direction “z” and γ is the non linear gain per unit length which is

connected to the pump intensity I_p and the non linear coefficient d_{eff} [†]:

$$\gamma = 0.172 \frac{d_{eff} \sqrt{I_p}}{\sqrt{\lambda_s \lambda_i n_p n_s n_i}}$$

Perfect phase-matching ($\Delta k_z = 0$) is achieved only for the main direction of propagation of the beams that experience a maximum gain: $G_i^{max}(\Delta k_z = 0) = sh^2(\gamma L)$.

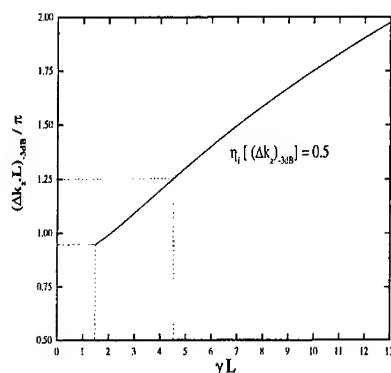


Figure 2: Phase-mismatch versus γL for $-3dB$ loss in the relative gain η_i .

$$\eta_i = \frac{G_i(\Delta k_z L)}{G_i^{max}} \quad (3)$$

For imaging applications, it is useful to consider $(\Delta k_z)_{-3dB}$ which corresponds to $\eta_i = 0.5$. Numerical calculations of $(\Delta k_z)_{-3dB}$ using equations (2) and (3) are shown in Figure 2 for typical values of γL . One notes that $(\Delta k_z)_{-3dB}$ can be *slowly increased* by increasing γL that is to say I_p or d_{eff} . Usually γL stands between 1 and 5, which leads to a value of $(\Delta k_z)_{-3dB} L / \pi$ close to unity. Then, from equation (1) the angular acceptances become straightforward:

$$\delta \phi_s \sim \delta \theta_s \approx \sqrt{1, 12 \times \frac{\lambda_p}{n_p L}} \quad (4)$$

Now, angular acceptances in and out of the principal plane are symetric and appear to depend only on the pump wavelength, refractive index and cristal length.

[†]Where I_p is in W/cm^2 , d_{eff} is in pm/V , λ_j in nm , L in cm and $n_{j=p,s,i}$ are the refractive indices of the three beams in the cristal.

General theory for highly non linear regime (protection):

If the input signal becomes strong, pump depletion and back-conversion lead to strong modulations of the transverse amplitudes and phases of the beams.^{13,14} These phenomena lead to the saturation of the non linear gain¹⁵⁻¹⁷ and interplay with anisotropic effects like walk-off, inhomogeneous diffraction or phase-mismatch.¹⁸⁻²⁰ A realistic description of three wave mixing in a highly non linear regime, has indeed to consider the full angular content of the beams, and the role played by anisotropy, both on linear propagation^{21,22} and non linear coupling.^{20,23} Decomposing the three beams into a continuum set of linearly polarised plane waves,²⁴ gives :

$$\vec{E}_{\omega_j}(x, y, z) = \frac{1}{(2\pi)^2} \int_{-\infty}^{+\infty} \sum_{n=\pm, -} \hat{e}_j(n; k_x, k_y) \tilde{E}_{\omega_j}(k_x, k_y, z) e^{i\vec{k}_j \cdot \vec{r}} dk_x dk_y \quad (5)$$

where $\hat{e}_j(n=\pm; k_x, k_y)$ are the two possible eigenmodes in a birefringent medium. As a first approximation, we consider that only the mode which fulfills phase-matching condition will be efficiently excited and we eliminate the summation over "n". Secondly, the variations of \hat{e}_j with k_x, k_y are small[†] so that we can keep the polarisation constant and drop it out of the integrals. Then the envelopes can be written as:

$$E_{\omega_j}(x, y, z) = \frac{1}{(2\pi)^2} \iint_{-\infty}^{+\infty} \tilde{E}_{\omega_j}(k_x, k_y, z) \times e^{ik_{jz}(k_x, k_y) \cdot z} e^{i(k_x x + k_y y)} dk_x dk_y$$

Thus, the non linear polarisations are written: $\vec{P}_{\omega_j}^{nl}(\vec{r}) = 2\varepsilon_0 \underline{\underline{d}} : \hat{e}_l \hat{e}_m E_{\omega_l}(\vec{r}) E_{\omega_m}^*(\vec{r})$ where the subscripts j, l, m stand for p, s or i . We replace the fields and the polarisations into the general propagation equation:[§]

$$\vec{\nabla}(\vec{\nabla} \cdot \vec{E}_{\omega_j}(\vec{r})) - \Delta \vec{E}_{\omega_j}(\vec{r}) - i\omega_j \mu_0 \sigma_j \vec{E}_{\omega_j}(\vec{r}) - \underline{\underline{\varepsilon}}(\omega_j) \frac{\omega_j^2}{c^2} \vec{E}_{\omega_j}(\vec{r}) = \mu_0 \omega_j^2 \vec{P}_{\omega_j}^{nl}(\vec{r})$$

and make use of the *slowly varying amplitude approximation* (SVEA). Identifying the terms with the same transverse components (k_x, k_y), leads to the propagation equation of the angular spectrum in the Fourier space:

$$\frac{\partial \tilde{E}_{\omega_j}}{\partial z} = \frac{\mu_0 \omega_j \sigma_j}{2\Gamma_j(k_x, k_y)} \tilde{E}_{\omega_j} - i \frac{\omega_j^2}{c^2} \frac{d_{eff}}{\Gamma_j(k_x, k_y)} \tilde{P}_{\omega_j}(k_x, k_y, z) e^{-ik_{jz}(k_x, k_y) \cdot z} \quad (6)$$

[†]this is always true provided the fact that we are not too close to the optical axes.

[§] σ_j is the conductivity and $\underline{\underline{\varepsilon}}(\omega_j)$ the dielectric tensor of the medium in the MKSA system.

where $\Gamma_j(k_x, k_y) = [(\vec{k}_j \cdot \hat{e}_j)e_{jz} - k_{jz}(k_x, k_y)]$ and $\tilde{P}_{\omega_l}(k_x, k_y, z) = \mathcal{F}[E_{\omega_m}(\vec{r})E_{\omega_n}^*(\vec{r})]$ are the Fourier transforms of the electric fields products in the real space. One notes that in the limit of a linear non absorbing medium, solution of (6) is straightforward:

$$E_{\omega_j}(x, y, z) = \frac{1}{(2\pi)^2} \int_{-\infty}^{+\infty} \tilde{E}_{\omega_j}(k_x, k_y, 0) \times e^{ik_{jz}(k_x, k_y) \cdot z} e^{i(k_x x + k_y y)} dk_x dk_y$$

This means that all propagation phenomena are self-contained in the phase factor $e^{ik_{jz}(k_x, k_y) \cdot z}$. Indeed, k_{jz} is a function of k_x and k_y :

$$k_{jz} = \sqrt{k_j^2 - k_x^2 - k_y^2} \quad \text{with:} \quad k_j(\omega_j) = \frac{\omega_j}{c} n_j(\omega_j) \quad (7)$$

and because of the anisotropy, k_j must also verify *Fresnel's equation of wave normals*:

$$\frac{(a_{xx}k_x + a_{xy}k_y + a_{xz}k_{jz})^2}{k_j^2 - K_x^2} + \frac{(a_{yx}k_x + a_{yy}k_y + a_{yz}k_{jz})^2}{k_j^2 - K_y^2} + \frac{(a_{zx}k_x + a_{zy}k_y + a_{zz}k_{jz})^2}{k_j^2 - K_z^2} = 1$$

where $K_\alpha = \frac{\omega}{c} n_\alpha(\omega)$ (for $\alpha = x, y, z$) is the wave vectors modulus along the principal axes, and " $a_{\alpha\beta}$ " the matrix coefficients that transform the dielectric referential into the cristal one. For each transverse components (k_x, k_y) , one should calculate $k_{jz}(k_x, k_y)$ solving Fresnel's equation together with (7). Looking to paraxial propagation ($k_x, k_y \ll k_j$) we can develop (7) as:

$$k_{jz}(k_x, k_y) \approx k_j(k_x, k_y) - \frac{1}{2} \frac{k_x^2 + k_y^2}{k_j(k_x, k_y)}$$

As k_x and k_y are proportional to the spherical coordinates in the dielectric frame, we can write them as small angulations $\delta\theta, \delta\phi$ around the central directions θ_j, ϕ_j :

$$k_j(k_x, k_y) \equiv k_j(\theta_j + \delta\theta, \phi_j + \delta\phi) \approx \frac{\omega_j}{c} \left[n_j(\theta_j, \phi_j) + \frac{\partial n_j}{\partial \theta} \Big|_{\theta_j} \delta\theta + \frac{\partial n_j}{\partial \phi} \Big|_{\phi_j} \delta\phi \right]$$

Because phase-matching occurs into a principal plane, the first derivative of the index in θ cancels. Then, using the well known relation: $tg\rho_j = -\frac{1}{n_j(\phi_j)} \frac{\partial n_j}{\partial \phi} \Big|_{\phi_j}$ we have:

$$k_j(\theta_j + \delta\theta, \phi_j + \delta\phi) \approx k_j(\theta_j, \phi_j) [1 - tg\rho \times \delta\phi]$$

Hence, the paraxial propagator will be: $e^{ik_{jz}(k_x, k_y) \cdot z} \approx e^{ik_j[1 - tg\rho \delta\phi] \cdot z} \times e^{i(k_x^2 + k_y^2) \cdot z / 2k_j(k_x, k_y)}$

showing clearly the walk-off contribution to the phase, as well as the inhomogeneous diffraction in the transverse plane. Indeed, this model will handle general propagation in an anisotropic biaxial medium without any approximation as long as one will calculate exactly k_{jz} for each couple of transverse coordinates (k_x, k_y) .

Now, in order to simplify numerical integration of (6), we remove the highly oscillatory terms²³ in the propagator by writing:²³

$$k_{jz}(k_x, k_y) = k_{j0z} + \delta k_{jz}(k_x, k_y)$$

k_{j0z} standing for the “ z ” component of the central direction of beam “ j ” and δk_{jz} containing all the terms of a development of $k_{jz}(k_x, k_y)$ in powers of k_x and k_y around the central direction of propagation[¶]. We can write the electric fields separating the slowly varying envelope and the rapid term: $E_{\omega_j}(\vec{r}) = A_{\omega_j}(\vec{r}) \times e^{ik_{j0z} \cdot z}$ with:

$$A_{\omega_j}(\vec{r}) = \frac{1}{(2\pi)^2} \iint_{-\infty}^{+\infty} [\tilde{E}_{\omega_j}(k_x, k_y, z) e^{i\delta k_{jz}(k_x, k_y) \cdot z}] \cdot e^{i(k_x x + k_y y)} dk_x dk_y$$

The non linear polarisations are also redefined as the product of the *slowly varying amplitudes* of the fields in the real space, so that their Fourier transforms are: $\tilde{P}'_{\omega_l}(k_x, k_y, z) = \mathcal{F}[A_{\omega_m}(\vec{r}) \cdot A_{\omega_n}^*(\vec{r})]$. Finally, we obtain:

$$\frac{\partial \tilde{E}_{\omega_p}}{\partial z} = \frac{\mu_0 \omega_p \sigma_p}{2\Gamma_p(k_x, k_y)} \tilde{E}_{\omega_p} - i \frac{\omega_p^2}{c^2} \frac{d_{eff}}{\Gamma_p(k_x, k_y)} \tilde{P}'_{\omega_p}(k_x, k_y, z) \times e^{-i\delta k_{pz}(k_x, k_y) \cdot z} e^{+i\Delta k_{0z} \cdot z}$$

$$\frac{\partial \tilde{E}_{\omega_s}}{\partial z} = \frac{\mu_0 \omega_s \sigma_s}{2\Gamma_s(k_x, k_y)} \tilde{E}_{\omega_s} - i \frac{\omega_s^2}{c^2} \frac{d_{eff}}{\Gamma_s(k_x, k_y)} \tilde{P}'_{\omega_s}(k_x, k_y, z) \times e^{-i\delta k_{sz}(k_x, k_y) \cdot z} e^{-i\Delta k_{0z} \cdot z}$$

$$\frac{\partial \tilde{E}_{\omega_i}}{\partial z} = \frac{\mu_0 \omega_i \sigma_i}{2\Gamma_i(k_x, k_y)} \tilde{E}_{\omega_i} - i \frac{\omega_i^2}{c^2} \frac{d_{eff}}{\Gamma_i(k_x, k_y)} \tilde{P}'_{\omega_i}(k_x, k_y, z) \times e^{-i\delta k_{iz}(k_x, k_y) \cdot z} e^{-i\Delta k_{0z} \cdot z}$$

$\Delta k_{0z} = \vec{\Delta k}_0 \cdot \vec{z} = (k_{s0,z} + k_{i0,z}) - k_{p0,z}$ is the usual phase-mismatch between central frequencies and appears to be null in our case as the waves are initially phase-matched. All other angular components of the beams will undergo a phase-mismatch which is implicitly contained in the source terms $[\tilde{P}'_{\omega_j}(k_x, k_y, z) \times e^{-i\delta k_{jz}(k_x, k_y) \cdot z}]$. In

[¶]This development is very similar to the previous one.

fact, polarisations can be written as a convolution products of the amplitudes ^{||}:

$$\begin{aligned} \tilde{P}'_{\omega_l}(k_x, k_y, z) \times e^{-i\delta k_{lz} \cdot z} &= \tilde{A}_{\omega_m}(k_x, k_y, z) \otimes \tilde{A}_{\omega_n}(k_x, k_y, z) \times e^{-i\delta k_{lz} \cdot z} \\ &= \iint_{-\infty}^{+\infty} \tilde{E}_{\omega_m}(k_x - k'_x, k_y - k'_y, z) \tilde{E}_{\omega_n}(k'_x, k'_y, z) e^{i[\delta k_{mz}(k_x - k'_x, k_y - k'_y) + \delta k_{nz}(k'_x, k'_y) - \delta k_{lz}(k_x, k_y)]z} dk'_x dk'_y \end{aligned}$$

The exponential factor appears as the difference between the phase of the created polarization and that of the initial wave propagating at the same frequency.

RESULTS:

Experiments:

Parametric image transposition and amplification were performed experimentally with the set-up shown in Figure 3. The Fundamental of a Q-switched Nd-YAG laser (7 nsec pulse duration) was used as the signal beam (1064 nm), and its first harmonic (532 nm) as the pump. A transmission USAF test target was illuminated by the signal and its image was mixed with the pump in a 1 cm long KTP cristal cut for type II degenerate non critical frequency doubling in the *XY* plane ($d_{eff} \approx 3$ pm/V). Signal and idler amplified images were separated at the output with a Glan polarizer, and re-imaged on the focal plane of a water-cooled silicium CCD camera (512×512 pixels). Pump peak intensity was 100 MW/cm², leading to a gain $\gamma L \approx 2$. In this case, we found $(\Delta k_z)_{-3dB} L \approx \pi$ so the expected angular acceptance is: $2\delta\theta_s \approx 2\delta\phi_s \approx 11$ mrad (18,5 mm⁻¹). On the amplified idler image (Figure 3.c), Group 5.1 of the target is still resolved (32 Line Pairs/mm). Considering the imaging magnification we used (G=3), we finally get an experimental resolution of 10,7 Line Pairs/mm (~ 21 mm⁻¹) which is in good agreement with the theoretical one.

Optical limiting of the idler intensity was also performed using the same set-up slightly modified. The target and the afocal were replaced by a converging lens in order to focalise the signal into the cristal. Then, signal energy was increased from zero up to 680 μ J for different pumping energies. Results are presented in Figure 4 and show clearly the amplification stage, followed by saturation.

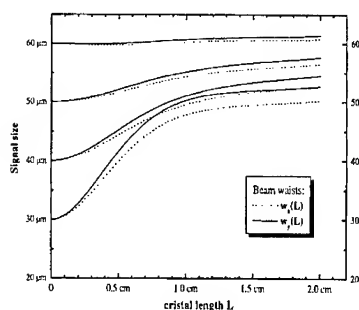
^{||}the notation: $\tilde{A}_{\omega_j}(k_x, k_y, z) = \mathcal{F}[A_{\omega_j}(x, y, z)] \equiv \tilde{E}_{\omega_j}(k_x, k_y, z) \times e^{i\delta k_{jz}(k_x, k_y) \cdot z}$ stands for the Fourier transform of amplitudes $A_{\omega_j}(x, y, z)$ in the transverse plane.

Numerical calculations:

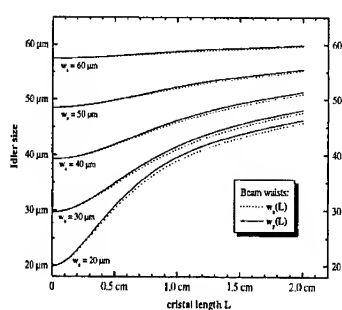
The model was implemented to simulate three wave propagation in this *KTP* cristal. The saturation of the non linear gain was simulated for the same previous experimental conditions, taking gaussian beams for pump and signal at the cristal input. Results can be seen on Figure 4 for a pump energy: $E_p = 0,74 \text{ mJ}$. The calculated points fit quite well the experimental curve, and the small discrepancy can be attributed to the pump profile which is not perfectly gaussian in the experiment. Transverse pump and idler beam profiles in the saturation regime ($E_s \approx 100$) μJ for different positions in the cristal are shown on Figures 5a-h. Depletion and backconversion strongly modulate the beams profiles that become ring shaped,^{13,18,19} and lead to an interesting cross-focusing effect.¹⁷ Finally, the evolution of the signal and idler waists in (w_x) and out (w_y) of the principal plane were investigated numerically in the parametric regime. Both are shown to be proportional to $1/\sqrt{L}$ (see figures below) in accordance with the equation (4).

Acknowledgments:

Authors want to thank D. Josse and J. Zyss^{††} for some useful ideas as well as helpful discussions and suggestions about this work.



(a) Evolution of signal waists sizes with crystal length



(b) Evolution of idler waists sizes with crystal length

^{††}Ecole Normale Supérieure de Cachan, Laboratoire de Photonique Quantique et Moléculaire (LPQM) 61, Av. du Président Wilson, F 94235-Cachan Cedex

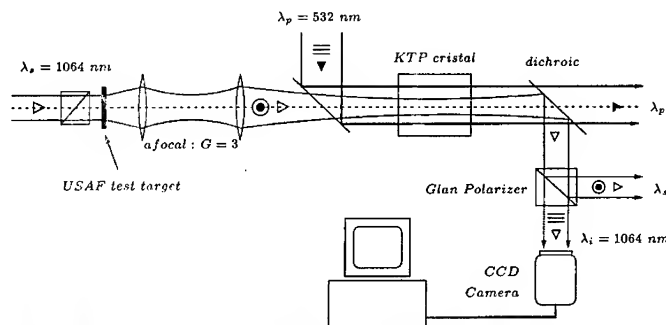


Figure 3: Experimental et-up for image transposition and amplification of a USAF test

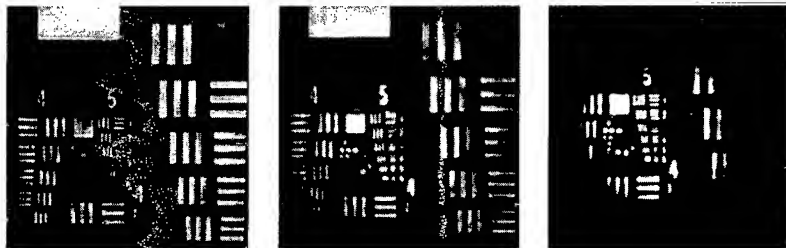
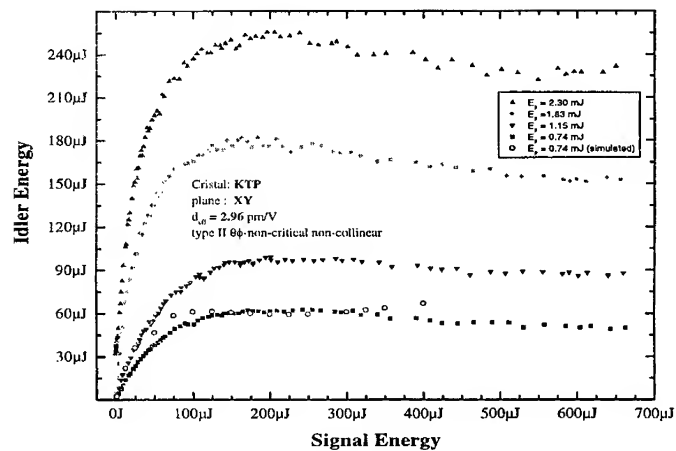
(a) Input signal image of
an USAF resolution target(b) Amplified signal image
of the target ($G_s \approx 2$)(c) Amplified idler image
of the target ($G_i \approx 2$)

Figure 4: Evolution of idler energy versus signal energy for DFG in a KTP crystal

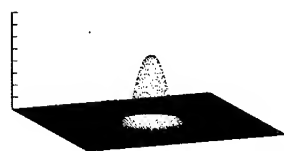
(a) Gaussian **pump** profile ($z = 0$)(b) Gaussian signal profile ($z = 0$)(c) **pump** profile ($z = 5 \text{ mm}$)(d) **idler** profile ($z = 5 \text{ mm}$)(e) **pump** profile ($z = 8 \text{ mm}$)(f) **idler** profile ($z = 8 \text{ mm}$)(g) **pump** profile ($z = 10 \text{ mm}$)(h) **idler** profile ($z = 10 \text{ mm}$)

Figure 5: Calculated transverse profiles of pump and idler beams for different propagation length

References

- [1] F. M. Johnson and J. A. Duardo. Laser Focus, page 31, 1967.
- [2] J. E. Midwinter. Appl. Phys. Lett., **12**(3):68, 1968.
- [3] A. Gavrielides, P. Peterson, and D. Cardimona. J. Appl. Phys., **62**(7):2640, 1987.
- [4] P. A. Laferriere, C. J. Wetterer, L. P. Schelonka, and M. A. Kramer. J. Appl. Phys., **65**(9):3347, 1989.
- [5] F. Devaux and E. Lantz. Optics Comm., **114**:295, 1995.
- [6] F. Devaux, E. Lantz, A. Lacourt, D. Gindre, H. Maillotte, P. A. Doreau, and T. Laurent. Nonlinear Optics, **11**:25, 1995.
- [7] S.X. Dou, D. Josse, and J. Zyss. J. Opt. Soc. Am. B, **8**(8):1732, 1991.
- [8] S.X. Dou, D. Josse, and J. Zyss. J. Opt. Soc. Am. B, **9**(8):1312-1319, 1992.
- [9] A. Lacourt E. Lantz, L. Han and J. Zyss. Optics Comm., **97**(3,4):245-249, 1993.
- [10] J.-P. Faure. PhD thesis, Université Paris VI, 1998. (to be published).
- [11] J.-P. Faure and O. Giraudo. (oral communication), ONERA, 1997.
- [12] S. E. Harris. Proc. IEEE, **57**(12):2096, 1969.
- [13] T. Nishikawa and N. Uesugi. J. Appl. Phys., **78**(11):6361, 1995.
- [14] T. Nishikawa and N. Uesugi. Optics Comm., **124**:512, 1996.
- [15] M. Nieto-Vesperinas and G. Lera. Optics Comm., **69**(3,4):329, 1989.
- [16] M. A. Dreger and J. K. McIver. J. Opt. Soc. Am. B, **7**(5):776-784, 1990.
- [17] P. Pliszka and P. P. Banerjee. J. Opt. Soc. Am. B, **10**(10):1810, 1993.
- [18] T. Nishikawa and N. Uesugi. J. Appl. Phys., **77**(10):4941, 1995.
- [19] T. Nishikawa and N. Uesugi. Optics Comm., **140**:277, 1997.
- [20] G. Arisholm. J. Opt. Soc. Am. B, **14**(10):2543, 1997.
- [21] J. A. Fleck and M. D. Feit. J. Opt. Soc. Am., **73**:920-926, 1983.
- [22] M. Trippenbach and Y. B. Band. J. Opt. Soc. Am. B, **13**(9):1403-1411, 1996.
- [23] Sam S. Ma, Dennis M. Guthals, Blair F. Campbell, and Patrick H. Hu. volume **1868**, page 135. Proc. SPIE, 1993.
- [24] J. W. Goodman. Introduction to Fourier Optics. (Mc Graw Hill, 1968).
- [25] S.-C. S. and A. E. Siegman. Phys. Rev. A, **21**(2):599, 1980.

THEORETICAL DESIGN OF ORGANIC CHROMOPHORES WITH LARGE TWO-PHOTON ABSORPTION CROSS-SECTIONS

D. BELJONNE¹, T. KOGEJ¹, S.R. MARDER^{2,3,4}, J.W. PERRY^{2,3,4}, J.L. BREDAS^{1,2}

¹ Service de Chimie des Matériaux Nouveaux, Centre de Recherche en Electronique
et Photonique Moléculaires, Université de Mons-Hainaut, Place du Parc 20,
B-7000 Mons, Belgium

² The Beckman Institute, California Institute of Technology, Pasadena,
California 91125

³ Jet Propulsion Laboratory, California Institute of Technology, Pasadena,
California 91109

⁴ Department of Chemistry, The University of Arizona*, Tucson,
Arizona 85721

* New permanent address

Abstract

Design strategies and structure-property relationships for two-photon absorption in conjugated molecules are described on the basis of correlated quantum-chemical calculations. We first focus on stilbene derivatives with centrosymmetric structures. We found that derivatization of the conjugated molecule with electroactive groups in a quadrupolar-like arrangement leads to a large increase in the two-photon absorption cross section, δ . Next, we consider a noncentrosymmetric dipolar compound built by grafting donor and acceptor end-groups on stilbene. In this case also, the calculations predict huge enhancement factors in δ upon substitution. In both cases (centrosymmetric and noncentrosymmetric compounds), the quantum-chemical description provides rich insight into the mechanisms for the two-photon absorption phenomenon.

1. INTRODUCTION

Two-photon absorption is a process by which, in the presence of intense laser pulses, a compound simultaneously absorbs two photons of light that can be of the same energy or of different energies. As a result, the compound reaches a (two-photon symmetry-allowed) excited state which is higher than the ground state by the sum of energies of the two absorbed photons. The process is illustrated in Figure 1, where we consider (as in the remainder of this work) absorption by two photons of the same energy $\hbar\omega$; after having been promoted to a two-photon excited state, the compound can undergo a number of photophysical phenomena, such as internal conversion down to the lowest excited state, intersystem crossing to the triplet manifold, excited-state absorption, or fluorescence emission. A major aspect to point out is that, while the transition probability for the usual one-photon absorption is linearly proportional to light intensity, that for the simultaneous absorption of two identical photons depends on the square of light intensity, I^2 . This is the reason why, although two-photon absorption was predicted as early as 1931,¹ it was experimentally observed only after the advent of lasers in 1961.²

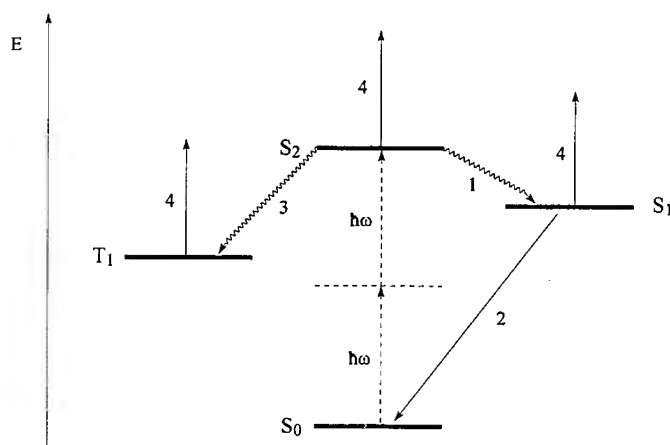


FIGURE 1 Sketch of two photon absorption from the ground state S_0 to excited state S_2 , also showing possible subsequent processes: (1) internal conversion down to S_1 ; (2) fluorescence from S_1 ; (3) intersystem crossing to the triplet manifold down to T_1 ; and (4) photoinduced absorption from S_1 , S_2 , or T_1 .

Molecules with a large two-photon absorption cross-section, δ , are in great demand for a variety of applications including two-photon excited fluorescence microscopy,³⁻⁴ optical limiting,⁵⁻⁷ three-dimensional optical data storage,⁸⁻⁹ and two-photon induced biological caging studies.¹⁰ Unfortunately, most known organic molecules have relatively small δ , and criteria for the design of molecules with large δ have not been well-developed.¹¹ As a result, the full utility of two-photon absorbing materials has still to be realized.

Since we are dealing with molecular materials, it is useful to recall that the polarization, $\vec{\mu}$, induced by an external electric field, \vec{E} (such as that associated to a laser light) writes:

$$\vec{\mu} = \alpha \cdot \vec{E} + \frac{1}{2!} \beta : \vec{E} \vec{E} + \frac{1}{3!} \gamma : \vec{E} \vec{E} \vec{E} + \dots \quad (1)$$

where α , β , and γ denote the first-, second-, and third-order molecular polarizabilities (and correspond to second-, third-, and fourth-rank tensors), respectively. While one-photon absorption at wavelength ω depends on the imaginary part of the linear polarizability $\alpha(-\omega; \omega)$, two-photon absorption is a third-order (four-wave mixing) phenomenon related to the imaginary part of the $\gamma(-\omega; \omega, \omega, -\omega)$ process. In contrast to second-harmonic generation which is a second-order process and is usually restricted to noncentrosymmetric media, two-photon absorption can occur in any medium, whatever its symmetry.

It is interesting to note that two-photon absorption has long been regarded as an adverse effect by the nonlinear optics community. This is especially true in the case of all-optical switching since two-photon absorption can quickly lead to strong attenuation of the signals and provoke damage to the samples due to severe heating; given this negative action, there has been therefore no desire to try and optimize two-photon absorption; quite the opposite, efforts were rather made to prevent its appearance. As is however often the case, what can be regarded as highly detrimental in a given context, can be exploited in other fields. The applications that are now envisioned for two-photon absorption rely on the two key features mentioned above: (i) the ability to access excited states using photons of half the nominal excitation energy; this can provide *improved*

penetration in absorbing or scattering media, such as for instance human tissues when considering medical imaging applications; and (ii) the I^2 dependence of the process, that allows for excitation of chromophores with a *high degree of spatial selectivity in three dimensions* using a tightly focused laser beam.

It is thus desirable to acquire a detailed understanding of the two-photon absorption phenomenon and of the elements that control it, thus to define the specific structure/property relationships pertaining to two-photon absorption. At this stage, it must be borne in mind that there is no single design strategy that could be valid for all third-order processes: each process actually has its own requirements. This is already clearly established in the case of second-order processes: while compounds exploitable for second-harmonic generation should be as transparent as possible, colored compounds can be used in electro-optics applications since in that case one works only at the fundamental frequency.¹²

In this contribution, we review some of our recent work on two-photon absorption. Section II provides a brief introduction to the theoretical modeling of third-order polarizabilities, on the basis of the widely exploited Sum-over-States expressions that are derived from perturbation theory. Section III describes design strategies and structure-property investigations for two-photon absorption (TPA) in *centrosymmetric* stilbene derivatives. These studies have recently resulted in the synthesis of fluorescent molecules with unprecedented δ values.¹³ In Section IV, the focus is on *noncentrosymmetric* (push-pull) stilbene compounds; we describe possible mechanisms of enhancement of the two-photon response on the basis of correlated quantum-chemical calculations.¹⁴

II. THEORETICAL MODELLING OF THE THIRD-ORDER MOLECULAR POLARIZABILITY

In the context of perturbation theory, the third-order polarizability and its wavelength dependence can be conveniently expressed following the Sum-over-States (SOS) approach described by Orr and Ward nearly thirty years ago.¹⁵ The contributions to γ appear as summations over all excited states of terms corresponding to quadruple

products of transition or state dipole moments over transition energies modulated by damping factors Γ . The SOS expression for the dynamic third-order polarizability tensor components is:

$$\gamma_{ijkl}(-\omega_\sigma; \omega_1, \omega_2, \omega_3) = \frac{1}{6\hbar^3} P(i, j, k, l; -\omega_\sigma, \omega_1, \omega_2, \omega_3) \left(\sum_{m \neq g} \sum_{n \neq g} \sum_{p \neq g} \frac{\langle g | \mu_i | m \rangle \langle m | \bar{\mu}_j | n \rangle \langle n | \bar{\mu}_k | p \rangle \langle p | \mu_l | g \rangle}{(\omega_{gm} - \omega_\sigma - i\Gamma_{gm})(\omega_{gn} - \omega_1 - \omega_2 - i\Gamma_{gn})(\omega_{gp} - \omega_1 - i\Gamma_{gp})} - \sum_{m \neq g} \sum_{n \neq g} \frac{\langle g | \mu_i | m \rangle \langle m | \mu_j | n \rangle \langle n | \mu_k | p \rangle \langle p | \mu_l | g \rangle}{(\omega_{gm} - \omega_\sigma - i\Gamma_{gm})(\omega_{gn} - \omega_1 - i\Gamma_{gn})(\omega_{gn} + \omega_2 + i\Gamma_{gn})} \right) \quad (2)$$

where:

- $P(i, j, k, l; -\omega_\sigma, \omega_1, \omega_2, \omega_3)$ is a permutation operator defined such as, for each permutation of indices (i, j, k, l) , a permutation of frequencies $(-\omega_\sigma, \omega_1, \omega_2, \omega_3)$ is made simultaneously;
- $\omega_1, \omega_2, \omega_3$ are the incident frequencies (pulsations); $\omega_\sigma = \omega_1 + \omega_2 + \omega_3$ is the resulting frequency
- i, j, k, l denote the molecular axes x, y, z ;
- $|m\rangle, |n\rangle$ et $|p\rangle$ symbolize electronic excited states, $|g\rangle$ is the electronic ground state;
- $\langle g | \mu_k | m \rangle$ corresponds to the electronic transition moment (coupling) between the $|g\rangle$ and $|m\rangle$ states;
- $\langle m | \bar{\mu}_k | n \rangle = (\langle m | \mu_k | n \rangle - \langle g | \mu_k | g \rangle) \delta_{mn}$ is the difference in state dipole moment between states $|m\rangle$ and $|g\rangle$;
- Γ_{gn} corresponds to the damping constant associated to excited state $|n\rangle$;
- $\omega_{gm}, \omega_{gn}, \omega_{gp}$ are the frequency differences separating $|m\rangle, |n\rangle$, and $|p\rangle$ with the ground state, respectively ($\hbar\omega_{gm}, \hbar\omega_{gn}, \hbar\omega_{gp}$ correspond to the transition energies between the ground state $|g\rangle$ and $|m\rangle, |n\rangle, |p\rangle$).

The state dipoles, transition dipoles, and transition energies can be computed accurately on the basis of correlated quantum-chemical methods, based for instance on a configuration interaction approach following semiempirical Hartree-Fock

calculations carried out with the CNDO (Complete Neglect of Differential Overlap)¹⁶ or INDO (Intermediate Neglect of Differential Overlap) Hamiltonian.¹⁷ The damping factors are much more difficult to evaluate since they are directly related to the lifetime broadening of the excited states; they are usually simply set on the basis of two approximate choices: either all factors are fixed to the same value or they are made to evolve linearly with transition energy¹⁸ (for conjugated compounds, ranges of Γ values between 0.05 and 0.2 eV are usually considered as reasonable).

In many cases, the full Sum-Over-States expression for the third-order polarizability can be simplified; this is especially true when a single low-lying excited state, $|e\rangle$, dominates the linear optical response.¹⁹ In that case, the summations over the excited states (electric-dipole) coupled to the ground state $|g\rangle$ can be limited to that excited state alone and the summations over upper lying excited states go over those few upper lying excited states $|e'\rangle$ that are strongly coupled to $|e\rangle$. Moreover, all systems investigated here present a highly anisotropic nonlinear optical response dominated by the longitudinal components. In the case of two-photon absorption ($\omega_1 = \omega_2 = \omega_3 = \omega$) the SOS expression (2) then reduces to:

$$\text{Im}\gamma = 24 \text{Im} \left[\begin{array}{l} \frac{M_{ge}^2 \Delta\mu_{ge}^2}{(E_{ge} - \hbar\omega - i\Gamma_{ge})(E_{ge} - 2\hbar\omega - i\Gamma_{ge})(E_{ge} - \hbar\omega - i\Gamma_{ge})} \quad \text{D} \\ \frac{M_{ge}^4}{(E_{ge} - \hbar\omega - i\Gamma_{ge})(E_{ge} - \hbar\omega - i\Gamma_{ge})(E_{ge} + \hbar\omega - i\Gamma_{ge})} \quad \text{N} \\ + \sum_{e'} \frac{M_{ge}^2 M_{ee'}^2}{(E_{ge} - \hbar\omega - i\Gamma_{ge})(E_{ee'} - 2\hbar\omega - i\Gamma_{ee'})(E_{ge} - \hbar\omega - i\Gamma_{ge})} \quad \text{T} \end{array} \right] \quad (3)$$

where M_{ge} , $\Delta\mu_{ge}$ and E_{ge} denote the longitudinal component of the transition moment, transition energy, and dipole moment difference between the $|g\rangle$ and $|e\rangle$ states, respectively; D is called the dipolar term since it exclusively appears in noncentrosymmetric systems; its expression is similar to that of the only term appearing in the two-state expression for β , the second-order polarizability.²⁰ Term T involves upper-lying (two-photon) excited states $|e'\rangle$ and is strongly dependent on the

coupling of $|e'\rangle$ with $|e\rangle$. The third term is the negative term, N ; since the expression of N presents the possibility of only one-photon resonances, the N term makes no contribution to two-photon absorption. In the D and T terms, two-photon resonances occur with respect to $|e\rangle$ and $|e'\rangle$, respectively; these are essential in the present context as they directly relate to two-photon absorption processes.

III. DESIGN OF CENTROSYMMETRIC PHENYLENEVINYLENE CHROMOPHORES WITH LARGE TWO-PHOTON ABSORPTION CROSS-SECTIONS

We have recently developed a strategy for the design of *centrosymmetric* molecules with large two-photon absorption cross-sections, δ . This strategy is based on the concept that symmetric charge transfer, from the ends of a conjugated system to the middle, or vice versa, upon excitation is correlated to enhanced values of δ . Newly synthesized bis-styrylbenzene derivatives with donor- π -donor, donor-acceptor-donor (D-A-D), and acceptor-donor-acceptor (A-D-A) structural motifs exhibit exceptionally large values of δ , up to ~400 times that of *trans*-stilbene.¹³ Quantum-chemical calculations performed on these new molecules indicate that substantial symmetric charge redistribution occurs upon excitation and provide δ values in good agreement with experiment.

Our strategy developed as follows. Initial optical studies revealed that 4,4'-bis(di-*n*-butyl)amino-*E*-stilbene, **2** (Figure 2), in toluene solution, exhibited a strong blue fluorescence that depended on I^2 when exposed to 5-ns laser pulses at 605 nm. Compound **2** has a linear absorption peak at 385 nm, an emission maximum at 410 nm, and a fluorescence quantum yield, Φ_f , of 0.90. The two-photon excited fluorescence spectrum for **2** was essentially identical to that excited by one-photon absorption into $|e\rangle$, suggesting that there was rapid relaxation of the state reached by two-photon absorption (taken to be $|e'\rangle$) to the $|e\rangle$ state, and subsequent fluorescence from that state. Measurement of the two-photon excitation cross section for **2** gave a maximum δ of $210 \times 10^{-50} \text{ cm}^4/\text{s/photon}$ at an excitation wavelength of 605 nm, which is almost 20 times greater than that of *trans*-stilbene, **1**,¹³ and is among the largest values of δ

reported for organic compounds. We conjectured that the large increase in the two-photon absorption for **2** relative to **1** was related to a symmetrical charge transfer from the amino nitrogens to the conjugated bridge of the molecule.

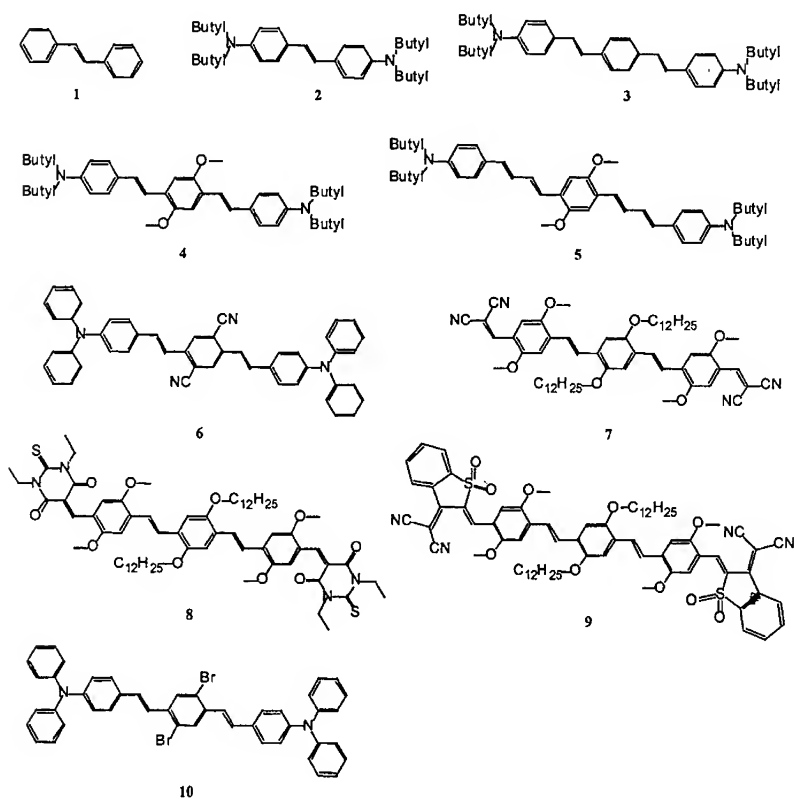


FIGURE 2 Structures and numbering scheme for the compounds studied in Section III of this work.

In order to gain insight into the origin of the large δ value for **2** relative to **1**, we performed quantum-chemical calculations on **1** and 4,4'-bis(dimethyl)amino-*E*-stilbene. Using geometries optimized with the AM1 semiempirical Hartree-Fock technique,²¹ the transition energies (*E*) and dipole moments (*M*) for the singlet excited

states of both compounds were calculated by combining the intermediate neglect of differential overlap (INDO) Hamiltonian¹⁷ with the multi-reference double configuration interaction (MRD-CI) scheme.²² The frequency dependence of δ , $\delta(\omega)$ is related to the calculated $\text{Im } \gamma(-\omega; \omega, \omega, -\omega)$ by the expression:²³

$$\delta(\omega) = (3\pi\hbar\nu^2 / n^2 c^2) L^4 \text{Im } \gamma(-\omega; \omega, \omega, -\omega) \quad (4)$$

where h is Planck's constant, n is the index of refraction of the medium (vacuum is assumed for the calculations), L is a local field factor (equal to 1 for vacuum), and c is the speed of light. We calculated $\text{Im } \gamma(-\omega; \omega, \omega, -\omega)$ using the Sum-over-States (SOS) expression (with the damping factor, Γ , set to 0.1 eV in all cases in this study).

As can be seen from Table 1, the calculations predict an order of magnitude enhancement in δ upon substitution of *trans*-stilbene with terminal dimethylamino groups, consistent with the experimental data presented above. This two-photon transition is from the ground-state ($|g\rangle$, $1A_g$) to the lowest excited state with A_g symmetry ($|e'\rangle$, $2A_g$). For both molecules, the $|e'\rangle$ state is located at about 0.8 eV above the lowest one-photon allowed excited state ($|e\rangle$, $1B_u$), see Figure 3. A simplified form of the SOS expression for the peak two-photon resonance value of $\delta(\omega)$ for the $|g\rangle \rightarrow |e'\rangle$ transition, $\delta_{ge'}$, is:

$$\delta_{ge'} \propto \frac{M_{ge} M_{ee'}}{(E_{ge} - \hbar\omega)^2 \Gamma} \quad (5)$$

where E_{ge} is the transition energy between the $|g\rangle$ and $|e\rangle$ states and $\hbar\omega = \frac{E_{ge'}}{2}$. This expression results from taking $|e\rangle$ as the dominant intermediate state and is valid when $(E_{ge} - \hbar\omega)$ is large compared to the damping factor for the $|g\rangle \rightarrow |e\rangle$ transition.

Based on the results of the calculations, as illustrated in Figure 3, we can rationalize the increase in $\delta_{ge'}$ on going from *trans*-stilbene to 4,4'-bis(dimethyl)amino-*E*-stilbene on the basis of: (i) a major increase in the $|e\rangle$ to $|e'\rangle$ transition dipole moment ($M_{ee'}$) from 3.1 to 7.2 D; (ii) an increase in the $|g\rangle$ to $|e\rangle$ transition dipole

moment (M_{ge}) from 7.1 D to 8.8 D; and (iii) a decrease in the one-photon detuning term, ($E_{ge} - \hbar\omega$), from 1.8 to 1.5 eV. This enhancement results from the electron donating properties of the terminal amino groups. The calculations also show that the electronic excitation from $|g\rangle$ to $|e\rangle$ is accompanied by a substantial charge transfer (~ 0.14 |e|) from the amino groups to the central vinylenic linkage, as we had hypothesized, leading to a large change in quadrupole moment upon excitation (a similar sense and magnitude of charge transfer is calculated for $|g\rangle \rightarrow |e'\rangle$ transition). This pronounced redistribution of the π -electronic density is correlated with an increase of electron delocalization in the first excited state and results in a significant increase in the $|e\rangle$ to $|e'\rangle$ transition dipole moment, which is the major contributor to the enhanced value of 4,4'-bis(dimethyl)amino-*E*-stilbene with respect to that of *trans*-stilbene. Another consequence of the terminal substitution with electron donors is a shift of the position of the two-photon resonance to lower energy.

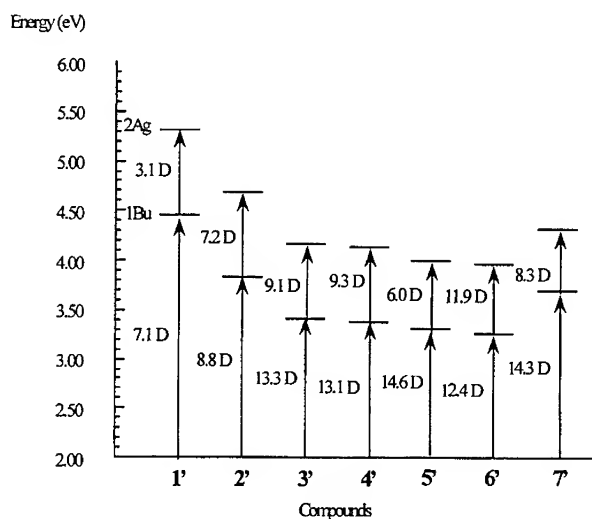


FIGURE 3 Scheme of the calculated energy levels and transition dipole moments (in Debye, D) for the three lowest singlet states for compounds 1' to 7' (which are model compounds for 1 to 7, wherein alkyl groups on amino or alkoxy groups and phenyl groups on terminal amino groups were replaced by methyl groups).

TABLE 1 Calculated and experimental two-photon excitation cross sections (δ) and peak positions (TPA λ_{\max}) for compounds in this work. Experimental δ values determined using nanosecond pulses and femtosecond pulses (given in parentheses) are reported. The uncertainty in the experimental δ values is estimated to be $\pm 15\%$. Also reported are single-photon absorption maxima (λ_{\max}), the wavelengths for fluorescence emission maxima (Emission λ_{\max}) and the fluorescence quantum yields (Φ_f). For the theoretical results, 1'-7' are model compounds for 1-7, wherein alkyl groups on amino or alkoxy groups and phenyl groups on terminal amino groups were replaced by methyl groups.

Theoretical results				Experimental results			
	TPA	δ		TPA	δ	Emission	Φ_f
	λ_{\max}			λ_{\max}		λ_{\max}	
Comp	(nm)	($10^{-50}\text{cm}^4\text{s}$ /photon)	Comp	(nm)	($10^{-50}\text{cm}^4\text{s}$ /photon)	(nm)	(nm)
1'	466	27.3	1	514	12		
				[ref. 13]	[ref. 13]		
2'	529	202.4	2	605	210	374	410
				(<620)	(110@620nm)		
3'	595	680.5	3	730	995	408	455
				(~725)	(635)		
4'	599	670.3	4	730	900	428	480
				(~725)	(680)		
5'	620	712.5	5	775	1250	456	509
				(~750)	(1270)		
6'	625	950.0	6	835	1940	472	525
				(810)	(3670)		
7'	666	570.4	7	825	480	513	580
				940	620		
				(815)	(650)		
				(910)	(470)		
-	-	-	8	970	1750	554	641
-	-	-	9	975	4400 ^a	618	745
				(945)	(3700)		
-	-	-	10	~800	450	424	490

^a There is a large uncertainty in this δ value due to a large uncertainty in the rather low value of Φ_f which is 0.0055($\pm 45\%$). The raw $\Phi_f \delta$ product determined using nanosecond pulses for this compound is $37.5 \times 10^{-50} \text{ cm}^4\text{s/photon}$ and using femtosecond pulses is $31.5 \times 10^{-50} \text{ cm}^4\text{s/photon}$. In the table, we have reported the upper estimate of Φ_f and the value of δ based on it, which gives the more conservative estimate for δ . The values of δ obtained using the average Φ_f (based on determinations in different laboratories) are $6800 \times 10^{-50} \text{ cm}^4\text{s/photon}$ (for nanosecond pulses) and $5700 \times 10^{-50} \text{ cm}^4\text{s/photon}$ (for femtosecond pulses).

These results suggested several strategies to enhance δ and tune the wavelength of the two-photon absorption peak for π -conjugated organic molecules. Because the symmetric charge transfer and change in quadrupole moment appear to be important, for molecules with small ground-state mesomeric quadrupole moments, we reasoned that structural features that could further enhance the change in quadrupole moment upon excitation could be beneficial for enhancing the corresponding transition dipole moments and the magnitude of δ . We therefore examined both theoretically and experimentally molecules in which: (i) The conjugation length was increased by inserting phenylene-vinylene or phenylene-butadienylene groups (compounds **3** to **5**) to increase the distance over which charge can be transferred. (ii) Electron-accepting cyano groups were attached to the central ring of the bis-styrylbenzene backbone (compound **6**), creating a D-A-D motif, to increase the extent of charge transfer from the ends of the molecule to the center. (iii) The sense of the symmetric charge transfer was reversed by substituting electron donating alkoxy donors on all three rings of the bis-styrylbenzene and attaching relatively strong accepting dicyanovinyl (compound **7**), thiobarbituric acid (compound **8**), or 3-(dicyanomethylidenyl)-2,3-dihydrobenzothiophene-2-ylidenyl-1,1-dioxide (compound **9**) electron accepting groups on both ends, creating A-D-A compounds. Finally, we were interested in introducing heavy atoms (for example, bromine atoms, compound **10**) with a large spin-orbit coupling to facilitate intersystem crossing from the $|e\rangle$ state to the lowest excited triplet state, T_1 , aiming to create a two-photon absorbing molecule that could act as an efficient triplet sensitizer.

We performed the same INDO-MRD-CI calculations described above on a series of model compounds (**3'** to **7'**) for **3** to **7** wherein alkyl groups on amino or alkoxy groups and phenyl groups on terminal amino groups were replaced by methyl groups. The results which are shown in Table 1 support our proposed design strategies. Increasing the conjugation length of the molecule or increasing the extent of symmetrical charge transfer from the ends of the molecule to the middle or *vice versa* leads to a large increase of δ and a shift of the two-photon absorption peak to longer wavelength relative to that of *trans*-stilbene.

The two-photon absorption cross sections of these molecules were measured using the two-photon fluorescence excitation method with nanosecond¹³ and

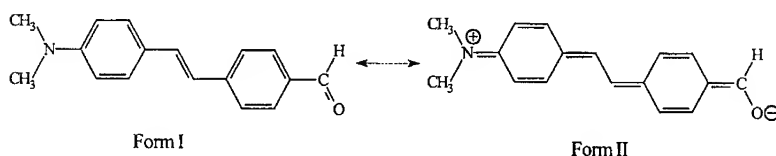
femtosecond²⁴ laser pulses. In both cases, measurements were performed using fluorophores with well characterized δ -values as reference standards¹³. The positions and magnitudes of the two-photon resonances, the fluorescence quantum yields, and positions of the one-photon absorption bands are shown in Table 1.

Several important conclusions can be drawn from the data in Table 1:

- (i) There is good agreement between the peak values of δ measured using femtosecond and nanosecond pulses, and calculated with the INDO-MRD-CI method.
- (ii) The INDO-MRD-CI calculations reproduce the trends in the evolution of the position of the two-photon absorption peak (although, as expected, the absolute excitation energies are systematically overestimated by theory, due to overcorrelation of the ground state with the MRD-CI scheme).
- (iii) Increasing the length of the molecule leads to a significant increase in δ , as can be seen by comparing results for **3**, **4**, and **5** with **2**.
- (iv) Our hypothesis that D-A-D and A-D-A compounds should have enhanced δ is borne out by the observation of large δ -values, in the range of 620×10^{-50} to $4400 \times 10^{-50} \text{ cm}^4/\text{s/photon}$, for **6** to **9** relative to bis-1,4-(2-methylstyryl)benzene for which δ is $55 \times 10^{-50} \text{ cm}^4/\text{s/photon}$.²⁵
- (v) There are significant shifts of the peak position of the two-photon absorption to longer wavelength upon increasing both the conjugation length and the extent of symmetric charge transfer.
- (vi) With the exceptions of **5**, **8**, **9**, and **10**, the compounds have very high fluorescence quantum yields indicating that they could be of interest as fluorescent probes for two-photon microscopy.
- (vii) The dibromo-substituted compound **10** has a reasonably large δ -value, and its fluorescence quantum yield is low in comparison to **3**, consistent with efficient intersystem crossing. Preliminary results indicate that **10** is a singlet O_2 sensitizer, which makes it a good candidate for cytotoxicity and photodynamic therapy studies in biological tissues.²⁶

IV. DESIGN OF PUSH-PULL STILBENE CHROMOPHORES WITH LARGE TWO-PHOTON ABSORPTION CROSS SECTIONS

Our attention here focuses on a *noncentrosymmetric* stilbene derivative since promising two-photon absorption cross sections have also been reported for such compounds.²⁷ The molecule under study is 4-dimethylamino-4'-formylstilbene, DAFS, a stilbene backbone end-capped with donor and acceptor groups. The degree of ground-state polarization in DAFS depends on the relative contributions of the neutral (aromatic-like) resonance form I and the charge-separated zwitterionic (quinoid-like) form II:



In analogy with our earlier studies,^{20,28} the evolution of two-photon absorption (with absorption of two photons of the same energy $h\nu$) was evaluated theoretically as a function of the degree of ground-state polarization, by imposing an external homogeneous field, F , directed such as to favor stabilization of charge transfer from the donor to the acceptor. Since application of the field modifies the geometry, its influence can also be cast in terms of the evolution of the degree of π bond-order alternation (BOA) within the vinyne segment.^{20,28} Equal contributions of I and II lead to the so-called cyanine limit for which BOA in the vinyne moiety tends to be vanishingly small (note that the cyanine limit is defined here as the situation where the lowest transition energy is minimum).

Full geometry optimizations have been performed with the INDO semiempirical Hamiltonian for applied electric field values ranging from 0 to 9×10^7 V/cm. We adopted a similar formalism to compute the two-photon absorption cross-section as in the case of the centrosymmetric compounds: (i) the ground state and singlet excited states for each field-dependent INDO-optimized geometry are evaluated with the INDO (Intermediate Neglect of Differential Overlap) Hamiltonian¹⁷ coupled

to an MRD-CI (MultiReference Double Configuration Interaction) formalism;²² (ii) the electronic characteristics of the excited states, as provided by the INDO/MRD-CI scheme, are then injected in the SOS expression for two-photon absorption to simulate the frequency-dependent curves.

First, we have analyzed two-photon absorption into the lowest $|e\rangle$ excited state of DAFS (whose wavefunction has characteristics similar to the strongly optically allowed B_u excited state of stilbene); here, $h\nu$ of light is then equal to half E_{ge} . From the simplified SOS expression of two-photon absorption (3), the D-term dominates such a process since it is the only one with two-photon resonance involving $|e\rangle$. The results are given in Figure 4.

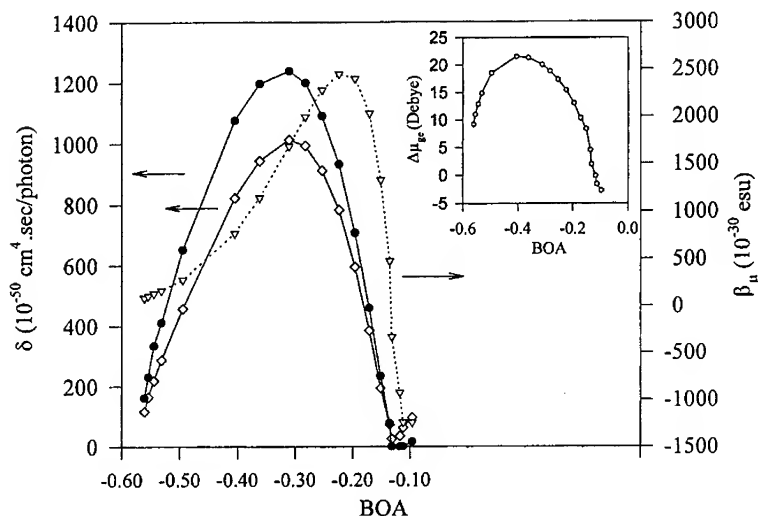


FIGURE 4 Evolution in DAFS, with respect to BOA, of: the fully converged SOS-calculated TPA cross-section δ (open losenges); the D-term contribution to δ (closed circles); the converged β_μ value (open triangles); in the inset, the difference in dipole moment between the ground state and $|e\rangle$, $\Delta\mu_{ge}$.

As expected, the D-term contribution matches the evolution of the fully converged SOS value for the two-photon absorption. As a result, the two-photon absorption evolution closely follows those of β and $\Delta\mu_{ge}$, see Figure 4, and peaks at an intermediate value of BOA between the neutral structure and the cyanine limit (note

that the difference in peak positions for instance between δ and β , is due to their different dependence on $\Delta\mu_{ge}$. At the peak, the two-photon absorption is strongly enhanced with respect to that of the neutral structure: by a factor of nearly 50 in $\text{Im } \gamma$ to reach ca. 1.4×10^5 in 10^{-36} esu units or by a factor of ca. 8 in the two-photon absorption cross-section δ in units of $10^{-50} \text{ cm}^4 \text{ sec/photon}$ (the difference in enhancement factor between γ and δ is due to the quadratic frequency dependence when going from γ to δ , as expressed above; as depicted in the inset of Figure 5, the E_{ge} transition energy strongly decreases, by nearly a factor of 3, in going from the neutral polyene structure to the cyanine limit)²⁹.

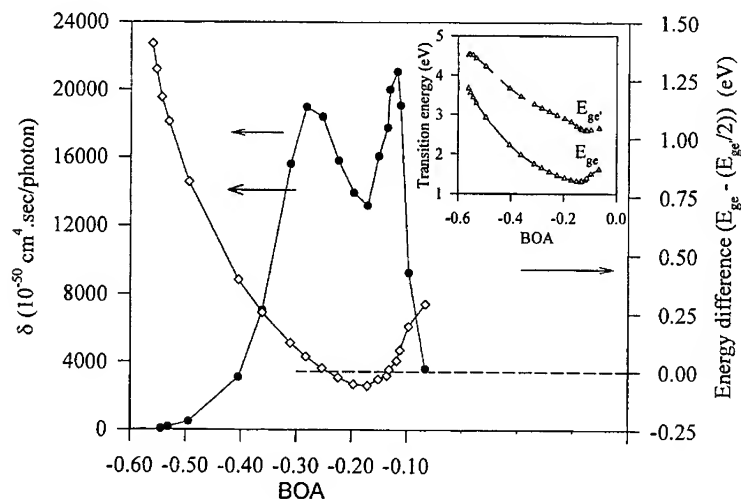


FIGURE 5 Evolution in DAFS, with respect to BOA, of: the TPA cross-sections associated to $|e'>$ (closed circles); the difference in energy between $E_{ge'}/2$ and E_{ge} (open losenges); in the inset, the E_{ge} ($S_0 \rightarrow |e'>$) and $E_{ge'}$ ($S_0 \rightarrow |e>$) transition energies.

Figure 5 also reports the evolution of the transition energy from the ground state to the second excited state $|e'>$ of DAFS (which possesses wavefunction characteristics reminiscent to those of the lowest two-photon A_g excited state of stilbene with significant two-photon absorption cross-section). In the case where two-photon absorption is directed into $|e'>$ ($h\nu = E_{ge'}/2$), the T term is then dominant since

it is the only term possessing two-photon resonance into $|e'\rangle$; this implies that two-photon absorption will be maximized in situations where the couplings between $|g\rangle$ and $|e\rangle$ and between $|e\rangle$ and $|e'\rangle$ are simultaneously large. This occurs, as shown in Figure 2, when one approaches the cyanine limit, a result which is consistent with previous findings on linear polymethines.^{20,28}

Two-photon absorption δ values as large as $2 \times 10^4 \times 10^{-50} \text{ cm}^4 \text{ sec/photon}$ are found for a fundamental wavelength of ca. $1 \text{ }\mu\text{m}$; this represents over a 100-fold increase with respect to two-photon absorption into $|e\rangle$ for the neutral structure of DAFS (in the absence of an applied field). It is most interesting to note that such large δ values are related to a near double-resonance process. Figure 5 indeed shows that around the cyanine limit, $E_{ge'}$ is approximately twice as big as E_{ge} . As a result, two-photon resonance with $|e'\rangle$ is accompanied with near one-photon resonance to $|e\rangle$, a feature which strongly enhances the T term. Although these δ values are exceptionally large, it can be argued that they will be experimentally significant only if absorption due to one-photon absorption is negligible at the fundamental wavelength; in this context, a positive aspect is that even when $E_{ge'}/2$ is detuned by 0.3 eV below E_{ge} ($\text{BOA} \approx -0.35$), our calculations suggest δ values that are as large as $1 \times 10^4 \times 10^{-50} \text{ cm}^4 \text{ sec/photon}$; if practically achievable, these values would be about one order of magnitude larger than those obtained above for centrosymmetric compounds.¹³ Perhaps fortuitously, cyanine molecules are prime candidates to fulfill such a criterion because the low energy side of their absorption bands is known to be exceptionally sharp (due to low damping and vibronic bandwidth). Thus, it may be possible to use a fundamental radiation whose energy approaches E_{ge} , while maintaining low linear loss due to single photon absorption.

V. CONCLUSIONS

Organic conjugated compounds with large two-photon absorption cross-sections have high technological potential for a broad range of applications in biology, medicine, three-dimensional optical memory, photonics,³⁰ optical limiting⁵ and materials science.³⁰

On the basis of detailed investigations of structure-property relationships in

phenylenevinylene-based materials, we have proposed several guidelines for the design of conjugated chromophores with enhanced two-photon absorption response: We have focused on two types of molecular architectures:

- (i) *Centrosymmetric* conjugated molecules substituted by electron-donating groups at both ends (D- π -D compounds), or by donating groups at the ends and electron-withdrawing groups in the middle (D-A-D compounds), or vice-versa (A-D-A compounds). Such derivatization patterns lead to a quadrupolar-like structure, in which electronic excitation induces a significant electron density flow from the extremities towards the center of the chain (or in the reverse direction). The change in quadrupole moment upon excitation is accompanied by an increase in the two-photon absorption response, with δ values up to 15 times larger than the best chromophores used up to now.¹³
- (ii) *Noncentrosymmetric dipolar* compounds in which donor and acceptor moieties are grafted in an asymmetric fashion on the outer parts of a conjugated segment (here, a stilbene unit). In that case, two strategies can be followed to enhance two-photon absorption in donor-acceptor stilbenes and related conjugated compounds:

One is to optimize the conditions (donor-acceptor strength, medium polarity, nature of conjugated segment) to have the structure leading near the maximum of β with two-photon absorption into the lowest excited state $|e\rangle$. Detailed guidelines and experimental studies which illustrate such molecules have been described and such molecules are currently under examination. However, as depicted in Figure 4, in the BOA regime where two-photon absorption peaks, E_{ge} gets significantly reduced so that the excitation wavelength falls beyond the $1\mu\text{m}$ limit. This sets an effective limit for the minimum BOA of ca. -0.45; in this case, enhancement with respect to the neutral aromatic-like structure can be as large as a factor of 5 (recent two-photon absorption measurements actually appear to be consistent with the calculated evolution).³¹

Another strategy is to consider two-photon absorption into the second excited state $|e'\rangle$ while driving the structure towards the cyanine limit and exploiting near double-resonance enhancement. Preliminary calculations on several cyanine-type compounds confirm that huge δ values can be reached with such an approach. Thus, we believe that if correctly designed to control the exact positions of $|e\rangle$ and $|e'\rangle$ states, certain

cyanine molecules can be particularly useful for two-photon fluorescence applications because in addition to potentially large values, they often have very high fluorescence quantum yields.

Acknowledgements

The work in Mons was carried out within the framework of the Belgium Prime Minister Office of Science Policy "Pôle d'Attraction Interuniversitaire en Chimie Supramoléculaire et Catalyse (PAI 4/11)" and is partly supported by the Belgium National Fund for Scientific Research (FNRS-FRFC) and an IBM-Belgium Academic Joint Study; DB is a Chercheur Qualifié FNRS; TK is a Ph.D. grant holder of FRIA (Fund for Research in Industry and Agriculture). Support from the National Science Foundation (Chemistry Division), Office of Naval Research, Air Force Office of Scientific Research (AFOSR) and its Defense University Research Instrumentation Program at Caltech is gratefully acknowledged. The research described in this paper was performed in part by the Jet Propulsion Laboratory (JPL) California Institute of Technology, as part of its Center for Space Microelectronics Technology and was supported by the Ballistic Missile Defense Initiative Organization, Innovative Science and Technology Office and AFOSR through an agreement with the National Aeronautics and Space Administration (NASA).

References

- [1] M. Göppert-Mayer, *Ann. Phys.* **9**, 273 (1931).
- [2] W. Kaiser, C.G.B. Garrett, *Phys. Rev. Lett.* **7**, 229 (1961).
- [3] W. Denk, J.H. Strickler, W.W. Webb, *Science* **248**, 73 (1990).
- [4] P.M. Rentzepis, D.A. Parthenopoulos, *Science* **245**, 843 (1989).
- [5] J.E. Ehrlich, X.L. Wu, I.-Y.S. Lee, Z.-H. Hu, H. Röckel, S.R. Marder, J.W. Perry, *Opt. Lett.* **22**, 1843 (1997).
- [6] A.A. Said, C. Wamsely, D.J. Hagan, E.W. Van Stryland, B.A. Reinhardt, P. Roderer, A.G. Dillard, *Chem. Phys. Lett.* **228**, 646 (1994).
- [7] G.S. He, R. Gvishi, P.N. Prasad, B. Reinhardt, *Opt. Commun.* **117**, 133 (1995).
- [8] D.A. Parthenopoulos, P.M. Rentzepis, *Science* **245**, 843 (1989).
- [9] J.H. Strickler, W.W. Webb, *Opt. Lett.* **16**, 1780 (1991).
- [10] D.L. Pettit, S.S.H. Wang, K.R. Gee, G.J. Augustine, *Neuron* **19**, 465 (1997).
- [11] C. Xu, W.W. Webb, *J. Opt. Soc. Am. B* **13**, 481 (1996).

- [12] J. Zyss in "Conjugated Polymeric Materials: Opportunities in Electronics, Optoelectronics, and Molecular Electronics", edited by J.L. Brédas and R.R. Chance (NATO ASI Series, Kluwer, Dordrecht, 1989), Vol. 182, p. 545.
- [13] M. Albota, D. Beljonne, J.L. Brédas, J.E. Ehrlich, J.-Y. Fu, A.A. Heikal, S. Hess, T. Kogej, M.D. Levin, S.R. Marder, D. McCord-Maughon, J.W. Perry, H. Röckel, M. Rumi, G. Subramaniam, W.W. Webb, X.-L. Wu, C. Xu, *Science* **281**, 1653 (1998).
- [14] T. Kogej, D. Beljonne, F. Meyers, J.W. Perry, S.R. Marder, J.L. Brédas, submitted.
- [15] B.J. Orr, J.F. Ward, *Mol. Phys.* **20**, 513 (1971).
- [16] S.J. Lalama, A.F. Garito, *Phys. Rev. A* **20**, 1179 (1979).
- [17] J.E. Ridley, M.C. Zerner, *Theoret. Chim. Acta* **32**, 111 (1973).
- [18] D. Beljonne, J. Cornil, Z. Shuai, J.L. Brédas, F. Röhlfing, D.D.C. Bradley, W.E. Torruellas, V. Ricci, G.I. Stegeman, *Phys. Rev. B* **55**, 1505 (1997).
- [19] J.L. Brédas, C. Adant, P. Tackx, A. Persoons, B.M. Pierce, *Chem. Rev.* **94**, 243 (1994).
- [20] F. Meyers, S.R. Marder, B.M. Pierce, J.L. Brédas, *J. Am. Chem. Soc.* **116**, 10703 (1994).
- [21] M.J.S. Dewar, E.G. Zoebish, E.F. Healy, J.J.P. Stewart, *J. Am. Chem. Soc.* **107**, 3902 (1985).
- [22] R.J. Buenker, S.D. Peyerimhoff, *Theoret. Chem. Acta*, **35**, 33 (1974).
- [23] M. Cha, W.E. Torruellas, G.I. Stegeman, W.H.G. Horsthuis, G.R. Möhlmann, *J. Meth. Appl. Phys. Lett.* **65**, 2648 (1994).
- [24] R.R. Birge *Acc. Chem. Res.* **19**, 138 (1986).
- [25] S.M. Kennedy, F.E. Lytle, *Anal. Chem.*, **58**, 2643 (1986); We have scaled the peak δ value reported in this paper by a factor chosen to match the long wavelength data reported therein with that of ref. 11.
- [26] M. Lipson, M. Levin, S.R. Marder, J.W. Perry, unpublished results.
- [27] B.A. Reinhardt, L.L. Brott, S.J. Clarson, A.G. Dillard, J.C. Bhatt, R. Kannan, L.Y. Yuan, G.S. He, P.N. Prasad, *Chem. Mater.* **10**, 1863 (1998).
- [28] S.R. Marder, C.B. Gorman, F. Meyers, J.W. Perry, G. Bourhill, J.L. Brédas, B.M. Pierce, *Science* **265**, 632 (1994).
- [29] The cyanine limit has been defined here as the situation where E_{gc} is minimum; it is obtained for a BOA value of ca. -0.12 and not 0 as in polymethines²⁸; this could be related to the nature of the conjugated backbone in DAFS where the vinylene segment is sandwiched between two phenylene rings.
- [30] B.M. Cumpston *et al.*, submitted.
- [31] J.W. Perry, unpublished data.

MICROSCOPIC THEORY AND MODELING OF ORGANIC OPTICAL POWER LIMITING MATERIALS

SHASHI P. KARNA

*US Air Force Research Laboratory, Space Electronics & Protection Branch, 3550
Aberdeen Ave, SE, Kirtland AFB, NM 87117-5776 USA*

Abstract: A formal theory describing the relationship between molecular two-photon absorption cross-section and third-order nonlinear optical (NLO) coefficients is presented. Quantum mechanical methods commonly used to calculate molecular NLO coefficients are described. Applicability of one of the methods is demonstrated by presenting the results for molecular second-hyperpolarizabilities for Li^+ and Na^+ encapsulated C_{60} molecule. The calculated results indicate that Li^+ and Na^+ encapsulation only marginally affect the NLO properties C_{60} molecule. Between the two metal ions, Li^+ appears to be more effective than Na^+ in increasing the NLO coefficients of C_{60} .

Keywords: optical power limiting, third order effects, two photon absorption

INTRODUCTION

Materials with an ability to control the intensity of light in a predetermined and predictable manner have important applications in eye and sensor protection against high power laser beams. Of particular interest in the recent years have been those materials which limit the power of incident light by virtue of their nonlinear optical (NLO) properties. Since organic materials exhibit exceptionally large NLO activity and ultrafast response to external laser source, there is considerable interest in the application of these materials for optical power limiting (OPL) applications. In particular, materials exhibiting two-photon absorption (TPA), which is a third-order resonant NLO process, have received much attention as potential candidates for OPL applications. Two recent articles^{2,3} provide good reviews on this topic.

In this paper we provide the details of the theoretical basis for modeling TPA-active organic OPL materials. The paper is organized in the following manner: First, a relationship is established between microscopic TPA cross-section and NLO coefficient. Then, two different approaches commonly used for the calculation of molecular NLO coefficients are described and their merits and limitations are discussed. Finally, results obtained for third-order NLO coefficients of Li^+ and Na^+ doped C_{60} molecule by one of the methods described are presented and compared with the corresponding results for the parent C_{60} molecule.

THEORY

A. Relation between molecular TPA cross-section and hyperpolarizabilities.

A detailed theory of NLO absorption can be found in References 2 and 3. In this paper, some of the basic equations are reviewed to establish the relationship between

molecular TPA cross-section and second-hyperpolarizabilities. The intensity, I , of a beam traversing a distance z in a material exhibiting one- and two-photon absorptions is given by the equation

$$\frac{\partial I}{\partial z} = -(\alpha I + \beta I^2) \quad (1),$$

where, α is the linear absorption coefficient and β is the TPA coefficient. Let us assume that for the angular frequency, ω , of the optical beam, the linear absorption in the medium is vanishingly small, so that $\alpha \approx 0$, then we can write Eq. (1) as

$$\frac{\partial I}{\partial z} = -\beta I^2 \quad (2).$$

Solving Eq. (2) gives²

$$I(L) = \frac{I_0}{(1 + \beta I_0 L)} \quad (3).$$

Here, L is the traverse length in the sample and I_0 is the intensity of the incident beam. It is clear from Eq. (3) that for a given traverse-length L in the material, the larger the value of TPA coefficient β , the smaller the value of the transmitted intensity, $I(L)$. Thus materials with large TPA coefficient greatly reduce the intensity of the incident beam. Also, for such materials, the transmitted intensity $I(L)$ decreases with the increase in I_0 , the intensity of the input beam.

The TPA coefficient β of a material is related to the imaginary part of its third-order NLO coefficient, $\chi^{(3)}(\omega)$, as²

$$\beta = \frac{3\omega}{2\epsilon_0 c^2 n^2} \text{Im}[\chi^{(3)}(\omega)] \quad (4).$$

In the above equation, ω is the angular frequency ($2\pi\nu$) of the incident beam, ϵ_0 and n are the dielectric constant and the refractive index of the medium, respectively, and c is the velocity of light. The third-order NLO coefficient $\chi^{(3)}(\omega)$ is related to the microscopic NLO coefficient, $\gamma(\omega)$, as¹

$$\chi^{(3)} = N_0 f_\omega^{(3)} \gamma(\omega) \quad (5),$$

where, N_0 is the number density of the material, $f_\omega^{(3)}$ is the local field factor experienced by individual polarizable units at frequency ω . The TPA coefficient β is related to the molecular TPA cross-section σ_2 as³

$$\sigma_2 = \frac{\hbar\omega\beta}{N_0} \quad (6),$$

where, $\hbar=h/2\pi$ with h representing the Planck constant. From Eqs. (4)-(6), we can write,

$$\sigma_2 = \frac{3\hbar\omega^2 f_\omega^{(3)}}{2\varepsilon_0 c^2 n^2} \text{Im}[\gamma(\omega)] \quad (7).$$

It is obvious from Eq. (7) that

$$\sigma_2 \propto \text{Im}[\gamma(\omega)] \quad (8),$$

i.e., the molecular TPA cross-section σ_2 , which is related to the TPA coefficient of a material via Eq. (6), at a given optical frequency, ω , is proportional to the imaginary part of the molecular second-hyperpolarizability, $\text{Im}[\gamma(\omega)]$. Eq. (8) thus provides a means for modeling efficient OPL materials via optimization of its third-order microscopic NLO coefficient.

The molecular second hyperpolarizability, $\gamma(\omega)=\text{Re}[\gamma(\omega)]+i \text{Im}[\gamma(\omega)]$, contains a real part and an imaginary part. The real part of $\gamma(\omega)$ quantifies the non-resonant or non-absorptive NLO properties of a molecule and has been the subject of numerous theoretical and experimental studies in the recent years.^{1,4} The imaginary part of $\gamma(\omega)$, on the other hand, quantifies the resonant or absorptive NLO properties, e.g. the TPA process. Therefore, the theoretical modeling of two-photon absorbing OPL materials depends on the accurate prediction of $\text{Im}[\gamma(\omega)]$. Unfortunately, accurate *a priori* prediction of $\text{Im}[\gamma(\omega)]$ is not straightforward. The main difficulty in the calculation of $\text{Im}[\gamma(\omega)]$ arises from a lack of reliable theoretical techniques. Therefore, quantum mechanical calculations on TPA-active organic materials have been fewer and generally within the framework of semi-empirical approaches.^{5,6}

Since TPA-active organic materials, in general, also exhibit enhanced non-resonant NLO effects, an alternate approach to model organic materials for OPL applications is to study their $\text{Re}[\gamma(\omega)]$. It is this latter approach that is taken in this paper. In the following sections, quantum mechanical methods to calculate $\text{Re}[\gamma(\omega)]$ are briefly reviewed. Results are presented for doped fullerene molecule and compared with those of the parent C_{60} molecule.

B. Quantum mechanical calculations of $\text{Re}[\gamma(\omega)]$.

Molecular hyperpolarizabilities are generally calculated via two different approaches of the time-dependent perturbation theory:⁷ (1) The uncoupled perturbation (UCP) approach and (2) the coupled perturbation (CP) approach. In the UCP method, also generally referred to as the sum-over-states (SOS) approach, the expression for $\gamma(\omega)$ can be written as⁸⁻¹⁰

$$\gamma_{abcd}(\omega_\sigma; \omega_1, \omega_2, \omega_3) = \frac{1}{6} K(\omega_\sigma; \omega_1, \omega_2, \omega_3) \wp(\omega_\sigma; \omega_1, \omega_2, \omega_3) \left\{ \sum_{l, m, n \neq g} \frac{\langle g | a | l \rangle \langle l | \bar{d} | m \rangle \langle m | \bar{c} | n \rangle \langle n | b | g \rangle}{(\Delta E_{lg} - \hbar\omega_\sigma)(\Delta E_{mg} - \hbar\omega_1 - \hbar\omega_2)(\Delta E_{ng} - \hbar\omega_1)} \right. \\ \left. + \sum_{m, n \neq g} \frac{\langle g | a | m \rangle \langle m | d | g \rangle \langle g | c | n \rangle \langle n | b | g \rangle}{(\Delta E_{mg} - \hbar\omega_\sigma)(\Delta E_{ng} - \hbar\omega_1)(\Delta E_{ng} + \hbar\omega_2)} \right\} \quad (9),$$

where, $\langle m | \bar{r} | n \rangle = \langle m | r | n \rangle - \langle g | r | g \rangle$; $\Delta E_{mn} = E_m - E_n$; g, l, m, n represent the electronic states with the corresponding state energy represented by $E_i (i=g, l, m, n, \dots)$; $\omega_1, \omega_2, \omega_3$ represent the angular frequencies of the incident beams while ω_σ represents the frequency of the output beam; $K(\omega_\sigma; \omega_1, \omega_2, \omega_3)$ is a constant that depends on the degeneracy among the input beams and their values; $\wp(\omega_\sigma; \omega_1, \omega_2, \omega_3)$ is a permutation operator that permutes the indices a, b, c, d (representing the Cartesian distance vector operators, x, y, z) in each summation along with the corresponding frequency argument. The numerical values of $K(\omega_\sigma; \omega_1, \omega_2, \omega_3)$ for different NLO process have been tabulated by Orr and Ward.¹⁰ The SOS method thus requires a knowledge of the moments of dipole transition between various states in the spectrum of the molecule and the energy of the electronic states. This approach is often used for phenomenological description of NLO processes in terms of dipole transitions involving a few molecular states. The SOS method is also easy to implement for the calculation of $\text{Im}[\chi(\omega)]$ by including in the denominator the phenomenological detuning factor.^{1,8-10}

The practical difficulty in using the SOS method for *ab initio* prediction of $\chi(\omega)$ lies in the complexity of accurately calculating the wavefunction and the energy of excited states. Therefore, except for a few simple atoms,¹¹ the SOS method does not easily lend itself to the *ab initio* calculations of hyperpolarizabilities. There have been some attempts in the recent years to surmount this problem by recasting the SOS expressions in terms of the molecular orbitals.¹² This allows the calculation of hyperpolarizabilities of relatively large molecular structures within the framework of the sum-over-orbital space (SOOS). Unfortunately, in the few cases that the SOOS method has been successfully applied, the calculated values of $\chi(\omega)$ are generally underestimated with respect to the corresponding coupled perturbation method.¹²

Unlike the UCP method, the CP approach does not require a knowledge of excited states.⁷ Rather, the $\chi(\omega)$ values in the CP methods are calculated from a knowledge of the perturbed ground state wavefunction, which is generally obtained from a self-consistent field (SCF) solution of the time-dependent Hartree-Fock (TDHF) equation.^{7,13} The expression for molecular second-hyperpolarizabilities in the TDHF approach, also sometimes referred to as the time-dependent coupled Hartree-Fock (TDCPHF) approach,¹⁴ can be written as¹³

$$\gamma_{abcd}(\omega_\sigma; \omega_1, \omega_2, \omega_3) = -\text{Tr}[\mathbf{h}_a^{(1)} \mathbf{D}_{bcd}^{(3)}(\omega_1, \omega_2, \omega_3)] \quad (10),$$

where,

$$\mathbf{h}_a^{(0)} = \langle \varphi | e\mathbf{a}(a = x, y, z) | \varphi \rangle \quad (11),$$

represents the atomic orbital basis dipole moment matrix, φ represents the set of atomic orbitals, e is the electronic charge, and

$$\mathbf{D}_{bcd}^{(3)}(\omega_1, \omega_2, \omega_3) = \mathfrak{R}_{bcd}^{(3)}(\omega_1, \omega_2, \omega_3) \mathbf{C}^{(0)} \quad (12)$$

represents the third-order perturbed density matrix. The subscripts b, c, d , as usual, represent the Cartesian components (x, y, z). $\mathbf{C}^{(0)}$ and $\mathfrak{R}^{(3)}$, respectively, represent the zero-order molecular orbital (MO) coefficient matrix and the transformation matrix calculated from the solution of the TDCPHF equations. Detail accounts of the TDCPHF method are given in the articles by Sekino and Bartlett¹³ for closed shell systems and by Karna¹⁵ for open-shell systems.

It is also possible to calculate molecular hyperpolarizabilities, $\chi(\omega)$, directly from the solution of the lower-order TDCPHF equations, thus avoiding expensive calculations of $\mathfrak{R}^{(3)}$ from the explicit solution of the third-order CPHF equations. As first pointed out by Sekino and Bartlett,¹³ this approach has been implemented by Karna and Dupuis¹⁴ and by others.¹⁵⁻¹⁷ The TDCPHF method is very well suited for the *ab initio* modeling of NLO properties of organic molecules. However, a practical difficulty often encountered in using this method for large molecules stems from the storage requirements and processing of the two-electron repulsion integrals in the Hamiltonian.¹³⁻¹⁷ This problem can be easily surmounted by the use of the "direct"-SCF technique^{18,19} for solving TDCPHF equations.²⁰

Unlike the SOS method, however, the TDCPHF method does not easily lend itself to describe the mechanism of NLO processes in a simple intuitive manner. Additionally, it is also not straightforward to represent and calculate $\text{Im}[\chi(\omega)]$ values by TDCPHF method.

CALCULATIONS

In order to demonstrate the applicability of *ab initio* methods for modeling organic OPL materials, we have calculated $\text{Re}[\chi(\omega)]$ values corresponding to several third-order NLO effects in Li^+ and Na^+ encapsulated C_{60} molecule. The purpose of selecting these systems was two-fold: 1) To demonstrate the applicability of *ab initio* TDCPHF technique for calculating NLO properties of large organic molecules. 2) To examine the changes due to metal-ion doping in the third-order NLO properties of C_{60} , which has emerged as a potentially useful OPL material.²¹⁻²⁴ In the recent years, there have been a number of quantum mechanical calculations²⁵⁻²⁸ on the geometry and properties of Li^+ and Na^+ encapsulated C_{60} complexes.

The calculations were performed via "direct" TDCPHF method²⁰ in conjunction with the HONDO-8 electronic structure code.²⁹ A minimal set of Cartesian Gaussian

basis functions was used in the calculations. Calculations were performed at two different geometrical arrangements of the metal ion: In the first case, the metal ion was placed at the center of the *ab initio* SCF optimized geometry of the C_{60} molecule. In the second case, the metal ion was placed slightly away from the center of the C_{60} cage. The latter geometry was obtained from *ab initio* SCF optimization of the $M^+(M=Li, Na)$ encapsulated complexes.

RESULTS

For the parent C_{60} molecule, the minimal basis optimized bond lengths were: C-C = 1.376 Å and C=C = 1.447 Å, in agreement with other theoretical calculations.^{30,31} The changes in the values of the C-C and C=C bond lengths due to metal ion doping were marginal. Calculated total energy, position of the metal atom with respect to the center of the C_{60} cage, and the dipole moment of the endohedral complexes are listed in Table I. The endohedral complex structures are lower in energy at their optimized geometry than at the parent (C_{60}) geometry. In the latter geometry, the metal is placed at the center of the C_{60} cage. At the optimized equilibrium geometry, the metal atom (Li, Na) is placed away from the center of the cage. The displacement, d , from the center in the equilibrium geometry for Li is about 1.7 times larger than that for Na. Accordingly, the dipole moment for the Li^+ -encapsulated complex is calculated to be much larger, by a factor of more than 2, than that for the Na^+ -encapsulated complex.

TABLE I. Calculated relative energy, ΔE , off-center displacement, d , of $M^+(M=Li, K)$ and the dipole moment of $M^+@C_{60}(M=Li, Na)$.

Molecule	$Li^+ @ C_{60}$	$Li^+ @ C_{60}$	$Na^+ @ C_{60}$	$Na^+ @ C_{60}$
Geometry	C_{60}	Optimized	C_{60}	Optimized
ΔE (a.u.) ^a	0.0	-0.035422	0.0	-0.011101
d (Å)	0.0	1.012	0.0	0.605
μ (D)	0.0	3.236	0.0	1.366

^aThe value of the total energy, E (a.u.), at the C_{60} geometry is: $E(Li^+@C_{60}) = -2251.4075279$, $E(Na^+@C_{60}) = -2404.0163213$ a.u.

Our calculated equilibrium displacement, d (Table I), is smaller by 0.46 Å for Li and about 0.6 Å for Na than that calculated by Whitehouse and Buckingham²⁶ using similar theoretical approach. The large difference between the results of the present calculations and those of Whitehouse and Buckingham²⁶ is surprising, considering the fact that the two calculations utilize very similar theoretical techniques.

For the Li^+ -encapsulated complex, a mixed valence basis *ab initio* Hartree-Fock calculation³¹ gives $d=1.297$ Å and a local density functional (LDF) theory calculation²⁵ gives $d=1.37$ Å. Both these values are closer to our calculated values than those reported by Whitehouse and Buckingham.²⁶ Previously calculated values of dipole moment for Li^+ -encapsulated complex range from about 1.35 D obtained from LDF calculations^{25,28} to 15.78 D obtained from semiempirical calculations.²⁷

As the focus of this paper, we now examine the calculated values for $\chi(\omega)$. Listed in Table II are the values of the mean second-hyperpolarizability, $\langle\chi(\omega)\rangle$, calculated from the tensor components as

$$\langle\chi\rangle = \frac{1}{15} \sum_{i,j} (\chi_{ijj} + \chi_{jij} + \chi_{jji}), \quad i, j = x, y, z \quad (13).$$

There have been a number of experimental³²⁻³⁶ and theoretical^{34,36-42} studies on the hyperpolarizability of C_{60} molecule. However, we are not aware of any previous studies of the hyperpolarizabilities of the Li^+ and Na^+ doped C_{60} molecules. For the undoped C_{60} molecule, the experimental values of $\chi(\omega)$ differ from each other by several orders of magnitude. A similar situation also exist among the calculated values.^{41,42} Previously calculated values of $\chi(\omega)$ for C_{60} molecule⁴¹ are also listed in Table II for comparison. These values (Table II) are smaller by a factor of 3 compared to the best literature data.³⁷ The theoretical method and the basis set used in the present study on $M^+@C_{60}$ ($M=Li, Na$) complexes are the same as that used in ref. [41]. Therefore, a similar deficiency as noted in the results of ref. [41] is expected in the results of $\chi(\omega)$ obtained in the present study. However, we believe that the qualitative trend and relative changes calculated in the values of $\chi(\omega)$ in going from C_{60} molecule to $M^+@C_{60}$ ($M=Li, Na$) are reasonably accurate.

TABLE II. Calculated values of $\langle\chi(\omega)\rangle(10^{-36}$ esu) for $Li^+@C_{60}$.^a

Molecule	$Li^+ @C_{60}$	$Li^+ @C_{60}$	$Na^+ @C_{60}$	$Na^+ @C_{60}$	C_{60} ^b
Geometry	C_{60}	Optimized	C_{60}	Optimized	Optimized
$\chi(0,0,0,0)$	1.395	1.403	1.377	1.389	1.364
$\chi(-\omega,0,0,\omega)$	1.470	1.482	1.452	1.466	1.440
$\chi(-\omega,\omega,\omega,-\omega)$	1.552	1.571	1.535	1.550	1.555
$\chi(-2\omega,0,\omega,-\omega)$	1.641	1.667	1.626	1.644	1.614

^aFrequency-dependent hyperpolarizabilities calculated at $\lambda = 1064$ nm.

^bTaken from ref. 41.

An examination of Table II reveals several noteworthy features of the $\chi(\omega)$ values for the M^+ ($M=Li, Na$) encapsulated C_{60} molecule. First, it can be noted that there is only a marginal change, generally increase, in going from the undoped to the doped C_{60} molecule. Second, the calculated values of $\chi(\omega)$ for the $M^+@C_{60}$ complex at the optimized geometry are larger than that at the C_{60} geometry. Third, the $\chi(\omega)$ values for the $Li^+@C_{60}$ complex are slightly larger in magnitude than that for the $Na^+@C_{60}$ complex. It is also noted that the calculated values of $\chi(\omega)$ corresponding to various third-order processes show substantial dispersion, with the absolute values showing the following order: $\chi(-2\omega,0,\omega,-\omega) > \chi(-\omega,\omega,\omega,-\omega) > \chi(-\omega,0,0,\omega) > \chi(0,0,0,0)$.

SUMMARY

A formal theory relating microscopic third-order NLO properties and the TPA absorption cross-section of molecules with a view to modeling organic structures for OPL applications has been presented. Quantum mechanical modeling of OPL materials

requires accurate prediction of molecular TPA cross-section and, therefore, the third-order NLO properties. Two different quantum mechanical approaches commonly used to calculate molecular NLO properties have been briefly reviewed. The applicability of one such method for the prediction of relevant third-order NLO properties in potentially useful OPL structures has been demonstrated by obtaining results for metal-ion encapsulated C_{60} molecule. The numerical results presented here for the NLO properties of $M^+@C_{60}$ ($M=Li, Na$) complexes indicate a number of interesting features. These results suggest that the metal-ion encapsulation only marginally changes (generally increases) the NLO coefficients of the C_{60} molecule. Additionally, it is noted that the greater the distortion of the charge distribution of C_{60} cage due to metal-ion encapsulation, the larger the changes in the NLO coefficient.

ACKNOWLEDGMENT

It is a pleasure to acknowledge useful discussions with Brett Dunlap.

References

1. *Introduction to Nonlinear optical Effects in Molecules and Polymers*, by P. N. Prasad and D. J. Williams (Wiley, New York, 1991).
2. L. W. Tutt and T. F. Boggess, *Progr. Quant. Electron.* **17**, 299 (1993).
3. J. D. Bhawalkar, G. S. He, and P. N. Prasad, *Rep. Prog. Phys.* **59**, 1041 (1996).
4. "Nonlinear Optical Materials: Theory and Modeling", Ed. S. P. Karna and A. T. Yeates, ACS Symposium Series, Vol. 628 (ACS Publication, Washington, DC, 1996).
5. R. R. Birge and B. M. Pierce, *J. Chem. Phys.* **70**, 165 (1979).
6. B. M. Pierce, *J. Chem. Phys.* **91**, 791 (1989).
7. P. W. Langhoff, S. T. Epstein, and M. Karplus, *Rev. Mod. Phys.* **44**, 602 (1972).
8. P. K. Franken and J. F. Ward, *Rev. Mod. Phys.* **35**, 23 (1963).
9. J. F. Ward, *Rev. Mod. Phys.* **37**, 1 (1965).
10. B. J. Orr and J. F. Ward, *Mol. Phys.* **20**, 513 (1971).
11. D. M. Bishop, *Adv. Quantum Chem.* **25**, 1 (1994).
12. R. Bursi, M. Lankhorst, and D. Feil, *J. Comp. Chem.* **16**, 545 (1995).
13. H. Sekino and R. J. Bartlett, *J. Chem. Phys.* **85** (1986).
14. S. P. Karna and M. Dupuis, *J. Comp. Chem.* **12**, 487 (1991).
15. S. P. Karna, *J. Chem. Phys.* **104**, 6590 (1993), *ibid*, **105**, 6091 (1996).
16. J. E. Rice, R. D. Amos, S. M. Colwell, N. C. Handy, and J. Sanz, *J. Chem. Phys.* **93**, 8828 (1990).
17. H. Årgen, O. Vahtras, H. Koch, P. Jørgensen, and T. Helgaker, *J. Chem. Phys.* **98**, 6417 (1993).
18. J. Almlöf, K. Fægri, Jr., and K. Korsell, *J. Comp. Chem.* **3**, 385 (1982).
19. M. Häser, and R. Ahlrichs, *J. Comp. Chem.* **10**, 104 (1989).
20. S. P. Karna, *Chem. Phys. Lett.* **214**, 186 (1993).
21. L. W. Tutt and A. Kost, *Nature* **356**, 225 (1992).
22. A. Kost, L. Tutt, M. B. Klein, T. K. Dougherty, and W. E. Elias, *Opt. Lett.* **18**, 334 (1993).

23. S. R. Flom, R. G. S. Pong, F. J. Bartoli, and Z. H. Kafafi, *Phys. Rev.* **46**, 15598 (1992).
24. M. P. Joshi, S. R. Mishra, H. S. Rawat, S. C. Mehendale, and K. C. Rustagi, *Appl. Phys. Lett.* **62**, 1763 (1993).
25. B. I. Dunlap, J. L. Ballaster, and P. P. Schmidt, *J. Phys. Chem.* **96**, 9781 (1992).
26. D. B. Whitehouse and A. D. Buckingham, *Chem. Phys. Lett.* **207**, 332 (1993).
27. Y. S. Li, D. Tománek, *Chem. Phys. Lett.* **221**, 453 (1994).
28. S. P. Karna, W. J. Lauderdale, B. I. Dunlap, Jorge L. Ballester, *SPIE Proc.* **2530**, 150 (1995).
29. M. Dupuis, A. Farazdel, S. P. Karna and S. Maluendes, in *Modern Techniques in Computational Chemistry*, Ed. E. Clementi (Escom Science Publishing, Leiden, 1991), p. 277.
30. B. I. Dunlap, *J. Phys. Chem.* **96**, 9781 (1992).
31. J. Ciosolowski and N. Nanayakkara, *J. Chem. Phys.* **96**, 8354 (1992).
32. Z. Kafafi, ed. *Fullerenes and Photonics*, *SPIE Proc.* Vol. **2284** (1994).
33. W. J. Blau, H. J. Byrne, D. J. Cardin, T. J. Dennis, P. J. Hare, W. H. Kroto, R. Taylor, and D. R. M. Walton, *Phys. Rev. Lett.* **67**, 1423 (1991).
34. G. B. Talapatra, N. Manickam, M. Samoc, M. Orczyk, S. P. Karna, and P. N. Prasad, *J. Phys. Chem.* **96**, 5206 (1992).
35. J. R. Lindle, R. S. Pong, F. J. Bartoli, and Z. F. Kafafi, *Phys. Rev. B* **48**, 8404 (1993).
36. F. Kajzar, C. Taliani, R. Danieli, S. Rossini, and R. Zamboni, *Phys. Rev. Lett.* **73**, 1617 (1994).
37. P. W. Fowler, P. Lazzaletti, and R. Zanasi, *Chem. Phys. Lett.* **165**, 79 (1990).
38. F. Willaime and L. M. Falicov, *J. Chem. Phys.* **98**, 6369 (1993).
39. M. R. Pederson and A. A. Quong, *Phys. Rev. B* **46**, 13584 (1992).
40. Z. Shuai and J.-L. Brédas, *Phys. Rev. B* **46**, 16135 (1992).
41. S. P. Karna and W. K. M. P. Wijekoon, *SPIE Proc.* **2284**, 111 (1994).
42. S. J. A. van Gisbergen, J. G. Snijders, and E. Baerends, *Phys. Rev. Lett.* **78**, 3097 (1997).

DESIGN CONSIDERATIONS FOR USING OPTICAL LIMITERS IN SIGHTING SYSTEMS

STEPHEN P MCGEOCH, IAN THOMSON, ALAN CHRISTIE
Pilkington Optronics, Barr & Stroud Ltd, Linthouse Road, Glasgow, G51 4BZ,
Scotland, UK
RICHARD C HOLLINS, JON MILWARD
DERA, St Andrews Road, Malvern, Worcs, WR14 3PS, England, UK

Abstract Some of the optical design issues and performance trade-offs incumbent upon the designer of a practical, pulsed laser-protected optical sight are addressed. The basic optical requirements of a sighting system are discussed, along with the additional features specific to the limiter device, such as accommodation and provision of sufficiently high intensities for operation of the device. Consideration is also given to the need to minimise the inherent transmission loss due to the limiter. Laser-induced damage of the limiter is discussed. Examples of optical designs for sighting systems are used to demonstrate the trade-offs which may have to be considered in order to achieve the required system specification. It is shown that the use of optical power limiters in sights is a systems engineering issue, and must be fully considered in the concept and design phases of system development.

INTRODUCTION

There has been increasing interest over recent years in non-linear optical power limiters. A primary application identified for these devices is in providing sensor and eye protection from pulsed lasers of unknown wavelength. However, there has been comparatively little reported work on the design issues involved in the use of optical limiters in real sighting systems. In this paper, we address some of the optical design issues and performance trade-offs in the design of a pulsed laser-protected optical sight.

In addition to the basic optical requirements of a sight, the optical design of a system protected by an optical limiter must provide an accessible location with suitable optical conditions for the limiting device. In practice, the high intensities required for the operation of a limiter mean that this is likely to be at the focal plane of the objective

lens or other intermediate focal plane (IFP). It must be recognised that a consequence of the limiter location is that it may be susceptible to laser-induced damage.

All known practical optical limiters have significant linear absorption. This is required to drive the non-linear process which provides the optical limiting action. Thus, the depth of the IFP affects the transmission and is an important parameter for the optimisation of the optical design.

The great majority of published work on optical limiters has been carried out using laboratory-standard devices such as glass cuvettes. However, it is noted that, for practical applications in optical sighting systems, it is necessary to use fully-engineered optical limiter devices with suitable optical, mechanical and environmental specifications.

GENERAL CONSIDERATIONS

System Optical Specification

The principal parameters of an optical design are set by the specification of the optical system or sight. These will include field of view, magnification and resolution, and some determinant of light-gathering ability such as f-number. There will also be physical constraints such as size and weight. In conjunction with magnification, the space available to the optics will go some way towards defining the focal length of the objective lens. Also to be considered is compatibility with other systems such as rangefinders and target locators; optically-injected information such as symbology, graphics, warning lights, and images from other sensors; and focal plane features such as gratitudes. Note that the advanced features of a complex sight tend to limit the available space at the IFP where it is usually a mechanically-preferred location for optical combination. The system will also have environmental requirements such as temperature and humidity ranges, which may affect choice of materials. The physical requirement in terms of mechanical shock and vibration must also be considered. Cost, determined by materials, complexity and manufacturing risk or yield, is also a significant parameter.

Limiter Requirements

When an optical power limiter is to be incorporated within a sight, then the optical design must be optimised for its use within the boundaries defined by the system performance parameters.

The design must provide suitable physical accommodation for the limiting device at a focal plane. The spot size at the focal plane must be sufficiently small to generate the intensity required by the limiter to provide the required attenuation at the specified input levels. This is readily achieved for the $n_f - n_c$ (486nm - 656nm) spectral band near and on-axis by most practical designs at the nominal operating temperature. However field-angle and temperature extrema must also be considered, and also, in some cases, an extended waveband. The entirety of the intermediate focal plane must be contained within the optical limiter, *ie* the foci for all wavelengths and field angles. As will be shown, this is an important design driver for the protected optical system.

These facts place considerable restrictions on the freedom of the optical designer. It is a commonplace of optical design that small aberrations present in the objective can be balanced using complementary aberrations in the eyepiece since the quality of the final image at the sensor or eye is paramount. However, in the case of a sight incorporating an optical limiter, the design must produce a high quality image at both the intermediate image and the sensor.

Insertion Loss

All effective optical limiters cause a significant loss of transmission due to absorption. This is required to drive the non-linear process which provides the optical limiting effect.

The majority of practical optical limiters for visible waveband applications are dye solutions or particle suspensions in liquid hosts. Examples are solutions such as metal-phthalocyanines and carbon-black suspensions. In practical concentrations, dye solutions have been shown¹ generally to offer optimum levels of attenuation at energy densities of $>10\text{Jcm}^{-2}$. Dyed solids are susceptible to laser induced damage at such levels. Liquid phase limiter has the great advantage of self-healing after laser-induced damage, and consequently much greater energy-handling capability.

In selecting an optical limiter for an application, it is necessary to choose one which is compatible with the waveband of the system. It is also essential early in the design process to estimate the approximate concentration requirement for the optical limiter. This can be carried out by measuring the output of a relatively-thick cell filled with the limiting material, for a range of concentrations, at the maximum specified input energy, incident at the system f-number. The measurements can be made mid-waveband and on-axis, and scaled later if necessary. Note that the output may be measured in terms of total energy or peak energy density, or whatever is required by the specification.

Taking the case of an optical limiter with 50% transmittance in a 1mm thickness as an example, it can be seen that increasing the thickness to 1.5mm leads to a corresponding transmittance of 35%, while 2mm gives only 25% (Figure 1). Note that any suitable transmission parameter may be chosen, *eg* integrated visual transmittance.

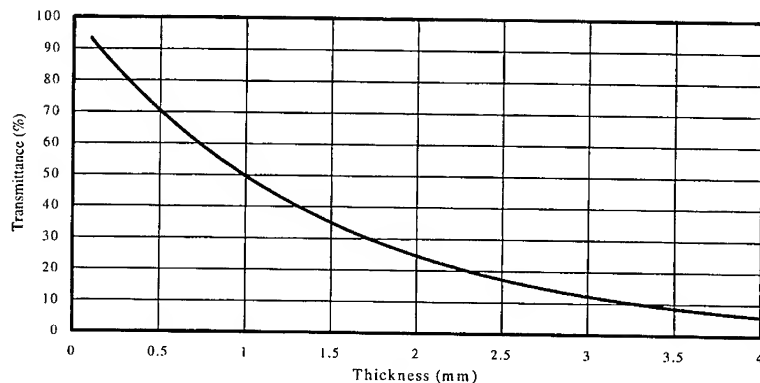


FIGURE 1 Variation of example limiter transmittance with device thickness

In practice, it is the task of the optical designer to minimise the depth of the IFP while meeting the system optical specification and the spot size requirement of the limiter. The IFP thickness will be determined by factors such as field of view, spectral waveband, effective focal length, temperature range of operation, and, in zoom or switchable systems, magnifications. It may also be necessary to account for laser parameters such as spatial or angular distribution of the input beam. These parameters

must be traded-off to optimise the design so that the IFP thickness requirement is minimised.

OPTICAL DESIGNS

To illustrate some of the complex design considerations and trade-offs associated with the incorporation of an optical limiter device in an optical sighting system, we consider three design examples for a representative specification based on an $f/6$, dual field-of-view sight.

In our figures, we shall illustrate the characteristics of the designs with respect to the following parameters: a mid-band wavelength (gr), the short (bl) and long (rd) wavelength extrema, the nominal design temperature (20°C), and low-temperature (lo-T) and high temperature (hi-T) extrema of the specification. As a convention, we use positive values of field position to represent the narrow field-of-view (NFOV) configuration, and negative values for the wide field-of-view (WFOV).

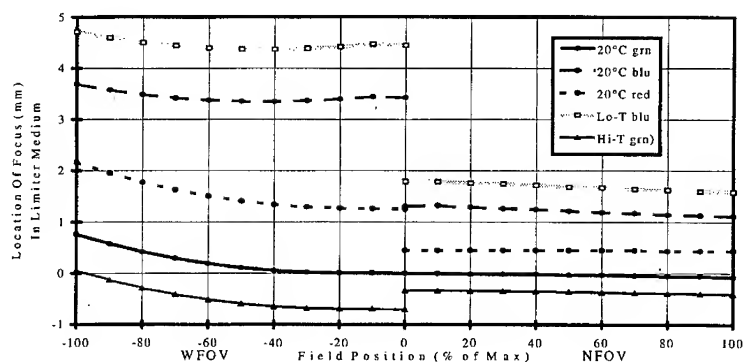


FIGURE 2 Variation of focus position at IFP in baseline optical design.

Baseline Design

Figure 2 shows the focal plane configuration for a baseline optical design for the sight. Only the extremes of the temperature excursion data are shown. This design is optimised for manufacturability to meet the specification with no attention paid to the requirements of an optical limiter. The focal plane locus is thickened to ~6mm by field

curvature, chromatism, the temperature range of the instrument, and the refractive index of the limiter device. For our example limiter, this would give a transmission of only 1.5%.

Design for optical limiter (I)

A possible improvement to the baseline to minimise the insertion loss due to the optical limiter is a flat-field design optimised to minimise chromatic focus range over the full spectral range of the optical system (apochromatic). This design requires the use of more exotic or difficult-to-work glasses. Glass types which have the necessary secondary spectrum characteristics required for such correction almost invariably have poor thermal behaviour. As Figure 3 shows, this design achieves a much tighter bounding of the focal plane at the design temperature at the nominal design temperature (20°C). The locus of foci is contained within a thickness of ~0.6mm; which corresponds to a transmission of 66% for our example limiter. This approach in which variance with wavelength is minimised would probably be necessary for sophisticated optical limiter concepts such as optimised concentration gradient² or tandem³ limiters.

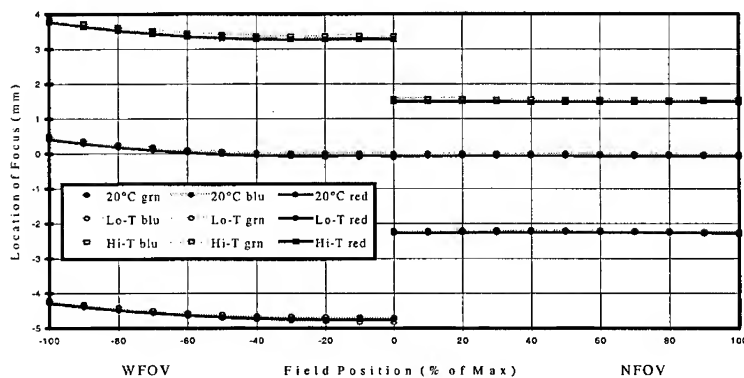


FIGURE 3 Variation of focus position at IFP in optical design (I).

However, there is significant drift of focal position with temperature, and this leads to a total thickness requirement of ~9mm (*ie* a transmission of only 0.1% using our example limiter). The thickness requirement over the temperature range could be minimised by

incorporating a temperature-controlled position adjustment for the limiter. This of course assumes that such a system could be physically accommodated and meet the environmental requirements, and that the penalties in terms of reliability and cost can be tolerated.

Design (I) - Spot Sizes

It is essential for the efficient operation of the optical limiter that the focal spot size is sufficiently small for all wavelengths, field angles and temperatures. These are shown in Figure 4 for the apochromatic design, plotted relative to the spot size for green, on-axis (for which, as might be expected, the smallest spot is achieved). For this design, the biggest spot is a factor of about 16 greater than the smallest, giving a significant reduction in intensity. Note that larger spots (and therefore less efficient limiting) occur predominantly at wider field angles, and that the loss of limiting performance may be offset to some extent by vignetting.

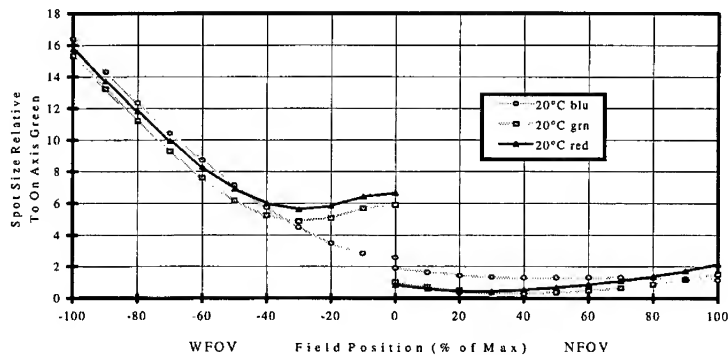


FIGURE 4 Relative variation of spot size at 20°C for optical design (I)

Design for optical limiter (II)

Another approach is to create a design which trades spectral co-location for thermal invariance. As with design (I), this athermal design has drawbacks from the point of view of manufacturing: it requires the use of glasses which are difficult to work and tight assembly tolerances. This design gives a thickness requirement for the limiter of ~1mm - a transmission of 50% for the example limiter (Figure 5).

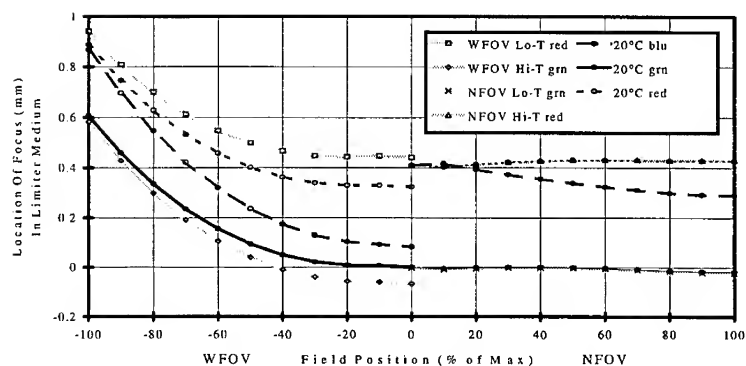


FIGURE 5 Variation of focus position at IFP in optical design (II).

Design (II) - Spot Sizes

The focal spot sizes for the athermal design (II) are shown in Figure 6, plotted relative to the spot size for green, on-axis.

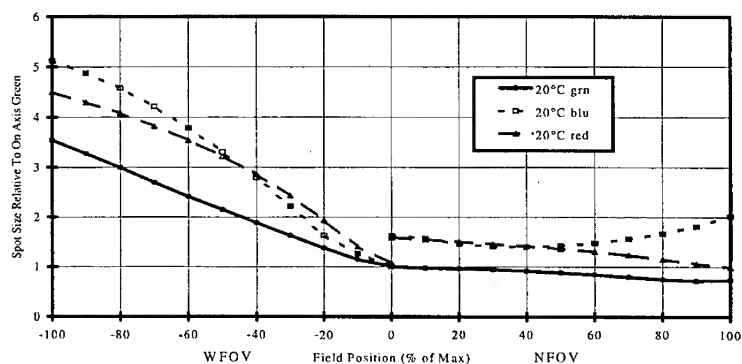


FIGURE 6 Relative variation of spot size at 20°C for optical design (II)

For this design, the biggest spot is a factor of about 5 greater than the smallest, giving significantly less reduction in intensity than the apochromatic design (I).

ADDITIONAL FACTORS IMPACTING ON SYSTEM TRANSMISSION

Limiter performance near the cell walls

Some additional cell thickness must be allowed because the limiting performance is not maintained all the way to the edges of the cell. The output of the limiter at the maximum specified input can be measured as a function of position using the z-scan configuration and representative optics. It can be assumed that the nominal minimum output has been chosen to match the requirement. This is shown for a carbon suspension device in Figure 7, and indicates a reduction in limiting over about 0.2mm at the front face and 0.7mm at the rear.

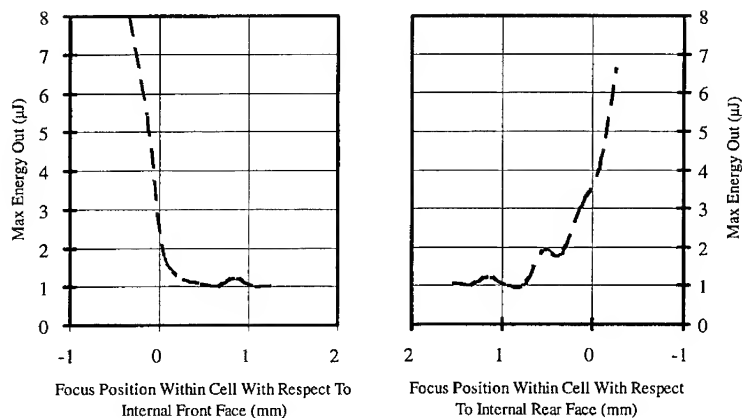


FIGURE 7 Variation in protection with focus position through cell

Laser-induced damage to the optical limiter

Although the liquid-phase non-linear optical limiting medium is self-healing for laser-induced damage, the design imperatives to achieve small spots and to minimise the limiter cell thickness means that the walls (particularly the input face) are at risk of optical damage.

In order to estimate the clearance required to avoid laser-induced damage of the cell walls, it is useful to scan a thick cell of the correct concentration through the focus of a representative optical system (z-scan configuration) over a range of input energies

up to the maximum requirement, using a mid-waveband, on-axis input. Note that for most optical designs, an axial monochromatic spot will be near diffraction-limited, so that a well-corrected, off-the-shelf lens of the correct f-number can be used for this assessment. The results can be scaled for other wavelengths and field angles using the spot size and focus location data generated by the optical design.

A picture showing the necessary clearance for the front and rear surfaces of the cell can readily be built up. Measurement over a range of energies reduces uncertainty in the measurements, and, as will be seen later, is important for the estimation of risk of damage.

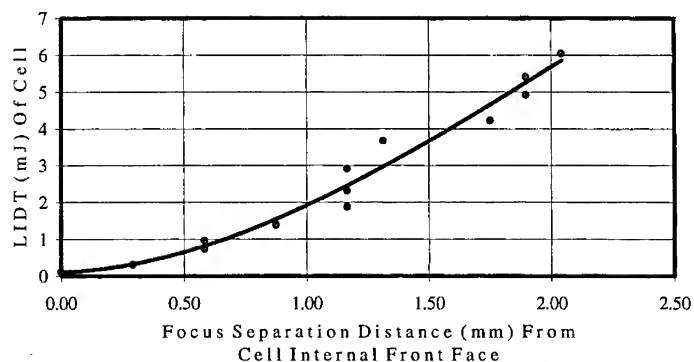


FIGURE 8 Variation in cell LIDT with focus distance from front face

In almost all cases the front face of the cell will be damaged more readily than the rear, and will, therefore, require greater clearance. This is because the cell protects the exit face. An example is shown in Figure 8, where the LIDT refers to the energy incident on the optical system. In this case, it was not possible to damage the rear face of the cell for any focus position and up to the maximum energy output of the test laser.

Note that the laser-induced damage threshold (LIDT) of the optical limiter cell is critically dependent on the choice of material for the cell construction. High-LIDT materials such as fused silica give significant advantage over simple glass cells.

DESIGN TRADE-OFFS

The locus of foci derived in the optimised optical design of the objective lens and the reduction in protection at the cell boundaries give the minimum optical limiter thickness required to provide protection to the sensor for all cases of wavelength, field angle and temperature.

The focal point to cell wall separation condition to prevent laser damage to the device, coupled with the focal spot location and size data, gives the additional limiter thickness requirement to avoid laser-induced damage to the limiter cell.

Damage to the optical limiter cell is potentially serious because the damage site is in the focal plane of the sight. It will be visible to the user, and may significantly degrade the functionality of the system.

For real systems, some risk of damage to the optical limiter will probably be acceptable if sufficient gain in transmission can be realised as a result. For example, small localised damage sites at wide field angles may have little effect on system performance. The risk is further reduced if this only occurs at extreme temperatures. If the optical limiter module can be made accessible, interchangeable and relatively cheap, then this may increase the acceptability of some risk of laser-induced damage. However, it will not generally be permissible to compromise protection of the sensor, particularly when this is the human eye. Note also that limiter damage will provide sacrificial protection to the sensor.

CONCLUSIONS

The incorporation of an optical limiter as a laser-protective device in an optical sighting system places significant demands on the optical design, and presents critical performance trade-off considerations to the systems engineer.

The optical design must provide a focal plane location for the limiter of a high quality to allow satisfactory limiting performance.

The transmittance penalty incurred upon the insertion of the optical limiter makes it imperative that the optical design is optimised to produce the minimum possible thickness of the locus of foci for all wavelengths and field angles throughout the

temperature range of the instrument. This localisation of the focal plane has its price in terms of materials cost and manufacturing cost and risk, but is essential for the current generation of optical limiter materials.

As well as providing protection from laser-induced damage to the sensor (and especially to the eye), it is essential that the optical limiter itself is laser-hardened, since it is in sharp focus to the user because of its location at the intermediate focal plane, and damage sites can cause severe disruption to the perception of the scene. Liquid-phase limiters are excellent choices in this regard since they are self-healing upon damage. However, the walls of the optical limiter cell are at risk since they are so close to the focal plane, and consequently suffer high levels of irradiance. This susceptibility to laser-induced damage can be obviated by increasing the cell thickness at the expense of loss of transmittance. A careful trade-off analysis must be carried out to optimise the balance between risk of damage and system performance.

Finally, it can be seen from the above that the use of an optical limiter is a fundamental design driver for a sighting system. It is important therefore that consideration to the requirements of the limiter be introduced into the design process at the earliest possible stage so that the optimum performance of the instrument can be realised.

REFERENCES

1. SP McGeoch, A Christie, GS Bahra and KR Welford, Materials for Optical Limiting, MRS Symp Proc 374, 381, (1995).
2. PA Miles, Appl Opt, 33(30), 6965 (1994).
3. DJ Hagen, T Xia, AA Said and EW Van Stryland, Nonlinear Optical Materials for Switching and Limiting, SPIE Proc 2229, 179 (1994).

OPTICAL POWER LIMITING USING NONLINEAR PERIODIC SEGMENTED WAVEGUIDES

PIERRE ASCHIERI, PASCAL BALDI, LOÏC CHANVILLARD, MARC P. DE
MICHELI AND DANIEL B. OSTROWSKY

Laboratoire de Physique de la Matière Condensée, Université de Nice Sophia
Antipolis, 06 108 Nice Cedex 2, France.

GAETANO BELLANCA AND PAOLO BASSI

Dipartimento di Elettronica Informatica e Sistemistica, University of Bologna,
2-40136 Bologna, Italy.

Abstract We present a numerical study of optical power limitation in nonlinear periodic segmented waveguides. We base our analysis on light propagation in linear periodic segmented waveguides which exhibits interesting properties for light attenuation if a Kerr-type nonlinear optical index is added.

INTRODUCTION

Segmented waveguides are formed by a periodic structure of high index refractive segments embedded in a low refractive index substrate¹ (see Figure 1). It has been shown that such waveguides exhibit several interesting properties. On the one hand, they have been used for linear applications such as tapers, mode filters and Bragg reflectors^{2,3} using the fact that changing the duty-cycle (DC), defined as the ratio of the high index segment over the period changes the spot size and the propagation constant. On the other hand, because of the periodic reversal of the nonlinear coefficient associated with such waveguides in some materials such as *KTP* or *LiNbO₃*, they have been employed to achieve efficient nonlinear guided wave interaction using the Quasi Phase Matching (QPM) or Balanced Phase Matching (BPM) schemes⁴. The use of such structures for power limiting is based on the fact that such waveguides have intrinsic losses which are very sensitive to the waveguide parameters. This means that in certain situations increasing or decreasing the index difference δn between the guiding parts of the structure and the substrate can lead to dramatic effects on the losses. Since an

optical power dependent index change in the guiding and non-guiding parts of the structure can be obtained using the Kerr effect or a χ^2 cascading process⁵, the structure can act as an optical limiter. In order to exploit the full potential of these particular waveguides, it is important to have first, a detailed numerical and/or analytical modelization of the linear problem in order to understand the guiding mechanism in such structures. Then, interesting properties can be derived for the nonlinear case such as optical limiting. In this paper, we present a study of light propagation in linear planar segmented waveguides using two different approaches: the Finite Difference Beam Propagation Method^{1,6} (FD-BPM) and the Coupled Mode Theory¹ (CMT) and then we extend the numerical (FD-BPM) approach to the nonlinear case.

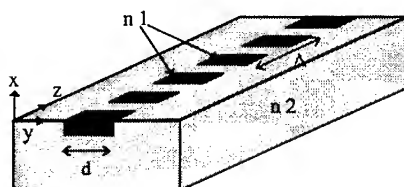


FIGURE 1 Segmented waveguide comprising of a linear array of high index regions embedded in lower index surrounding.

METHOD DESCRIPTION

It is well known that segmented waveguides can support light propagation with low losses, and the effective index of the guided mode can be calculated using the equivalent waveguide model. An essential problem with such waveguides is the evaluation of the loss.

CMT and FB-BPM are used here to analyze periodic segmented waveguides. A similar approach has been employed earlier by Weismann and Hardy¹, except that we now use Finite Differences instead of the Fast Fourier Transform (FFT) for the BPM. We introduce a Kerr-type nonlinear index dependence in waveguide segments using the Leap-Frog⁶ scheme.

Using the CMT, we derive a simple analytical formula for the loss in linear waveguides and show a very good agreement with the linear results of FD-BPM.

Nevertheless, those two methods are complementary; the CMT can give immediately the loss value while the FD-BPM takes some computation time (typically 1 or 2 mn for 1cm length waveguides) but can also give the field profile. We confirm a strong dependence, as in Ref.1, of the propagation losses of segmented waveguides on the waveguides parameters. In the following sections, both the CMT and FD-BPM methods are briefly described.

FD-BPM

For the FD-BPM, the starting point is the scalar Helmholtz equation

$$\Delta E + k^2 E = 0 \quad (1)$$

with $k^2 = \epsilon \mu_0 \omega^2$ and the usual assumption of time dependence having the form $\exp(i\omega t)$. Using the slowly varying envelope approximation, the field can be written as $E = E(x, z) \exp(-i k_0 n_0 z)$ which leads to the following scalar parabolic wave equation for $E(x, z)$ with the parabolic approximation $\partial^2 E(x, z) / \partial x^2 \ll -2 i k_0 n_0 \partial E(x, z) / \partial z$

$$\partial^2 E(x, z) / \partial x^2 - 2 i k_0 n_0 \partial E(x, z) / \partial z + k_0^2 (n^2(x, z, |E|^2) - n_0^2) E(x, z) = 0 \quad (2)$$

with $n^2(x, z, |E|^2) = n^2(x, z) + \alpha(x, z) |E|^2$ as the nonlinear refractive index of the structure and where $\alpha(x, z)$ is the nonlinear coefficient ($\alpha=0$ for the linear case). This equation is solved using Finite Differences associated with the Leap-Frog scheme. If p represents the z -component and i the x -component of the field, then one can write: $E(x, z) = E_i^p$; using this notation, we will evaluate all the terms of equation (1):

The first derivative along z is describe as:

$$\frac{\partial E}{\partial z} \approx \frac{E_i^{p+1} - E_i^{p-1}}{2\Delta z}$$

The second derivative for the transversal component x is approximated by:

$$\frac{\partial^2 E}{\partial^2 x} \approx \frac{1}{2} \left[\frac{E_{i-1}^{p+1} - 2E_i^{p+1} + E_{i+1}^{p+1}}{\Delta x^2} + \frac{E_{i-1}^{p-1} - 2E_i^{p-1} + E_{i+1}^{p-1}}{\Delta x^2} \right]$$

and the nonlinear term is evaluated as follows:

$$k_0^2 (n^2(x, z, |E|^2) - n_0^2) E \approx \frac{k_0^2}{2} \left[\left((n_i^{p+1})^2 + \alpha_i^p |E_i^p|^2 - n_0^2 \right) E_i^{p+1} + \left((n_i^{p-1})^2 + \alpha_i^p |E_i^p|^2 - n_0^2 \right) E_i^{p-1} \right]$$

We also use Transparent Boundary Conditions⁷ (TBC) thus avoiding the problem of reflections. The losses are calculated simply by looking at the power remaining in the computation window after a sufficient distance of propagation for given input power.

CMT

We start again with the equation (Eq.1). Using the perturbation approach, one can assume that the segmented waveguide can be represented as a periodically perturbed uniform waveguide, the uniform unperturbed waveguide is assumed to be the equivalent waveguide as defined in Ref.1. Then the wave equation becomes:

$$\Delta E + \varepsilon \mu_0 \omega E = -\Delta \varepsilon \mu_0 \omega^2 E$$

where ε represent the permittivity profile of the equivalent waveguide model, $\Delta \varepsilon = \Delta(\varepsilon_0 n^2(x, z)) \approx 2\varepsilon_0 n_{eq} \Delta n$ represents the periodic perturbation of the refractive index along the z-direction; n_{eq} is the weighted average index of the guiding film. In a uniform waveguide, guided modes and radiation modes are not coupled, but here, the periodic perturbation couples these two kind of modes. The coupling of power from the guided mode to the radiation mode spectrum due to the periodic perturbation is then responsible for the loss associated with a segmented waveguide. The coupling¹ is a function of the overlap between guided and radiation modes. Because it is a periodic structure, coupling takes place predominantly to those radiation modes which satisfy the phase matching condition: $\beta \approx \beta_g - p \cdot 2\pi/\Lambda$ where β_g is the propagation constant of the

guided mode of the unperturbed waveguide, Λ the period of the perturbation and $p=1,2,3,\dots$ is the coupling order. Using the CMT, we can evaluate the amount of power coupled by different orders. We have noted, that for a duty-cycle equal to 0.5, the coupling is very strong with the first order; higher order coupling becomes significant for other duty-cycles. In both FD-BPM and CMT analyses, backward reflections, normally negligible outside the reflection band, are ignored and we assume that the Bragg conditions are not satisfied. We may mention that there are different methods that can be used to estimate losses in segmented waveguides. Segmented waveguides can be seen as a lamellar grating with light incident at angle $\theta_i=\pi/2$. One numerical method⁸, derived from grating analysis is based on the well known Bloch-Floquet theorem applied to periodic structures. Another approach using the "Kronig-Penney" model⁹ has also been applied to study segmented waveguides.

LINEAR PERIODIC SEGMENTED WAVEGUIDE

As mentioned previously, we will base our study of optical power limiting beginning with a presentation of some interesting linear properties of segmented waveguides.

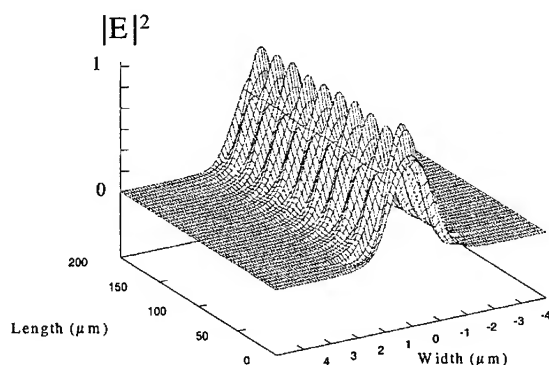


FIGURE 2 Mode profile in a linear periodic segmented waveguide, Parameter values: wavelength $\lambda=0.85\mu\text{m}$, $\Lambda=20\mu\text{m}$, DC =0.5, $d=3\mu\text{m}$

Calculations have been performed for a planar segmented waveguide and some results are shown in the following figures. Figure 2 represents the mode profile intensity distribution in a periodic segmented waveguide. One can note the amplitude modulation due to the periodic index change along the propagation direction. The

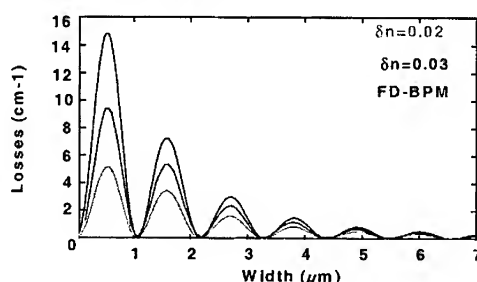


FIGURE 3 Losses as a function of the width d calculated with FD-BPM and CMT for different δn , Parameter values: $\lambda = 0.85 \mu\text{m}$, $\Lambda = 5 \mu\text{m}$, $DC = 0.5$

period of the modulation corresponds to the period Λ of the waveguide. Figure 3 shows the variation of loss with the width d of the waveguide. Some important observations are that the loss decreases when the width increases, which can be understood from the fact that as the width increases the guided mode becomes more confined and a bigger part of diffracted light from the homogeneous space is coupled to the next guiding segment. There are oscillations which lead to a strong dependence with the width; changing the width for $0.5 \mu\text{m}$ can multiply loss by a factor of 20. These oscillations can be clearly understood if we use the CMT model. We know that losses are due to the coupling between guided and radiation modes. The radiation modes have an oscillatory field distribution in the guiding film and the cladding layers; a small change of the guided mode size due to a change in width of the waveguide results in a corresponding change in the overlap of the guided and radiation modes. This leads to loss oscillation as a function of width. Furthermore, if δn changes, for example if δn increases, the shape of the curve remains almost the same, but the magnitude of loss increases for all values of width; this is again expected, since increasing the index discontinuity increase losses.

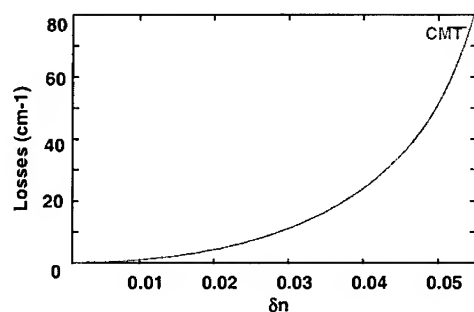


FIGURE 4 Losses as a function of the index difference δn ,
Parameter values: $\lambda=0.85\mu\text{m}$, $\Lambda=20\mu\text{m}$, $DC=0.5$, $d=5\mu\text{m}$

This can be also seen with Figure 4 which represent the loss variation with the index difference δn ; the losses increase with the index difference. Finally, Figure 5 shows the loss variation as a function of the period Λ . This also shows an interesting behavior; as one can expect, increasing the period might lead to increasing losses in general, but low losses can also be attained for specific values for large periods. This is also due to the overlap between guided and the radiation modes. Nevertheless, it is normally preferable to have short periods. Short periods leads to a small number of radiation modes and wide diffraction angles which reduces the overlap.

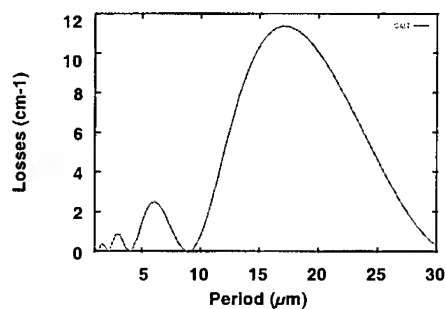


FIGURE 5 Losses as a function of the period, Parameter
values: $\lambda=0.85\mu\text{m}$, $DC=0.5$, $d=2\mu\text{m}$

It can be clearly seen with these results that losses are very sensitive to waveguide parameters. An optical power dependent index change in the high index region will modify the waveguide properties and for a certain set of parameters light can be coupled into radiation modes and the structure can act as an optical power limiter. This behavior is expected looking at Figure 4 where losses increase -coupling into radiation modes- with the index difference. That can be obtained using the Kerr effect or a χ^2 cascading process as will be shown in the following section.

NONLINEAR PERIODIC SEGMENTED WAVEGUIDE

In this sections we present a the numerical analysis of a nonlinear periodic segmented waveguide. The calculations are performed using the FD-BPM Leap-Frog scheme defined previously. We analyze a periodic segmented waveguide with an intensity dependent refractive index change in the guiding part of the structure of the form $n(|E|^2)=n_1+\alpha|E|^2$.

The intensity field profile for low input power is very close to that of Figure 2 corresponding to the same linear waveguide. The output power remaining in the waveguide is 98% of the input power. The difference is due to intrinsic losses induced by the segmentation. For high input power, the field intensity distribution is given by Figure 6 where one can see the amplitude attenuation of the mode and the strong light coupling into radiation modes.

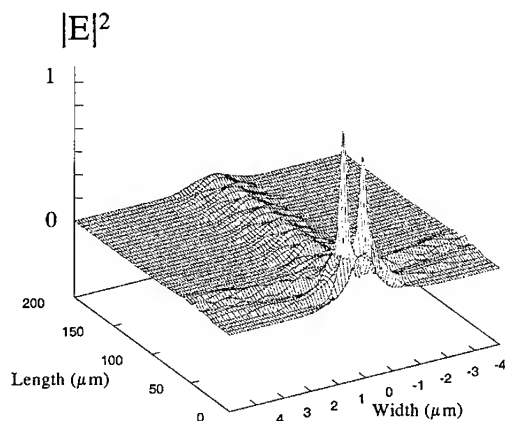


FIGURE 6 Field profile for a high input power, waveguide parameters: $\lambda=0.85\mu\text{m}$, $\Lambda=20\mu\text{m}$, $DC=0.5$, $d=3\mu\text{m}$

Figure 7 shows the power remaining in a nonlinear periodic segmented waveguide and a nonlinear straight waveguide as a function of the input power. We can see that while the behavior of these two waveguides is similar for low input power, this is no longer the case for high input power. While the output power is still increasing with the input power for the straight waveguide it is no longer true for the segmented waveguide. For the segmented waveguide a saturation occurs very rapidly. An explanation of such behavior is that the increasing input power increases the index difference because of the nonlinear power dependent high index segments and this leads to higher losses according to Figure 5. Another explanation is based on the strong loss dependence of the waveguide parameters. Choosing low loss waveguide parameters for a linear case will lead to higher losses with a nonlinear index change. Because the overlap between guided and radiation modes is minimum for the linear case, it is then perturbed by the nonlinearity and induces higher losses. Nevertheless, numerical simulations have shown that this effect is not as important as the increase of

the index difference mentioned previously. In any case, it is preferable to choose low loss parameters for the linear case in order to have the maximum efficiency transmission for a low input power.

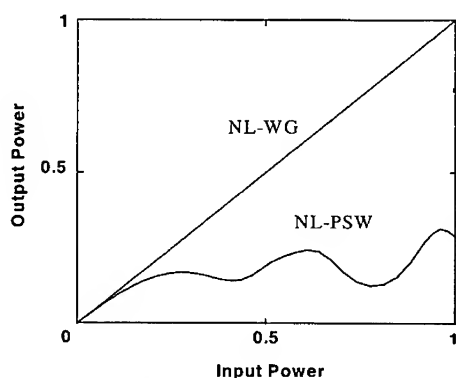


FIGURE 7 Output power for nonlinear segmented waveguide and a straight nonlinear waveguide as a function of the input power in arbitrary units

A limitation of such a device is that the phenomena involved for the optical limitation requires high optical intensity. Typically, the estimated nonlinear index change required in order to see such phenomena is around $\delta n = 0.005$ which can not be obtained in classical nonlinear materials such as *KTP*, *LiNbO₃* with reasonable intensities. It is necessary to use materials with higher Kerr coefficients such as *PTS*, *DAN* or *Optimized Stilbene*, where on the order of several Watts of input power is enough to see optical power attenuation. For example, in a $5\mu\text{m}^2$ *LiNbO₃* waveguide, 10kW pump is necessary with Lithium Niobate whereas only 100 mW would be enough to see optical attenuation in an identical *Optimized Stilbene* waveguide.

In this paper we have analyzed a waveguide containing an ideal configuration with a high nonlinear Kerr-type contrast since the nonlinearity is present only in the high index segments and null in the surrounding media. This configuration can be made using a cascaded χ^2 process in the segments. More generally, we can consider realizing nonlinear periodic segmented waveguides using a dopant in the high index segments which increase the Kerr-type nonlinear contrast but without destroying the

Kerr effect in the substrate. The expecting behavior of optical limiting is still valid but at the expense of an increasing input power.

CONCLUSION

Starting our analysis with the linear properties of segmented waveguides, we have demonstrated numerically that the introduction of nonlinearities in such waveguides can exhibit interesting new phenomena. In particular a nonlinear optical Kerr type segmentation can be used to realize an optical power limiter. The light powers involved in such phenomena require nonlinear materials with higher cascaded or Kerr type coefficient than usual materials.

Acknowledgments

Partial financial support is provided by the Conseil Régional Provence Alpes Côte d'Azur.

REFERENCES

1. Z. Weissman and A. Hardy, *J. Lightwave Technol.*, **11**, pp. 1831-1837, (1993).
2. M.H. Chou, M.A. Arbore, and M.M. Fejer, *Opt. Lett.*, **17**, pp. 794-796, (1996).
3. W.P. Risk, S.D. Lau, and M.A. Mc. Cord, *OSA Technical Digest Series*, **1**, (Optical Society of America, Washington, D.C., 1993), paper CWI14.
4. J.D. Bierlein, D.B. Laubacher, J.B Brown, C.J. van der Poel, *Appl. Phys. Lett.*, **56**, pp. 1725-1727, (1990).
5. G.I. Stegeman, *Quantum Semiclass. Opt.*, **9**, pp. 139-153, (1997).
6. J.C. Strikwerda, *Finite Difference Scheme and Partial Differential Equations*, (Wadsworth, New York, 1989).
7. G.R. Hadley, *Opt. Lett.*, **16**, pp. 624-629, (1991).
8. L. Li and J.J. Burke, *Opt. Lett.*, **17**, pp. 1195-1197, (1992).
9. D.D. Stancil, *Appl. Opt.*, **35**, pp. 4767-4771, (1996).

Large Second-Order Optical Nonlinearity in Ge-Doped Silica Glass

AKIRA J. IKUSHIMA and TAKUMI FUJIWARA
Research Center for Advanced Photon Technology
Toyota Technological Institute
Nagoya 468-8511, Japan

Abstract Large second-order optical nonlinearity in Ge-doped silica glass induced by simultaneous applications of a high DC voltage and UV irradiation is reported. The nonlinearity thus induced has been found to be quite relevant to the GeE' center. The d coefficient so far obtained exceeds the second biggest d-tensor component of LiNbO_3 .

[Keyword: optical nonlinearity, silica glass, UV-poling, defects, GeE' center]

INTRODUCTION

Silica glass is in many respects the most typical glass. Silica glass is also the very key material for photonics applications. Optical fibers made of silica glass has been exclusively used for long-distance transmission network.

Glass is the material which has the inversion symmetry. Therefore, glass should not have in principle any second-order, or more precisely the even-order, optical nonlinearities. This has brought the glass materials only to passive usages like fibers in photonics, while the second-order optical nonlinearity is the property absolutely required to active, not passive, applications in photonics. The active applications include to switch optical signals, to convert light frequency, to direct laser light, and so on. So far, devices which require the second-order nonlinearity have been realized with organic and inorganic crystals.

Several years ago, second-order nonlinearity was first induced in silica glass by a

treatment. The treatment was to apply a high electric voltage while a glass sample was at an elevated temperature, and this treatment has been called *thermal-poling*.¹ More recently, Fujiwara et al. has discovered in their pioneer work that an appreciable electro-optic effect could be induced in a Ge-doped silica fiber if the fiber sample was shone by UV laser light while a high voltage was applied.² This method, now commonly called *UV-poling*, has attracted much attention since then. And, the present authors and their colleagues have confirmed that the second-order nonlinearity can be induced with the UV-poling method in Ge-doped silica glass.³

The appearance of the second-order nonlinearity is a direct evidence that the inversion symmetry is broken in thus treated glass. We are not aware of any results reported as a direct experimental evidence of breaking of the inversion-symmetry in glasses induced by poling. Studies on the effect are therefore to make clear the points:

- (1) What kind(s) of defects produced during the thermal- and UV-polings are responsible to the nonlinearity ?
- (2) How do such defects work to produce the nonlinearity ?

The present authors and their colleagues have been devoting to this topic.^{3, 6-10}

The effect, which had never been thought to exist in glass, should really bring a big breakthrough in photonics. Glass-based active devices will be not only high functional as themselves, but also they can probably sweep out almost all of the problems related to connection between optical fibers and crystal-based devices. The problems are such as optical loss caused by the different cross-sectional shape of optical waveguides, optical loss and troublesome worries caused by the difference of thermal expansion coefficients, appreciable costs of crystal preparation, cutting and polishing, and also the cost of pig-tailing, etc.

PHOTO-CHEMICAL REACTIONS AND DEFECTS IN THE GLASS

Figure 1 shows thinkable major defects in Ge-doped silica glass. Here, GEC represents Ge-related electron-trapped centers, NOMV and NODV are two oxygen-deficient

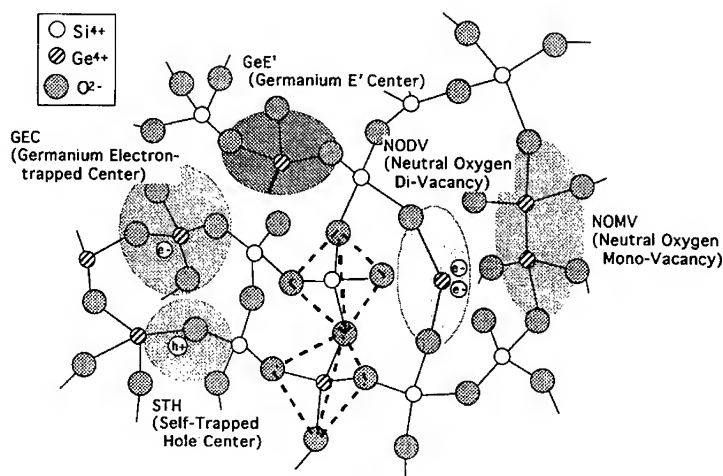
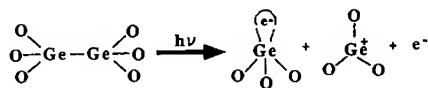


FIGURE 1 Defects in Ge-doped silica glass

vacancies, and are neutral oxygen mono-vacancy and neutral oxygen di-vacancy, respectively.^{4,5} Among those, probably the most important defect in the present issue is GeE' center, which consists of a Ge atom with a dangling bond and three oxygen atoms covalently-bonded to Ge. The GeE' center is thought to give optical absorption at 6.2 eV or 200 nm. Such centers would exist already in Ge-doped silica glass from the beginning if we judge from the optical absorption spectrum. New GeE' centers are freshly produced by the following photo-chemical reaction from oxygen-deficit defects, where



one of Ge atoms may be replaced by a Si atom. The first term on the right is the GeE' center and electrons are also released correspondingly. Therefore, a complex consist of an oxygen vacancy neighboring to a Ge atom is the precursor of producing a GeE' center.

EXPERIMENTAL PROCEDURE AND RESULTS

Sample and Poling

A Ge-doped SiO_2 glass (15.7 GeO_2 -84.3 SiO_2 in mole%) fabricated by VAD (Vapor Axial Deposition) method as a fiber preform was used in the experiment. Glass samples for the present experiment were cut from the preform to 10x10x1 mm in size, and therefore the measurements were carried out using these bulk, not fiber samples. With a poling electric-field up to 3×10^5 V/cm across the electrodes, glass samples were irradiated by a pulsed ArF excimer laser at its wavelength of 193 nm.

Polings of the samples were done with two electrodes put from upper and lower faces of a sample so that as a high voltage as possible could be applied, avoiding possible dielectric breakdown of air.

Nonlinearity Induced by UV-Poling

For measuring the induced SHG (d coefficient) in UV-poled glasses, the Maker-fringe patterns were obtained by using Q-switched Nd:YAG laser pulses. The rotational axis of samples was always chosen to be parallel to the direction of poling electric-field.

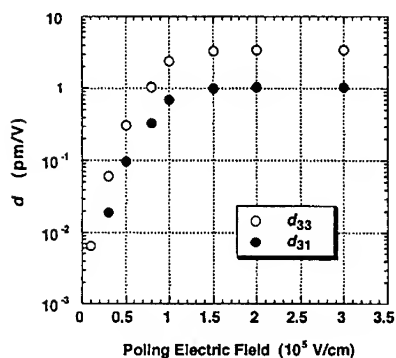


FIGURE 2 d coefficients as a function of poling electric field

A Y-cut quartz with $d_{qz} = 0.5$ pm/V was used as a reference sample to obtain the absolute value of d coefficient.

The induced d coefficients, d_{33} and d_{31} , as a function of poling electric-field strength are shown in Fig. 2. d_{33} and d_{31} were obtained from the Maker-fringe patterns of s-s and p-s polarizations, respectively, where s-s and p-s mean relations of polarizations between fundamental-SHG lights. Both d_{33} and d_{31} increase with increasing the poling

field up to about 1.5×10^5 V/cm, and then the value gets saturated. The largest values measured in that work were 3.4 ± 0.3 pm/V for d_{33} and 1.1 ± 0.2 pm/V for d_{31} .³ The value of d_{33} is exactly 3 times as large as that of d_{31} in all range of the poling electric-

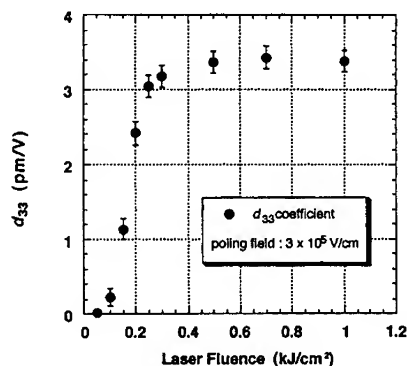


FIGURE 3 d coefficient vs laser fluence

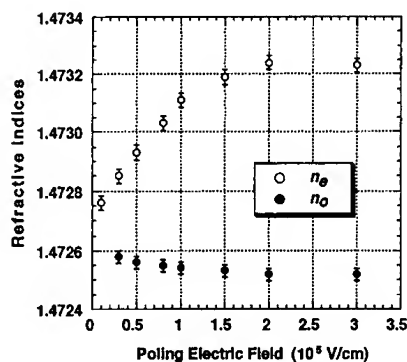


FIGURE 4 Refractive indices as a function of poling electric field

field. It should be emphasized that the value of d_{33} should be compared with d_{22} in LiNbO_3 , which is 2.6-3.0 pm/V.

Figure 3 shows variation of the induced nonlinearity as a function of fluence spent for the UV-poling. The behavior is somewhat complicated, and the dependence during the initial stage of poling is proportional to the fourth power of the fluence.

From the dependence of SHG on the polarization direction of fundamental light, the refractive indices at fundamental frequency are plotted in Fig. 4 as a function of the poling electric-field strength.⁶ n_e and n_o are the extraordinary and ordinary refractive indices, respectively, corresponding to the polarizations of fundamental light. n_e increases with increasing the poling field strength up to about 1.5×10^5 V/cm, and then saturates. n_o , on the other hand, decreases with increasing poling field, in contrast to the increase of n_e .

Decay Behaviors of the Induced Nonlinearity

Quantitative studies of decay behaviors of both d coefficient and optical absorption induced by the UV-poling should be the most interesting to reveal the role of defects in the induced second-order nonlinearity.

(a) d coefficient

The decay of induced d coefficient was investigated at various elevated temperatures. Values of d_{33} coefficient normalized by d_{33} at time $t = 0$ are plotted in Fig. 5 as functions of t . As shown in the Figure, single-exponential decays of the induced SHG were observed in all cases.

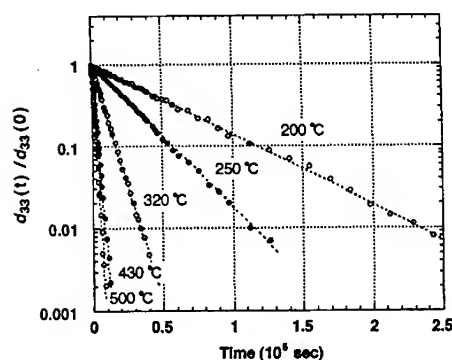


FIGURE 5 Decay of d_{33} at various elevated temperatures

The activation energy of decay time-constant of induced d_{33} coefficient, τ , has been deduced to be (0.41 ± 0.05) eV in the temperature range from 200°C to 500°C. The decay time-constant at 15°C was estimated by extrapolation as $\tau = (2.34 \pm 0.07) \times 10^7$ sec or approximately 280 days. To confirm this value, we actually measured the decay at 15°C, and the result at the temperature was

$(2.48 \pm 0.08) \times 10^7$ sec, in an excellent agreement with the extrapolation.⁷

(b) Optical Absorption

All of the optical measurements were carried out at room temperature. Before the UV-poling, an intense absorption band is usually observed around 5 eV, which has been known as due to oxygen-deficient vacancies such as neutral oxygen mono-vacancy

(NOMV) and neutral oxygen di-vacancy (NODV). After the poling, the absorption coefficient was increased in the region from 3.0 eV to 6.3 eV, as it produced various kinds of defects. Based on previous work⁴, the absorption spectrum was deconvoluted into four Gaussian components, which were assigned to Ge(1), NOMV, Ge(2), and GeE' centers with the respective absorption peaks at 4.5 eV, 5.1 eV, 5.5 eV, and 6.3 eV. Here, as was claimed in Ref. 4, Ge(1) and Ge(2) are the Ge-related electron-trapped centers (GEC) associated with fourfold-coordinated Ge ions with 1 or 2 next-nearest neighbor Ge ions, respectively. Excellent least-squares fitting was obtained, where respective peak positions and full widths at half-maximum (FWHM) were quite the same as those previously reported.⁸

After the poling, samples were kept at various elevated temperatures for measuring

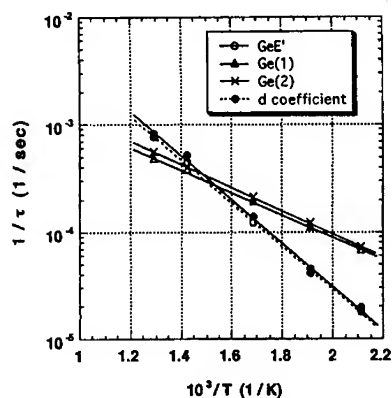


FIGURE 6 Arrhenius plot of τ

decays of the extra optical absorption.

Figure 6 is plots of decay time-constants of the peak heights deconvoluted as due to Ge(1), Ge(2), and GeE' centers.

Decay time-constant of the d coefficient is shown together in Fig. 6. This Figure clearly indicates that the induced non-linearity are very relevant to GeE' centers in the sense of the activation energy.

The activation energy of the decay of GeE' centers seen from the optical absorption is (0.40 ± 0.10) eV.

(c) Electrical Conductivity

To understand the decay mechanism of induced nonlinearity, DC electrical conductivity in the dark was measured at various temperatures as a function of time after the UV-poling. The measurement was carried out using the guard electrode technique. The dark

conductivity decay time again exhibited the Arrhenius behavior against temperature, and the activation energy was deduced to be (0.44 ± 0.05) eV.⁹ The value is quite close to those of both d coefficient and optical absorption attributed to GeE' centers.

Enhancement of the Induced SHG

When a sample was heat-treated at an elevated temperature in vacuum, and then UV-poled, the induced second-order nonlinearity was remarkably increased. This is just what one could expect from the relevance of GeE' centers to the second-order nonlinearity. The largest magnitude of d so far obtained is 5.1 pm/V.¹⁰ The value is exceeding the second largest coefficient of LiNbO₃, d_{13} , which is 4.7 pm/V. This result strongly indicates a possibility to enhance the nonlinearity with increasing GeE' centers and further improvement through defects control.

DISCUSSION

The large second-order nonlinearity induced in Ge-doped silica glass seems to be very relevant to the GeE' centers. However, the mechanism of how GeE' centers produce the effect is still unclear.

There are at least two possible mechanisms. One is that electrical dipoles of GeE' centers are oriented by the strong electric field during the UV-poling. This should not be the sole mechanism, however, because the behaviors shown in Fig.2 is not described by the Langevin function. The other is that the third-order term of polarization, $\chi^{(3)}EEE$, would work as a second-order term if one of the electric fields is any DC field. In the present case, one may think that an internal DC field in glass, E_0 , is built up probably from the free carriers released during the poling. Then, the third-order term, $[\chi^{(3)}E_0]EE$, acts like another second-order term. In this sense, a very suggestive fact is that the decay of dark conductivity gives quite a similar activation energy to those of d coefficient and optical absorption attributed to GeE' centers.

To summarize, in UV-poled silica glass doped with GeO₂ we have found the

following remarkable results:

- (1) A large d coefficient exceeding d_{13} of LiNbO_3 , was induced.
- (2) Formation and/or orientation of GeE' centers are quite relevant to the second-order nonlinearity induced by the UV-poling.
- (3) Enhancement of the induced nonlinearity with increasing number of GeE' center is possible through defects control.

As a whole, the UV-poling of the glass is quite promising to create innovative glass materials with an appreciable second-order nonlinearity, comparable to that in crystals. Quantitative measurements are still very necessary to understand basic mechanisms of the nonlinearity induced by the UV-poling.

From the standpoint of applications, lifetime of the induced nonlinearity should be as long as 10 years or even longer. This requirement also demands full understanding of the mechanism.

ACKNOWLEDGMENTS

The present authors thank Drs. K. Saito, M. Takahashi, Messrs. M. Ohama, and H. Yoshida for their assistance during the experiment.

REFERENCES

1. R. A. Myers, N. Mukherjee, and S. R. J. Brueck, *Opt. Lett.*, **16**, 1732 (1991).
2. T. Fujiwara, D. Wong, Y. Zhao, S. Fleming, S. Poole, and M. Sceats, *Electron. Lett.*, **31**, 573 (1995).
3. T. Fujiwara, M. Takahashi, and A. J. Ikushima, *Appl. Phys. Lett.*, **71**, 1032 (1997).
4. H. Hosono, Y. Abe, D. L. Kinser, R. A. Weeks, K. Muta, and H. Kawazoe, *Phys. Rev.*, **B46**, 11445 (1992).
5. J. Nishii, K. Fukumi, H. Yamada, K. Kawamura, H. Hosono, and H. Kawazoe, *Phys. Rev.*, **B52**, 1661 (1995).
6. T. Fujiwara, M. Takahashi, and A. J. Ikushima, *Jpn. J. Appl. Phys.*, **37**, 15 (1998).
7. T. Fujiwara, M. Takahashi, and A. J. Ikushima, *Electron. Lett.*, **33**, 980 (1997).

8. M. Takahashi, T. Fujiwara, T. Kawachi, and A. J. Ikushima, *Appl. Phys. Lett.*, **71**, 993 (1997).
9. T. Fujiwara, M. Ohama, and A. J. Ikushima, to be published.
10. T. Fujiwara, H. Yoshida, M. Ohama, and A. J. Ikushima, to be published.

EXPERIMENTAL EVIDENCE OF LASER BEAM SELF-FOCUSING IN
PHOTOREFRACTIVE MEDIA FROM THE NANOSECOND TIME-SCALE
TO STEADY-STATE

DELPHINE WOLFERSBERGER^{a,b}, NICOLAS FRESSENGEAS^{a,b}, JEAN
MAUFOY^a, GODEFROY KUGEL^b

^a Supélec, 2 rue Edouard Belin, 57078 METZ Cedex 3, FRANCE

^b Laboratoire Matériaux Optiques à Propriétés Spécifiques, Centre Lorrain
d'Optique et d'Electronique des solides, 2 rue Edouard Belin, 57078 METZ Cedex
3, FRANCE

Abstract This paper presents a way to achieve efficient optical limiting using the self-focusing process of a laser pulse in photorefractive medium on a nanosecond time-scale. A fundamental experimental investigation of the propagation characteristics in biased $\text{Bi}_{12}\text{TiO}_{20}$ of a continuous He-Ne laser beam at low power level is first reported and evidences the possibility to generate spatial solitons. Regarding the results obtained with such laser beams, systematic investigations have been achieved with a pulsed laser to study the self-focusing process on a nanosecond time-scale. We evidences that a laser pulse can be self-focused during the very short time of its transmission in the photorefractive media and by that way, we show that photorefractive materials can be used in optical power limiting devices.

INTRODUCTION

Laser beam self-focusing in photorefractive materials at microwatt power level has recently been the object of intense theoretical and experimental research, regarding the space-charge field build-up and its influence on the self-focusing properties. In particular, bright spatial solitons have been predicted¹⁻⁴ and observed⁵⁻⁹ in properly biased photorefractive media illuminated by a continuous laser. Theoretical studies have thus been recently developed on the time behavior of the self-focusing process¹⁰⁻¹¹, which allow to foresee that a beam can be self-focused in a time as short as desired if its intensity is high enough.

In this paper, we report experimental results on photorefractive self-focusing of both a continuous He-Ne laser beam and a ns pulsed doubled YAG-Nd laser beam in biased $\text{Bi}_{12}\text{TiO}_{20}$, which validate our predictions¹⁰⁻¹¹ and which provide a better understanding of the behavior of self-focused transversally bi-dimensional beams.

We have evidenced that the initial circular gaussian beam is asymmetrically self-focused, being more focused in the direction parallel to the field than in the other direction, leading to an elliptically shaped output beam. We have also evidenced a transient overfocusing behavior that appears for high laser powers (significantly higher than the dark irradiance): in that case, the beam rapidly self-focuses and relaxes to a less focused state. This phenomenon behaves qualitatively as earlier theoretical studies predicted, leading to reasonable extrapolations for much higher optical intensities and much shorter time scales.

Regarding the results obtained with continuous laser beams, we have achieved systematic investigations in $\text{Bi}_{12}\text{TiO}_{20}$ (BTO) to study the self-focusing process on a nanosecond time-scale. An experimental set-up using a KTP doubled YAG-Nd laser beam with pulse duration around 5 nanoseconds has been developed. Systematic measurements in BTO have thus been achieved to study the self-focusing process on a nanosecond time scale. Qualitative and quantitative results are then reported evidencing that photorefractive materials can be used in optical power limiting devices. Furthermore,

numerical simulations of the space-charge field build-up in a $\text{Bi}_{12}\text{SiO}_{20}$ crystal illuminated by a short pulse have been developed and bring to the fore a self-focusing process¹².

SELF-FOCUSING AND OPTICAL LIMITING : PRINCIPLE

One way to achieve efficient optical limiting is to build an optical system that modifies itself as a function of the incident beam intensity. For instance, if an inner beam waist was to be shifted in space for a high intensity incident beam, this latter would not focus on the detector anymore, thus avoiding its destruction. If the incident beam is self-focused within a nonlinear crystal, as for example in a spatial soliton like way, the beam waist is shifted and the goal is achieved (Figure 1).

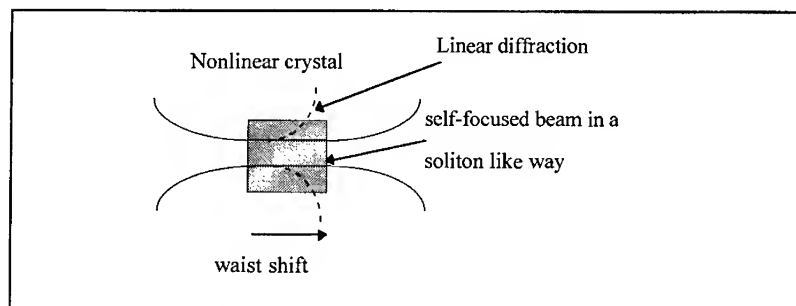


FIGURE 1 Principle of optical limiting by using a photorefractive crystal.

The main advantage of using a photorefractive crystal to do optical limiting is that this phenomenon is only sensible to the energy density and not to the power density of the laser beam, this for considerably lower energy than Kerr effects (5 mJ/cm^2). Furthermore, photorefractive materials have a low absorption coefficient so that the excess of received energy is not stocked in the medium.

CONTINUOUS WAVE LASER INVESTIGATION

We have carried out a systematic experimental investigation on photorefractive self-focusing in $\text{Bi}_{12}\text{TiO}_{20}$, using a continuous laser beam at low power level (in the microwatt range). Indeed, a spatially cleaned He-Ne laser is focused on the entrance face of the crystal using plano-convex lenses, to a beam waist w of $20\text{ }\mu\text{m}$. Using the apparatus described on Figure 2, where the light transmitted through a far field aperture is proportional to the beam diameter on the crystal output face, the output beam diameter is monitored during a few tens of seconds, for both the directions parallel to the applied electric field and perpendicular to it. These measurements have been made systematically as a function of the ratio r of the beam peak intensity over background irradiance and as a function of the applied electric field E_{ext} .

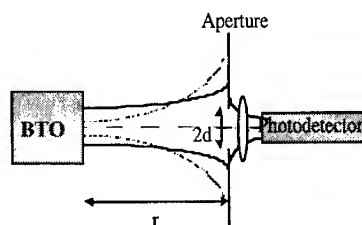


FIGURE 2 Principle of the indirect observation for quantitative measurements

Figure 3 shows a parallel self-focusing measurement in the direction of the applied electric field. It evidences, at the application of the field, the occurrence of a temporally short over self-focusing state, which relaxes toward a steady-state behavior until the field is switched off. We showed from a reasonable extrapolation of our results that the self-focalised beam can be obtained at time scales as short as desired for much higher intensities¹³.

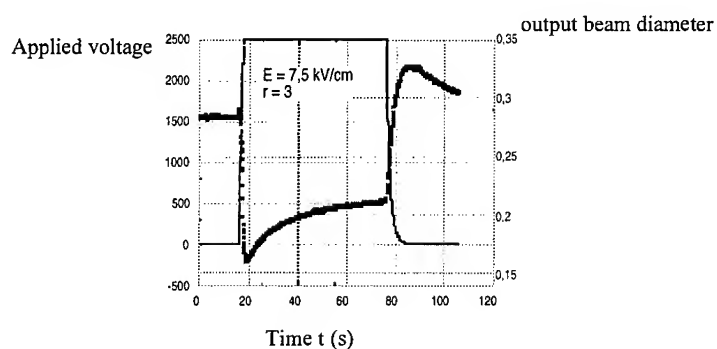


FIGURE 3 Typical time dependence of the output beam diameter measured before, during and after DC field application on a BTO crystal with $E_{\text{ext}} = 7.5$ kV/cm, $r=3$, $I=10$ mW/cm² and $w=20$ μ m.

EXPERIMENTAL STUDY OF THE SELF-FOCUSING PROCESS IN THE PULSED REGIME

Experimental apparatus

The experiments were performed on an experimental set-up represented on Figure 4, specially designed for the observation of self-focusing effects in photorefractive (PR) crystals under the influence of a short pulse. A KTP doubled YAG-Nd laser pulse of various intensity is focused on the sample entrance face on a PR medium with an adjustable waist (between 10 and 30 μ m). The polarization of the laser beam can be chosen using a half-wave plate along the transverse or the perpendicular direction of the DC electric field applied (which can vary from 0 to 6.2 kV/cm). Between two pulses, we use a uniform illumination to erase the crystal in order to avoid memory effects from successive pulses. The output face of the crystal is observed by two different techniques : by a CCD camera to take qualitative measurements (direct observation); by a spatial filtering technique (measuring the pulse intensity on a photodiode) to measure the output beam waist (indirect observation).

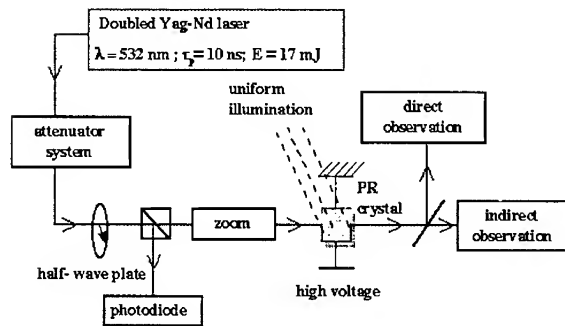


FIGURE 4 Experimental set-up for measuring the self-focusing process in the pulse regime

We have performed systematic investigation on a crystal of $\text{Bi}_{12}\text{TiO}_{20}$ (BTO) provided by D.Rytz from FEE Idar-Oberstein (Germany). The measurements on BTO have been done for different input waists (10, 20 and 30 μm) as a function of the field (from 0 to 6.2 kV/cm) and for different values of the energy densities of the input beam (between 1 and 5 mJ/cm^2).

Qualitative measurements

By the direct observation system using a CCD camera, we observe the output face of the crystal to evidence qualitatively the self-focusing process. First, we take an image when a laser pulse passes through the crystal without any applied electric field: in this case, we just see the natural diffraction. Secondly, we take an image when a light pulse passes through the crystal when a high voltage is applied. We compare the two images and bring to the fore a significant self-focusing process in BTO. These first experiments have been performed with a laser pulse self-focused at the entrance face of the crystal with a waist of 15 μm and an energy density d_e of 40 mJ/cm^2 under the influence of an external electric field of 6.2 kV/cm.



FIGURE.5 Images of the output face of the BTO crystal for a waist $w = 15 \mu\text{m}$, $d_e = 40 \text{ mJ/cm}^2$, output polarization = 0° (parallel to the field) (a) without any applied electric field (b) for $U = 2500 \text{ V} \Rightarrow E_{\text{ext}} = 6.2 \text{ kV/cm}$

Figure 5 shows the two images taken in such a case. The first one shows the natural diffraction; on the second, we remark that the intensity in the center of the beam is enhanced : working with pulses of same overall energy, this tends to show that the beam is self-focused.

Quantitative measurements

The direct observation is a method which permits to evidence the phenomenon of self-focusing qualitatively, but it does not allow to observe easily the evolution of the beam output waist with time during the pulse duration. In order to estimate the diffraction coefficient $\alpha(t)$, defined as the ratio of the output over the input beam diameters, as a function of time, we used the indirect observation method described before.

Systematic measurements have been performed in order to determine the beam width evolution of and during the light pulse with the electric field OFF and ON. The time evolution of the diffraction coefficient of the pulse is then obtained by making the point to point ratio of the first over the latter. Figure 6 represents a typical measured output beam diameter during one pulse. This figure confirms that the laser beam is self-focused during the pulse duration and show that the process becomes more intense for higher voltage.

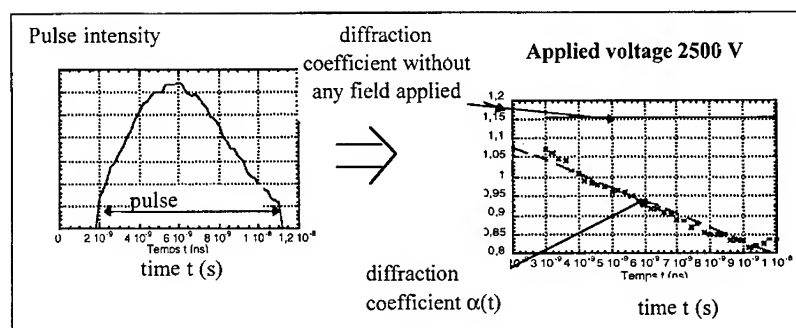


FIGURE 6 Typical time dependence of the diffraction coefficient during the pulse duration in biased BT0 for a waist $w=20 \mu\text{m}$, $d_e=5 \text{ mJ/cm}^2$, output polarization = 0° (parallel to the field).

As we can see on Figure 6, the diffraction coefficient is decreasing with time during the pulse duration; this is due to the memory effect of BTO crystals. Indeed the apparent linearity of the coefficient is due to the fact that self-focusing is sensitive to the fluence of the beam. Since we have to consider only the points over a given significant pulse intensity, this quantity behave quasi-linearly with time within our condition of measurements.

To analyze those systematic studies, we focused our analysis on two characteristic values of $\alpha(t)$: the value at $t=\tau_p/2$ and at $t=\tau_p$, where τ_p represents the pulse duration. Figure 7 reports the diffraction coefficients as a function of the applied voltage at those two different times. It emphasizes that the self-focusing process seems linear with the electric field applied; the effect is more intense at $t=\tau_p$ than at $t=\tau_p/2$.

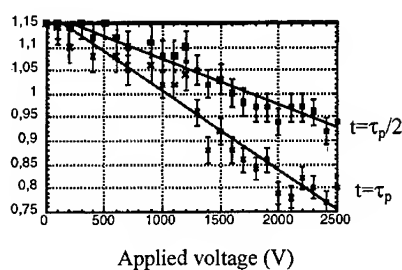
diffraction coefficient α 

FIGURE 7 Applied voltage dependence of the diffraction coefficients corresponding to $t = \tau_p/2$ and $t = \tau_p$

CONCLUSION

We have investigated experimentally the self-focusing process in photorefractive materials from the continuous laser light to nanosecond time scale pulses, in order to use this phenomenon for optical power limiting. Results in the continuous regime show that the transient self-focusing process can be reached in a very short time for high power lasers. Measurements in the pulse regime with a pulse duration of 5 ns confirm this result: we succeeded in self-focusing a laser pulse in a BTO crystal while it passes through the crystal. This result demonstrates that the photorefractive phenomenon can be used for optical limitation. More measurements are on the way in different experimental configurations, to test the self-focusing process with different intensities of the laser pulse, different polarizations, different types of crystals.

ACKNOWLEDGEMENTS

The authors wish to thank D.Rytz, from the Forschungsinstitut für Mineralische und Metallische Werkstoffe Edelsteine / Edelmetalle GmbH (D-55716 Idar-Oberstein, Germany), for useful discussion and for his $\text{Bi}_{12}\text{TiO}_{20}$ crystal on which our experimental studies have been conducted.

REFERENCES

1. M.Segev, B.Crosignani, A.Yariv, Phys.Rev.Lett., **68**, p. 923 (1992)
2. B.Crosignani, M.Segev, D.Engin, P.Di Porto, A.Yariv, G.Salamo, J.Opt.Soc.Am.B, **10**, p. 446 (1993)
3. M.Segev, B.Crosignani, P. Di Porto, G.C.Duree, G.Salamo, E.Sharp, Opt. Lett., **19**, p. 1296 (1994)
4. D.N.Cristodoulides, M.I.Carvalho, Optics Letters, **19**, p. 1714 (1994)
5. G.C.Duree, J.L.Schultz, G.J.Salamo, M.Segev, A. Yariv & al., Phys.Rev.Lett., **71**, p. 533 (1993)
6. G.Duree, G.Salamo, M. Segev, A.Yariv, B.Crosignani, P.Di Porto, E.Sharp, Optics Letters, **19**, p. 1195 (1994)
7. M.D.Iturbe Castillo, P.A.Marquez Aguilar, J.J.Sanchez Mandragon, S.Stepanov, V.Vysloukh, Appl.Phys.Lett., **64**, p. 408 (1994)
8. M.F.Shih, M.Segev, G.C.Valley, G.Salamo, B.Crosignani, P.Di Porto, Elec.Lett., **31**, p. 826 (1995)
9. M.T.Taya, M.C.Bashaw, M.Segev, G.C.Valley, Phys.Rev.A, **52**, p. 3095 (1995)
10. A.A.Zozulya, D.Z.Anderson, Opt. Lett., **20**, p. 837 (1995)
11. N.Fressengeas, J.Maufoy, G.Kugel, Phys. Rev. E, **54**, p. 6866 (1996)
12. D.Wolfersberger, N.Fressengeas, J.Maufoy, G.Kugel, Journ.KoreanPhys.Soc., **32**, pp. S436-S438 (1998)
13. N.Fressengeas, D.Wolfersberger, J.Maufoy, G.Kugel, Opt.Comm., **145**, p. 393 (1998)

ELECTROOPTICAL PROPERTIES OF POLYVINYLSHALOGENCARBAZOLE'S

JERZY SANETRA^a, JACEK NIZIOŁ^b, PAWEŁ ARMATYS^a, RYSZARD CHRZĄSZCZ^a,
STANISŁAW NIZIOŁ^b, IVAN KITIK^c, A. MEFLEH^d

^aCracow University of Technology, Cracow, Poland

^bUniversity of Mining and Metallurgy, Cracow, Poland

^cPedagogical University of Częstochowa, Częstochowa, Poland

^dInstitute of Physics, University of Perpignan, France

Abstract PVK modified by substituting chlorine in positions 3 and 6 was studied in order to determine its photo and electroluminescence characteristics as well as electrooptic properties. Halogens as electronegative atoms strongly influence the electron structure of a carbazole group modifying its UV and VIS spectrum and dielectric properties. The studies concerning electrooptic properties, photoluminescent and electroluminescent spectrum for the LED-type structure have been performed on the following polymers: PVK, P3ClVK and P3,6ClVK. Photoluminescent spectra in the temperature range 80 – 300 K were obtained. The experimental results were correlated with the calculations of the molecular orbitals (MO) using the ab initio non-local pseudopotential method.

KEYWORDS: polymer, PVK, NLO, LED

INTRODUCTION

PVK has been a research subject for a number of years now. It displays a wide range of physical and chemical properties, which are interesting as far as basic research and applications are concerned. The materials are also stable and relatively easy to process. Several derivatives of N-vinylcarbazole have been used in the synthesis of a new group of polymers which shows semiconductivity as well as photosensitive and dielectric properties.¹

Polysiloxanes, which were modified by pendant carbazole groups using electrochemical method, have electrochromic properties. They are prepared as thin films which may be transparent depending whether they are in a reduced or oxidized state². Recently studies on the photoluminescence (PL) and electroluminescence (EL) of PVK, particularly its blends used in multilayer devices have been extensively performed; e.g. electroluminescence of pure poly(N-vinylcarbazole) and its blends with a multiblock copolymer (CNMBC) were presented by B. Hu & all³. These blends EL spectra maximum vary from green to blue as the weight ratio of the components is changed. A new peak in EL emission spectrum appears which is not present in either of the two components in their pure form. In this case the formation

of an exciplex between the components is suggested.

Introducing new substituents into the aromatic carbazole group results in considerable changes in the physical and chemical properties of the obtained polymers. It significantly influences luminescent and photorefractive properties. The materials which show photorefractive effects must be characterized by large photoconductivity and secondary non-linear optical properties; namely, by the Pockels effect.

This article presents the results of the research on pure PVK and on the PVK's with chlorine substituted in the position 3 and in the positions 3 and 6 (Fig. 1).

It concerns the following properties:

- dependence of a temperature upon the photoluminescent properties
- electroluminescent properties of the LED - type structures ITO/PVK/Ca/Al,
- photorefractive properties.

MATERIALS

Monomers:

N-vinylcarbazole /Fluka AG/ was crystallized from methanol.

N-vinylchlorocarbazoles:

Suitable 3 and 3,6 chlorine-carbazole derivatives were chlorineethylated towards chlorinoderivatives of N-(2-chloroethyl)-carbazole by ethylene chloride under PTC conditions. Then monomers were obtained by elimination of hydrochloride from chlorinoderivatives with N-(2-chloroethyl)-carbazole in the ethanolic solution base. Finally, monomers were purified by crystallization of ethanol. The purity of monomers was tested by means of the GCMS method.

The polymerization procedure:

First the monomers were polymerized at 60°C in a dry DMS solution in the presence of AIBN (conc. 0.005 ml/l). The polymerization was carried out in the argon atmosphere. Then, the polymer was put in methanol in the Soxhlett apparatus for 24 hours; finally, it was precipitated and dried in vacuum.

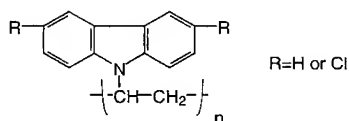


FIGURE 1. Molecular structure of PVHK.

SPECTROSCOPIC RESEARCH

Absorption spectra

Optical absorption spectra were obtained using the Perkin-Elmer UV-VIS LAMBDA 19 spectrometer in the range from 180 to 400 nm. The investigated samples were prepared as thin films on a quartz substrate. UV-Vis absorption spectra of PVK, P3CIVK and P3,6CIVK are presented in the Fig. 2. With regard to pure PVK, the results of survey comply quite well with those presented in the work¹. As for P3CIVK and P3,6CIVK, the spectra structures are similar. However, a clear red shift of the absorption maximum, greater for double Cl substituted carbazole group than for single substituted one, could be observed. The obvious influence of the substituted atoms of Cl on the energy of excitons may also be seen.

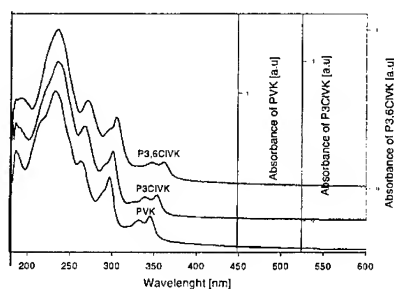


FIGURE 2. Photoabsorption spectra of PVK, P3CIVK and P3,6CIVK

Photoluminescence spectra

Photoluminescent properties were investigated using ORIEL MULTISPEC II spectrometer with fiber optics and a pulse N_2 laser ($T=5$ ns, $\lambda=337$ nm) as the source of the exciting light. The samples were prepared using the spin-coating method as thin films (about 100 nm thin) on a leucosapphire substrate. THF was used as a dissolvent. Then, they were (together with the substrate) placed on the cryostat holder. The leucosapphire substrate was fixed to the cooper holder along the circle with the radius of 5 mm and the width of 1.5 mm. The temperature was controlled by means of thermocouple Au-chromel, which was in direct contact with the sample. The temperature in the investigated ranges was stabilized along the sample's radius exact to 1K. The experiment lasted 120 s. The measurements were done in the temperature ranging from 293 K to 82 K. The results of the investigations for PVK, P3CIVK and P3,6CIVK are presented respectively in the Fig. 3, 4 and 5.

The spectrum of the photoluminescence was observed in the spectral range from 350 nm to 700 nm. It was considerably influenced by the presence of chlorine substitute. The spectra of PVK and P3ClVK are similar. At room temperature, in the range from 370 nm to 450 nm there is a maximum for $\lambda = 420$ nm with a certain fine structure present on a shorter wavelength shoulder. In the range of 470 nm to 600 nm the intensity of the spectrum is smaller changing with the length of the waves. Lowering the sample's temperature causes significant changes in the photoluminescence spectrum. Then an increase in the intensity of the spectrum around 420 nm and also in the spectral structure is clearly seen. A maximum for $\lambda = 380$ nm, whose intensity is higher than the intensity for $\lambda = 420$ nm, appears.

At low temperature there are no significant changes in the intensity of the spectrum for PVK (Fig.3) in the range higher than 450 nm. As for P3ClVK photoluminescence spectrum, similar behavior can be observed what is showed in Fig.4. Together with a general tendency to increase of overall intensity the new peak, around 380 nm, becomes dominant.

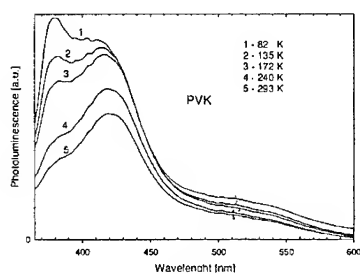


FIGURE 3. PL spectra of PVK

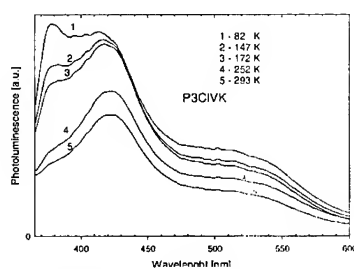


FIGURE 4. PL spectra of P3ClVK

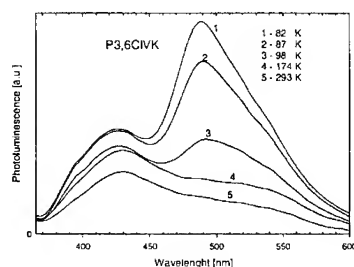


FIGURE 5. PL spectra of P3,6ClVK

On the other hand, for double Cl substitutes (P3,6ClVK) the photoluminescent spectrum differs

considerably from the ones described above. At the room temperature there is a weak and wide peak for $\lambda=430$ nm in the spectrum, while at low temperatures strong, wide maximum for $\lambda=500$ nm appears.

The absorption and photoluminescent spectra prove that the states of excitation in the investigated PVK are possible to obtain. Therefore, there is a possibility of receiving the electroluminescent signal.

Electroluminescence spectra

A sandwich-like structure of the indium-tin-oxide/PVK(or P3ClVK or P3,6ClVK)/Ca/Al LED was employed for investigation of electroluminescence spectra of various poly(N-vinyl-carbazoles). Thin polymer films with thickness of about 100 nm were obtained by spin-coating THF solution onto a ITO substrate. The injected carries have a low mobility because they move by hopping and they recombine giving excitons in organic layers. The electroluminescence spectra obtained for PVK's are presented in

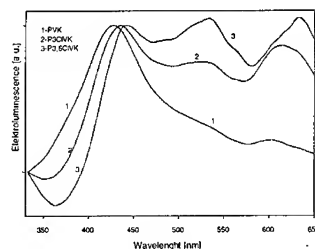


FIGURE 6. EL spectra of PVK, P3ClVK and P3,6ClVK

Fig. 6⁴. Apparently the results depend on the polymer compositions used. By changing the halogen substituents in the carbazole ring additional electroluminescence bands are generated: namely, EL spectrum of PVK possesses two peaks. One of them at 428 nm is caused by the formation of excitons in the carbazole molecule and the other (around 618 nm) appears due to the excimers emission⁴. These results are consistent with those one presented by Hu³. Introducing a chlorine atom into the carbazole molecule profoundly changes the luminescent spectrum, that is, the intensity around the peak of 618 nm increases and also an additional electroluminescent band appears around 530 nm.

NLO properties

Substitution of the halogens, such as Cl, in the carbazole ring generates the effect of charge transfer electron, which is important for the nonlinear optics.

Two main ways of enhancing such interactions and changing NLO susceptibility properties are proposed. The first one is connected with applying an external electric field or a photon illumination while

the second one deals with the possibility of chemical modifications by halogen ions, which causes a considerable essential charge transfer both on the intra- and the intermolecular levels.

The optical and non-linear optics methods have been chosen in the experiment as an effective tool to detect the appearing changes. They are very sensitive both to the changes of electron density distribution as well as to the electron-vibration anharmonic interactions.

All the powder-like specimens were embedded and mixed into the liquid photopolymer oligoetheracrylate photo composition⁵. The photopolymer solidification was performed using UV nitrogen laser ($\lambda=337$ nm) with the light power density of 45 W/cm^2 . Consequently, the homogenous distribution of the embedded powders was received. This mixture was embedded into the interplate quartz space. The distance between the two quartz determines the specimen thickness. ITO electrodes allow to perform electropoling within the electric field of the strength ranging from 10 to 1000 V/cm. Birefringence was measured by the standard Senarmont method for the He-Ne laser wavelength ($0.633 \mu\text{m}$). As a source of the photoinduced changes YAG-Nd laser with the power 35 MW and pulse duration 0.8...60 ps was used.

The obtained results for P3CIVK are presented in Fig. 7 and 8. The applied electrostatic field leads to a great increase both of the electrooptic coefficient r_{22} and the photoinduced birefringence Δn_{ij} . An increase of the material thickness forces a smooth increase of the r_{22} .

The results comply with the data calculated using the method described below. For the other samples (PVK, P3,6CIVK) the changes of r_{22} were smaller. The competition between the creation of the non-centrosymmetry electronic charge density distribution and the external induced-electron-vibration anharmonic states is the main cause of the observed irreversible and reversible changes. The observed phenomena are caused by photogeneration of electrons from occupied to nonoccupied conducting states and by the interaction of the electron-vibration excited states.

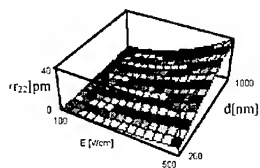


FIGURE 7. Dependence of electrooptical coefficient r_{22} versus applied electric field E to the specimens embedded within the oligoetheracrylate matrices with the thickness d .

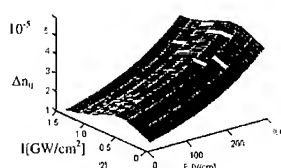


FIGURE 8. Dependence of the photoinducing birefringence Δn_{ij} versus external applied electrostatic field E and photoinducing beams I .

Molecular dynamics geometry optimization of the separate molecule was performed employing the force field MM⁺ method⁶. Intermolecular interactions were calculated using solid state quasi-Brillouine

zone approach. Plane wave basis set and Bachelet Hamann Schluter norm-conserving nonlocal pseudopotential⁷ basis set was used for the calculations. Total energy minimisation was carried out by the orthogonalization to the LCAO wavefunctions by the procedure described in⁸. According to the MO electronic wavefunctions obtained in a way described above, the vibration modes were recalculated and hyperfine MO electron-vibration was estimated, all of which is presented in the Fig 9. The considerable contribution (up to 33%) of electron-phonon interactions to the absolute values of the electrooptic tensor r_{22} have, then, been revealed. Calculated MO wave functions for the HOMO states for the different pure carbazole and modified specimens: 3-Cl-carbazole, 3,6-Cl-carbazole indicate the redistribution of the MO wave functions in the area of the Cl atoms.

CONCLUSIONS

The results of the calculations for the monomer VK, 3CIVK, 3,6CIVK allow to explain in the qualitative way the changes that appear in the photoluminescent spectra and depend on the temperature. Basing on the experimental results using UPS method, the UV-VIS absorption and the photoluminescence as well as the calculations described above one may identify the energy structure of the excited states, which are shown in the fig. 9, as the Jablonski's diagram. Those diagrams made for the investigated samples are similar. The only thing different is the energy of the levels. A difference can be observed for the photoluminescent spectrum. The analyze of the calculations makes it evident that the photoluminescence is emitted from the band 2 (fig. 9) for PVK and P3CIVK when the temperature decreases. On the other hand, for P3,6CIVK in low temperatures the emission from 1 band appears in the range of 500 nm, what cannot be seen in the cases of PVK nor P3CIVK.

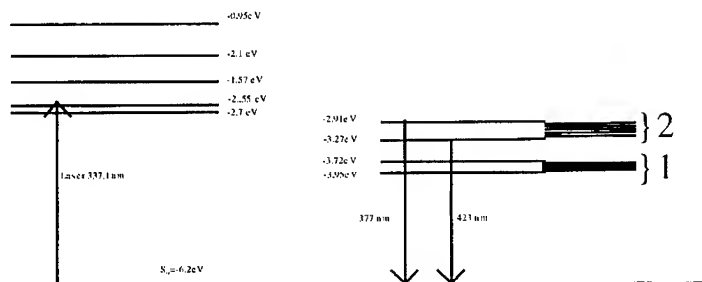


FIGURE 9. Jablonski's diagram for P3CIVK

The electrooptical coefficient r_{22} obtained for PVHK polymers can also be described within the presented model of electron-vibration interactions.

ACKNOWLEDGEMENTS

The Polish Committee for Scientific Research (KBN) financially supported this work through Grant No. 3T09B06615.

Stimulating and valuable discussions with Professor J. Pielichowski and Dr. D. Bogdal as well as Dr. P. Barta are gratefully acknowledged.

REFERENCES

1. J. Pielichowski, Z. Kowalczyk, *Tetrahedron*, 1403, **37** (1981)
2. I.D. Bartellet and A.R. Hepbutu, *Synthetic Metals*, 1241, **70** (1995)
3. B. Hu, Z. Yang and R.E. Karasz, *J. Appl. Phys.*, 2419, **76** (1994)
4. J. Sanetra, P. Barta, S. Nizioł & all, *Synthetic Metals*, 123, **94** (1998)
5. I.V. Kityk, R.I. Mervinskii, J. Kasperczyk & S. Jossi, *Materials Letters*, 233, **27**, (1996).
6. A.D. Becke, *J. Chem. Phys.*, 1372, 98, (1993).
7. G.B. Bachelet, D.R. Hamann, M. Schluter, *Phys. Rev.*, 4199, **26B**, (1982).
8. I.V. Kityk, J. Kasperczyk, B. Andrievskii, *Physics Letters*, 161, **216 A**, (1996).

PHOTOINDUCED TRANSPARENCY AND TWO-PHOTON ABSORPTION IN SOME MODIFIED FULLERENES

B. SAHRAOUI and X. NGUYEN PHU
University of Angers, POMA Laboratory, EP CNRS 130
2 bd Lavoisier, UFR Sciences, 49045, Angers, France

I. V. KITYK
Institute of Physics WSP, Al. Armii Krajowej 13/15,
Czestochowa, PL-42201, Poland

P. HUDHOMME
Laboratoire de synthese Organique, UMR CNRS 6513
Universite de Nantes, 2 rue de la Houssiniere 44332, Nantes cedex, France

A. GORGUES
Laboratoire d'Ingenierie Moleculaire et Materiaux Organiques, UMR CNRS 6501
Universite d'Angers, 2 bd Lavoisier, France

KEYWORDS: fullerene, two-photon absorption, photoinduced phenomena

Abstract The subject of study is fullerene modified by 2-thioxo-1,3-dithiole cycloadduct (CA) and tetrathiafulvalene (TTF) derivatives. Phototransparency (PT) and two-photon absorption (TPA) were measured versus pressure and time delay between the pump and probe beams at $\lambda=530$ nm. A guest-host photopolymer technique was used to manufacture the investigated samples. The performed measurements show that maximal photoinduced changes are observed at temperature about 88 K and time delay between the pump and probe light within the 0.2 - 0.5 ps time range. An essential role of a nature the organic donor TTF or CA chains on the observed photoinduced effects is shown. It was found that length of the organic donors essentially varies behavior of the pressure-induced optical and nonlinear optical susceptibilities. As an explanation of the observed behaviors could serve the charge density redistribution's, bending of the CA or TTF planes and intermolecular charge transferring.

INTRODUCTION

Recently one can observe an increasing interest to the non-linear optical properties of the fullerene-like compounds^{1,2}. One of the promising directions to enhance the non-linear optical susceptibilities consists in addition of the prolonged donor-like organic molecule. In order to investigate the influence of the molecule on the optical response of the fullerenes we have added 2-thioxo-1,3-dithiole cycloadduct and tetrathiafulvalene derivatives to the proper fullerenes. The corresponding chemical formula and notation are presented in the Fig. 1 a and Fig. 1b.

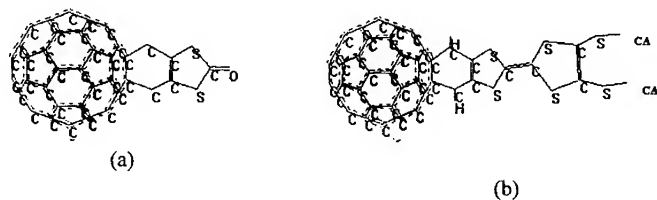


Figure 1. Chemical formula of the C₆₀-2thioxo-1,3-dithiole cycloadduct – (a); C₆₀ with the added tetrathiafulvalene derivatives: (b)- CA=S(CH₂)₄-CH₃; (C)-CA=CH₃.

An addition of the prolonged TTF or the CA groups leads to essential delocalisation of the intra- and intermolecular electronic charge density distribution. The later one leads to an increase of the matrix dipole moment determining the main optical susceptibilities.

In the present work we study an influence of the mentioned chemical groups on the PT and non-linear optical susceptibilities, particularly on the TPA. To clarify physical mechanisms of the observed effects all the measurements were performed versus applied hydrostatic pressure (up to 19 GPa) using pump-probe time delay laser technique. Relaxation times contributing to the PT (linear optical response) and TPA (imaginary part of the third order non-linear optical response) are different due to

different orders of photon-electron interactions. Our prevailing molecular dynamics calculation indicates a possibility of bending the TTF or CA planes under the applied hydrostatic pressure and simultaneously changes intermolecular interaction and charge transfer³.

Varying temperature we searched maximal values of the corresponding optical responses. The performed investigations are interesting both for the pure scientific point of view as well for applied aspect for searching new non-linear optical materials.

EXPERIMENTAL METHODS

The chemical synthesis of the mentioned compounds using the Diels-Alder reaction is described in works^{4,5}. To perform the optical investigations the newly synthesized powder-like specimens were embedded and dissolved in the oligoetheracrylate photopolymer liquid composition. An external electrostatic field of the strength 300 - 800 kV/cm was applied to order the embedded chromophores (electropoling procedure) along the CA- or TTF chains (direction x). Detailed technology of the specimen preparation is presented in the Ref. 6. Control of the specimen field-induced orientation was carried out using optical polarized method. Solidification of the liquid photopolymer with the embedded modified fullerene-like compounds was carried out using nitrogen laser ($\lambda=337$ nm, $W=45$ W/cm²) during 3 min. The obtained specimens have a form of parallelepipeds with the sizes of 5 mm x 4 mm x 3mm. Space non-uniformity of transparency through the sample surface was about 7 %. Due to relatively high level of the space transparent non-uniformity we carried out the measurements in different points of the samples. To evaluate absolute values of the TPA coefficients we prepared using the similar technology the solidified specimens with embedded LBO and pure C₆₀ compounds. The TPA values for these compounds are well known. Using technique of correlational analysis we evaluated the absolute values of the TPA in the modified fullerenes.

The pumping process was provided using picosecond pulses of $\lambda=530$ nm generated by the doubled YAG:Nd laser light. The laser light beams were polarized using a rotating Fresnel polariser and the output light intensities were detected using a

FEU-79 (FEU-39) photomultipliers. The measurements were performed in a single-pulse regime, with a pulse frequency repetition of 12 Hz and a tunable pulse duration within 1 ps. The TPA coefficients were determined from expression $T \approx 1 - \beta \ell I_p$, where β is the TPA coefficient, ℓ is the thickness of investigated sample, and T is the intensity dependent transparency. The polarization of the pumping and probing beams was carried out using Glan-Thompson polarisers with the polarization degree of about 99.996 % at wavelength of 530 nm. The measurement technique is similar to the described in Ref. 9 ones.

To evaluate absolute values of the TPA coefficients, the LBO crystallites embedded in the liquid oligoetheracrylate matrices were used. Independently we carried out the measurements for the samples of C_{60} and solidified oligoetheracrylate matrices. This is necessary to extract an influence of the host polymer background. The nonlinear contribution was extracted from the intensity-dependent transparency measurements using a standard method⁷. Simultaneously we extracted an influence of linear absorption (220 cm^{-1} , $\lambda=530 \text{ nm}$) and the Fresnel reflection 0.048. The choice of the oligoetheracrylate matrices is caused by low value of their TPA coefficient (below 0.002 cm/GW). An averaging statistics through the sample surface was performed to avoid a space optical non-uniformity within the oligoetheracrylate matrix.

To perform time delaying measurements we use the $\text{Li}_2\text{B}_4\text{O}_7$ single crystals. The splitting between the probe and pump beams is done using the quartz splitter. Detections of the output signal is performed using the boxcar (Hiyu-95 with the time gate 250 ps).

To exclude an influence of the hyper-Raman scattering, the additional investigations of the scattered light up to 3000 cm^{-1} have been carried out starting from the wavelength $\lambda=530 \text{ nm}$. We have detected three hyper-Raman maxima within $1200 \text{ cm}^{-1} \dots 1800 \text{ cm}^{-1}$ spectral range. Intensities of these maxima were at least 8 times weaker than the measured signal. In the case of the Raman and hyper-Raman measurements argon laser at 522 nm Ar^+ laser line and Spex Triplemate spectrometer have been used. A position-sensitive photomultiplier calibrated using helium-neon gaseous mixture discharge was used to detect the scattering light.

For optical measurements under applied hydrostatic pressures we have used a

special thermo-baro chamber with sapphire windows that allowed to perform the corresponding measurements in the high-pressure atmosphere within the temperature range 77- 450 K. A Mao and Bell type diamond anvil cell supplied with diamond optical windows was used for the measurements. The pressure and the temperature were changed within the 0.1-20 GPa and 77 - 300 K, receptively.

RESULTS AND DISCUSSION

From the Fig. 2 one can clearly see that the highest TPA values are observed for the (C) specimens. An appearance of the two-photon processes is observed at the pumping intensity $I=0.75 \text{ GW/cm}^2$. For the specimen (A) the corresponding processes appeared at the 1.14 GW/cm^2 . For the specimens (A) the two-photon processes are observed only for the $I=1.50 \text{ GW/cm}^2$. We present the values of the transparency in the arbitrary units because due to the space non-uniformity absolute values will be different for the different sample parts.

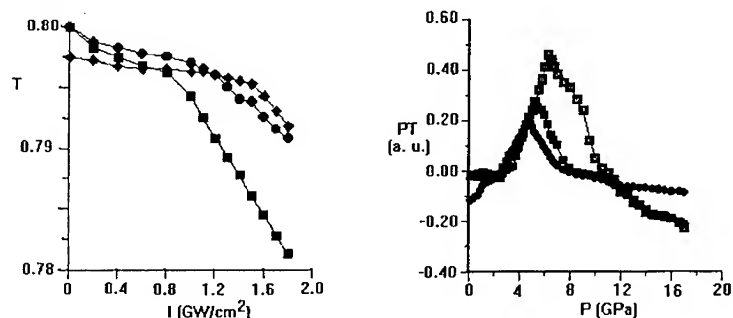


Figure 2. Behavior of the transparency (in arbitrary units) versus the pumping light intensity for the three different specimens for the different pump-probe samples: ■ - sample (B); • - sample (A); ♦ - sample (C). Measurements were done at $T = 88 \text{ K}$.

and we averaged all the data through the specimen surface. To obtain the

absolute values of the β we carry out correlational analysis with the LBO and C_{60} compounds. We present here all the data only for the 88 K because within the temperature range 77 - 105 K the observed PT and TPA achieve the maximal values.

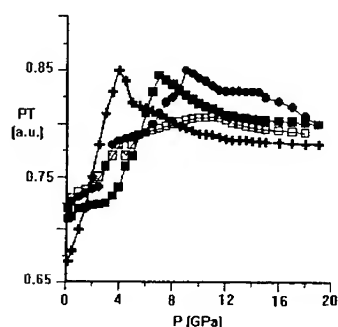


Figure 4. Behavior of the PT (in arbitrary units) for the compound (C) versus hydrostatic pressure for different delaying time between the pumping and probing beams: \circ - 0.2 ps; \blacksquare - 0.4 ps; \bullet - 0.6 ps; \square - 0.8 ps. The measurements were done at $T=88$ K.

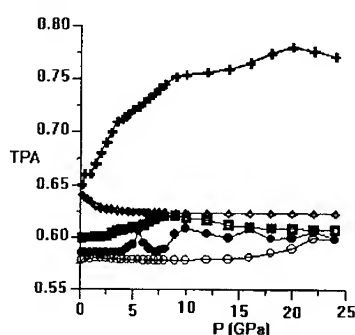


Figure 5. TPA dependencies (in arbitrary units) for the (C) versus the hydrostatic pressure for different delaying times t between the pumping and probing beams: \circ - 0.15 ps; \blacksquare - 0.4 ps; \bullet - 0.20 ps; \square - 0.25 ps; \diamond - 0.3 ps; $+$ - 0.26 ps.

In the Fig. 3 are shown dependencies of the PT versus the hydrostatic pressure p for different delaying time between the pumping and probing beams. First of all it is necessary to note changes of a sign in the PT- p dependencies with the varying pressures (at 3.45 - 3.67 GPa and 9.1 - 9.6 GPa). The pressure-dependent maxima are increased and shifted towards the higher pressures with the increasing hydrostatic pressures within the time region 0.8 - 0.2 ps. At higher pressures there exist at least two peaks in the corresponding PT- p dependencies.

In the case of the (C) specimens (see Fig. 4) the sign of the PT remains unchanged. The shapes of the PT- p curves are similar to the previous case. However the corresponding maxima decrease with increasing pressure and are shifted towards the higher pressures with increasing pump-probe time delay. The drastical changes begin at the times higher than 0.6 ps. The PT- p dependencies are relatively smooth. In the case

of the (A) compound the corresponding dependencies are very similar.

The TPA processes seem to be very sensitive to the pump-probe delaying time (see Fig. 5) with increasing pressure. With enhancing the time one can observe a change of the sign in the TPA-P derivatives. The maximum of the TPA-P changes are observed for the delaying times about 0.26 ps. Within the times about 0.20 ... 0.25 ps one can see a pressure-modulated TPA dependencies. The similar dependencies (but on the lower levels) are observed for the (A) and (B) compounds.

Table. Typical values of the TPA tensor components at $T = 88$ K.

Sample	β_{xyy} (cm/GW)	β_{xxx} (cm/GW)
C ₆₀	12.7	8.9
A	14.8	8.2
B	21.6	13.6
C	17.3	12.1

The obtained results show that the modification of fullerenes by the prolonged TTF and CA donor chains play an important role in the observed PT and TPA. The higher effects are observed for the intermediate TTF length (compound (B)). The applied external hydrostatic pressure changes the intermolecular interaction and the rotational degree of freedom. The observed changes indicate the key role of the prolonged S(CH₂)-CH₃ chain in the observed optical effects. All the effects are observed for the relaxation times typical for the electronic subsystem. Therefore one can eliminate contribution of the electron-vibration subsystem and to conclude the dominating role of the electronic parts the CA and TTF donor chains. The latter one have the typical relaxation times lying within the 0.2 - 2.6 ps³. Moreover, the performed *ab initio* molecular dynamics simulation under the applied hydrostatic pressures establish the three main mechanisms effectively contributing to the observed dependencies: intermolecular charge transfer, pressure-induced CA or TTF plane bending and intermolecular interactions. The latter one lead to essential changes of the matrix dipole moment determining the nonlinear optical susceptibilities. As a confirmation of the such prediction can serve the relatively high difference between the diagonal and off-diagonal TPA β tensor coefficients (see

Table). Moreover for the off-diagonal tensor components this difference increases with increasing absolute values of the β coefficients.

The similar photoinduced measurements were performed for the pure fullerenes⁸. The authors have revealed that the maximal value of the observed photoinduced changes was observed at temperatures about 90 K and time delay of 1.4 ps. This is in agreement with the obtained by us data. But the obtained values of the β in the Ref.8 are lower. It could be caused by an absence of the electropoling procedure essentially changing long-range correlation's in the mentioned work.

CONCLUSIONS

Essential influence of the CA and TTF donors on the photoinduced PT and PTA was revealed. The length of the CA planes essential role in the absolute values of the PT and the TPA as well in their pressure dependencies. The more detailed changes of the pressure-dependent PT and TPA features are observed within the delaying time within the 0.26 ... 1.5 ps. This ones indicates a dominant role of the electronic subsystem in the observed dependences. Hydrostatic pressure allows continuously to operate by the photoinduced optical parameters due to the possibility of changes the inter- and intramolecular interactions. With the increasing absolute value of the TPA the difference between the β_{xxxx} and β_{yyyy} increases also.

REFERENCES

1. W.J.Blau, H.J.Byrne, D.J.Cardin, T.J.Dennis, J.P.Hare, H.W.Kroto, R.Taylor, D.R.M.Walton *Phys.Rev.Letters*, 1423, 67, (1991).
2. F.Kajzar, C.Taliani, R.Danieli, S.Rossini and R.Zamboni *Chem. Phys.Lett.*, 418, 217, (1994).
3. B.Sahraoui, I.V.Kityk, X.Nguyen Phu, P.Hudhomme, A.Gorgues *Phys.Rev B*, (to be published).
4. C.Boulle, J.M.Rabreau, P.Hudhomme, M.Cariou, M.Jubault, A.Gorgues, J.Orduna and J.Garin, *Tetrahedron Letters*, 3909, 38, (1997).
5. C.Boulle, P.Hudhomme, M.Cariou, A.Gorgues, and J.Orduna *Tetrahedron Letters*.

81, 38, (1997).

6. I.V.Kityk, R.I.Mervinskii, J.Kasperczyk & S.Jossi.

Materials Letters. V. 27. N 4-5. 233, 27, (1996).

7. S.Cheng and L.Xin, In book: Proc 2 Photoinduced measurements
in condensed matters. Singapore, World Scientific, 1993, 210 p.

8. S.K.Anisimov, P.Petrakov J.Appl.Spectrosc., 567, 58, (1995)

NOTES FOR CONTRIBUTORS TO NONLINEAR OPTICS

As Gordon and Breach moves into the delivery of journals in electronic format, it becomes essential that authors prepare their manuscripts according to established specifications. The effectiveness of the search capabilities offered by electronic delivery will depend upon the care used by authors in preparing their manuscripts. Therefore, contributors are strongly encouraged to read these instructions carefully before preparing a manuscript for submission, and to check the manuscript for compliance with these notes before submitting it for publication.

Gordon and Breach online "offices" enable our authors to submit abstracts and full-text articles in virtually any file format, from anywhere in the world, at any time. Visit http://www.gbhap.com/Nonlinear_Optics/ to access a full range of internet author services.

MANUSCRIPTS

Papers should be typed with double spacing and wide (3 em) margins on good quality paper, and submitted in triplicate to any of the editors, or via a member of the Editorial Advisory Board. Submission of a paper to *Nonlinear Optics* will be taken to imply that it represents original work not previously published, that it is not being considered elsewhere for publication, and that if accepted for publication it will not be published elsewhere in the same form, in any language, without the consent of editors and publisher.

Language: English language is preferred, but French or German papers will be accepted if an English summary of 200–300 words is also supplied.

Abstract: Each paper requires an abstract of 100–150 words summarizing the significant coverage and findings. Non-English papers should have a similar abstract in the language, but must also contain an English-language abstract of 200–300 words.

It is a condition of acceptance by the editor of a typescript for publication that the publishers acquire automatically the copyright in the typescript throughout the world.

FIGURES

All figures should be numbered with consecutive arabic numbers, have descriptive captions, and be mentioned in the text. Keep figures separate from the text, but indicate an approximate position for each in the margin.

Preparation: Figures submitted must be of a high enough standard for direct reproduction. Line drawings should be prepared in black (India) ink on white paper or tracing cloth, with all lettering and symbols included. Alternatively, good sharp photoprints ("glossies") are acceptable. Photographs intended for half-tone reproduction must be good glossy original prints, of maximum contrast. Clearly label each figure with the author's name and figure number; indicate 'top' where this is not obvious. Redrawing or retouching of unusable figures will be charged to authors.

Size: The preferred width of submitted line drawings is 20 to 23 em with capital lettering 4mm high, to accommodate reduction to single-column width. Photographs for halftone reproduction should be about twice the desired size.

Color Plates: Whenever the use of color is an integral part of the research, or where the work is generated in color, the journal will publish the color illustrations without charge to the authors. Reprints in color will carry a surcharge. Please write to the Editor for details.

EQUATIONS AND FORMULAE

Mathematical: Mathematical equations should preferably be typewritten, with subscripts and superscripts clearly shown. It is helpful to identify unusual or ambiguous symbols in the margin when they first occur. To simplify typesetting, please use:

- (1) the "exp" form of complex exponential functions; (2) fractional exponents instead of root signs; and (3) the solidus (/) to simplify fractions—e.g. $\exp x^{1/2}$.

Chemical: Ring formulae, and other complex chemical matter, are extremely difficult to typeset. Please, therefore, supply reproducible artwork for equations containing such chemistry. Long reaction sequences should be designated as "Schemes" and treated like figures; i.e. keep artwork separate from the text, indicate in the margin an appropriate position, and supply a separate list of scheme captions. Where necessary, individual chemical formulae can be identified with bold arabic numbers. Chemical equations referred to in the text should be indicated with arabic numbers set over to the right, and in parentheses.

Marking: Where chemistry is straightforward and can be set (e.g. single-line formulae), please help the typesetter by distinguishing between, e.g. double bonds and equal signs and single bonds and hyphens, where there is ambiguity. The printer finds it extremely difficult to identify which symbols should be set

in roman (upright) or italic or bold type, especially where the paper contains both mathematics and chemistry. Therefore, please underline all mathematical symbols to be set italic and put a wavy line under bold symbols. Other letters not marked will be set in roman type.

TABLES

Number tables consecutively with roman numerals, and give each a clear descriptive caption at the top. Avoid the use of vertical rules in tables. Indicate in the margin where the printer should place tables.

REFERENCES

References and notes are indicated in the text by consecutive superior arabic numbers in brackets. The full list should be collected and typed at the end of the paper in numerical order. Listed references should be complete in all details, but excluding article titles in journals. Authors' initials should precede their names; journal title abbreviations should conform to *Chemical Abstracts* style. Examples:

1. A. B. Smith and C.D. Jones, *J. Appl. Phys.* **34**, 296 (1965).
2. R. B. Brown, *Molecular Spectroscopy* (Gordon and Breach, New York, 1970), 3rd ed., Chap. 6. pp. 95-106.

FOOTNOTES

Authors are encouraged to minimize the use of footnotes. A footnote may include the designation of a corresponding author of the paper, current address information for an author (if different from that shown in the affiliation), and traditional footnote content. Information concerning grant support of research should appear in a separate Acknowledgments section at the end of the paper, not in a footnote. Acknowledgments of the assistance of colleagues or similar notes of appreciation also properly belong in an Acknowledgments section, not in footnotes.

Footnotes should be indicated in the text by the following symbols: * (asterisk or star), † (dagger), ‡ (double dagger), ¶ (paragraph mark), § (section mark), || (parallels), # (number sign). Do not use numerals for footnote call-outs, as they may be mistaken for bibliographical reference call-outs or exponents. Type each footnote at the bottom of the typescript page on which its text call-out appears.

Footnotes within a table should be indicated by the same symbols listed above. Reinitialize symbol sequence within tables. Type footnotes to a table directly beneath the table.

It is assumed that, with the development of the World Wide Web (WWW), authors and/or the publisher will propose distribution of articles or parts of articles on the WWW. If the author knows the HTTP address of a referenced article on the WWW, this information should be added at the end of the reference. Please use the following style:

< www: http://www.blouk.com/article.html >

where http://www.blouk.com/article.html is the HTTP address.

TEXT CALL-OUTS TO FIGURES, TABLES, SECTIONS, SCHEMES

Text call-outs to figures, tables and other elements are the basis for searching articles on electronic delivery. Therefore, proper designation of text call-outs to figures and other elements is essential to the success of electronic delivery. When referring to a figure, table or other element within an article, always call the element by its full name: "See Table 1", "Figure 1 illustrates...", "Refer to Scheme 1". Do not use ambiguous call-outs (for example, "I illustrates...") that do not clearly denote the element being referred to.

SUBMISSION OF ARTICLES ON DISK

The Publisher welcomes article submission on disk. Disk files should be submitted with the final hard copy manuscript. The disk file and hard copy must match exactly.

When typing the article, do not include design or formatting information. Type all text flush left, unjustified and without hyphenation. Do not use indents, tabs or multi-spacing. If an indent is required, please note it by a line space; also mark the position of the indent on the hard copy manuscript. Indicate the beginning of a new paragraph by typing a line space. Leave one space at the end of a sentence, after a comma or other punctuation mark, and before an opening parenthesis. Be sure not to confuse lower case letter "l" with numeral "1", or capital letter "O" with numeral "0". Distinguish opening quotes from close quotes. Do not use automatic page numbering or running heads.

Tables and displayed equations may have to be rekeyed by the typesetter from your hard copy manuscript.

Articles prepared on most word processors are acceptable. If equations and/or scientific symbols have been imported into the article from another program, please provide details of the program used and the procedures followed. If author-created macros have been used, please include them as well.

Illustrations that are available in an electronic format are acceptable; please supply them on a separate disk. Please clearly indicate on the disk the file format and/or program used to produce them, and supply a high-quality hard copy of each illustration as well.

If more than one disk is submitted, please number each disk. Please mark each disk with the journal title, author name, abbreviated article title and file names. Retain a back-up copy of each disk submitted and pack the disks carefully before shipping. Complete the Author Disk Submission form that appears at the back of the journal (forms also may be obtained from the publisher and journal editor in chief) and submit it with the disk and hard copy manuscript.

SUBMISSION OF ANIMATION

Author-supplied animation related to articles accepted for publication will be included in the journal CD-ROM at no cost to authors. Animations are limited to a time duration of 30 seconds. Animation should be submitted to the journal editor with the final manuscript, after it has completed the refereeing process.

Animation in the following forms (in order of preference) can be accepted from authors:

- Video tape
- AVI or QuickTime files
- A sequence of still images.

The following formats can be accepted:

- all uncompressed formats widely used on PC, Mac and UNIX
- JPEG for colored and compressed images
- TIFF with a group IV compression for black and white compressed images
- FLI and FLC format from AutoDesk

Authors who submit animations are requested to provide the following information:

- Video tape - format used. (i.e. NTSC, PAL etc.)
- AVI or QuickTime files - version used, and system used for disk file creation.
- Sequence of still images - format used, version and system used for disk file creation.

Authors who are unable to supply video tape, AVI or QuickTime files may provide the publisher with a set of sequential still images. Note that an animated sequence will consist of 13 to 15 still images per second of animation; e.g., if an animated sequence is 10 seconds in duration, it is made up of 130 images.

Authors who are unable to submit in any of the above-mentioned formats are advised to contact the publisher to discuss other options with the Publisher prior to submission.

Animation should be mentioned in the text. Indicate an approximate location for the animation call-out in the margin.

PROOFS

Authors will receive page proofs (including figures) by air mail for correction, which must be returned to the printer within 48 hours of receipt. Please ensure that a full postal address is given on the first page of the typescript, so that proofs are not delayed in the post. Authors' alterations in excess of 10% of the original composition cost will be charged to authors.

Reprints: 25 free reprints will be provided to the first-named author of each article. Additional reprints may be ordered by completing the appropriate form sent with proofs.

PAGE CHARGES

There are no page charges to individuals or to institutions.

Disk Specifications

Journal name _____

Date _____ Paper Reference Number _____

Paper title _____

Corresponding author _____

Address _____

_____ Postcode _____

Telephone _____

Fax _____

E-mail _____

Disks Enclosed (file names and descriptions of contents)

Text

Disk 1 _____

Disk 2 _____

Disk 3 _____

PLEASE RETAIN A BACK-UP COPY OF ALL DISK FILES SUBMITTED.

GORDON AND BREACH PUBLISHERS • HARWOOD ACADEMIC PUBLISHERS

Figures

Disk 1 _____

Disk 2 _____

Disk 3 _____

Computer make and model _____

Size/format of floppy disks

☐ 3.5"

☐ 5.25"

☐ Single sided

☐ Double sided

☐ Single density

☐ Double density

☐ High density

Operating system _____

Version _____

Word processor program _____

Version _____

Imported maths/science program _____

Version _____

Graphics program _____

Version _____

Files have been saved in the following format

Text: _____

Figures: _____

Maths: _____

PLEASE RETAIN A BACK-UP COPY OF ALL DISK FILES SUBMITTED.

GORDON AND BREACH PUBLISHERS • HARWOOD ACADEMIC PUBLISHERS

(Continued from inside front cover)

nonreceipt of issues will be honored if made within three months of publication of the issue. **See Publication Schedule Information** Subscriptions are available for microform editions; details will be furnished upon request.

All issues are dispatched by airmail throughout the world.

Subscription Rates Base list subscription price per volume: EUR 128.00.* This price is available only to individuals whose library subscribes to the journal OR who warrant that the journal is for their own use and provide a home address for mailing. Orders must be sent directly to the Publisher and payment must be made by personal check or credit card.

Separate rates apply to academic and corporate/government institutions. Postage and handling charges are extra.

*EUR (Euro). The Euro is the worldwide base list currency rate; payment can be made by draft drawn on Euro currency in the amount shown, or in any other currency within the eurozone at the euro-denominated rate. All other currency payments should be made using the current conversion rate set by the Publisher. Subscribers should contact their agents or the Publisher. All prices are subject to change without notice.

Publication Schedule Information To ensure your collection is up-to-date, please call the following number for information about the latest issue published: +44 (0) 118-956-0080 ext. 391; +1 973 643-7500 ext. 290; or web site: <http://www.gbhap.com/reader.htm>.

Note: If you have a rotary phone, please call our *Customer Service* at the numbers listed below.

Orders should be placed through one of the addresses below:

IPD Marketing Services
PO Box 310
Queen's House, Don Road
St. Helier, Jersey
Channel Islands JE4 0TH
Telephone: +44 (0) 118-956-0080
Fax: +44 (0) 118-956-8211

PO Box 32160
Newark NJ 07102 USA
Telephone: +1 800 545-8398
Fax: +1 973 643-7676

Kent Ridge, PO Box 1180
Singapore 911106
Republic of Singapore
Telephone: +65 741-6933
Fax: +65 741-6922

Yohan Western Publications Distribution Agency
3-14-9, Okubo, Shinjuku-ku
Tokyo 169-0072, Japan
Telephone: +81 3 3208-0186
Fax: +81 3 3208-5308

Enquiries can also be sent by e-mail: <info@gbhap.com> and the world wide web: <http://www.gbhap.com>.

Rights and Permissions/Reprints of Individual Articles

Permission to reproduce and/or translate material contained in this journal must be obtained in writing from the Publisher.

This publication and each of the articles contained herein are protected by copyright. Except as allowed under national "fair use" laws, copying is not permitted by any means or for any purpose, such as for distribution to any third party (whether by sale, loan, gift, or otherwise); as agent (express or implied) of any third party; for purposes of advertising or promotion; or to create collective or derivative works. A photocopy license is available from the Publisher for institutional subscribers that need to make multiple copies of single articles for internal study or research purposes. Any unauthorized reproduction, transmission or storage may result in civil or criminal liability. Copies of articles may be ordered through SCAN, the Publisher's own document delivery service. SCAN provides customers with the current contents and abstracts to all Gordon and Breach and Harwood Academic journals. Please contact one of the addresses listed above to receive SCAN, or view current contents and abstracts directly on the Web at <http://www.gbhap.com>, and for ordering.

The Publisher is also a member of Copyright Clearance Center.

The Canada Institute for Scientific and Technical Information (CISTI) provides a comprehensive, worldwide document delivery service for Gordon and Breach/Harwood Academic journals. For more information, or to place an order for a copyright-cleared Gordon and Breach/Harwood Academic document, please contact Client Assistant, Document Delivery, CISTI, National Research Council Canada, Ottawa, Canada, K1A 0S2 (Tel: 613-993-9251; Fax: 613-993-7619; e-mail: <cisti.docdel@nrc.ca>).

Voluntary Page Charges The United States National Science Foundation has extended the allowance of page charge funds for payments to journals regardless of the Publisher's commercial status. Previously this was reserved for only nonprofit society-sponsored journals. Voluntary page charge payments are now accepted for this journal, and authors may elect to pay any amount up to a maximum of \$25.00 per page. Payments will be refunded in the form of a voucher at 100% value of total payment. This voucher can be used by the author or the author's university library for any product or service offered by the Publisher, and thereby can be used to supplement library funding.

Article Vouchers The principal author of each article will receive a voucher for his contribution in the amount of EUR 18.00 (USD 20.00, JPY 2,500), which can also be used to purchase the Publisher's products directly or through university libraries, thereby reducing costs of publications to those authors supporting the journal.

This journal is sold CIF with title passing to the purchaser at the point of shipment in accordance with the laws of The Netherlands. All claims should be made to your agent or the Publisher.

Printed in Malaysia

June 1999